Crystallography Reports, Vol. 46, No. 5, 2001, pp. 701–706. Translated from Kristallografiya, Vol. 46, No. 5, 2001, pp. 775–780.

DIFFRACTION AND SCATTERING OF X-RAY AND SYNCHROTRON RADIATION

Dedicated to the memory of B.K. Vainshtein

Beam Focusing on Stations with a Sibir'-2 Synchrotron Source for Single-Crystal Studies of Atomic Structures

D. M. Kheiker, V. A. Shishkov, M. E. Andriyanova, and D. V. Smagin

Shubnikov Institute of Crystallography, Russian Academy of Sciences, Leninskiĭ pr. 59, Moscow, 117333 Russia

Received November 14, 2000

Abstract—A scheme for obtaining a stationary monochromatic beam that can be focused in the horizontal and the vertical planes and rapidly tuned to a desirable wavelength with the aid of a bending magnet on a Sibir'-2 synchrotron source has been designed. The channel parameters and the size and profile of a sagittally bent single crystal of the double-crystal monochromator were chosen with the use of numerical simulation. © *2001 MAIK "Nauka/Interperiodica".*

INTRODUCTION

The use of synchrotron radiation (SR) in structural studies of single crystal enables one to reduce the collection time of X-ray data, increase the angular resolution of X-ray patterns, decrease the spectral range, reduce the background, and tune to any desirable wavelength.

The beam generated by a bending magnet installed on Sibir'-2 source exerts moderate thermal loads on the focusing optics and a sample, which provides the reproducibility and precision of the measurements of X-ray diffraction intensities. This beam allows precision structure studies based on X-ray intensities measured under the conditions anomalous scattering.

The structural studies of single crystals require SR beam focusing providing a spot with a diameter 0.3–0.7 mm on the sample. The beam divergent in the horizontal plane should be focused in the maximum possible angular range to provide the maximum intensity. However, the better the angular convergence of the incident beam, the lower the angular resolution of the X-ray diffraction pattern and the smaller the maximum possible unit-cell parameters of the crystals studied.

Earlier, a scheme of the station for X-ray studies of proteins was proposed [1] which provided the admissible compromise between these conflicting requirements.

The scheme of the station involved a (1, –1) double-crystal monochromator with the fixed position of the monochromatic beam and sagittal bending of the second crystal focusing the beam in the horizontal direction and a segmented mirror of the total external reflection focusing it in the vertical direction and excluding harmonics. The station designed for studies of single crystals with small unit-cell parameters will also be based on an analogous scheme for primary-beam focusing.

A holder of the second crystal in the monochromator allows the use of computer-controlled step motors providing rotation of the crystal through the θ_2 angle with the change of the wavelength; the displacement of the crystal along the primary beam incident on the first crystal in order to fix the position of the monochromatic beam in the space, the change the radius of the sagittal bending with the change in the wavelength, and the displacement the crystal along the reflecting-surface normal to compensate the change in the sagitta. In addition to the above movement, two adjusting movements are

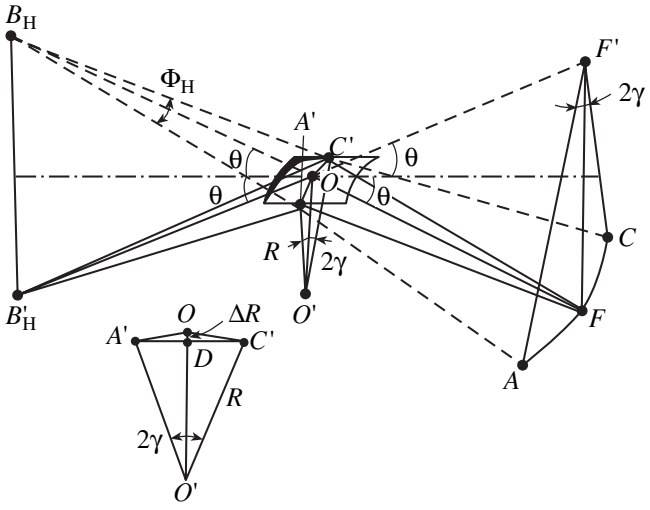

Fig. 1. Horizontal focusing of the synchrotron-radiation beam in the case of sagittal bending: $B_HO = P_1$; $OF = P_2$; $A'C' = P_1\Phi_H$, $AC = (P_1 + P_2)\Phi_H$; $FF' = 2P'\sin\theta$.

1063-7745/01/4605-0701$21.00 © 2001 MAIK "Nauka/Interperiodica"

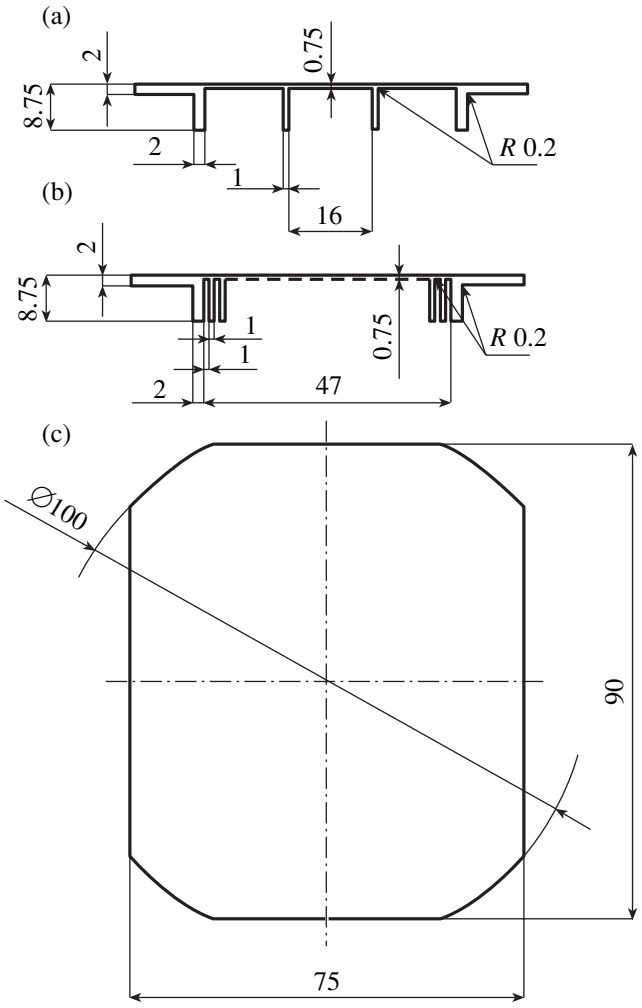

Fig. 2. Configurations of focusing crystals based on sagittal bending: (a) profile of crystal *2*a; (b) profile of crystal *2*b; (c) reflecting surfaces of crystals *2*a and *2*b.

possible—crystal rotation about the axis of sagittal bending and a rotation of this axis about the reflecting-surface normal.

FOCUSING IN THE HORIZONTAL PLANE IN THE CASE OF SAGITTAL BENDING OF THE CRYSTAL

As can be seen from Fig. 1, in a sagittally bent crystal, the rays of the divergent beam are displaced in the sample plane by the distance of $\gamma FF' = \gamma 2P_2 \sin\theta$. Upon focusing, the ray deflected from the mean line by the angle $\Phi_H/2$ in the horizontal plane should be displaced by $(\Phi_H/2)(P_1 + P_2) = \gamma 2P_2 \sin\theta$.

The angle of bending γ, the bending radius $R = \Phi_H P_1/2\gamma$, the sagitta $\Delta R = R(1 - \cos\gamma)$ for different wavelengths, the interplanar spacings of the crystal-monochromator, and different parameters of the channel (P_1P_2, and Φ_H) can readily be determined from the above equation. If the beam diverges from the mean line in the horizontal plane [2, 3], then, in the general case of a sagittally bent second crystal, the angle (θ_2) of beam incidence onto the second crystal differs from the angle of incidence onto the first crystal (θ_1) by the following value:

$$\theta_1 - \theta_2 = (\Phi_H/2)^2(P_1/R)[1/\cos\theta - P_1 \tan\theta/2R].$$

The equality $\theta_1 = \theta_2$ is fulfilled only on the condition that $P_1 = 3P_2$ [2]. In the station considered here, P_1 = 10 m and P_2 = 6 m for λ = 1.0 Å and the Si(111) plane; $\theta_1 - \theta_2 = 0.6''$. This cannot cause noticeable intensity losses, because the rocking curve half-width is 4.5″. The chosen value of the P_1/P_2 ratio is a compromise between the value $P_1/P_2 = 3$ and the desire to obtain the highest possible intensity (the large Φ_H value) at a low beam convergence on the sample ($\Phi_H' = (P_1/P_2)\Phi_H$).

FOCUSING IN VERTICAL PLANE

Vertical focusing is attained by the use of the mirror providing the total external reflection, which consists of eight planar segments of polished glass with the dimensions 200 × 50 × 25 mm and roughness less than 10 Å. The individual adjustment of each segment provides the vertical size of the focus of 0.62 mm. If the segments are tangential to the cylindrical surface, the vertical size of the focus is 0.75 mm [1].

REDUCTION OF MERIDIONAL BENDING

Sagittal bending leads to compression of inner layers of the crystal and extension of its outer layers resulting in crystal bending in the meridional (diffraction) plane with the curvature radius $R_M = -R/\sigma$, where σ is the Poisson ratio (σ = 0.262 for Si(111)). As a result, the crystal adopts a saddlelike shape.

To reduce the meridional bending, the crystal was cut in a way to have stiffness ribs of height *h* and width *W*, spacings *S*, and interspace thickness *t*. The ratio of the bending radii is given the following equation [3]: $R_M/R = -1/\sigma[1 + (W/S)(h/t)^3(1 - \sigma^2)]$.

Another way for reducing the meridional bending involves rigid crystal fixation and an increase of the face length (*b*) of crystal *2* parallel to the diffraction plane [4, 5] (*a* is the lateral size):

$$R_M/R = -(8/15\sigma)(b/a)^4(1 + a^2/b^2).$$

Using the crystal-monochromators and their profiles such that they provide both ways of decreasing the meridional bending simultaneously (Fig. 2), we calculated the coordinates *z*, the derivatives *dz*/*dy* (the inclination angle), and the bending radii $R_M(y) = [d^2z/(dy)^2]^{-1}$ along the mean line in the meridional plane for *y* ranging from 0 to 20 mm.

All the computations were performed by numerical simulation in finite elements with the aid of the

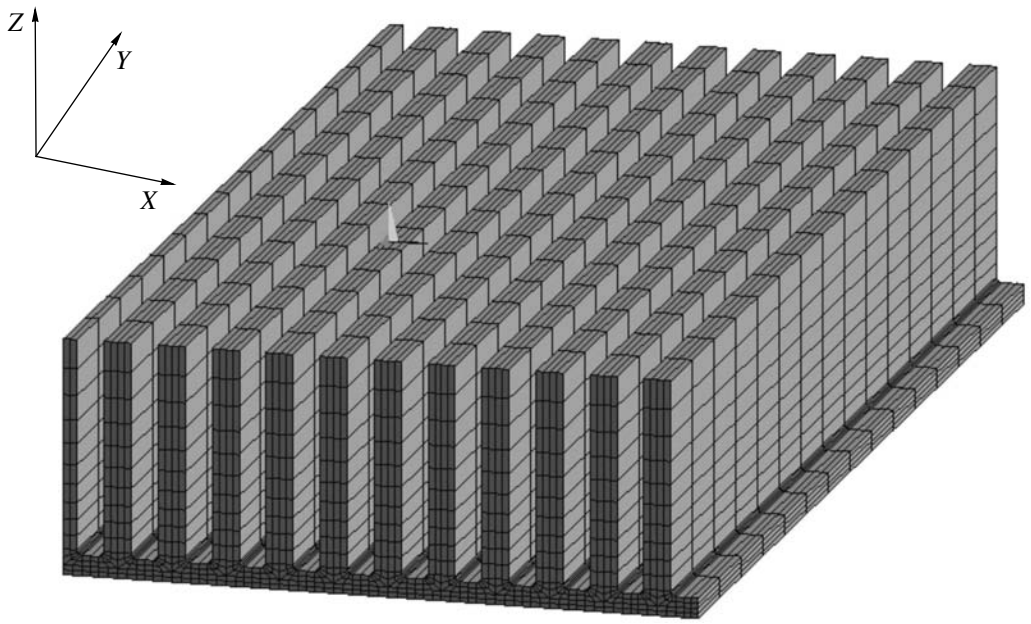

Fig. 3. Net of finite elements for crystal *2*b.

ANSYS.5.5 program using the bilinear volume unit SOLID95 [6]. To decrease the dimensionality of the problem to be solved, we considered the symmetry of the bent crystal in the vertical and horizontal planes (0*yz* and 0*xz*), but under the condition that forbids the displacement of finite elements in the symmetry planes in the directions normal to these planes. The models of crystals *2*a and *2*b consisted of 19044 and 12540 finite elements, respectively. The three-dimensional net of finite elements for the model of crystal *2*b is shown in Fig. 3. The rotation of one lateral face of the crystal-monochromator was preassigned. Since a finite element used possesses no rotational degrees of freedom, the rotation of the crystal-monochromator face was specified by coupling equations. For a (111) Si crystal, we used the following constants: $\sigma = 0.262$ and the Young's modulus $E = 167$ GPa (17000 kgf/mm^2).

Because of the meridional bending, the difference $\theta_1 - \theta_2$ was determined from the *dz*/*dy* curves (Fig. 4) as

$$\Delta\theta_M = \theta_1 - \theta_2 = (P_1/R_M)\Phi_v/2\sin\theta = dz/dy.$$

For the profile *2*a we have: $\lambda = 1.0$ Å, $P_1 = 10$ m, $y = 10$ mm, $\Phi_v = 0.3$ mrad, $\theta = 9.15°$, $R_M = 1$ km, $\Delta\theta_M = 1.9''$ (10^{-5} rad).

For the profile *2*b we have: $\lambda = 1.0$ Å, $P_1 = 10$ m, $y = 10$ mm, $\Phi_v = 0.3$ mrad, $\theta = 9.15°$, $R_M = 3.6$ km, $\Delta\theta_M = 0.55''$ (0.3×10^{-5} rad).

Therefore, profile *2* is preferable, and the error in θ_2 does not noticeably change the monochromatic-beam intensity.

EVALUATION OF DEFOCUSING CAUSED BY RIBS

In the case of sagittal bending, the presence of ribs distorts the circumference into a "polygon" which gives rise to defocusing. The deviation of the polyhedron from a circumference is determined from the analysis of the model of a bent crystal in finite elements. The model allows the determination of the bending radius $R = [d^2z/(dx)^2]^{-1}$ as a function of *x*. As can be seen from Fig. 5, the radius under the ribs increases up to 2.4 m, between the ribs, the radius is 0.85 m (the average radius equals 1.2 m and is comparable with the value obtained in [7]).

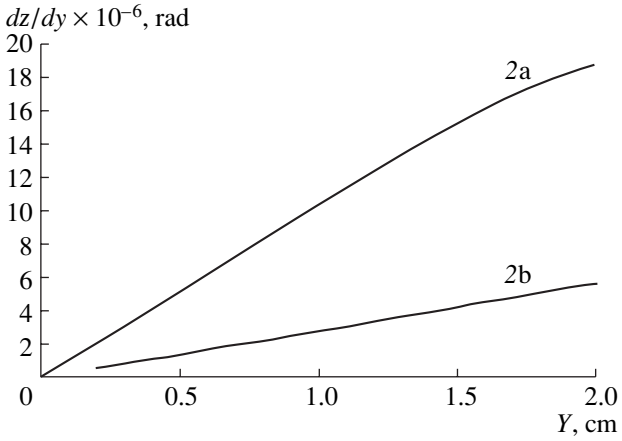

Fig. 4. Dependence of the angle of rotation in the meridional direction *dz*/*dy* (in the plane *y*0*z*) on the coordinate *y* at the average bending radius $R = 1200$ mm on the reflecting surface and at a depth of 0.25 mm for crystals *2*a and *2*b, respectively.

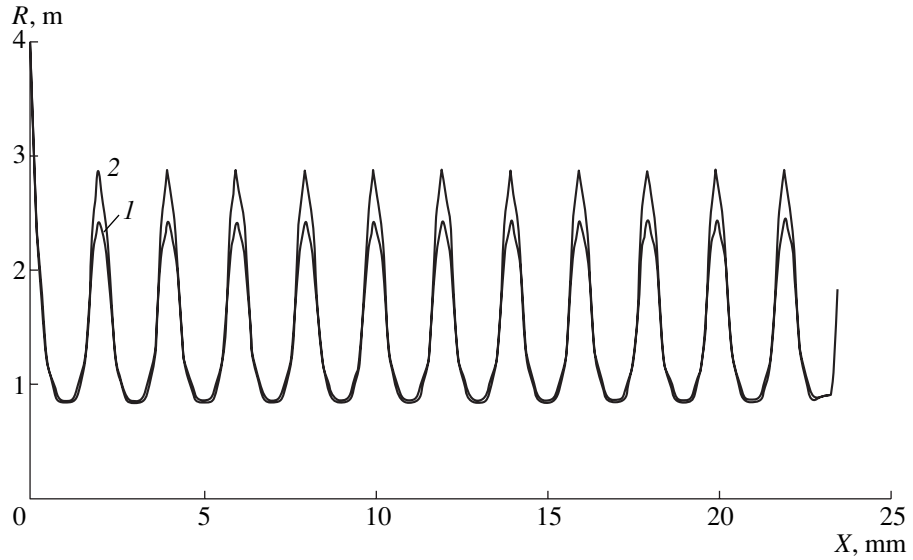

Fig. 5. Dependence of the bending radius R in the $x0z$ plane on the coordinate x on the reflecting surface (crystal *2*a) and at a depth of 0.25 mm (crystal *2*) at the average bending radius R = 1200 mm (crystal *2*b).

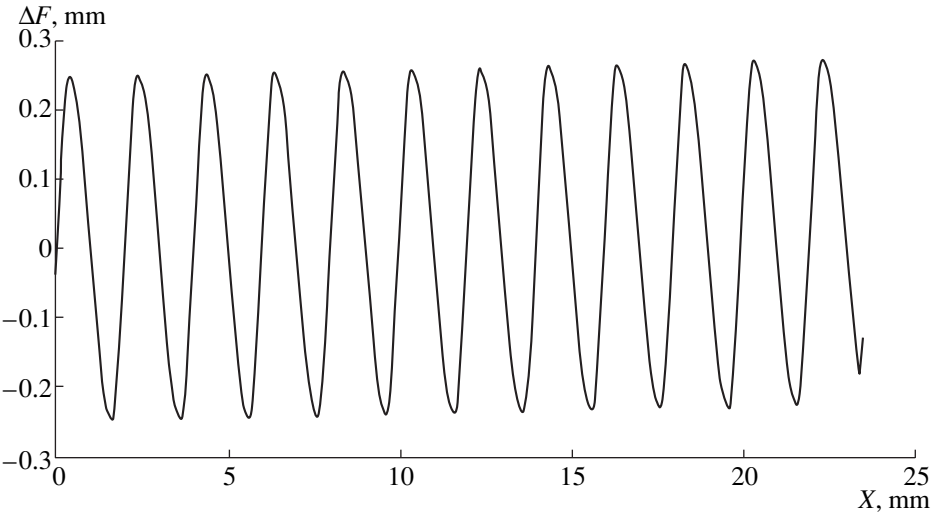

Fig. 6. Dependence of defocusing $\Delta F = (dz/dx - x/R)R(P_1 + P_2)/P_1$ on the coordinate x (crystal *2*b).

The inclination angle γ at a distance x from the mean line obtained by simulating dz/dx was compared with the analogous value for the cylinder, x/R. The error $\Delta\gamma(x) = dz/dx - x/R$ leads to defocusing ΔF (the displacement of the focus from the mean line in the sample plane):

$$\Delta F = R[dz/dx - x/R](P_1 + P_2)/P_1.$$

As can be seen from Fig. 6, the maximum defocusing ΔF for a beam with $\lambda = 1$ Å and the horizontal divergence Φ_H = 1 mrad (x ranges from –5 to 5 mm) is ±0.25 mm. This defocusing leads to an increase of the beam spot in the sample plane $F = B_H P_2/P_1$ = 0.44 mm up to $\sqrt{F^2 + (2\Delta F)^2}$ = 0.67 mm. The coefficient $(P_1 + P_2)/P_1 = 1.6$ reduces this value almost by a factor of two in comparison with the $(P_1 + P_2)/P_1 = 2.4$ obtained in [8].

THE MAXIMUM TENSILE STRESSES

The maximum tensile stresses in the (111) plane were determined by numerical simulation (Fig. 7). In the bent crystal with the curvature radius of 1200 mm, these stresses are 10 and 9 kgf/mm^2 (for the crystals *2*b and *2*a, respectively). If the bending radius is 720 mm, the tensile stresses increase in the proportion 1200 : 720 and attain the values of 17 and 15 kgf/mm^2, respec-

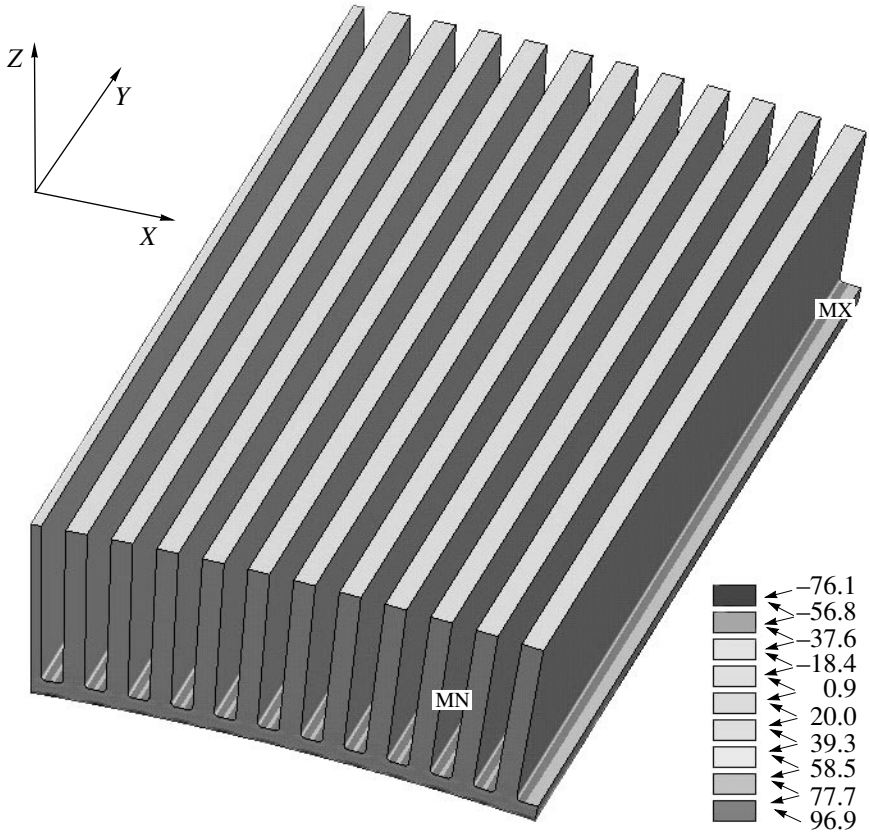

Fig. 7. Tensile stresses (MPa) in crystal *2*b; the bending radius is 1200 mm, and the radius of curvature is 0.2 mm.

tively, which are more than an order of magnitude lower than the breaking point along the [110] direction in silicon crystals (0.02 of the Young modulus) [9]. The maximum stresses are formed within the reentrant angles (between ribs and horizontal segments). The stresses were determined at the bending radius of 0.2 mm.

PROGRAMS CONTROLLING MONOCHROMATOR, MIRROR, AND SLITS

The positions of the slits, the monochromator, and the segmented mirror are set by a personal computer using the CAMAK interface. Step drives all the necessary movements. The monochromator can be controlled in two modes: (1) λ scan by varying θ_1 and θ_2 at a step of $1''$; and (2) by setting to the a certain wavelength.

The change of the θ_1 and θ_2 angles gives rise to the change in the distance between the crystals $l = h\cot 2\theta$ (to ensure the stationary diffracted beam), the change in the bending radius of the second crystal $R = 2P_1P_2\sin\theta/(P_1 + P_2)$ (to preserve the focusing), and by the displacement T_2 of the second crystal along the reflecting-surface normal (to compensate the change in the sagitta $T_2 = (x_{max})^2/2R$.

Control over the mirror envisages inclination and displacement of the mirror as a whole, its cylindrical bending with the change of the bending radius, and the individual rotation of each segment for its adjustment along the elliptical cylinder.

The control of the slits consisting of four independent shutters envisages the changes in their widths and heights and their horizontal and vertical translations.

CONCLUSIONS

A comparatively simple scheme for formation of a stationary monochromatic beam tunable to the desired wavelength and focused in both horizontal and vertical planes has been suggested. The channel parameters and the dimensions and profiles of crystal-monochromators are determines with the use of numerical simulation. These parameters ensure the necessary focusing on the stations designed for structural studies of 0.3–0.7-mm-large single crystals.

ACKNOWLEDGMENTS

This study was supported by the Russian Foundation for Basic Research, project nos. 99-02-16191 and 00-02-16636.

REFERENCES

1. É. G. Arutyunyan, D. M. Kheĭker, M. V. Koval'chuk, *et al.*, Poverkhnost, No. 2, 88 (1999).
2. C. J. Sparks, Jr., B. S. Borie, and J. B. Hastings, Nucl. Instrum. Methods **172**, 237 (1980).
3. C. J. Sparks, G. E. Ice, Jr., J. Wong, *et al.*, Nucl. Instrum. Methods **194**, 73 (1982).
4. S. Ferrer, M. Krisch, F. Bergevin, *et al.*, Nucl. Instrum. Methods Phys. Res. A **311**, 444 (1992).
5. V. I. Kushnir, J. P. Quintana, and P. Georgopoulos, Nucl. Instrum. Methods Phys. Res. A **328**, 588 (1993).
6. *ANSYS* (Inc. – Ansys Elements Reference, Canonsburg, September, 1997).
7. J. L. Hazemann, K. Nayouf, and F. Bergevin, Nucl. Instrum. Methods Phys. Res. B **97**, 547 (1995).
8. G. S. Khapp, M. Ramanathan, H. L. Nian, *et al.*, Rev. Sci. Instrum. **63** (1), 465 (1992).
9. L. A. Shuvalov, A. A. Urusovskaya, I. S. Zheludev, *et al.*, *Modern Crystallography*, Vol. 4: *Physical Properties of Crystals*, Ed. by B. K. Vainshtein, A. A. Chernov, and L. A. Shuvalov (Nauka, Moscow, 1981; Springer-Verlag, Berlin, 1988).

Translated by T. Safonova

Crystallography Reports, Vol. 46, No. 5, 2001, pp. 707–716. Translated from Kristallografiya, Vol. 46, No. 5, 2001, pp. 781–790.

DIFFRACTION AND SCATTERING OF X-RAY AND SYNCHROTRON RADIATION

Dedicated to the memory of B.K. Vainshtein

Structure of the Interfaces of the $In_xGa_{1-x}As$ Quantum Well from X-ray Diffraction Data

A. M. Afanas'ev[1], M. A. Chuev[1], R. M. Imamov[2], and A. A. Lomov[2]

[1] *Institute of Physics and Technology, Russian Academy of Sciences, Nakhimovskiĭ pr. 36/1, Moscow, 117218 Russia*

[2] *Shubnikov Institute of Crystallography, Russian Academy of Sciences, Leninskiĭ pr. 59, Moscow, 117333 Russia*

Received October 17, 2000

Abstract—The structure of the interfaces of a 10-nm-thick $In_xGa_{1-x}As$ quantum well buried in the semiconductor GaAs matrix has been studied by the method of double-crystal X-ray diffractometry. It has been shown that, in comparison with the well-known photoluminescence method, the X-ray diffraction method has considerable advantages in characterization of multilayer systems. The detailed analysis of the rocking curves provided the reconstruction of the profiles of indium distributions in quantum wells for specimens with different indium concentrations. *© 2001 MAIK "Nauka/Interperiodica".*

1. INTRODUCTION

Heterostructures consisting of thin layers, including quantum wells, form the basis for creating elements with extremely good electrophysical and optical characteristics for modern microelectronics [1–6]. The state-of-the-art of the modern technology provides the creation of systems with the layer thicknesses from several nanometers to hundreds of nanometers with well-developed sharp interfaces. Small thicknesses of the layers make the creation of such systems rather difficult and require the rigid control of the thickness, composition, and other parameters of growing layers. The most widespread technique for analyzing these systems is the photoluminescence method, which is used to evaluate layer thicknesses. However, the interpretation of the photoluminescence data requires detailed information on the electron band structure of the corresponding materials which is not always accessible. Thus, for the $In_xGa_{1-x}As$ compounds, there is no information even on elastic constants; moreover, the published data on the fundamental characteristic of the material—the ratio of the conduction-band bottom to the valence-band ceiling—differ by a factor of 1.5. Thus, it is necessary to develop new methods for analyzing these structures.

As was shown in a number of recent publications, these requirements are satisfied by double-crystal X-ray diffractometry. The existence of sharp interfaces can be revealed from rocking curves, where they are seen as pronounced interference oscillations [7–10]. Naturally, the layer interfaces are not absolutely sharp, and X-ray diffraction methods record a such diffusion of interfaces rather easily. The X-ray diffraction method has a much higher informative power and precision than the photoluminescence method in the determination of the layer thicknesses, compositions, and interface diffusion.

Below, we demonstrate the possibilities of X-ray diffraction method on an example of the $GaAs/In_xGa_{1-x}As/GaAs$ structure with $x \approx 0.1$–0.2 and a 10-nm-thick quantum well. The technology of structure growth and the experimental conditions are considered in Section 2. In Section 3, the experimental rocking curves are analyzed by the method described in [7].

2. SPECIMEN PREPARATION AND EXPERIMENTAL METHOD

Heterostructures were grown on semi-insulating GaAs(100) substrates misoriented by three angular seconds from the [110] direction on a Tsna-18 setup used for molecular beam epitaxy (MBE). Two structures with a single $In_xGa_{1-x}As$ quantum well were grown (the specimens *A* and *B*, respectively). Proceeding from the measured dependences of the equivalent pressures of the molecular Ga and In beams on the temperature of the molecular sources and the results of growth-rate calibration of the GaAs and $In_xGa_{1-x}As$ layers, we assumed that the molar fraction of indium, *x*, in different quantum wells can vary from 0.08 to 0.25.

To provide a high conductivity of these two-dimensional channels, the growth temperature of In-containing layers was set 30–40°C higher than the conventional growth temperatures. To avoid impurity and defect diffusion from the substrate to the active part of the heterostructure, we first prepared a ~0.5-μm-thick

Table 1. Structure parameters used in the growth technology and obtained from the analysis of the rocking curves

Specimen		MBE			Rocking curve	
		T_s, °C	l_j, nm	x	l_j, nm	x
A	GaAs	610	100		107.60(2)	
	$In_xGa_{1-x}As$	580	13.5	0.08	12.13(2)	0.071(1)
	Buffer GaAs layer	610	500		500	
B	GaAs	610	100		109.64(1)	
	$In_xGa_{1-x}As$	555	13.5	0.17	12.91(2)	0.155(1)
	Buffer GaAs layer	610	500		500	

buffer GaAs layer for all the specimens. The $In_xGa_{1-x}As$ quantum wells were separated from the film surfaces by a 50-nm-thick GaAs layer. During growth, the crystals were not intentionally doped. The substrate temperature during GaAs growth was 610°C; the growth rate of GaAs was 0.6 μm/h. The ratio of the equivalent As and Ga flow pressures was 20 : 1. During the formation of both $In_xGa_{1-x}As$ interfaces, the growth in the As flow was ceased for 90 s to smoother the interfaces and to change the substrate temperature. The substrate temperature was first decreased to a certain temperature dependent on the quantum-well composition, and then, upon the completion of growth of $In_xGa_{1-x}As$ layers, it was increased again to 610°C. To avoid possible thermal desorption from the subsurface layer and minimize possible thermally stimulated segregation of indium atoms, the growth of the upper interface of the quantum well with the substrate temperature was stopped upon deposition of three GaAs monolayers. In the growth of a quantum well in the specimen *B*, this operation was not used at all. The expected quantum-well ($In_xGa_{1-x}As$) parameters and the corresponding growth temperatures are shown in the MBE column in Table 1.

Rocking curves from a number of specimens were recorded according to the scheme shown in Fig. 1. An incident X-ray beam is formed by a slit triple-reflection monochromator prepared from a perfect Ge(004) crystal. Diffraction curves were recorded from the (004) reflection in the $\theta/(1+\beta)\theta$ scanning (where β is the asymmetry coefficient) with the use of a narrow (8 angular minutes) slit placed before the detector. The radiation source was an 1.1-kW-X-ray tube with a copper anode. The reflection diffraction curves were recorded in the stepwise mode according to the set signal statistics at each measurement point. The other details of the experimental method were similar to those described in [7]. The rocking curves measured from specimens *A* and *B* are shown in Fig. 2. In both cases, the curves consist of a large number of oscillations, which indicates a high quality of the quantum wells, i.e., the formation of rather sharp interfaces. On the other hand, a large number of well-pronounced oscillations allows one to extract reliable data on the quantum-well parameters (see below).

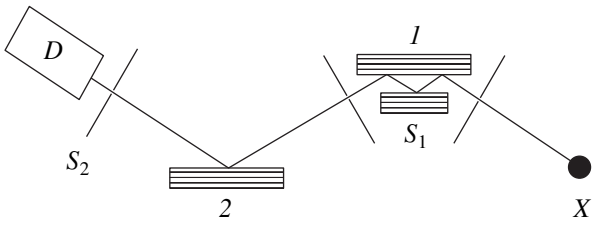

Fig. 1. Schematic of a double-crystal X-ray diffractometer. *X* is the radiation source, *D* is a detector, *1* is the monochromator block, *2* is the specimen, S_1 is the system of slits of the monochromator block, and S_2 is the detector slit reducing the background component.

3. METHOD FOR ANALYZING AND CHARACTERIZING QUANTUM WELLS

Represent a multilayer system as a set of homogeneous sublayers whose number is not necessarily coincident with the number of technologically grown layers. The introduction of such layers is necessary for the adequate description of multilayer structures. Each of these sublayers is characterized by the thickness l_j, the crystal-lattice parameter a_j, and the static Debye–Waller factor w_j, setting the degree of the layer amorphization,

$$f_j = \exp(-w_j) = \exp(-\langle(\mathbf{Ku})^2\rangle_j), \qquad (1)$$

where **K** is the reciprocal-lattice vector and **u** is the random displacement of an atom from its regular position. Inside each sublayer, the parameters a_j and f_j are assumed to be constant.

With due regard for the above, the calculation of X-ray rocking curve as a function of the parameters l_j, a_j, and f_j was performed by the formulas of the dynamical theory, which, in this case, reduced to the recurrent formulas relating the amplitude $R_{h,N}$ of reflection from N layers with the reflection, $R_{h,1}$, and the transmission, $R_{0,1}$, amplitudes from the upper layer and the amplitudes of the subsequent $(N-1)$ layers of the type

$$R_{h,N} = [R_{h,1} + R_{h,N-1}(R_{0,1}R_{0,1} - R_{h,1}R_{h,1})] \times (1 - R_{h,N-1}R_{h,1})^{-1}. \qquad (2)$$

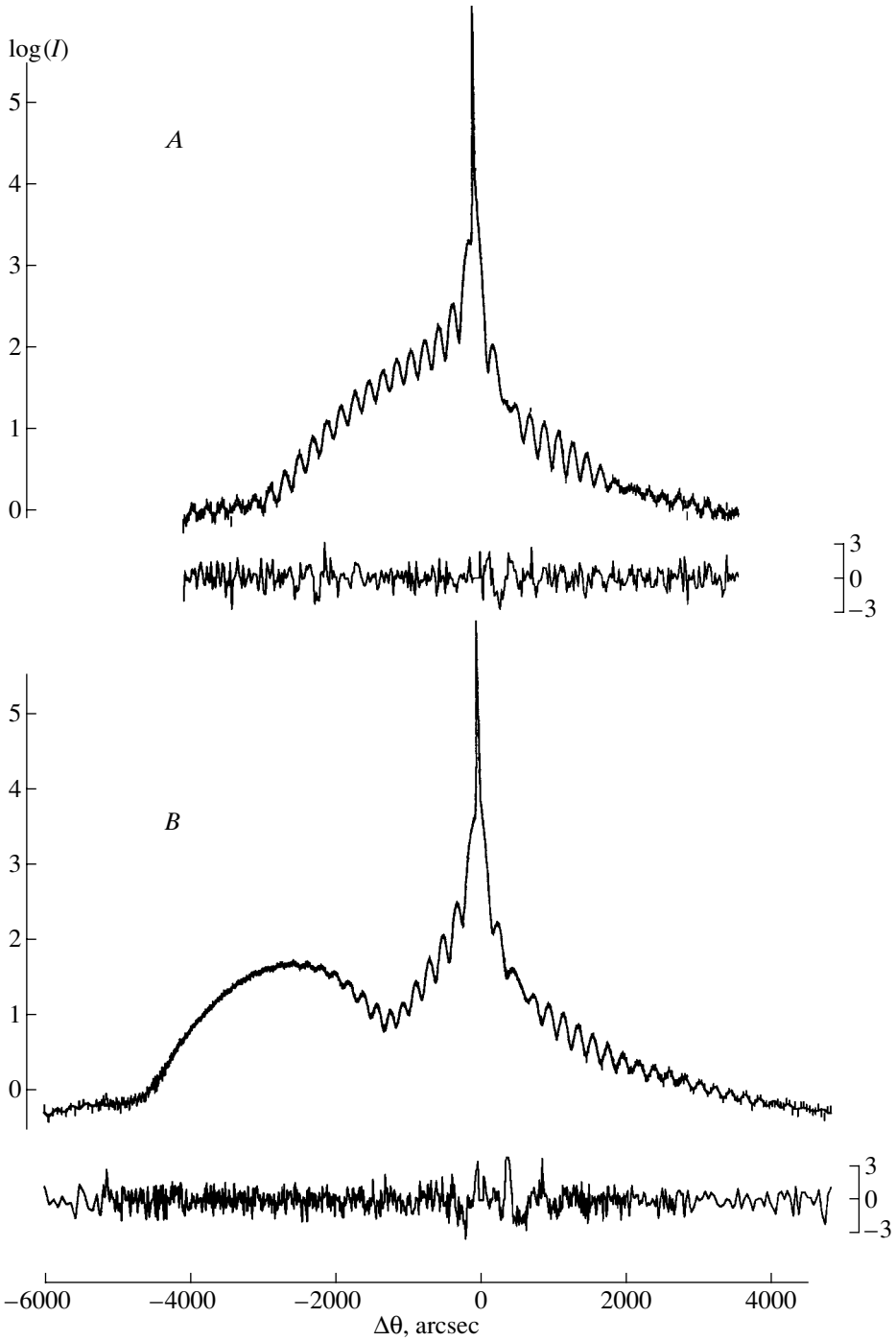

Fig. 2. Experimental rocking curves from the specimens *A* and *B* (vertical primes) and the calculated curves (solid lines) for the resulting modes ($\chi^2 = 1.06$ and 1.07, respectively). Under each curve, the deviations of the calculated rocking curve from the experimental rocking curve normalized to the experimental error are indicated.

The reflection and the transmission amplitudes for an individual layer are determined in terms of the parameters l_j, a_j, and f_j by the well-known formulas of the dynamical theory (see, e.g., [11]). In what follows, we assume that the parameters of the buffer layer only slightly differ from those of the substrate, so that both layers can be considered as one layer of an infinite thickness.

The structure parameters were determined by the well-known χ^2 method by minimizing the following functional:

$$\chi^2 = \frac{1}{n - n_p}\sum_{i=1}^{n}\frac{(I_i^e - I_i^{(t)})^2}{s_i^2}, \quad (3)$$

where n is the number of points of the rocking curve,

n_p is the number of the parameters to be determined, and $I_i^{(e)}$ and $I_i^{(t)}$ are the measured and the theoretically calculated intensities of the reflected wave, respectively.

In addition to the intensity of pure diffraction scattering $I_i^{(D)}$, one has also to take into account in the calculations the intensity $I_i^{(d)}$ diffusely scattered by thermal phonons and the lattice imperfections:

$$I_i^{(t)} = I_i^{(D)} + I_i^{(d)}. \quad (4)$$

The intensity of the diffraction scattering with due regard for averaging over polarization in the dispersion-free scheme is

$$I_i^{(D)} = \frac{I_0}{A_m^\pi + A_m^\sigma} \sum_{\alpha = \pi, \sigma} \int P_{R_m}^\alpha(\theta_i - \theta) P_{R_s}^\alpha(\theta) d\theta, \quad (5)$$

where I_0 is the intensity of the radiation reflected by the monochromator,

$$A_m^\alpha = \int P_{R_m}^\alpha(\theta) d\theta \quad (6)$$

are the integrated reflection coefficients from the monochromator for the α-polarization, $P_{R_m}^\alpha(\theta)$ is the coefficient of reflection from the monochromator,

$$P_{R_s}^\alpha(\theta) = \frac{1}{\beta}|R_{h,N}|^2 \quad (7)$$

is the coefficient of reflection from the specimen, and β is the asymmetry coefficient.

The rigorous calculation of diffuse scattering is rather complicated and requires the knowledge of many additional parameters such as the type and the density of various defects (dislocations, point defects, etc.). Obviously, unlike diffraction scattering, diffuse scattering is an incoherent process and, thus, cannot have oscillations. Therefore, it can be approximated by a piecewise function of the type

$$I_i^{(d)} = B_j + (B_{j+1} - B_j)\frac{\theta_i - \theta_j}{\theta_{j+1} - \theta_j} \quad (8)$$

for

$$\theta_i \in (\theta_j, \theta_{j+1}),$$

where the angular intervals (θ_j, θ_{j+1}), in which the function $I_i^{(D)}$ has a continuous derivative, should considerably exceed the periods of oscillations observed on the reflection curve. The coefficients B_j are the parameters to be varied.

This scheme of the analysis also implies that the relative change in the lattice parameter in the $In_xGa_{1-x}As$ bulk is related to the concentration x by the Vegard's law

$$\varepsilon = \frac{x(a_{InGaAs} - a_{GaAs})}{a_{GaAs}}. \quad (9)$$

In thin $In_xGa_{1-x}As$ layers, $\varepsilon_\parallel = 0$, and the layers are characterized by tetragonal distortions with

$$\varepsilon_\perp = \varepsilon\frac{1 + \nu_{In_xGa_{1-x}As}}{1 - \nu_{In_xGa_{1-x}As}}, \quad (10)$$

where $\nu_{In_xGa_{1-x}As}$ is the Poisson ratio, which, similar to formula (9) [12], linearly depends on the concentration x.

The process of fitting of the theoretical and the experimental data requires the selection of some initial parameters, which is quite a complicated and delicate problem. It is natural to use as the initial approximation the structural parameters set by the growth technology. Figure 3a shows the rocking curve for the specimen *A* calculated with the use of the technological parameters listed in the MBE column of Table 1. It is seen from Fig. 3a that the technological parameters coincide with the specimen parameters quite well. The number and the shape of the rocking-curve oscillations and even the amplitudes of the theoretical curve are quite consistent with the corresponding experimental data. (The pronounced difference in the oscillation amplitudes is associated with the logarithmic scale of the reflection intensities, which will be considered somewhat later.) On the other hand, the peak positions on the theoretical and the experimental curves considerably differ, and the value of χ^2 equals 88, whereas the adequate model yields the value close to unity. It is clear that the real structure differs from that expected from the growth technology, and that this difference can be detected by the X-ray diffraction method.

Thus, the variation of the quantum-well width, the indium concentration in this quantum well, and the thickness of the upper layer lead to a drastic decrease of the parameter χ^2 down to a value of 18.5 (Fig. 3b). In this case, the positions of the maxima and the minima on the experimental and the calculated curves coincide with good accuracy, whereas the layer thicknesses and the In concentrations in the layers differ within 10% from the values envisaged by technology (see the rocking-curve column in Table 1). Moreover, as follows from the errors listed in Table 1, the X-ray diffraction method provides the detection of the parameter variation several times smaller than in the case considered above. This example demonstrates the possibilities provided by the X-ray diffraction method in the determination of the layer thicknesses and layer compositions.

The fitting quality attained for this simplest model is still far from the desirable quality, because, in terms of mathematics, the value of χ^2 normalized in accordance

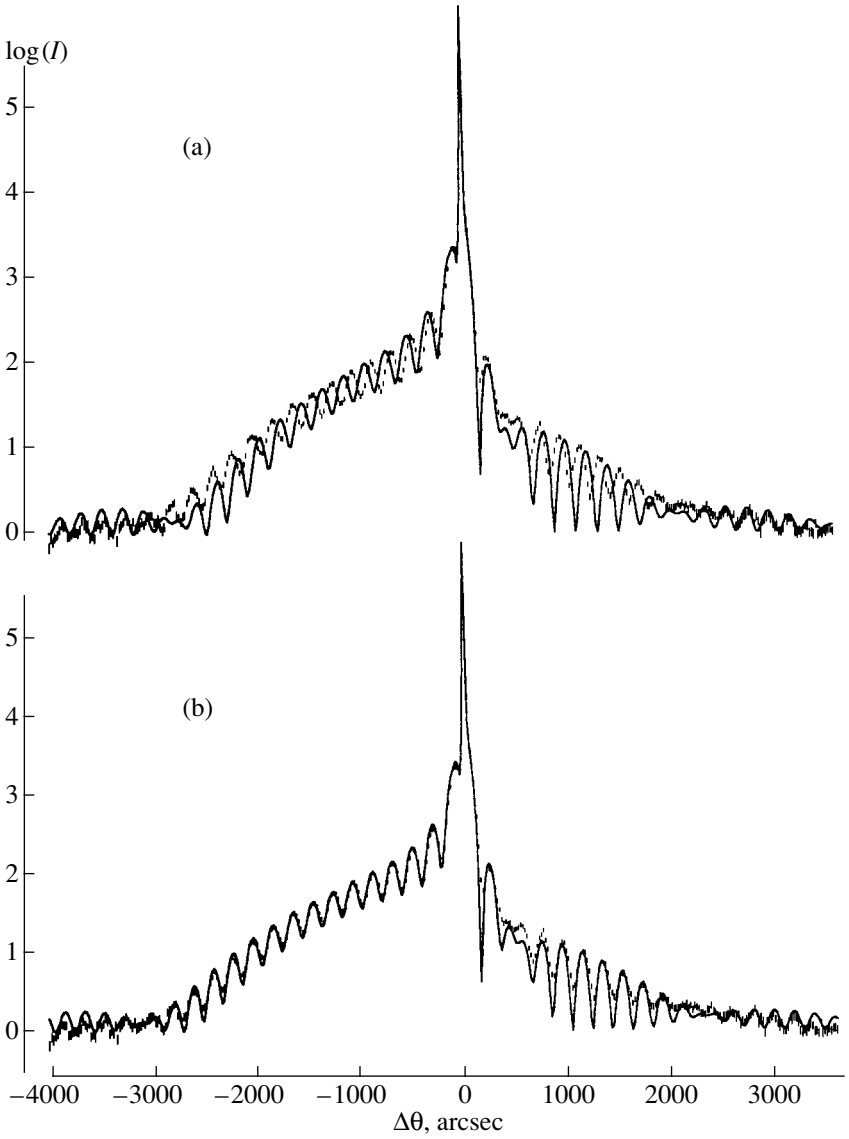

Fig. 3. Experimental rocking curve from the specimen *A* and the theoretical curves calculated for the model (a) with the technological parameters ($\chi^2 = 88$) and (b) the varying parameters of the main layers ($\chi^2 = 18$).

with Eq. (3) should lie within the limits $(1 - \Delta)$–$(1 + \Delta)$, where

$$\Delta = \sqrt{\frac{2}{n - n_p}}. \quad (11)$$

In our case, the number of points on the reflection curve is ~800, with the $\Delta\chi^2$ being 0.05.

There are still possibilities for better fitting. First of all, the parameters of the upper layer and those of the substrate can be somewhat different because of the differences in their growth conditions. Moreover, one can expect the formation of point defects or dislocations in the quantum well and, thus, the deterioration of the crystal-lattice quality described in our model by the static Debye–Waller factor f_j. Crystal defects give rise to diffuse scattering, which can also arise because of the crystal-lattice vibrations. And finally, the changes in the shape of the theoretically calculated curve can be caused by diffusion of the quantum-well interfaces.

In this case, the most considerable reduction of χ^2 is attained due to the allowance for the diffuse-scattering contribution made according to the scheme considered above. Thus, the parameter χ^2 was reduced to a value of 6.5. The variation of the parameters f_j and the crystal-lattice parameter for the upper layer resulted in a further decrease of χ^2 to a value of 2.1. This stage of the fitting procedure is illustrated by Fig. 4a and Table 2. There is good agreement between the experimental and the calculated curves. Visually, these curves differ only at the left edge of the rocking curve in the range from –4000 to –2500 arcsec (Fig. 5a). According to this model, the

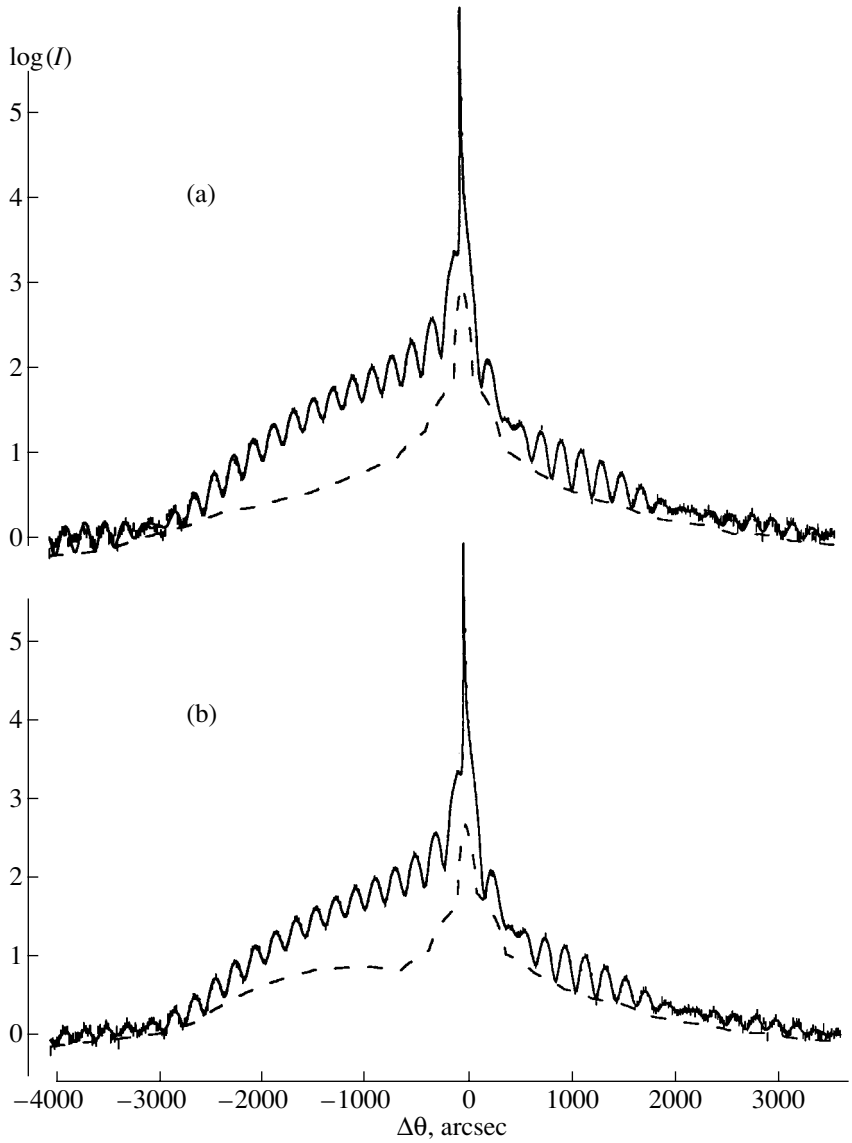

Fig. 4. Experimental rocking curve from the specimen *A* and the theoretically calculated curve with due regard for the diffuse-scattering contribution (dashed lines) for the models (a) without ($\chi^2 = 2.1$) and (b) with ($\chi^2 = 1.27$) sublayers.

main parameters of the quantum well and the upper layer vary only insignificantly. The change in the crystal-lattice parameter of the upper layer with respect to the substrate parameter is also rather weak. Moreover, the static Debye–Waller factors only slightly differ from unity, which indicates the existence of some defects in the film and stresses in the layers. The diffusion-scattering contribution is rather small, and, for the

Table 2. Structure parameters for specimen *A* for models without and with sublayers

Layer	Model without sublayers			Layer	Model with sublayers		
	l_j, nm	$\Delta a_j/a$, %	f_j		l_j, nm	$\Delta a_j/a$, %	f_j
1	107.1(1)	−.007(1)	0.854(4)	1	105.2(8)	−0.008(1)	0.83(1)
				2'	2.1(7)	0.12(8)	0.86(1)
2	12.8(1)	0.952(5)	0.91(1)	2	10.7(2)	0.962(8)	0.86(1)
				2"	3.2(1)	0.51(4)	0.82(1)
3	500	0	0.86(1)	3	500	0	0.88(1)

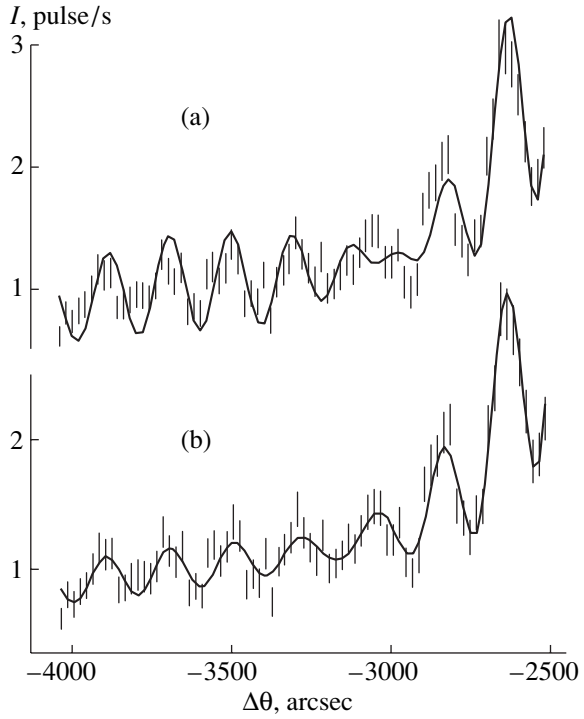

Fig. 5. The tail of the experimental rocking curve from the specimen *A* and the theoretically calculated curves for the models (a) without and (b) with sublayers.

most part, the rocking curve does not exceed 3 pulse/s. Only in the vicinity of the Bragg peak in the central region, is its contribution more pronounced. An increase of the diffuse-scattering intensity in the central part of the curve is associated with the well-known anomalies in diffuse scattering, scattering from dislocations, and first-order point defects. The change in the crystal-lattice parameter of the upper layer is also insignificant and does not exceed 0.01%.

A further improvement of fitting can be attained if one takes into account the diffusion of the quantum-well interfaces. At the next fitting stage, we used the structure model with two additional sublayers on both sides of the quantum well. Along with the parameters of the main layers, we also varied the thicknesses, the concentration, and the static Debye–Waller factors of these sublayers. The results obtained at this fitting stage are illustrated by Fig. 4b and Table 2. The χ^2 parameter decreased to a value of 1.27. Visually, the results of the two latter fitting stages are almost the same in the whole range of the spectrum, except for the left edge of the range of negative angles. Figure 5 shows the tails of the experimental curves and the curves calculated in this angular range for the two latter models, with the rocking curves being represented not on the logarithmic, but on a linear scale. It is seen that the latter model describes this spectrum range more adequately than the previous model. Figure 5 also shows that the conclusion on the existence of the interfaces having the dimensions indicated in Table 2 is based on the assumption on the existence of the upper interface with a thickness of ~2 nm and the lower interface with a thickness of ~3 nm. It should also be emphasized that the existence of these layers can be established by analyzing the rocking curves measured far from the Bragg peak (at $|\theta| > 3000$ arcsec). In the remaining spectrum range (at $|\theta| < 3000$ arcsec), no essential differences in the description of the experimental data by two last models is seen visually.

At first glance, the data presented in Fig. 5 can hardly help in choosing between the last two models, because both indicate the existence of the interfaces and provide their possible detection despite the fact that the previous model (having no interfaces) also describes the experimental data sufficiently well. The conclusion drawn from the latter model is more advantageous and can be drawn from the theory of hypotheses, according to which (see, e.g., [13]), each model is

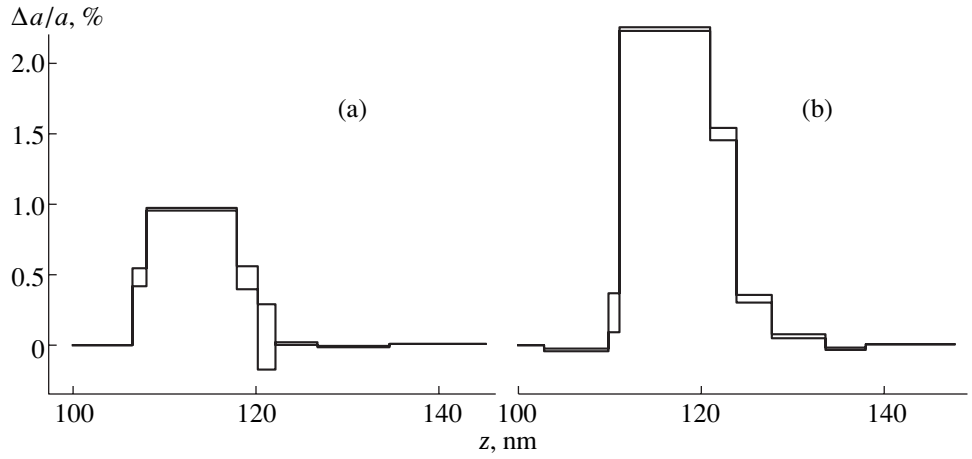

Fig. 6. Profiles of the crystal-lattice parameter distribution over the layer depth in the vicinity of the quantum well for the specimens (a) *A* and (b) *B*.

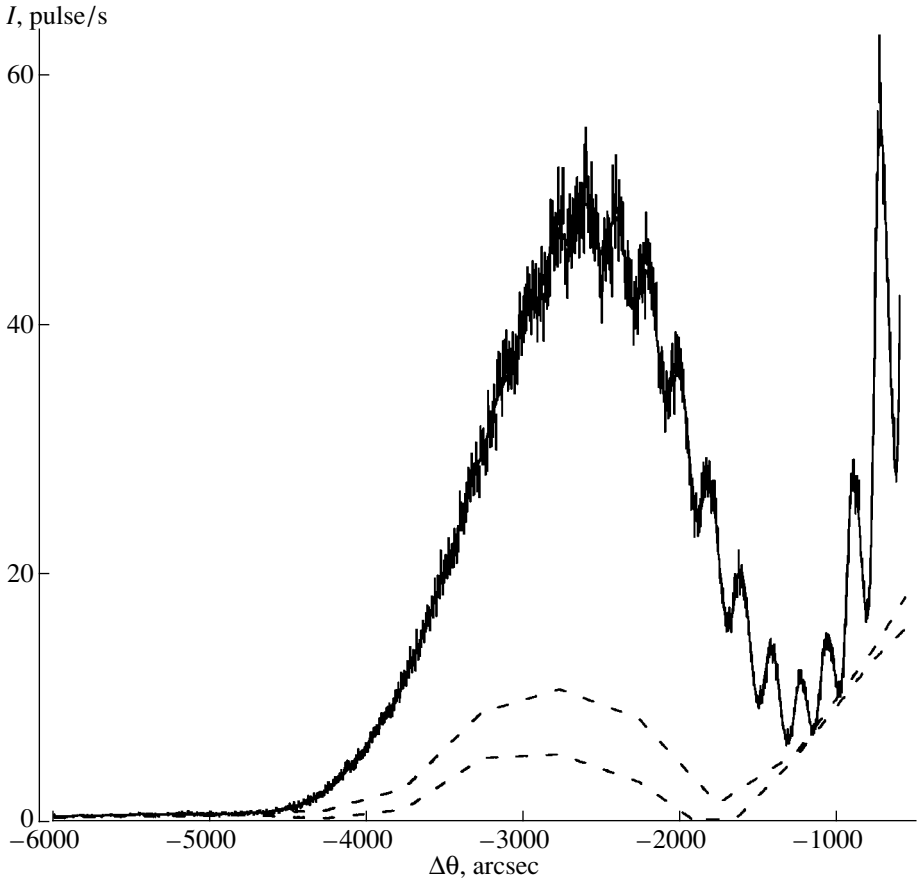

Fig. 7. The tail of the experimental rocking curve from the specimen *B* and the theoretical curve calculated for the resulting model. The diffuse-scattering contribution with due regard for the root-mean-square error in the parameters B_j is shown by dashed lines.

characterized by the so-called first-order error *r*, which determines the probability of erratic rejection of the correct model. Consider the model without additional sublayers and assume that it is correct and that the high value of χ^2 equal to 2.1 follows from a certain random fluctuation. For the true model, the distribution of χ^2, which is a random quantity at a large number of measured points, is set by the Gaussian distribution

$$P(\chi^2) = \frac{1}{\sqrt{2\pi}\Delta}\exp\left[-\frac{(\chi^2-1)^2}{2\Delta^2}\right], \qquad (12)$$

where Δ is determined by Eq. (11). The probability that the fluctuation in the experiment under consideration provides the minimum value of χ^2 (considered here as the characteristic of the fitting quality) is determined by the integral

$$r = \frac{1}{\sqrt{2\pi}\Delta}\int_{\chi^2}^{\infty}\exp\left[-\frac{(x-1)^2}{2\Delta^2}\right]dx \qquad (13)$$

having the sense of the first-order error. For the model with $(\chi^2 - 1) \gg \Delta$, formula (13) yields a simpler estimate of *r*, namely,

$$r \approx \frac{1}{\sqrt{2\pi}}\frac{\Delta}{\chi^2-1}\exp\left[-\frac{(\chi^2-1)^2}{2\Delta^2}\right]. \qquad (14)$$

In our case (the model without interface sublayers), $r \approx 10^{-75}$, i.e., the probability of erroneous rejection of the correct model is infinitely low. It should be indicated that the smallness of the first-order error is associated, first of all, with the smallness of the quantity Δ provided by a large number *n* of experimental points and a small number n_p of the fitting parameters used. In experiments of other types, where the number of measurement points is by an order of magnitude lower but χ^2 is the same, the value of *r* would have been of the order of 10^{-7}. The value corresponding to the latter model is $r \approx 10^{-5}$, i.e., although much higher, it is still rather small and requires the model refinement.

Further analysis was performed upon the introduction of additional sublayers. This reduced the χ^2 value to 1.06, which, in terms of mathematics, is quite good. Introducing three more sublayers at the interfaces, we improved the fitting procedure even further (Figs. 2a and 6a and Table 3). Then, new layers were succes-

Table 3. Structure parameters in the resulting models for specimens *A* and *B*

Layer	Specimen *A*			Layer	Specimen *B*		
	l_j, nm	$\Delta a_j/a$, %	f_j		l_j, nm	$\Delta a_j/a$, %	f_j
				1	2.2(2)	−0.8(3)	0.29(4)
				2	2.8(1)	−0.19(6)	0.67(2)
1	106.5(2)	−0.009(1)	0.84(1)	3	97.9(6)	−0.001(1)	0.81(1)
2	1.6(2)	0.5(1)	0.95(2)	4	7.2(8)	−0.05(1)	0.74(1)
3	9.8(2)	0.97(2)	0.85(2)	5	1.2(4)	0.1(3)	0.95(3)
4	2.3(16)	0.6(2)	0.80(5)	6	10.1(3)	2.23(2)	0.90(3)
5	2(1)	0.3(5)	0.90(6)	7	2.9(1)	1.45(9)	0.90(3)
6	5(2)	0.01(2)	0.90(2)	8	3.9(3)	0.30(5)	0.86(2)
7	8(1)	−0.005(8)	0.86(2)	9	5.8(9)	0.04(2)	0.90(1)
				10	4.4(9)	−0.04(1)	0.88(1)
8	500	0	0.90(2)	11	500	0	0.93(1)

sively introduced until their number provided the root-mean square deviations in the layer bulk not exceeding the average thickness of these sublayers.

A similar analysis was also performed for the specimen *B* differing from the specimen *A* by the In concentration in the quantum well, $x \approx 0.17$, and somewhat different growth mode. The rocking curves for the specimen *B* were obtained within a wider range of angles and are shown in Fig. 2b. The broad peak in the vicinity of –3000 arcsec corresponds to the diffraction reflection from the quantum well. Similar to the case of specimen *A*, there is a large number of oscillations attenuating in the vicinity of the peak due to the quantum well, which, as will be shown below, is associated with a higher defect concentration in the specimen *B* in comparison with their concentration in the specimen *A*. Varying the layer thicknesses, the static Debye–Waller factors, interplanar spacings, and introducing new sublayers with due regard for diffuse scattering, we managed to attain quite a good agreement between the calculated and experimental rocking curves with $\chi^2 = 1.07$. The results of the fitting procedure are illustrated by Figs. 2b and 6b and are listed in Table 3. The most impressive result here is only slight spreading of the quantum well interface from the side of the upper layer, which is quite consistent with the changes in the growth technology for specimen *B*. The upper layer, immediately following the quantum well, was grown in this specimen at a lower temperature than in the specimen *A*. At the same time, the well interface from the substrate side is considerably diffused, and the thorough analysis provides the detailed description of this interface (Fig. 6b).

Another important result is the detection of a higher number of defects in the specimen *B* than in the specimen *A*, which is seen from the reduced Debye–Waller factor for the quantum well (Table 3) and a more pronounced contribution of diffuse scattering to the rocking curve. Especially large diffuse-scattering contribution is observed at negative angles in the vicinity of the peak caused by the quantum well. This region is considered in more detail in Fig. 7, where the refection intensity is shown on a linear scale. It is seen that the diffuse-scattering contribution is quite pronounced but still is too small in comparison with the contribution of the diffraction scattering, which indicates the presence of coherent interfaces between the neighboring layers. It is well known that an increase of the indium concentration in the quantum well above a certain critical value results in the appearance of misfit dislocations and deterioration of coherent interfaces between the layers. It should also be noted that the errors in the determination of deformation in the quantum well and in sublayers (determined mainly by the indium distributions in different layers) in the specimen *B* is much less than in the specimen *A*. This fact is explained by a larger angular range of the rocking curve measured for the specimen *B*.

CONCLUSION

Thus, the analysis performed in this study shows that X-ray diffraction is a very promising method for characterization of multilayer systems. It provides the determination of the thicknesses and the compositions of individual layers, interfaces, and the defect concentration in individual layers. In this respect, the X-ray diffraction method has obvious advantages in comparison with the photoluminescence method despite the fact that this method is slower. The measurement of the rocking curves with the necessary statistics (Fig. 2) requires almost 24 h if conventional X-ray tubes are used. More powerful radiation sources, such as the synchrotron-radiation source, would allow, on the one hand, the reduction of the measurement time, and, on the other hand, the increase of the volume of information extracted from the rocking curves because of a

higher statistical quality of the experimental curve and broadening of the angular range of the measurements.

ACKNOWLEDGMENTS

The authors are grateful to Yu.G. Sadof'ev and D.S. Shipitsyn for the specimens.

This study was supported by the Russian Foundation for Basic Research, project no. 00-02-17716 and the Ministry of Industry, Science, and Technology of the Russian Federation [subprogram *Promising Technologies and Devices for Micro- and Nanoelectronics*, project no. 204-8(00)-P].

REFERENCES

1. M. N. Herman, D. Bimberg, and J. Christen, J. Appl. Phys. **70**, R1 (1991).
2. H. Juergen, T. P. E. Broekaert, and C. G. Fonstad, J. Appl. Phys. **71**, 2475 (1992).
3. N. N. Ledentsov, V. A. Shchukin, M. Grundmann, *et al.*, Phys. Rev. B **54**, 8743 (1996).
4. F. Diette, D. Langrez, J. L. Codron, *et al.*, Electron. Lett. **32**, 848 (1996).
5. Y. Shiraishi, N. Furuhata, and A. Okamoto, J. Appl. Phys. **76**, 5099 (1994).
6. S. V. Evstigneev, Yu. V. Kopaev, Yu. G. Sadof'ev, *et al.*, Mikroélektronika **27** (4), 317 (1998).
7. A. M. Afanas'ev, M. A. Chuev, R. M. Imamov, *et al.*, Kristallografiya **42** (3), 514 (1997) [Crystallogr. Rep. **42**, 467 (1997)].
8. A. M. Afanas'ev, A. A. Zaĭtsev, R. M. Imamov, *et al.*, Kristallografiya **43** (1), 139 (1998) [Crystallogr. Rep. **43**, 129 (1998)].
9. A. M. Afanas'ev, A. A. Zaĭtsev, R. M. Imamov, *et al.*, Kristallografiya **43** (4), 677 (1998) [Crystallogr. Rep. **43**, 628 (1998)].
10. A. M. Afanas'ev, M. A. Chuev, R. M. Imamov, *et al.*, Kristallografiya **43** (5), 926 (1998) [Crystallogr. Rep. **43**, 872 (1998)].
11. L. Tapfer, M. Ospelt, and H. von Kanel, J. Appl. Phys. **67**, 1298 (1990).
12. C. Ferrari, M. R. Bruni, F. Martelli, and M. G. Simeone, J. Cryst. Growth **126**, 144 (1993).
13. W. T. Eadie, D. Drijard, F. E. Janus, *et al.*, *Statistical Methods and Experimental Physics* (North-Holland, Amsterdam, 1971; Atomizdat, Moscow, 1976).

Translated by L. Man

Crystallography Reports, Vol. 46, No. 5, 2001, pp. 717–721. Translated from Kristallografiya, Vol. 46, No. 5, 2001, pp. 791–795.

DIFFRACTION AND SCATTERING OF X-RAY AND SYNCHROTRON RADIATION

Dedicated to the memory of B.K. Vainshtein

Triple-Crystal X-ray Spectroscopy of Diffuse Scattering from Tracks

V. N. Peregudov and E. M. Pashaev

Shubnikov Institute of Crystallography, Russian Academy of Sciences, Leninskiĭ pr. 59, Moscow, 117333 Russia

e-mail: vlad@dni.polyn.kiae.su

Received January 24, 2000

Abstract—A theoretical model is presented for studying the structure of tracks of charged particles in crystals. Two structurally different track regions are considered: the track proper and its elastically deformed vicinity. A computer program is written for determining the contributions from a track and its elastically deformed vicinity to the experimental diffuse-scattering data and their quantitatively evaluating dimensions and other parameters. The effect of the model parameters on the shape of diffuse-scattering curves is also considered. © *2001 MAIK "Nauka/Interperiodica".*

INTRODUCTION

A shape of a diffuse maximum in the triple-crystal X-ray spectroscopy is determined by defects in the crystal structure. The possibilities provided by triple crystal X-ray spectroscopy for studying long-range fields of elastic displacements caused by various defects in crystals were considered elsewhere [1]. Diffuse scattering by the fields of elastic displacements caused by spherical clusters and dislocation loops was studied earlier [2] for the case of symmetric diffraction with the reciprocal-lattice vector **b** being normal to the crystal surface [2]. The use of triple-crystal X-ray spectroscopy for studying the nature of the asymptotic diffuse scattering [3] yielded rich information about the size, orientation, and symmetry of various microdefects in silicon-doped GaAs single crystals. For complete characterization of defects, the method of q_z-scanning was used [3], which allowed the study of diffuse scattering in various sections of the reciprocal space, the anisotropy due to defects, and the corresponding displacement fields. The analysis of the asymptotic diffuse scattering in GaAs crystals [4] showed a considerable difference in the microdefect concentration in the space between the plate edge and its center and revealed large (~1 μm) dislocation loops. Knowing the sign of the asymmetric component of the diffuse-scattering intensity, one can identify the microdefects with negative and positive dilatation [5] and determine their concentrations [6]. The use of triple-crystal X-ray spectroscopy [7] allowed one to reveal considerable negative deformations with $\Delta d/d \sim -10^{-3}$ in the subsurface layers in $CsDSO_4$ and $CsHSO_4$ crystals. The coherent nature of the maxima on the diffuse-scattering curves from Si-doped GaAs single crystals obtained in the double-crystal scheme was established in [8].

Below, we demonstrate the possibilities of the simplest model of a track for studying defects induced by ion irradiation of crystals.

TRACK MODEL

A track of a charged particle in a crystal is a region, which absorbs the energy of an incident ion and expands (dilatation) due to atomic displacements. The atomic density inside the track region $\rho < \rho_0$ can be somewhat lower than the atomic density n_0 of the initial crystal. The track region exerts a certain pressure onto the surrounding crystal structure, thus inducing a field of elastic atomic displacements. Figure 1 shows the region of the track A and the elastically deformed vicinity of the track B. Below, we analyze only the case where the direction of the track axis coincides with the direction of the normal to the irradiated surface. We limit our consideration to an isotropic crystal and the case where atomic displacements in the region B have only the radial component. The radial decrease of the displacement $u(\rho)$ in the region B is determined by the equilibrium equation [9], which, for the azimuthal symmetry with due regard for the conditions $L \gg r_0$, yields the solution $u = c/\rho$ for $\rho \geq \rho_0$ (where L is the track length, r_0 is the entrance radius of the track on the irradiated surface).

Under the assumption that the residual pressure in the track region is constant and proportional to the density of the energy evolved by an ion at a depth z,

$$p \sim \rho_0^{-2} d\varepsilon/dz,$$

1063-7745/01/4605-0717$21.00

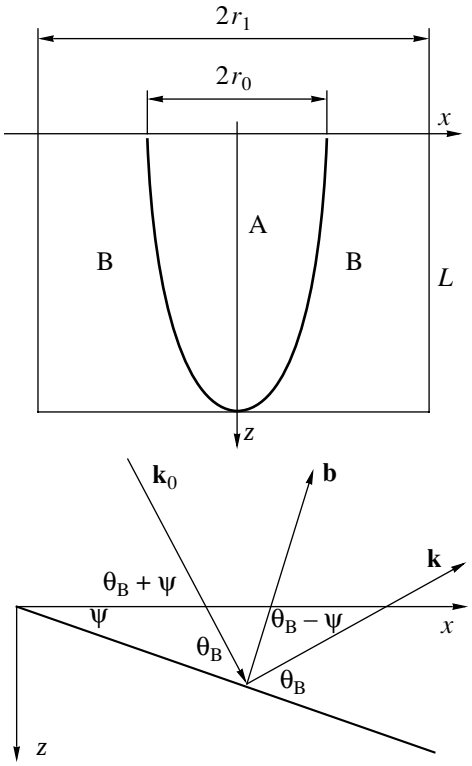

Fig. 1. Track region (A), the elastically deformed region around the track (B), and the asymmetric scattering scheme in the (*x*, *z*) plane.

one can obtain a simple expression for the radial component of the displacement field in the region B as a function of ρ and *z* for low energetic (ε) incident ions with the deceleration losses $d\varepsilon/dz \sim \varepsilon^{1/2}$:

$$u_r(\rho, z) = c_0 r_0^2 (1 - z/L)/\rho, \quad (1)$$

where

$$c_0 = p(1 + \sigma)/E. \quad (2)$$

Here σ is Poisson's ratio, and *E* is Young's modulus. Formu-la (1) describes the field of elastic displacements in the region B. We assume that the lattice atoms in the region A are displaced only along the *z*-axis, whereas the interatomic distances in this region remain constant and, therefore, the atomic displacements are given by the constant quantity

$$\langle u \rangle_z = \gamma c_0 r_0, \quad (3)$$

where γ is the dimensionless parameter characterizing the relative displacement of atoms in the region A. Within the above assumptions and at low energies of the incident ions, the region *A* has the shape of a paraboloid $\rho_0^2 = r_0^2(1 - z/L)$. Then the track model considered here is reduced either to the impression of this paraboloid into the region B or to its repulsion from this region.

In what follows, we ignore the distortion of the displacement field in the vicinity of the surface, the track ends, and the region where the fields of the neighboring tracks overlap. We also introduce into consideration the maximum radius r_1 beyond which the effect of the track can be ignored. All the tracks are assumed to be of the same length *L*; at larger length, i.e., at $z > L$, the effect of tracks onto the crystal structure can be ignored.

CALCULATION OF DIFFUSE SCATTERING

In the general case, the diffuse-scattering intensity can be represented as [2]

$$I(\mathbf{q}) = I_0 N |F(\mathbf{q})|^2, \quad (4)$$

where I_0 is the intensity of the X-ray beam incident onto the crystal and *N* is the number of tracks formed,

$$F(\mathbf{q}) = \int d^3 r(\mathbf{bu}) \exp(i\mathbf{qr}) \quad (5)$$

is the diffuse-scattering amplitude dependent on the transferred pulse $\mathbf{q} = \mathbf{k} - \mathbf{k}_0 - \mathbf{b}$, the direction of the reciprocal-lattice vector **b**, and the field of the elastic displacements. It follows from (5) that for tracks normal to the surface, the symmetric diffraction scheme yields the zero diffuse-scattering amplitude for atoms displaced in the region B if (**bu**) = 0.

Thus, "track defects" should be studied in the asymmetric diffraction scheme for a system of crystallographic planes in which the reciprocal-lattice vector has a considerable projection onto the irradiated surface. Choosing the Cartesian coordinate system in such a way that scattering occurs in the (*x*, *z*) plane, we obtain the following simple expressions for the transferred-pulse components [3]:

$$\begin{aligned} q_x &= k_0 \sin(\theta_B - \psi)[(1 + \beta)\alpha - \Delta\theta], \\ q_z &= k_0 \cos(\theta_B - \psi)\Delta\theta. \end{aligned} \quad (6)$$

Here $k_0 = 2\pi/\lambda$ is the pulse of the incident X-ray radiation, ψ is the angle formed by the reflecting planes and the irradiated crystal surface, θ_B is the Bragg angle for the system of reflecting planes, α is the angle of deviation of the crystal from the exact Bragg position, Δθ determines the angular position of the crystal–analyzer, and $\beta = \sin(\theta_B + \psi)/\sin(\theta_B - \psi)$ is the asymmetry coefficient for the chosen Bragg reflection. Figure 1 shows the asymmetric scattering scheme in the (*x*, *z*) plane. To compare the calculated and observed diffuse-scattering intensities, we have to average $|F(\mathbf{q})|^2$ over the transferred pulses q_y in the direction normal to the scattering plane. As a result, we arrive at the sought dependence of the diffuse-scattering intensity on angles α and Δθ in the form

$$I(\alpha; \Delta\theta) = I_0 N \frac{1}{2q_0} \int_{-q_0}^{q_0} dq_y |F(\mathbf{q})|^2, \quad (7)$$

where q_0 is the aperture parameter equal to the maximum value of the pulse transferred in the direction normal to the scattering plane, which is determined by the size of the corresponding slit.

In our case, the diffuse-scattering amplitude (5) is a sum of the amplitudes of scattering from the track, F_A, and from the elastically deformed region, F_B. A considerable contribution to the diffuse-scattering intensity also comes from the interference of these two amplitudes.

Integration over the region A in formula (5) yields the scattering amplitude F_A in the form

$$F_A = \pi b_z \gamma c_0 r_0^3 L \sum_{k=0}^{\infty} (-1)^k a_k (q_x^2 + q_y^2)^k r_0^{2k} \Phi_{k+1}(q_z L), \quad (8)$$

where $\Phi_m(z) = \int_0^1 dx(1-x)^m \exp(izx)$, $a_k = \dfrac{k+1}{[(k+1)!]^2 4^k}$.

Integration over the elastically deformed region B yields the expression for F_B,

$$F_B = i\frac{\pi}{2} b_x c_0 r_0^2 r_1^2 q_x L \sum_{k=0}^{\infty} (-1)^k b_k (q_x^2 + q_y^2)^k \times r_1^{2k}\left[\Phi_1(q_z L) - \left(\frac{r_0}{r_1}\right)^{2k+2} \Phi_{K+2}(q_z L)\right], \quad (9)$$

where

$$b_0 = 1/2, \quad b_1 = 1/16, \quad b_{k+1} = b_k/(2k+4)^2 \ldots.$$

One has to pay attention to the linear dependence $F_B \sim q_x$, which, as will be shown later, results in the characteristic angular dependence of diffuse scattering from the elastically deformed region.

On the basis of the above model, we wrote the computer program to calculate the complete diffuse-scattering intensity by formula (7), the contributions $|F_A|^2$ and $|F_B|^2$ from the regions A and B, respectively, and also the interference term $2\mathrm{Re}F_A F_B^*$, which can make a noticeable contribution to the diffuse-scattering curve and the sign reversal with the change of the displacement direction. The program allows one to vary the parameters defining the region dimensions (L, r_0, r_1) and relative atomic displacements (γ), the residual pressure (p) in the region A, and also the parameters of the asymmetric scattering scheme.

DISCUSSION OF RESULTS

The curves in Fig. 2 show the contributions of the diffuse scattering intensity that come from the regions A and B, the interference contribution $2\mathrm{Re}F_A F_B^*$, and the total intensity $|F_A + F_B|^2$ calculated for the CuK_α radiation with the wavelength $\lambda = 1.54$ Å scattered from the

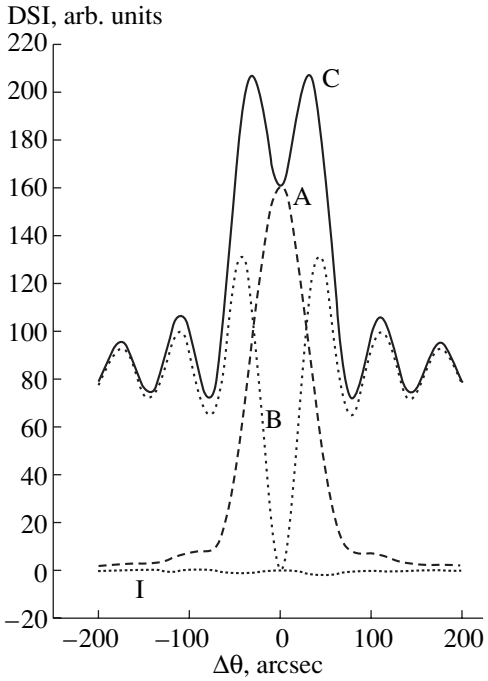

Fig. 2. Total diffuse-scattering curve (C) and the contributions from the regions A and B and their interference (I).

(511) planes of an ion-irradiated Si(111) crystal, which corresponds to the angles $\theta_B = 47.476°$ and $\psi = 38.94°$ and the asymmetry coefficient $\beta = 6.72$. The computations were performed at $\alpha = 0$ and the following values of the track parameters: $r_0 = 0.6$, $r_1 = 60$, $L = 500$ nm, $\gamma = 1$, $p(1+\sigma)/E = 10^{-5}$. The residual pressure in the computation of the diffuse-scattering curve is set by the dimensionless quantity $p(1+\sigma)/E$. Figure 2 demonstrates the characteristic differences of the diffuse scattering from the regions A and B. Within the track model used, the diffuse-scattering curve from the region A is similar to the diffusion-scattering curve with the characteristic maximum, whose height and width are determined by the parameters r_0, L, and γ, and whose position corresponds to the Bragg angle of the displaced lattice. The elastically deformed region in the vicinity of the track is characterized by the diffusion-scattering curve with the characteristic minimum at $\Delta\theta = \alpha(1+\beta)$ [because $F_B \sim q_x$, see (9)] and the oscillations at the wings. The period and the amplitude of these oscillations depend on the dimensions of the region B (L, r_0, r_1), whereas the residual pressure p determines the total scale of the diffuse scattering. As is seen from Fig. 2, at the given values of the parameters, the main contributions to the diffuse-scattering curve come from the regions A and B, whereas the interference contribution is rather small.

The effect of the parameters r_0 and r_1 on the shape of the diffuse-scattering curve is illustrated by Figs. 3 and 4, respectively. All the computations were performed for the values of the parameters used in Fig. 2.

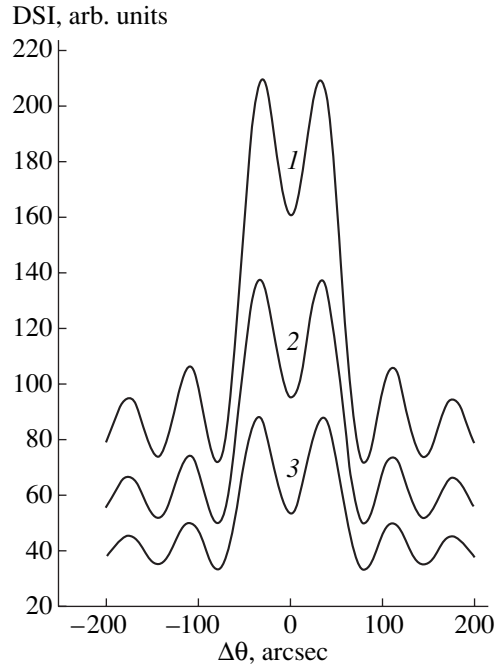

Fig. 3. Effect of the initial track radius r_0 on the shape of the diffuse-scattering curve: r_0 = (*1*) 0.6, (*2*) 0.55, and (*3*) 0.5 nm.

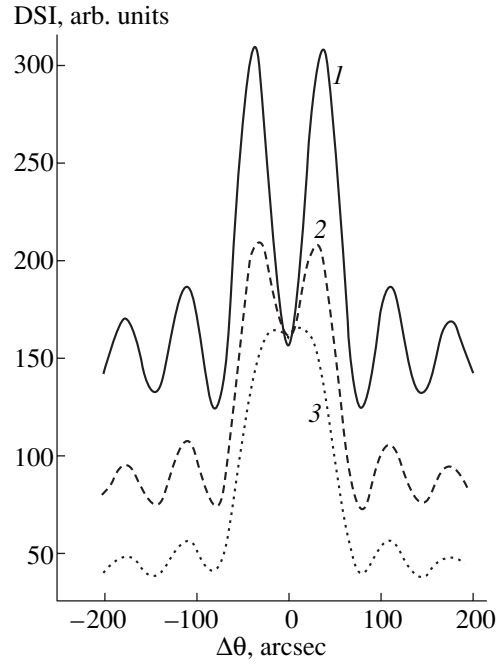

Fig. 4. Effect of the radius r_1 of elastically-deformed region on the diffuse-scattering curve: r_1 = (*1*) 70, (*2*) 60, and (*3*) 50 nm.

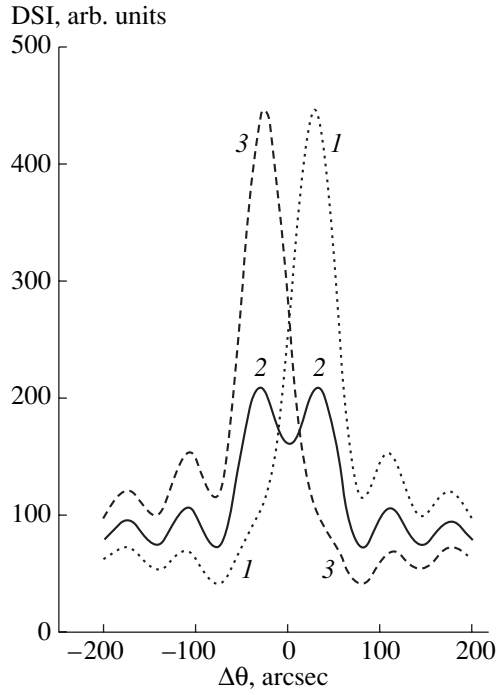

Fig. 5. Effect of crystal rotation on the shape of the diffuse-scattering curve: α: (*1*) –3, (*2*) 0, and (*3*) 3.

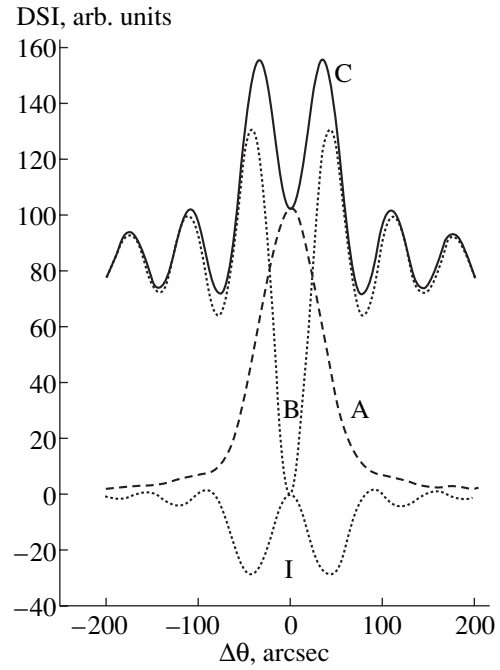

Fig. 6. Total diffuse-scattering curve (C), and the contribution from the A and B regions and interference (I) for the model displacement field in the region A with the components $u_r = c_0\rho$ and $u_z = \gamma c_0(\rho_0 - \rho^2/\rho_0)$ at $\gamma = 5$.

It is seen that a decrease of the track radius r_0 results diminishes the effect of the region A (Fig. 3), whereas a decrease of the radius r_1 reduces the effect of the region B (Fig. 4). The variations in the track length L change the relative contributions of the regions A and B to the total diffuse-scattering curve, because the dimensions of these regions depend on L. A decrease of the atomic displacement $\langle u \rangle$ in the region A and the track

radius r_0 (Fig. 3) diminish the contribution of this region to diffuse scattering. At $\gamma = \sim 0.8$, the contributions to the diffuse-scattering curve from the regions A and B become comparable.

At considerable displacements in the region A with $\gamma \geq 1$ and at larger track radii r_0, the main contribution to the diffuse-scattering curve comes from the region A, whereas the region B is responsible for small maxima at the curve wings. If measurements are made at $\alpha \neq 0$, the maxima at the wings of the diffuse-scattering curve are shifted because of the linear dependence $F_B \sim q_x \sim [\alpha(1 + \beta) - \Delta\theta]$.

Figure 5 illustrates the transformation of the diffuse-scattering curve for the crystal deviating from the exact Bragg position by an angle of $\alpha = \pm 3$ s. In this case, the contributions to the diffuse-scattering curve that come from the interference and the region B are shifted by an angle of $\Delta\theta = \alpha(1 + \beta) \sim \pm 23''$, which makes the curves asymmetric.

For comparison, Figure 6 shows the results of the computations for the case, where atoms in the A region have both radial, $u_r = c_0\rho$ and longitudinal, $u_z = \gamma c_0(\rho_0 - \rho^2/\rho_0)$, displacement components. We also took into account the nonuniform displacement along the track and expansion along the radius. Here, the parameter γ determines the maximum atomic displacement along the track axis. This model is characterized by an increase of the interference contribution. The corresponding computations were made at the same parameter values as in Fig. 2, with the only exception—in the latter case, $\gamma = 5$.

CONCLUSIONS

Thus, the high sensitivity of diffuse scattering to the parameters of the track models allows one to use the experimental curves for qualitative estimation of the contributions of the regions A and B to the diffuse scattering. The further fitting of the theoretical curve to the experimental one can also yield the averaged values of the parameters for the regions A and B.

The expressions obtained for the amplitudes F_A and F_B can considerably simplify the study of the track structure. Thus, it is clear from Eqs. (8) and (9) that the above model allows the experimental determination of the contribution of the longitudinal displacement from the region A to the diffuse-scattering curve by the method of q_z-scanning and, thus, facilitates the analysis of the track structure.

ACKNOWLEDGMENTS

The authors are grateful to V.A. Bushuev for the fruitful discussion of the asymmetric diffraction scheme and valuable advice.

This study was supported by the Russian Foundation for Basic Research, project no. 00-15-96 580.

REFERENCES

1. A. M. Afanas'ev, P. A. Aleksandrov, and R. M. Imamov, *X-ray Diffraction of Submicron Layers* (Nauka, Moscow, 1989).
2. P. A. Aleksandrov and A. M. Afanas'ev, Kristallografiya **29** (5), 1019 (1984) [Sov. Phys. Crystallogr. **29**, 598 (1984)].
3. A. A. Lomov, V. A. Bushuev, R. M. Imamov, *et al.*, Kristallografiya **44** (4), 674 (1999) [Crystallogr. Rep. **44**, 625 (1999)].
4. L. A. Charniy, A. N. Morozov, V. T. Bublic, *et al.*, J. Cryst. Growth **118** (2), 163 (1992).
5. V. T. Bublik and K. D. Shcherbachev, Kristallografiya **40** (1), 122 (1995) [Crystallogr. Rep. **40**, 110 (1995)].
6. K. D. Shcherbachev, V. T. Bublik, and O. É. Daricheva, Kristallografiya **40** (5), 868 (1995) [Crystallogr. Rep. **40**, 803 (1995)].
7. A. A. Lomov, N. V. Shitov, and V. A. Bushuev, Kristallografiya **37** (2), 444 (1992) [Sov. Phys. Crystallogr. **37**, 230 (1992)].
8. V. T. Bublik, S. B. Evgen'ev, S. P. Ivanov, *et al.*, Kristallografiya **44** (5), 890 (1999) [Crystallogr. Rep. **44**, 829 (1999)].
9. L. D. Landau and E. M. Lifshitz, *Course of Theoretical Physics*, Vol. 7: *Theory of Elasticity* (Nauka, Moscow, 1965; Pergamon Press, New York, 1986).

Translated by L. Man

Crystallography Reports, Vol. 46, No. 5, 2001, pp. 722–729. From Kristallografiya, Vol. 46, No. 5, 2001, pp. 796–804.

DIFFRACTION AND SCATTERING OF ELECTRONS

Dedicated to the memory of B.K. Vainshtein

Size Effect in X-ray and Electron Diffraction Patterns from Hydroxyapatite Particles[1]

E. I. Suvorova* and P.-A. Buffat**

** Shubnikov Institute of Crystallography, Russian Academy of Sciences, Leninskiĭ pr. 59, Moscow, 117333 Russia*

*** Centre Interdepartemental de Microscopie Electronique, EPFL Lausanne, Switzerland*

e-mail: suvorova@ns.crys.ras.ru

Received January 19, 2001; in final form, May 14, 2001

Abstract—High-resolution transmission electron microscopy (HRTEM), electron microdiffraction, and X-ray diffraction were used to study hydroxyapatite specimens with particle sizes from a few nanometers to several hundreds of nanometers. Diffuse scattering (without clear reflections in transmission diffraction patterns) or strongly broadened peaks in X-ray diffraction patterns are characteristic for agglomerated hydroxyapatite nanocrystals. However, HRTEM and microdiffraction showed that this cannot be considered as an indication of the amorphous state of the matter but rather as the demonstration of size effect and the morphological and structural features of hydroxyapatite nanocrystals. © *2001 MAIK "Nauka/Interperiodica"*.

INTRODUCTION

Precipitation of hydroxyapatite in aqueous solutions is, in fact, mass crystallization with the formation of large numbers of small crystals during the chemical reaction between phosphate and calcium ions. At pH > 4, hydroxyapatite is the least water-soluble calcium phosphate modification of the four (hydroxyapatite, octacalcium phosphate, brushite, and monetite). The mechanisms of nucleation and growth of hydroxyapatite crystals are still subject to controversy and numerous experimental and theoretical studies because of the promising properties of hydroxyapatite for production of efficient bioimplants and artificial bone tissue.

Posner's theory on the mechanism of formation of hydroxyapatite is the earliest and the best-known work. On the basis of X-ray diffraction patterns [1] and IR spectra [2], Posner suggested that at the initial stage of the reaction, an amorphous phase is formed; its particles gradually become crystals. The interpretation of radial-distribution functions on X-ray diffraction patterns led to the model of this amorphous phase. Its structure consists of $Ca_9(PO_4)_6$ clusters, with Ca- and PO_4-groups occupying approximately the same positions as in crystalline hydroxyapatite [3]. The deposit of amorphous substance was considered to be a precursor of the growth of hydroxyapatite crystals. Recently, this cluster model has been developed in both experimental and theoretical directions. Thus, the presence of 0.7 to 1.0 nm clusters in the solutions was detected by the method of dynamical scattering of light [4–6]; the stability of $[Ca_3(PO_4)_2]_n$ clusters in the amorphous phase was calculated in [7, 8].

The amorphous state was confirmed by the absence of clear peaks in X-ray diffraction patterns. However, as was indicated by Pinsker [9] and Vainshtein [10], at the early stage of the development of electron diffraction, the reflection broadening is associated mainly with small sizes of particles. It was also indicated [9] that reflection broadening is accompanied by weakening and redistribution of reflection intensities due to scattering from very small particles. Vainshtein [10] made an exhaustive study of the intensity redistribution on electron diffraction patterns from ideal single crystal and polycrystalline films with different grain sizes. As Heidenrech [11] has shown, a sharp decrease in the diffracted intensity and a broadening of the peaks occurs when the size of a one-dimensional crystal is reduced by four times, i.e., from eight, four, and two atoms.

However, the importance of the size effect has not been recognized in the following studies and the transition from the amorphous phase into crystalline hydroxyapatite was considered as a number of successive phase transformations [12–16].

The high-resolution transmission electron microscopy (HRTEM) and electron diffraction study of calcium phosphates [17, 18] precipitated from aqueous solutions under different conditions always showed the formation of crystalline hydroxyapatite. The X-ray dif-

[1] This article was submitted by the authors in English.

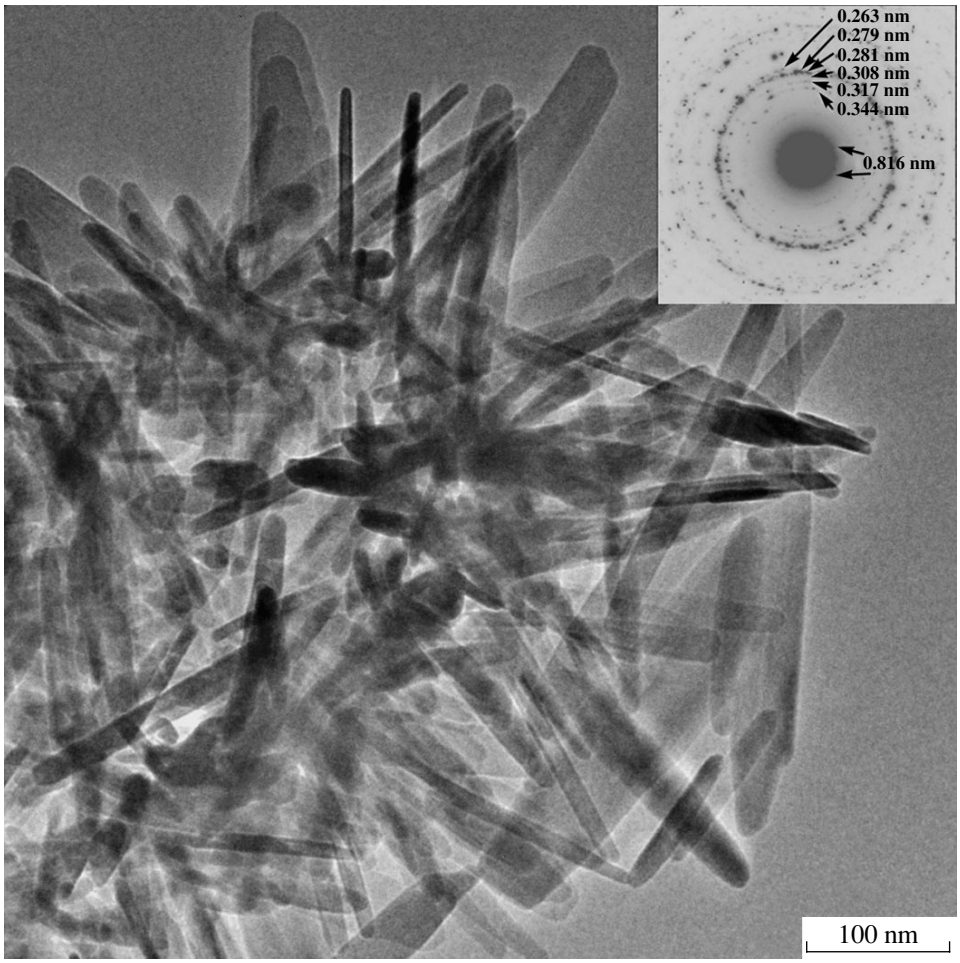

Fig. 1. Hydroxyapatite microcrystals and the corresponding SAED pattern taken from an area about 0.8 μm in diameter.

fraction (XRD) and selected area electron diffraction (SAED) method applied to the smallest hydroxyapatite particles provided the formation of only "amorphous-like" broad rings. The objective of the present work is to compare the results obtained by X-ray and electron diffraction from small hydroxyapatite particles and to consider some factors that cause strong reflection broadening. We should like to show that only a combination of all the above methods can provide the adequate interpretation of the experimental data for the determination of the phase composition and the morphology of hydroxyapatite particles.

EXPERIMENTAL

Hydroxyapatite samples were precipitated from aqueous solutions during the chemical reaction between calcium ions with phosphate ions. The concentration of the stock solutions, the rate of their mixing, and the duration of crystallization was varied over wide ranges. The temperature ranged between 25 and 40°C; after mixing but prior the precipitation, pH was 6.5–7.5. A detailed description of the growth conditions can be found elsewhere in [18–20].

Dry powders of all the samples were examined by X-ray diffraction in a D/max-IIIC X-ray diffractometer (Rigaku Int. Corp., Tokyo, Japan) over wide angular interval (from 3° up to 60°).

A Philips CM300 UT FEG microscope (300 kV field emission gun, 0.65 mm spherical aberration, and 0.17 nm resolution at Scherzer defocus) was used to study the crystal morphology and the structure at the atomic level. Because of spherical aberration, the minimum diameter of the sample part providing the formation of the diffraction pattern in selected area diffraction (SAED) cannot be smaller than 0.1 μm. To obtain a diffraction pattern from areas a few nanometers in diameter, it is necessary to use a microdiffraction mode with a beam focused into a thin parallel probe and illuminating only the area of interest. To provide this, the first condenser lens was highly excited, whereas the second condenser was supplied with a small aperture (30 μm or less). To compensate the loss in the intensity

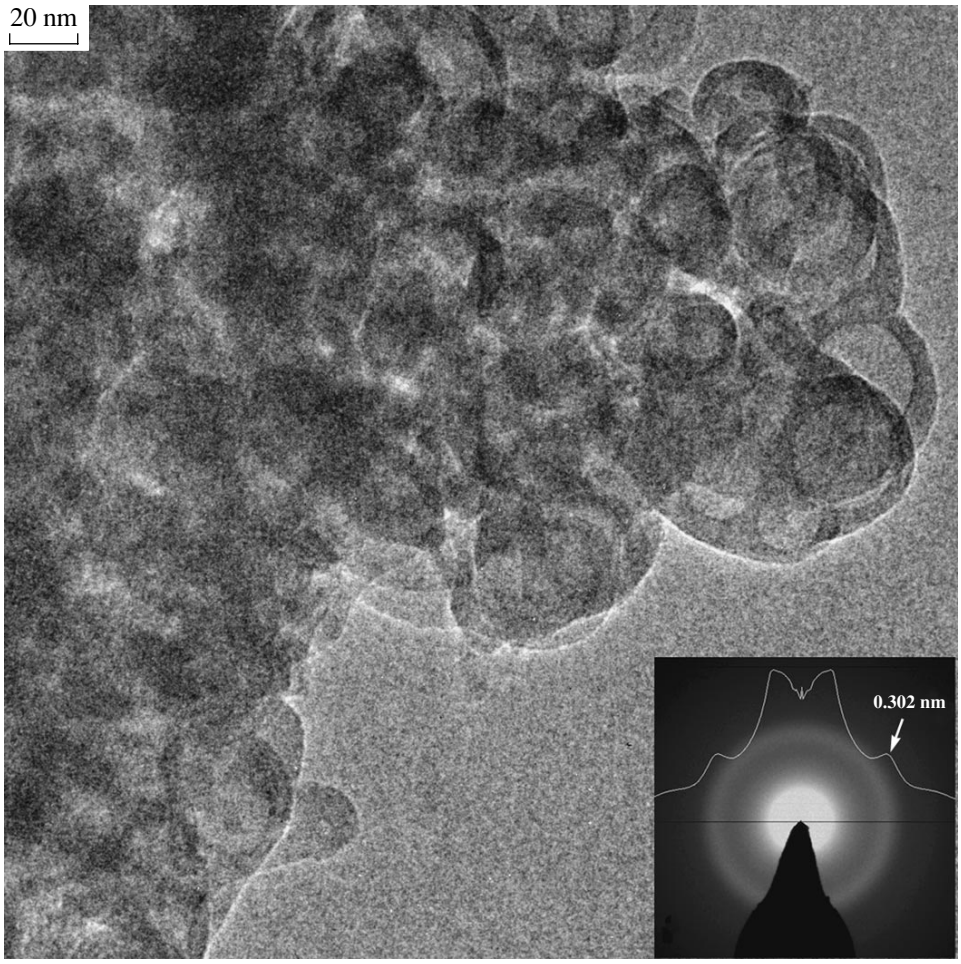

Fig. 2. Hydroxyapatite nanocrystals and the corresponding SAED pattern taken from an area about 0.8 μm in diameter.

of the beam (with parallel probes of about 3.5–10 nm in diameter), it was necessary to use a field emission gun. In a CM 300 UT FEG microscope, a Schottky emitter was used with a tungsten tip partly covered by zirconium oxide and with a curvature radius less than 1 μm that gives a source size (crossover) of about 10 nm and a brightness about one thousand times higher than conventional W thermionic emitters. All these conditions provided the formation of fine reflections and preserved the sample from fast radiation damage. However, to avoid severe irradiation damage, it was necessary to take all the necessary precautions so that the beam would never be focused to its minimum diameter.

The images were recorded in a Gatan 797 slow scan CCD camera and processed with the Gatan DigitalMicrograph 3.3.3 software (Gatan, Inc., Pleasanton, Calif.), including Fourier filtering and diffraction pattern analysis.

The HRTEM images and electron diffraction patterns were calculated at the given electron-optical parameters and structural data of hydroxyapatite [21] (hexagonal unit cell $P6_3/m$ with the lattice parameters $a = 0.942$ and $c = 0.688$ nm) with the use of the EMS software package [22] and its new version JEMS (JAVA EMS) [22]. These simulations provided unambiguous phase determination and also the estimation of the precipitated crystal thickness.

RESULTS AND DISCUSSION

The sizes of hydroxyapatite crystals varied in the range from a few nanometers to several hundreds of nanometers depending on the rate of mixing of the stock solutions and the crystallization duration at temperatures below 40°C in neutral solutions. Figure 1 shows the TEM image of the agglomerated hydroxyapatite crystals with sizes usually less than 0.5 μm and elongated in the [0001] direction and also the SAED pattern taken from an area about 0.8 μm in diameter. The rings on the SAED pattern consist of individual thin reflections from different crystallites differently oriented with respect to the electron beam. The crystal planes {0002}, $\{21\bar{3}1\}$, $\{11\bar{2}2\}$, $(03\bar{3}0)$ and $\{02\bar{2}2\}$ with interplanar spacings $d = 0.344$, 0.281, 0.279, 0.272

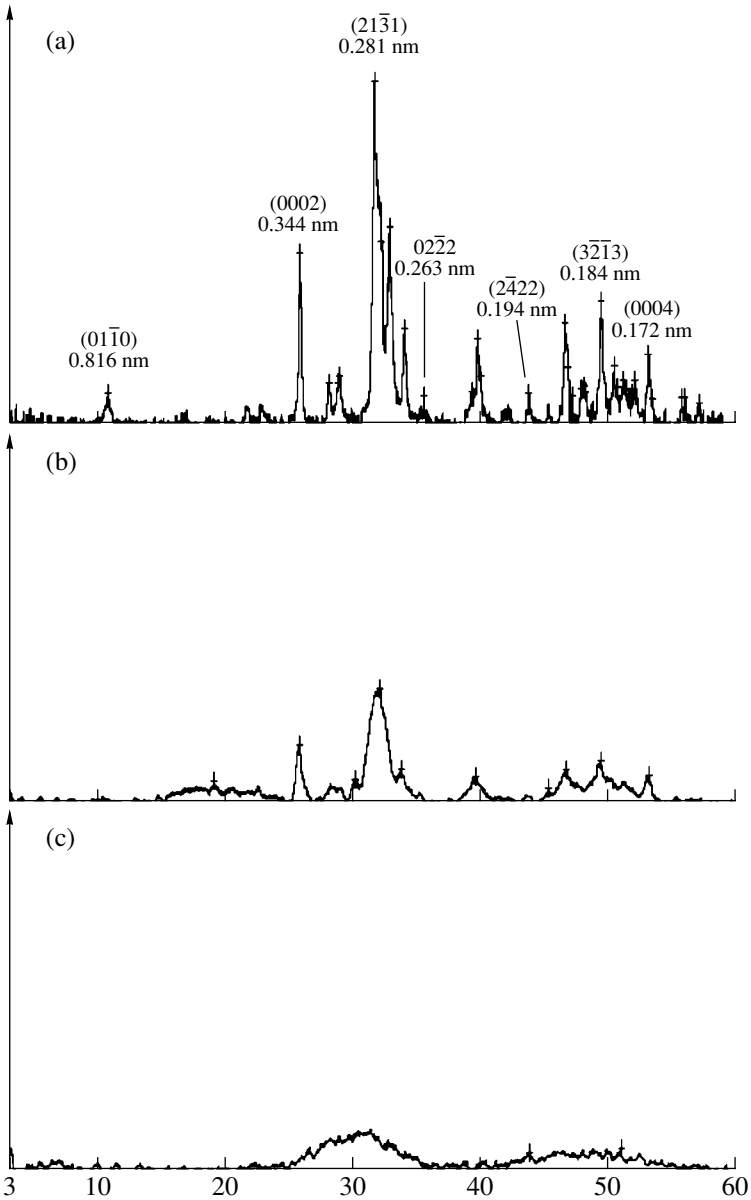

Fig. 3. X-ray diffraction patterns obtained from hydroxyapatite samples grown under different conditions: (a) microcrystals of a length up to 0.5 μm, (b) microcrystals at the initial stage of faceting of the average length 0.1–0.2 μm, (c) rounded nanocrystals with a diameter less than 50 nm.

and 0.263 nm, respectively, give the most intense reflections. If the diameter of the sample area is increased by a factor of 10, all the reflections merge and form continuous rings. With the appearance of some noticeable broadening (instrumental, size effect, etc.), the overlap of the reflections with interplanar spacings from 0.272 nm (03$\bar{3}$0) to 0.308 nm (21$\bar{3}$0) provides the formation of a wide ring with the strongest intensity [17].

Figure 2 shows small (<50 nm in diameter) rounded hydroxyapatite particles and the corresponding SAED pattern taken from an area 0.8 nm in diameter. Thus, the particle size decreased by 10 times in comparison with the size of the previous sample, whereas the SAED diffraction pattern no longer exhibit sharp rings. Now, it has two wide and diffuse rings without speckles and looks like the diffraction pattern from an "amorphous" material. It should be noted that the maximum intensity of the first diffuse ring is observed at the 0.3 nm between the 0002 reflection (d = 0.344 nm) and the 02$\bar{2}$2 reflections (d = 0.263 nm).

Three X-ray diffraction patterns taken from hydroxyapatite precipitates are shown in Fig. 3. X-ray diffraction pattern of submicron-scale hydroxyapatite (up to 0.5 μm in length) clearly exhibit all the reflections of this phase (Fig. 3a), in particular the reflections

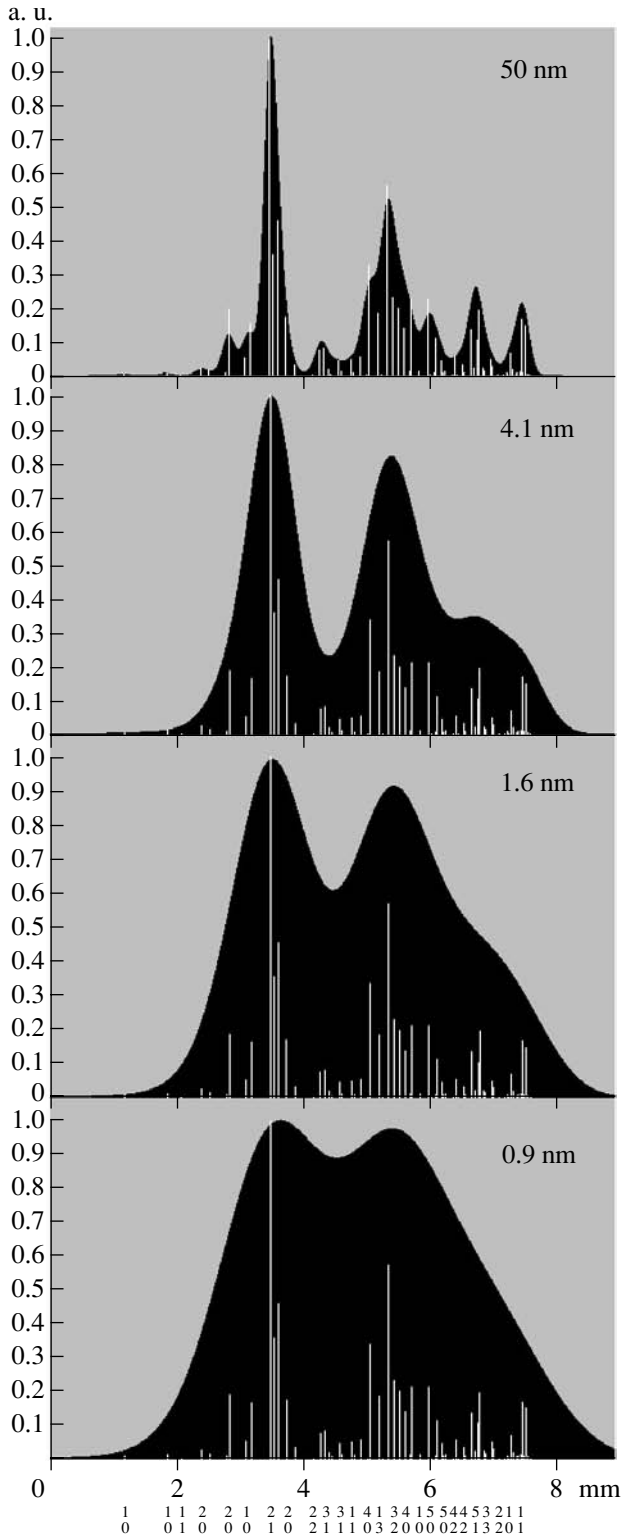

Fig. 4. Simulation of the isotropic size effect for hydroxyapatite crystals using the JEMS software. Broadening of diffraction reflections with a decrease of the particle size: particles of 50, 4.1 (equivalent of the thickness of 5 unit cells), 1.6 (thickness of 2 unit cells), 0.9 nm (thickness of 1 unit cell).

from the $\{01\bar{1}0\}$ atomic planes with the 0.816 nm spacing; these reflections are well resolved and can be used for reliable identification of hydroxyapatite. Figure 3b shows an X-ray diffraction pattern from smaller crystals (with the average length of about 0.1 μm). Now reflections are broader, and the $01\bar{1}0$ reflection cannot be seen against the background and noise. The XRD pattern from nanoparticles (Fig. 3c) has very broad peaks, so that it is impossible to make any definite conclusion on the phase composition or the material structure. These broad maxima lie in the area of strong reflections from HAP planes in the range of reflections 0002–$21\bar{3}1$–$02\bar{2}2$ (first broad maximum) and $24\bar{2}2$–$3\bar{2}\bar{1}3$–0004 (second broad maximum).

These XRD patterns show the method limitations in the phase analysis of small particles. Even selected-area electron diffraction patterns taken from relatively large samples can be interpreted erroneously. The results of the simulation of the size effect for random spherical hydroxyapatite particles (JEMS software [23]) are shown in Fig. 4 for crystals with decreasing sizes (50, 4.1, 1.6, and 0.9 nm in diameter). The three last values correspond to crystal thicknesses corresponding to the thickness of 5, 2, and 1 unit cell. Similar to the case of experimental patterns, reflection broadening is observed and the intensity maxima of these broad peaks are located close to the positions of strong reflections.

The use of electron microprobes 3.5–10 nm in diameter provides probing of only very thin parts of the sample and the formation of the diffraction pattern only from this part. Now the strongest reflections, $21\bar{3}1$ and $20\bar{2}2$, appear in the microdiffraction pattern (Fig. 5).

The HRTEM studies confirm the crystalline character of the nanoparticles. Figure 6 shows two images of the same particle. In Fig. 6a, only part of the regular structure is seen. Figure 6b shows that a sample slightly tilted with respect to the electron beam provides recording of the whole lattice of the particle. This indicates that the absence of visible lattice should not be interpreted as a lack of crystallinity, rather it is only a sign of the fact that the particle is, first, out of diffraction conditions, and, second, that the particles are either bent or consist of individual grains. The zone-axis orientation was first determined from the fast Fourier transform (FFT) of square areas with regular lattice. Then HRTEM simulation was performed for several thicknesses of the sample, several tilts to the beam, and objective defocusing, and the data obtained were compared with the experimental image. Thus, we managed to estimate the actual sample orientation and the sample thickness. The best fit between the simulation and experiment is shown in the inset M1 in Fig. 6a for a crystal 0.8 nm in thickness (one unit-cell parameter). The noise-filtered image (inverse FFT) is given below for better comparison and also to show the size of the

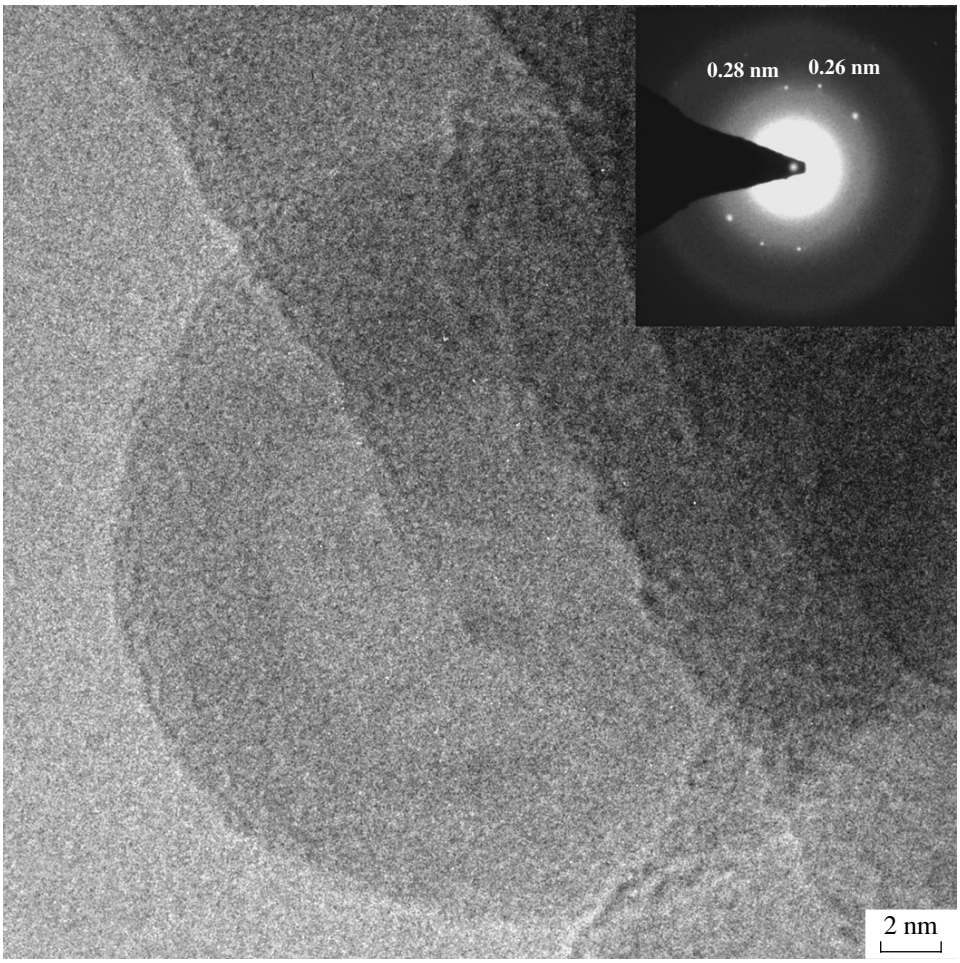

Fig. 5. Hydroxyapatite nanocrystals and the microdiffraction pattern obtained with an electron nanoprobe 5 nm in diameter. Some of the strongest reflections always appear in the pattern. Usually, polycrystal nanodiffraction patterns are observed because of the superposition of several particles and their bending.

area considered. This pattern was obtained at defocusing of 15 nm, a thickness of 0.8 nm and a sample tilt of 0.7° toward $(2\bar{1}\bar{1}4)$ close to $[4\bar{2}\bar{2}\bar{3}]$. The same analysis illustrated by Fig. 6b on approximately the same sample area led to 16 and 0.8 nm and 1°, respectively.

We believe that the crystallization of hydroxyapatite under the electron beam does not give any explanation of the difference observed between the XRD and SAED results, on one hand, and HRTEM and microdiffraction results, on the other hand. First, this material has a large unit cell consisting of 44 atoms and including PO^{4-} and OH-groups. Second, it is rapidly and irreversibly destroyed by the beam.

Stacking faults and, more generally, crystal defects are known to give rise to some broadening of diffraction reflections [24], crystal-lattice distortions and strains [25], and dislocations and point defects [26]. However, these defects are inherent in both nano- and microcrystals. During crystallization, crystal length increases along the [0001] direction, while the increase in their width or thickness is very feebly marked [17, 18]. Moreover, the X-ray and SAED patterns from larger crystals show sharp reflections. Thus, the presence of defects cannot account for the significant reflection broadening observed for small particles.

Further work would allow us to refine the results obtained by using new algorithms for calculating the broadening of reflections from platelets (anisotopic size effect) and by taking in account the contribution of coherent, incoherent, and inelastic scattering in powders prepared from large or small crystals. Microcrystals are slightly thicker than nanocrystals. Within the kinematical approximation, the diffracted intensities are proportional to the squared crystal thickness. Thus, of two equivalent volumes containing the same number of diffracting planes, the volume consisting of nanocrystals would produce lower diffracted intensities than the one containing larger crystals.

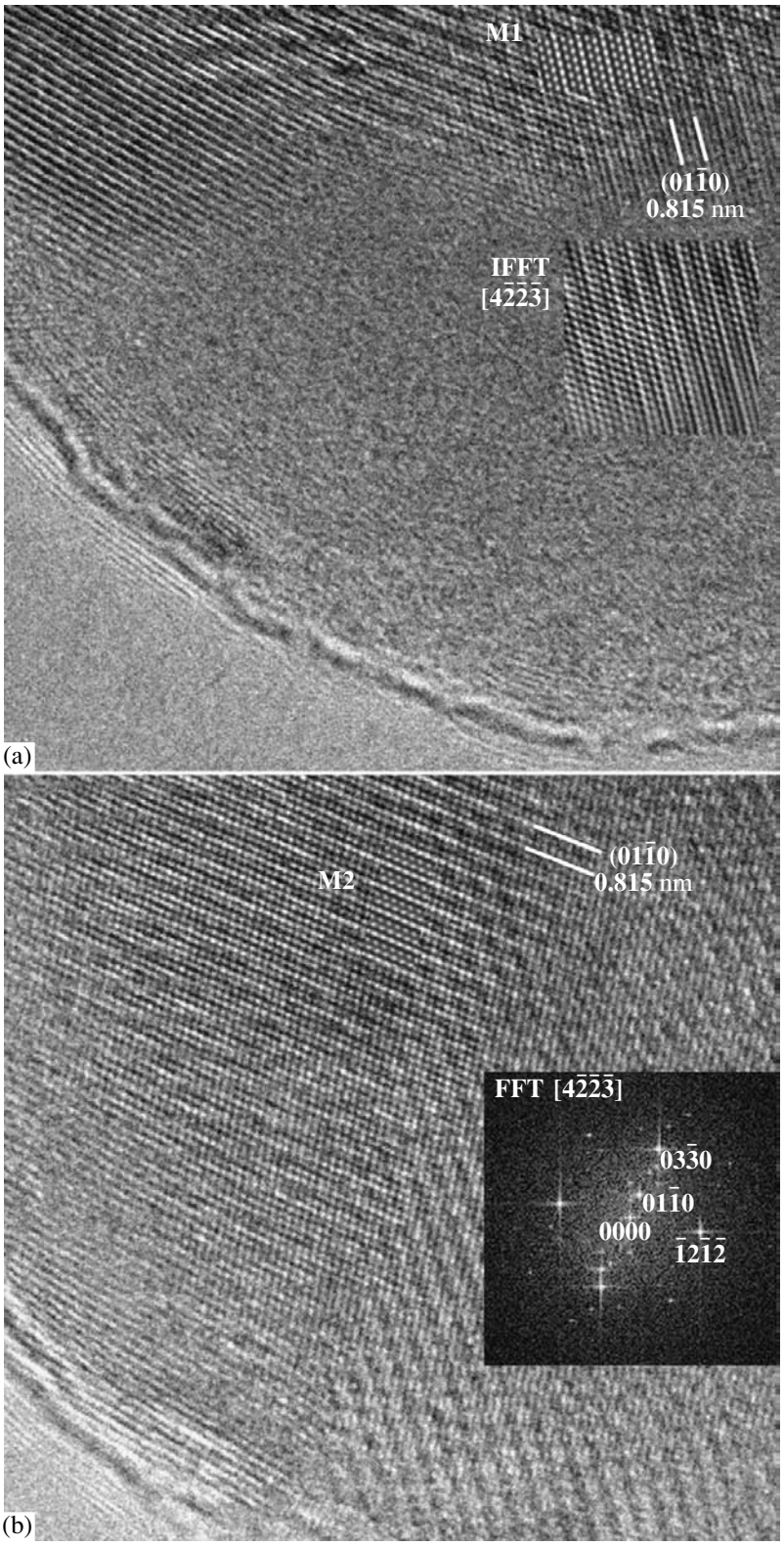

Fig. 6. HRTEM images of the same hydroxyapatite nanocrystal obtained at different illumination angles: (a) untilted crystal; in the inset M1: the simulated image best fitted to the experimental one; obtained from a 0.8-nm-thick crystal, 15-nm-defocusing, and the zone axis [4$\bar{2}\bar{2}$3] forming an angle of 0.7° with the beam along the direction of the 2$\bar{1}\bar{1}$4 reflection; the inset shows the filtered image; (b) tilted crystal. The images of atomic planes are well seen over the whole area. The Fourier transform and the theoretical simulation (the inset M2) are made for a 0.8-nm-thick crystal, defocusing 16 nm. The zone axis [4$\bar{2}\bar{2}$3] is at an angle of 1° to the beam in the direction of the 2$\bar{1}\bar{1}$4 reflection.

CONCLUSIONS

The methods of HRTEM and electron microdiffraction (nanodiffraction) of hydroxyapatite particles precipitated at moderate pH and temperatures always showed the formation of crystalline hydroxyapatite irrespectively of the particle sizes. The clear reflections observed in X-ray and electron diffraction patterns taken from the large sample areas of microcrystals had very broad peaks or diffuse rings due to nanocrystals. The broadening of reflections and weakening of the scattered intensity is due to the size effect. The closeness of some interplanar spacings enhances the overlapping of reflections and lead to the formation of very broad peaks around the two most intense reflections. Nevertheless, microdiffraction with the use of thin and parallel electron nanoprobes allows the study of the crystal structure of nanoparticles and the use of HRTEM to identify them with hydroxyapatite.

The authors highly appreciate the collaboration with Prof. H.E. Lundager Madsen (Chemistry Department, Royal Veterinary and Agricultural University, Denmark) and Prof. I.V. Melikhov and Dr. V.F. Komarov (Chemistry Department, Moscow State University, Russia) who provided us with calcium phosphate specimens and Prof. V.V. Klechkovskaya for very helpful discussions. The financial support from Contraves Space AG, Zurich (Switzerland) is gratefully acknowledged. This study is also supported by the Russian Foundation for Basic Research, project no. 01-02-16176.

REFERENCES

1. E. D. Eanes, I. H. Gillessen, and A. S. Posner, Nature **208**, 365 (1965).
2. J. D. Termine and A. S. Posner, Nature **211**, 268 (1966).
3. A. S. Posner and F. Betts, Acc. Chem. Res. **8**, 273 (1975).
4. K. Onuma, A. Ito, T. Tateishi, and T. Kameyama, J. Cryst. Growth **154**, 118 (1995).
5. K. Onuma and A. Ito, J. Mineral. Soc. Jpn. **29**, 17 (2000).
6. K. Onuma and A. Ito, Chem. Mater. **10**, 3346 (1998).
7. G. Treboux, N. Kanzaki, K. Onuma, and A. Ito, J. Phys. Chem. A **103**, 8118 (1999).
8. G. Treboux, P. Layrolle, N. Kanzaki, *et al.*, J. Phys. Chem. A **104**, 9111 (2000).
9. Z. G. Pinsker, *Electron Diffraction* (Akad. Nauk SSR, Moscow, 1949; Butterworths, London, 1953).
10. B. K. Vainshtein, *Structure Analysis by Electron Diffraction* (Akad. Nauk SSSR, Moscow, 1956; Pergamon, Oxford, 1964).
11. R. Heidenreich, *Fundamentals of Transmission Electron Microscopy* (Interscience, New York, 1964; Mir, Moscow, 1966).
12. G. H. Nancollas and J. Tomazic, J. Phys. Chem. **78**, 2218 (1974).
13. A. L. Boskey and A. S. Posner, J. Phys. Chem. **80**, 40 (1976).
14. G. H. Nancollas, A. Tsortos, and A. Zieba, Scanning Microsc. **10** (2), 499 (1996).
15. J. Christoffersen, M. Christoffersen, W. Kibalczyc, and F. A. Andersen, J. Cryst. Growth **94**, 767 (1989).
16. F. Abbona and A. Baronnet, J. Cryst. Growth **165**, 98 (1996).
17. E. I. Suvorova and P. A. Buffat, J. Microsc. **196** (1), 46 (1999).
18. E. I. Suvorova and P. A. Buffat, Eur. Cells Mater. **1**, 27 (2001); http://www.eurocelmat.org.uk.
19. E. I. Suvorova, L. E. Polyak, V. F. Komarov, and I. V. Melikhov, Kristallografiya **45** (5), 930 (2000) [Crystallogr. Rep. **45**, 857 (2000)].
20. E. I. Suvorova, F. Christensson, H. E. Lundager Madsen, and A. A. Chernov, J. Cryst. Growth **186**, 262 (1998).
21. M. I. Kay and R. A. Young, Nature **204**, 1050 (1964).
22. P. Stadelmann, Ultramicroscopy **21**, 131 (1987).
23. P. Stadelmann, JEMS. EMS JAVA version, 2001; http://cimewww.epfl.ch/people/Stadelmann/jemsWebsite/jems.html.
24. V. A. Drits, *Structural Investigations of Crystals* (Nauka, Moscow, 1996).
25. L. M. Utevskiĭ, *Diffraction Electron Microscopy in Physical Metallurgy* (Metallurgiya, Moscow, 1973).
26. M. Sauvage and E. Parthé, Acta Crystallogr., Sect. A: Cryst. Phys., Diffr., Theor. Gen. Crystallogr. **A28**, 607 (1972).

Crystallography Reports, Vol. 46, No. 5, 2001, pp. 730–733. Translated from Kristallografiya, Vol. 46, No. 5, 2001, pp. 805–808.

STRUCTURE OF INORGANIC COMPOUNDS

Dedicated to the memory of B.K. Vainshtein

Crystal Structure of Lepidocrocite FeO(OH) from the Electron-Diffractometry Data

A. P. Zhukhlistov

Institute of Geology of Ore Deposits, Petrography, Mineralogy, and Geochemistry, Russian Academy of Sciences, Staromonetnyĭ per. 35, Moscow, 109017 Russia
e-mail: zvyagin@genome.eimb.relarn.ru

Received February 16, 2001

Abstract—The crystal structure of lepidocrocite γ-FeO(OH) with the lattice parameters a = 3.072(2), b = 12.516(3), c = 3.873(2) Å, sp. gr. *Cmcm* has been refined by the electron-diffractometry data for 135 crystallographically nonequivalent reflections up to R = 0.048. Using the difference syntheses of the Fourier potential, we established, for the first time, the anisotropy in the distribution of the electrostatic potential of hydrogen and the statistical occupancy (with the probability of 1/2) by hydrogen atoms of two positions in the *m* plane normal to the *a*-axis at a distance of 0.27 Å from the twofold axis. The O–H distance equals 0.97(3) Å, the O–H···O angle, 135°. The average Fe–O distance in octahedra is 2.022 Å. © *2001 MAIK "Nauka/Interperiodica".*

The crystal structure of lepidocrocite γ-FeO(OH) (sp. gr. *Cmcm*) was first determined by the X-ray diffraction method by Ewing in 1935 [1]. The structure is built by double layers of Fe-octahedra, with the hydroxyl groups being located on their external surfaces and providing hydrogen bonding between the layers. It was assumed that hydrogen atoms occupy the centers of inversion and are located at the same distances from two oxygen atoms of the adjacent layers, thus forming continuous O–H–O–H–O chains with symmetric hydrogen bonds.

In the following years, the atomic positions of hydrogen atoms in lepidocrocite [2, 3], its aluminum analogue boehmite (γ-AlO(OH) [4], and their deuterium varieties [5, 6] were refined mainly by the method of powder neutron diffraction (the Rietveld profile analysis). It was established that hydrogen atoms in these structures form asymmetric hydrogen bonds. The refinement was performed within two models—with hydrogen atoms statistically occupying (with the probability 1/2) two positions in the plane *m* normal to the *a*-axis (sp. gr. *Cmcm*) and orderly occupying one of these positions (sp. gr. $Cmc2_1$). The most probable model for lepidocrocite [5] and boehmite [4, 6] seems to be the model with the statistically disordered distribution of hydrogen atoms in sp. gr. *Cmcm*.

At the same time, the positions of hydrogen atoms in lepidocrocite determined by the powder neutron-diffraction method differ considerably. Thus, hydrogen atoms are located at the centers of symmetry with the O–H distance being 1.35 Å [2]. At the same time, the orderly distributed H-atoms are displaced from these positions toward one of the oxygen atoms participating in hydrogen bonding and are located in the vicinity of the line connecting these oxygen atoms, O–H = 0.93 and H···O = 1.75 Å and the angle O–H···O = 178° [3]. In the deuterium variety of lepidocrocite [5], the D(H) atoms are statistically disordered and are displaced from the line connecting the O atoms of the adjacent layers with the interatomic distances O–D(H) = 0.86, D(H)···O = 1.95 Å, and the angle O-D(H)···O = 157.9°. The angle θ formed by the vector O–H with the direction [010] is 48° [3] and 31.8° [5], respectively. Moreover, it was established that in the lepidocrocite structure, both average interatomic Fe^{3+}–O distances in octahedra vary within 2.00–2.04 Å, and the individual Fe^{3+}–O distances show considerable scatter [1–3, 5]. All these facts make the structure refinement of lepidocrocite by data provided by the oblique-texture electron diffraction patterns (where all the reflections superimposed on powder neutron diffraction patterns are resolved) quite timely. It is also possible to use the advantages offered by electron diffractometry. The efficiency of the latter method was demonstrated in the studies of hydrogen-containing brucite $Mg(OH)_2$ [7] and serpentine mineral—lizardite 1*T* [8].

The crystal structure of natural lepidocrocite FeO(OH) was refined by oblique-texture electron diffraction pattern from the specimen from the Chukhrov collection (no. 2184). The parameters of the orthorhombic unit cell of lepidocrocite determined from the electron diffraction patterns with the internal standard (NaCl) are a = 3.072(2), b = 12.516(3), and c = 3.873(2) Å.

The oblique-texture electron diffraction patterns were obtained on an electron diffractometer based on an EMR-102 industrial electron diffraction camera

1063-7745/01/4605-0730$21.00 © 2001 MAIK "Nauka/Interperiodica"

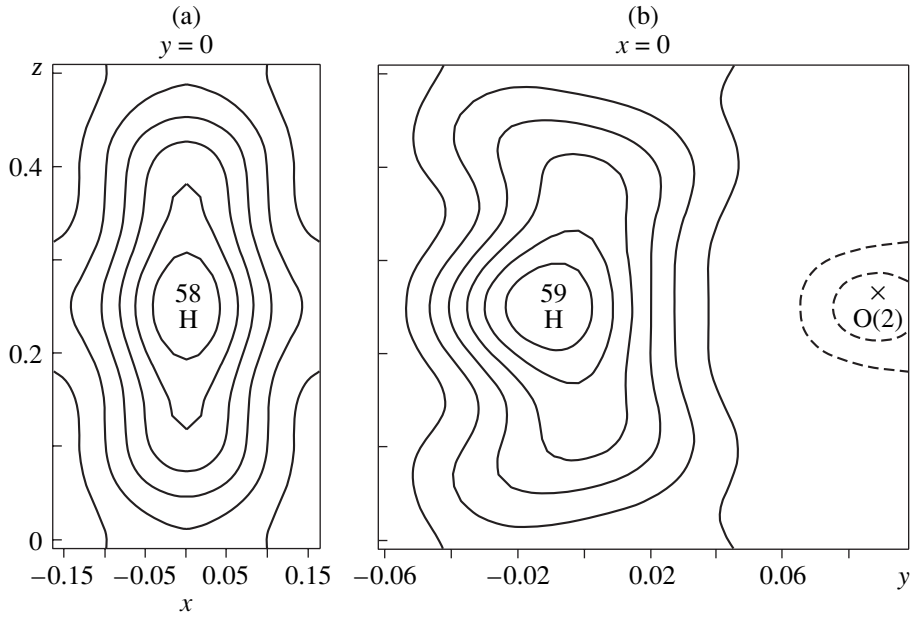

Fig. 1. Sections of the electrostatic potential passing through the hydrogen atoms for lepidocrocite (with subtracted oxygen atoms): (a) the *x*0*z* section; the elongation of the isolines in the *c*-direction favors the two-positional model for H atoms; (b) the 0*yz* section; the cross indicates the positions of the O(2) located, as well as the H atom, on the twofold axis parallel to the *b*-axis. The isolines are spaced by 10 V. The figures indicate the values of the potential at the maxima.

modified for recording two-dimensional intensity distributions in the digital form [9]. The reflection intensities and intensity-distribution profiles across individual archlike reflections were measured by scanning the diffraction pattern along the radial directions and the immobile detector (scinitillator, photoelectron multiplier). All the reflection intensities were normalized to the intensity of the reference reflection. The reflection intensities were determined as the sums of the intensities recorded at each point of the transverse profile with the subtraction of the background. The transition from the intensities, I_{hkl}, to the structure factors, F_{hkl}, was made by the formula for local intensities: $|F_{hkl}(\exp)| = \sqrt{I_{hkl}(\exp)/d_{hkl}d_{h0l}p}$, where the *h*0*l* and *hkl* indices are attributed to the reflections of the same *hl* ellipse and *p* is the repetition factor [10]. The structural computations were performed by the AREN-90 complex of programs [11] with the use of the atomic scattering factors for neutral atoms. We used the intensities of 135 crystallographically independent reflections up to $\sin\theta/\lambda = 1.01$ located on 37 ellipses. The analysis of the reflection intensities showed that for most reflections, scattering occurs by the kinematic law. The intensities of 021, 002, 022, and 152 reflections were corrected for primary extinction in the Blackman two-beam approximation by the technique described elsewhere [12] with the calculated average effective crystallite thicknesses being $t_{av} = 324$ Å.

The lepidocrocite structure was refined within the sp. gr. *Cmcm* with the use the coordinates of nonhydrogen atoms of the ideal model as the starting coordinates. The LSM refinement of the coordinates and the thermal parameters of Fe and O atoms on the difference *x*0*z* and 0*yz* sections of the Fourier potential revealed the maximum elongated in the direction of the *c*-axis with its center being on twofold symmetry axis parallel to the *b*-axis. The maximum was attributed to a hydrogen atom (Fig. 1). The observed anisotropy in the distribution of the electrostatic potential indicates the possible superposition of two maxima located in the plane *m* normal to the *a*-axis and related by the twofold axis, which correspond to the statistic (with the probability 1/2) occupancy by hydrogen atoms of the positions displaced from the twofold axes. The refinement of the lepidocrocite structure with the split hydrogen position by the least-squares method in the anisotropic approximation up to $R = 0.048$ yielded the atomic coordinates and the anisotropic thermal parameters listed in Table 1 and the interatomic distances listed in Table 2. The structure refinement with hydrogen atom on the twofold axis up to $R = 0.049$ indicated much more pronounced thermal vibrations along the *c*-axes, which, in turn, indicated that hydrogen atoms are statistically distributed over the structure.

Taking into account the possible ordered distribution of H atoms over one of two statistically occupied positions, the lepidocrocite structure was also refined in the noncentrosymmetric sp. gr. $Cmc2_1$ (to $R = 0.054$). Lepidocrocite structures refined within the sp. gr. *Cmcm* and $Cmc2_1$ showed the most pronounced differences in the *z*-coordinates of the O(1) and O(2) atoms. However, the *z*-coordinates refined in the sp. gr. $Cmc2_1$ yield the standard deviations exceeding the differences

Table 1. Atomic coordinates and anisotropic thermal parameters ($Å^2 \times 10^{-4}$) for the lepidocrocite structure

Atom	*x*/*a*	*y*/*b*	*z*/*c*	B_{11}	B_{22}	B_{33}	B_{23}
Fe	1/2	0.1778(1)	1/4	62(12)	15(1)	127(10)	
O(1)	0	0.2889(4)	1/4	108(36)	22(3)	112(29)	
O(2)	0	0.0738(4)	1/4	105(42)	24(3)	212(31)	
H	0	–0.001(3)	0.179(10)	360(240)	30(27)	300(212)	–5(154)

Table 2. Interatomic distances (Å) in the lepidocrocite structure

Octahedron				Interlayer space	
Fe–O(1) × 2	2.072(3)	O(1)–O(1) × 4	2.657(3)	O(2)–H	0.97(3)
–O(1) × 2	1.981(1)	O(1)–O(2) × 2	2.692(7)	H–O(2)	1.89(3)
–O(2) × 2	2.013(3)	O(1)–O(1) × 4	3.010(4)	O(2)–O(2)	2.676(4)
Average	2.022	O(1)–O(1)	3.072(2)		
		O(2)–O(2)	3.072(2)		
		Average	2.850		

in the *z*-coordinates of oxygen atoms in these structures. Moreover, the H atoms in the sp. gr. $Cmc2_1$ are characterized by a considerable increase of atomic thermal vibrations along the *c*-axis. Thus, the electron-diffraction refinement of the lepidocrocite structure justified the choice of the sp. gr. *Cmcm* and disordered distribution of H atoms over two positions.

The interatomic distances in the lepidocrocite structure are O(2)–H = 0.97(3), H···O(2)' = 1.89(3), and O(2)···O(2)' = 2.676(5) Å; the angle O(2)–H···O(2)' equals 135°. The angle θ formed by the O–H vector with the [010] direction equals 17°. Figure 2 shows the positions statistically occupied by H atoms in the interlayer spaces of lepidocrocite structure. In fact, the H atoms in the structure occupy one of two positions (H or H') and form two different types of chains of hydrogen bonds (solid and dashed lines). Disordering can be caused by the variations either inside the chains of one type or in the chains of both types. As is seen from Fig. 2, each oxygen atom of hydroxyl groups participates in the formation of two hydrogen bonds—either as a donor or as an acceptor.

The average interatomic Fe^{3+}–O distance equals 2.022 Å (in goethite α-FeOOH [13] and hematite F_2O_3 [14]); the interatomic distances $(Fe^{3+}–O)_{av}$ are equal to 2.021 and 2.025 Å, respectively. The Fe–Fe distance for Fe atoms located within one octahedral lepidocrocite sheet equals 3.072(2) Å; in the adjacent octahedral sheets, 2.062(2) Å; whereas the shared octahedron edges are equal to 2.692(7) and 2.657(3) Å, with the average O–O distance in the octahedron being 2.850 Å. The octahedron distortions are caused by the necessity of screening the mutual repulsion of Fe^{3+} cations. Thus, an increase in the Fe–Fe distance within one octahedral sheet is caused by a considerable elongation of the octahedron edge in the direction of the *a*-axis (3.072 Å) in comparison with edge elongation in the direction of the *b*-axis (2.692 Å), so that the octahedron section by the *ab* plane is an elongated rectangle and not a square. An additional increase in the Fe–Fe distance in the adjacent octahedral sheets of the double layer is attained due to stagger of octahedron vertices [the O(1) atoms] along the *b*-axis. In the projection onto the *ab* plane, the octahedron vertices are displaced by 0.37 Å from the center

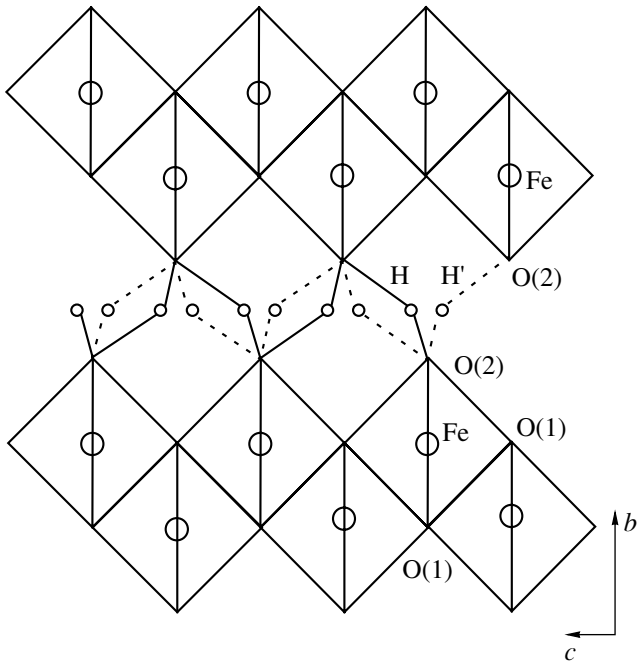

Fig. 2. Hydrogen bonding in the lepidocrocite structure, H and H' are the hydrogen positions statistically (with the probability of 1/2) occupied by hydrogen atoms located in the plane *m* normal to the *a*-axis. Solid and dashed lines indicate two types of chains of hydrogen bonds, O(2)–H···O(2) and O(2)–H'···O(2).

of the rectangle and, thus, give rise to the additional displacement of the octahedral sheets along the *b*-axis with respect to one another in the layer (in an ideal structure, this displacement equals 1/8*b*).

Comparing the electron-diffraction data for lepidocrocite, the most reliable single-crystal X-ray diffraction data for boehmite refinement [4] and the powder neutron-diffraction data (the Rietveld analysis) for the deuterium analogue of boehmite [6] with the unit-cell parameters $a = 2.865$, $b = 12.221$, $c = 3.693$ Å, we see the essential similarity of the structural features of individual layers. The octahedra in these structures are distorted in a similar way, the individual *M*–O distances in the octahedra are also distributed in the same way. Thus, the distances from the octahedral cation to the oxygen atom of the hydroxyl group in lepidocrocite and boehmite are approximately equal to the average *M*–O distance, which is determined by the valence strength *1* for this oxygen atom from the side of the octahedral cations. Despite different unit-cells parameters *b*, the distances between the closest oxygen atoms of hydroxyl groups in the adjacent layers are almost the same (2.676 for lepidocrocite and 2.705 Å for boehmite), which is explained by a certain increase of the interlayer distance in boehmite (1.977 Å) in comparison with this distance in lepidocrocite (1.847 Å).

The most pronounced differences were revealed for hydrogen positions. At the statistical distribution (with the probability 1/2) of hydrogen atoms characteristic of both structures, the hydrogen (deuterium) atom is located in the vicinity of the line connecting the oxygen atoms of the adjacent layers, the O(2)–H···O(2)' angle is 176° [4] and 179° [6] at the interatomic O–H distance 0.75 Å (H was determined from the difference electron-density synthesis without using the LS procedure) and 0.97°, respectively. According to the electron diffraction data, hydrogen atoms in lepidocrocite are located in the vicinity of the twofold axis (the O(2)–H···O(2)' angle equals 135°) at a distance of 0.27 Å from it. It should also be indicated that according to the calculation of the energy by the semiempirical method of molecular orbitals suggested by Hückel for a boehmite cluster consisting of nine hydrogen atoms, the minimum energy was obtained for θ-angle ranging within 22°–32° depending on the orientation of hydroxyl groups OH [4], which corresponded better to the angle θ obtained for lepidocrocite (17° in this study and 31.8° in [5]) than for boehmite (45° [4] and 44° [6]). The angle θ determined for lepidocrocite by the electron diffraction data is on the side of smaller angles, whereas the angle θ determined for lepidocrocite in [3, 5] and boehmite in [4, 6], on the side of large angles with respect to the indicated range of θ angles corresponding to the minimum energy.

ACKNOWLEDGMENTS

The author is grateful to B.B. Zvyagin for his interest in this study and useful discussions. The study was supported by the Russian Foundation for Basic Research, project no. 99-05-65430.

REFERENCES

1. F. J. Ewing, J. Chem. Phys. **3**, 420 (1935).
2. A. Oles, A. Szytula, and A. Wanic, Phys. Status Solidi **41**, 173 (1970).
3. N. Christensen and A. N. Christensen, Acta Chem. Scand. A **32** (1), 87 (1978).
4. R. J. Hill, Clays Clay Miner. **29** (6), 435 (1981).
5. A. N. Christensen, M. S. Lenmann, and P. Convert, Acta Chem. Scand. A **36** (4), 303 (1982).
6. C. E. Corbato, R. N. Tettenhorst, and G. G. Christoph, Clays Clay Miner. **33** (1), 71 (1985).
7. A. P. Zhukhlistov, A. S. Avilov, D. Ferraris, *et al.*, Kristallografiya **42** (5), 841 (1997) [Crystallogr. Rep. **42**, 774 (1997)].
8. A. P. Zhukhlistov and B. B. Zvyagin, Kristallografiya **43** (6), 1009 (1998) [Crystallogr. Rep. **43**, 950 (1998)].
9. B. B. Zvyagin, A. P. Zhukhlistov, and V. P. Plotnikov, in *Structural Studies of Minerals* (Nauka, Moscow, 1996), p. 228.
10. B. K. Vainshtein, *Structure Analysis by Electron Diffraction* (Akad. Nauk SSSR, Moscow, 1956; Pergamon, Oxford, 1964).
11. V. I. Andrianov, Kristallografiya **32** (1), 228 (1987) [Sov. Phys. Crystallogr. **32**, 130 (1987)].
12. B. K. Vainshtein, B. B. Zvyagin, and A. S. Avilov, in *Electron Diffraction Techniques* (Oxford Univ. Press, Oxford, 1992), Vol. 1, p. 216.
13. J. B. Forsyth, I. G. Hedley, and C. E. Johnson, J. Phys. C **1**, 179 (1968).
14. R. E. Newnham and Y. M. Haan, Z. Kristallogr. **117**, 235 (1962).

Translated by L. Man

Crystallography Reports, Vol. 46, No. 5, 2001, pp. 734–740. Translated from Kristallografiya, Vol. 46, No. 5, 2001, pp. 809–815.

STRUCTURE OF INORGANIC COMPOUNDS

Dedicated to the memory of B.K. Vainshtein

Atomic Structure of Boron Suboxycarbide $B(C,O)_{0.155}$

N. B. Bolotina[1], T. I. Dyuzheva[2], and N. A. Bendeliani[2]

[1] *Shubnikov Institute of Crystallography, Russian Academy of Sciences, Leninskiĭ pr. 59, Moscow, 117333 Russia*

e-mail: bolotina@ns.crys.ras.ru

[2] *Vereshchagin Institute of High-Pressure Physics, Russian Academy of Sciences, Troitsk, Moscow oblast, 142092 Russia*

Received December 26, 2000

Abstract—The structure of a high-pressure boron suboxycarbide $B(C,O)_{0.1555}$ single crystal has been studied for the first time. The unit-cell parameters are $a_h = 5.618(1)$, $c_h = 12.122(1)$ Å, $V = 331.38(1)$ Å^3, sp. gr. $R\bar{3}m$, $R_{hkl} = 0.0479$. The established common structural features of the interstitial rhombohedral α-boron-based B(C,O) phases and the data on the known carbides and boron suboxides allowed the characterization of the new phase. © *2001 MAIK "Nauka/Interperiodica".*

INTRODUCTION

Interstitial phases based on the rhombohedral α-boron modification have long attracted the attention of researchers because of their physical–mechanical properties. Unlike the well studied boron carbides, the oxygen-containing compounds—suboxides—and, to a lesser degree, boron suboxycarbides have become the objects of systematic study only in the past ten years. The successful synthesis of these compounds under high pressures allowed the variation of the number and the assortment of the interstitial atoms over wide ranges. However, the insufficient reaction volume, characteristic of the high-pressure experiments, and small atomic weights of the elements create certain difficulties for determination of both chemical composition and density, and, thus, determination of the number of atoms in the unit cell of the interstitial phase synthesized. The absence of the data on the corresponding single crystals is one of the factors that hinder the structural diagnostics of boron suboxides and suboxycarbides. The known boron suboxides have the composition B_6O_{1-x} and are characterized by a certain deficit of oxygen atoms (up to the $x = 0.28$). The concepts on their atomic structure are based on the postulated models refined by the powder diffraction data with the use of the Rietveld method [1–4]. The structural models of boron suboxycarbide have never been discussed at such a level. The present article describes the results of the X-ray diffraction analysis of the boron suboxycarbide $B(C, O)_x$ single crystal synthesized under high pressures.

EXPERIMENTAL

The brown–red transparent crystals up to 250 μm in size were obtained as a result of the one-hour chemical reaction between B_4C and B_2O_3 compounds in the 1 : 1 ratio in a boron-nitride container under a pressure of 5.5 GPa and a temperature of 1400 K. The single crystal selected for the X-ray diffraction study had a flake-like shape with the maximum linear dimension of about 100 μm. The chemical composition was calculated as follows. It was established that crystals are trigonal with the rhombohedral unit-cell parameters a = 5.182(1) Å and α = 65.65(1)° (or the hexagonal parameters of the *R*-cell $a_h = 5.618(1)$, $c_h = 12.122(1)$ Å, $V = 331.38(1)$ Å^3. The X-ray diffraction experiment in the hexagonal setting was performed on an automated RED-4 X-ray diffractometer with a graphite monochromator, MoK_α-radiation. At the stage of data collection, we recorded 842 diffraction reflections with noticeable intensities within a reciprocal-space hemisphere ($l \geq 0$, $\sin\theta/\lambda < 0.9$). Upon averaging the intensities of the crystallographically equivalent reflections in the diffraction class $\bar{3}m$ (*R* factor 0.0398), the further structure study was performed in the sp. gr. $R\bar{3}m$ over the data set containing 191 independent reflections with the intensities $I > 3\sigma(I)$.

SELECTION OF STRUCTURE MODEL

The preliminary analysis confirmed that the crystal structure of the specimen and the structures of the known α-boron-based interstitial phases are of the same type (Fig. 1). The structure framework is formed by slightly distorted B_{12} or $B_{11}C$ icosahedra with the

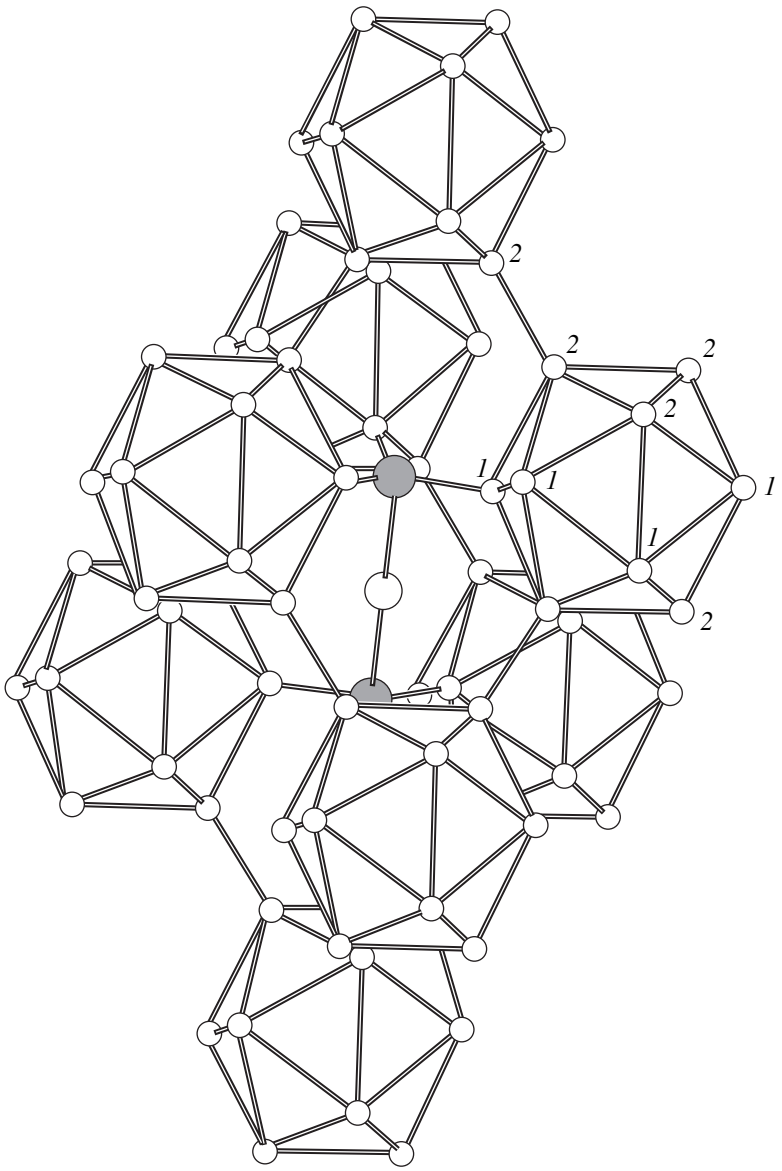

Fig. 1. Fragment of the $B(C,O)_x$ structure. The centers of the $B_{11}C$ icosahedra form a rhombohedral unit cell. Figures *1* and *2* indicate the positions of B(1) and B(2) atoms, respectively. The filled circles on the threefold axis of the rhombohedron indicate the atoms of the linear groups in the side positions, the open circle indicates the atom in the central position.

centers coinciding with the points of the rhombohedral lattice. Six atoms in the icosahedron bind the polyhedron with six other polyhedra along the five-fold axis of the icosahedron. The remaining six atoms form a corrugated hexagon along the icosahedron perimeter. The voids between the icosahedra are filled with B, C, and O atoms located on the threefold axes and forming the linear groups consisting of three (sometimes, two) atoms. Each of the boron atoms located along the icosahedron perimeter is related to five atoms of the given icosahedron and the side atom of the linear group.

The color and the degree of transparency of the specimen characteristic of boron suboxycarbides allowed us to identify it with the phase of the composition B(C,O) formed due to the replacement of some carbon atoms in the initial $B(C,O)_x$, structure by boron and oxygen. According to the modern concepts [5, 6], the B_4C structure is built by $B_{11}C$ icosahedra and linear CBC groups. The preliminary estimation shows that the chemical effect of B_2O_3 is the most important for the linear groups. The calculations indicate that different distributions of atoms in the linear groups can provide equally low *R*-factors. It was reliably established that the occupancy of the central 3*b* (0, 0, 1/2) position was always lower than 100%, although it depended on the kind of the chosen atom. The side positions 6*c* (0, 0, 1/2 $\pm\delta$) were always fully occupied. It was established that filling the side positions with the atoms of different kinds

Table 1. Unit-cell parameters of α-boron-based carbides and suboxides

Compound	a_h(Å)	c_h(Å)	V(Å^3)	Z	x	V/Z	$V/Z(1)$	S
B_{12} [7]	4.927(3)	12.564(7)	264.13	36	0	7.337	7.336	36
$B_{19}C$ [8]	5.640(20)	12.165(5)	335.12	41	0.10	8.174	8.180	45.1
$B_{9.3}C$ [9]	5.6720(3)	12.1428(2)	338.32	41.33	0.107	8.185	8.233	45.77
$B_{13}C_2$ [10]	5.633(1)	12.164(2)	334.26	39	0.154	8.571	8.565	45
B_4C [11]	5.6039(4)	12.079(1)	328.51	36	0.25	9.125	9.127	45
$B_6O_{0.96}$ [4]	5.3902(1)	12.3125(2)	309.80	36	0.16	8.605	8.606	41.76
$B_6O_{0.93}$ [1]	5.374(2)	12.331(3)	308.41	36	0.155	8.567	8.572	41.58
$B_6O_{0.89}$ [4]	5.3872(1)	12.3152(3)	309.53	36	0.148	8.598	8.525	41.33
$B_6O_{0.87}$ [1]	5.362(2)	12.328(3)	306.96	36	0.145	8.527	8.504	41.22
$B_6O_{0.84}$ [3]	5.3761(3)	12.326(1)	308.52	36	0.14	8.570	5.470	41.04
$B_6O_{0.79}$ [3]	5.3824(4)	12.322(1)	309.15	36	0.132	8.587	8.414	40.75
$B_6O_{0.77}$ [1]	5.367(1)	12.328(2)	307.53	36	0.128	8.543	8.386	40.61
$B_6O_{0.77}$ [4]	5.3696(4)	12.3258(6)	307.77	36	0.128	8.549	8.386	40.61
$B_6O_{0.72}$ [2]	5.361(1)	12.340(1)	307.14	36	0.12	8.532	8.329	40.32

Note: a_h and c_h are the parameters of the hexagonal unit cell, V is the unit-cell volume, Z is the number of B(C, O)$_x$ formula units per unit cell, $S = Z(1 + x)$ is the number of atoms per unit cell; $(V/Z)(1)$ are the values calculated by Eq. (1).

in the proportion providing the effective scattering power of the position, z_{eff}, approximately equal to the scattering power of carbon z_C also lead to reduction of the reliability factor. Similar information was also obtained from the Fourier syntheses of electron density. It was shown that two ratios are valid in all the models with different formulas of the linear groups characterized by low reliability factors: the electron density in the positions of the side-group was always 6/5, whereas in the central position, it was 95% of the z_B value for the icosahedral positions. This fact allowed us to predict the number of atoms in the structure unit cell. To provide the necessary value of $z_{eff} = z_C$ in the side positions (which can contain the atoms of all the three kinds), the members of oxygen and boron atoms should relate as 1 : 2. Unlike the rust-color nontransparent B_4C crystals, the reddish crystal studied was transparent. This indicates that the considerable number of oxygen atoms are incorporated into the crystal. Since oxygen atoms can hardly occupy the positions in icosahedra, we made an attempt to place oxygen atoms into the central position in a linear group. In the first approximation, the side positions were filled with carbons. We begin the process at 95%-occupancy of the central position with boron, and start replacing boron with small amounts of oxygen with the introduction of the corresponding corrections into z_{eff}. The minimum R-value was attained when the position contained 2.32 boron and 0.33 oxygen atoms. Unfortunately, we have no other data which would have allowed us to state that, in principle, oxygen can fill the central position. According to the known data, the centers of the linear groups in boron carbides are usually occupied by boron and not carbon atoms. The structure model containing only boron atoms in the centers of the groups is considered in the Discussion section. The other kinds of atoms were distributed over the structure positions proceeding from the other established facts which are discussed below.

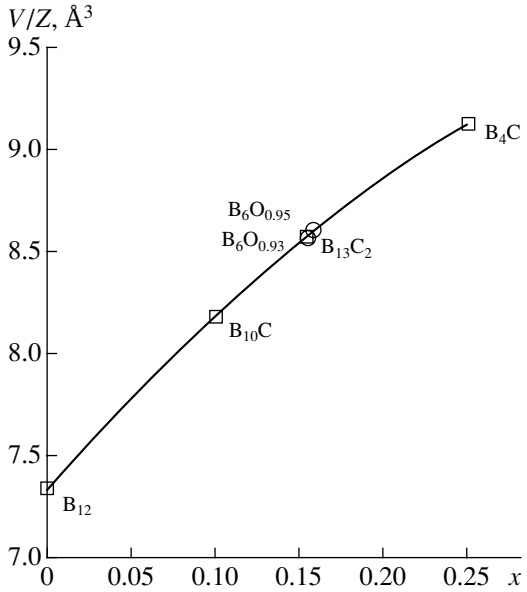

Fig. 2. Specific volume of the unit cell V/Z as a function of x for α-boron and boron carbides (squares) and suboxides (circles).

COMPOSITION AND STRUCTURE

The x value in the formula unit B(C,O)$_x$ and the number of such formula units per unit cell were calcu-

Table 2. Occupancies, positional and thermal atomic parameters u_{ij} (Å^2) in the B(C, O)$_{0.155}$ structure

Atom	Occupancy	x/a	z/c	u_{11}	u_{22}	u_{12}	u_{13}
B(1)	1	0.1680(4)	0.6413(5)	0.1039(8)	0.095(3)	0.060(1)	−0.005(1)
B(2)	1	0.2296(5)	0.7771(4)	0.094(1)	0.099(3)	0.046(2)	0.002(1)
(B, C, O)	1	0	0.6215(5)	0.114(2)	0.069(4)	0.057(1)	0
(B, O)	0.88	0	0.5	0.047(4)	0.180(5)	0.024(2)	0

Note: $y/b = x/a$; the temperature factor is defined as $\exp(2\pi^2 \Sigma h_i h_j a_i^* a_j^* u_{ij})$; for the B(1) and B(2) atoms, $u_{22} = u_{11}$, $u_{23} = -u_{13}$, and for the remaining atoms $u_{22} = u_{11}$, $u_{12} = u_{11}/2$, $u_{23} = u_{13} = 0$.

lated with the use of the following empirical dependence. As is seen from Table 1 listing the data on the well-known boron carbides and suboxides, the specific unit-cell volume V/Z per formula unit B(C,O)$_x$ is a monotonic function of x. We used as such a function the second-order polynomial with the coefficients obtained by linear approximation from the reliable structure data for α-boron and some of the related carbon-containing compounds (B_4C, $B_{13}C_2$, and $B_{10}C$),

$$V/Z = 7.336 + 9.296x - 8.534x^2, \quad (1)$$

where V is the unit-cell volume and Z is the number of the formula units in the unit cell. This dependence is illustrated by Fig. 2. As is seen, the figurative points of boron suboxides $B_6O_{0.95}$ and $B_6O_{0.93}$ fit this plot quite satisfactorily. This allows us to assume the universal character of the dependence determined for the interstitial α-boron-based phases of the general composition B(C, O)$_x$. Knowing the total number of atoms in the unit cell $S = Z(1 + x)$, one can readily select the appropriate x value. In our case, we have $S = 44.65$, $V = 331.38$ Å^3, whence, using Eq. (1), we obtain $x = 0.155$; the number of boron atoms in the unit cell is $Z = 38.66$, the number of non-boron atoms in the unit cell is $Zx = 5.99$. According to the modern concepts on the structure of the known boron carbides, three carbon atoms occupy the positions in icosahedra. Subtracting 0.33 oxygen atom in the central position from Zx, we arrive at 2.66 non-boron atoms and 3.34 boron atoms in the six side positions. Among the non-boron atoms, we have 1.67 of oxygen atoms (50% of boron atoms) and 0.99 of carbon atoms. Different atoms are distributed over the unit cell in the following way: 1.67 + 0.33 = 2.0 of oxygen atoms, 3 + 0.99 = 3.99 of the carbon atoms, and 33 + 3.34 + 2.32 = 38.66 of boron atoms. Now, let us analyze the model thus constructed with due regard of the mechanism of the transitions from the B_4C to the $B_{13}C_2$ structure suggested in [5]. According to [5], the linear CBC groups characteristic of B_4C are gradually replaced by the BBC groups and, upon the completion of the group replacement (which corresponds to the composition $B_{13}C_2$), a further increase in boron concentration is accompanied by the replacement of the $B_{11}C$ icosahedra by B_{12}. Unfortunately, we have not had access to the complete text of the article [5]. The interpretation of the results obtained in [5] and made in [12] can be understood in such a way that upon the attainment of the 50% boron concentration in the side positions, boron cannot be incorporated into the linear groups any more and is incorporated into icosahedra. Extending the facts observed in boron carbides to boron suboxycarbides, we modified the above model in such a way that the six side positions included only 3 (instead of 3.34) boron atoms, 1.5 oxygen atoms, and 1.5 carbon atoms, whereas 0.34 of a boron atom replaced carbon in icosahedra. On the whole, the modified unit cell contains 1.5 + 0.33 = 1.83 oxygen atoms and 1.5 + (3 – 0.34) = 4.16 carbon atoms. If one assumes that the replacement occurs in both icosahedra and linear groups simultaneously, then there are 1.83–2 oxygen atoms and 4.16–3.99 carbon atoms in the unit cell.

The structural parameters were refined by the LS method over the set of the structure factors F within the sp. gr. $R\bar{3}m$ with the use of the weighting scheme $w(F) = 1/\sigma^2(F) + (0.01F)^2$. The values of the weighted and conventional R factors upon the refinement by the JANA98 program [13] are $R = R_w = 0.0479$, the $GOF = 2.57$. The

Table 3. The elements of the tensors of the third to the sixth order for the parameters of anharmonic thermal vibrations in the Gram–Charlier expansion

*C*111	*C*112	*C*113	*C*122	*C*123	*C*133
*C*222	*C*223	*C*233	*C*333		
*D*1111	*D*1112	*D*1113	*D*1122	*D*1123	*D*1133
*D*1222	*D*1223	*D*1233	*D*1333	*D*2222	*D*2223
*D*2233	*D*2333	*D*3333			
*E*11111	*E*11112	*E*11113	*E*11122	*E*11123	*E*11133
*E*11222	*E*11223	*E*11233	*E*11333	*E*12222	*E*12223
*E*12233	*E*12333	*E*13333	*E*22222	*E*22223	*E*22233
*E*22333	*E*23333	*E*33333			
*F*111111	*F*111112	*F*111113	*F*111122	*F*111123	*F*111133
*F*111222	*F*111223	*F*111233	*F*111333	*F*112222	*F*112223
*F*112233	*F*112333	*F*113333	*F*122222	*F*122223	*F*122233
*F*122333	*F*123333	*F*133333	*F*222222	*F*222223	*F*222233
*F*222333	*F*223333	*F*233333	*F*333333		

Table 4. Parameters of anharmonic thermal vibrations of atoms in the $B(C, O)_{0.155}$ structure

B(1)	−0.148(15)	−0.085(3)	0.011(5)	0.085(3)	−0.014(5)	−0.015(2)
	0.148(15)	0.011(5)	0.015(2)	−0.005(2)		
	−0.192(13)	−0.155(2)	0(0)	−0.200(3)	0(0)	0(0)
	−0.155(2)	0(0)	−0.008(3)	0.005(1)	−0.192(13)	0(0)
	0(0)	−0.005(1)	−0.007(1)			
	−0.532(13)	−0.255(1)	−0.025(5)	−0.0661(5)	−0.031(2)	−0.010(2)
	0.066(5)	−0.0153(4)	0(0)	0.0043(8)	0.255(1)	−0.031(2)
	0(0)	0.0047(9)	−0.0030(4)	0.532(13)	−0.025(5)	0.010(2)
	0.0043(8)	0.0030(4)	−0.0009(4)			
	−1.29(3)	−0.781(6)	−0.029(11)	−0.547(1)	−0.044(3)	−0.020(3)
	−0.439(2)	−0.0216(3)	−0.008(1)	0.006(1)	−0.547(1)	0.0216(3)
	−0.0061(2)	0(0)	−0.0052(7)	−0.781(6)	0.044(3)	−0.008(1)
	0(0)	−0.0030(7)	0(0)	−1.29(3)	0029(11)	−0.020(3)
	−0.006(1)	−0.0052(7)	0(0)	−0.0029(4)		
B(2)	0(0)	0(0)	0.025(4)	0(0)	0.015(4)	−0.003(1)
	0(0)	0.025(4)	0.003(1)	−0.005(1)		
	−0.22(2)	−0.039(14)	0.036(6)	0(0)	0.015(2)	−0.021(2)
	−0.039(14)	−0.015(2)	−0.027(3)	0.002(1)	−0.22(2)	−0.036(6)
	−0.021(2)	−0.002(1)	−0.006(1))			
	−0.11(2)	−0.044(7)	0.033(5	−0.0230(8)	0.012(2)	−0.004(2)
	0.0230(8)	0.0113(5)	−0.0017(5)	0.0058(9)	0.044(7)	0.012(2)
	0.0017(5)	0.006(1)	0(0)	0.11(2)	0.033(5)	0.004(1)
	0.0058(9)	0(0)	0(0)			
	−0.607(51)	−0.244(17)	0.075(9)	−0.274(1)	0.045(2)	−0.042(2)
	−0.271(2)	0.0125(3)	−0.0291(8)	0.002(1)	−0.274(1)	−0.0125(3)
	−0.0260(2)	0(0)	−0.0037(7)	−0.244(17)	−0.045(2)	−0.0291(8)
	0(0)	−0.0035(7)	0(0)	−0.607(51)	−0.075(9)	−0.042(2)
	−0.0002(1)	−0.0037(7)	0(0)	−0.0049(7)		
(B, C, O)	−0.254(18)	−0.127(9)	−0.027(8)	0.127(9)	−0.013(4)	0
	0.254(18)	−0.027(8)	0	−0.003(1)		
	−0.47(4)	−0.235(21)	−0.033(12)	−0.235(21)	−0.016(6)	−0.026(4)
	−0.235(21)	0.016(6)	−0.013(2)	0	−0.47(4)	0.033(12)
	−0.026(4)	0	0.0048(7)			
	−0.500(17)	−0.250(8)	0.051(14)	−0.050(2)	0.026(7)	0.012(2)
	0.050(2)	0.026(7)	0.006(1)	−0.009(1)	0.250(8)	0.026(7)
	−0.006(1)	−0.0044(7)	0	0.500(17)	0.051(14)	−0.012(2)
	−0.009(1)	0	−0.0007(1)			
	−0.38(5)	−0.19(3)	0(0)	−0.36(4)	0.023(16)	−0.083(7)
	−0.44(6)	0(0)	−0.042(3)	−0.002(1)	−0.36(4)	0(0)
	−0.042(3)	0(0)	0(0)	0	0(0)	−0.042(3)
	0(0)	0(0)	0	0	0(0)	−0.083(7)
	0(0)	0(0)	0	0.0010(1)		
(B, O)	0.12(3)	0.058(14)	0(0)	0.058(14)	0(0)	−0.095(11)
	0.058(14)	0(0)	−0.048(6)	0	0.12(3)	0(0)
	−0.095(11)	0	−0.034(6)			
	0.058(14)	0.029(7)	−0.029(13)	0(0)	−0.014(7)	−0.012(4)
	0(0)	−0.003(1)	−0.007(2)	0(0)	0(0)	0.003(1)
	−0.07(2)	0.002(1)	−0.037(6)	0	0.014(7)	−0.007(2)
	−0.002(1)	−0.018(3)	0	0	0.029(13)	−0.014(4)
	0(0)	−0.037(6)	0	−0.049(2)		

Note: The values C(Å^3), D(Å^4), E(Å^5), and F(Å^6) are multiplied by 10^3, 10^4, 10^5, and 10^6, respectively. In the (B, O) position, no odd-order zero tensors (C and E) exist.

occupancies, coordinates of the atomic positions, and the parameters of anisotropic thermal vibrations are listed in Table 2. Table 3 lists the elements of the tensors of orders from three to six for the parameters of anharmonic thermal vibrations in the Gram–Charlier expansion. Table 4 lists the parameters of anharmonic thermal vibration of atoms in the $B(C,O)_{0.155}$ structure and Table 5, the interatomic distances.

DISCUSSION OF RESULTS

Consider first the model with only boron in the centers of the linear groups. At the 95% occupancy of the central position with boron, the total number of the atoms in the unit cell amounts to 44.85. The calculation by Eq. (1) yields $x = 0.191$, $Zx = 7.19$, and $Z = 37.66$. Thus, one can readily see that if the unit cell contains 7.19 non-boron atoms, the side positions can contain only 0.9 of an oxygen atom. Such a low oxygen percentage would have hardly provided the color of the crystal and its transparency observed experimentally. At the same time, the oxygen fraction in the centers of groups cannot be high, because its increase would have been accompanied by a reduction of the total number of atoms in the unit cell. At $x = 0.11$, this number is minimal, 44.59, i.e., only slightly differs from the established value of 44.65.

The question about the causes of vacancy formation in the central positions of the linear groups is still open. One can assume that the linear CBC groups characteristic of boron carbides and the BBC groups [5] can hardly lose the central atom. From the geometrical consideration it follows that such a loss is most probable for the BBB groups. The typical B–B bond lengths ranging within 1.60–1.85 Å are inconsistent with the value determined in our study, 1.465 Å. If the atoms of the BBB triad are to be located along the space diagonal of the rhombohedron, they should either be displaced from the calculated positions or push out the central atom from its position. In our model with the 44.65 atoms per unit cell, the percentage of vacancies in the center is low, whereas the percentage of boron in the side position is quite considerable. Therefore, it is most probably that most vacancies in the centers correspond not to the B–B but to the oxygen pairs as is the case in boron suboxides of the composition B_6O_{1-x}.

The approach to diagnostics of new interstitial phase in the B–C–O system suggested here was tested on other similar phases. Thus, in [12], two compounds were considered, which, in accordance with the results obtained by the PEELS method, have the composition $B_6C_{1.1}O_{0.33}$ with the unit cell volume 325.5 Å^3 and $B_6C_{1.28}O_{0.31}$ with the unit cell volume 327 Å^3. Substituting the value $x = 0.238$ into Eq. (1) for the first compound, we obtain $Z = 35.89$, $Zx = 8.54$, and $S = 44.43$. For the second compound at $x = 0.265$, we have $Z = 35.57$, $Zx = 9.43$, and $S = 44.99$. The structures of similar interstitial phases of the general composition have not been studied as yet, but, in accordance with the unit-cell parameters, they should be similar to the structure considered in our article. This allows us to compare these compounds with our structure. The number of atoms in the unit cell of the first structure (44.43) makes it similar to our structure (the number of atoms in the unit cell 44.65). It should also have a considerable number of vacancies in the central position. Comparing this structure with the structures studied here, we see that the number of non-boron atoms is considerably higher (8.54 in comparison with 5.99 in our structure), whereas the fraction of boron atoms is lower (35.89 in comparison with 38.66 in our structure). An increase of the fraction of atoms with a lower value of the effective radius agrees with the lower value of the unit-cell volume (325.5 Å^3 in comparison with 331.38 Å^3 for our structure). It should also be indicated that the O/C ratio in the $B_6C_{1.1}O_{0.33}$ and $B_6C_{1.28}O_{0.31}$ structures equals 0.30 and 0.24, respectively. Our models contain a higher fraction of oxygen with respect to carbon, 0.50–0.44, although the total percentage of non-boron atoms with respect to boron is rather low—15.5 instead of 23.8 and 26.5% in the two above indicated structures.

Table 5. Interatomic distances in the $B(C, O)_{0.155}$ structure

Atoms	Distance, Å	Type of bonding
B(1)–B(1)	1.727(5) × 2	in the icosahedron face
B(1)–B(2)	1.740(7) × 2	in the icosahedron face
B(1)–B(2)	1.757(9)	in the icosahedron face
B(2)–B(2)	1.769(5) × 2	in the icosahedron face
B(2)–B(2)	1.815(6)	between icosahedra
B(1)–(B, C, O)	1.655(4)	icosahedron–linear group
(B, C, O)–(B, O)	1.465(10)	linear group–linear group

Concluding the article, return to the analysis of Table 1. The second part of this table lists the known data on boron suboxides of the composition B_6O_{1-x}. The compounds $B_6O_{0.95}$ and $B_6O_{0.93}$ fit the plot in Fig. 2 quite well, but with an increase of deficit in oxygen, the (V/Z) values obtained from the structural data start differing from the $(V/Z)_f$ values and form a curve running above the plot. We can only assume that, with an approach to the ordinate axis, the second curve either dramatically decreases in order to pass through the point of the α-boron or there is no smooth transition from boron suboxides to pure boron at all, or, else, the structural data on boron suboxides are somewhat erroneous. If the empirical characteristics established in our work are correct, then the unit cells of all the remaining phases (except for $B_6O_{0.95}$ and $B_6O_{0.93}$) should contain either more oxygens in the linear groups of the side positions or some additional boron atoms in the side or central positions.

ACKNOWLEDGMENTS

This study was supported by the Russian Foundation for Basic Research, projects nos. 98-03-32736, 00-15-96633, and 00-02-16636.

REFERENCES

1. M. Kobayachi, I. Hogachi, C. Brodhag, and F. Thevenot, J. Mater. Sci. **28**, 2129 (1993).
2. T. Lundstom and H. Bolmgren, in *Proceedings of the 11th International Symposium on Boron, Borides and Related Compounds, Tsukuba, 1993*, Ed. by R. Uno and I. Higashi, JJAP Ser. **10**, 1 (1994).
3. T. Lundstom and Y. G. Andreev, Mater. Sci. Eng., A **209**, 16 (1996).
4. H. Hubert, L. A. J. Garvie, B. Devouard, *et al.*, Chem. Mater. **10**, 1530 (1998).
5. D. Emin, Mater. Res. Soc. Symp. Proc. **97**, 3 (1987).
6. H. Ripplinger, K. Schwarz, and P. Blaha, J. Solid State Chem. **133** (1), 51 (1997).
7. B. Morozin, A. W. Mullendore, D. Emin, and G. A. Slack, in *Boron-Rich Solids*, Ed. by D. Emin *et al.* (American Inst. of Physics, New York, 1986), AIP Conf. Proc. **140**, 70 (1986).
8. D. Gosset and M. Colin, J. Nucl. Mater. **183**, 161 (1991).
9. H. L. Yakel, Acta Crystallogr., Sect. B: Struct. Crystallogr. Cryst. Chem. **B31**, 1797 (1975).
10. A. Kirfel, A. Gupta, and G. Will, Acta Crystallogr., Sect. B: Struct. Crystallogr. Cryst. Chem. **B35**, 1052 (1979).
11. A. C. Larson, in *Boron-Rich Solids*, Ed. by D. Emin *et al.* (American Inst. of Physics, New York, 1986), AIP Conf. Proc. **140**, 109 (1986).
12. H. Hubert, L. A. J. Garvie, P. R. Buseck, *et al.*, J. Solid State Chem. **133**, 356 (1997).
13. *JANA'98: Crystallographic Computing System*, Ed. by V. Petricek and M. Dusek (Inst. of Physics, Prague, 1998).

Translated by L. Man

Crystallography Reports, Vol. 46, No. 5, 2001, pp. 741–747. Translated from Kristallografiya, Vol. 46, No. 5, 2001, pp. 816–822.

STRUCTURE OF INORGANIC COMPOUNDS

Dedicated to the memory of B.K. Vainshtein

Synthesis and X-ray Diffraction Study of $K_{2.92}Nb_{2.58}Ti_{1.42}P_{2.5}O_{17}$ Single Crystals

O. A. Alekseeva[1], N. I. Sorokina[1], I. A. Verin[1], T. Yu. Losevskaya[2], V. I. Voronkova[2], V. K. Yanovskiĭ[2], and V. I. Simonov[1]

[1] *Shubnikov Institute of Crystallography, Russian Academy of Sciences, Leninskiĭ pr. 59, Moscow, 117333 Russia*

e-mail: zalexandr@mtu-net.ru

[2] *Moscow State University, Vorob'evy gory, Moscow, 119899 Russia*

Received May 10, 2001

Abstract—Single crystals of the composition $K_{2.92}Nb_{2.58}Ti_{1.42}P_{2.5}O_{17}$ possessing ionic conductivity $\sigma = 10^3\ \Omega^{-1}\ cm^{-1}$ at 300°C were grown by the method of spontaneous crystallization from flux in the quaternary K_2O–TiO_2–Nb_2O_5–P_2O_5 system. The X-ray diffraction study of the single crystals grown showed that they are monoclinic with the unit-cell parameters $a = 13.800(1)$, $b = 6.412(2)$, $c = 16.893(3)$ Å, $\beta = 83.33(1)°$, $Z = 16$, sp. gr. $P2/n$ and provided the determination of the structure of this new compound. The Nb and Ti atoms statistically (with different probabilities) occupy four crystallographically independent octahedra. The (Nb,Ti) and P-tetrahedra form the three-dimensional framework with the channels along the diagonal [101] direction occupied by potassium atoms. *© 2001 MAIK "Nauka/Interperiodica".*

INTRODUCTION

The systematic studies of the rich family of crystals with the $KTiOPO_4$ (KTP) structure are dictated by the unique set of physical properties inherent in these compounds. All these compounds have a ferroelectric phase transition, superionic conductivity, and nonlinear optical properties. The establishment of the regular relationships between the atomic structure and the physical properties of crystals allows the purposeful change of the above characteristics of the crystals with the aid of isomorphous replacements. The special attention of the researchers is attracted to KTP-type crystals with isomorphous additions of Nb atoms (KTNP) [1, 2]. Doping with niobium considerably increases the ionic conductivity and birefringence of the crystals. The crystals with titanium partly replaced by niobium seem to be a very promising material for increasing the frequency of the yttrium–aluminum garnet-based lasers [3, 4]. However, as was shown in [5], the KTP-type structure is also preserved if a crystal is doped only with a small amount of niobium (up to 11.3 at. % Nb in [5]). If the niobium concentration exceeds the titanium concentration, the crystals have a different symmetry and atomic structure. We had the aim to grow single crystals with high niobium concentration and perform their complete X-ray diffraction study.

GROWTH OF SINGLE CRYSTALS AND THEIR INITIAL STUDY

The crystals were grown by the method of spontaneous crystallization from flux in the quaternary K_2O–TiO_2–Nb_2O_5–P_2O_5 system. Two different initial melts were used—with the same content of K_2O (40 mol %) and P_2O_5 (27 mol %) and different concentration ratio of niobium and titanium Nb/(Nb + Ti)—66.6 and 75.5 at. %. In the course of the growth experiments, the mixture of K_2CO_3, Nb_2O_5, TiO_2, and $NH_4H_2PO_4$ reagents of extrapure grade was heated up to 600°C to remove the volatile components, crushed into powder, milled in an agate ball mill, and then was placed into 50-ml-large platinum crucibles and subjected to resistive heating at temperatures up to 1100°C. For further homogenization, the melts were kept for 24 h at this temperature and then were cooled at a rate of 1 deg/h down to 850°C. The remaining melt was poured out, the crystals grown on the crucible walls were cooled at a rate of 20 deg/h down to room temperature and washed from the solvent in hot water. The crystals thus obtained had the dimensions of the order of several millimeters. They were well faceted and transparent. According to the X-ray microanalysis data, the composition of KTNP crystals can be written as $K_{2.85}Ti_{1.31}Nb_{2.62}P_{2.62}O_{17}$ and $K_{2.64}Ti_{1.07}Nb_{2.68}P_{2.55}O_{17}$, the hydrostatic density measured in toluene equals 3.63 ± 0.01 and 3.45 ± 0.01 g/cm^3, respectively. The analysis of the growth form of the crystals indicated the point

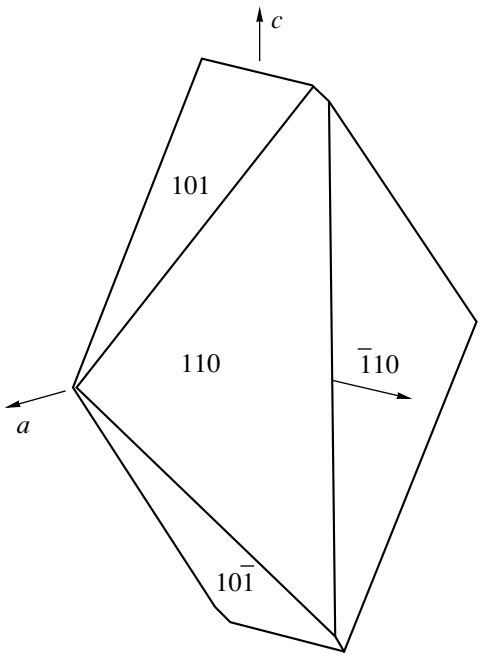

Fig. 1. Typical morphology of KTNP crystals.

symmetry group 2/*m*. The typical faceting consisted of rhombic prisms and pinacoids (Fig. 1). X-ray diffraction patterns obtained on a DRON-2.0 diffractometer confirmed that the crystals are monoclinic with the unit-cell parameters a = 13.804, b = 6.413, c = 16.918 Å, $\beta = 83°$ and a = 13.768, b = 6.407, c = 16.938 Å, $\beta = 83°$. The structure of these crystals was determined in our earlier study [6].

The temperature dependence of the dielectric constant measured on specimens of different orientations at a frequency of 1 MHz in the temperature range from room temperature to 900°C showed no anomalies. Electric conductivity of the crystals seems to be purely ionic and equals $10^{-3}\ \Omega^{-1}\ cm^{-1}$ at 300°C. Thus, the ionic conductivity of these crystals with respect to potassium ions is close to the conductivity of the best superionics. Both checking of a possible piezoelectric effect by the static method test and for the second optical-harmonics generation by the Kurtz method gave negative results. This indicates the possible existence of the center of inversion in the crystals. This conclusion is also consistent with the growth forms observed for single crystals.

X-RAY DIFFRACTION ANALYSIS

The complete X-ray diffraction analysis was performed on a single crystal obtained from the initial melt with 66.6 at. % Nb. The spherical samples for X-ray diffraction study were obtained from an optically homogeneous crystal. The experiment was performed on one of these samples (0.216(3) mm in diameter), which gave the best X-ray diffraction pattern. The experiment was performed on a CAD-4F Enraf-Nonius diffractometer (MoK_α radiation, graphite monochromator, $\omega/2\theta$ scan, $(\sin\theta/\lambda)_{max} = 1.0$). The reflection intensities were recorded within the reflection hemisphere of the reciprocal space. The total number of recorded reflections with $I \geq 3\sigma_I$ was 15625. The analysis of the data set confirmed that crystals are monoclinic. The reflection intensities were recalculated into the structure-factor moduli with due regard for the Lorentz and polarization factors and X-ray radiation absorption in the sample with $\mu = 3.605\ mm^{-1}$. Upon averaging of the symmetrically equivalent structure factors, the working set of reflections consisted of 7860 independent structure factors. The reliability factor of averaging was R = 1.58%, which indicated a high quality of the experimental data set. The parameters of the monoclinic unit cell were refined by the least squares method over 24 reflections: a = 13.800(1), b = 6.412(2), c = 16.893(3) Å, $\beta = 83.33(1)°$. The analysis of the extinction law indicated two possible space groups—acentric *Pn* and centrosymmetric *P*2/*n*. The crystal properties indicate that the space group *P*2/*n* (Z = 16) is preferable. It was also confirmed by the structure refinement by the JANA'96 package of programs [7]. The initial model of the structure was taken from [6], where a $K_{2.47}Nb_{2.85}Ti_{1.15}P_{2.5}O_{17}$ crystal was studied. The most serious difficulty in the structure refinement was associated with the determination of the Nb and Ti positions in four independent octahedra and localization of potassium atoms in the structure channels. Considering the data [6] and the chemical composition of the crystal, we assumed that all the octahedra are 100% occupied with isomorphous mixtures of Nb and Ti atoms. The X-ray diffraction data provided the most reliable localization of niobium (the heaviest atoms of the structure, Z_{Nb} = 41), whereas titanium atoms (Z_{Ti} = 22) complement the occupancy of each of the four octahedra to 100%. As a result of the refinement, the occupancies of the octahedral positions were determined as follows: $(Nb_{0.73}Ti_{0.27})$ (1), $(Nb_{0.75}Ti_{0.25})$ (2), $(Nb_{0.45}Ti_{0.55})$ (3), and $(Nb_{0.65}Ti_{0.35})$ (4). Thus, similar to the structure of $K_{2.47}Nb_{2.85}Ti_{1.15}P_{2.5}O_{17}$, the Ti atoms in the structure studied enter all the four niobium positions with different probabilities.

The difference electron-density syntheses revealed the residual electron-density peaks of various heights in the vicinity of all four (Nb,Ti) positions (Fig. 2). Their formation can be caused either by the different electronic structure of the Ti and Nb atoms resulting in their slightly different positions in octahedra or by the noticeable anharmonism of thermal vibrations of these atoms. The attempt to split the Ti and Nb positions in the refinement process revealed strong correlations between the structural parameters, which did not allow the creation of a reliable model of Ti and Nb distribution over two close positions. Then we analyzed the variant of the interpretation of the residual electron-density maps with due regard for anharmonic thermal vibrations of Ti and Nb atoms located in the same posi-

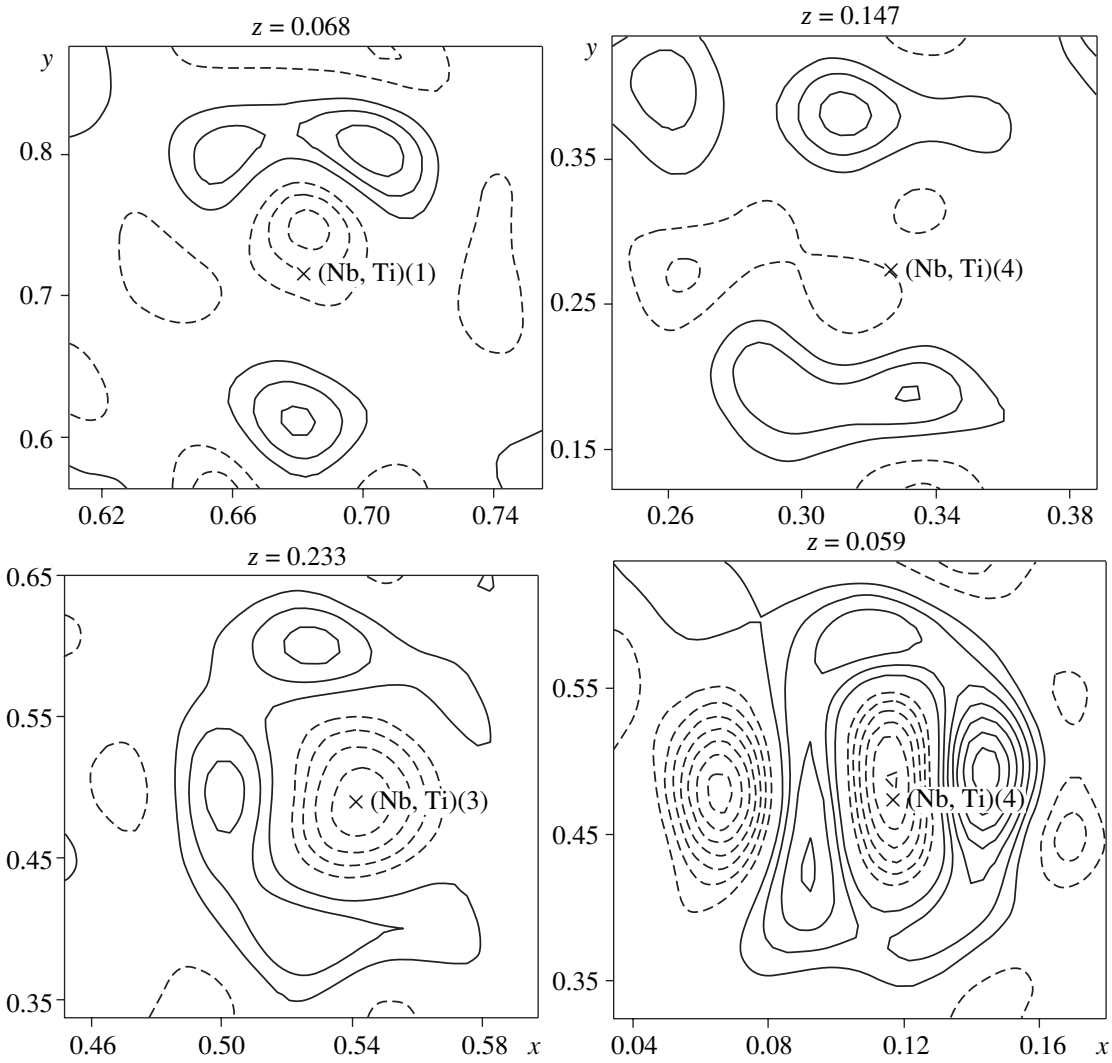

Fig. 2. Sections of the difference electron-density distribution in the vicinity of the (Nb,Ti) atoms [(1), (2), (3), and (4)]. The result of the structure refinement with due regard for the anisotropy of atomic thermal vibrations.

tion. The anharmonism of thermal vibrations was taken into account by expanding the probability density function of atomic displacements from the equilibrium position into the Gram–Charlier series with allowance for the terms up to the fourth order. The difference electron-density syntheses calculated with due regard for anharmonism (Fig. 3) show the adequate allowance for the electron-density distribution in the vicinity of Nb and Ti atoms.

The localization of potassium atoms was more difficult. Similar to the $K_{2.47}Nb_{2.85}Ti_{1.15}P_{2.5}O_{17}$ structure, the K(1) and K(2) atoms have close coordinates and 100% occupancies, whereas the situation with the remaining potassium atoms has changed. Figures 4a and 4b present the sections of the difference electron-density syntheses showing the K(3) atom in the $K_{2.47}Nb_{2.85}Ti_{1.15}P_{2.5}O_{17}$ structure and the structure studied here. The syntheses are constructed upon the structure refinement with due regard for anharmonism of thermal vibrations of (Nb, Ti) atoms and harmonic thermal vibrations of the K, P, and O atoms. These syntheses clearly show the differences in the positions of K(3) atom and the existence of additional potassium positions in both structures. In the $K_{2.47}Nb_{2.85}Ti_{1.15}P_{2.5}O_{17}$ structure, the position of the K(3) atom is split into two positions spaced by 1.07 Å, whereas in the structure studied in this work, the K(3) position is split into four positions hereafter denoted as K(4) (with occupancy 0.330) spaced by 1.857 Å from the K(3) atom; K(5) (with occupancy 0.265) spaced by 1.139 Å from the K(3) atom. The attempts to localize the K(6) atom spaced a distance of 0.909 Å from the K(5) atom encountered some difficulties because of the correlation in the coordinates of the K(5) and K(6) atoms, occupancies of these positions, and thermal vibrations of the atoms located in these positions. To overcome these difficulties, we used the refinement with the step-by-step scanning of strongly correlating parameters [8].

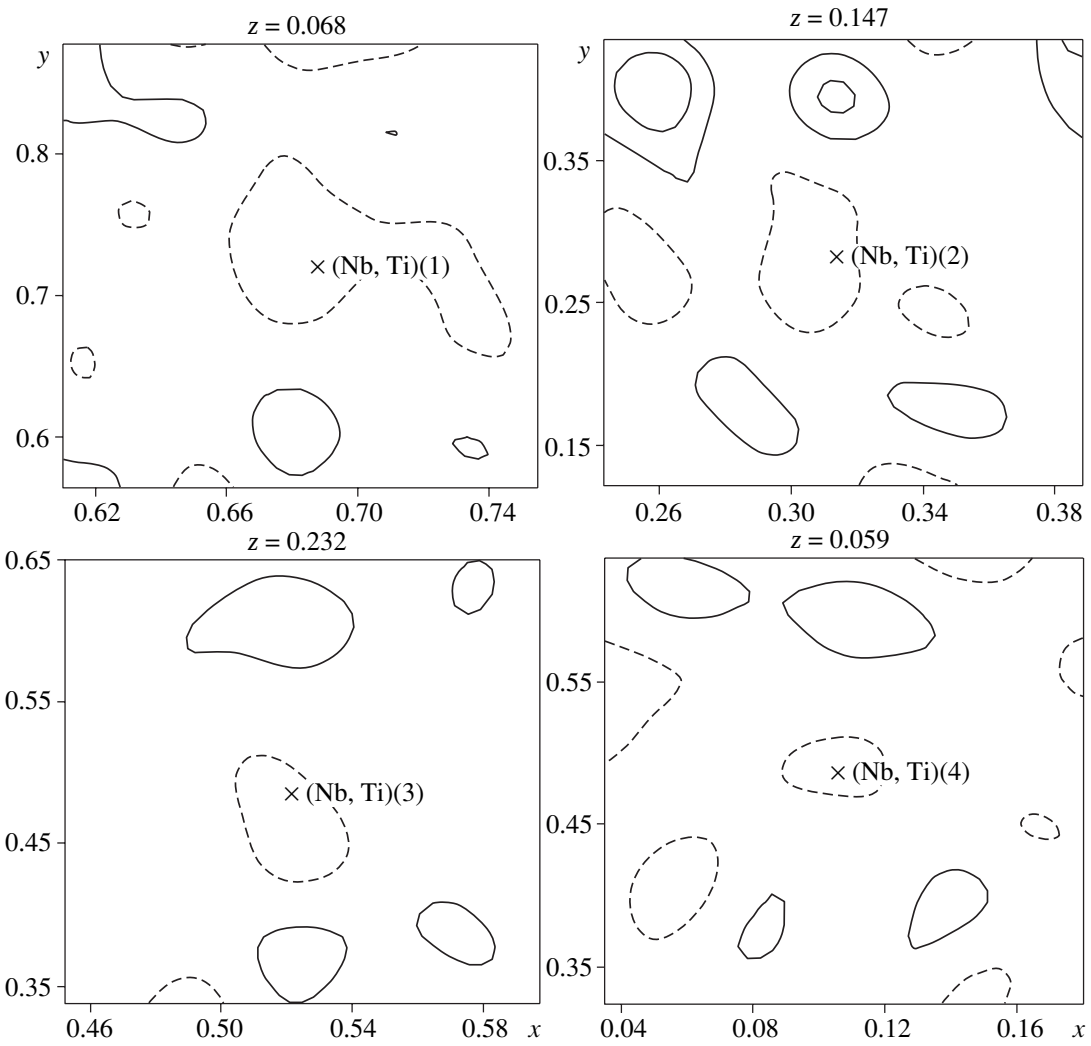

Fig. 3. Sections of difference electron-density distribution similar to the sections in Fig. 2 upon the structure refinement with due regard for the anharmonism of atomic thermal vibrations.

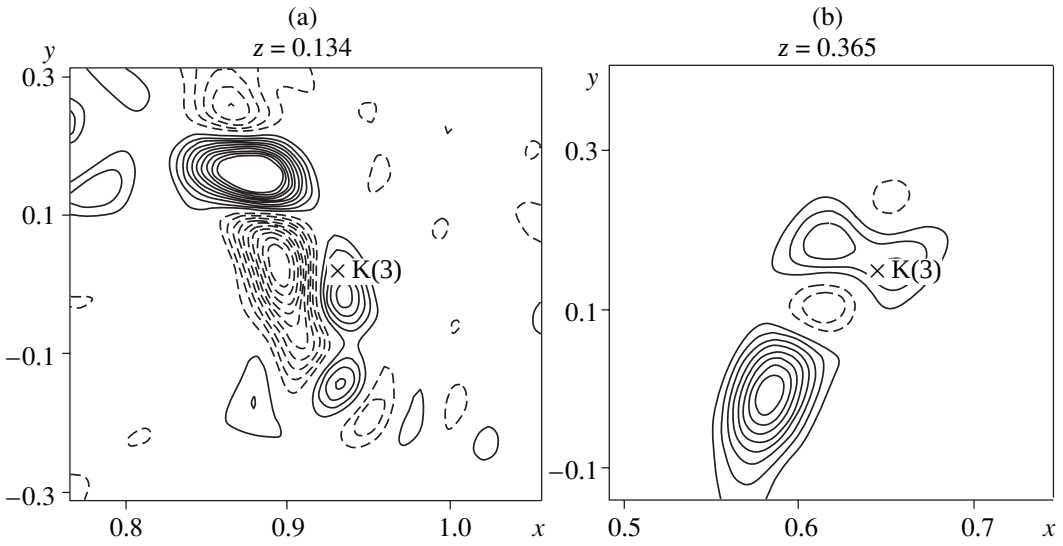

Fig. 4. Sections of difference electron-density distribution in the vicinity of the K(3) atom for the (a) $K_{2.92}Nb_{2.58}Ti_{1.42}P_{2.5}O_{17}$ and (b) $K_{2.47}Nb_{2.85}Ti_{1.15}P_{2.5}O_{17}$ structures.

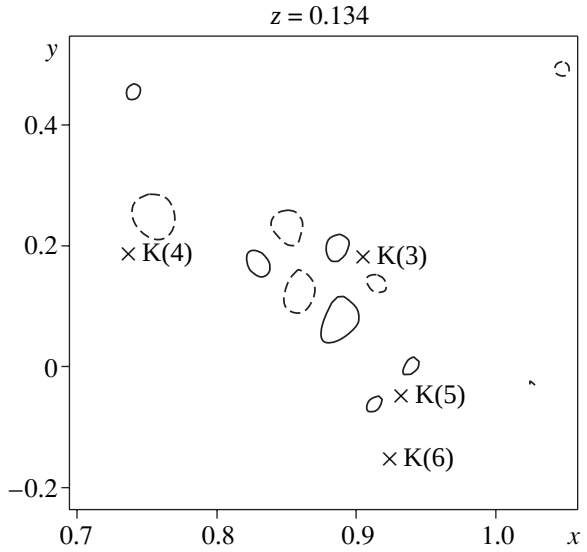

Fig. 5. Section of difference electron-density distribution for the model of the $K_{2.92}Nb_{2.58}Ti_{1.42}P_{2.5}O_{17}$ structure with the statistical distribution of potassium atoms over four independent positions, K(3), K(4), K(5), and K(6) (the section passes through these atoms).

We consistently fixed the occupancy of the position by the K(6) atom at a step of 0.01 and refined the coordinates and the thermal parameters of all the atoms of the structure including the occupancy by the K(5) atom of its position. For K(5) and K(6) atoms, this procedure yielded the following parameters: $q_{K(5)} = 0.265$ and $q_{K(6)} = 0.383$. Using these parameters, we constructed the zeroth electron-density synthesis. Figure 5 shows the section of this synthesis that reveals the K(3), K(4), K(5), and K(6) atoms. The final structure-model refinement was performed with due regard for the Becker–Coppens correction for extinction with the misorientation of the blocks of the crystal mosaics (type 1). The refinement was performed up to the conventional and the weighted reliability factors $R = 2.38$ and $Rw = 2.78\%$, respectively.

The coordinates of the basis atoms of the structure, occupancies q of the crystallographic positions with atoms, and the equivalent isotropic parameters of their thermal motion B_{eq} are indicated in the table. Using the occupancy values, the refined chemical formula of the crystal can be written as $K_{2.92}Nb_{2.58}Ti_{1.42}P_{2.5}O_{17}$.

DISCUSSION OF RESULTS

The $K_{2.92}Nb_{2.58}Ti_{1.42}P_{2.5}O_{17}$ crystal structure [64.50 at. % Nb/(Nb + Ti)] is a three-dimensional framework of sharing-vertex $(Nb,Ti)O_6$-octahedra and PO_4-tetrahedra. Similar to the $K_{2.47}Nb_{2.85}Ti_{1.15}P_{2.5}O_{17}$ structure [71.25 at. % Nb/(Nb + Ti)] [7], the framework of the structure has two types of the channels along the diagonal [101] direction (Fig. 6) filled with K^+ cations. Some K^+ cations concentrated in a wider channel [the average distances are K(1)–O 2.95 Å, K(2)–O 3.14 Å] are localized with the occupancy of 100% as is the case in the $K_{2.47}Nb_{2.85}Ti_{1.15}P_{2.5}O_{17}$ structure. However, the distribution of potassium cations in a narrower channel differs from that observed in the latter structure, where not two but four positions of potassium atoms exist (the average distances are K(3)–O 3.04, K(4)–O 2.85, K(5)–O 3.00, and K(6)–O 2.99 Å and the probabilities of the K(3) occupancy are 44, K(4) 33, K(5) 27, and K(6) 38%).

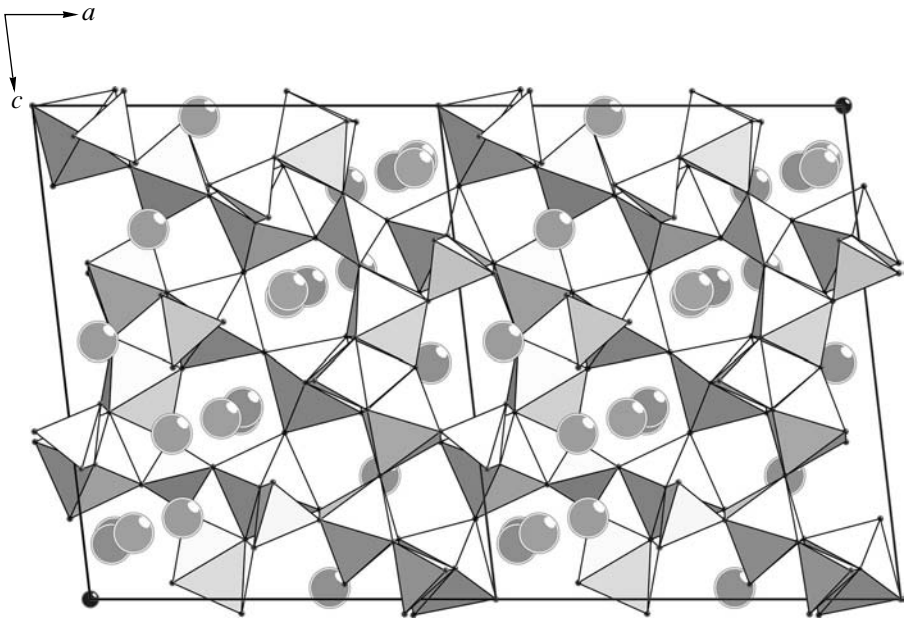

Fig. 6. The model of the KTNP structure: $(Nb,Ti)_6$ octahedra and PO_4-tetrahedra; K atoms are represented by spheres.

Atomic coordinates, position occupancies (q), and the equivalent isotropic thermal parameters B_{eq} (Å^2) in the $K_{2.92}Nb_{2.58}Ti_{1.42}P_{2.5}O_{17}$ structure

Atom	*x*/*a*	*y*/*b*	*z*/*c*	*q*	$Ç_{eq}$
Nb(1)	0.68269(1)	0.72020(3)	0.06812(1)	0.730(1)	0.56(1)
Ti(1)	0.68269(1)	0.72020(3)	0.06812(1)	0.270(1)	0.56(1)
Nb(2)	0.31587(1)	0.27830(3)	0.14726(1)	0.747(1)	0.66(1)
Ti(2)	0.31587(1)	0.27830(3)	0.14726(1)	0.253(1)	0.66(1)
Nb(3)	0.52473(1)	0.49378(3)	0.23224(1)	0.451(1)	0.74(1)
Ti(3)	0.52473(1)	0.49378(3)	0.23224(1)	0.549(1)	0.74(1)
Nb(4)	0.10760(1)	0.48072(3)	0.05948(1)	0.648(1)	1.23(1)
Ti(4)	0.10760(1)	0.48072(3)	0.05948(1)	0.352(1)	1.23(1)
K(1)	0.25	0.77332(6)	0.25	1	2.22(1)
K(2)	0.40685(2)	0.75557(5)	0.02214(2)	1	2.52(1)
K(3)	0.8782(1)	0.1518(2)	0.13382(6)	0.442(2)	4.45(4)
K(4)	0.74801(7)	0.2188(1)	0.16247(6)	0.330(1)	2.02(2)
K(5)	0.9193(1)	–0.0023(5)	0.12702(9)	0.265(2)	4.04(6)
K(6)	0.93296(6)	–0.1372(2)	0.11350(5)	0.383(2)	2.15(2)
P(1)	0.51492(1)	0.99604(3)	0.18145(1)	1	0.53(1)
P(2)	0.17016(1)	0.99465(3)	0.05130(1)	1	0.52(1)
P(3)	0.75	0.65682(5)	0.25	1	0.59(1)
O(1)	0.51566(5)	0.8049(1)	0.23643(4)	1	0.79(1)
O(2)	0	0.5	0	1	0.88(2)
O(3)	0.02753(5)	0.4824(1)	0.16298(4)	1	0.88(1)
O(4)	0.79230(5)	0.5533(1)	0.03269(4)	1	0.80(1)
O(5)	0.36893(5)	0.2823(1)	0.02991(4)	1	0.81(1)
O(6)	0.54897(5)	0.1855(1)	0.22665(4)	1	0.83(1)
O(7)	0.58223(5)	0.9619(1)	0.10405(4)	1	0.97(1)
O(8)	0.22349(5)	0.4681(1)	0.12245(4)	1	0.78(1)
O(9)	0.40916(5)	0.4639(1)	0.18104(4)	1	0.82(1)
O(10)	0.60087(5)	0.5282(1)	0.12061(4)	1	0.85(1)
O(11)	0.11516(5)	0.7873(1)	0.05739(4)	1	0.87(1)
O(12)	0.09218(5)	0.1678(1)	0.06150(4)	1	0.89(1)
O(13)	0.83999(5)	0.5147(1)	0.23241(4)	1	0.86(1)
O(14)	0.23778(5)	0.0095(1)	0.11630(4)	1	0.86(1)
O(15)	0.74044(5)	0.7942(1)	0.17702(4)	1	0.83(1)
O(16)	0.77038(5)	–0.0110(1)	0.03063(4)	1	0.77(1)
O(17)	0.25	0.2223(1)	0.25	1	0.97(2)
O(18)	0.41137(5)	0.0282(1)	0.16035(4)	1	0.93(1)

Compare the arrangement of (Nb,Ti) atoms over four positions in the $K_{2.47}Nb_{2.85}Ti_{1.15}P_{2.5}O_{17}$ and the structure studied. The Nb occupancies in these positions in $K_{2.92}Nb_{2.58}Ti_{1.42}P_{2.5}O_{17}$ was determined as $q_{Nb(1)} = 0.73$, $q_{Nb(2)} = 0.75$, $q_{Nb(3)} = 0.45$, and $q_{Nb(4)} = 0.65$. For the $K_{2.47}Nb_{2.85}Ti_{1.15}P_{2.5}O_{17}$ structure, the occupancies are somewhat different: $q_{Nb(1)} = 0.86$, $q_{Nb(2)} = 0.80$, $q_{Nb(3)} = 0.53$, and $q_{Nb(4)} = 0.67$ [6]. It is seen that with an increase of the Nb content from 64.50 at. % (the $K_{2.92}Nb_{2.58}Ti_{1.42}P_{2.5}O_{17}$ structure) to 71.25 at. % (the $K_{2.47}Nb_{2.85}Ti_{1.15}P_{2.5}O_{17}$ structure), its distribution over the positions becomes nonuniform. The increase in the Nb content is maximal for the (Nb,Ti)(1) position ($\Delta q_{Nb(1)} = 0.13$), then there follow the positions (Nb,Ti)(3) ($\Delta q_{Nb(3)} = 0.08$), ($\Delta q_{Nb(2)} = 0.05$), and (4) ($\Delta q_{Nb(4)} = 0.02$). As is well known [8, 9], niobium atoms have the tendency to deviate from the center of the oxygen octahedron coordinating them

with the variation in the distances of the type 3 + 3 (three short distances in the *trans*-positions to three long ones), or 2 + 2 + 2, or 1 + 4 + 1. In the TiO_6 octahedra, the distances to six oxygen atoms usually almost coincide, however, one has to indicate, that in the compounds with the $KTiOPO_4$-type structure, the distances to four equatorial oxygen atoms in TiO_6 octahedra are practically equal, whereas the Ti–O distances to axial oxygen atoms are considerably different [10]. Similar to the $K_{2.47}Nb_{2.85}Ti_{1.15}P_{2.5}O_{17}$ structure, one can separate in the structure studied here, the (Nb,Ti)(1) and (Nb,Ti)(2) octahedra with high Nb concentration and three long (Nb,Ti)–O distances (2.126, 2.133, 2.146 and 2.032, 2.113, 1.230 Å, respectively) and three short ones (1.834, 1.886, 1.886 and 1.845, 1.895, 1901 Å, respectively). For two other octahedra with a higher Ti-concentration, (Nb,Ti)(3) and (Nb,Ti)(4), one can separate the shortest (Nb,Ti)–O distance (1.831 and 1.882 Å, respectively) and the longest one (2.058 and 2.035 Å, respectively). The four remaining (Nb,Ti)–O distances for these octahedra range within 1.916–2.019 and 1.950–2.015 Å, respectively. The average values of the (Nb,Ti)–O distances in the octahedra are as follows: (Nb,Ti)(1) 2.002, (Nb,Ti)(2) 1.986, (Nb,Ti)(3) 1.970, and (Nb,Ti)(4) 1.9971 Å.

The synthesis of the niobium compound $K_5Nb_8P_5O_{34}$ was reported in [11]. A polycrystal was obtained by the method of solid-phase synthesis in vacuum at 1000°C. The parameters of the monoclinic unit cell were reported as a = 13.874, b = 6.456, c = 20.622 Å, β = 124.96° and the sp. gr. $P2/c$. However, changing the setting by the transformations $\mathbf{A} = \mathbf{a}$, $\mathbf{B} = \mathbf{b}$, and $\mathbf{C} = \mathbf{a} + \mathbf{c}$, we obtained different unit-cell parameters A = 13.874, B = 6.456, C = 17.026 Å, β' = 83.06°, sp. gr. $P2/n$. To preserve the balance of valences in the $K_{2.5}Nb_4P_{2.5}O_{17}$ compound in our notation, one has to assume that some niobium atoms are in the reduced four-valent state $K_{2.5}(Nb^{5+})_3(Nb^{4+})P_{2.5}O_{17}$ and play the role of titanium always present in the form of Ti^{4+} cations in our compounds.

ACKNOWLEDGMENTS

This study was supported by the Russian Foundation for Basic Research, projects nos. 00-02-16059, 01-02-06407, 00-02-017802 and the Federal Program on Support of Prominent Scientists and Leading Scientific Schools, project no. 00-15-96633.

REFERENCES

1. P. A. Thomas and B. E. Watts, Solid State Commun. **73** (2), 97 (1990).
2. T. Yu. Losevskaya, E. P. Kharitonova, V. I. Voronkova, *et al.*, Kristallografiya **44** (1), 95 (1999) [Crystallogr. Rep. **44**, 90 (1999)].
3. L. T. Cheng, L. K. Cheng, R. L. Harlow, and J. D. Bierlein, Appl. Phys. Lett. **64** (2), 155 (1994).
4. J. Wei, J. Wang, Y. Liu, *et al.*, Chin. Phys. Lett. **13** (3), 203 (1996).
5. T. Yu. Losevskaya, O. A. Alekseeva, V. K. Yanovskiĭ, *et al.*, Kristallografiya **45** (5), 809 (2000) [Crystallogr. Rep. **45**, 739 (2000)].
6. O. A. Alekseeva, N. I. Sorokina, M. K. Blomberg, *et al.*, Kristallografiya **46** (2), 215 (2001) [Crystallogr. Rep. **46**, 176 (2001)].
7. *JANA'96: Crystallographic Computing System*, Ed. by V. Petricek and M. Dusek (Inst. of Physics, Prague, 1996).
8. L. A. Muradyan, S. F. Radaev, and V. I. Simonov, in *Methods of Structural Analysis* (Nauka, Moscow, 1989), p. 5.
9. T. S. Chernaya, B. A. Maksimov, I. A. Verin, *et al.*, Kristallografiya **42** (3), 421 (1997) [Crystallogr. Rep. **42**, 375 (1997)].
10. J. Tordjman, R. Masse, and J. C. Guitel, Z. Kristallogr. **139**, 103 (1974).
11. A. Leklaire, M. Guerioune, M. Borel, *et al.*, Eur. J. Solid State Inorg. Chem. **29**, 473 (1992).

Translated by L. Man

Crystallography Reports, Vol. 46, No. 5, 2001, pp. 748–751. Translated from Kristallografiya, Vol. 46, No. 5, 2001, pp. 823–826.

STRUCTURE OF INORGANIC COMPOUNDS

Low-Temperature Structural Variations and Interlayer Charge Transfer in Cuprate Superconductors

S. Sh. Shil'shtein[1], I. P. Makarova[2], and V. N. Molchanov[2]

[1] *Russian Research Centre Kurchatov Institute, Moscow, pl. Kurchatova 1, 123182 Russia*

[2] *Shubnikov Institute of Crystallography, Russian Academy of Sciences, Leninskiĭ pr. 59, Moscow, 117333 Russia*

e-mail: vladimol@ns.crys.ras.ru

Received October 30, 2000

Abstract—The analysis of the structural variations in cuprates with different types of conductivity has shown that cooling from room temperature prior to the transition into the superconducting state results in transfer of a small part of the charge (approximately several hundredths of an electron charge per unit cell) from the reservoir to the conducting layers. The sign of the charge corresponds to the conductivity type and is positive for a hole conductor and negative for an electron one. © *2001 MAIK "Nauka/Interperiodica".*

INTRODUCTION

The study of the specific features of the structural variations in high-temperature superconductors, especially in the range of the transition to the superconducting state, attracts the ever growing attention of experimentalists despite numerous difficulties associated with the solution of this problem. In some studies [1–4], specific behavior of interatomic distances in the direct vicinity of the critical temperature for cuprates with the hole-type conductivity was revealed (e.g., of the length of the apical copper–oxygen bond), although the small changes in the positional parameters observed in these studies practically did not exceed the experimental errors. Below, we analyze the results of the structural studies of doped cuprates with electron conductivity [5, 6] in terms of the concepts that explain the observed atomic displacements by the charges of the neighboring layers. It is shown that above the critical temperature, all doped cuprates are characterized by the temperature-dependent charge transfer between the layers prior to the transition into the superconducting state.

ANALYSIS OF EXPERIMENTAL DATA

The most typical experimental data on the structural changes in cuprates with hole conductivity and its relation to the charge transfer were obtained for the BaO layer in the lattice of all these cuprates located between the conducting CuO_2 layer and the MeO_δ layer (the charge reservoir) (Fig. 1). The BaO layer interacting with the neighboring layers having opposite charges is split into two layers with the barium ions being displaced toward the negatively charged conducting layer and the oxygen ions being displaced toward the positively charged layer (the so-called reservoir). As follows from the empirically established correlation [7], splitting Δ is a linear function of the difference Q in the charges of the neighboring layers, Q_1 and Q_2. For BaO layers it has the form

$$\Delta \sim (Q_1 - Q_2)/4 = Q/4, \quad (1)$$

where splitting is measured in angstroms and the charges, in the *e*-units (where *e* is the electron charge); the latter are normalized to the unit cell. Knowing the splitting value and using relationship (1), one can directly obtain information about the variations in the charges of the neighboring layers [8, 9].

The analysis of the structural changes was performed by determining the splitting value in the BaO layer from the positional parameters obtained in the original studies and constructing the corresponding temperature dependence. It is well known that the variations in the layer charge change, in turn, the splitting values of these layers [8, 9]. Therefore, we assumed

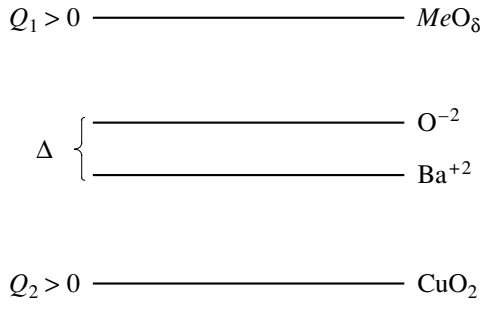

Fig. 1. Schematic arrangement of the layers in cuprates with the hole conductivity (MeO_δ corresponds to the HgO_δ layer in mercury cuprates; TlO, in thallium cuprates; and CuO, in yttrium–barium cuprates). For notation see the text.

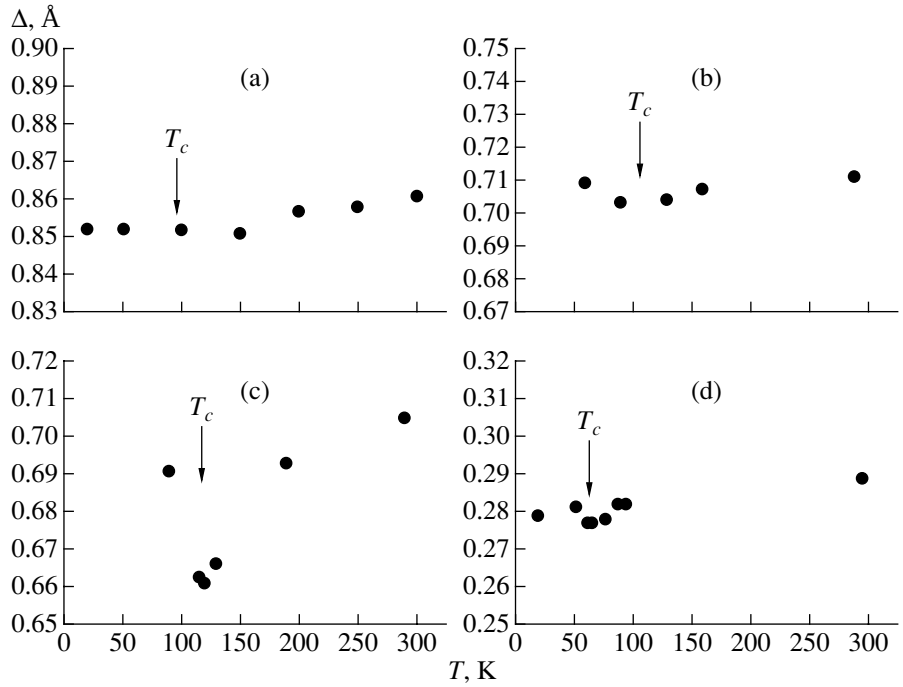

Fig. 2. Temperature variation of splitting (Δ) of the BaO layer in (a) mercury cuprate 1201, (b) thallium cuprate 2212, (c) thallium cuprate 2223, and (d) yttrium–barium cuprate 124.

that the changes in splitting are caused only by the variations in the layer charge (and their Coulombian interactions) and ignored the possible effect of all the other factors such as the temperature variations in the mutual layer repulsion and any other interactions in the crystals.

Considering the experimental powder neutron diffraction data [1] for $HgBa_2CuO_{4+\delta}$, we constructed the temperature dependence of splitting of the BaO-layer (Fig. 2a). Splitting decreases in the temperature range 300–150 K, and then attains a constant value. In fact, we observed no specific behavior of splitting in the vicinity of T_c. The numerical value of splitting ($\delta\Delta \cong 0.01$ Å) corresponds to a decrease by $\delta Q \cong 0.04$ of the charge difference between the HgO_δ and CuO_2 layers. In other words, the positive charge $\delta Q_1 = 1/2\delta Q = 0.02$ is transferred from the mercury layer (reservoir) to the conducting copper layer.

The X-ray diffraction data for a $Tl_2Ba_2CaCu_2O_8$ single crystal [2] show that splitting of the BaO layer decreases by 0.007 Å in the temperature range 290–130 K (Fig. 2b). In this case, there is a very weak broad minimum. The positive charge transferred from the reservoir (the TlO layer) to the conducting CuO_2 layer equals $\delta Q_1 \cong 0.014$, which is close to the experimental error of the layer-charge determination ($\simeq 0.01$). Although the observed structural changes are at the limit of the diffraction-experiment sensitivity, the nature of these changes is the same as in other compounds considered.

Analyzing the X-ray diffraction data on the changes in the positional parameters for $Tl_2Ba_2Ca_2Cu_3O_{10}$ crystals [3], we arrived at the following conclusions. The change in splitting in the range 290–120 K is well seen, and, in the vicinity of T_c, shows a clear minimum (Fig. 2c). The total decrease in BaO splitting is 0.045 Å, which corresponds to the transfer of the charge $\delta Q_1 \simeq 0.09$ from the TlO to the CuO_2 layer. The X-ray diffraction data for a $YBa_2Cu_4O_8$ single crystal [4] clearly show a decrease in splitting for the BaO layer ($\delta\Delta \simeq 0.01$ Å) despite the fact that the splitting value is much less than in mercury and thallium cuprates (Fig. 2d). The charge transferred from the layer of the "chain copper" CuO into the layer of the "in-plane copper" CuO_2 at the temperatures 300–100 K equals $\delta Q_1 \cong 0.02$. These data could be obtained only in sophisticated complex experiments with the measurement and detailed processing of the intensities of hundreds of reflections at each temperature.

Thus, in all the cuprates studied, splitting of the BaO layer at lower temperatures is considerably less [1–4]. This cannot result from the lattice compression, because a decrease in splitting of this layer ranges from one to several percent, whereas a decrease of the lattice parameters in the same temperature range does not exceed 0.2–0.3%. One can state that these split layers are a "weak link" during the cooling of cuprates with hole conductivity. Similar facts were also observed in these structures under high pressures [10]. A decrease in splitting indicates that the common feature of the behavior of all the cuprates with the hole conductivity

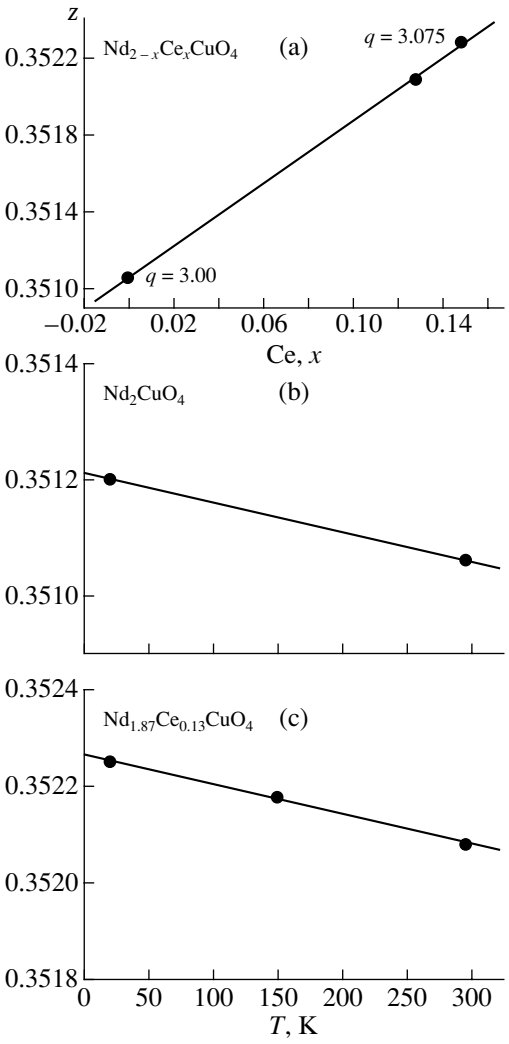

Fig. 3. Variation in the positional parameter of neodymium in the $Nd_{2-x}Ce_xCuO_4$ lattice with the change of the (a) cerium concentration and (b, c) temperature.

is the transfer of the positive charge into the conducting planes during a temperature decrease down to T_c. A temperature decrease provides the formation of additional holes in the structure prior to the system transition into the superconducting state. Usually, the total hole concentration in cuprate superconductors is estimated as 0.2–0.3 of the charge of an electron. The temperature-dependent charge transfer (0.02–0.09) is about 10–30% of the total charge necessary for the transition to superconductivity in cuprates.

The temperature variations in the positional parameters in cuprate-type high-temperature superconductors are very small. However, the qualitative changes in the structure (a decrease in splitting of the BaO layer in a number of cuprates with the hole conductivity established by different research groups by various experimental methods) fully coincide. Thus, we can state that in the cooling of these cuprates, the superconducting transition is preceded by the additional positive-charge transfer from the reservoir to the conducting layers. The efforts of all the experimentalists were directed mainly to the study of the specific features of the structure behavior in the vicinity of the critical temperature, whereas the temperature variation in the splitting of the BaO layer had not been given due attention for quite a long time. However, the analysis of the whole set of the data shown in Fig. 2 leads to the conclusion that the rate of the charge transfer increases with the approach to the transition into the superconducting state.

Cuprates with the electron-type conductivity are based on Nd_2CuO_4 compound: with the replacement of several percent of Nd by Ce (in $Nd_{2-x}Ce_xCuO_4$ with x = 0.13–0.15), the semiconductor compound is transformed into a superconducting metal. In the Nd_2CuO_4 lattice, a layer of Nd ions is located between the CuO_2 and O_2 layers. Such an asymmetric environment results in the fact that the Nd layer is located not in the middle between these layers but somewhat closer to the O_2 layer. The positional parameter z of neodymium is close to 0.35 (instead of 0.375 for the middle position). This difference is explained by the partly Coulombian interaction of this layer with the neighboring ones: both layers are charged negatively, but the charge of the O_2 layer has a larger absolute value. Therefore, the layer of Nd^{3+} ions is much more strongly attracted to the O_2 layer and, thus, is located at a longer distance from the CuO_2 layer. The Coulombian displacement should be proportional to the product of the neodymium-ion charge, q, by the difference in the charges between the neighboring layers, Q,

$$\Delta z_c \sim qQ = q[Q_{(CuO_2)} - Q_{(O_2)}]. \qquad (2)$$

As a result of the replacement of Nd by Ce, the neodymium layers increase their charge, and, in order to provide the crystal neutrality, the charges of some other layers should be reduced. Oxygen in the initial Nd_2CuO_4 has the valence –2 and cannot become "more electronegative." Therefore, the introduction of cerium should reduce the charge of copper ions. As a result of the changes in the average charge of ions in the neodymium layer by $+\delta q$, the difference in Q in Eq. (2) would change by the value $-2\delta q$ (since only one copper layer corresponds to two neodymium ones). At higher cerium concentrations, the Coulombian displacement (deviation of the z-parameter from the value 0.375) should decrease, whereas the z itself should increase. Figure 3a shows the variation in z with the introduction of cerium into Nd_2CuO_4 according to data [5, 11]. The sign of the change, i.e., a decrease of the Coulombian displacement with introduction of cerium, corresponds to Eq. (2). Therefore, the Coulombian model qualitatively describes the change in the positional parameter of neodymium with the change of the composition. The change of x = 0 by x = 0.15 results in an increase by 0.075 of the ion charge in the neodymium layer, and the corresponding decrease by 0.15 of the charge of the copper ions. This signifies that the transition to the

superconducting state is caused by transfer of the charge $\delta q_l = -0.15$ into the conducting layers.

The low-temperature changes in the Nd_2CuO_4 and $Nd_{1.85}Ce_{0.15}CuO_4$ structures were determined as a result of the X-ray study of the corresponding single crystals. It was established that the positional parameter of neodymium increases by about 0.00015–0.00018 with cooling of the crystal from 295 to 20–25 K [6, 12] (Fig. 3b). Such a change in the doping process corresponds to an increase of x by about 0.02. We assumed again that this increase is caused by the changes in the layer charges, because there is no other reason for the changes in the structural parameter. Under this assumption, cooling of the "pure" and doped neodymium cuprate results in the transfer of the negative charge to the conductive layers. The value of the transferred charge is about 10% of the total charge which is necessary to transfer during doping to provide the electron conductivity of the crystal and its subsequent transition to the superconducting state. The sign of the transferred charge should correspond to an increase in the number of electrons in the CuO_2 layer.

CONCLUSION

The characteristic feature common to all the cuprate high-temperature superconductors during their cooling from room to helium temperatures is the change in the mutual layer location such that it would correspond to the transfer of an additional charge to the conducting layers—positive in the case of the hole conductivity and negative in the case of the electron conductivity. Cooling seems to be accompanied by "preparing" the crystal to the transition to the superconducting state—the appearance of an additional charge of the required sign in CuO_2 layers. The value of this charge is several times less than the value of the total additional charge necessary for the semiconductor–superconducting metal transition.

ACKNOWLEDGMENTS

The authors are grateful to V.I. Simonov and V.A. Somenkov for fruitful discussions. This study was supported by the Federal Scientific and Technological Subprogram *Modern Trends in Condensed State Physics*, project no. 96-038 and the Russian Foundation for Basic Research, project no. 96-15-96473.

REFERENCES

1. J. L. Wagner, P. G. Radaelli, D. G. Hinks, *et al.*, Physica C (Amsterdam) **210**, 447 (1993).
2. V. N. Molchanov, R. A. Tamazyan, V. I. Simonov, *et al.*, Physica C (Amsterdam) **229**, 331 (1994).
3. M. Hasegawa, Yo. Matsushita, and H. Takei, Physica C (Amsterdam) **267**, 31 (1996).
4. V. N. Molchanov, V. I. Simonov, M. K. Blomberg, and M. Merisalo, Pis'ma Zh. Éksp. Teor. Fiz. **66**, 502 (1997) [JETP Lett. **66**, 534 (1997)].
5. I. P. Makarova, V. N. Molchanov, R. A. Tamazyan, *et al.*, Kristallografiya **38** (9), 24 (1993) [Crystallogr. Rep. **38**, 435 (1993)].
6. I. P. Makarova, V. I. Simonov, M. K. Blomberg, and M. Merisalo, Acta Crystallogr., Sect. B: Struct. Sci. **B52**, 93 (1996).
7. S. Sh. Shil'shteĭn, A. S. Ivanov, and V. A. Somenkov, Sverkhprovodimost **7**, 903 (1994); Physica C (Amsterdam) **245**, 181 (1995).
8. S. Sh. Shil'shteĭn and A. S. Ivanov, Fiz. Tverd. Tela (St. Petersburg) **37**, 3268 (1995) [Phys. Solid State **37**, 1796 (1995)].
9. S. Sh. Shil'shteĭn, Fiz. Tverd. Tela (St. Petersburg) **40**, 1980 (1998) [Phys. Solid State **40**, 1793 (1998)].
10. V. L. Aksenov, A. M. Balagurov, B. N. Savenko, *et al.*, Physica C (Amsterdam) **275**, 87 (1997).
11. I. P. Makarova, A. Bram, J. Markl, *et al.*, Physica C (Amsterdam) **223**, 1 (1994).
12. I. P. Makarova, in *Proceedings of the Workshop "Structure and Properties of Crystalline Materials" Dubna, 1997*, Ed. by A. M. Balagurov, V. V. Sikolenko, *et al.*, p. 55.

Translated by L. Man

Crystallography Reports, Vol. 46, No. 5, 2001, pp. 752–757. Translated from Kristallografiya, Vol. 46, No. 5, 2001, pp. 827–832.

STRUCTURE OF INORGANIC COMPOUNDS

Modular Structure of a Sodium-Rich Analogue of Eudialyte with the Doubled *c*-Parameter and the *R*3 Symmetry

R. K. Rastsvetaeva* and A. P. Khomyakov**

** Shubnikov Institute of Crystallography, Russian Academy of Sciences, Leninskiĭ pr. 59, Moscow, 117333 Russia*

e-mail: rast@ns.crys.ras.ru

*** Institute of Mineralogy, Geochemistry, and Crystal Chemistry of Rare Elements, ul. Veresaeva 15, Moscow, 121357 Russia*

Received January 30, 2001

Abstract—The structure of a new sodium-rich representative of the eudialyte group with the ideal formula $(Na,Sr,K)_{35}Ca_{12}Fe_3Zr_6TiSi_{51}O_{144}(O,OH,H_2O)_9Cl_3$ was established by the X-ray diffraction analysis ($R = 0.054$ based on 3503 $|F|$). The unit-cell parameters are $a = 14.239(1)$, $c = 60.733(7)$ Å, $V = 10663.9$ Å^3, sp. gr. $R3$. The mineral structure is characterized by in-layer order of cations resulting in doubling of the *c*-parameter and the formation of two modules, the composition and the structure of one of which corresponds to eudialyte (with an impurity of kentbrooksite), the prototype of the second module is alluaivite. Lowering of the symmetry is caused by ordering of Ca atoms and the Ca-replacing elements in the alluaivite module and by the displacements of the alkali cations from the *m* plane. *© 2001 MAIK "Nauka/Interperiodica".*

The minerals of the eudialyte group are actively studied both by Russian and Western researchers [1]. We were the first to discover and study the specific specimens of this group characterized by doubled *c*-parameter. These are alluaivite (sp. gr. $R\bar{3}m$) [2] and titanium- and potassium-rich analogues of eudialyte (the acentric sp. gr. $R3m$) [3, 4]. In this study, we describe the structure of a low-symmetry eudialyte-like mineral with the double unit cell (the sp. gr. $R3$).

The mineral under study was discovered in pegmatites from the Eveslogchorr mountain of the Khibiny alkaline massif (the Kola Peninsula). The mineral exists

Table 1. Crystallostructural data and details of X-ray diffraction study

Characteristic	Data and conditions
Unit-cell parameters, Å	$a = 14.239(1)$, $c = 60.733(7)$
Unit-cell volume, Å^3	$V = 10663.9$
Density, g/cm^3: ρ_{calc}; ρ_{exp}	2.87; 2.88
Sp. gr., λ, z	$R3$; 3 (for the idealized formula)
Radiation; λ, Å	CuK_α; 1.54180
Crystal dimensions, mm	$0.3 \times 0.25 \times 0.2$
Diffractometer	SYNTEX $P2_1$
$\sin\theta/\lambda$, Å^{-1}	<0.59
Ranges of the indices of measured reflections	$-16 < h < 16$, $-16 < k < 16$, $0 < l < 70$,
R_{int} for equivalent reflections	0.038
Total number of reflections	6206 $I > 2\sigma(I)$
Number of independent reflections	3503 $F > 4\sigma(F)$
Program used in computations	AREN [5]
Program for absorption correction	DIFABS [6]
Number of independent positions	108
R factor upon anisotropic refinement	0.054

Table 2. Atomic coordinates and equivalent thermal parameters of the framework atoms

Atom	*x*/*a*	*y*/*b*	*z*/*c*	B_{eq}, Å^2
Zr(1)	0.1659(1)	0.3321(1)	0.0829(1)	1.35(1)
Zr(2)	−0.0012(1)	0.4992(1)	0.2481(1)	1.29(1)
Ca(1)	0.0727(1)	0.6678(1)	0.1658(1)	1.08(3)
Ca(1)'	0.5945(1)	0.6679(1)	0.1658(1)	0.99(3)
Ca(2)	−0.0004(1)	0.2620(1)	−0.0009(1)	0.89(3)
Ca(2)'	0.2615(1)	0.2620(1)	−0.0008(1)	0.96(3)
Si(1)	0.3248(2)	0.0551(1)	0.1182(1)	1.29(9)
Si(1)'	0.3263(1)	0.2685(1)	0.1178(1)	1.15(8)
Si(2)	0.2496(1)	0.1253(1)	0.2948(1)	1.13(9)
Si(3)	0.0641(1)	0.3419(1)	0.2841(1)	1.00(9)
Si(3)'	0.2766(1)	0.3401(1)	0.2839(1)	1.96(8)
Si(4)	0.5979(1)	0.4037(1)	0.2910(1)	0.96(8)
Si(5)	0.0710(1)	0.1428(1)	0.0408(1)	0.98(8)
Si(6)	0.4044(1)	0.5962(1)	0.2068(1)	0.93(8)
Si(7)	0.5418(2)	0.4589(2)	0.1281(1)	1.82(9)
Si(8)	0.2625(1)	0.5261(1)	0.1252(1)	1.10(9)
Si(9)	0.0054(1)	0.6088(1)	0.0486(1)	1.15(9)
Si(9)'	0.0070(1)	0.3970(1)	0.0484(1)	1.25(8)
Si(10)	0.1243(2)	0.2485(2)	0.2038(1)	1.61(9)
Si(11)	0.4173(1)	0.2091(1)	0.0369(1)	1.18(9)
Si(12)	0.3398(1)	0.0636(1)	0.2141(1)	1.24(9)
Si(12)'	0.3384(1)	0.2736(1)	0.2145(1)	1.07(8)
O(1)	0.3551(6)	0.1766(5)	0.1089(1)	2.1(3)
O(2)	0.3083(5)	0.1521(5)	0.3182(1)	1.8(3)
O(3)	0.5157(4)	0.0326(5)	0.1518(1)	1.2(2)
O(4)	0.3856(4)	0.2808(3)	0.0534(1)	0.8(2)
O(4)'	0.3875(6)	0.1063(6)	0.0534(1)	3.2(2)
O(5)	0.0729(5)	0.3691(5)	0.3089(1)	1.7(3)
O(5)'	0.2917(5)	0.3688(5)	0.3092(1)	0.8(2)
O(6)	0.0300(5)	0.2585(6)	0.1038(1)	2.2(3)
O(6)'	0.2257(5)	0.2542(6)	0.1039(1)	2.5(2)
O(7)	0.3111(6)	0.1549(5)	0.2231(1)	2.2(3)
O(8)	0.1008(5)	0.4032(5)	0.0632(1)	2.0(3)
O(8)'	0.3028(5)	0.4070(5)	0.0636(1)	2.0(3)
O(9)	0.0566(7)	0.1175(6)	0.2051(1)	4.0(3)
O(10)	0.5687(5)	0.1407(5)	0.2664(1)	2.1(3)
O(11)	0.2344(5)	0.4731(6)	0.1013(1)	2.6(3)
O(12)	0.2986(4)	0.2515(3)	0.1438(1)	0.6(2)
O(12)'	0.3007(5)	0.0467(5)	0.1437(1)	1.8(3)
O(13)	0.5523(4)	0.4493(4)	0.3103(1)	1.2(2)
O(14)	0.2715(5)	0.5439(5)	0.2054(1)	1.9(3)
O(15)	0.0353(4)	0.6268(4)	0.0224(1)	1.4(2)
O(15)'	0.0351(6)	0.4037(5)	0.0229(1)	2.2(3)
O(16)	0.3666(4)	0.2871(4)	0.1883(1)	1.2(3)
O(16)'	0.3634(6)	0.0765(5)	0.1884(1)	2.4(3)

Table 2. (Contd.)

Atom	*x*/*a*	*y*/*b*	*z*/*c*	B_{eq}, Å^2
O(17)	0.1232(4)	0.0606(4)	0.0395(1)	1.2(3)
O(18)	0.5423(5)	0.2692(5)	0.2935(1)	1.9(3)
O(19)	0.0572(5)	0.2937(6)	0.2189(1)	2.2(3)
O(19)'	0.2332(4)	0.2871(4)	0.2188(1)	0.8(2)
O(20)	0.5067(4)	0.0190(5)	0.0564(1)	1.6(2)
O(21)	0.3965(4)	0.6061(4)	0.1273(1)	1.5(2)
O(22)	0.0924(5)	0.1875(5)	0.0654(1)	1.6(2)
O(23)	0.0684(5)	0.6341(4)	0.2683(1)	1.6(3)
O(23)'	0.5677(5)	0.6324(6)	0.2682(1)	1.3(3)
O(24)	0.1558(4)	0.3178(5)	0.2739(1)	1.7(3)
O(25)	0.4381(6)	0.3640(6)	0.2288(1)	2.9(3)
O(25)'	0.4358(5)	0.0712(5)	0.2287(1)	2.3(3)
O(26)	0.5468(5)	0.2715(7)	0.0333(1)	3.9(4)
O(27)	0.1135(5)	0.2300(5)	0.0218(1)	2.0(3)
O(28)	0.2201(4)	0.4411(5)	0.1445(1)	1.5(2)
O(29)	0.1031(6)	0.5511(5)	0.1874(1)	2.3(3)
O(30)	0.2792(4)	0.2278(4)	0.2788(1)	0.8(2)
O(30)'	0.2766(8)	0.0498(6)	0.2788(1)	3.8(2)
O(31)	0.6037(7)	0.2118(7)	0.1253(1)	3.6(3)
O(32)	0.4354(5)	0.3849(5)	0.1127(1)	2.6(3)
O(32)'	0.6122(8)	0.5684(8)	0.1126(1)	5.2(2)
O(33)	0.1199(5)	0.0576(8)	0.2996(1)	4.0(3)
O(34)	0.1504(5)	0.3031(5)	0.1804(1)	2.3(3)
O(35)	0.4303(5)	0.5732(5)	0.2313(1)	2.2(3)
O(36)	0.3601(5)	0.1765(4)	0.0144(1)	1.5(3)

Note: Hereinafter, the scheme of atomic numbering corresponds to that used in [4]; the atoms related by the pseudosymmetry plane *m* are primed.

as impregnations of pink spherical grains with the diameter of 0.5 to 1 cm. The mineral composition determined with the aid of an electron-probe microanalyzer corresponds to the empirical formula $Na_{33.30}K_{1.45}Sr_{0.74}Ca_{11.77}Fe^{2+}_{2.19}Mn_{0.87}Ce_{0.10}Zr_{5.94}Ti_{0.52}Si_{51.26}O_{144.48}(OH)_{4.80}Cl_{2.95}F_{0.36} \cdot 3H_2O$ ($Z = 3$).

The idealized formula can be represented as $(Na,Sr,K)_{35}Ca_{12}Fe_3Zr_6TiSi_{51}O_{144}(O,OH,H_2O)_9Cl_3$. In comparison with the typical eudialyte, this mineral has much higher sodium- and a lower iron-content (2.7 wt % of FeO in comparison with 5–7 wt % typical of eudialytes).

The X-ray diffraction data were collected from an isometric single crystal. The crystal characteristics and the details of the X-ray diffraction study are indicated in Table 1.

Proceeding from the similar composition and unit-cell parameters of the mineral under study and its potassium-rich analogue, we assumed that the two minerals are structurally similar. As the initial approximation, we used the coordinates of the framework positions indicated in [4]. The positions of all extraframework atoms were revealed from a series of Fourier syntheses. At the final stage, the partly occupied positions were localized from the difference electron-density synthesis. The allowance for the impurity atoms made with the use of mixed atomic-scattering curves did not lead to low *R*-factor but led to the unreasonably high atomic thermal parameters. The refinement within the sp. gr. *R*3 resulted in a substantially lower *R*-factor and the atomic thermal parameters. Lowering of the symmetry in comparison with the usual sp. gr. *R*3*m* (observed for a number of structures of the eudialyte group) is most often associated with the ordering of Ca atoms and some Ca-replacing elements in the positions of the six-membered rings. The crystal of the sodium-rich mineral with the double unit-cell contains two independent rings, in one of which the Ca and (Ca,Sr) atoms are ordered. Another reason of symmetry lowering is a large amount of Na ions, which do not provide the stabilization of the double-volume structure observed for

Table 3. Coordinates and equivalent thermal parameters of the extraframework atoms, multiplicities (Q) and occupancies (q) of the positions

Atom	*x/a*	*y/b*	*z/c*	*Qq*	B_{eq}, Å^2
Si(13)	0	0	0.1938(1)	3 1	2.1(1)
Si(14)	0	0	0.2888(1)	3 1	1.4(1)
Si(15)	0.6667	0.3333	0.0441(1)	3 1	1.6(1)
Si(16)	0.6667	0.3333	0.1346(8)	3 0.20(2)	6.8(4)*
Ti	0.6667	0.3333	0.1421(1)	3 0.52(1)	3.3(2)
Fe	0.3253(2)	0.1613(2)	0.1663(1)	9 0.73(1)	2.31(4)
Mn	0.3839(4)	0.1918(4)	0.1644(1)	9 0.27(1)	2.0(1)
Na(1)	0.0971(3)	0.5479(3)	0.3033(1)	9 1	2.5(2)
Na(2)	0.2205(3)	0.1110(3)	0.0760(1)	9 1	2.4(2)
Na(3)	0.2143(3)	0.4300(3)	0.0281(1)	9 1	2.6(2)
Na(4*a*)	0.4391(5)	0.5604(5)	0.0889(1)	9 0.35(1)	2.8(1)
Na(4*b*)	0.1687(9)	0.5859(8)	0.0817(1)	9 0.65(1)	6.1(2)
Na(5)	0.5659(2)	0.4352(2)	0.1903(1)	9 1	2.5(5)
Na(6)	0.2202(3)	0.4413(3)	0.2425(1)	9 1	2.9(2)
Na(7)	0.4911(4)	0.2451(4)	0.2497(1)	9 1	3.9(1)
Na(8*a*)	0.096(2)	0.166(1)	0.2486(3)	9 0.29(1)	7.8(4)
Na(8*b*)	0.156(1)	0.127(1)	0.2470(2)	9 0.49(2)	7.1(4)
Na(8*b*)’	0.154(2)	0.035(3)	0.2449(6)	9 0.22(2)	6.9(7)
Na(9*a*)	0.5032(5)	0.2563(6)	0.0861(1)	9 0.80(1)	5.2(2)
Na(9*b*)	0.521(2)	0.331(3)	0.0831(4)	9 0.20(2)	4.9(6)*
Na(10*a*)	0.0926(4)	0.1835(4)	0.1439(1)	9 0.63(1)	2.4(7)
Na(10*b*)	0.1054(4)	0.2143(5)	0.1405(1)	9 0.37(1)	3.3(1)
Na(11)	−0.007(1)	0.494(1)	0.0025(2)	9 0.41(1)	2.7(2)
Na(12)	0.5604(3)	0.4390(3)	0.0018(1)	9 0.57(1)	2.1(1)
Na(13)	0.1147(4)	0.5585(3)	−0.0031(1)	9 0.53(1)	2.0(1)
OH(1)	0	0	0.2631(1)	3 1	2.1(4)
OH(2)	0.6667	0.3333	0.0711(2)	3 1	2.7(4)
OH(4)	0.556(2)	0.281(2)	0.1639(3)	9 0.50(2)	4.7(3)*
OH(5)	0.6667	0.3333	0.159(2)	3 0.20(5)	7.8(5)*
OH(7)	0	0	0.1681(2)	3 1	5.2(5)*
H_2O(1)	0.3333	0.6667	0.2628(3)	3 1	7.2(3)*
H_2O(3)	0.3333	0.6667	0.076(1)	3 0.66(8)	9(5)*
H_2O(4)	0.6667	0.3333	0.2090(6)	3 0.32(6)	4(1)*
H_2O(5)	0	0	0.1198(2)	3 0.86(5)	3.1(2)
C1(1)	0.3333	0.6667	0.3118(1)	3 1	3.7(2)
C1(3*a*)	0.3333	0.6667	0.0200(1)	3 0.90(2)	3.5(1)
C1(3*b*)	0.3333	0.6667	0.046(1)	3 0.10(1)	3(1)*
C1, F	0.6667	0.3333	0.2164(1)	3 0.68(2)	2.2(1)

* Isotropic thermal parameters.

Table 4. Characteristics of the coordination polyhedra

Position	Coordination number	Cation–anion distances		
		limiting		average
Zr(1)	6	2.057	2.130	2.082
Zr(2)	6	2.035	2.067	2.047
Ca(1)	6	2.303	2.439	2.378
Ca(1)'	6	2.287	2.428	2.362
Ca(2)	6	2.324	2.374	2.340
Ca(2)'	6	2.344	2.451	2.381
Si(13)	4	1.550	1.603	1.589
Si(14)	4	1.560	1.610	1.603
Si(15)	4	1.615	1.640	1.621
Si(16)	4	1.40	1.60	1.55
Ti	6	1.810	1.900	1.850
Fe	4	2.022	2.069	2.045
Mn	5	2.082	2.192	2.137
Na(1)	7	2.416	2.957	2.622
Na(2)	8	2.518	2.770	2.645
Na(3)	7	2.400	2.960	2.608
Na(4*a*)	9	2.569	2.860	2.670
Na(4*b*)	8	2.060	2.970	2.58
Na(5)	11	2.556	3.140	2.774
Na(6)	9	2.444	3.040	2.674
Na(7)	7	2.460	2.962	2.637
Na(8*a*)	5	2.23	2.80	2.55
Na(8*b*)	5	2.26	2.88	2.69
Na(8*b*)'	8	2.28	3.17	2.67
Na(9*a*)	9	2.21	3.11	2.77
Na(9*b*)	6	2.18	2.87	2.59
Na(10*a*)	8	2.587	3.176	2.793
Na(10*b*)	7	2.500	2.923	2.685
Na(11)	4	2.06	2.27	2.16
Na(12)	7	2.434	2.980	2.775
Na(13)	7	2.389	3.036	2.766

Note: The compositions of the mixed positions ($Z = 1$): Ca(2)' = $Ca_{8.55}Sr_{0.45}$; Na(4*a*) = $Na_{2.35}Sr_{0.8}$; Na(5) = $Na_{7.1}SK_{1.9}$; Na(10*a*) = $Na_{3.2}K_{2.46}$; Na(10*b*) = $Na_{2.73}Sr_{0.6}$; Na(12) = $Na_{4.83}Sr_{0.15}Ce_{0.15}$; Na(13) = $Na_{4.42}Sr_{0.2}Ce_{0.15}$.

a potassium-rich analogue. As a result, the alkali cations are systematically displaced from the *m* plane. These deviations are seen in the fourth decimal place (in some cases, even in the third decimal place), which exceed the accuracy of the determination of the atomic coordinates. The most substantial displacements are observed in the cavities between the rings where Na-atoms have the highest mobility. The Na atoms are disordered over one cavity in two subpositions and over three subpositions in another cavity. The absence of the plane *m* is also evidenced by the X-ray diffraction data. Thus, upon averaging the experimental structure amplitudes, which are equivalent within the sp. gr. *R*3 (the diffraction class $C_{3i} = -3$), the averaging *R* factor was half that within the sp. gr. *R*3*m* ($D_{3d} = -3m$). The final atomic coordinates are given in Tables 2 and 3. The principal characteristics of the polyhedra (except for the Si-tetrahedra of the rings) are listed in Table 4.

The main mineral composition characteristics and the modular structure of the mineral are reflected in its crystallochemical formula ($Z = 1$):

$$\{Zr_9Ca_{18}[Si_{72}O_{216}][Si_{3.6}\square_{0.84}Ti^{[VI]}_{1.56}][Fe^{[IV]}_{6.66}Mn^{[V]}_{2.34}] \cdot Na_{36}[Na_{7.1}K_{1.9}][(OH)_{5.06}(H_2O)_{3.96}O_{3.22}ClF]\}\{Zr_9Ca_9 \cdot [Ca_{8.55}Sr_{0.45}][Si_{72}O_{216}][Si_6][Na^{[IV]}_{3.69}(Na_{4.83}Sr_{0.15}Ce_{0.15})^{[VII]} \cdot (Na_{4.42}Sr_{0.2}Ce_{0.15})^{[VII]}][Na_{35.2}Sr_{0.8}][Na_{5.94}K_{2.46}Sr_{0.6}] \cdot [(OH)_6Cl_6(H_2O)_{4.56}]\}.$$

In this formula, the compositions in braces correspond to the eudialyte (including "kentbrooksite") and "alluaivite" modules, respectively. (The compositions of the key positions are written in brackets, and the coordination numbers of the cations are given by Roman numerals in brackets.) The structure modules correspond to the layered fragments of the structure with *z* ranging from –0.055 to 0.11 and from 0.11 to 0.275, respectively; together, they form a two-layer ~20.2 Å-thick packet.

The main characteristic features of the "alluaivite" fragment are the high sodium concentration and the existence of the group consisting of three Na-polyhedra. Two of these polyhedra are seven-vertex polyhedra separated by the third Na in the square coordination (Fig. 1). The polyhedra are distributed statistically, because their simultaneous presence is impossible owing to too short distances [1.43(1) and 1.50(1) Å, the average distance is 1.46 Å] between the position in the Na(11)-square and the positions in the Na(12)- and Na(13)-seven-vertex polyhedra, respectively. Similar to all sodium-rich eudialytes, the square centers are occupied by sodium atoms, whereas the positions in the seven-vertex polyhedra are occupied by statistically Na together with Sr and Ce. In potassium-rich eudialyte [4], in which these positions are occupied by K, the average distance between these positions increases to 1.61 Å. The minimum distance (1.41 Å) is found in alluaivite [2], where the seven-vertex polyhedra are occupied exclusively by Na. Therefore, the distance between the cationic positions correlates with the average radius of the cations located in these positions. Another characteristic feature of the cationic layer in alluaivite is the centers of the nine-membered rings completely filled with additional Si atoms, with the corresponding tetrahedra being aligned along the threefold axis in the opposite direction with respect to the Si-tetrahedra of the eudialyte module. The latter fact is also responsible for doubling of the period along this axis.

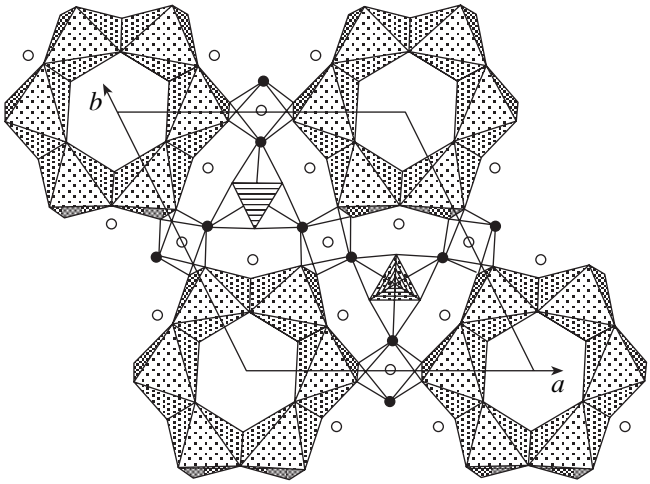

Fig. 1. Cationic layer in sodium-rich eudialyte corresponding to the "alluaivite" module projected onto the (001) plane; the Si-tetrahedra are hatched with solid lines; the Na atoms in the seven-vertex polyhedra are indicated by filled circles; the remaining Na atoms are indicated by empty circles.

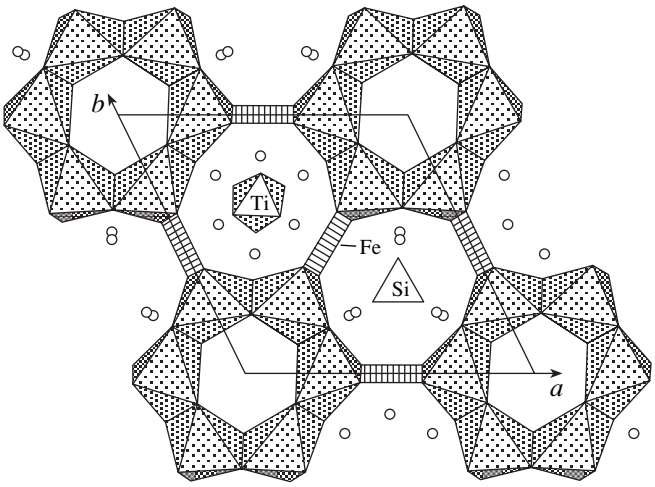

Fig. 2. Cationic layer of the structure corresponding to the eudialyte module; the Fe-squares are hatched; the Na atoms are indicated by empty circles.

The eudialyte module (Fig. 2) characterized by the presence of the Fe atom in the square position is statistically (~25%) complemented with the "kentbrooksite" module containing the Mn-five-vertex polyhedra, with the replacement of a Nb-octahedron located on the threefold axis by a Ti-octahedron. Taking into account that the alluaivite type of cavity filling with cations is also characteristic of the zirconosilicate, but not the titanosilicate framework, one can state that although the main features of these modules coincide with those of their known prototypes, these structures are not identical. This is also true for the modular structures of the eudialyte group studied in [3, 4].

In conclusion, it should be noted that recently, considerable attention in mineralogy has been paid to the modular aspects [7] because crystal structures can usually be considered as consisting of fragments or modules inherent in other simpler structures. New more complicated structures are modeled by combining such modules. Thus, it is possible to predict the existence of compounds with still unknown compositions and structures. The modular structure discovered in minerals of the eudialyte group for the first time gives grounds to predict both new complex eudialyte-like minerals with the n-fold larger period *c* and simple structures that compose the structures of these complex minerals.

ACKNOWLEDGMENTS

This study was supported by the Russian Foundation for Basic Research, project no. 99-05-65035.

REFERENCES

1. O. Johnsen, J. D. Grice, and R. A. Gault, Eur. J. Mineral. **10**, 207 (1998).
2. R. K. Rastsvetaeva, A. P. Khomyakov, V. I. Andrianov, and A. I. Gusev, Dokl. Akad. Nauk SSSR **312** (6), 1379 (1990) [Sov. Phys. Dokl. **35**, 492 (1990)].
3. R. K. Rastsvetaeva, A. P. Khomyakov, and G. Chapuis, Z. Kristallogr. **214**, 271 (1999).
4. R. K. Rastsvetaeva and A. P. Khomyakov, Kristallografiya **46**, 454 (2001) [Crystallogr. Rep. **46**, 647 (2001)].
5. V. I. Andrianov, Kristallografiya **32** (1), 228 (1987) [Sov. Phys. Crystallogr. **32**, 130 (1987)].
6. N. Walker and D. Stuart, Acta Crystallogr., Sect. A: Found. Crystallogr. **A39** (2), 158 (1983).
7. *Modular Aspects of Minerals (University Textbook)*, Ed. by S. Merlino (MondAt Ltd., Budapest, 1997), Vol. 1.

Translated by T. Safonova

Crystallography Reports, Vol. 46, No. 5, 2001, pp. 758–770. Translated from Kristallografiya, Vol. 46, No. 5, 2001, pp. 833–844.

STRUCTURES OF COORDINATION COMPOUNDS

X-ray Diffraction Study of Phase Transitions in Iron(II) Trisnioximate Hexadecylboronate Clathrochelate Complex

I. I. Vorontsov*, K. A. Potekhin, M. Yu. Antipin*, Ya. Z. Voloshin***, A. I. Stash***, V. K. Belsky***, I. I. Dubovik*, and V. S. Papkov***

** Nesmeyanov Institute of Organoelement Compounds, Russian Academy of Sciences, ul. Vavilova 28, Moscow, 117813 Russia*

*** Vladimir State Pedagogical University, pr. Stroiteleĭ 11, Vladimir, 660020 Russia*

**** Karpov Research Institute of Physical Chemistry (Russian State Scientific Center), ul. Vorontsovo pole 10, Moscow, 103064 Russia*

Received September 18, 2000

Abstract—Crystals of the iron(II) nioximate hexadecylboronate clathrochelate complex—FeNx_3(BHd)$_2$ [tris(μ-1,2-cyclohexanedionedioximato-*O*:*O*')di-*n*-hexadecyldiborato(2–)-*N*,*N*',*N*'',*N*''',*N*'''',*N*''''']iron(II)—are investigated by differential scanning calorimetry and X-ray diffraction. Two structural phase transitions are revealed at T_{cr1} = 290(3) K and T_{cr2} = 190(3) K. The crystal structures of phases **I**, **II**, and **III** are determined by X-ray diffraction analysis at 303, 243, and 153 K, respectively. It is demonstrated that the **I** ⟷ **II** phase transition is due to a change in the system of translations, and the **II** ⟷ **III** phase transition is accompanied only by a jumpwise change in the unit cell parameters. The possible mechanisms of phase transitions are discussed in terms of geometry and molecular packing of FeNx_3(BHd)$_2$ in all three phases. © *2001 MAIK "Nauka/Interperiodica".*

INTRODUCTION

Systematic investigations into phase transitions in molecular crystals of organic and metalloorganic compounds are few in number (see [1] and references therein). Traditionally, these phase transitions are classified into the ferrodistortion transitions (when the number Z of formula units in the unit cell remains unchanged) and the antiferrodistortion transitions (with a multiple increase in Z) [2].

Complex FeNx_3(BHd)$_2$, where *Hd* is the hexadecyl substituent and Nx^{2-} is the 1,2-cyclohexanedione dioxime (nioxime) dianion, belongs to the series of clathrochelate complexes with a Fe^{2+} ion encapsulated into a bulk cavity of the macrobicyclic ligand [3, 4].

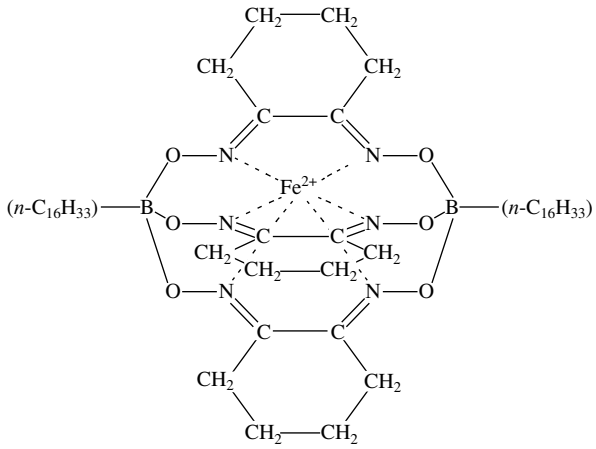

Scheme 1.

1063-7745/01/4605-0758$21.00 © 2001 MAIK "Nauka/Interperiodica"

According to ^{57}Fe Mössbauer spectroscopy [5], crystals of this compound are characterized by jumpwise changes in the quadrupole splitting at temperatures of 290 and 190 K, which can be associated with two phase transitions. In the present work, we investigated the phase transitions in a FeNx_3(BHd)$_2$ crystal by differential scanning calorimetry (DSC) and X-ray diffraction.

EXPERIMENTAL

Differential scanning calorimetry. Two phase transitions at T_{cr1} = 289(2) K and T_{cr2} = 190(2) K were revealed by differential scanning calorimetry of the FeNx_3(BHd)$_2$ complex. This is in agreement with the ^{57}Fe Mössbauer spectroscopic data. The measurements were carried out on a DSM-2M differential scanning microcalorimeter in the temperature range 120–330 K. The sample was preliminarily cooled to 120 K and was then heated at a rate of 8 K/min. The sample weight was 16.3 mg. The thermogram (Fig. 1) shows two endothermal effects with maxima at 190 and 289 K (their magnitudes are 1.8 and 8.8 J/g, respectively).

Crystal data and experimental details. According to X-ray diffraction data, single crystals of FeNx_3(BHd)$_2$ in the temperature range 303–150 K undergo two reversible phase transitions: triclinic modification **I** ⟷ triclinic modification **II** at T_{cr1} and triclinic modification **II** ⟷ triclinic modification **III** at T_{cr2}. The molecular and crystal structures of phases **I**, **II**, and **III** were determined at temperatures of 303(1),

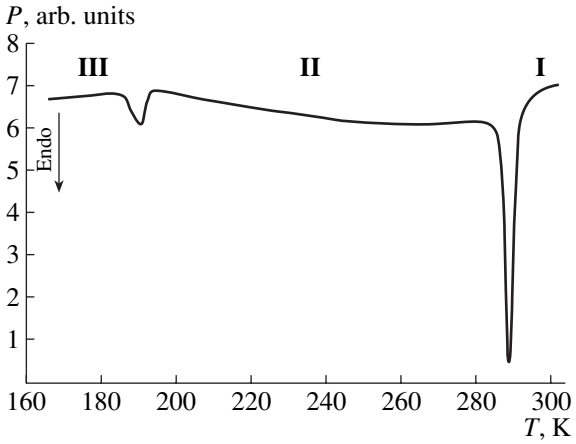

Fig. 1. Thermogram of FeNx_3(BHd)$_2$ crystals. Heating rate is 8 K/min.

Table 1. Main crystal data and structure-refinement parameters for the FeNx_3(BHd)$_2$ crystal ($C_{50}H_{90}N_6O_6B_2Fe$, M = 948.75 g/mol)

Parameter	Phase **I**	Phase **II**	Phase **III**
Temperature, K	303(1)	243(3)	153(3)
Sample size, mm	0.40 × 0.40 × 0.20	0.50 × 0.50 × 0.20	0.50 × 0.50 × 0.20
Diffractometer	Bruker SMART	Syntex $P2_1$	Siemens $P3/PC$
a, Å	15.3313(6)	18.146(12)	18.071(6)
b, Å	21.2648(8)	21.070(13)	20.998(8)
c, Å	19.4648(7)	19.363(13)	19.311(6)
α, deg	82.733(1)	84.23(5)	83.15(3)
β, deg	59.958(1)	62.87(4)	62.14(2)
γ, deg	86.486(1)	55.73(5)	55.84(2)
V, Å^3	5449.2(4)	5320(6)	5257(3)
Space group	$P1$	$P1$	$P1$
Z	4	4	4
d_{cal}, g/cm^3	1.156	1.184	1.199
μ, mm^{-1}	0.326	0.334	0.338
Absorption correction	semiempirical	absent	absent
Scan mode	ω	ω/2θ	ω/2θ
$2\theta_{max}$, deg	54	54	54
Number of unique reflections	34723	20716	18582
Number of parameters	2324	2279	2268
Number of reflections with $F^2 > 2\sigma(F^2)$	11474	12027	15559
$R_1(F)$	0.064	0.067	0.068
$wR_2(F^2)$	0.195	0.185	0.164
Goof	0.784	0.905	1.077

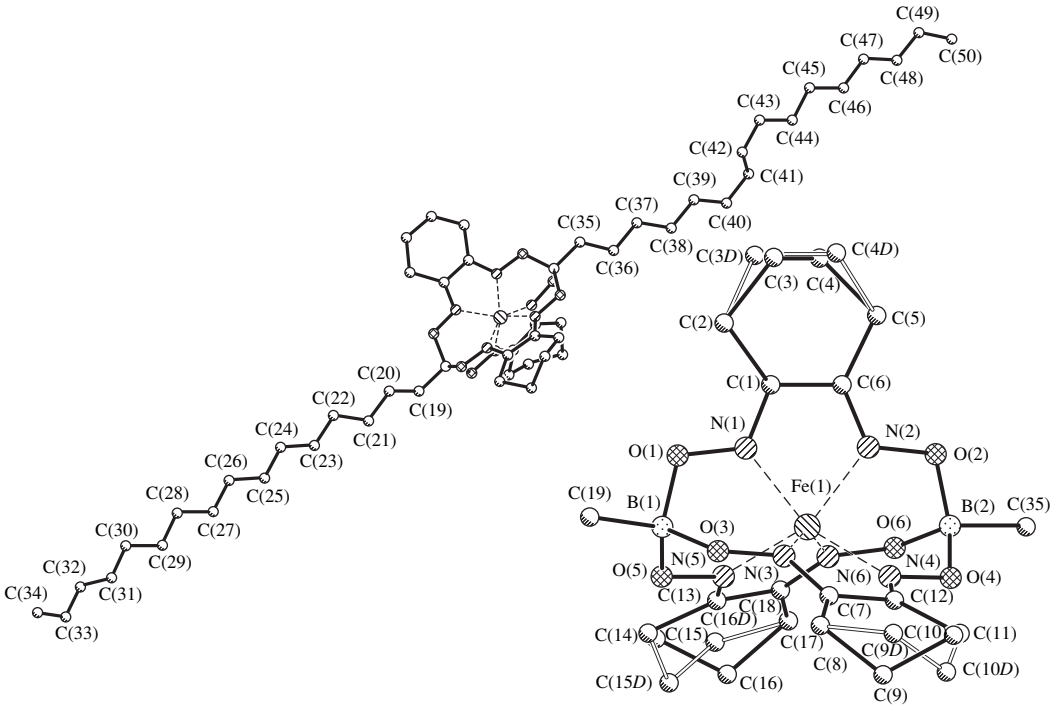

Fig. 2. A general view of one independent molecule in the FeNx_3(BHd)$_2$ complex and the atomic numbering (hydrogen atoms are omitted). For the other three molecules, the atomic numbering (except for iron atoms) differs by adding the letters *A*, *B*, and *C*. The second positions of disordered atoms are designated by the letters *D*, *E*, *F*, and *G*, respectively. The iron atoms are labeled as Fe(1), Fe(2), Fe(3), and Fe(4).

243(3), and 153(3) K, respectively. X-ray diffraction data (MoK_α radiation, λ = 0.7107 Å, graphite monochromator) were collected for three different, approximately isometric, dark orange single crystals on Bruker SMART 1K CCD (303 K), Syntex $P2_1$ (243 K), and Siemens P3/PC (153 K) automated diffractometers. The intensities of experimental reflections were corrected for Lorentz and polarization factors [6, 7]. Absorption correction for **I** was semiempirically included in calculations with the SADABS program [8]. The main crystal data are listed in Table 1.

All three phases are triclinic (space group $P\bar{1}$ and Z = 4); i.e., the unit cell in crystals in all three phases contains four independent molecules (260 independent non-hydrogen atoms). When solving structures **I** and **II**, the positions of iron atoms were determined by the Patterson method and the remaining non-hydrogen atoms were located from difference Fourier syntheses.

Table 2. Mean lengths of chemically equivalent bonds (Å) and mean bond angles (deg) in the FeNx_3(BHd)$_2$ molecule

Bond	Phase **I**	Phase **II**	Phase **III**	Angle	Phase **I**	Phase **II**	Phase **III**
Fe(1)–N(1)	1.90(1)	1.90(1)	1.91(1)	N(1)–Fe–N(2)	77.9(5)	78.1(5)	78.5(4)
B(1)–O(1)	1.48(1)	1.49(1)	1.50(1)	N(1)–Fe(1)–N(3)	85.5(5)	85.6(5)	85.8(4)
O(1)–N(1)	1.38*	1.38(1)	1.37(1)	N(1)–Fe(1)–N(4)	143.9(5)	146.0(5)	148.5(4)
C(1)–N(1)	1.30*	1.30(1)	1.31(1)	N(1)–Fe(1)–N(6)	124.9(5)	122.1(5)	119.6(4)
C(1)–C(2)	1.51*	1.51*	1.49(1)	N(1)–O(1)–B(1)	113.1(8)	112.8(8)	112.5(7)
C(1)–C(6)	1.46*	1.46*	1.44(1)	C(1)–N(1)–O(1)	116.2(8)	116.0(8)	116.3(7)
C(2)–C(3)	1.54*	1.54*	1.54*	C(1)–N(1)–Fe(1)	119.1(7)	118.9(7)	118.7(6)
B(1)–C(19)	1.60*	1.57(2)	1.59(2)	O(1)–B(1)–O(2)	109.5(8)	109.5(8)	109.3(7)
C(19)–C(20)	1.53*	1.53*	1.53*	O(1)–B(1)–C(19)	109.4(9)	109.4(9)	109.6(8)
				N(1)–C(1)–C(2)	124.9(9)	125.0(9)	125.4(8)
				N(1)–C(1)–C(6)	111.7(9)	111.8(9)	112.5(8)

* Bond lengths are fixed according to the data taken from [10].

For the solution of structure **III**, the atomic coordinates of structure **II** were used as a starting model. A general view of the molecule and the atomic numbering are depicted in Fig. 2. In six-membered carbocycles, the β-carbon atoms [the C(3), C(4), C(9), C(10), C(15), and C(16) atoms and the corresponding atoms in the remaining independent molecules] are disordered over two positions. Note that their disordering decreases with a decrease in the temperature: all 12 rings are disordered in phase **I**, while 11 and 6 cycles are disordered in phases **II** and **III**, respectively. Moreover, the terminal carbon atoms [the C(49) and C(50) atoms and the corresponding atoms in the other independent molecules] in four out of eight hexadecyl substituents in phase **III** are disordered over two positions. We failed to reveal a similar disordering in phases **I** and **II** because of the high-frequency thermal atomic vibrations.

The structures were refined by the full-matrix least-squares procedure (on F^2) according to the SHELXTL97 software package [9]. All the non-hydrogen atoms, except for the disordered carbon atoms, were refined in the anisotropic approximation. The unit cells in all the phases contain four independent molecules of the complex, which leads to a large number of refined parameters (≈2300). For this reason, in the course of the structure refinement, the lengths of all carbon–carbon bonds were taken equal to the standard values (1.54 and 1.53 Å for the –C–C– bonds in carbocycles and hexadecyl substituents, respectively; and 1.46 Å for the =C–C= bonds and 1.51 Å for the =C–C– bonds in the carbocycles [10]) and the C–C–C bond angles were taken equal to 112° for structures **I** and **II**; the O–N, C–N, and B–C bond lengths (1.38, 1.30, and 1.60 Å, respectively [10]) were fixed in structure **I**; and only the –C–C– bond lengths in the hexadecyl substituents were fixed in structure **III** (Table 2). In other cases, the scatter in lengths of chemically equivalent bonds was limited by 3σ, where σ = 0.01 Å. The positions of hydrogen atoms were calculated geometrically and then were included in the refinement within the rider model with the displacement parameters $U_{iso}(H) = 1.2U_{eq}(C)$ [$1.5U_{eq}(C)$ for methyl groups], where $U_{eq}(C)$ is the isotropic equivalent displacement parameter for the carbon atom.

The results of the structure refinement and the final discrepancy factors are presented in Table 1. The mean bond lengths and angles in structures **I**, **II**, and **III** are given in Table 2. The coordinates of non-hydrogen atoms are available from the authors.

DISCUSSION

Comparison of the unit cell parameters. In both cases, a multiple increase in the unit cell volume is not observed upon phase transitions. The unit cell parameters for phases **II** and **III** are close to each other (Table 1), and their change in the temperature range 153–243 K does not exceed 1.3%. The **I** ⟷ **II** phase transition is accompanied by the change in the translational symmetry of the lattice (Table 1), and the correspondence is revealed only for three parameters (*b*, *c*, and α): $b_{\mathbf{I}} \approx b_{\mathbf{II}}$, $c_{\mathbf{I}} \approx c_{\mathbf{II}}$, and $\alpha_{\mathbf{I}} \approx \alpha_{\mathbf{II}}$. The translations $a_{\mathbf{I}}$ and $a_{\mathbf{II}}$ lie in the same crystallographic plane and are related by the vector expression $a_{\mathbf{II}} \approx a_{\mathbf{I}} + b_{\mathbf{I}}/2$.

Table 3. Parameters of the common cell in **I*A*** and **II*A*** and the distribution of the observed [$I > 2\sigma(I)$] diffraction reflections (*HKL*) over parity classes

Parameter	**I*A***	**II*A***
Temperature, K	303	283
a_{com}, Å	30.665(7)	30.326(7)
b_{com}, Å	21.264(5)	21.179(5)
c_{com}, Å	19.459(4)	19.395(4)
α_{com}, deg	82.75(2)	83.54(2)
β_{com}, deg	60.06(2)	60.89(2)
γ_{com}, deg	86.40(2)	89.72(2)
V_{com}, Å^3	10907(5)	10796(5)
Reflections (*HKL*)	Number of reflections with $I > 2\sigma(I)$ ($I > 10\sigma(I)$)	
$H = 2n$	225(50)	171(49)
$H = 2n + 1$	0	89(14)
$H + K = 2n$	159(38)	260(63)
$H + K = 2n + 1$	66(12)	0

Note: The number of reflections with $I > 10\sigma(I)$ is given in parentheses.

In order to analyze the change in the translational symmetry upon the **I** ⟷ **II** phase transition, additional investigations were carried out on a Bruker SMART automated diffractometer at temperatures of 303 (**IA**) and 283 K (**IIA**). At these temperatures, the diffraction patterns of the same single crystal with a fixed orientation with respect to the goniometer axes were examined in detail in the low-angle range ($2\theta \leq 30°$). The unit cell parameters for **IA** and **I** coincide to within the limits of experimental error (Table 1), and the unit cell parameters for **IIA** are as follows: a = 18.537(5) Å, b = 21.179(5) Å, c = 19.395(4) Å, α = 83.54(2)°, β = 62.47(2)°, γ = 54.89(2)°, and V = 5398(3) Å^3. Over a range of 20 K, the unit cell volume varies by 57(3) Å^3 (~1%).

A common cell with comparable parameters and the volume $V_{com} = 2V$ (Table 3) was chosen for comparing the crystal lattices of phases **I** and **II**. The common cell for phase **I** is obtained by doubling the parameter $a_{\mathbf{I}}$ of the primitive cell, and the common cell for phase **II** is the *C* centered cell; in this case, the $a_{\mathbf{II}}$ translation centers the *C* face. (The common cell for phase **III** is chosen in the same way as for **II**.) The mean deviation of the

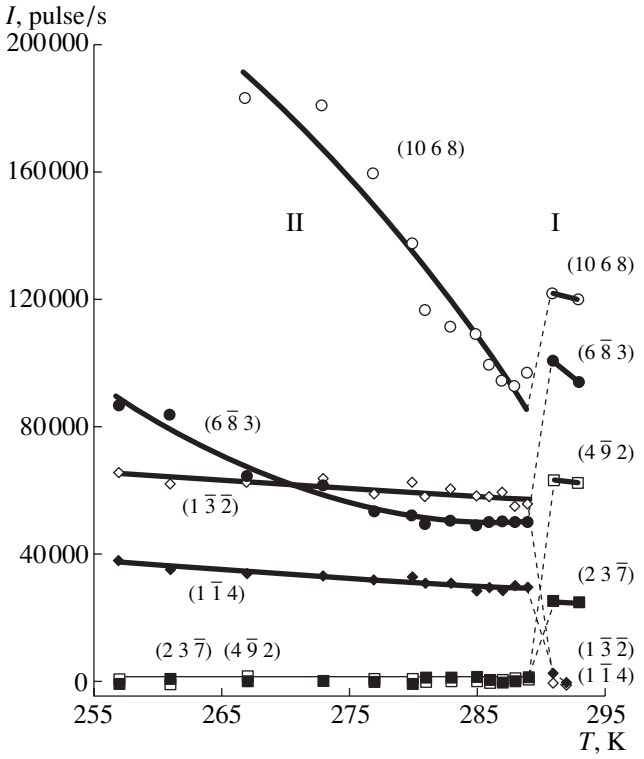

Fig. 3. Temperature dependences of the integrated intensities of six reflections: the (10 6 8) and (6 $\bar{8}$ 3) reflections common to phases **I** and **II**, the (4 $\bar{9}$ 2) and (2 3 $\bar{7}$) reflections characteristic of phase **I**, and the (1 $\bar{3}$ $\bar{2}$) and (1 $\bar{1}$ 4) reflections characteristic of phase **II**. Reflection indices correspond to the reciprocal spaces of common sublattices. The vertical size of symbols is ~2σ.

orientation matrix components for the common cells is equal to 4%, which confirms the correctness of our choice of these cells.

Out of the entire set of diffraction reflections obtained with identical parameters of scanning and integration for phases **IA** and **IIA**, we chose 349 pairs of reflections with the same indices (*HKL*) in the reciprocal space of common sublattices (described by the aforementioned common cells) and the intensities $I > 2\sigma(I)$ (at least, for one of the reflections involved in a pair). The distribution of these reflections over the parity classes (Table 3) revealed that the reflections with odd *H* are absent and the reflections with the odd sums $H + K$ are present in phase **IA**. This implies that the primitive translation $a_{\mathbf{I}} = a_{com}/2$ occurs and the centering translation $a_{\mathbf{II}}$ is absent in phase **IA**. By contrast, the $a_{\mathbf{II}}$ translation centering the common cell is observed (the sums $H + K$ are only even) and the $a_{\mathbf{I}}$ translation is absent (the presence of reflections with odd *H*) in phase **IIA**. Consequently, the structural phase transition **I** ⟷ **II** is attended by the disappearance of one primitive translation and the appearance of another translation. Note also that, upon phase transition, the intensities of reflections "common" to both phases change, on average, by 5σ for reflections with $I > 2\sigma(I)$ and by 9σ for 34 reflections with $I > 10\sigma(I)$.

Therefore, the structural phase transitions **I** ⟷ **II** and **II** ⟷ **III** are different-type ferrodistortion phase transitions which are characterized by a partial change in a system of translations in the former case (**I** ⟷ **II**) and only by its distortion in the latter case (**II** ⟷ **III**).

Analysis of structure-sensitive reflections. As can be seen from Table 3, among the (*HKL*) reflections, there are reflections typical of each phase—the reflections with $H + K = 2n + 1$ for the common sublattice of phase **I** and $H = 2n + 1$ for phase **II**. These reflections can be called the "characteristic" reflections of each phase. The appearance and disappearance of characteristic reflections upon the **I** ⟷ **II** phase transition can be used for the refinement of the transition temperature T_{cr1}. For this purpose, in the temperature range 250–296 K with a step of 3 K, we measured the integrated intensities of six reflections (Fig. 3), of which two reflections [(10 6 8) and (6 $\bar{8}$ 3)] are common and should be observed in both phases, two reflections [(4 $\bar{9}$ 2) and (2 3 $\bar{7}$)] are characteristic of phase **I**, and two reflections [(1 $\bar{3}$ $\bar{2}$) and (1 $\bar{1}$ 4)] are characteristic of phase **II**.

The experiment was performed on a Syntex $P2_1$ four-circle automated diffractometer. The orientation matrix components for the common cells at 296(3) (phase **I**) and 278(3) K (phase **II**) differed, on average, by 5%. The correspondence between the cells was revealed from the positions of the common reflections.

As is seen from Fig. 3, the intensities of the reflections common to both phases partly regain their values upon phase transition but exhibit a jump. The intensities of characteristic reflections in the phase transition range drastically decrease and become comparable to the background level. The obtained temperature $T_{cr1} = 290 \pm 3$ K agrees well with the DSC data. This experiment also confirms the aforementioned character of the change in the translational symmetry upon the **I** ⟷ **II** phase transition.

Temperature dependence of the unit cell parameters. In order to characterize the temperature dependences of the lattice parameters for the $Fe Nx_3(B Hd)_2$ complex upon phase transitions in the range 120–313 K, we determined the parameters of the common cell. The data shown in Figs. 4a and 4b were obtained for four single crystals on the Siemens *P*3/PC, Syntex $P2_1$, and Bruker SMART 1K CCD diffractometers.

The **I** ⟷ **II** phase transition in the temperature range 285–296 K is accompanied by a jumpwise change in the volume and parameters of the common cell: $\Delta V_{com} = 145(9)$ Å^3, $\Delta a_{com} = 0.367(12)$, $\Delta b_{com} = 0.139(12)$, $\Delta c_{com} = 0.084(8)$ Å, $|\Delta\alpha_{com}| = 0.85(4)°$, $|\Delta\beta_{com}| = 0.97(3)°$, and $|\Delta\gamma_{com}| = 3.31(4)°$. Note that the linear parameters (*a*, *b*, and *c*) decrease and the angular

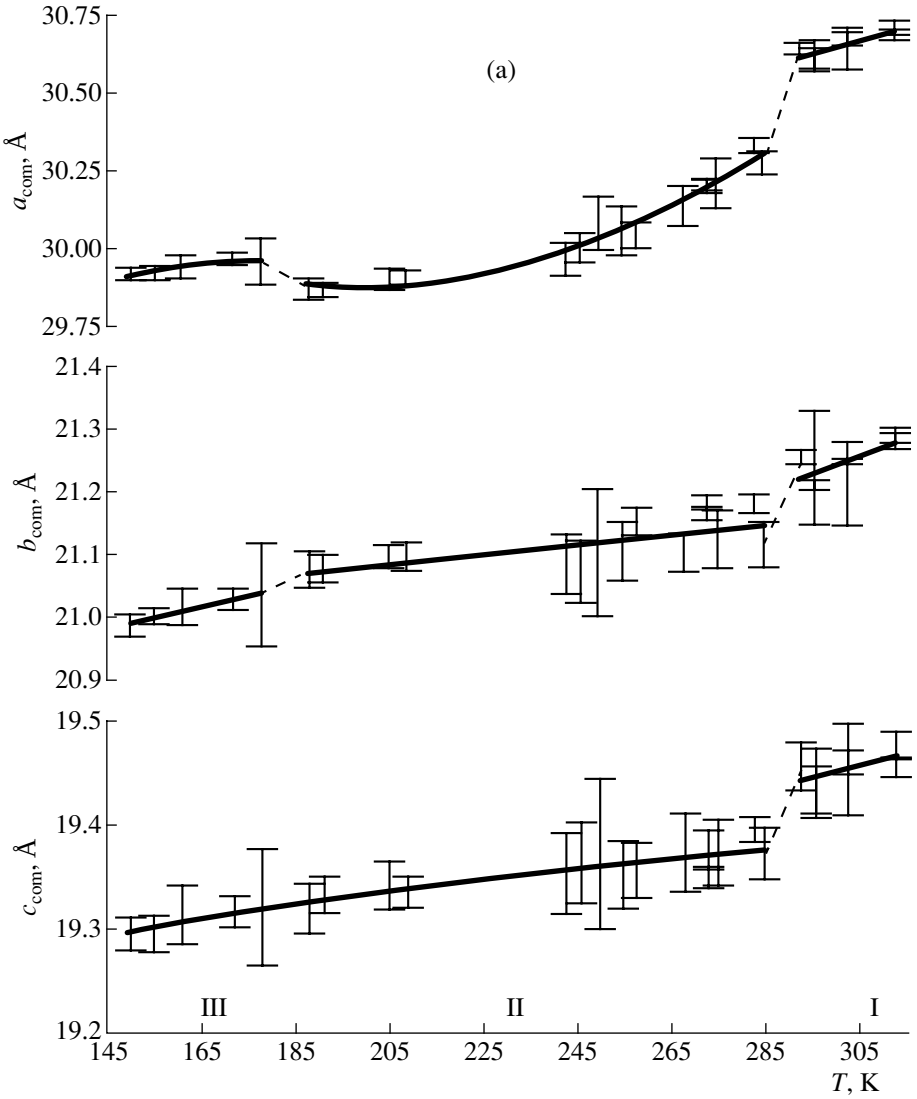

Fig. 4. Temperature dependences of (a) the linear parameters and (b) the angular parameters and the volume of the common cell for the FeNx_3(BHd)$_2$ crystal. Errors correspond to 3σ.

parameters (α, β, and γ) increase. The **II** ⟷ **III** phase transition occurs in the temperature range 172–188 K, which is in agreement with the calorimetric data. This transition is attended by an abrupt change in the parameters a_{com}, α_{com}, and γ_{com}: Δa_{com} = 0.097(10) Å, $|\Delta\alpha_{com}| = 1.19(3)°$, $|\Delta\gamma_{com}| = 0.71(4)°$. At the same time, the c_{com} and V_{com} parameters vary gradually. Variations in the remaining parameters (b_{com} and β_{com}) in the same temperature range are small and do not exceed 6σ.

Analysis of the thermal expansion of the crystal revealed two specific directions [0 $\bar{1}$ 1] and [0 1 1] in the crystallographic plane (100) of the common sublattice that are most sensitive to phase transitions. The temperature dependences of the $t_{[0\bar{1}1]}$ and $t_{[011]}$ translations (which correspond to these directions) and the interplanar distance D_{100} (this distance is equal to twice the interplanar distance d_{100} in the primitive lattices) are displayed in Fig. 5. The values of $t_{[0\bar{1}1]}$ in phase **I** and $t_{[011]}$ in phase **III** remain virtually constant with a change in the temperature, whereas the behavior of $t_{[0\bar{1}1]}$ in phase **II** indicates the negative linear thermal expansion coefficient along the [0 $\bar{1}$ 1] direction. It can be seen that the interplanar distance D_{100} varies in a gradual manner over the entire range 153–303 K (upon the **II** ⟷ **III** phase transition, its change is equal to ≈6σ).

Molecular geometry. The FeNx_3(BHd)$_2$ molecule (Fig. 2) contains three fragments: the clathrochelate skeleton with an encapsulated iron(II) ion (central fragment) and two hexadecyl substituents. The molecule has a strongly extended structure owing to two long-

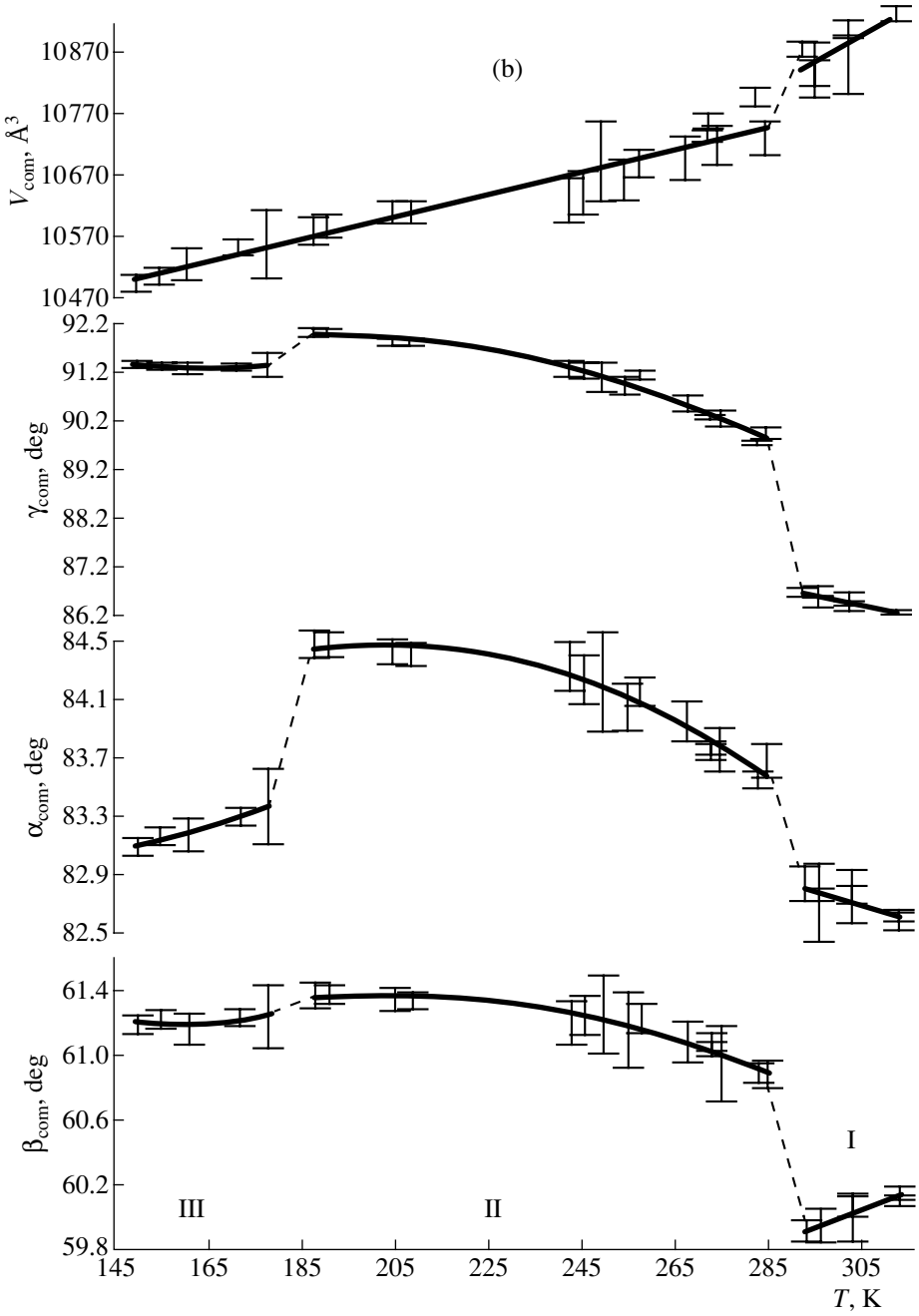

Fig. 4. (Contd.)

chain alkyl substituents: at 303 K, the "length" of the molecule (the distance between the terminal carbon atoms) is equal to 45.1–46.3 Å, and the angle between the long molecular axis (director) and the B··B pseudoaxis (passing through the boron atoms) of the central fragment is ~11°.

The central fragment has approximately a threefold symmetry with axis 3 coinciding with the B··B line and resembles a three-bladed propeller in its shape. Three α-dioximate fragments form almost planar "blades" (the six-membered carbocycles adopt a half-chair conformation in which the mean deviation of β-carbon atoms from the plane of the remaining atoms is equal to 0.38 Å). As a whole, the structure of the central fragment is characteristic of clathrochelates of this type [11, 12]; i.e., this fragment is twisted around the B··B axis. This twisting is described by the distortion angle φ (for a prism, φ = 0) of the iron coordination polyhedron $\{FeN_6\}$ formed by six donor nitrogen atoms. Four independent molecules can be separated into two pairs A, A' and B, B' with close values of the φ angle. Upon phase transitions, the φ angles change and become equal to

17° and 10° for molecules of the A and B types in phase **I**, 19° and 14° in phase **II**, and 20° for all the molecules in phase **III**.

The conformation of hexadecyl substituents in all the phases is considerably distorted. Analysis performed with the use of the Cambridge Structural Database for of twenty molecules containing an aliphatic chain n-$C_{16}H_{33}$ as a terminal fragment demonstrated that this chain in all compounds has a "classical" planar transoid structure [13], in which the mean deviation of carbon atoms from the root-mean-square plane is equal to 0.03 Å and the total chain length (the distance C···C between the first and last carbon atoms) is ~19.07 Å. In the temperature range 153–303 K, the length of hexadecyl substituents in the FeNx_3(BHd)$_2$ complex varies in the range 17.6–19.0 Å, which is noticeably less than the above value (Table 4). The possibility that the geometric features discussed below for hexadecyl substituents in the FeNx_3(BHd)$_2$ complex stem from the unresolved disordering must not be ruled out. Nonetheless, these features were rather regular and reproducible in the course of the structure refinement. The shortest substituent C(35B)···C(50B) with a length of 17.6 Å is observed in phase **I**, which is due to the *gauche* conformation of the terminal part of the chain and a substantially nonplanar chain geometry (the mean deviation of carbon atoms from the root-mean-square plane is 0.24 Å). Moreover, compared to the completely transoid aliphatic chain, the substituents involving two segments with a *gauche* configuration (the corresponding torsion angles are close to 60°) are considerably shortened (by approximately 1 Å). In phases **I** and **II**, this geometry is observed only in one substituent (Fig. 2). At the same time, in phase **III**, one substituent in each independent molecule is twisted in a similar manner (Table 4). In other cases, a decrease in the substituent length is associated with different combinations and the number of segments with a "nontransoid" configuration. It is worth noting that the mean length of carbon skeletons in phases **I** (18.3 Å) and **III** (18.2 Å) increases upon transition to phase **II** (18.6 Å). This can be explained by the fact that their configuration approaches the classical geometry.

Thus, both phase transitions in the FeNx_3(BHd)$_2$ complex are accompanied by the change in the molecular geometry, which, in particular, manifests itself in an increase in the twisting of the central fragments and a change in the effective length of hexadecyl substituents.

Molecular packing. In the subsequent discussion, we will use the primitive cells of phases **I**–**III** (Table 1). Because the parameters b, c, and α of the unit cell and the parameters b_{com}, c_{com}, and α_{com} of the common cell (as well as the translations $t_{[0\bar{1}1]}$ and $t_{[011]}$) are identical, the mutual displacements of molecules in the (100) layer will be discussed with the use of Figs. 4 and 5, which show the temperature dependences of the parameters of the common cell.

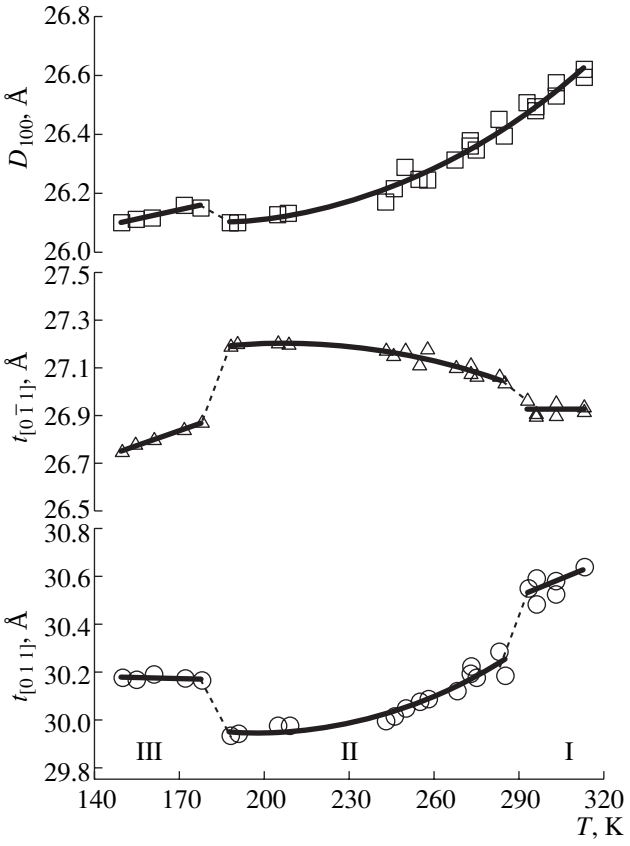

Fig. 5. Temperature dependences of the interplanar distance D_{100} and the translations $t_{[0\,1\,1]}$ and $t_{[0\,\bar{1}\,1]}$ of the common sublattice for the FeNx_3(BHd)$_2$ crystal.

In all three phases, the molecular packing of FeNx_3(BHd)$_2$ is typical of tilted smectic mesophases [14]. All four independent molecules (A, A', B, and B') form layers (Fig. 6) aligned parallel to the crystallographic plane (100). The directors of all molecules are parallel and form an angle of ~15° with the (100) plane. In the layer, the centers of mass of all the molecules, which actually coincide with the positions of iron atoms, are coplanar: the maximum deviation from the root-mean-square plane lying parallel to the (100) plane does not exceed 0.5 Å. In the temperature range 150–313 K, the interplanar distance d_{100} is equal to 13.05–13.31 Å. The adjacent (100) layers are related by the translation.

A distinguishing feature of the molecular packing in phases **I**–**III** is the formation of dimers from molecules A and B (dimer AB) and A' and B' (dimer A'B') (Fig. 7). The distance between the iron atoms in the molecules forming a dimer (8.41 Å in phase **I** and 8.37 Å in phases **II** and **III**) is almost 2 Å less than any one intermolecular distance Fe···Fe in the (100) layer. The B···B axes of molecules in the dimer lie approximately in the same

Table 4. Intermolecular distances Fe···Fe and carbon skeleton lengths of hexadecyl substituents in the FeNx_3(BHd)$_2$ molecule (Å)

Group	Atoms	Phase **I**	Atoms	Phase **II**	Phase **III**
1	Fe(1)···Fe(4)[1]	47.46	Fe(1)···Fe(4)[1]	48.56	48.09
	C(35)···C(50)	17.7(*)		18.3(*)	17.9(*)
			C(35)···C(50*D*)		17.7(*)
	C(35*C*)···C(50*C*)	18.2	C(35*A*)···C(50*A*)	17.9	17.9
			C(35*A*)···C(50*E*)		18.3
2	Fe(3)···Fe(2)[2]	48.17	Fe(3)···Fe(4)[1]	48.55	48.08
	C(35*B*)···C(50*B*)	17.6		18.7	18.2
			C(35*B*)···C(50*F*)		18.9
	C(35*A*)···C(50*A*)	18.6	C(35*C*)···C(50*C*)	18.2	17.9(*)
			C(35*C*)···C(50*G*)		17.6(*)
3	Fe(2)···Fe(1)[2]	28.33	Fe(2)···Fe(3)[1]	28.78	28.35
	C(19*A*)···C(34*A*)	18.8		18.9	18.3(*)
	C(19)···C(34)	18.4	C(19*B*)···C(34*B*)	18.8	18.1(*)
4	Fe(4)···Fe(3)[2]	28.33	Fe(4)···Fe(1)[2]	28.87	28.90
	C(19*C*)···C(34*C*)	18.7		19.0	19.0
	C(19*B*)···C(34*B*)	18.6	C(19)···C(34)	19.0	19.0

Note: Contacting molecules in the adjacent (100) layers are separated into groups: groups 1 and 2 involve contacts of the substituent–substituent type, and groups 3 and 4 contain contacts of the substituent–blade type. Designations of the corresponding distances in phases **II** and **III** are given in the fourth column. Symmetry transformations relating the symmetrically equivalent atoms: [1] $1 + x, -2 + y, 1 + z$; [2] $1 + x, -1 + y, 1 + z$.

* Hexadecyl substituent has the same geometry as the *C*(35)···*C*(50) substituent shown in Fig. 2.

plane and form an angle of ~20° (Fig. 7). The packing of dimers in the (100) layer (Fig. 7) differs from the herring-bone packing, which is characteristic of smectics [14], and has approximately the $p(\bar{1})$ symmetry (dimers AB and A'B' are approximately related by the inversion center) [15].

A decrease in the temperature leads to the displacement of dimers as a unit with respect to each other in the (100) layer. The general character of molecular displacements can be attributed to variations in the $t_{[011]}$ and $t_{[0\bar{1}1]}$ translations. As can be seen from Fig. 5, upon the **I** ⟶ **II** phase transition, dimers in the (100) layer noticeably approaches each other in the [0 1 1] direction (perpendicular to the molecular directors in Fig. 7). This necessarily gives rise to steric stresses between

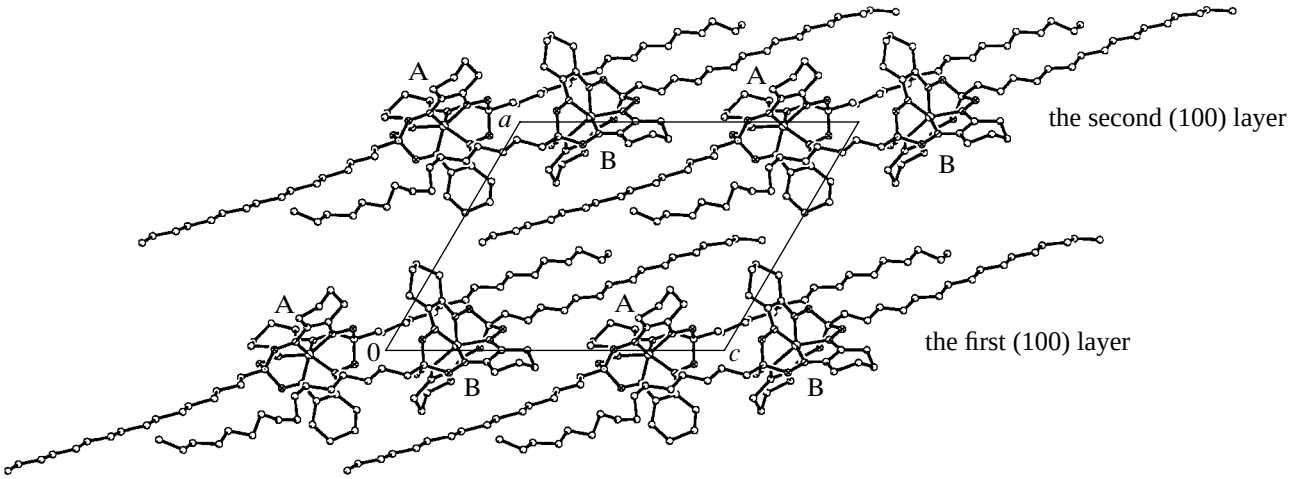

Fig. 6. Partial projection of the crystal structure of the FeNx_3(BHd)$_2$ clathrochelate in phase **I** along the *b*-axis.

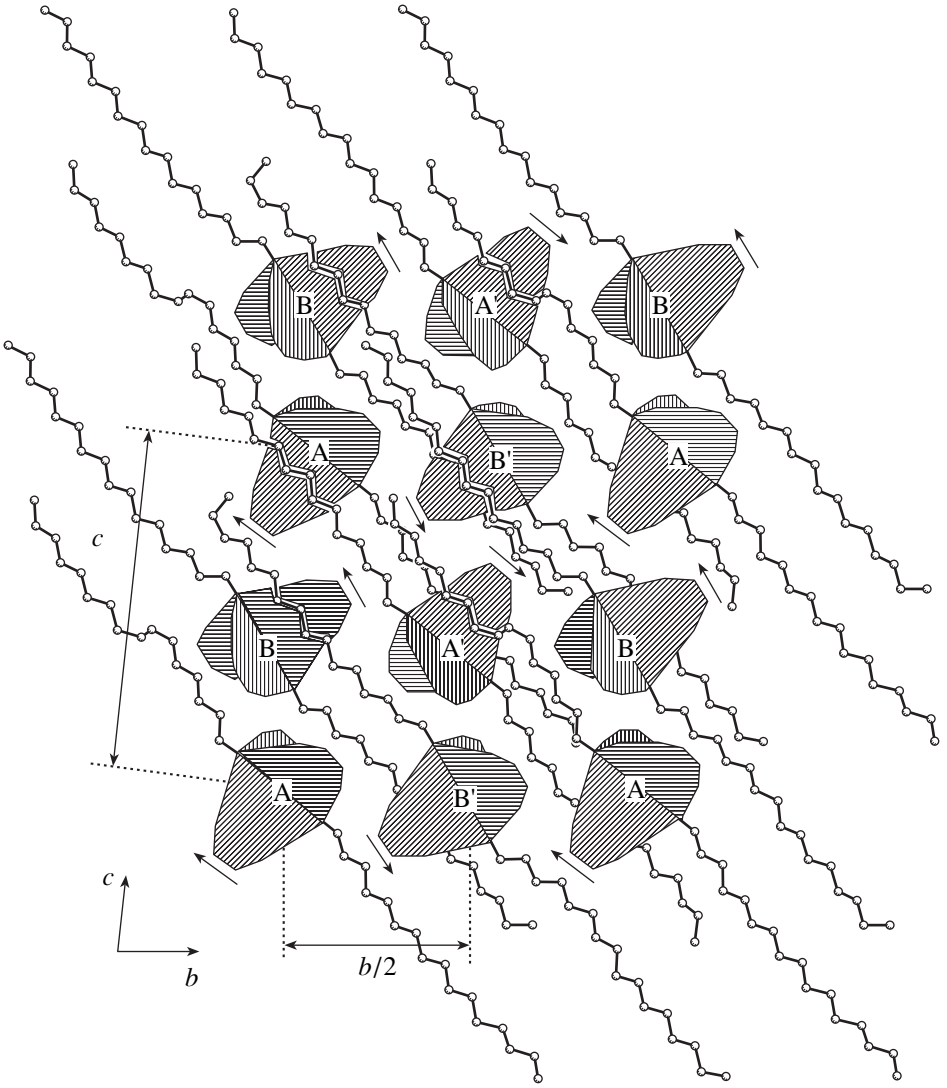

Fig. 7. A schematic representation of the molecular packing in the (100) layer for $FeNx_3(BHd)_2$ crystal (similar packing is observed for all the phases). Arrows indicate the directions of rotation of the central fragments (around iron atoms), resulting in the apparent displacement of the (100) layer by *b*/2.

blades of different dimers. These stresses are relieved when the distance between the dimers in the perpendicular direction [0 $\bar{1}$ 1] increases, i.e., due to their displacement along long molecular axes (Fig. 7), which manifests itself in an increase in $t_{[0\bar{1}1]}$. The reverse situation is observed upon the **II** ⟶ **III** phase transition: the packing in the (100) layer in phase **III** becomes similar to that in phase **I**. This can be judged from the $t_{[011]}$ and $t_{[0\bar{1}1]}$ translations and the α angle, which tend to regain their values observed in phase **I** (Figs. 4b, 5). However, it should be emphasized that, despite a certain lability, the (100) molecular layer has a similar structure in all the phases.

The character of stacking the (100) layers is clearly seen from the projection of the structure onto the crystallographic plane $(10\bar{1})$ (Fig. 8). The substituent of each molecule "meets" either a hexadecyl substituent (molecules A and A', B and B' in phase **I**; A and B, A' and B' in phase **II**) or a blade (molecules A and B, A' and B' in phase **I**; A and A', B and B' in phase **II**) of a complex in the adjacent (100) layer (Fig. 8). In each phase, two contacts of the substituent–substituent type and four contacts of the substituent–blade type are observed in the two-dimensional primitive cell of the $(10\bar{1})$ layer (Table 4).

Structural transformations upon phase transitions. The two-dimensional cells of the $(10\bar{1})$ layer in phases **I** and **II** are depicted by the solid lines in Figs. 8a and 8b, respectively. A comparison of Figs. 8a and 8b gives the impression that the **I** ⟶ **II** phase transition consists in displacing the second (100) layer

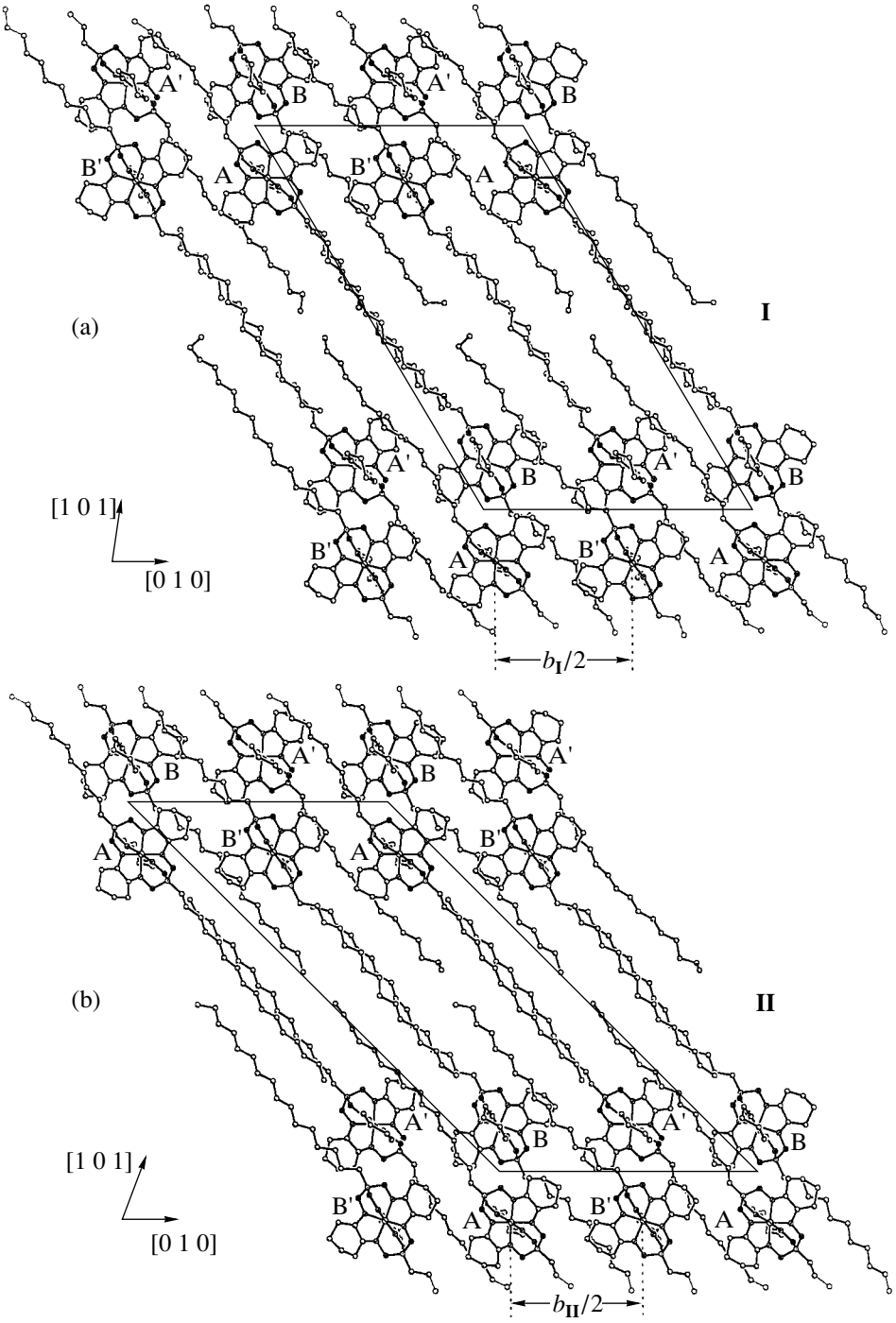

Fig. 8. Projections of the crystal structure of phases (a) **I** and (b) **II** onto the (1 0 $\bar{1}$) plane. Solid lines show the two-dimensional primitive cells of the (1 0 $\bar{1}$) layer.

by the distance $b/2$. A similar pattern of structural transformations in 4,4'-dichlorobenzophenone was observed earlier in [16]. In this structure, a decrease in the temperature is accompanied by the phase transition (in the range of 190 K) from the phase with the space group $C2/c$ to the phase with the space group $I2/c$ without a change in the parameters and the number of formula units in the unit cell. This implies that the phase transition is attended by the disappearance of the translation centering the C face and the appearance of the translation centering the unit cell volume. As a result, each second layer is displaced by the distance $c/2$. Unlike the **I** ⟶ **II** phase transition in $FeNx_3(BHd)_2$, the phase transition in 4,4'-dichlorobenzophenone occurs over a temperature range of ~20 K through a disordered intermediate state (with the unit cell parameter $c/2$) which

can transform either into the high-temperature *C* phase or into the low-temperature **I** phase, depending on the direction of the temperature variation.

For the **I** ⟶ **II** phase transition in FeNx_3(BHd)$_2$, no intermediate state is found. In this case, we can propose another mechanism of the structural transformation when all molecules in each second layer undergo a conformational transition which results in the apparent displacement of the layer by one-half the translation. By considering only the arrangement of the directors and the centers of mass of the molecules, it can be seen that the "subtranslation" equal to ~*b*/2 occurs in the crystal structure of FeNx_3(BHd)$_2$ (Figs. 7, 8). The realization of the primitive translation $a_{\mathbf{I}}$ (phase **I**) or $a_{\mathbf{II}}$ (phase **II**) in the superlattice with the parameter *b*/2 (in which both translations $a_{\mathbf{I}}$ and $a_{\mathbf{II}}$ take place) is determined by the mutual orientation of the central fragments in the adjacent (100) layers. For example, molecules A and B' in Fig. 8a would be translationally identical if the B···B axis of the B' molecule were rotated through an angle of 20°. This rotation in one molecule leads to the rotation of the B···B axes of the central fragments in all the remaining molecules in the (100) layer, as is shown in Fig. 7. As a consequence, the (100) layer would appear as though it were displaced by *b*/2.

As the stacking of the (100) layers changes upon the **I** ⟶ **II** phase transition, the distance along the hexadecyl substituents increases by 1.1 Å (Table 4). In this case, the length of the substituents being in contact with blades of molecules in the adjacent (100) layers (Fig. 7) increases and can initiate the aforementioned conformational transition.

In the temperature range from 243 to 153 K (the **II** ⟶ **III** phase transition), the length of the region occupied by the hexadecyl substituents decreases, on average, by 0.5 Å for six substituents (Table 4). This gives rise to steric stresses and brings about a decrease in the effective length of the substituents. As a result, at 153 K, already four substituents (in contrast with one substituent at 243 K) have two segments with a *gauche* conformation. Therefore, the change in the conformation of hexadecyl substituents can be associated, to a large measure, with the phase transition at T_{cr2}.

CONCLUSION

The FeNx_3(BHd)$_2$ single crystal was investigated by X-ray diffraction and differential scanning calorimetry. It was found that the crystal undergoes two different-type reversible phase transitions at T_{cr1} = 290(3) K and T_{cr2} = 190(3) K without a change in the number of formula units in the unit cell. The transition between phases **I** and **II** results in the disappearance of one primitive translation and the appearance of another translation, so that each second molecular (100) layer turns is displaced by ~*b*/2. This transformation is confirmed by the diffraction patterns of the same single crystal and the temperature dependence of the integrated intensity of the structure-sensitive diffraction reflections. Steric stresses that arise between contacting molecules of the adjacent (100) layers play an important role in the mechanism of the phase transition in the vicinity of T_{cr1}. Both transitions are accompanied by the distortion of the molecular geometry, specifically by the deviation from the planar transoid conformation of hexadecyl substituents. This distortion is associated, to a large measure, with the transition between phases **II** and **III**. As a whole, the mechanisms of both transitions have a complex character and can be considered a superposition of processes of the displacement and intramolecular distortion types. The characteristic structural features of the clathrochelate complex under consideration are the high lability of hexadecyl substituents and the central fragment and also its compact structure. These features favor the realization of a series of phase transitions in the crystal. In this aspect, clathrochelate complexes are similar to another family of organometallic compounds, namely, metallocenes and their derivatives [1].

ACKNOWLEDGMENTS

We are grateful to Z.A. Starikova for helpful remarks in discussing the results and É.V. Pol'shin for providing the ^{57}Fe Mössbauer spectroscopic data for the FeNx_3(BHd)$_2$ compound.

This work was supported by the Russian Foundation for Basic Research, project nos. 97-03-33783, 96-15-97367, 99-07-90133, and 00-03-32578.

REFERENCES

1. I. I. Vorontsov, K. A. Potekhin, M. Yu. Antipin, and I. E. Zanin, Kristallografiya **45** (2), 266 (2000) [Crystallogr. Rep. **45**, 234 (2000)].
2. R. Blinc and B. Zeks, in *Soft Modes in Ferroelectrics and Antiferroelectrics* (North-Holland, Amsterdam, 1974), p. 1.
3. N. A. Kostromina, Ya. Z. Voloshin, and A. Yu. Nazarenko, *Clathrochelates: Synthesis, Structure, and Properties* (Naukova Dumka, Kiev, 1992).
4. Ya. Z. Voloshin, Ross. Khim. Zh. **42** (1–2), 5 (1998).
5. I. I. Vorontsov, M. Yu. Antipin, K. A. Potekhin, and Ya. Z. Voloshin, in *Proceedings of the School–Conference of Young Scientists "Metalloorganic Chemistry on the Threshold of the 21th Century", Moscow, 1999*, p. 60.
6. *SMART and SAINT: Area Detector Control and Integration Software, Release 5.0* (Bruker AXS, Analytical X-ray Instruments, Madison, 1998).
7. V. A. Strel'tsov and V. E. Zavodnik, Kristallografiya **34** (6), 1369 (1989) [Sov. Phys. Crystallogr. **34**, 824 (1989)].
8. G. M. Sheldrick, *SADABS: A Program for Exploiting the Redundancy of Area-Detector X-ray Data* (Univ. of Göttingen, Göttingen, 1999).

9. G. M. Sheldrick, *SHELXTL97: An Integrated System for Solving, Refining and Displaying Crystal Structures from Diffraction Data, Version 5.10* (Bruker AXS, Madison, 1997).
10. F. H. Allen, O. Kennard, D. G. Watson, *et al.*, J. Chem. Soc., Perkin Trans. 2, S51 (1987).
11. Y. Z. Voloshin, T. E. Kron, V. K. Belsky, *et al.*, J. Organomet. Chem. **536**, 207 (1997).
12. Y. Z. Voloshin, O. A. Varzatskii, T. E. Kron, *et al.*, Inorg. Chem. **39**, 1907 (2000).
13. A. I. Kitaigorodsky, *Molecular Crystals* (Nauka, Moscow, 1971).
14. P. M. Zorky, T. V. Timofeeva, and A. P. Polishchuk, Usp. Khim. **58**, 1971 (1989).
15. *Modern Crystallography*, Vol. 1: *Symmetry and Methods of Structural Crystallography*, Ed. by B. K. Vainshtein, A. A. Chernov, and L. A. Shuvalov (Nauka, Moscow, 1979; Springer-Verlag, Berlin, 1994, 2nd ed.).
16. V. V. Mitkevich, V. G. Lirtsman, M. A. Strzhemechny, *et al.*, Acta Crystallogr., Sect. B: Struct. Sci. **B55**, 799 (1999).

Translated by O. Borovik-Romanova

Crystallography Reports, Vol. 46, No. 5, 2001, pp. 771–778. Translated from Kristallografiya, Vol. 46, No. 5, 2001, pp. 845–852.

STRUCTURES OF COORDINATION COMPOUNDS

Effect of the Acid–Base Interactions in a Solution on the Composition of the Coordination Sphere of Aluminum and Gallium Complexonates

A. B. Ilyukhin and S. P. Petrosyants

Kurnakov Institute of General and Inorganic Chemistry, Russian Academy of Sciences, Leninskiĭ pr. 31, Moscow, 119991 Russia

e-mail: ilyukhin@ionchran.rinet.ru

Received June 15, 2000

Abstract—Hydroxocomplexonate K_2[Ga*Edta*(OH)] · $6H_2O$ (**I**) and nitronium salts *B*H$^+$Ga*Edta* · $4H_2O$ (**II**) and *B*H$^+$Al*Edta* · $4H_2O$ (**IV**) are synthesized from aqueous solutions at pH 8, 6, and 7, respectively. AlH*Edta*(H_2O) (**III**) is isolated from an acid solution (pH 1.5). Structures **I**, **II**, and **IV** are determined by single-crystal X-ray diffraction. The X-ray powder diffraction analysis of **III** has revealed that its crystals are not isostructural with those of similar complexes of other metals. Crystals **I**–**IV** are monoclinic. The unit cell parameters are a = 10.482(1), 15.735(4), 5.768(4), and 15.756(4) Å; b = 10.442(2), 12.511(2), 14.884(11), and 12.453(3) Å; c = 19.590(4), 17.330(5), 19.113(12), and 17.328(6) Å; β = 101.30(2)°, 104.54(2)°, 90.74(5)°, and 104.75(2)° for **I**–**IV**, respectively. © *2001 MAIK "Nauka/Interperiodica".*

INTRODUCTION

Earlier [1], we found that the acid–base interactions in a solution affect both the deprotonation of GaH*Edta*(H_2O) (where H_4*Edta* is ethylenediaminetetraacetic acid), which results in the formation of the Ga*Edta*$^-$ anion, and the substitution of the acido ligand (F^- or NCS^-) for coordinated water molecules.

In the present work, we studied the formation of AlH*Edta*(H_2O), gallium hydroxocomplexonate, and *MEdta*$^-$ anions (*M* = Al or Ga) in the presence of the organic base (*B*) 4,5-dihydro-1,4-diphenyl-3,5-phenylimino-1,2,4-triazole (nitron).

EXPERIMENTAL

All except one of the reagents used in this work were commercial products. The GaH*Edta*(H_2O) compound was prepared according to the procedure described in [1].

Synthesis K_2[Ga*Edta*(OH)] · $6H_2O$ (I). GaH*Edta*(H_2O) (1.4 mmol) and KOH (2.8 mmol) were mixed in 80 ml H_2O (pH 8). The solution was allowed to concentrate at room temperature until the solid phase precipitated. The crystals were separated on a glass filter funnel, washed with ethanol, and dried in a desiccator over silica gel. The yield was 86%.

***B*H$^+$Ga*Edta* · $4H_2O$ (II).** GaH*Edta*(H_2O) (1.3 mmol) and nitron (1.3 mmol) were mixed in 50 ml H_2O and stirred with a magnetic agitator for 2.5 h on heating. After five days, the solution obtained (pH 6) afforded crystals, which were filtered off on a glass filter funnel, washed with ethanol and acetone, and dried at 80°C. The yield was 55%.

AlH*Edta*(H_2O) (III). A solution of $AlCl_3$ containing 10 mmol of aluminum was neutralized with ammonium hydroxide. Aluminum hydroxide was isolated, washed with water, and mixed with H_4*Edta* (10 mmol) in water (80 ml) on heating and stirring. The solution obtained (pH 1.5) was filtered off and evaporated on a water bath to 1/4 of the initial volume. The crystalline precipitate (H_4*Edta*) was separated out. The mother liquor was evaporated to 5 ml, and the finely disperse precipitate obtained in this volume was separated on a glass filter funnel, washed with water, and dried in air at 90°C. The yield was 30%.

***B*H$^+$Al*Edta* · $4H_2O$ (IV).** Nitron (1 mmol) and AlH*Edta*(H_2O) (1 mmol) were refluxed on stirring with a magnetic agitator for 3 h. The brown solution (pH 7) was filtered off under a crystallizing dish. After six days, crystals **IV** precipitated. They were washed with water and acetone and dried at 80°C. The yield was 40%.

Aluminum and gallium were determined as M_2O_3 by gravimetric analysis. The H, C, and N contents were determined according to the standard procedures with a Carlo Erba analyzer. The results are listed in Table 1.

The IR spectra were recorded on a Specord 75 IR spectrometer in the range 400–4000 cm^{-1}. The samples were prepared as suspensions in petrolatum oil or KBr pellets.

The X-ray powder diffraction study was performed with a FR-502 monochromating camera

Table 1. Data of the elemental analysis

Compound	Formula	Content (found/calcd), %			
		C	N	H	*M*
$K_2[GaEdta(OH)] \cdot 6H_2O$	$C_{10}H_{25}O_{15}N_2GaK_2$	21.56/21.38	4.96/4.98	6.97/4.44	
$BH^+GaEdta \cdot 4H_2O$	$C_{30}H_{37}O_{12}N_6Ga$	48.43/48.42	10.45/11.30	6.24/4.98	9.76/9.38
$AlHEdta(H_2O)$	$C_{10}H_{15}O_9N_2Al$	35.03/35.90	8.21/8.38	5.35/4.49	7.35/8.08
$BH^+AlEdta \cdot 4H_2O$	$C_{30}H_{37}O_{12}N_6Al$	50.74/51.43	10.84/12.00	7.66/5.98	3.95/3.85

Table 2. X-ray diffraction pattern of compound **III**

h	*k*	*l*	d_{exp}, Å	d_{calcd}, Å	*I*	*h*	*k*	*l*	d_{exp}, Å	d_{calcd}, Å	*I*
0	2	1	6.99	6.93	100	1	5	2	2.542	2.546	<1
1	0	0	5.77	5.77	90	0	5	4	2.514	2.526	<1
1	1	0	5.38	5.38	5	0	6	0	2.480	2.481	1
1	1	–1	5.20	5.19	30	2	3	–2	2.419	2.419	5
1	1	1	5.14	5.16	10	0	3	7	2.391	2.392	<1
1	0	–2	5.00	4.97	5	0	1	8	2.357	2.359	<1
1	0	2	4.94	4.91	20	1	2	7	2.332	2.332	<1
0	2	3	4.83	4.84	<1	1	5	4	2.308	2.308	<1
0	0	4	4.77	4.78	2	2	1	–5	2.284	2.289	<1
1	2	–1	4.44	4.44	20	2	4	1	2.260	2.261	<1
0	3	2	4.40	4.40	20	1	4	6	2.228	2.224	<1
0	2	4	4.01	4.02	5	2	3	4	2.199	2.200	<1
0	3	3	3.952	3.914	1	1	5	5	2.168	2.169	<1
1	3	0	3.780	3.761	1	2	1	–6	2.132	2.130	<1
0	4	1	3.619	3.652	1	0	7	1	2.112	2.113	<1
1	1	–4	3.602	3.593	20	2	3	–5	2.094	2.099	<1
1	1	4	3.540	3.551	5	2	4	–4	2.065	2.066	5
1	3	–2	3.511	3.510	1	1	1	–9	1.982	1.983	<1
0	3	4	3.435	3.442	3	2	5	3	1.964	1.964	<1
1	2	–4	3.317	3.315	10	2	2	–7	1.930	1.927	<1
1	3	3	3.227	3.251	1	2	5	–4	1.908	1.907	<1
0	0	6	3.172	3.185	<1	3	1	–2	1.876	1.874	<1
1	4	–1	3.092	3.089	<1	0	4	9	1.844	1.844	<1
1	4	1	3.074	3.082	1	2	5	–5	1.829	1.828	1
0	3	5	3.016	3.028	1	1	2	10	1.757	1.756	<1
1	3	–4	2.967	2.968	<1	1	5	9	1.652	1.651	<1
1	2	5	2.912	2.914	2	0	6	9	1.613	1.613	<1
0	5	2	2.855	2.842	1	2	1	10	1.575	1.575	<1
2	1	1	2.790	2.795	2	2	4	–9	1.562	1.562	<1
2	0	–2	2.771	2.771	20	2	8	–3	1.521	1.521	<1
2	0	2	2.750	2.751	<1	2	7	–7	1.455	1.455	<1
0	5	3	2.699	2.697	<1	4	5	2	1.284	1.284	<1
2	1	3	2.575	2.575	1						

Table 3. Main crystal data and structure-refinement parameters for **I–IV**

Compound	**I**	**II**	**III**	**IV**
Formula	$C_{10}H_{25}O_{15}N_2GaK_2$	$C_{30}H_{37}O_{12}N_6Ga$	$C_{10}H_{15}O_9N_2Al$	$C_{30}H_{37}O_{12}N_6Al$
Crystal system	Monoclinic	Monoclinic	Monoclinic	Monoclinic
a, Å	10.482(1)	15.735(4)	5.768(4)	15.756(4)
b, Å	10.442(2)	12.511(2)	14.884(11)	12.453(3)
c, Å	19.590(4)	17.330(5)	19.113(12)	17.328(6)
β, deg	101.30(2)	104.54(2)	90.74(5)	104.75(2)
Z	4	4	4	4
V, Å^3	2102.6(6)	3302.3(14)	1641(2)	3287.9(16)
Space group	$P2_1/c$	$P2_1/c$	$P2_1/c$	$P2_1/c$
d, g/cm^3	1.773	1.495	1.353	1.415
μ, mm^{-1}	1.780	0.906		0.134
θ_{max}	40	25		26
N_c/N_o^*	5343/5331	4632/4632		6686/6457
N_p^*	271	442		582
R_1/wR_2 ($I > 2\sigma$)**	0.0496/0.1271	0.0297/0.0692		0.0410/0.1095
R_1/wR_2 (all data)	0.0515/0.1287	0.0346/0.0710		0.0748/0.1270
*Goof***	1.064	0.849		1.011

Note: For compounds **I**, **II**, and **IV**, the data were collected on an Enraf–Nonius CAD4 diffractometer (MoK_α radiation).

* N_c is the number of unique reflections measured, N_o is the number of reflections with $I > 2\sigma(I)$, and N_p is the number of parameters refined.

** $R_1 = \Sigma||F_o| - |F_c||/\Sigma|F_o|$, $wR_2 = \{\Sigma[w(F_o^2 - F_c^2)^2]/\Sigma[w(F_o^2)^2]\}^{1/2}$, and $Goof = \{\Sigma[w(F_o^2 - F_c^2)^2]/(N - N_p)\}^{1/2}$.

(λCuK_α); the intensities were estimated visually. The X-ray diffraction pattern was indexed analytically. The unit cell parameters were refined with the POWTOOL program [2]. The X-ray diffraction pattern is represented in Table 2 [$F30 = 6.2$ (0.065, 74); $M20 = 2.3$].

The X-ray structure analysis. The main crystallographic parameters and the results of the structure refinement are summarized in Table 3. Structures **I**, **II**, and **IV** were solved by combinations of the direct method and the difference Fourier syntheses (SHELXS97 and SHELXL97 [3, 4]). In structures **I** and **II**, the positions of all aliphatic and aromatic hydrogen atoms were calculated from geometric considerations and the remaining hydrogen atoms were located from the difference Fourier syntheses. The hydrogen atoms in **I** and **II** were fixed in the refinement of the structures by the full-matrix least-squares procedures. In structure **IV**, all hydrogen atoms were located and refined isotropically. The atomic coordinates and thermal parameters are listed in Table 4.

RESULTS AND DISCUSSION

Reaction of GaH*Edta*(H_2O) with KOH at pH 5 gave K[Ga*Edta*] · $2H_2O$ (80%), in which the OH^- ligand was not included in the coordination sphere of gallium [1]. Formation of the hydroxide derivative requires higher pH of the reaction solution. Actually, the gallium complexonate with a coordinated hydroxo group, K_2[Ga*Edta*(OH)] · $6H_2O$, is formed in a high yield (86%) at pH 8. Its composition and structure were confirmed by elemental analysis, spectroscopic date, and

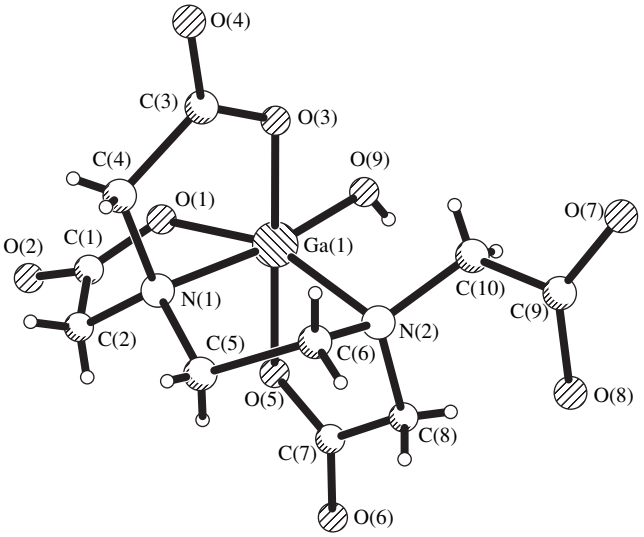

Fig. 1. Structure of the anionic complex in **I**.

Table 4. Atomic coordinates and equivalent (isotropic) thermal parameters ($Å^2$) in structures **I**, **II**, and **IV**

Atom	*x*	*y*	*z*	U_{eq}/U_{iso}
		I		
Ga(1)	0.33638(3)	0.66783(3)	0.17787(1)	0.01631(7)
K(1)	0.14205(9)	1.06369(9)	−0.16702(4)	0.03642(16)
K(2)	0.33558(7)	1.01153(7)	0.02701(3)	0.02766(13)
O(1)	0.4303(2)	0.7227(2)	0.26964(11)	0.0247(4)
O(2)	0.5683(4)	0.6524(3)	0.36169(13)	0.0417(4)
O(3)	0.40416(19)	0.7985(2)	0.12079(11)	0.0222(4)
O(4)	0.5775(3)	0.8697(3)	0.08287(18)	0.0437(7)
O(5)	0.2840(2)	0.5111(2)	0.22355(10)	0.0239(4)
O(6)	0.1964(3)	0.3175(2)	0.20999(13)	0.0318(5)
O(7)	0.1449(4)	0.6335(3)	−0.09361(13)	0.0415(7)
O(8)	0.1582(4)	0.4395(3)	−0.04756(14)	0.0449(8)
O(9)	0.1867(2)	0.7624(2)	0.17302(12)	0.0255(4)
O(10)	0.1413(3)	1.1691(3)	−0.02951(18)	0.0437(6)
O(11)	0.0597(3)	1.3302(3)	−0.17515(14)	0.0346(5)
O(12)	−0.1114(4)	1.0622(3)	−0.26352(15)	0.0465(8)
O(13)	0.1112(3)	0.9306(3)	0.06781(17)	0.0416(6)
O(14)	0.3077(5)	0.8522(4)	−0.0883(2)	0.0621(11)
O(15)	−0.0141(4)	0.8556(3)	−0.13541(19)	0.0498(8)
N(1)	0.5242(2)	0.5847(2)	0.17835(11)	0.0181(4)
N(2)	0.2787(2)	0.5448(2)	0.08548(11)	0.0171(4)
C(1)	0.5232(3)	0.6492(3)	0.29891(15)	0.0252(5)
C(2)	0.5742(3)	0.5527(3)	0.25270(15)	0.0248(5)
C(3)	0.5238(3)	0.7922(3)	0.11557(16)	0.0232(5)
C(4)	0.6048(2)	0.6839(3)	0.15407(16)	0.0247(5)
C(5)	0.5040(3)	0.4717(3)	0.13150(16)	0.0241(5)
C(6)	0.4031(3)	0.5045(3)	0.06681(14)	0.0226(5)
C(7)	0.2312(3)	0.4180(3)	0.18565(14)	0.0207(4)
C(8)	0.2074(3)	0.4347(3)	0.10717(15)	0.0255(5)
C(9)	0.1665(3)	0.5572(3)	−0.04316(15)	0.0243(5)
C(10)	0.1997(3)	0.6211(3)	0.02858(14)	0.0217(4)
		II		
Ga(1)	0.70798(2)	0.47211(2)	0.77767(2)	0.0355(1)
O(1)	0.63210(11)	0.48266(15)	0.85235(9)	0.0399(4)
O(2)	0.58245(14)	0.59112(17)	0.93311(11)	0.0639(6)
O(3)	0.81868(12)	0.49479(15)	0.85369(9)	0.0453(5)
O(4)	0.92905(15)	0.60870(19)	0.87562(12)	0.0717(6)
O(5)	0.68174(14)	0.32255(14)	0.76982(10)	0.0491(5)
O(6)	0.56621(14)	0.21469(18)	0.73373(13)	0.0708(6)
O(7)	0.76914(11)	0.47226(14)	0.69274(10)	0.0452(5)
O(8)	0.76308(12)	0.46537(16)	0.56458(10)	0.0526(5)
O(9)	0.36140(15)	0.50982(19)	0.73933(12)	0.0747(6)
O(10)	0.44437(15)	0.4271(2)	0.89697(13)	0.0819(7)
O(11)	0.57230(16)	0.80999(19)	0.99179(12)	0.0819(7)
O(12)	0.6871(2)	0.5767(2)	0.41951(13)	0.1024(9)
N(1)	0.70231(13)	0.63934(18)	0.78160(11)	0.0395(5)
N(2)	0.60029(13)	0.48393(17)	0.67919(11)	0.0365(5)
N(3)	0.94365(14)	0.40019(18)	0.58746(12)	0.0443(6)
N(4)	0.90301(13)	0.23867(18)	0.51265(11)	0.0408(5)
N(5)	1.01661(13)	0.21325(16)	0.47078(11)	0.0362(5)
N(6)	1.03228(13)	0.30664(17)	0.51602(12)	0.0401(5)
C(1)	0.62406(18)	0.5738(2)	0.88228(16)	0.0459(7)
C(2)	0.6657(2)	0.6679(2)	0.85086(15)	0.0507(7)
C(3)	0.8528(2)	0.5879(2)	0.84628(15)	0.0466(7)
C(4)	0.79347(17)	0.6708(2)	0.79516(15)	0.0457(7)
C(5)	0.64199(17)	0.6711(2)	0.70403(15)	0.0420(7)
C(6)	0.56462(18)	0.5923(2)	0.68233(15)	0.0476(7)

Table 4. (Contd.)

Atom	*x*	*y*	*z*	U_{eq}/U_{iso}
C(7)	0.6006(2)	0.3027(3)	0.73506(16)	0.0515(8)
C(8)	0.54505(19)	0.3956(2)	0.69445(16)	0.0519(8)
C(9)	0.73001(18)	0.4677(2)	0.62233(16)	0.0434(7)
C(10)	0.63100(16)	0.4667(2)	0.60660(14)	0.0437(7)
C(11)	1.00240(17)	0.4841(2)	0.62164(14)	0.0394(6)
C(12)	0.96910(18)	0.5592(2)	0.66384(15)	0.0434(7)
C(13)	1.0187(2)	0.6462(2)	0.69736(15)	0.0501(7)
C(14)	1.10189(18)	0.6584(2)	0.68910(15)	0.0464(7)
C(15)	1.1366(2)	0.5823(3)	0.64887(16)	0.0546(8)
C(16)	1.08556(18)	0.4954(2)	0.61368(15)	0.0462(7)
C(17)	0.96243(16)	0.3201(2)	0.54120(13)	0.0361(6)
C(18)	0.81668(16)	0.2234(2)	0.52729(14)	0.0397(6)
C(19)	0.74254(17)	0.2262(2)	0.46549(16)	0.0499(7)
C(20)	0.66192(19)	0.2070(3)	0.48002(19)	0.0579(8)
C(21)	0.6569(2)	0.1849(2)	0.5565(2)	0.0618(9)
C(22)	0.7321(2)	0.1807(2)	0.61794(18)	0.0584(8)
C(23)	0.81141(19)	0.1985(2)	0.60262(16)	0.0502(7)
C(24)	0.93951(17)	0.1760(2)	0.46918(4)	0.0414(7)
C(25)	1.08352(17)	0.1764(2)	0.43372(14)	0.0396(6)
C(26)	1.0606(2)	0.0970(2)	0.37632(17)	0.0601(8)
C(27)	1.1262(2)	0.0654(3)	0.34034(18)	0.0620(9)
C(28)	1.2078(2)	0.1077(3)	0.36065(18)	0.0627(9)
C(29)	1.22808(18)	0.1854(3)	0.41785(17)	0.0539(8)
C(30)	1.16497(18)	0.2202(2)	0.45410(14)	0.0492(7)
		IV		
Al(1)	0.70732(4)	0.47332(5)	0.77592(3)	0.0351(2)
O(1)	0.63506(10)	0.48289(12)	0.84729(8)	0.0469(4)
O(2)	0.58230(11)	0.58599(14)	0.92887(10)	0.0614(5)
O(3)	0.81232(9)	0.49330(12)	0.84992(8)	0.0462(4)
O(4)	0.92749(11)	0.60310(15)	0.87668(11)	0.0695(5)
O(5)	0.68308(10)	0.32858(11)	0.76745(8)	0.0451(3)
O(6)	0.57026(13)	0.21529(15)	0.73555(13)	0.0768(6)
O(7)	0.76922(8)	0.47545(11)	0.69596(8)	0.0394(3)
O(8)	0.76271(9)	0.46546(13)	0.56656(8)	0.0487(4)
O(9)	0.35904(14)	0.5084(2)	0.73852(13)	0.0775(6)
O(10)	0.44229(17)	0.4268(2)	0.89638(15)	0.0864(7)
O(11)	0.57166(16)	0.8065(2)	0.99011(13)	0.0845(6)
O(12)	0.6887(2)	0.5786(2)	0.42087(15)	0.1026(9)
N(1)	0.70051(11)	0.63878(13)	0.77943(10)	0.0384(4)
N(2)	0.59961(10)	0.48542(13)	0.67996(9)	0.0371(4)
N(3)	0.94383(12)	0.39868(14)	0.58744(11)	0.0433(4)
N(4)	0.90183(10)	0.23781(14)	0.51222(9)	0.0380(4)
N(5)	1.01686(10)	0.21370(13)	0.47122(9)	0.0366(4)
N(6)	1.03279(10)	0.30576(13)	0.51645(10)	0.0383(4)
C(1)	0.62396(14)	0.57334(18)	0.87831(12)	0.0451(5)
C(2)	0.66525(18)	0.66828(19)	0.84826(15)	0.0495(5)
C(3)	0.85140(14)	0.58469(18)	0.84483(13)	0.0472(5)
C(4)	0.79386(14)	0.67029(19)	0.79383(15)	0.0471(5)
C(5)	0.64107(15)	0.67304(18)	0.70242(14)	0.0457(5)
C(6)	0.56372(14)	0.59554(18)	0.68125(14)	0.0466(5)
C(7)	0.60197(16)	0.30462(18)	0.73534(14)	0.0499(5)
C(8)	0.54356(15)	0.3961(2)	0.69494(15)	0.0507(6)
C(9)	0.72734(12)	0.46905(16)	0.62202(11)	0.0375(4)
C(10)	0.62876(13)	0.4659(2)	0.60602(12)	0.0429(5)
C(11)	1.00065(12)	0.48382(16)	0.62120(11)	0.0384(4)

Table 4. (Contd.)

Atom	*x*	*y*	*z*	U_{eq}/U_{iso}
		IV		
C(12)	0.96711(14)	0.55939(18)	0.66468(12)	0.0443(5)
C(13)	1.01724(16)	0.64621(19)	0.69808(13)	0.0491(5)
C(14)	1.10130(16)	0.65927(19)	0.68923(13)	0.0495(5)
C(15)	1.13487(15)	0.58301(19)	0.64822(14)	0.0503(5)
C(16)	1.08583(14)	0.49496(19)	0.61361(14)	0.0457(5)
C(17)	0.96123(12)	0.31884(16)	0.54075(11)	0.0368(4)
C(18)	0.81587(12)	0.22077(16)	0.52624(11)	0.0379(4)
C(19)	0.74277(14)	0.2247(2)	0.46395(14)	0.0509(5)
C(20)	0.66193(16)	0.2056(2)	0.47903(17)	0.0610(7)
C(21)	0.65601(17)	0.1826(2)	0.55520(17)	0.0610(7)
C(22)	0.73044(18)	0.1802(2)	0.61687(17)	0.0603(7)
C(23)	0.81138(16)	0.1984(2)	0.60311(4)	0.0515(5)
C(24)	0.93978(13)	0.17345(17)	0.46876(12)	0.0395(4)
C(25)	1.08248(12)	0.17547(16)	0.43406(12)	0.0387(4)
C(26)	1.06089(17)	0.0980(2)	0.37554(16)	0.0548(6)
C(27)	1.12450(18)	0.0646(2)	0.33867(18)	0.0640(7)
C(28)	1.20735(17)	0.1061(2)	0.36072(16)	0.0597(6)
C(29)	1.22786(16)	0.1834(2)	0.41886(15)	0.0568(6)
C(30)	1.16489(14)	0.2200(2)	0.45577(13)	0.0476(5)
H(1)	0.376(2)	0.584(3)	0.737(2)	0.093
H(2)	0.386(2)	0.480(3)	0.784(2)	0.093
H(3)	0.487(2)	0.467(3)	0.904(2)	0.104
H(4)	0.427(3)	0.411(4)	0.927(3)	0.104
H(5)	0.560(2)	0.728(3)	0.971(2)	0.101
H(6)	0.618(2)	0.858(3)	0.957(2)	0.101
H(7)	0.708(3)	0.536(4)	0.455(3)	0.123
H(8)	0.664(3)	0.544(3)	0.375(3)	0.123
H(9)	0.8892(18)	0.402(2)	0.5848(15)	0.058(7)
H(10)	0.6250(17)	0.724(2)	0.8349(16)	0.066(8)
H(11)	0.7137(17)	0.695(2)	0.8919(16)	0.064(7)
H(12)	0.8053(16)	0.738(2)	0.8196(15)	0.063(7)
H(13)	0.8103(15)	0.6718(19)	0.7455(15)	0.052(7)
H(14)	0.6753(14)	0.6700(18)	0.6643(14)	0.047(6)
H(15)	0.6194(17)	0.742(2)	0.7029(16)	0.067(8)
H(16)	0.5280(14)	0.5971(17)	0.7211(13)	0.043(6)
H(17)	0.5235(16)	0.616(2)	0.6291(15)	0.059(7)
H(18)	0.5053(17)	0.363(2)	0.6475(17)	0.070(8)
H(19)	0.5078(16)	0.421(2)	0.7277(15)	0.057(7)
H(20)	0.6047(16)	0.515(2)	0.5646(15)	0.057(7)
H(21)	0.6118(14)	0.3933(19)	0.5857(13)	0.045(6)
H(22)	0.9085(15)	0.5491(19)	0.6706(14)	0.050(6)
H(23)	0.9946(17)	0.699(2)	0.7288(16)	0.068(7)
H(24)	1.1346(16)	0.719(2)	0.7080(15)	0.061(7)
H(25)	1.1905(16)	0.588(2)	0.6432(15)	0.060(7)
H(26)	1.1085(16)	0.446(2)	0.5879(15)	0.064(8)
H(27)	0.7474(15)	0.238(2)	0.4124(16)	0.061(7)
H(28)	0.6146(19)	0.209(2)	0.4356(18)	0.079(9)
H(29)	0.6010(18)	0.162(2)	0.5697(16)	0.070(8)
H(30)	0.7279(17)	0.164(2)	0.6662(17)	0.065(8)
H(31)	0.8656(16)	0.196(2)	0.6429(15)	0.058(7)
H(32)	0.9159(14)	0.1123(18)	0.4427(13)	0.041(6)
H(33)	1.0064(17)	0.071(2)	0.3610(15)	0.059(7)
H(34)	1.110(2)	0.009(3)	0.2982(19)	0.092(10)
H(35)	1.2513(16)	0.085(2)	0.3362(15)	0.059(7)
H(36)	1.2868(17)	0.218(2)	0.4324(15)	0.063(7)
H(37)	1.1791(15)	0.279(2)	0.4944(15)	0.058(7)

X-ray diffraction analysis. The IR spectra of **I** contain a smeared band in the range 3300–3500 cm^{-1}, which is attributed to $\nu(H_2O)$. The ν(COO–Ga) stretching vibrations of the coordinated carboxylate groups are observed at 1625 cm^{-1}. The deprotonated acetate arm which is not involved in the gallium coordination sphere, is characterized by the ν(COO) stretching vibrations at 1580 cm^{-1}.

In the Ga*Edta*$(OH)^{2-}$ anion, as in other mixed-ligand gallium compounds [1], the monodentate ligand occupies the *trans* position relative to one of the nitrogen atoms of the aminocarboxylate (Fig. 1). The bond lengths in the Ga*Edta*$(OH)^{2-}$ polyhedron are listed in Table 5. Based on the data reported in [1] and Table 5, the hard monodentate *X* ligands producing the *trans*-effect in the mixed-ligand Ga*Edta*X complexonates can be arranged in order of increasing Ga–N bond length as follows:

X =	H_2O	NCS^-	F^-	OH^-
Ga–N Å =	2.075	2.102	2.114	2.150

Reaction of equimolar amounts of aluminum hydroxide and H_4*Edta* resulted in the precipitation of up to 50% of the ligand from the solutions obtained (pH 1.5). The neutral complexonate AlH*Edta*(H_2O) was obtained in a low yield (30%) upon separation of the unreacted ligand. In acid solutions, the protonation of the H_4*Edta* ligand impedes the formation of complexonate **III**. This behavior of the aluminum system differs significantly from that of similar gallium solutions in which GaH*Edta*(H_2O) precipitates in a high yield [1].

The data of the elemental analysis (Table 1) agree with the formation of the AlH*Edta*(H_2O) complexonate. The spectral data indicate that, in this complexonate, one of the acetate arms of the ligand is protonated (H*Edta*) and does not participate in coordination. In the IR spectrum of **III**, the stretching vibrations of the protonated acetate group ν(COOH) appear as a band at 1735 cm^{-1} and the absorption of the coordinated carboxylate groups ν(COO–Al) is observed at 1635 cm^{-1}.

The X-ray powder diffraction analysis (Table 2) revealed that complex **III** is not isostructural with similar compounds *M*H*Edta*(H_2O) of other metals (*M* = Ga [1], Cr [5], Fe [6], Ru [7], and Rh [8]). The CoH*Edta*$(H_2O) \cdot 3H_2O$ compound with a close composition also has a different crystal structure [9].

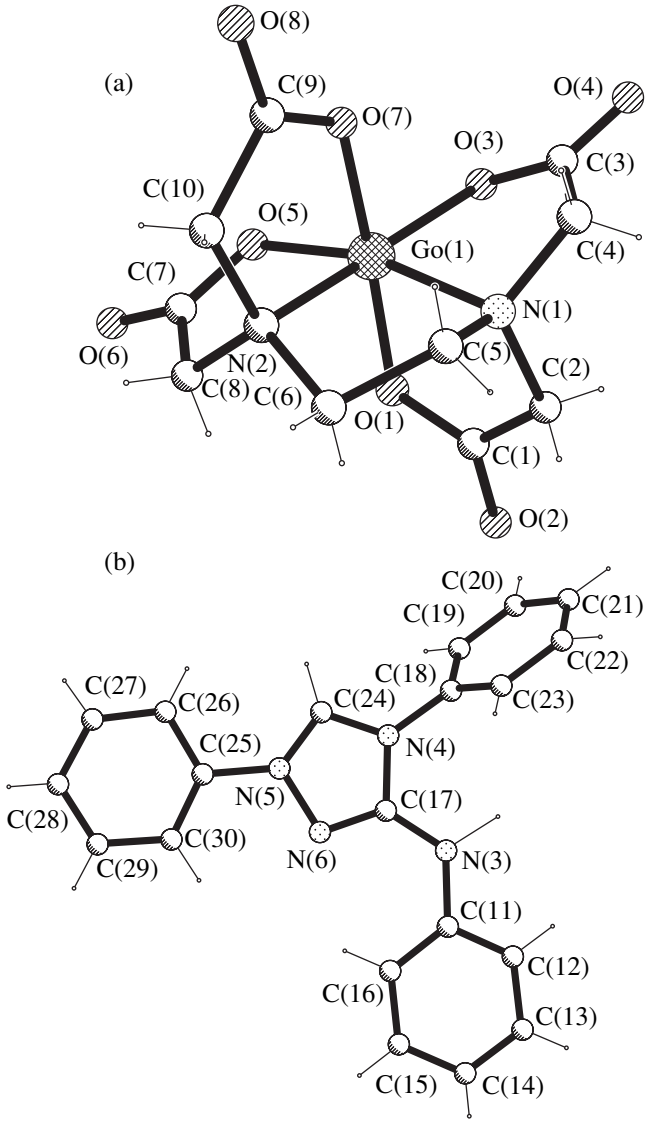

Fig. 2. Structures of (a) the [Ga*Edta*]$^-$ anionic complex and (b) the BH^+ cation in **II**.

Table 5. Bond lengths (Å) in the coordination polyhedra of aluminum and gallium in structures **I**, **II**, and **IV**

I		**II**		**III**	
Ga(1)–O(9)	1.841(2)	Ga(1)–O(5)	1.9136(19)	Al(1)–O(3)	1.8338(16)
Ga(1)–O(1)	1.959(2)	Ga(1)–O(3)	1.9231(18)	Al(1)–O(5)	1.8406(15)
Ga(1)–O(3)	1.982(2)	Ga(1)–O(7)	1.9502(18)	Al(1)–O(1)	1.8860(15)
Ga(1)–O(5)	1.994(2)	Ga(1)–O(1)	1.9734(17)	Al(1)–O(7)	1.8868(15)
Ga(1)–N(1)	2.150(2)	Ga(1)–N(2)	2.086(2)	Al(1)–N(2)	2.0568(18)
Ga(1)–N(2)	2.205(2)	Ga(1)–N(1)	2.096(2)	Al(1)–N(1)	2.0650(18)

The formation of $BH^+MEdta \cdot 4H_2O$ [M = Al (**IV**) or Ga (**II**)] results from the protonation of nitron by the coordinated H*Edta* ligand, which enters into the composition of the $MHEdta(H_2O)$ complexonates. Nitronium salts **II** and **IV** are isolated from solutions with pH 6 and 7, respectively. In the IR spectra of **II** and **IV**, the bands attributed to the ν(COO–*M*) stretching vibrations are observed at 1635 and 1625 cm^{-1} for aluminum and gallium, respectively. The crystallization water molecules manifest themselves in the IR spectra of **II** and **IV** as a broad band of the $\nu(H_2O)$ stretching vibrations near 3400 cm^{-1} and the intense absorption at 1660 cm^{-1}, which corresponds to the δ(HOH) mode.

Compounds **II** and **IV** are isostructural. In complexes **II** and **IV**, the protonated nitron BH^+ has no short contacts with the coordination sphere of the metal (Fig. 2). The geometric parameters of the $GaEdta^-$ anions in **II** and [H*Bipy*][Ga*Edta*] $\cdot H_2O$ [1] are virtually independent of the outer-sphere cation.

ACKNOWLEDGMENTS

This work was supported by the Russian Foundation for Basic Research, project no. 00-15-97432.

REFERENCES

1. S. P. Petrosyants, A. B. Ilyukhin, and Yu. A. Buslaev, Zh. Neorg. Khim. **43** (11), 1816 (1998).
2. V. A. Efremov, in *Collected Abstracts of the International Conference "Powder Diffraction and Crystal Chemistry," St. Petersburg, 1994*, p. 31.
3. G. M. Sheldrick, *SHELXS97: Program for the Solution of Crystal Structures* (Univ. of Göttingen, Göttingen, 1997).
4. G. M. Sheldrick, *SHELXL97: Program for the Refinement of Crystal Structures* (Univ. of Göttingen, Germany, 1997).
5. L. E. Gerdom, N. A. Baenziger, and H. M. Goff, Inorg. Chem. **20** (5), 1606 (1981).
6. T. Mizuta, T. Yamamoto, K. Miyoshi, and Y. Kushi, Inorg. Chim. Acta **175**, 121 (1990).
7. K. Okamoto, J. Hidaka, I. Iida, *et al.*, Acta Crystallogr., Sect. C: Cryst. Struct. Commun. **C46** (12), 2327 (1990).
8. G. H. Y. Lin, J. D. Leggett, and R. M. Wing, Acta Crystallogr., Sect. B: Struct. Crystallogr. Cryst. Chem. **B29** (5), 1023 (1973).
9. H. Okazaki, K. Tomioka, and H. Yoneda, Inorg. Chim. Acta **74**, 169 (1983).

Translated by I. Polyakova

Crystallography Reports, Vol. 46, No. 5, 2001, pp. 779–785. Translated from Kristallografiya, Vol. 46, No. 5, 2001, pp. 853–859.

STRUCTURES OF COORDINATION COMPOUNDS

Crystal Structure and Thermochromism of Bisguanidinium Tetrachlorocuprate Dihydrate at 123 and 293 K

V. K. Belsky*, V. Fernandez, V. E. Zavodnik*, I. Diaz**, and J. L. Martinez*****

** Karpov Research Institute of Physical Chemistry, State Scientific Center, ul. Vorontsovo pole 10, Moscow, 103064 Russia*

e-mail: belsky@cc.nifhi.ac.ru

*** Departamento de Quimica Inorganica, Universidad Autonoma de Madrid, Madrid, Spain*

**** Instituto de Ciencia de Materiales, CSIC, Cantoblanco, 28049 Madrid, Spain*

Received September 26, 2000

Abstract—The crystal structure of bisguanidinium tetrachlorocuprate dihydrate is determined by X-ray diffraction at $T = 293$ and 123 K with the purpose of revealing the crystal-chemical factors responsible for the thermochromic transition. © *2001 MAIK "Nauka/Interperiodica".*

Completing the series of our studies of the relationship between the structural and thermochromic properties of the copper(II) halide complexes with nitrogen-containing ligands [1–3], we performed the structure analysis of bisguanidinium tetrachlorocuprate dihydrate $2[CNH_2)_3]^+ \cdot [CuCl_4]^{2-} \cdot 2H_2O$, which colors yellowish green at room temperature and brown above 373 K but virtually loses its color below 150 K.

EXPERIMENTAL

A solution of copper chloride dihydrate in an ethanol–water (30 : 70) mixture was gradually added to a guanidine solution in the 1 : 2 molar ratio on dropwise addition of 12 M hydrochloric acid and continuous stirring. The reaction mixture was allowed to stand, and after an hour, the crystals of the complex began to precipitate. After three weeks, the crystals were filtered off, washed with *n*-pentane, and dried.

The crystallographic parameters, details of the X-ray data collection, and characteristics of the refinement are summarized in Table 1. The structure was solved by the heavy-atom method. The positions of the H atoms were found from the difference Fourier syntheses and included in the refinement with the isotropic thermal parameters. The set of experimental data was processed using the PROFIT program [4]. All the calculations were performed with the SHELX97 software package [5]. Correction for X-ray absorption was introduced with due regard for the real faceting of the crystal. The coordinates of the non-hydrogen atoms are listed in Table 2, and the interatomic distances and bond angles are given in Table 3.

RESULTS AND DISCUSSION

Unlike the earlier-studied structure of the anhydrous complex of bis(dimethylguanidinium) tetrachlorocuprate [3], in which the isolated pseudotetrahedral

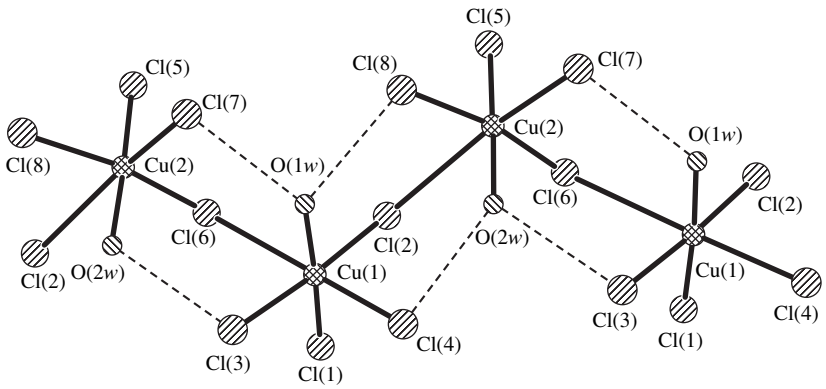

Fig. 1. Packing of the anions in the structure (dashed lines indicate the OH···Cl hydrogen bonds).

1063-7745/01/4605-0779$21.00 © 2001 MAIK "Nauka/Interperiodica"

Table 1. Main crystal data and parameters of X-ray data collection and structure refinement

Empirical formula		$C_2H_{16}Cl_4CuN_6O_2$	
Molecular weight		343.53	
Crystal size, mm		$0.64 \times 0.18 \times 0.16$	
Crystal shape		Parallelepiped	
Temperature, K		293(2)	123(2)
Color		Yellowish green	Colorless
Crystal system		Monoclinic	
Space group		$P2_1/c$	
Z		8	
Unit cell parameters:	a, Å	8.084(2)	8.024(2)
	b, Å	18.484(3)	18.444(3)
	c, Å	16.939(3)	16.741(3)
	β, deg	91.44(2)	91.71(2)
Unit cell volume, Å^3		2530(9)	2476.5(9)
Density (calcd), g/cm^3		1.804	1.843
Diffractometer		CAD4	
Scan mode		θ/2θ	
Radiation		λMoK_α = 0.71073 (beta-filtered)	
Absorption coefficient, mm^{-1}		2.553	2.608
F(000)		1384	
2θ range, deg		2.51–22.47	2.43–22.47
Index range		$0 \le h \le 8$, $0 \le k \le 19$, $-18 \le l \le 18$	
Total number of reflections		2645	2429
Unique reflections		2443 [$R(int)$ = 0.0214]	2249 [$R(int)$ = 0.0159]
Absorption correction		Numerical integration	
T_{max} and T_{min}		0.688 and 0.616	0.683 and 0.603
F(000)		1384	
Number of standard reflections		3	
Frequency of standard reflections		60 min	
Intensity decay		0.5 %	
Refinement technique		Full-matrix least-squares procedure on F^2	
Number of reflections/Number of parameters		2433/366	2249/366
Goodness-of-fit on F^2		1.045	1.035
R factors [$I \ge 2\sigma(I)$]		R_1 = 0.025	R_1 = 0.025
		wR_2 = 0.065	wR_2 = 0.066
Extinction coefficient		0.0008(3)	0.0003(3)
Residual (maximum and minimum) densities (e/Å^3)		0.406 and –0.723	0.498 and –0.834

Table 2. Coordinates ($\times 10^4$) and equivalent isotropic thermal parameters ($Å^2 \times 10^3$) of non-hydrogen atoms

Atom	*x*/*a*	*y*/*b*	*z*/*c*	U_{eq}	Atom	*x*/*a*	*y*/*b*	*z*/*c*	U_{eq}
Cu(1)	2465(1)	5928(1)	3011(1)	31(1)	N(3)	11204(6)	8457(3)	1418(2)	57(1)
	2432(1)	5946(1)	2994(1)	12(1)		11099(5)	8449(2)	1419(2)	20(1)
Cu(2)	7565(1)	6543(1)	1528(1)	31(1)	N(4)	5945(5)	5743(2)	5039(2)	42(1)
	7502(1)	6553(1)	1513(1)	12(1)		5904(5)	5743(2)	5029(2)	17(1)
Cl(1)	2224(1)	6231(1)	4290(1)	43(1)	N(5)	7444(6)	6233(2)	4055(2)	38(1)
	2198(1)	6254(1)	4288(1)	17(1)		7417(5)	6241(2)	4038(2)	16(1)
Cl(2)	4380(1)	6824(1)	2824(1)	37(1)	N(6)	8738(6)	5652(2)	5084(3)	43(1)
	4366(1)	6839(1)	2798(1)	15(1)		8734(5)	5646(2)	5077(2)	18(1)
Cl(3)	446(1)	5044(1)	3096(1)	37(1)	N(7)	−2300(6)	8581(3)	2863(2)	63(1)
	392(1)	5061(1)	3092(1)	14(1)		7713(5)	8588(3)	2835(2)	27(1)
Cl(4)	4907(1)	4852(1)	3136(1)	39(1)	N(8)	−2532(6)	8034(2)	4054(3)	60(1)
	4835(1)	4872(1)	3129(1)	15(1)		7418(5)	8036(2)	4045(2)	22(1)
Cl(5)	7642(1)	7644(1)	950(1)	46(1)	N(9)	−2899(6)	9248(2)	3938(3)	60(1)
	7561(1)	7658(1)	927(1)	17(1)		7030(5)	9255(3)	3916(2)	21(1)
Cl(6)	9345(1)	6923(1)	2529(1)	36(1)	N(10)	1995(6)	9310(2)	4038(3)	57(1)
	9326(1)	6933(1)	2513(1)	14(1)		1987(5)	9331(2)	4013(2)	22(1)
Cl(7)	9804(1)	5957(1)	625(1)	34(1)	N(11)	1832(7)	8097(3)	4130(3)	64(1)
	9732(1)	5974(1)	596(1)	13(1)		1757(5)	8098(2)	4101(2)	24(1)
Cl(8)	5336(1)	6192(1)	744(1)	43(1)	N(12)	3377(5)	8599(3)	3184(2)	55(1)
	5276(1)	6192(1)	706(1)	16(1)		3395(4)	8605(3)	3168(2)	21(1)
O(1*W*)	2526(5)	5698(2)	1866(2)	32(1)	C(1)	12461(4)	8041(2)	1235(2)	30(1)
	2490(4)	5708(2)	1840(2)	14(1)		12401(4)	8042(2)	1230(2)	10(1)
O(2*W*)	7423(4)	5581(1)	2070(2)	33(1)	C(2)	7383(4)	5870(2)	4730(2)	27(1)
	7373(4)	5590(2)	2056(2)	15(1)		7352(4)	5870(2)	4717(2)	11(1)
N(1)	12141(5)	7381(2)	980(2)	42(1)	C(3)	−2561(5)	8621(2)	3623(2)	41(1)
	12136(5)	7388(2)	955(2)	16(1)		7392(5)	8629(2)	3606(2)	15(1)
N(2)	13981(5)	8265(2)	1299(2)	46(1)	C(4)	2413(5)	8671(2)	3787(2)	37(1)
	13917(5)	8294(3)	1302(2)	17(1)		2386(5)	8679(3)	3768(2)	14(1)

Note: For each atom, the upper and the lower rows refer to T = 293 and 123 K, respectively.

anions $CuCl_4^{2-}$ are linked by the intermolecular hydrogen bonds NH···Cl, the coordination polyhedra of the copper atoms in the hydrated structure transform into the tetragonal pyramids due to the coordination of water molecules. These water molecules are located in the planar base of the pyramid. The magnetic measurements demonstrated that the inequality of the Cu–Cl bond lengths is due to the Jahn–Teller effect. In the temperature range 200–300 K, the magnetic moment is 1.48 μB and the variation in the magnetic susceptibility with a change in temperature follows the Curie–Weiss law.

A comparison of the Cl–Cu–Cl bond angles at different temperatures revealed that the largest changes

Table 3. Interatomic distances (Å) and bond angles (deg)

Bonds	Interatomic distances		Bonds	Bond angles	
	293 K	123 K		293 K	123 K
Cu(1)–O(1*W*)	1.987(3)	1.983(3)	O(1*W*)–Cu(1)–Cl(4)	83.50(10)	83.38(9)
Cu(1)–Cl(1)	2.251(1)	2.253(1)	Cl(1)–Cu(1)–Cl(4)	166.30(3)	166.30(3)
Cu(1)–Cl(2)	2.293(1)	2.294(1)	Cl(1)–Cu(1)–Cl(6')	90.89(4)	90.70(3)
Cu(1)–Cl(3)	2.317(1)	2.321(1)	Cl(1)–Cu(1)–Cl(6')	94.60(3)	94.70(4)
Cu(1)…Cl(4)	2.807(1)	2.768(1)	Cl(1)–Cu(1)–Cl(6')	82.50(3)	82.60(3)
Cu(1)…Cl(6')	3.210(1)	3.172(1)	O(1*W*)–Cu(1)–Cl(6')	85.02(4)	85.50(4)
Cu(2)–O(2*W*)	2.006(3)	1.999(3)	O(2*W*)–Cu(2)–Cl(5)	177.66(9)	177.74(10)
Cu(2)–Cl(5)	2.260(1)	2.263(1)	O(2*W*)–Cu(2)–Cl(8)	87.74(10)	87.73(10)
Cu(2)–Cl(8)	2.305(1)	2.305(1)	Cl(5)–Cu(2)–Cl(8)	91.95(4)	91.79(4)
Cu(2)–Cl(6)	2.305(1)	2.300(1)	O(2*W*)–Cu(2)–Cl(6)	88.59(9)	88.90(9)
Cu(2)…Cl(7)	2.634(1)	2.620(1)	Cl(5)–Cu(2)–Cl(6)	91.21(4)	91.15(4)
Cu(2)…Cl(2)	3.464(1)	3.400(1)	Cl(8)–Cu(2)–Cl(6)	166.92(4)	168.43(3)
N(1)–C(1)	1.317(5)	1.306(5)	O(2*W*)–Cu(2)–Cl(7)	87.04(9)	87.13(10)
N(2)–C(1)	1.299(5)	1.304(5)	Cl(5)–Cu(2)–Cl(7)	9529(4)	95.11(3)
N(3)–C(1)	1.317(5)	1.333(5)	Cl(8)–Cu(2)–Cl(7)	95.02(4)	93.98(3)
N(4)–C(2)	1.308(5)	1.309(5)	Cl(6)–Cu(2)–Cl(7)	97.32(4)	96.90(4)
N(5)–C(2)	1.328(5)	1.330(5)	Cl(2)–Cu(2)–Cl(5)	99.70(5)	99.20(4)
N(6)–C(2)	1.299(5)	1.313(5)	Cl(2)–Cu(2)–Cl(6)	87.11(5)	87.70(5)
N(7)–C(3)	1.311(5)	1.325(5)	Cl(2)–Cu(2)–Cl(7)	164.30(4)	164.89(5)
N(8)–C(3)	1.309(5)	1.320(5)	Cl(2)–Cu(2)–Cl(8)	79.90(5)	80.81(6)
N(9)–C(3)	1.308(6)	1.032(5)	Cl(2)–Cu(2)–O(1*W*)	77.91(7)	78.52(5)
N(10)–C(4)	1.303(6)	1.314(5)	N(2)–C(1)–N(1)	120.0(4)	120.3(4)
N(11)–C(4)	1.303(6)	1.316(6)	N(2)–C(1)–N(3)	121.9(4)	120.8(4)
N(12)–C(4)	1.307(6)	1.315(5)	N(1)–C(1)–N(3)	118.1(4)	119.0(4)
Bonds	Bond angles		N(6)–C(2)–N(4)	120.5(4)	120.6(4)
O(1*W*)–Cu(1)–Cl(1)	175.87(10)	176.07(10)	N(6)–C(2)–N(5)	120.3(4)	119.4(4)
O(1*W*)–Cu(1)–Cl(1)	89.21(10)	89.06(9)	N(4)–C(2)–N(5)	119.2(4)	120.0(4)
Cl(1)–Cu(1)–Cl(2)	91.65(4)	91.85(4)	N(9)–C(3)–N(8)	120.5(4)	120.8(4)
O(1*W*)–Cu(1)–Cl(3)	86.83(10)	87.17(9)	N(9)–C(3)–N(7)	120.4(4)	119.4(4)
Cl(1)–Cu(1)–Cl(3)	92.12(4)	91.75(4)	N(8)–C(3)–N(7)	119.6(4)	119.7(4)
Cl(1)–Cu(1)–Cl(3)	175.27(3)	175.48(3)	N(10)–C(4)–N(11)	120.8(4)	120.8(4)
Cl(1)–Cu(1)–Cl(4)	100.40(3)	100.38(4)	N(10)–C(4)–N(12)	119.6(5)	119.5(4)
Cl(1)–Cu(1)–Cl(4)	92.60(3)	93.06(4)	N(11)–C(4)–N(12)		
Cl(1)–Cu(1)–Cl(4)	8949(4)	88.98(4)			

Note: The Cl(6') and Cl(6) atoms are related by the symmetry transformation [$x - 1, y, z$].

Table 4. Intermolecular hydrogen bonds

D	H	*A*	*D*–H, Å	H···*A*, Å	*D*···*A*, Å	D–H–A angle, deg	Symmetry transformation
N(1)	H(1)*n*1	Cl(7)	0.77	2.66	3.289	141	*x*, *y*, *z*
			0.77	2.65	3.287	133	
N(2)	H(2)*n*1	Cl(8')	0.85	2.57	3.383	172	*x* + 1, *y*, *z*
			0.82	2.57	3.423	174	
N(2)	H(1)*n*2	Cl(5')	0.86	2.54	3.230	148	*x* + 1, *y*, *z*
			0.78	2.42	3.242	138	
N(2)	H(2)*n*2	Cl(4')	0.91	2.45	3.213	168	2 – *x*, .5 + *y*, .5 – *z*
			0.78	2.49	3.208	158	
N(3)	H(1)*n*3	Cl(5)	0.76	2.30	3.276	160	*x*, *y*, *z*
			1.02	2.45	3.326	163	
N(3)	H(2)*n*3	Cl(3')	0.89	2.69	3.315	132	1 – *x*, .5 + *y*, .5 – *z*
			0.84	2.86	3.335	120	
N(4)	H(1)*n*4	Cl(4')	0.81	2.67	3.356	160	1 – *x*, 1 – *y*, 1 – *z*
			0.72	2.65	3.370	166	
N(4)	H(2)*n*4	Cl(1)	0.74	2.51	3.324	168	*x*, *y*, *z*
			0.83	2.57	3.359	172	
N(5)	H(1)*n*5	Cl(2)	0.79	2.48	3.350	159	*x*, *y*, *z*
			0.92	2.53	3.379	159	
N(5)	H(2)*n*5	Cl(6)	0.90	2.78	3.274	134	*x*, *y*, *z*
			0.66	2.77	3.296	140	
N(6)	H(1)*n*6	Cl(3')	0.66	2.66	3.384	164	1 – *x*, 1 – *y*, 1 – *z*
			0.75	2.69	3.391	159	
N(6)	H(2)*n*6	Cl(1')	0.74	2.60	3.309	174	*x* + 1, *y*, *z*
			0.72	2.64	3.330	176	
N(7)	H(1)*n*7	Cl(6)	0.69	2.67	3.366	168	*x*, *y*, *z*
			0.71	2.68	3.394	153	
N(7)	H(2)*n*7	Cl(4')	0.77	2.72	3.491	143	1 – *x*, .5 + *y*, .5 – *z*
			0.91	2.69	3.555	148	
N(8)	H(1)*n*8	Cl(8')	0.98	2.79	3.605	155	*x* , 1.5 – *y*, .5 + *z*
		Cl(5')	0.88	2.79	3.447	141	
N(8)	H(2)*n*8	Cl(6)	0.80	2.98	3.646	143	*x*, *y*, *z*
			0.79	3.17	3.600	124	
N(9)	H(1)*n*9	O(1*W*')	0.77	2.15	2.993	170	1 – *x*, .5 + *y*, .5 – *z*
			0.86	2.21	3.025	166	
N(9)	H(2)*n*9	Cl(8')	0.84	2.76	3.449	154	*x* , 1.5 – *y*, .5 + *z*
			0.74	2.82	3.503	150	
N(10)	H(1)O(1)	Cl(7')	0.76	2.62	3.300	151	*x* – 1, 1.5 – *y*, .5 + *z*
			0.75	2.45	3.293	163	
N(10)	H(1)O(2)	O(2*W*')	0.88	2.13	2.986	164	1 – *x* , .5 + *y*, .5 – *z*
			0.88	2.41	3.051	162	
N(11)	H(1)11	C(1)	0.67	2.56	3.432	145	*x*, *y*, *z*
			1.00	2.77	3.474	150	
N(11)	H(1)12	Cl(7')	0.79	2.87	3.475	155	*x* – 1, 1.5 – *y*, .5 + *z*
			0.66	2.94	3.517	150	

Table 4. (Contd.)

D	H	*A*	*D*–H, Å	H···*A*, Å	*D*···*A*, Å	D–H–A angle, deg	Symmetry transformation
N(12)	H(1)21	Cl(2)	0.65	2.65	3.410	171	*x*, *y*, *z*
			0.77	2.75	3.438	172	
N(12)	H(1)22	Cl(4')	0.69	2.71	3.518	160	1 – *x* , 1.5 + *y*, .5 – *z*
			0.85	2.73	3.527	161	
O(1*W*)	H(1)1*W*	Cl(7')	0.83	2.33	3.034	160	*x* – 1, *y*, *z*
			0.84	2.26	3.043	171	
O(1*W*)	H(1)2*W*	Cl(8)	0.78	2.96	3.107	164	*x*, *y*, *z*
			0.84	2.49	3.131	165	
O(2*W*)	H(2)1*W*	Cl(3')	0.66	2.30	3.095	168	*x* + 1, *y*, *z*
			0.81	2.30	3.124	167	
O(2*W*)	H(2)2*W*	Cl(4)	0.83	2.45	3.057	156	*x*, *y*, *z*
			0.65	2.39	3.066	157	

Note: For each parameter, the upper and the lower rows refer to T = 293 and 123 K, respectively.

are observed for the Cl(8)–Cu(2)–Cl(7) (θ_1) and Cl(8)–Cu(2)–Cl(6) (θ_2) angles (Table 3). Substituting both values (θ_1 and θ_2) into the known equation ν_{max} = (144.5θ – 974) cm^{-1} [6], we obtain that the Δν differences in the positions of the maxima of the absorption spectra are 150.28 and 182.0 cm^{-1}, respectively. This confirms the proposition that thermochromism depends on the coordination geometry of a chromophoric metallocomplex.

Examination of the packing of different fragments of the complex also revealed remarkable details. The additional longer Cu···Cl contacts, which are neverthe-

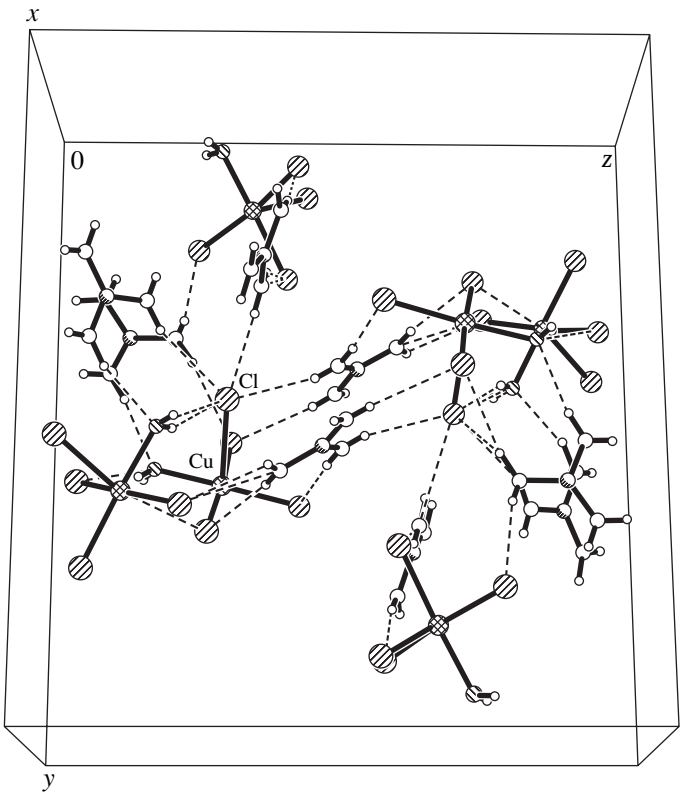

Fig. 2. A fragment of the unit cell and hydrogen bonding (dashed lines).

less shorter than the sum of the van der Waals radii [7], complement the coordination polyhedra of the symmetrically independent copper atoms to the tetragonal bipyramids. The bipyramids are linked into infinite chains through these contacts (Fig. 1). The guanidinium ions and water molecules are located between the chains and form a complex three-dimensional network of intermolecular NH···Cl, NH···O, and OH···Cl hydrogen bonds (Table 4, Fig. 2).

ACKNOWLEDGMENTS

V.K. Belsky and V.E. Zavodnik acknowledge the support of the Russian Foundation for Basic Research, project no. 00-03-32578.

REFERENCES

1. I. Diaz, V. Fernandez, V. K. Belsky, and J. L. Martinez, Z. Naturforsch. B **54**, 718 (1999).
2. V. E. Zavodnik, V. K. Belsky, I. Diaz, and V. Fernandez, Kristallografiya **44** (4), 623 (1999) [Crystallogr. Rep. **44**, 575 (1999)].
3. V. Fernandez, J. L. Martinez, V. K. Belsky, and V. E. Zavodnik, Kristallografiya **44** (5), 849 (1999) [Crystallogr. Rep. **44**, 790 (1999)].
4. V. A. Strel'tsov and V. E. Zavodnik, Kristallografiya **34** (6), 1369 (1989) [Sov. Phys. Crystallogr. **34**, 824 (1989)].
5. G. M. Sheldrick, *SHELX97: Program Complex for Structure Solution and Refinement* (Univ. of Göttingen, Göttingen, 1997).
6. R. L. Harlow, W. J. Wells, G. W. Watt, and S. H. Simonsen, Inorg. Chem. **14**, 1768 (1975).
7. S. S. Batsanov, Zh. Neorg. Khim. **36**, 3015 (1991).

Translated by I. Polyakova

Crystallography Reports, Vol. 46, No. 5, 2001, pp. 786–791. Translated from Kristallografiya, Vol. 46, No. 5, 2001, pp. 860–865.

STRUCTURE OF ORGANIC COMPOUNDS

Molecular and Crystal Structures of 1*R*,4*S*-2-(4-Carbomethoxy)benzylidene-*n*-Menthan-3-one

S. V. Shishkina*, T. G. Drushlyak*, L. A. Kutulya*, O. V. Shishkin*, and J. W. Goodby**

** Institute of Single Crystals, National Academy of Sciences of Ukraine, pr. Lenina 60, Kharkov, 61001 Ukraine*

*** Department of Chemistry, University of Hull, Hull HU6 7RX, United Kingdom*

e-mail: kutulya@isc.kharkov.com

e-mail: shishkin@xray.isc.kharkov.com

Received May 17, 2000; in final form, October 31, 2000

Abstract—The molecular and crystal structures of chiral 1*R*,4*S*-2-(4-carbomethoxy)benzylidene-*n*-menthan-3-one (**I**) are determined by X-ray diffraction analysis. Crystals **I** are orthorhombic; at 20°C: $a = 11.961(3)$ Å, $b = 26.453(8)$ Å, $c = 5.400(2)$ Å, space group $P2_12_12_1$, and $Z = 4$ ($C_{19}H_{25}O_3$). In molecule **I**, the cyclohexanone ring with the axial methyl and isopropyl substituents adopts a chair conformation. It is found that the enone and arylidene fragments of compound **I** have a substantially nonplanar structure. The shortened intramolecular contacts between atoms of the arylidene grouping and the α fragment of the cyclohexanone ring and their associated distortions of bond angles at the sp^2 carbon atoms are the common structural features of 2-arylidene-*n*-menthan-3-ones irrespective of the stereochemical configuration of the C(4) chiral center. © *2001 MAIK "Nauka/Interperiodica".*

INTRODUCTION

2-Arylidene-*n*-menthan-3-ones have attracted considerable interest, because they serve as efficient chiral dopants to induced cholesteric [1–3] and ferroelectric liquid-crystal composites [4]. These compounds are also attractive as molecular models that can be used to elucidate the interrelation between the molecular structure and the properties of chiral dopants in liquid-crystal systems and to reveal the most important structural criteria for their efficient use. Moreover, they can serve as interesting objects in investigations into the effect of electronic and steric factors on the conformation state of the cyclohexanone ring and the π-electron fragment in fixed *s-cis* enone molecular systems.

For these compounds, the structure of molecules with an 1*R*,4*R*-*cis* configuration has been studied thoroughly by X-ray diffraction [5–10] and spectroscopic techniques (IR and ^{1}H NMR spectroscopy) [11, 12] in combination with theoretical conformational analysis within the framework of the molecular mechanics method. It was found that, in all the cases, the cyclohexanone ring with axial methyl and equatorial isopropyl substituents in crystals of the studied compounds adopts a chair conformation. According to the spectroscopic data and molecular mechanics calculations, conformers with a chair-type cyclohexanone ring also predominate in solutions of these compounds. It was demonstrated that the cinnamoyl fragment in molecules of 1*R*,4*R* diastereomers is nonplanar. The degree of nonplanarity considerably depends on the electronic nature of a substituent in the aryl group [9] and, most likely, on the energy of intermolecular interaction between the π-electron groupings in crystals [10].

As regards the molecular structure of 1*R*,4*S*-*trans* diastereomers, only one compound with the phenyl substituent in the 2-arylidene grouping was investigated by X-ray diffraction [13]. The cyclohexanone ring in crystals of this compound exhibits a twist conformation in distinction to its 1*R*,4*R* isomer with a chair-type cyclohexanone fragment. As follows from the molecular mechanics calculations for this compound, the steric energies for chair-type (with axial 1,4-substituents) and twist conformers are close to each other in magnitude, and, hence, each of these conformers can exist in the crystalline state. In this respect, the structural investigation of new compounds of the 2-arylidene-*n*-menthan-3-one series with an 1*R*,4*S* configuration is important for stereochemistry of chiral cyclohexanone systems with a fixed *s-cis* enone grouping.

In the present work, we investigated the molecular and crystal structures of the recently synthesized 2-(4-carbomethoxy)benzylidene-*n*-menthan-3-one (**I**) [14] with a hypothetical 1*R*,4*S*-*trans* configuration. The results obtained were compared with the available data for the earlier-studied compound **II** [13] (which has the same configuration but a different substituent in the 2-arylidene grouping) and compounds **III** and **IV** of the

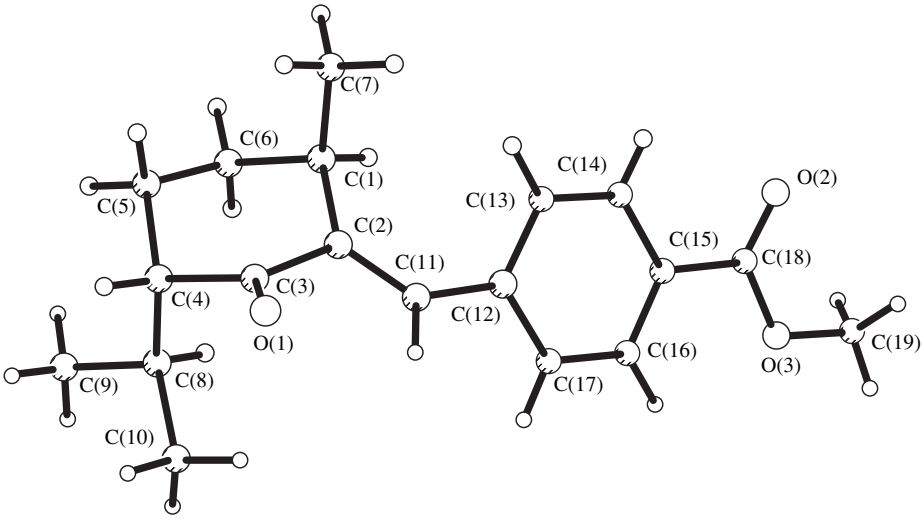

Fig. 1. Molecular structure of compound **I**.

1*R*,4*R* diastereomeric series with electron-acceptor substituents (*R* = Cl and NO_2) [9]:

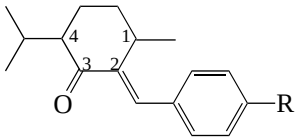

1*R*,4*S*-*trans* diastereomers: *R* = $COOCH_3$ (**I**) and C_6H_5 (**II**); 1*R*,4*R*-*cis* diastereomers: *R* = Cl (**III**) and NO_2 (**IV**).

RESULTS AND DISCUSSION

Compound **I** was characterized by X-ray structure analysis. Figure 1 displays the molecular structure of compound **I** with the atomic numbering. The bond lengths, bond angles, and selected torsion angles are listed in Tables 1–3. For comparison, the selected torsion angles and puckering parameters for compounds **II**–**IV** [15] are also presented in Table 3.

As follows from the X-ray diffraction data, compound **I** is the 1*R*,4*S*-*trans* diastereomer. The cyclohex-

Table 1. Bond lengths (*l*, Å) in structure **I**

Bond	l	Bond	l
O(1)–C(3)	1.215(4)	O(2)–C(18)	1.207(5)
O(3)–C(18)	1.335(5)	O(3)–C(19)	1.453(5)
C(1)–C(2)	1.514(4)	C(1)–C(6)	1.534(5)
C(1)–C(7)	1.541(5)	C(2)–C(11)	1.340(5)
C(2)–C(3)	1.497(4)	C(3)–C(4)	1.515(5)
C(4)–C(5)	1.536(5)	C(4)–C(8)	1.543(6)
C(5)–C(6)	1.525(5)	C(8)–C(9)	1.524(4)
C(8)–C(10)	1.530(5)	C(11)–C(12)	1.475(4)
C(12)–C(17)	1.384(5)	C(12)–C(13)	1.401(4)
C(13)–C(14)	1.385(4)	C(14)–C(15)	1.384(5)
C(15)–C(16)	1.384(4)	C(15)–C(18)	1.489(5)
C(16)–C(17)	1.382(5)		

Table 2. Bond angles (ω, deg) in structure **I**

Angle	ω	Angle	ω
C(2)C(1)C(6)	110.7(3)	C(6)C(1)C(7)	111.3(3)
C(2)C(1)C(7)	109.7(3)	C(11)C(2)C(1)	126.6(3)
C(11)C(2)C(3)	116.8(3)	O(1)C(3)C(2)	121.2(3)
C(3)C(2)C(1)	116.5(3)	C(2)C(3)C(4)	116.9(3)
O(1)C(3)C(4)	121.9(3)	C(3)C(4)C(8)	109.7(3)
C(3)C(4)C(5)	108.4(3)	C(6)C(5)C(4)	112.7(3)
C(5)C(4)C(8)	113.9(3)	C(9)C(8)C(10)	108.6(3)
C(5)C(6)C(1)	112.7(3)	C(10)C(8)C(4)	112.5(4)
C(9)C(8)C(4)	111.8(4)	C(17)C(12)C(13)	117.8(3)
C(2)C(11)C(12)	130.8(3)	C(13)C(12)C(11)	123.2(3)
C(17)C(12)C(11)	118.9(3)	C(15)C(14)C(13)	121.0(3)
C(14)C(13)C(12)	120.4(3)	C(16)C(15)C(18)	122.3(4)
C(16)C(15)C(14)	119.0(3)	C(17)C(16)C(15)	120.0(3)
C(14)C(15)C(18)	118.7(3)	O(2)C(18)O(3)	123.5(4)
C(16)C(17)C(12)	121.8(3)	O(3)C(18)C(15)	112.5(3)
O(2)C(18)C(15)	124.0(4)	C(18)O(3)C(19)	116.0(3)

Table 3. Selected torsion angles (φ_i) and puckering parameters for cyclohexanone rings in molecules **I**–**IV**

φ_i	Atoms	**I**	**II** [13]	**III** [5]	**IV** [9]
		φ_1, deg			
φ_1	C(1)C(2)C(3)C(4)	44.6(4)	33.2(3)	40.4	43.2
φ_2	C(2)C(3)C(4)C(5)	−48.0(4)	−9.2(3)	−53.1	−42.2
φ_3	C(3)C(4)C(5)C(6)	54.5(4)	−39.8(2)	62.2	49.0
φ_4	C(4)C(5)C(6)C(1)	−58.0(4)	69.6(2)	−53.7	−58.2
φ_5	C(5)C(6)C(1)C(2)	49.7(4)	−44.9(2)	41.6	55.6
φ_6	C(6)C(1)C(2)C(3)	−43.1(4)	4.7(3)	−37.4	–47.2
φ_7	C(7)C(1)C(2)C(3)	80.2(4)	118.4(2)	81.1	75.6
φ_8	C(7)C(1)C(6)C(5)	−72.6(4)	–167.2(2)	–	−67.1
φ_9	C(8)C(4)C(3)C(2)	76.9(4)	119.8(2)	–173.4	–173.7
φ_{10}	C(8)C(4)C(5)C(6)	−67.9(4)	–166.5(2)	–	179.8
φ_{11}	O(1)C(1)C(2)C(11)	43.5(5)	30.6(3)	38.5	42.0
φ_{12}	C(2)C(11)C(12)C(13)	36.7(6)	−32.6(4)	42.7	42.4
φ_{13}	C(3)C(4)C(8)C(9)	177.1(3)	−59.2	–	–160.3
φ_{14}	C(5)C(4)C(8)C(10)	176.3(3)	−58.0	–	−55.7
φ_{15}	C(5)C(4)C(8)C(9)	−61.2(4)	68.6	–	69.9
φ_{16}	C(3)C(4)C(8)C(10)	54.6(4)	174.2	–	74.0
φ_{17}	O(1)C(3)C(4)C(8)	−99.8(4)	−56.8	–	11.0 (4)
		Puckering parameters			
	θ, deg	5.49	63.92	9.73	6.32
	ψ, deg	7.02	26.87	27.57	5.95
	S	1.03	0.82	1.01	1.03

anone ring in this compound adopts a chair conformation (see the φ_1–φ_6 torsion angles and puckering parameters in Table 3) with an axial orientation of methyl and isopropyl groups (the φ_7–φ_{10} torsion angles lie in the range 68°–80°). The alkyl substituents are in the *trans* position with respect to the cyclohexanone ring as judged from the deviations of the C(7) and C(8) atoms in opposite directions (by 1.42 and –1.43 Å, respectively) from the root-mean-square planes passing through pairs of the C(3)–C(4) and C(1)–C(6) opposite bonds in the cyclohexanone ring. It should be noted that the *R* configuration of the C(1) chiral center distant from the carbonyl group remains unchanged in the course of the chemical reactions used in synthesizing 2-arylidene derivatives of diastereomeric *n*-menthan-3-ones [16, 17]. Therefore, the *trans* orientation of 1,4-alkyl substituents with respect to the cyclohexanone ring unambiguously indicates that the C(4) center has an *S* configuration.

The conformation of the cyclohexanone ring in structure **I** substantially differs from that in structure **II** with the same 1*R*,4*S* configuration but with the biphenyl group in the arylidene fragment (see the φ_1–φ_6 torsion angles in Table 3). As was shown earlier in [13], the cyclohexanone ring in compound **II** adopts a twist conformation. Moreover, it was revealed that 2-arylidene derivatives of the same diastereomeric series of 1*R*,4*S*-*trans*-*n*-menthan-3-ones have structures with different conformations of the cyclohexanone ring (depending on the nature of a substituent in the arylidene fragment). In general, these findings are consistent with the results of the molecular mechanics simulation [18]. As was already mentioned, the close steric energies for the chair and twist alternative conformations in compound **II** and its model analogue **IIa** (*R* = H) were obtained in conformational calculations within the framework of the MMX force field with inclusion of the π-electron conjugation [13, 19].

All the previously studied 2-arylidene derivatives of the 1*R*,4*R*-*cis*-*n*-menthan-3-one series exhibit a chair conformation with the axial methyl group. Hence, it is expedient to compare the structural characteristics of the cyclohexanone ring in compound **I** with those in compounds **III** and **IV** of the 1*R*,4*R* diastereomeric

Table 4. Shortened intramolecular contacts (Å) in structures **I**, **II**, and **IV**

Contact	Structure			Contact	Structure	
	I	**II** [13]	**IV** [9]		I	IV [9]
H(1)···H(13)	2.27	2.16	2.28	H(9*B*)···C(5)	2.77	2.89
H(1)···C(13)	2.69	2.84	2.68	H(10*C*)···C(3)	2.61	2.80
C(1)···H(13)	2.79	2.84	2.83	H(5*A*)···H(10*B*)	–	2.32
H(1)···C(12)	2.83	–	2.81	H(5*A*)···C(10)	–	2.73
H(7*A*)···H(13)	2.32	–	2.34	H(10*B*)···C(5)	–	2.80
H(5*B*)···H(9*B*)	2.17	–	2.29	H(6*A*)···H(8)	2.29	–
H(5*B*)···C(9)	2.71	–	2.78	H(8)···C(6)	2.82	–

* The sums of the van der Waals radii are as follows [20]: H···H, 2.32 Å and H···C, 2.87 Å.

series with electron-acceptor substituents in the arylidene grouping.

In compound **I**, the conformation of the cyclohexanone ring is best described as a chair-2,5 (with the ethylene group in the "head"): the atoms involved in the pair of the C(1)–C(6) and C(3)–C(4) opposite bonds in the ring are coplanar to within 0.006 Å and the C(2) and C(5) atoms deviate from the root-mean-square plane in opposite directions by 0.66 and 0.50 Å, respectively. The geometry of the cyclohexanone ring can be approximated as a chair-3,6 (or chair-1,4) with an appreciably lower accuracy: the atoms involved in the C(1)–C(2) and C(4)–C(5) [C(2)–C(3) and C(5)–C(6)] bonds are coplanar only to within 0.04 (0.05) Å. It is evident that the cyclohexanone ring exhibits different chair-type conformations in diastereomeric structures **I** (1*R*,4*S* isomer), **III** (1*R*,4*R* isomer), and **IV** (1*R*,4*R* isomer) with the electron-acceptor substituents $COOCH_3$, Cl, and NO_2, respectively. According to [9], the conformation of the cyclohexanone ring in compound **IV** can be characterized as a chair-1,4 with a rather high accuracy. In structure **III** with a weaker electron-acceptor substituent (Cl) compared to the nitro group [8], the chair-type conformation of the cyclohexanone ring is more "symmetrical" and can be described, with the same accuracy, as a chair-1,4 or chair-2,5. The difference in the geometries of the cyclohexanone rings in these compounds also manifests itself in changes in the endocyclic torsion angles (Table 3).

As in structures with an 1*R*,4*R* conformation and electron-acceptor substituents [5–7, 9], the enone and arylidene groupings in structure **I** are substantially nonplanar (cf. the φ_{11} and φ_{12} torsion angles). The nonbonded interactions (steric hindrances) between the *ortho* atoms (H and C) of the aryl group and atoms of the $>C(1)HCH_3$ fragment in the cyclohexanone system also manifest themselves in these structures (see the relevant intramolecular contacts in Table 4). These interactions lead to a noticeable distortion of the bond angles at the C(sp^2) atoms of the arylidene grouping (Table 2): the C(1)C(2)C(11), C(2)C(11)C(12), and C(11)C(12)C(13) bond angles considerably exceed 120°.

As in the 1*R*,4*R* diastereomeric compounds **III** and **IV** [5, 9], the maximum distortion is observed for the C(2)C(11)C(12) bond angle.

Thus, the shortened intramolecular contacts between atoms of the arylidene grouping and the α fragment of the cyclohexanone ring and their related distortions of the bond angles at the sp^2 carbon atoms (as manifestations of the steric strain of molecules) are the common structural features of 2-arylidene-*n*-menthan-3-ones irrespective of the stereochemical configuration of the C(4) chiral center.

It is worth noting that the nonplanarity of the enone grouping and the acoplanarity of the double bond with the benzene ring in structure **I** (in which the cyclohexanone ring adopts a chair conformation) are considerably more pronounced than those in structure **II** (cf. the φ_{11} and φ_{12} torsion angles in Table 3) with a twist conformation of the cyclohexanone ring [13]. A substantial flattening of the cinnamoyl fragment involving the biphenyl group is also characteristic of the corresponding compound of the 1*R*,4*R*-*cis* series [10]. It is quite possible that a considerable decrease in the intramolecular energy due to the conjugation in the O=C–C=CH–$C_6H_4C_6H_5$ cinnamoyl fragment favors the formation of a twist conformation of the cyclohexanone ring in compound **II**. In the presence of the electron-acceptor substituent $COOCH_3$ in the aryl group (compound **I**), this interaction is appreciably weakened and the dominant effect of steric factors is responsible for the formation of a chair conformation of the cyclohexanone fragment.

The differences in the configurations of the C(4) chiral centers and, correspondingly, in the orientations of the isopropyl substituents with respect to the chair-type cyclohexanone ring in diastereomeric compounds **I**, **III**, and **IV** determine the conformational features of

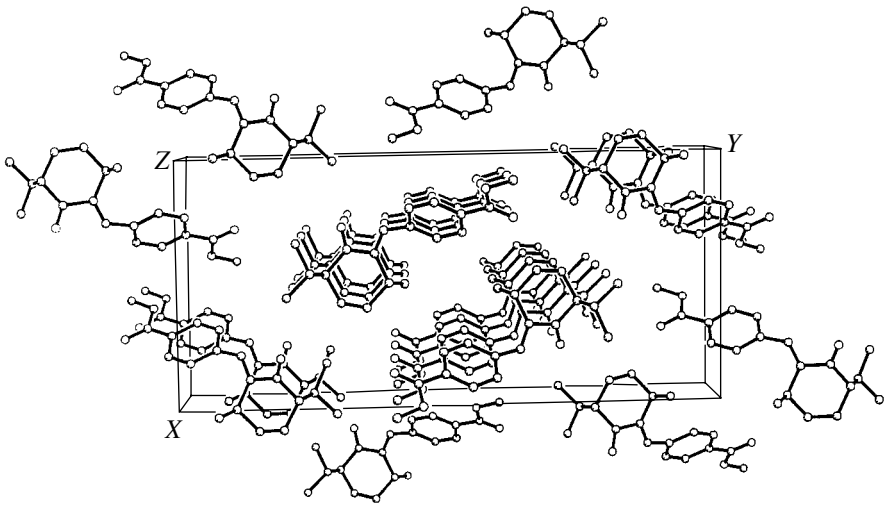

Fig. 2. Molecular stacks in the crystal of compound **I**.

the isopropyl grouping. Unlike the *gauche* orientation of the C(8)–H(8) and C(4)–H(4) bonds, which is typical of the 1*R*,4*R*-*cis* structures [7, 9, 10], the structure of the 1*R*,4*S* diastereomeric compound **I** is characterized by a transoid arrangement of these bonds (Fig. 1). Consequently, the methyl groups of the isopropyl substituent are arranged symmetrically about the cyclohexanone ring as judged from the φ_{13}–φ_{16} torsion angles (Table 3). This orientation of the isopropyl grouping in molecule **I** in the crystal brings about a slight shortening of the intramolecular contacts between the C(9) and H(9*B*) atoms of the methyl groups in the isopropyl fragment and the C(5) and H(5*B*) atoms of the 5-methylene group in the cyclohexanone ring and also a considerable shortening of the contact between the H(10*C*) methyl hydrogen atom and the C(3) carbon atom of the carbonyl group (Table 4). In the structure of the 1*R*,4*R* diastereomeric compound **IV**, the corresponding contacts are either shortened to a substantially lesser extent or close to the standard sum of the van der Waals radii of the relevant atoms [20]. By contrast, certain of the intramolecular contacts in the above fragment, which are noticeably shortened in the structure of 1*R*,4*R* diastereomeric compound **IV** with the *para*-nitro-substituted 2-arylidene grouping [the H(5*A*)···C(10) and H(10*B*)···C(5) contacts], are larger than the standard sums of the van der Waals radii in the structure of compound **I**. Thus, the intramolecular contacts between atoms in the studied compounds indicate that diastereomeric structures **I** and **IV** considerably differ in the steric strain in the molecular fragments containing the C(4) chiral center and the carbonyl and 5-methylene groups attached to C(4). The carbonyl group and the C(4)–C(8) bond in compound **I** are nearly orthogonal (see the φ_{17} torsion angle), unlike their more or less eclipsed orientation in the 1*R*,4*R* structures [9, 10].

It is interesting that the methyl groups of the isopropyl fragment in structures **I** and **II** with the same 1*R*,4*S* configuration but different (chair and twist, respectively) conformations exhibit different orientations with respect to the cyclohexanone ring (the φ_{13}–φ_{17} torsion angles in Table 3).

As could be expected, the carbomethoxy group in compound **I** is planar and lies in the plane of the benzene ring [the C(14)C(15)C(18)O(2) torsion angle is equal to –0.9(6)°].

In the crystal, the molecules of compound **I** form stacks along the *c*-axis (Fig. 2).

EXPERIMENTAL

Compound **I** was synthesized according to the procedure described in [14]. Single crystals suitable for X-ray diffraction analysis were grown from an octane–methanol mixture (at a volume ratio of 1 : 1).

Crystals **I** are orthorhombic ($C_{19}H_{25}O_3$); at 20°C: a = 11.961(3) Å, b = 26.453(8) Å, c = 5.400(2) Å, V = 1708.6(9) Å^3, M = 300.38, Z = 4, space group $P2_12_12_1$, d_{calcd} = 1.168 g/cm^3, $\mu(MoK_\alpha)$ = 0.077 mm^{-1}, and $F(000)$ = 648. The unit cell parameters and the intensities of 1770 unique reflections were measured on a Siemens P3/PC automated four-circle diffractometer (MoK_α radiation, graphite monochromator, $2\theta/\theta$ scan mode, $2\theta_{max}$ = 50°). The *hkl* index ranges are as follows: $0 < h < 14$, $0 < k < 31$, and $0 < l < 6$.

The structure was solved by the direct method using the SHELX97 software package [21]. The hydrogen atoms were located from the electron-density difference synthesis and refined using a riding-atom model with the thermal parameters $U_{iso} = nU_{eq}$ for the non-hydrogen atom bonded to the refined hydrogen atom (n = 1.5 for the hydrogen atoms of the methyl group and n = 1.2 for the remaining hydrogen atoms). The structure was refined on F^2 by the full-matrix least-squares procedure in the anisotropic approximation for

Table 5. Coordinates of non-hydrogen atoms ($\times 10^4$) and equivalent isotropic thermal parameters ($Å^2 \times 10^3$) for structure **I**

Atom	*x*	*y*	*z*	U_{eq}
O(1)	2374(2)	−1944(1)	15490(6)	85(1)
O(2)	2836(3)	−1033(1)	6639(7)	100(1)
O(3)	3941(2)	552(1)	4263(6)	79(1)
C(1)	283(3)	−1107(1)	13056(7)	50(1)
C(2)	1424(3)	−1353(1)	12955(7)	45(1)
C(3)	1546(3)	−1848(1)	14275(7)	55(1)
C(4)	620(3)	−2231(1)	13905(7)	54(1)
C(5)	−508(3)	−1964(1)	14286(8)	62(1)
C(6)	−642(3)	−1499(1)	12644(7)	58(1)
C(7)	136(3)	−833(1)	15553(8)	75(1)
C(8)	746(3)	−2484(1)	11345(8)	57(1)
C(9)	−131(3)	−2894(1)	10932(10)	86(1)
C(10)	1905(3)	−2717(1)	10969(11)	85(1)
C(11)	2324(3)	−1182(1)	11739(7)	51(1)
C(12)	2489(3)	−719(1)	10263(8)	46(1)
C(13)	2007(3)	−253(1)	10877(7)	53(1)
C(14)	2247(3)	174(1)	9494(7)	56(1)
C(15)	2970(3)	152(1)	7495(7)	50(1)
C(16)	3440(3)	−309(1)	6863(8)	58(1)
C(17)	3203(3)	−735(1)	8247(7)	57(1)
C(18)	3229(3)	626(1)	6130(8)	61(1)
C(19)	4243(4)	998(2)	2841(11)	97(2)

non-hydrogen atoms up to $wR_2 = 0.136$ for 1770 reflections [$R_1 = 0.047$ for 1139 reflections with $F > 4\sigma(F)$ and $S = 0.990$]. The final coordinates of non-hydrogen atoms are listed in Table 5.

ACKNOWLEDGMENTS

This work was supported by the International Association of Assistance for the promotion of co-operation with scientists from the New Independent States of the former Soviet Union, project no. INTAS-1997 1730.

REFERENCES

1. L. A. Kutulya, I. B. Nemchenok, and T. V. Khandrimaĭlova, Kristallografiya **35** (5), 1234 (1990) [Sov. Phys. Crystallogr. **35**, 724 (1990)].
2. L. A. Kutulya, Proc. SPIE **3488**, 84 (1998).
3. V. Vashchenko, T. Dryshlyak, N. Shkolnikova, and L. Kutulya, Mol. Cryst. Liq. Cryst. **328**, 245 (1999).
4. E. V. Popova, A. P. Fedoryako, V. V. Vashchenko, and L. A. Kutulya, Zh. Fiz. Khim. (in press).
5. V. I. Kulishov, L. A. Kutulya, V. E. Kuz'min, *et al.*, Zh. Obshch. Khim. **61** (1), 155 (1991).
6. L. A. Kutulya, V. P. Kuznetsov, E. E. Lakin, *et al.*, Kristallografiya **38** (5), 86 (1993) [Crystallogr. Rep. **38**, 630 (1993)].
7. L. A. Kutulya, V. V. Vashchenko, V. P. Kuznetsov, *et al.*, Kristallografiya **40** (6), 1015 (1995) [Crystallogr. Rep. **40**, 941 (1995)].
8. V. P. Kuznetsov, V. I. Kulishov, L. A. Kutulya, *et al.*, Kristallografiya **44** (2), 229 (1999) [Crystallogr. Rep. **44**, 196 (1999)].
9. L. A. Kutulya, V. P. Kuznetsov, V. I. Kulishov, *et al.*, Kristallografiya **44** (3), 475 (1999) [Crystallogr. Rep. **44**, 435 (1999)].
10. A. S. Tolochko, V. I. Kulishov, L. A. Kutulya, *et al.*, Kristallografiya **46** (2), 254 (2001) [Crystallogr. Rep. **46**, 214 (2001)].
11. L. A. Kutulya, N. S. Pivnenko, I. B. Nemchenok, *et al.*, Zh. Obshch. Khim. **57**, 397 (1987).
12. L. A. Kutulya, T. V. Khandrimaĭlova, V. I. Biba, *et al.*, Zh. Obshch. Khim. **58** (8), 1793 (1988).
13. L. A. Kutulya, V. P. Kuznetsov, L. D. Patsenker, *et al.*, Kristallografiya **39** (5), 860 (1994) [Crystallogr. Rep. **39**, 782 (1994)].
14. T. G. Drushlyak, V. V. Vashchenko, L. A. Kutulya, *et al.*, in *Book of Abstracts of the European Conference on Liquid Crystals, Hersonissos, Greece, 1999*, P3-060.
15. N. S. Zefirov, V. A. Palyulin, and E. E. Dashevskaya, J. Phys. Org. Chem. **3**, 147 (1990).
16. L. A. Kutulya, Doctoral Dissertation in Chemistry (Kharkov, 1992).
17. L. A. Kutulya, V. V. Vashchenko, V. P. Kuznetsov, *et al.*, Zh. Strukt. Khim. **35** (5), 133 (1994).
18. U. Burkert and N. Allinger, *Molecular Mechanics* (American Chemical Society, Washington, 1982; Mir, Moscow, 1986).
19. L. V. Chepeleva, Candidate's Dissertation in Chemistry (Kharkov, 1997).
20. Yu. V. Zefirov and P. M. Zorky, Usp. Khim. **58** (5), 713 (1989).
21. G. M. Sheldrick, *SHELX97, PC Version: A System of Computer Programs for the Crystal Structure Solution and Refinement. Rev. 2*, 1998.

Translated by O. Borovik-Romanova

Crystallography Reports, Vol. 46, No. 5, 2001, pp. 792–800. Translated from Kristallografiya, Vol. 46, No. 5, 2001, pp. 866–874.

STRUCTURES OF MACROMOLECULAR COMPOUNDS

Dedicated to the memory of B.K. Vainshtein

Topology of the Polypeptide Chain in the Complex of Agglutinin from Castor Bean Seeds with β-*D*-Galactose in the Crystalline State

N. V. Konareva[1], A. G. Gabdulkhakov[1,2], S. Eschenburg[3], S. Stoeva[4], A. N. Popov[1], R. Krauspenhaar[3], M. E. Andrianova[1], Yu. Savochkina[1,5], I. I. Agapov[5], A. G. Tonevitskiĭ[5], A. N. Kornev[1,6], V. V. Kornilov[1,6], V. N. Zaitsev[1], W. Voelter[4], Ch. Betzel[3], S. V. Nikonov[2], B. K. Vainshtein[1,†], and A. M. Mikhailov[1]

[1] *Shubnikov Institute of Crystallography, Russian Academy of Sciences, Leninskiĭ pr. 59, Moscow, 117333 Russia*

[2] *Institute of Protein Research, Russian Academy of Sciences, Pushchino, Moscow oblast, 142292 Russia*

[3] *Institute of Physiological Chemistry, University Hospital, c/o DESY, Build. 22a, Notkestrasse 85, Hamburg, 22603 Germany*

[4] *Department of Physical Biochemistry, Institute of Physiological Chemistry, University of Tübingen, Hoppe-Seyler-Strasse 4, Tübingen, 72076 Germany*

[5] *State Research Center of Genetics and Selection of Industrial Microorganisms, VNIIGENETIKA, Pervyi Dorozhnyi proezd 1, Moscow, 113545 Russia*

[6] *Institute of Cell Biophysics, Russian Academy of Sciences, Pushchino, Moscow oblast, 142292 Russia*

e-mail: amm@biostr.crystal.msk.ru

Received April 25, 2001

Abstract—The three-dimensional structure of the complex of agglutinin from *Ricinus communis* with β-*D*-galactose was established and refined at 2.5 Å resolution by X-ray structure analysis. Biocrystals were obtained using dialysis through a semipermeable membrane. X-ray intensity data (R_{merge} = 4.6%) were collected from one crystal at 100 K using synchrotron radiation at the DESY outstation [European Molecular Biology Laboratory (EMBL), Hamburg, Germany]. The initial phases were calculated by the molecular replacement method. The atoms of both protein and sugar molecules were localized. Unlike ricin, the ricinlike heterodimer RcA contains only one galactose-binding center in the region of the *Asn*46–*Gly*25–*Trp*37–*Lys*40 site in the first domain of the *B* subunit, whereas the second galactose-binding site of the *B* subunit is lost. One functionally important water molecule, which is bound to the residues *Tyr*123–*Glu*176–*Arg*179–*Glu*207, was revealed in the region of the active center in the *A* subunit. © *2001 MAIK "Nauka/Interperiodica".*

INTRODUCTION

Agglutinin from castor bean seeds (*Ricinus communis Agglutinin*, RcA) belongs to type-II ribosome-inactivating proteins (RIP-II). Proteins of this group are bound to the cell receptor and transport of the polypeptide to cell cytosol, thus terminating the ribosomal protein synthesis. Type-II ribosome-inactivating proteins belong to plant toxins that are most poisonous to mammalian cells. Only one molecule of plant toxin penetrated into cytosol can cause cell death.

The RcA molecule, like all type-II ribosome-inactivating proteins, is composed of two subunits differing in both three-dimensional structure and function. The *A* subunit of agglutinin (RcA/*A*) with the molecular weight of 32 kDa consists of 266 amino acid residues [1]. This subunit represents a catalytic polypeptide and removes specific *N*-glycosidase of adenine from the loop of 28S ribosomal RNA, which results in termination of the ribosomal protein synthesis. The loss of ability to synthesize protein leads to cell death.

The *B* subunit of agglutinin (RcA/*B*) with the molecular weight of 37 kDa belongs to lectins. This subunit consists of 262 amino acid residues and can be bound to glycoproteins and glycolipids containing terminal galactose. The *A* and *B* subunits form the *AB* heterodimer through hydrophobic interactions and one covalent bond. This heterodimer is characteristic of all the type-II ribosome-inactivating proteins. Unlike the

† Deceased.

best studied RIP-II protein from *Ricinus communis Ricin* (RcR) consisting of one *AB* heterodimer, RIP-II from *Ricinus communis Agglutinin* belongs to tetrameric proteins and is composed of two ricinlike *AB* heterodimers linked by a disulfide bond.

The *A* subunits of type-II ribosome-inactivating proteins are widely used for constructing efficient immunotoxins possessing highly specific activity and employed primarily in the treatment of oncological diseases. It should be noted that one of the tetrameric type-II ribosome-inactivating proteins, namely, viscumin (*Mistletoe Lectin I* from *Viscum album*, MLI), is presently used in pharmacology as an efficient extract to stimulate the immune system.

Type-II ribosome-inactivating proteins are promising biomolecules for studying transport pathways and mechanisms of protein–cell interactions. There is evidence that the activity of immunotoxins substantially depends on the efficient intracellular transport of the toxic portion of a molecule, which is, apparently, determined primarily by the three-dimensional structure of toxins.

Hence, investigation and comparative analysis of the structural characteristics of type-II ribosome-inactivating proteins and their complexes are of interest in both fundamental and applied aspects.

MATERIALS AND METHODS

Agglutinin was *isolated and purified* at 4°C using the procedure whose principal characteristics are described elsewhere [2]. A 5 mM sodium phosphate buffer (pH 7.4) containing 200 mM NaCl was added to a homogenate of castor bean seeds. The protein was extracted within 24 h.

The homogenate obtained was centrifuged for 20 min at 8000 g, and the protein was precipitated by adding 2.5 M ammonium sulfate and 200 mM NaCl to the resulting supernatant. One-day incubation was followed by the protein precipitation by 30-min centrifugation at 8000 g. The centrifugate was dissolved in a 5 mM sodium phosphate buffer (pH 7.4) containing 200 mM NaCl. The suspension was clarified by 10-min centrifugation at 10 000 g. The concentration of sulfate ammonium in the supernatant was brought to 2 M, and the above-described operations associated with the precipitation and clarification of the protein fraction were repeated.

The second stage of purification of RIP-II from the resulting extract was performed by affine chromatography on a column packed with galactosyl-Sepharose 4B equilibrated with a 5 mM sodium phosphate buffer (pH 7.4). The column was washed with a 5 mM sodium phosphate buffer (1 l) at pH 7.4, and RIP-II was eluted from the column with a solution of 0.1 M galactose in the same buffer. The proteins RcR and RcA were separated by gel filtration on a column with Sephadex G250. The purity and homogeneity of agglutinin were analyzed by electrophoresis in an SDS-containing polyacrylamide gel.

Crystallization of the agglutinin complex with 50 mM β-D-galactose was made by both hanging- and sitting-drop vapor diffusion techniques, as well as dialysis of a precipitant through a semipermeable membrane (Serva, Germany) [3, 4].

X-ray diffraction data collection. The Fourier spectrum of intensities for RcA was measured from crystals cooled to 100 K. Prior to freezing, the crystals were soaked for one hour in a cryoprotector composed of glycerol (25% v/v) and 1.7 M ammonium sulfate in a 0.1 M sodium phosphate buffer at pH 6.5.

The three-dimensional X-ray diffraction data were collected on a BW7A beam line with a DORIS storage ring at the DESY synchrotron outstation (EMBL, Hamburg, Germany). The Fourier spectrum of RcA was recorded and processed using the DENZO and SCALEPACK program packages [5].

DETERMINATION OF THE THREE-DIMENSIONAL STRUCTURE

The model for RcA was constructed by the molecular replacement and computer graphics methods using the AMoRe [6] and O [7] program packages. The structure of ricin established by X-ray diffraction analysis at 2.5 Å resolution was used as the starting model.

The primary and tertiary structures of the agglutinin complex with β-D-galactose were modified, and the three-dimensional structure was refined using the CNS (Brünger) and O [7] program packages.

RESULTS AND DISCUSSION

Crystals of the RcA complex (0.34×0.70 mm) were grown from a crystallization solution (40 μl) consisting of the protein (2%) in a 0.1 M sodium phosphate buffer (pH 6.7), 50 mM β-D-galactose, and NaN_3 (0.02%) by equilibrium dialysis through a semipermeable membrane at 20°C within four weeks. A reservoir solution (2 ml) consisted of 2.5 M ammonium sulfate and NaN_3 (2%) in a 0.1 M sodium phosphate buffer at pH 6.7. The choice of the crystallization procedure was dictated primarily by the necessity of growing crystals of the necessary dimensions (0.5–0.7 mm) with the minimum mosaicity.

Rapid freezing of the crystals made it possible to record the Fourier spectrum of the agglutinin molecule from one crystal in the resolution range from 20 to 2.5 Å. The data were collected on a BW7A beam line at the wavelength of 0.9 Å at the synchrotron outstation (DORIS, DESY, EMBL, Hamburg, Germany). The completeness of the data set was 91% (R_{merge} = 4.6%). The details of X-ray data collection and the characteristics of the data set are indicated in Table 1.

It was shown that agglutinin and ricin from castor bean seeds are produced by different genes [8]. It is

Table 1. Geometric parameters of the direct and the reciprocal spaces for RcA and the statistics of the refined model

Sp. gr.	$P3_2$
Unit-cell parameters: $a = b$, Å	98.824
c, Å	209.490
Number of molecules per unit cell	3
Mathews coefficient, Å^3/Da	4.5
Solvent concentration in the unit cell, %	64
Number of crystals used for X-ray data collection	1
Temperature of X-ray data collection, K	100
Wavelength, Å	0.9
Rocking angle, deg	0.5
Number of two-dimensional Fourier images	135
Resolution range, Å	20–2.5
Number of measured reflections	469452
Number of independent reflections	72014
$R_{merg}(I)$/Completeness of the set, %	4.6/90.9
Number of the refined non-hydrogen atoms:	
of the RcA molecule	8530
of the galactose molecule	120
of water molecules bound to the protein	808
R_f/R_{free}, %	23.8/30.2
Rms deviations from the ideal values:	
for bond lengths, Å	0.018
for dihedral angles, deg	2.4
Average B factor, Å^2:	
for non-hydrogen atoms of the protein	37.1
for atoms of galactose	35.8
for oxygen atoms of water molecules	44.5
Statistics of the* φ- and ψ-angle distribution,* %:	
in allowed regions	82
in additionally allowed regions	16

* Based on the Ramachandran plot for all the residues, except for Gly and Pro.

assumed that the ricin gene is formed first. Its duplication and subsequent evolution mutation give rise to the synthesis of the *AB* heterodimer of agglutinin. Unlike the dimeric structure of ricin, the ricinlike heterodimers undergo posttranslational modification and are linked in pairs, and, thus, form the tetrameric agglutinin structure. The primary structures of RcR and RcA (Tables 2 and 3) are highly homologous [1]. The nucleotide sequence of the RcA/*A* chain is shorter by three bases than that of the RcR/*A* chain, which corresponds to Ala130 deletion. On the whole, the *A* chains of ricin and agglutinin from *Ricinus communis* differ by 18 amino acid residues and are 93% homologous. The *B* chains of these proteins differ by 41 amino acid residues and are 81% homologous. Of all 59 different amino acid residues, 22 substitutions cause no essential changes in the protein properties, because the amino acid residues are replaced by the residues with similar properties. The most substantial difference between RcA and RcR reduces to two additional cysteine residues in the RcA/*A* chain. Functionally, the most important is the replacement of Tyr248 of a highly affine carbon-binding center in the RcR/*B* subunit by His248 in the RcA/*B* subunit.

The above structure-function analysis of the primary sequences of the RcA and RcR molecules dictated the choice of the molecular replacement method for the solution of the phase problem. We used as the starting model the ricin structure at 2.5 Å resolution (the Brookhaven Protein Data Bank, ID code 2AAI).

The starting model composed of two complete ricin molecules, including side-chain atoms (at 2.5 Å resolution), was located, oriented, and refined in the unit cell of RcA using the modules of structure amplitudes in the resolution range from 8 to 3 Å. The calculations were performed with the integration radius of 30 Å and the structure amplitudes larger than 10σ. The translation and rotation functions were calculated using the molecular-replacement AMoRe program package [6]. The only arrangement of the RcR molecules in the unit cell of agglutinin was found. The relatively low value of the correlation factor ($R_f = 0.425$, $R_c = 0.504$) characterizing the solution is explained by the fact that the starting model, as was mentioned above, was composed not only by the main-chain atoms, but also by the side-chain atoms of all the amino acid resides of the RcR chains. This approach substantially simplified the construction of the model of the agglutinin molecule at the subsequent stages of the structure solution RcA.

In the starting model, the amino acid residues of ricin were replaced by the amino acid residues of agglutinin with due regard for the alignment of the corresponding primary sequences (Tables 2 and 3) using the *merge* and *lego-side-chain* procedures from the O program package [7]. Then the structure of agglutinin represented as individual blocks was refined in the rigid-body mode. First of all, the RcA molecule was divided into two blocks (*A*1*B*1 and *A*2*B*2). At the second stage, the *B*1, *A*1, *A*2, and *B*2 subunits were refined separately.

It is well known that the *B* chains of RIP-II consist of two virtually identical dimers. Hence, the subsequent refinement was performed considering the A1 and A2 chains, the first and second domains of the *B*1 chain, and the first and second domains of the *B*2 chain as rigid bodies. Finally, after the refinement of the positions of all the amino acid residues as individual rigid bodies, the construction of the RcA molecule in the block form was completed. This above-described pro-

Table 2. Comparison of the primary structures of the RcA/*A* and RcR/*A* chains

		1sssss 1hhhhhhhhhhhhhh* 2ss**	
RcA/A	1	IFPKQYPIINFTTADATVESYTNFIRAVRSHLTTGADVRHEIPVLPNRVG	50
		:::::::::::::: ::: :::::::::: ::::::::: :::::::::***:	
RcR/A	1	IFPKQYPIINFTTAGATVQSYTNFIRAVRGRLTTGADVRHDIPVLPNRVG	50
		3ssssssssss 4sssssssssssssss 5ss 2hh	
RcA/A	51	LPISQRFILVELSNHAELSVTLALDVTNAYVVGCRAGNSAYFFHPDNQED	100
		::: ::::::::::::::::::::::::::::: ::::::::::::::::	
RcR/A	51	LPINQRFILVELSNHAELSVTLALDVTNAYVVGYRAGNSAYFFHPDNQED	100
		hhhh 6sssss 3hhhhhhhh h	
RcA/A	101	AEAITHLFTDVQNSFTFAFGGNYDRLEQL–GGLRENIELGTGPLEDAISA	149
		::::::::::::: :::::::::::::: : :::::::: :::: ::::	
RcR/A	101	AEAITHLFTDVQNRYTFAFGGNYDRLEQLAGNLRENIELGNGPLEEAISA	150
		4hhhhhhhhhhhhhhhhhhhhhhhhhhhhhhhhhhhh	
RcA/A	150	LYYYSTCGTQIPTLARSFMVCIQMISEAARFQYIEGEMRTRIRYNRRSAP	199
		:::::: ::: ::::::: :::::::::::::::::::::::::::::	
RcR/A	151	LYYYSTGGTQLPTLARSFIICIQMISEAARFQYIEGEMRTRIRYNRRSAP	200
		5hhhhhhhhhhhhhhhhhh 7ssssssss 8sssss	
RcA/A	200	DPSVITLENSWGRLSTAIQESNQGAFASPIQLQRRNGSKFNVYDVSILIP	249
		:: :::::::::	
RcR/A	201	DPSVITLENSWGRLSTAIQESNQGAFASPIQLQRRNGSKFSVYDVSILIP	250
		9ss	
RcA/A	250	IIALMVYRCAPPPSSQF	266
		:::::::::::::::::	
RcR/A	251	IIALMVYRCAPPPSSQF	267

* Helix.

** β-ribbon.

*** Homologous amino acid residues.

cedure for the construction of the three-dimensional agglutinin model was performed by the FROG program [9] based on $|F| > 5\sigma$ in the resolution range from 10 to 3.5 Å. The model of the agglutinin molecule obtained at this stage is characterized by $R_f = 0.36$. The representation of the protein molecule by a block is efficient only at the initial stages of the model construction. In our opinion, the structure solution based on the block model is a necessary stage of the X-ray structure analysis of biomacromolecules and their complexes. This stage is of particular importance if the starting phases are calculated from the "homologous model" localized in the unit cell by the molecular replacement method.

The subsequent refinement of the three-dimensional RcA structure was performed by the CNS and O program packages and computer graphics with a gradual increase of the number of the structure-factor moduli. The manual correction of the positions of the amino acid residues and individual atoms was alternated with the refinement using the CNS program package. At this stage, we analyzed both omit maps and electron-density syntheses with the coefficients ($3F_o$–$2F_c$ and $2F_o$–$2F_c$). At the final stage, we included into the refinement the water molecules, which were placed into chemically reasonable positions with the difference in the electron densities on the map exceeding 3σ. The galactose molecules were localized from the several electron density syntheses. At all stages, the positions of these molecules were refined together with the position of the agglutinin molecule.

The parameters of the refined structure is given in Table 1. The quality of the RcA structure was checked by the Procheck program [10]. The estimated characteristics of the structure had either good or admissible values.

The RcA molecules occupy only 36% (Table 1) of the unit-cell volume. The remaining volume is occupied by solvent molecules. Such molecular packing of the crystal is too loose even for biomacromolecules. The RcA molecules (Fig. 1) are surrounded by solvent molecules occupying the cavities with the linear dimensions of 70 Å (the diameter of the RcA molecule is 40 Å). The large percentage of the solvent leads to a sharp decrease in the intensities of higher harmonics in

Table 3. Comparison of the primary structures of the RcA/*B* and RcR/*B* chains

		1ssss 1hh* 2ssss** 3s	
RcA/*B*	1	ADVCMDPEPIVRIVGRNGLCVDVTGEEFFDGNPIQLWPCKSNTDWNQLWT	50
		::::::::::::::::::::::: : :: :::::::::::: :::::***:	
RcR/*B*	1	ADVCMDPEPIVRIVGRNGLCVDVRDGRFNHNAIQLWPCKSNTDANQLWT	50
		ss 4ss 5sss 6sss 7sssss 8sss 9ss	
RcA/*B*	51	LRKDSTIRSNGKCLTISKSSPRQQVVIYNCSTATVGATRWQIWDNRTIIN	100
		: : ::::::::::: :: : :: : :: :::::::::: ::::	
RcR/*B*	51	LRKDNTIRSNGKCLTTYGYSPGVYVMIYDCNTAATDATRWQIWDNRTIIN	100
		ss 10ssss 11ssss 2hh 12ssss s	
RcA/*B*	101	PRSGLVLAATSGNSGTKLTVQTNIYAVSQGWLPTNNTQPFVTTIVGLYGM	150
		::: ::::::::::::: :::::::::::::::::::::::::::::::::::	
RcR/*B*	101	PRSGLVLAATSGNSGTTLTVQTNIYAVSQGWLPTNNTQPFVTTIVGLYGM	150
		13sss 14sss 3hhs15s 16sss 17sss	
RcA/*B*	151	CLGANSGKVWLEDCTSEKAEQQWALYADGSIRPQQNRDNCLTTDANIKGT	200
		::::::: :: ::: ::::::::::::::::::::::::::::::: : :::::	
RcR/*B*	151	CLGANSGQVWIEDCSSEKAEQQWALYADGSIRPQQNRDNCLTSDANIKET	200
		18sss 19s 20s 21sss 4hh 22ss	
RcA/*B*	201	VVKILSCGPASSGQRWMFKNDGTILNLYNGLVLDVRRSDPSLKQIIVHPF	250
		:::::::::::::::::::::::::::::::: :::::::::::::::::::: :	
RcR/*B*	201	VVKILSCGPASSGQRWMFKNDGTILNLYNGLVLDVRRSDPSLKQIILYPL	250
		23ss	
RcA/*B*	251	HGNLNQIWLPLF	262
		:: :::::::::	
RcR/*B*	251	HGDPNQIWLPLF	262

* Helix.

** β-ribbon.

*** Homologous amino acid residues.

the Fourier spectrum of the molecule. As a result, it is impossible, in principle, to collect the X-ray diffraction data at the atomic resolution using the currently available X-ray instruments. However, the formation of RcA complexes with a wide variety of reagents in the crystalline state is highly probable because of the existence of the above-mentioned channels. This fact opens new possibilities for modeling the pathways of biochemical reactions in the RcA crystals. In the crystal, the interactions between the RcA molecules are primarily of the polar and the hydrophobic nature. The principal intermolecular bonds are indicated in Table 4.

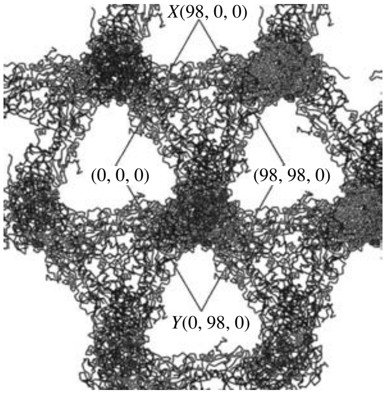

Fig. 1. RcA molecule projected along the *c*-axis.

Two ricinlike dimers, *B*1*A*1 and *A*2*B*2, form the tetrameric structure of the agglutinin molecule mainly due to covalent interactions between the Cys156 residues in the *A*1 and *A*2 subunits (Fig. 2). The S–S bond length of the disulfide bridge equals 2.13 Å, i.e., is somewhat longer than the corresponding bond lengths (2.08–2.10 Å) determined from the X-ray data for small molecules. In our opinion, this difference is associated mainly with insufficient resolution of the Fourier spectrum (2.5 Å) used for the structure solution. Evidently, this bond length can be discussed in detail only upon the refinement of the tetramer structure on the basis of the Fourier spectrum at high (atomic) resolution. It should be emphasized that this is the first example of dimerization of ricinlike dimers via covalent bonding in

Table 4. Intermolecular hydrogen bonds

Subunit, residue						*d**, Å	*s***	*t****
Atoms								
1			2					
*A*1	Glu137	N	*B*1	Ser70	O*G*	3.13	2	*–a – b*
*A*1	Asp145	O*D*1	*B*1	Lys117	N*Z*	3.48	2	*–a – b*
*A*1	Asp145	O*D*2	*B*1	Lys117	N*Z*	3.39	2	*–a – b*
*A*1	Cys156	O	*B*1	Thr122	N	4.44	2	*–a – b*
*A*1	Gly157	O	*B*1	Gln73	N*E*2	3.14	2	*–a – b*
*A*1	Gkn159	N	*B*1	Gln73	O*E*1	2.77	2	*–a – b*
*A*1	Thr162	O*G*1	*B*1	Gln73	O*E*1	2.84	2	*–a – b*
*A*1	Arg165	N*E*	*B*1	Pro71	O	3.37	2	*–a – b*
*A*1	Arg196	N*H*1	*B*1	Ser70	O	3.22	2	*–a – b*
*A*1	Asp15	O*D*2	*B*2	Arg102	N*H*2	4.64	1	*–b*
*A*1	Glu67	O*E*1	*B*2	Thr84	O*G*1	3.64	1	*–b*
*B*1	Ser114	N	*B*2	Ser69	O	2.54	3	*–a – b*
*B*1	Ser114	O*G*	*B*2	Ser103	O	2.50	3	*–a – b*
*B*1	Asp188	O*D*1	*B*2	Gln73	N*E*2	3.22	3	*–a – b*
*B*1	Asp196	N*D*2	*A*2	Gly157	O	3.59	3	*–b*
*B*1	Tyr228	O*H*	*A*2	Thr155	O*G*1	2.66	3	*–b*

Note: 1: *x, y, z*; 2: *–y, x – y*, 2/3 + *z*; 3: *y – x, –x*, 1/3 + *z*.
* Bond length.
** Symmetry operation.
*** Translation.

the case of tetrameric RIP-II. In addition, two RcA/*A* subunits are linked through polar interactions between the compactly arranged amino acid residues 113–118.

The toxic *A* subunit is a globular enzyme (Fig. 3) terminating the eukaryotic ribosomal protein synthesis. Similar to the corresponding subunits in other RIP-II, the RcA/*A* subunit can be represented by three domains (Fig. 3). The first domain contains both helical regions and β-ribbons (Fig. 3, Table 3); the second domain consists only of helical regions; and the third domain is formed by two short antiparallel β-ribbons and a rather long helical region. A branched network of salt bridges

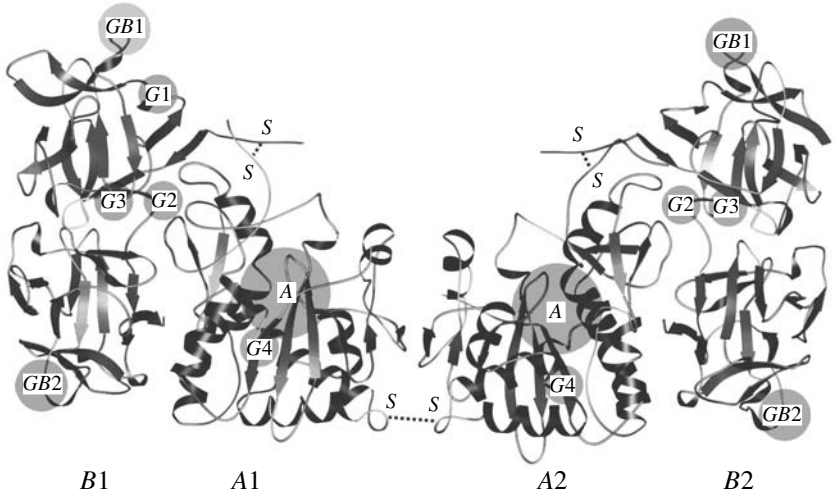

Fig. 2. Polypeptide-chain folding represented as secondary-structure elements of the RcA molecule; *B*1, *A*1, *A*2, and *B*2 are polypeptide chains of the RcA molecule; S···S are disulfide bonds; *A* is the region of the active center of the RcA/*A* subunit.

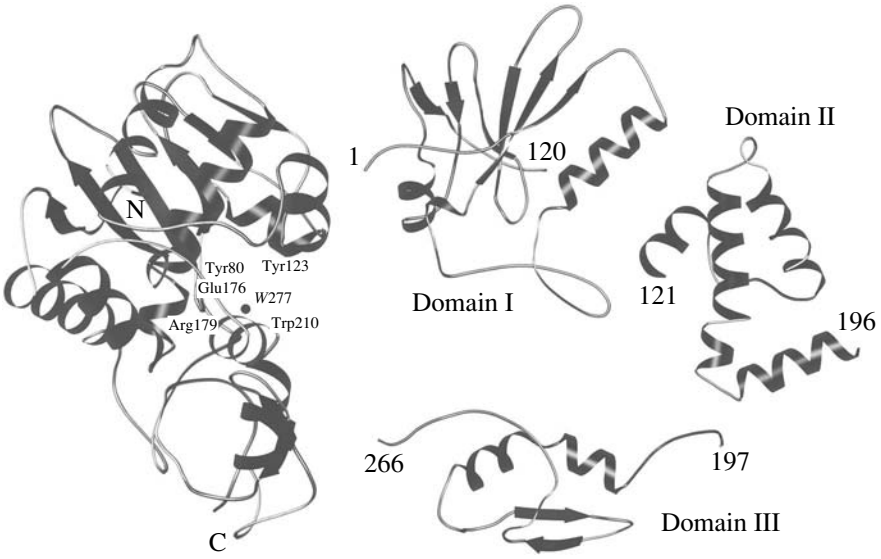

Fig. 3. Three-dimensional structure of the *A* chain and its three domains represented as the secondary-structure elements. The principal amino acid residues and the bound water molecule (*W*277) in the pocket of an active center in the RcA/*A* subunit are labelled.

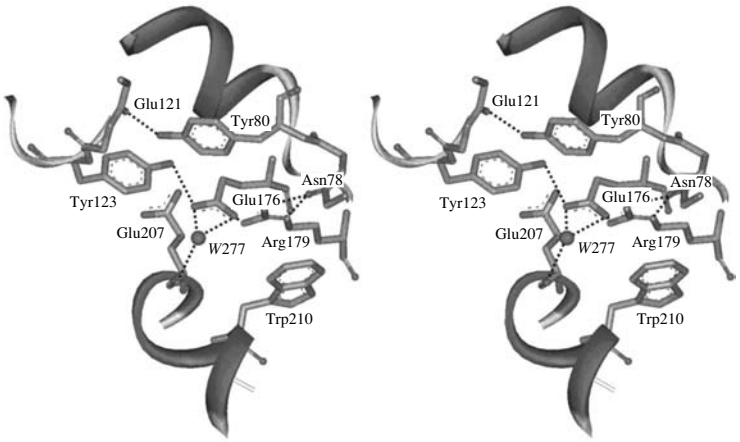

Fig. 4. Stereoview of the active center of the *A* subunit.

plays an important role in the stabilization of the tertiary RcA/*A* structure.

The amino acid residues Tyr80, Tyr123, Glu176, Arg179, and Trp210 forming the site responsible for *N*-glycosidase activity are located in an open pocket of the *A* subunit (Fig. 3). The catalytic residues of RcA/*A* are conservative, not only in tetrameric RIP-II, but also in heterodimeric ricin (Tyr80, Tyr123, Glu177, Arg180, and Trp211) (Table 2). However, a pocket of the active center of viscumin [11] contains several water molecules playing an important role in toxin functioning, whereas, in RcA/*A*, only one water molecule (*W*277) is revealed (Figs. 3 and 4). This fact supports the opinion that the mechanisms of functioning of the catalytic subunits of these two tetrameric proteins are somewhat different. The oxygen atom of *W*277 in the pocket of the RcA/*A* subunit forms hydrogen bonds with OE1 Glu176 (the bond length is 3.00 Å), OE2 Glu176 (2.66 Å), NH1 Arg279 (2.52 Å), and O Gln207 (2.90 Å).

The RcA/*B* subunit belongs to lectins. It is bound to galactose-containing receptors at the cell surface, thus creating the prerequisites for penetration of the toxic RcA/*A* chain into the cell via endocytosis. The *B* subunit of RcA (Fig. 5) consists of two structurally similar domains. Each domain, in turn, is built of four subdomains, three of which (α, β, and γ, Fig. 5) are structurally similar and consist of approximately equal numbers of amino acid residues. The subdomains are arranged symmetrically with respect to the local threefold quasi-symmetry axis to form a globule with a hydrophobic core (Fig. 5). This arrangement of the amino acid residues is typical of the lectin family [12].

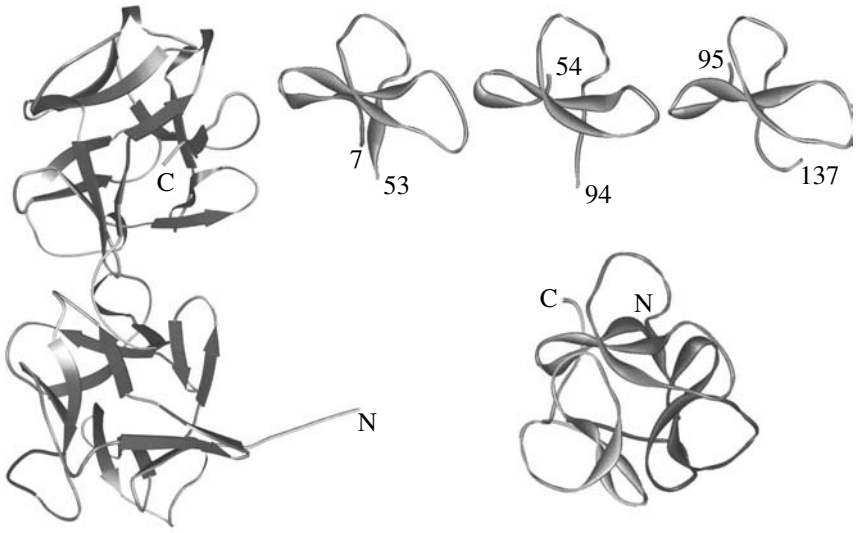

Fig. 5. Three-dimensional structure of the *B* subunit of RcA (at left), the α, β, and γ subdomains (at top), and their quasi-symmetrical arrangement in RcA/*B* (at lower right).

The first seven amino acid residues of each domain in the RcA/*B* subunit form the 1λ and 2λ subdomains, respectively. The RcA/*A* and RcA/*B* chains are linked through the 1λ subdomain (Fig. 2), and the first and the second domains of the RcA/*B* subunit are linked via the 2λ subdomain (Fig. 5). Virtually, there are no helical regions among the secondary-structure elements forming the three-dimensional structure of the RcA/*B* subunit (Table 3).

As follows from the consideration of the primary and three-dimensional structures of the RcA/*B* and RcR/*B* subunits, the replacement of Tyr248 by His248 is the most essential mutation in the RcA chain. As a result of this substitution, the RcA molecule loses the second galactose-binding center existing in the RcR/*B* subunit. The inspection of the electron-density synthesis in the region of the Arg237, His248, and His251 residues revealed no sugar residues in the pocket, despite the fact that the external pocket shape was retained. Therefore, in distinction from RcR/*B*, the first domains of each agglutinin molecule retain only one galactose-binding site (*GB*1, see Fig. 2). It should be noted that Asp22 (the *OD*2 atom, the bond length is 2.5 Å), Lys40 (NZ, 2.56 Å), Asn46 (N*D*2, 2.66 Å), and Gly25 (N, 3.13 Å) are the major residues of the sugar-binding sites (Fig. 6) involved in hydrogen bonding with oxygen atoms of sugar.

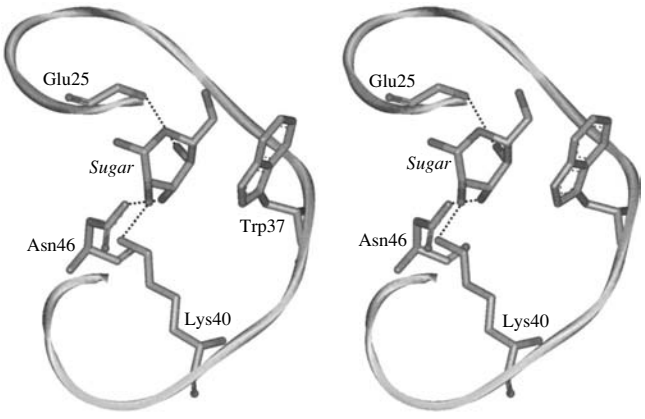

Fig. 6. Stereoview of the region of the galactose-binding site (*GB*1) in the RcA/*B* subunit.

Eight additional sugar-binding sites (*G*1, *G*2, *G*3, and *G*4, see Fig. 2) in the RcA complex with galactose were located from the electron-density synthesis and then were refined. These sites are in the vicinity of the Arg58, Asn95, Asn135, and Asn10 (2.76 Å) amino acid residues, respectively.

The interactions between the RcA/*A* and RcA/*B* subunits are of the nature similar to the nature of the interactions observed in ricin and viscumin, with the hydrophobic and polar interactions being prevalent. In addition, the *A* and *B* subunits are linked by one disulfide bond between Cys256 (*A*) and Cys4 (*B*) (2.18 Å). It should be noted that the sugar molecule is located in the region of the contact between the *A* and *B* subunits (*G*2, see Fig. 2).

ACKNOWLEDGMENTS

This study was supported by the Russian Foundation for Basic Research, project no. 00-04-48321, and by the Federal Ministry of Education, Science, Research and Technology (Germany, Bundesministerium für Bildung, Wissenschaft, Forschung und Technologie, BMBF, grant no. RUS 00/214).

REFERENCES

1. L. M. Roberts, F. I. Lamb, D. J. C. Pappin, *et al.*, J. Biol. Chem. **260** (29), 15682 (1985).
2. A. G. Tonevitsky, O. S. Zhukova, N. V. Mirimanova, *et al.*, FEBS Lett. **299**, 209 (1990).
3. A. G. Tonevitsky, D. E. Temyakov, E. C. Sweeney, *et al.*, Kristallografiya **41** (6), 1018 (1996) [Crystallogr. Rep. **41**, 966 (1996)].
4. E. Yu. Morgunova, A. M. Mikhaĭlov, and B. V. Mchedlishvili, Mol. Genet., Mikrobiol. Virusol. **3**, 29 (1989).
5. Z. Otwinovski and W. Minor, Methods Enzymol. **276**, 307 (1997).
6. J. Navaza, Acta Crystallogr., Sect. A: Found. Crystallogr. **A50**, 157 (1994).
7. T. A. Jones, J. Appl. Crystallogr. **11**, 268 (1978).
8. M. Ready, K. Wilson, M. Piatak, and J. D. Robertus, J. Biol. Chem. **259**, 15252 (1984).
9. A. G. Urzhumtsev, V. Yu. Lunin, and E. A. Vernoslova, J. Appl. Crystallogr. **22**, 500 (1989).
10. R. A. Laskowski, M. W. MacArthur, D. S. Moss, and J. M. Thornton, J. Appl. Crystallogr. **26**, 283 (1993).
11. R. Krauspenhaar, S. Eschenburg, M. Perbandt, *et al.*, Biochem. Biophys. Res. Commun. **257**, 418 (1999).
12. B. Hazes, Protein Sci. **5**, 1490 (1996).

Translated by T. Safonova

Crystallography Reports, Vol. 46, No. 5, 2001, pp. 801–809. Translated from Kristallografiya, Vol. 46, No. 5, 2001, pp. 875–883.

CRYSTAL CHEMISTRY

Crystal Chemistry of Li,Ge^{VI}-Germanates: Combinatorial–Topological Analysis and Modeling of Crystal Structures

G. D. Ilyushin and L. N. Demianets

Shubnikov Institute of Crystallography, Russian Academy of Sciences, Leninskiĭ pr. 59, Moscow, 117333 Russia

e-mail: ilyushin@mail.ru

Received November 5, 1998; in final form, November 9, 2000

Abstract—The combinatorial–topological analysis of the structures of framework Li,Ge-germanates of the compositions $Li_2Ge^{VI}Ge_2^{IV}O_6(OH)_2$ (sp. gr. B_2/b), $Li_2Ge^{VI}Ge_3^{IV}O_9$ (sp. gr. *Pcca*), $Li_4Ge_2^{VI}Ge_7^{VI}O_{20}$ (sp. gr. $C2$), and $Li_2Ge^{VI}Ge_6^{IV}O_{15}$ (sp. gr. *Pbcn*) has been made with the separation of subpolyhedral structural units (SPSUs) built by octahedra and tetrahedra. The topologically invariant SPSUs are separated in three-dimensional frameworks of the structures. A possible mechanism of the matrix assemblage from the SPSU invariants in crystal structures of the framework Li,Ge-germanates is suggested. © *2001 MAIK "Nauka/Interperiodica".*

INTRODUCTION

The class of Li-germanates consisting of 11 compounds is the most informative model system among the families of alkali germanates/silicates for studying the role of Li-atoms in the processes of crystal-structure formation. Earlier [1–5], a similar analysis of the role of sodium and potassium atoms in the formation of complicated silicate/germanate structures was performed for the crystallochemical families of nine Na,*Me*-germanates (*Me* = Ti, Sn, Zr, Hf) and five K,Zr-silicates. For Na- and K-containing phases, various topological invariants—subpolyhedral structural units (SPSUs) consisting of octa- and tetrahedra—were separated. Then, crystal structures formed by these SPSUs by the mechanism of the matrix assemblage were modeled [1, 6, 7].

Crystal structures of five Li-germanates contain $[GeO_4]$-tetrahedra as the simplest structural invariants [8]; the structures of six other compounds (germanogermanates) are characterized by the location of germanium atoms in $[GeO_6]$-octahedra (*M*) and $[GeO_4]$-tetrahedra (*T*). The topological classification of the family over the simplest structural units (SSUs) and the mechanisms of their conjugation with one another and formation of crystal structures is given in our earlier paper [8]. Four compounds are related to the group with the MT-framework formed by the *M*- and *T*-polyhedra in which three-dimensional polyhedron "condensation" occurs only at the vertices; these are $Li_2Ge^{VI}Ge_2^{IV}O_6(OH)_2$ (the MT_2-framework is formed by *M*- and *T*- polyhedra in the ratio 1 : 2, sp. gr. $B2/b$ [9]), $Li_4Ge_2^{VI}Ge_7^{IV}O_{20}$ (the M_2T_7-framework, sp. gr. $C2$ [10]), $Li_2Ge^{VI}Ge_3^{IV}O_9$ (the MT_3-framework, sp. gr. *Pcca* [11]), and $Li_2Ge^{VI}Ge_6^{IV}O_{15}$ (the MT_6-framework, sp. gr. *Pbcn* [12]).

The traditional classification of 20 germanogermanates over the types of tetrahedral Ge-radicals (similar to the case of silicates) with the separation of *T*-chains and *T* layers was made in [13].

Among the structures of Li-germanates, the compounds with the M,T-frameworks—the topological analogues of the Na,*Me*-germanates and K-zirconosilicates considered earlier—are of special interest. Below, we perform the combinatorial–topological analysis of the Li,Ge-germanate structures with the separation of the SPSUs. A possible mechanism of the matrix assemblage of crystal structures is considered on the basis of the separated SPSU-invariants.

METHODOLOGY OF THE CRYSTALLOCHEMICAL ANALYSIS

Consider the general approach to the analysis of the structure and the search for the crystallochemical contacts in the Li,Ge-germanates suggested earlier [1–8]. The analysis is performed at three levels of the structural organization of compounds—atomic, polyhedral, and subpolyhedral.

1063-7745/01/4605-0801$21.00

At the atomic level, the models are characterized by the number and types of the regular systems of points occupied by the atoms in the fundamental domains (stereons [14]) sp. gr. *G*.

At the polyhedral level, polyhedra around the Ge atoms are constructed in stereons and the role of these polyhedra as the simplest subunits forming the structure framework is determined. The Li-atoms in the similar structure models occupy the framework voids [8]. Within the polyhedral models of structures, the information on the bond length and the bond angles is not used any more. The tetrahedra and octahedra sharing the vertices are considered as SSUs. The structures of the Li,Ge-germanates, as well as the alkali Zr-silicates (germanates), are related to the topological family of the framework MT-structures, which are, in fact, the periodic three-dimensional lattices with the six- and fourfold bonds [15].

At the subpolyhedral level, the topological invariants consisting of topologically equivalent SSUs are sought in the local parts of the structures in the first, second, and higher coordination spheres surrounding the polyhedron selected as the central. The concept of the connectedness index in the fragments of a higher level is introduced. The classification of the SPSUs over the indices of their connectedness in the SPSUs of a higher level is introduced.

The framework Li.Ge-germanates are obtained under close physical–chemical conditions so that these compounds can regularly replace one another in the crystallization system [8]. One can assume that, similar to the case of alkali Zr-silicates (germanates), the three-dimensional lattices of structures of the Li,Ge-germanates contain the topologically equivalent regions in the second and third coordination spheres and provide the information on the initial stages of the formation of the first structure-forming MT-fragments, e.g., in the form of topologically different short chains or rings with a small number of links. The crystallochemical analysis of the framework sodium and potassium zirconosilicates and zirconogermanates [1] showed that these stable MT-fragments (usually of the same topological type) control all the processes of the further development of the crystal-forming MT complex, thus making the formation of a SPSU of a higher level possible. Sometimes, the MT-frameworks are built by two topologically different MT-fragments such as, e.g., four-link *trans*- and *cis*-type chains (as in the $KTiO_4$ crystals). The complicated structure of the MT-framework is determined by the number of crystallographically independent M-octahedra (the structure of the M-sublattice). The presence of one such octahedron in the M-sublattice indicates the appearance of the crystal-forming MT-complexes of one type [1]. The same structural feature of the M-sublattice of Li,Ge-germanates and, therefore, the symmetry control (all the octahedra are related by certain symmetry elements) in growth of the SPSU at all the stages of the MT-complex transformations were described earlier [8].

COMBINATORIAL–TOPOLOGICAL ANALYSIS

Polyhedral composition and symmetry characterization of stereons. Within the framework of the atomic–polyhedral model of the Li,Ge-germanate structure, the sets of crystallographically independent framework-forming polyhedra and Li-atoms entering the stereons can be described as follows:

$Li_2Ge^{VI}Ge_2^{IV}O_6(OH)_2$: one M-octahedron, one T-tetrahedron, two Li-atoms (a stereon in the sp. gr. *B*2/*b*);

$Li_2Ge^{VI}Ge_3^{IV}O_9$: one M-octahedron, two T-tetrahedra, two Li-atoms (a stereon in the sp. gr. *Pcca*);

$Li_4Ge^{VI}{}_2Ge^{IV}{}_7O_{20}$: one M-octahedron, four T-tetrahedra, three Li-atoms (a stereon in the sp. gr. *C*2);

$Li_2Ge^{VI}Ge_6^{IV}O_{15}$: one M-tetrahedron, three T-tetrahedra, two Li-atoms (a stereon in the sp. gr. *Pbcn*).

Table indicates the sets of regular point systems (Wyckoff positions) with the point symmetry of these groups including twofold rotation axes and centers of inversion lying on the stereon surfaces. There is no *m* planes in any of the space groups. Germanates can be crystallized in the space groups most often encountered in organic and inorganic structures ($P\bar{1}$, $P2_1/b$, *B*2/*b*, and *Pbcn* [16]) and in relatively unusual space groups (*C*2 and *Pcca*), which confirms the specific structures of these germanates.

Separation of invariant. To separate a topological invariant, we used the methods of the local (crystallostructural) intersection of space groups *G* describing the structures of the phases considered in [1]. The algorithm of the search for invariants reduces to the following.

The unit cell is divided into stereons of volume V_{min} (i.e., into fundamental domains) for each of the group *G*; the total number of stereons, $n = V/V_{min}$, equals the order of the group *G*.

Then, all possible stereon fragments composed of the basic polyhedra related to one another are constructed.

Then, the consistent "extension" of the regular point systems possessing certain point symmetry in the groups *G* is made, with the points being located on the stereon surface. The stereons share the mutually complementing parts of their surfaces, which is determined by the symmetry operations of the given group.

Finally, the topology of each fragment thus obtained (consisting of vertex-sharing polyhedra) in the symmetrized stereon [14] is analyzed, and the topologically equivalent fragments are selected.

Consider the structures of the Li,Ge-germanates described by the centrosymmetric groups *G* (all the groups are of the eighth order) with the following sets of the coded Wyckoff positions for the various space groups.

Regular point systems of the special position in the triclinic, monoclinic, and orthorhombic space groups G, which characterize the stereons in the crystal structures and the types of the crystal-forming periodic structures $S_3^1(g)$, $g \subset G$ of Li,Ge-germanates and Na/K,Zr-germanates (silicates)

Framework germano- and zirconogermanates [1, 9–12]	Sp.gr. G	Multiplicity of the general position	Elements g with the point symmetry				Elements g with the translation symmetry			Some symmetrically allowed types of the structures $S_3^1(g) = SPSU)\hat{g}$ SPSU $\hat{g}$ …, $\hat{g} \subset G$.
			2/*m*	–1	2	*m*	2_1	*c*	*n*	
$Na_2ZrGe_2O_7$	*P*–1	2*i*	–	8	–	–	–	–	*	S(–1) = SPSU(–1) –1 SPSU(–1) –1…
$K_2ZrSi_2O_7$	$P2_1/c$	4*e*	–	4	–	–	+	+	–	S(2_1) = SPSU(–1) 2_1 SPSU(-1) 2_1…
$Li_4Ge_2Ge_7O_{20}$	*C*2	4*c*	–	–	2	–	+	–	–	S(2_1) = SPSU(2) 2_1 SPSU(2) 2_1…
$Li_2GeGe_2O_6(OH)_2$	*C*2/*c*	8*f*	–	4	1	–	+	+	–	S(–1) = SPSU(–1) –1 SPSU(–1) –1…
$Li_2GeGe_3O_9$	$P2_1/c2/c2/a$	8*f*	–	2	3	–	+	+	–	S(–1) = SPSU(–1) –1 SPSU(–1) –1…
$Li_2GeGe_6O_{15}$	$P2_1/b2/c2_1/n$	8*d*	–	2	1	–	+	+	+	S(–1) = SPSU(–1) –1 SPSU(–1) –1…

*B*2/*b*: centers of inversion (the 4*a*, 4*b*, 4*c,* and 4*d* positions) and twofold axes (the 4*e* positions);

Pcca: centers of inversion (the 4*a* and 4*b* positions) and twofold axes (the 4*c*, 4*d*, and 4*e* positions);

Pbcn: centers of inversion (the 4*a* and 4*b* positions) and twofold axes (the 4*c* positions);

The topological variant common to all the structures was obtained by the extending of points of the position 4*b* characterized by the centers of inversion (the only possible solution for these MT-frameworks).

We also singled out the SPSU in the form of a dimer in the unit cells (the number n_M of M-polyhedra equals 2), which is a subpolyhedral MT-fragment containing two symmetry-related octahedra. The prefixes di-, tetra-, etc., indicate the numbers of symmetry-related octahedra in the M,T-fragments (2, 4, etc.) [1]. The invariant thus obtained has the shape of a ringlike centrosymmetric complex [the $D(\bar{1})$ dimer of the composition M_2T_4] consisting of six polyhedra (two M-octahedra and two diorthogroups, Fig. 1). In all the cases, only one of the crystallographically independent Li-atoms (of their total number of two or three) is located within the extended sphere of the crystallographic points 4*b*. This Li-atom can be located with respect to the complex center as follows.

In the $Li_2Ge^{VI}Ge_2^{IV}O_6(OH)_2$ structure—above and under the center of the M_2T_4 ring (the Li1-atoms [9], the extension of the centrosymmetric position 1/2, 0, 0 in the *B*-cell);

in the $Li_2Ge^{VI}Ge_3^{IV}O_9$ structure—in the center of the ring (the Li1 position [11], the extension of the position 0, 1/2, 0 in the *P*-cell);

in the $Li_2Ge^{VI}Ge_6^{IV}O_{15}$ structure—in the center of the ring (the Li1 position [12], the extension of the position 1/2, 1/2, 1/2 in the *P*-cell).

For the $Li_4Ge_2^{VI}Ge_7^{IV}O_{20}$ germanate crystallizing in the polar symmetry group *C*2 of the fourth order, the extension of the crystallographic points located on twofold axes (the 2*a* positions 1/2, *y*, 0) also results in the separation of the ringlike M_2T_4-fragment consisting of six polyhedra. This fragment is equivalent to the M_2T_4-fragment whose central Li2-atom lies on the twofold axis (Fig. 1) [10].

Thus, there is a topological invariant common to all the framework Li,Ge-germanates—a ringlike M_2T_4-fragment consisting of six polyhedra with geometrically different variants of location of Li-atoms in the vicinity of the ring center. These Li-atoms play an active part in the formation (stabilization) of the ring structure of the dimer, whereas the remaining crystallographically independent Li-atoms (one or two) are located at the complex periphery and occupy the voids caused by the formation of new fragments of the MT-framework.

Unlike the Na,Zr-germanates (silicates) structures, the framework structures of Li,Ge-germanates have no topological analogues among the known alkali-containing silicates and alkali-free phosphates of polyvalent-metals. In the Na,Zr germanates, three of five known MT-structures have the topological analogues among the polyvalent-metal alkali-free phosphates [1]. In this case, the presence of sodium atom is not necessary for the formation of the MT-framework, and their structural role at all the levels of the SPSU formation reduces to filling the framework voids.

The highest symmetry of the separated M_2T_4-fragment is described by the orthorhombic point group D_{2h} = 2/*m* 2/*m* 2/*m*. The total number of free vertices or condensation centers equals 16. In the germanate structures, the complexes preserve the center of inversion (in three phases) and the twofold axis (in one phase). The topology of the M_2T_4-fragment allows the conformations with the appearance of different numbers of new diorthogroups relating two octahedra; the total number

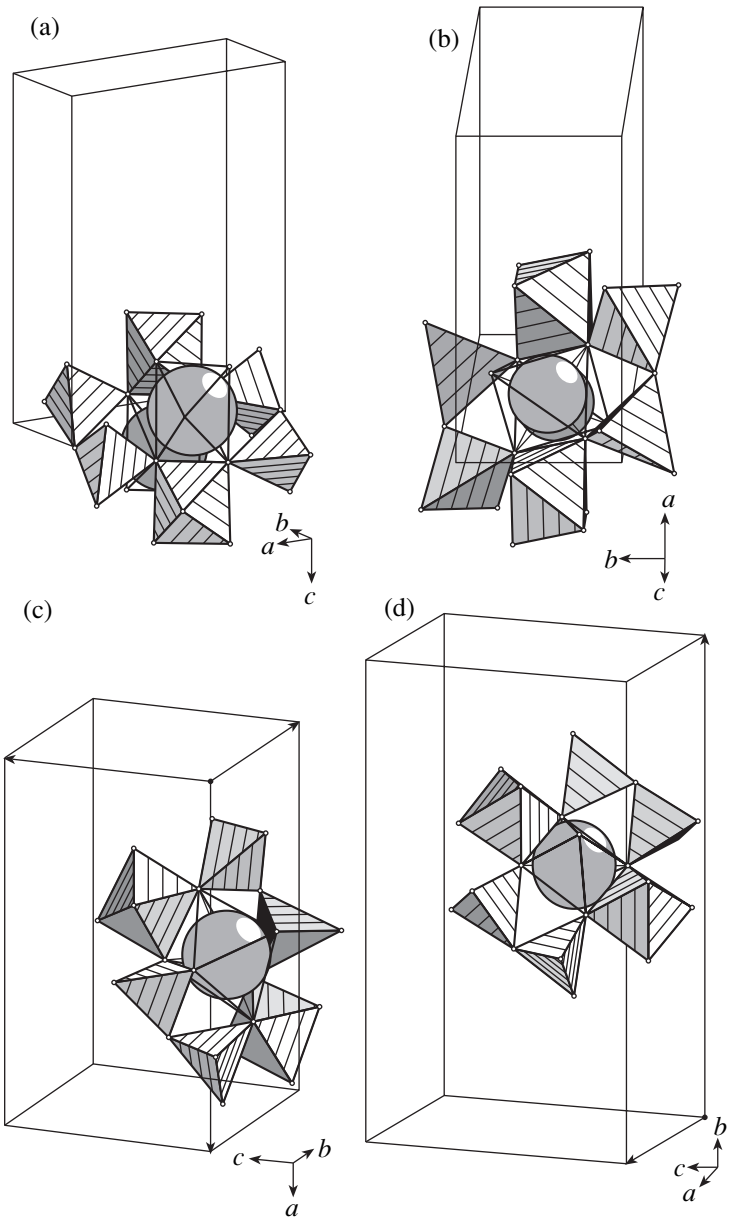

Fig. 1. Structural–topological invariant in the form of ringlike M_2T_4-fragment consisting of six polyhedra (two M GeO_6 octahedra and two Ge_2O_7 diorthogroups) in the Li,Ge-germanate structures (a) $Li_2Ge^{VI}Ge_2^{IV}O_6(OH)_2$, (b) $Li_2Ge^{VI}Ge_3^{IV}O_9$, (c) $Li_4Ge_2^{VI}Ge_7^{IV}O_{20}$, and (d) $Li_2Ge^{VI}Ge_6^{IV}O_{15}$. One can see Li-atoms located in the center of the MT-fragment and their relation to the surrounding oxygen atoms.

of "binding" diorthogroups for two octahedra can increase up to four (as will be shown later, this really takes place in the structures of two germanates).

MODELING OF CRYSTAL STRUCTURES

Model of matrix assembly. Within the framework of the model of structure assembly from SPSU [7, 8], we suggest the following mechanism of the structure formation.

Because of the existence of one invariant common to all the structures, the initial stage of structure formation is the same for all the analyzed Li,Ge-germanates. The crystal-forming SPSU invariants in the form of the ringlike M_2T_4-fragments consist of two octahedra and four tetrahedra.

If the ratio of the numbers of octahedra and tetrahedra in the three-dimensional structure $MT_2 = M_2T_4$ [i.e., (T/M) = 2] and in the composition of the subpolyhedral structural invariant M_2T_4 [i.e., (T/M) = 2] coin-

cide, the crystal structure of the compound is obtained as a result of packing of the invariant SPSUs. Such a ratio is observed in the $Li_2GeGe_2O_6(OH)_2$ germanate.

In the remaining cases, the structure is formed on the basis of the SPSU-invariant with participation of additional tetrahedra (in three germanates).

The mechanisms of complex condensation during their assemblage from the SPSUs of the three-dimensional structures of the framework Li,Ge-germanates can be written in the form

SPSU-type:	dimer D	→	tetramer T	→	octamer O…	→	framework S_3^3
MT-composition:	M_2T_4		$2M_2T_4$		$4M_2T_4$		NM_2T_4

The number n_b of the binding tetrahedra participating in the formation of the framework is $n_b = 0$ in $Li_2Ge^{VI}Ge_2^{IV}O_6(OH)_2$ with the MT_2-framework, $n_b = 1$ in $Li_2Ge^{VI}Ge_3^{IV}O_9$ with the MT_3-framework, $n_b = 1.5$ in $Li_2Ge_2^{VI}Ge_7^{IV}O_{20}$ with the $MT_{3,5}$-framework, and $n_b = 4$ in $Li_2Ge^{VI}Ge_6^{IV}O_{15}$ with the MT_6-framework. The binding tetrahedra (their numbers and position in the unit cell) were identified upon the "subtraction" from the MT-framework structure of the SPSU invariants whose composition includes all the M-octahedra and the related Ge_2O_7 diorthogroups. As a result, the unit cell of the structure is composed only by the shared or isolated tetrahedra.

Selection of SPSU-tetramers according to the connectedness index. The dimer condensation into tetramers is the most probable along the crystallographic direction along which a certain characteristic is the most pronounced, e.g., the highest degree of dimer binding with one another. If the connectedness indices along different crystallographic directions are equal, the processes of dimer condensation in these directions are equiprobable. Thus, the rule of the tetramer selection in the unit cell, which is used for the further dimer transformation into tetramers, can be formulated as follows.

All the pairs of symmetrically related dimers $D\hat{g}D$ are constructed with the operator $\hat{g}$ belonging to the group G;

these tetramers are ordered in accordance with the degree of dimer connectedness to each other;

a tetramer with the maximum connectedness index is selected.

If the dimer connectedness is the same along the crystallographically different directions, tetramers are formed by the bifurcation mechanism (the condensation probabilities in all the directions are the same).

The behavior of a dimer during condensation is determined by the distribution of the condensation centers (16 free polyhedron vertices—eight vertices of M-octahedra and eight vertices of the *T*-tetrahedra) over its surface. With due regard for six possible condensation directions (X, –X), (Y, –Y), (Z, –Z), four variants of the distribution of 16 free vertices are possible. Then, these vertices can participate in condensation with the formation of the following periodic structures: 16 = 12 + 2 + 2 (variant I); 16 = 10 + 4 + 2 (variant II); 16 = 8 + 4 + 4 (variant III), and 16 = 6 + 6 + 4 (variant IV).

Mechanism of tetramer formation. Figures 2–5 show the tetramers separated in germanates and obeying the selection rules. In all these figures, six polyhedra in the M_2T_4 complexes are indicated by bold lines. Depending on the number of the binding tetrahedra, the structural transformation (modification) of dimers into tetramers occurs in several stages.

In $Li_2Ge^{VI}Ge_2^{IV}O_6(OH)_2$ (the MT_2-framework), the direct dimer condensation under the action of the symmetry operators along the unit-cell diagonals in the *XZ* plane is observed (the bifurcation mechanism of tetramer assemblage). The connectedness index of dimers D in a centrosymmetric tetramer T($\bar{1}$) is $c = 2$ (Fig. 2) along all the directions. Of total 16 free vertices, eight (indicated by figures in Fig. 2) participate in the layer formation (four vertices along each direction). Thus, we arrive at variant III (of the type 4 + 4 + 8) of the condensation centers over three crystallographic directions. Of eight remaining vertices, four vertices of T-tetrahedra take part in dimer binding along the third crystallographic directions (along the Y- and –Y-axes). Four vertices of the M-octahedra in the three-dimensional germanate structure are in the form of free OH groups.

In $Li_2Ge^{VI}Ge_3^{IV}O_9$ (the MT_3-framework) the appearance of T_c-tetrahedra modifying the tetramer structure, and the process of the structure formation can be described as follows.

Stage 1. Dimer condensation under the effect of the symmetry operator $g = \bar{1}$ along the Y-axis. The index of the dimer connectedness in the centrosymmetric tetramer is $c = 4$ (Fig. 3).

Stage 2. Modification of the tetramer with the aid of two additional tetrahedra located at the tetramer boundaries. This increases the connectedness index from $c = 4$ to $c = 8$. The additional T_c tetrahedra (tetrahedra 1 and 2 in Fig. 3) bind four free vertices of four M octahedra.

In $Li_2Ge^{VI}{}_2Ge_7^{IV}O_{20}$ (the framework of $MT_{3,5}$), two variants of structural transformation with the

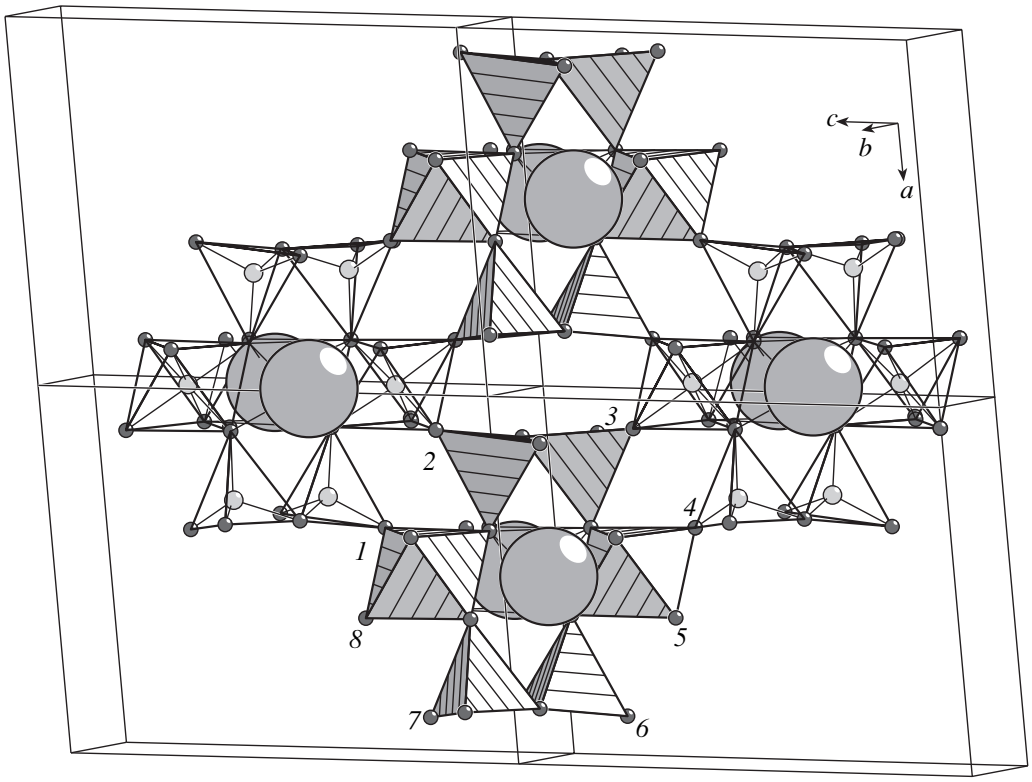

Fig. 2. $Li_2Ge^{VI}Ge_2^{IV}O_6(OH)_2$ germanate. The structure of the octamer. Small circles denote Ge-atoms, large circles, Li-atoms. Figures *1–8* show the vertices of Ge-polyhedra participating in dimer condensation along four directions.

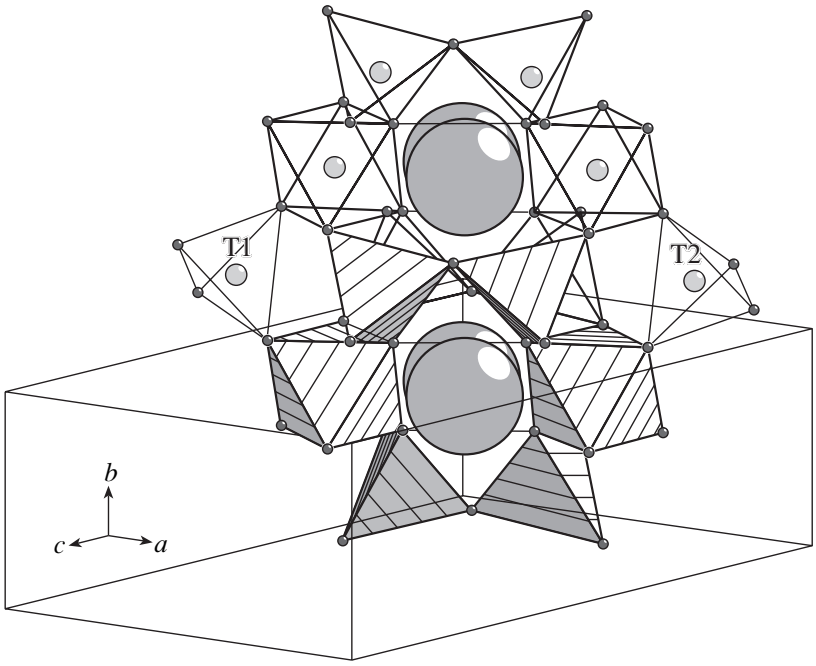

Fig. 3. $LiNaGe_4O_9$ ($Li_2Ge^{VI}Ge_3^{IV}O_9$) germanate. The structure of the modified tetramer. Binding tetrahedra are denoted as T1 and T2.

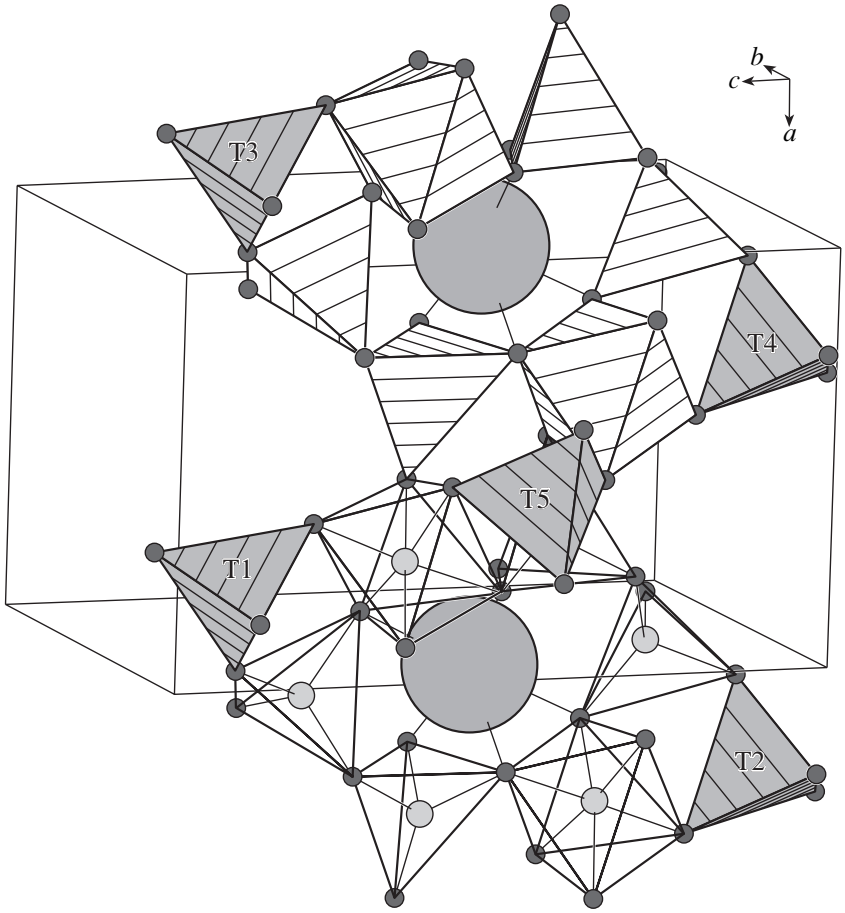

Fig. 4. $Li_4Ge_2^{VI}Ge_7^{IV}O_{20}$ germanate. The structure of the modified tetramer. Binding tetrahedra are denoted as T1–T5.

change of the order of the SPSU modification by the binding tetrahedra are possible.

Variant A

Stage 1. Direct dimer condensation under the action of the symmetry operator $\hat{g} = 2$ along the direction of the Y-axis. The connectedness index of dimers D in T(2) with $c = 2$ (Fig. 4).

Stage 2. An increase of the connectedness index up to $c = 2 + 2$ occurs with the addition of the tetrahedron T_c localized on the twofold axis (tetrahedron 5 in Fig. 4).

Stage 3. The formation at the tetramer boundaries of two new tetrahedra T_c (tetrahedra 1, 2, 3, and 4 in Fig. 4 for each dimer, respectively) without a further increase of the connectedness D in the tetramer structure.

Variant B

Stage 1. Modification of a dimer by two T_c tetrahedra (by the mechanism 3A).

Stage 2. Direct condensation of the modified dimers *D* (by the mechanism 1A).

Stage 3. An increase in the connectedness index of the tetramer (by the mechanism 2A).

In $Li_2Ge^{VI}Ge_6^{IV}O_{15}$ (the MT_6-framework), the structure formation can proceed in the following way.

Stage 1. Conformational modification of the dimer by two additional diorthogroups with the formation of the M_2T_8 complex and preservation of the local symmetry of the dimer $D(\bar{1})$. The centers of inversion relate tetrahedra 1, 2 to tetrahedra 3, 4, and tetrahedra 5, 6 to tetrahedra 7, 8 (Fig. 5). The direct dimer condensation under the action of the symmetry operator $\hat{g} = \bar{1}$ is impossible, because the dimers–invariants share no vertices (the diorthogroups composed by SPSUs shown by bold lines have no common bonds).

Stage 2. Direct condensation of the dimers modified under the action of the operator $\hat{g} = \bar{1}$ along the direction of the *X*-axis; the connectedness index of dimers *D* in the centrosymmetric tetramer $T(\bar{1})$ is $c = 4$.

Stage 3. Localization of two new diorthogroups at the tetramer boundaries (tetrahedra 9, 10 and 11, 12 for each diorthogroup in Fig. 5, respectively), and, as a

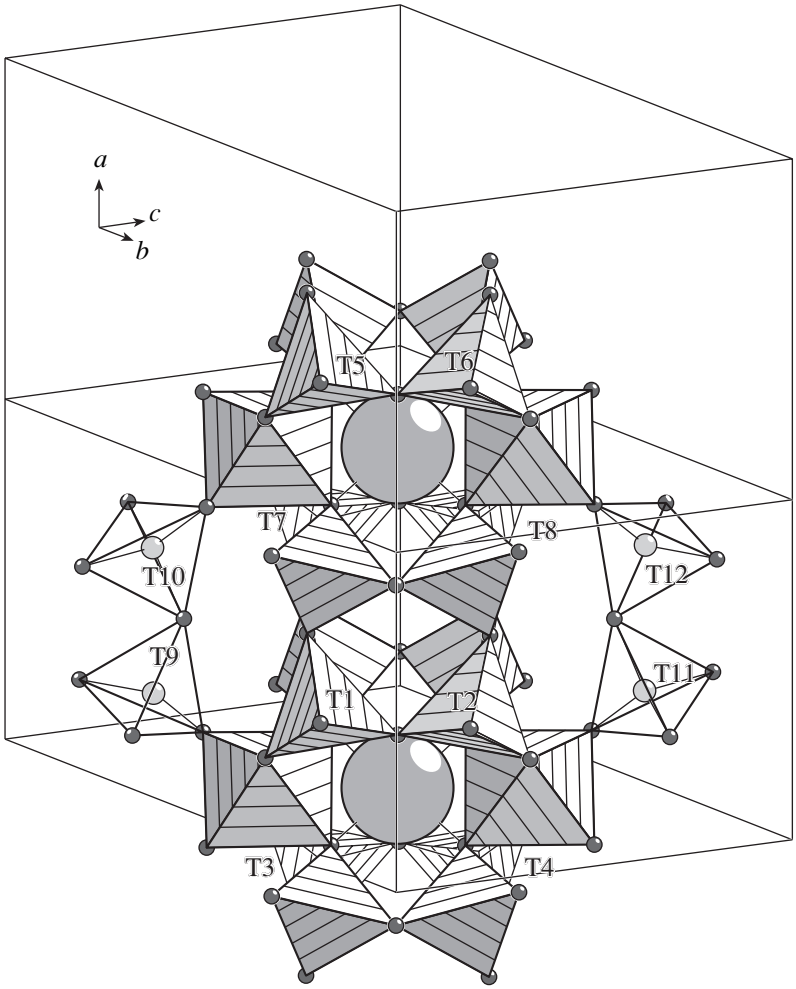

Fig. 5. $Li_2Ge^{VI}Ge_6^{IV}O_{15}$ germanate. The structure of the modified tetramer. Binding tetrahedra are denoted as T1–T12.

result, an increase of the connectedness index of dimers in the tetramer up to $c = 4 + 4$.

CONCLUSIONS

The common topological invariant of the composition M_2T_4 in the form of a ringlike MT-fragment consisting of six polyhedra (two M-octahedra, and two diorthogroups) has been separated in the structures of the framework Li,Ge-germanates.

The mechanism of the assemblage of the crystal structures from invariant SPSU dimers has been suggested. The topological diversity of the frameworks is determined by the differences in the SPSU condensation during tetramer formation. The structural role of all the crystallographically independent polyhedra forming the framework of the germanate structures have been established. In the Li-sublattice, the Li-atoms playing an active part in the formation of the ringlike structure of the dimer and the Li-atoms (one or two) filling the voids of the MT-framework have been revealed.

ACKNOWLEDGMENTS

This study was supported by the Russian Foundation for Basic Research, project no. 98-64883.

REFERENCES

1. G. D. Ilyushin and L. N. Dem'yanets, Itogi Nauki Tekh., Ser. Kristallokhim. **22**, 176 (1989).
2. G. D. Ilyushin and L. N. Dem'yanets, Zh. Strukt. Khim. **29** (4), 178 (1988).
3. G. D. Ilyushin, Kristallografiya **34** (4), 846 (1989) [Sov. Phys. Crystallogr. **34**, 506 (1989)].
4. G. D. Ilyushin and L. N. Demianets, in *Growth of Crystals*, Ed. by E. I. Givargisov and A. M. Melnikova (Consultant Bureau, New York, 1996), Vol. 20, p. 89.
5. G. D. Ilyushin and L. N. Demianets, Kristallografiya **42** (6), 1124 (1997) [Crystallogr. Rep. **42**, 1047 (1997)].

6. G. D. Iljushin and L. N. Demianets, in *Proceedings of the 19th European Crystallographic Meeting, Nancy, 2000*, p. 362.
7. G. D. Ilyushin and L. N. Demianets, in *Proceedings of the IX National Conference on Crystal Growth, Moscow, 2000*, p. 187.
8. G. D. Ilyushin and L. N. Demianets, Kristallografiya **45** (4), 684 (2000) [Crystallogr. Rep. **45**, 626 (2000)].
9. N. N. Nevskiĭ, L. N. Ivanova, V. V. Ilyukhin, and N. V. Belov, Dokl. Akad. Nauk SSSR **242** (6), 1330 (1978) [Sov. Phys. Dokl. **23**, 705 (1978)].
10. H. Völlenkle, A. Wittmann, and H. Nowotny, Monatsch. Chem. **100** (1), 79 (1969).
11. H. Völlenkle, A. Wittmann, and H. Nowotny, Monatsch. Chem. **102** (1–4), 361 (1971).
12. H. Völlenkle, A. Wittmann, and H. Nowotny, Monatsch. Chem. **101** (1), 56 (1970).
13. D. Yu. Pushcharovskiĭ, *Structural Mineralogy of Silicates and Their Synthetic Analogues* (Nedra, Moscow, 1986).
14. B. K. Vainshtein, *Modern Crystallography*, Vol. 1: *Fundamentals of Crystals: Symmetry and Methods of Structural Crystallography*, Ed. by B. K. Vainshtein, A. A. Chernov, and L. A. Shuvalov (Nauka, Moscow, 1979; Springer-Verlag, Berlin, 1994, 2nd ed.).
15. A. Wells, *Structural Inorganic Chemistry* (Clarendon Press, Oxford, 1984; Mir, Moscow, 1988), Vol. 1.
16. B. K. Vainshtein, V. M. Fridkin, and V. L. Indenbom, *Modern Crystallography*, Vol. 2: *Structure of Crystals*, Ed. by B. K. Vainshtein, A. A. Chernov, and L. A. Shuvalov (Nauka, Moscow, 1979; Springer-Verlag, Berlin, 1995, 2nd ed.).

Translated by L. Man

Crystallography Reports, Vol. 46, No. 5, 2001, pp. 810–812. From Kristallografiya, Vol. 46, No. 5, 2001, pp. 884–886.

STRUCTURE OF REAL CRYSTALS

Dislocations in BZS and PMN Pyrochlores[1]

A. Mergen

Eti Holding A. S., Research and Development Department, Istanbul Yolu Üzeri, 9 Km, Güvercinlik, Ankara, Turkey

Received September 11, 2000

Abstract—The dislocations observed in $Bi_{3/2}ZnSb_{3/2}O_7$ (BZS) and $Pb_{1.83}Mg_{0.29}Nb_{1.71}O_{6.39}$ (PMN) pyrochlores are described. An attempt is made to determine the Burgers vectors. *© 2001 MAIK "Nauka/Interperiodica".*

The crystal structure of the pyrochlore mineral $(Ca, Na)_2(Nb, Ta)_2O_6(OH, F)$ was first determined by von Gaertner [1] in 1930 to belong to the space group *Fd*3*m* (No. 227). Since then a large number of other compounds with a similar structure have been discovered, including many compounds with potentially useful properties. The structure of simple pyrochlore is a face-centered cubic lattice with eight molecules per unit cell and a cell edge of approximately 10 Å. Pyrochlore compounds have the general formula $A_2B_2X_6Z$ or $A_2B_2X_7$, where *A* and *B* are cations and *X* and *Z* are anions. By replacing a combination of *A* and *Z* ions, a variety of defect structures can be produced, for example, $A_2B_2X_6$ and AB_2X_6.

This paper describes observations of dislocations in both $Bi_{3/2}ZnSb_{3/2}O_7$ (BZS) and $Pb_{1.83}Mg_{0.29}Nb_{1.71}O_{6.39}$ (PMN) pyrochlores and an attempt to determine the Burgers vectors.

Pure pyrochlore-type BZS and PMN powders were produced using conventional mixed-oxide methods [2, 3]. Uniaxially pressed pellets of the calcined powders were sintered at 1200°C for 4 h (BZS) and at 1260°C for 2 h (PMN). The samples suitable for transmission electron microscopy (TEM) were prepared using standard ceramographic techniques and Ar^+ ion beam thinning. Burgers vectors of dislocations were determined using the invisibility criterion $\mathbf{g}, \mathbf{b} = 0$ [4], where **g** is the operating reflection and **b** is the Burgers vector of the dislocation. At least two invisibility criteria should be satisfied using two nonparallel reflections ($\mathbf{g}_1$ and $\mathbf{g}_2$), for which dislocations must go out of contrast ($\mathbf{g}_1\mathbf{b} = 0$ and $\mathbf{g}_2\mathbf{b} = 0$, so that $\mathbf{b} \propto \mathbf{g}_1 \times \mathbf{g}_2$). However, $\mathbf{gb} = 0$ is the condition sufficient for invisibility only for pure screw dislocations, and the invisibility of a pure edge dislocation also requires that $\mathbf{gb} \times \mathbf{u} = 0$ (**u** is the unit vector parallel to the dislocation line). Thus, the invisibility of an edge dislocation and of a dislocation of a mixed character is not expected for any reflection, even though the condition $\mathbf{gb} = 0$ is satisfied, because $\mathbf{gb} \times \mathbf{u} \neq 0$. In addition, for complete invisibility, the sample should be elastically isotropic, because, in anisotropic crystals, no planes remain flat around edge and screw dislocations [5]. Therefore, the invisibility method for determining Burgers vectors often relies on finding conditions which result in a weak contrast rather than in complete invisibility.

Analysis of the Burgers vectors of dislocations in the BZS pyrochlore shown in Fig. 1 suggests that **b** belongs to the ⟨011⟩ type family. This is not conclusive since two invisibility criterion were not obtained for any of the dislocations marked in Fig. 1a. As can be seen from Fig. 1, all dislocations (marked as *A*, *B*, *C*, and *D*) are in contrast for $\mathbf{g} = 262$ (Fig. 1a) and have a double image for $\mathbf{g} = 040$ (Fig. 1b; i.e., $\mathbf{gb} = 2$). Moreover, the *B* and *D* dislocations are out of contrast, respectively, for $\mathbf{g} = 6\bar{2}2$ and $\mathbf{g} = 044$ (Figs. 1c, 1d). A possible **gb** analysis for the dislocations shown in Fig. 1 is given in Table 1.

[1] This article was submitted by the author in English.

Table 1. Possible values of **gb** for dislocations observed in the BZS pyrochlore under different reflections in Fig. 1

Dislocation	**g**↓	**b** × 1/2					
		[110]	[101]	[011]	[1⁻0]	[10⁻]	[0⁻1]
All visible (Fig. 1a)	262	4	2	4	$\bar{2}$	0	$\bar{2}$
Double image (Fig. 1b)	$2\bar{4}0$	$\bar{2}$	0	$\bar{2}$	2	0	2
B is invisible (Fig. 1c)	$6\bar{2}2$	2	4	0	4	2	2
D is invisible (Fig. 1d)	$04\bar{4}$	2	$\bar{2}$	0	$\bar{2}$	2	$\bar{4}$

1063-7745/01/4605-0810$21.00

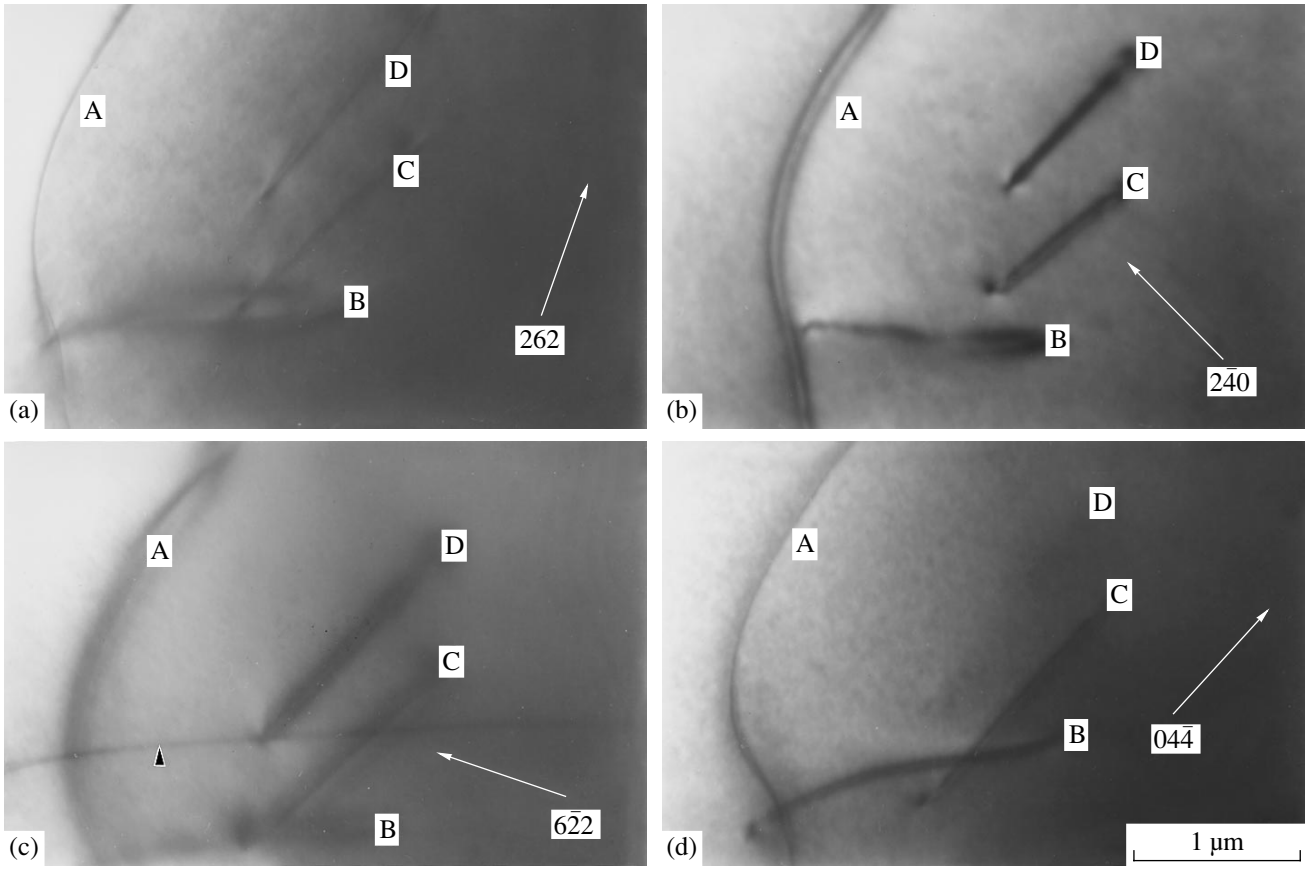

Fig. 1. Analysis of the Burgers vectors of dislocations in the BZS pyrochlore sintered for 4 h at 1200°C: (a) **g** = 262 from the [0⁻3] zone, (b) **g** = 040 from the [001] zone, (c) **g** = 622 from the [011] zone, and (d) **g** = 044 from the [011] zone. In Fig. 1c, the arrowed mark is an artifact which appeared on the negative on developing.

Analysis of the Burgers vectors of dislocations in a network in the PMN pyrochlore was also performed (see Fig. 2). Although no two invisibility criteria were obtained for any dislocations, the analysis suggests that **b** belongs to the ⟨011⟩ type. While the dislocations observed in the BZS pyrochlore were intragranular, those investigated in the PMN pyrochlore formed a low-angle grain boundary. The whole dislocation network was in contrast for **g** = $\bar{6}2\bar{6}$ (Fig. 2a), whereas *A* was out of contrast for **g** = 440 (Fig. 2b), *B* for **g** = 400 (Fig. 2c), and *C* for **g** = $26\bar{2}$ (Fig. 2d). Possible values of **b** for dislocations are given in Table 2. The values of **b** for the dislocations (*A*, *B*, and *C*), which formed a network in the PMN pyrochlore, can be checked using the Frank rule [5]. This rule indicates that the sum of the **b** vectors is zero when the **b** signs are defined looking out from the node (i.e., the sum of the **b** vectors is zero at a node, e.g., $b_A + b_B + b_C = 0$, where subscripts indicate the dislocations shown in Fig. 2). If the Frank rule is applied to these dislocations, then [1⁻0] + [011] + [⁻0⁻] = 0, which indicates that consistent indexing of the Burgers vectors has been made.

Table 2. Values of **gb** for different reflections shown in Fig. 2 for dislocations observed in the PMN pyrochlore

Dislocation	**g**↓	**b** × 1/2					
		[110]	[⁻0⁻]	[011]	[1⁻0]	[10⁻]	[0⁻1]
All visible (Fig. 2a)	$\bar{6}2\bar{6}$	$\bar{2}$	6	$\bar{2}$	$\bar{4}$	0	$\bar{4}$
A is invisible (Fig. 2b)	440	4	$\bar{2}$	2	0	2	$\bar{2}$
B is invisible (Fig. 2c)	400	2	$\bar{2}$	0	2	2	0
C is invisible (Fig. 2d)	$26\bar{2}$	4	0	2	$\bar{2}$	2	$\bar{4}$

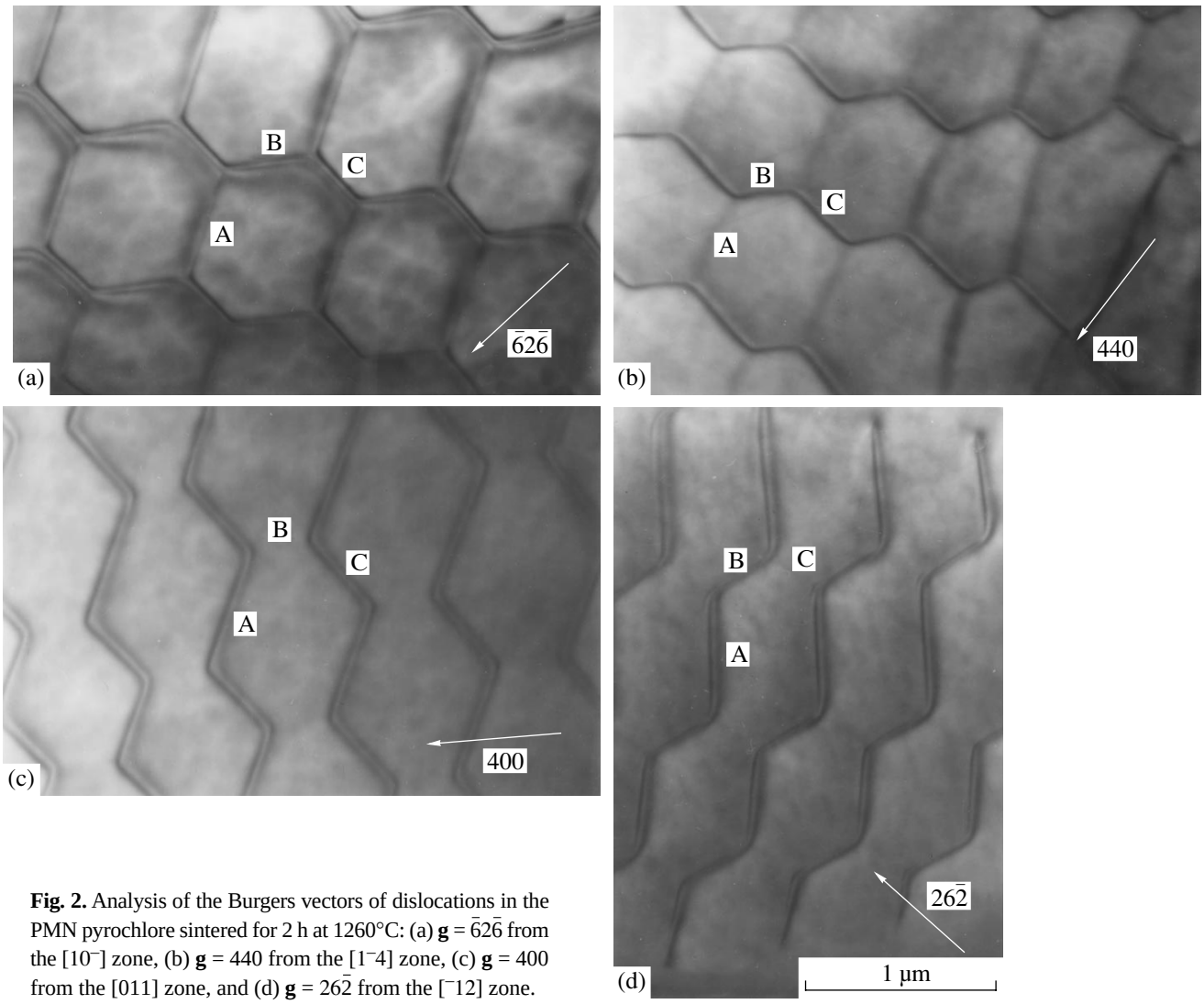

Fig. 2. Analysis of the Burgers vectors of dislocations in the PMN pyrochlore sintered for 2 h at 1260°C: (a) **g** = $\bar{6}2\bar{6}$ from the [10^{-}] zone, (b) **g** = 440 from the [1^{-}4] zone, (c) **g** = 400 from the [011] zone, and (d) **g** = $26\bar{2}$ from the [$^{-}$12] zone.

While not conclusive, it is likely that the Burgers vectors of the dislocations belong to the ⟨011⟩ type. For metals, it is generally expected that crystals slip most easily on close-packed planes in close-packed directions [6]. The most likely Burgers vector for dislocations in face-centered cubic (fcc) structures is of the type 1/2⟨110⟩ [5]. In ceramics, the slip systems are generally as expected [7], although the complexity and ionic nature of the crystal structure can raise additional considerations [6]. For example, MgO and $MgAl_2O_4$ have fcc structures, and the Burgers vectors of their dislocations belong to the 1/2⟨1^{-}0⟩ type [6]. The BZS and PMN pyrochlores, which have fcc Bravais lattices, are most likely to have dislocations with **b** = 1/2⟨110⟩. N. Doukhan and J. Doukhan [8] determined the **b** vectors of dislocations in $BaTiO_3$ and $CaTiO_3$ perovskites, which are tetragonal and orthorhombic, respectively, to be ⟨1^{-}0⟩ (although $BaTiO_3$ is tetragonal at room temperature, it can be considered cubic because the distortion is small).

REFERENCES

1. H. R. von Gaertner, Neues Jahrb. Mineral., Geol. Palaeontol. **61**, 1 (1930).
2. A. Mergen and W. E. Lee, J. Eur. Ceram. Soc. **16** (10), 1041 (1996).
3. A. Mergen and W. E. Lee, J. Eur. Ceram. Soc. **17** (8), 1033 (1997); **17** (8), 1049 (1997).
4. A. C. McLaren, *Transmission Electron Microscopy of Minerals and Rocks* (Cambridge Univ. Press, Cambridge, 1991).
5. D. Hull and D. J. Bacon, *Introduction to Dislocations* (Pergamon, Oxford, 1984).
6. T. E. Mitchell, J. Am. Ceram. Soc. **62**, 254 (1979).
7. W. E. Lee and W. M. Rainforth, *Ceramic Microstructures: Property Control by Processing* (Chapman and Hall, London, 1994).
8. N. Doukhan and J. C. Doukhan, Phys. Chem. Miner. **13**, 403 (1986).

Crystallography Reports, Vol. 46, No. 5, 2001, pp. 813–819. Translated from Kristallografiya, Vol. 46, No. 5, 2001, pp. 887–893.

PHYSICAL PROPERTIES OF CRYSTALS

Dedicated to the memory of B.K. Vainshtein

Properties of Nonlinear Elastic Waves Propagating along Acoustic Axes

A. L. Shuvalov* and A. Radowicz**

** Shubnikov Institute of Crystallography, Russian Academy of Sciences, Leninskiĭ pr. 59, Moscow, 117333 Russia*

*** Kielce University of Technology, ul. Tysiacelecia Panstwa, Polskigo 7, Kielce, 25-314, Poland*

Received March 28, 2000

Abstract—Amplitudes and polarization of nonlinear elastic harmonics exited along an arbitrary acoustic axis of the conic type have been studied as functions of the rotation angle of the polarization vector of the degenerate reference wave. When the reference polarization is rotated by an angle of π, the resulting rotation angle for the polarization vector of the second harmonic turns out to be equal to either zero or 2π or –2π. The actual type of the behavior of the second harmonic propagating along the given acoustic axis is determined by an algebraical criterion for elastic moduli of the second and the third order for the medium. For polarization of the reference wave, we determined the orientations corresponding to the maximum and minimum for the amplitude of the second harmonic. Similar results were obtained for different cases of collinear interactions between degenerate waves, in particular, for the excitation of longitudinal harmonics. The possible control of nonlinear interactions with the use of degenerate-wave polarization in optics and acoustooptics is also discussed. © *2001 MAIK "Nauka/Interperiodica".*

INTRODUCTION AND BASIC RELATIONSHIPS

In crystals, phase velocities of bulk elastic waves coincide along some directions referred to as acoustic axes. The degeneracy of these waves with respect to velocities gives rise to peculiar features of the elastic waves and acoustic phonons [1–10]. In particular, the ambiguity (arbitrariness) in the orientation of the polarization vector of degenerate waves results in the topological singularity of the vector field characterizing the polarization in the vicinity of the acoustic axis. It is clear that such an ambiguity in the polarization of the reference wave affects the properties of the nonlinear harmonics under the conditions of elastic nonlinearity. These harmonics are generated along the acoustic axes of the conic type (i.e., the axes not coinciding with the symmetry axes of the even order, along which no shear harmonics are excited). Thus, the possible rotation of the reference-polarization along the acoustic axis provides an additional parameter that can be used to control the nonlinear interaction. The results of theoretical and experimental studies of the polarization behavior were reported for the second and combined transverse harmonics along the three-fold axis [2]. In this paper, we analyze the polarization and the amplitude effects at different types of the nonlinear interaction for the general case of an arbitrarily (non-symmetrically) oriented acoustic axis of the conic type. The case of symmetry axes is discussed in relation to the excitation of the longitudinal harmonic. We also consider the examples of the polarization-based control of the nonlinear interactions involving the degenerate waves in optics and acoustooptics.

Consider an anisotropic elastic medium of the density ρ characterized by tensors c_{ijkl} and c_{ijklmn} of the second- and the third-order elastic coefficients, respectively. First, write the basic relationships for the propagation direction **m** of the general type, where three nondegenerate bulk plane waves are nondegenerate, i.e., have different velocities v_α and mutually orthogonal polarizations $\mathbf{A}^{(\alpha)}$ ($\alpha = 1, 2, 3$). Let one of these modes with the frequency ω, which relates, for example, to the $\alpha = 1$ branch propagate along **m**; then we have

$$\mathbf{u}^{(l)} = U\mathbf{A}^{(1)}\cos(k_1 x - \omega t), \tag{1}$$

where $k_1 = \omega/v_1$, $x = \mathbf{m} \cdot \mathbf{r}$. The self-interaction of the reference wave described by Eq. (1) causing the formation of the double-frequency wave $\mathbf{u}^{(nl)}$ is described by the equation of nonlinear acoustics. In the leading approximation under condition $x \ll \lambda^2/U$ (λ is the wavelength), this equation can be reduced, to the following linear inhomogeneous equation [2]:

$$\rho u_i^{(nl)} - c_{ijkl} u_{k,jl}^{(nl)} = f_i, \tag{2}$$

where the comma in the subscript indicates the differ-

entiation with respect to the components of **r**. The vector **f** of the nonlinear force in Eq. (2) has the components $f_i = C_{ijklmn} u^{(l)}_{m,n} u^{(l)}_{k,jl}$, where the tensor

$$C_{ijklmn} = c_{ijklmn} + c_{ijln}\delta_{mk} + c_{njkl}\delta_{im} + c_{ljmn}\delta_{ik} \quad (3)$$

contains the contributions due to elastic and geometrical nonlinearities [2]. Substituting Eq. (1) into Eq. (2), we obtain

$$\mathbf{f} = \frac{1}{2}U^2 k_1^3 \mathbf{F}^{(11)} \sin 2(k_1 x - \omega t), \quad (4)$$

where

$$F_i^{(11)} = C_{ikm}^{(\mathbf{m})} A_k^{(1)} A_m^{(1)}, \quad (5a)$$

$$C_{ikm}^{(\mathbf{m})} = C_{ijklmn} m_j m_l m_n. \quad (5b)$$

Note that the due account for the electromechanical coupling in the calculation of amplitude $\mathbf{F}^{(11)}$ of the nonlinear interaction in piezoelectric crystals gives rise to the new terms [2] added to the "purely elastic" tensor $C_{ikm}^{(\mathbf{m})}$ in Eq. (5a). However, these corrections do not influence the general approach to the examination of polarization-related features of the nonlinear wave, which are related to the quadratic dependence of $\mathbf{F}^{(11)}$ on the polarization of the reference mode $\mathbf{A}^{(1)}$. Therefore, for the sake of brevity, we omit here cumbersome expressions of the contribution of electromechanical coupling.

A solution to Eq. (2) is sought in the form of superposition $\mathbf{u} = \mathbf{u}^{(l)} + \mathbf{u}^{(nl)}$. Taking into account the boundary condition corresponding to vanishing nonlinear modes at $x = 0$, we find from Eqs. (2) and (4) [2] that

$$\mathbf{u}^{(nl)} = \frac{1}{4}U^2 k_1^3 \sum_{\alpha=1}^{3} (\mathbf{F}^{(11)} \cdot \mathbf{A}^{(\alpha)})\mathbf{A}^{(\alpha)} \times \frac{\sin[(k_1 - k_\alpha)x]}{\rho v_\alpha^2 (k_1^2 - k_\alpha^2)} \cos[(k_1 + k_\alpha)x - 2\omega t]. \quad (6)$$

According to Eq. (6), the reference wave described by Eq. (1) in the range $x \ll \lambda^2/U$ excites the second harmonic with the vector amplitude linearly increasing with x and parallel to the polarization of the reference wave $\mathbf{A}^{(1)}$. Denote the second harmonics as $\mathbf{u}^{(2\omega)}$. Two other modes with the double frequencies polarized along $\mathbf{A}^{(2)}$ and $\mathbf{A}^{(3)}$ exhibit spatial beatings.

In the same way, the interaction of two reference waves with the frequencies ω_1 and ω_2 results in the generation of the combination waves at the sum and difference frequencies, $\omega_1 \pm \omega_2$. For example, at the collinear interaction of the copropagating reference waves belonging to the branches $\alpha = 1$ and $\alpha = 2$, the combination waves propagating in the same direction have the form [2]

$$\mathbf{u}^{(nl)} = \frac{1}{4}U_1 U_2 k_1 k_2 (k_1 \pm k_2) \times \sum_{\alpha=1}^{3} (\mathbf{F}^{(12)} \cdot \mathbf{A}^{(\alpha)})\mathbf{A}^{(\alpha)} \frac{\sin[(k_1 \pm k_2 - K_\alpha)x]}{\rho v_\alpha^2 [(k_1 \pm k_2)^2 - K_\alpha^2]} \times \cos\left[\frac{1}{2}(k_1 \pm k_2 + K_\alpha)x - (\omega_1 \pm \omega_2)t\right], \quad (7)$$

where $F_i^{(12)} = C_{ikm}^{(\mathbf{m})} A_k^{(1)} A_m^{(2)}$, $k_1 = \omega_1/v_1$, $k_2 = \omega_2/v_2$, $K_\alpha = (\omega_1 \pm \omega_2)/v_\alpha$. Under the lock-in condition $k_1 \pm k_2 = K_\alpha$, the amplitude of the mode polarized parallel to $\mathbf{A}^{(\alpha)}$ linearly grows with x. The lock-in conditions for interacting counter propagating waves have the opposite sign commutation [2].

The above general relationships describe excitation of nonlinear waves in the direction which is not an acoustic axis. In the following sections, these relationships will be considered for some particular cases and analyzed for the nonlinear interaction of the waves degenerate along the acoustic axes.

SECOND HARMONIC ALONG AN ACOUSTIC AXIS

Consider the direction of the acoustic-axis propagation $\mathbf{m}_d$ and introduce the following notation:

$$v_1(\mathbf{m}_d) = v_2(\mathbf{m}_d) \equiv v_d \neq v_3(\mathbf{m}_d) \equiv v_3, \quad \mathbf{A}^{(3)}(\mathbf{m}_d) \equiv \mathbf{A}^{(3)}. \quad (8)$$

Denote the polarization plane of degenerate waves normal to the polarization $\mathbf{A}^{(3)}$ of the non-degenerate mode by **P**. Let the reference wave described by Eq. (1) be a degenerate wave with the wavevector $k_d = \omega/v_d$ and the polarization

$$\mathbf{A}^{(d)} = \begin{pmatrix} \cos\Omega \\ \sin\Omega \end{pmatrix} \quad (9)$$

in the **P** plane. According to Eq. (6), the wave $\mathbf{u}^{(nl)}$ caused by the nonlinear self-interaction at the double frequency involves the beating mode polarized parallel to $\mathbf{A}^{(3)}$ and the second harmonic $\mathbf{u}^{(2\omega)}$ with the linearly increasing amplitude

$$\mathbf{u}^{(2\omega)} = \frac{1}{8}U^2 \frac{k_d^2 x}{\rho v_d^2} \mathbf{a}^{(2\omega)} \cos[2(k_d x - \omega t)], \quad (10)$$

where $\mathbf{a}^{(2\omega)} = \mathbf{F}^{(11)}(\mathbf{1} - \mathbf{A}^{(3)} \otimes \mathrm{A}^{(3)})$ is the non-normalized polarization vector of the second harmonic, which lies the **P** plane ($\otimes$ is the dyadic product). With due

regard for Eq. (5a), the components of this vector in the coordinate system with the x_3 axis directed along $\mathbf{A}^{(3)}$ are written in the form

$$a_i^{(2\omega)} = C_{ikm}^{(\mathbf{m}_d)} A_k^{(1)} A_m^{(1)}, \quad i, k, m = 1, 2, \qquad (11)$$

where $C_{ikm}^{(\mathbf{m}_d)}$ is the convolution described by Eq. (5b) symmetric over all the indices of the tensor C_{ijklmn} with $\mathbf{m}_d$. If there are four- and sixfold symmetry axes, providing degeneracy of the tangent type (touching sheets of the slowness surface), we have $\mathbf{a}^{(2\omega)} = 0$, and, hence, no second harmonic can be generated for shear waves [2]. The further consideration in this section relates to the case of conic type degeneracies. Such degeneracy arises along the acoustic axes of any nonsymmetric orientation and also along threefold symmetry axes. The necessity to take into account weakened second-harmonic generation (because of conic refraction and the effect of the finite width of the reference beam) imposes an additional limitation on the wave path from above [2, 11].

According to Eq. (11), polarization of the second harmonic, $\mathbf{a}^{(2\omega)} \in \mathbf{P}$, depends quadratically on polarization of the degenerate reference mode, $\mathbf{A}^{(d)}$. Possible types of this dependence can be classified in terms of the topology of planar vector fields [12]. Assume that the vector $\mathbf{A}^{(d)}$ is rotated in $\mathbf{P}$ through an angle of π. Obviously, as a result, the vector $\mathbf{a}^{(2\omega)}$ should return to the position parallel to the initial one. Then a question arises: what number of rotations through an angle of π in the plane $\mathbf{P}$ does the vector make? Denote the total rotation of vector $\mathbf{a}^{(2\omega)}$ during rotation of vector $\mathbf{A}^{(d)}$ through an angle of π as $\pi p^{(2\omega)}$. It is easy to see that, formally, the problem of finding $p^{(2\omega)}$ is analogous to the calculation of the Poincaré index of a planar bilinear field described by Eq. (13) in the vicinity of the singular point.[1] Applying the methods considered in [12], we obtain, as in [3, 8, 13], the following result:

$$p^{(2\omega)} = [1 + \operatorname{sgn}(4B_1B_2 - B_3^2)]\operatorname{sgn} B_1, \qquad (12)$$

where

$$\begin{aligned} B_1 &= C_{111}^{(\mathbf{m}_d)} C_{122}^{(\mathbf{m}_d)} - (C_{112}^{(\mathbf{m}_d)})^2, \\ B_2 &= C_{112}^{(\mathbf{m}_d)} C_{222}^{(\mathbf{m}_d)} - (C_{122}^{(\mathbf{m}_d)})^2, \\ B_3 &= C_{111}^{(\mathbf{m}_d)} C_{222}^{(\mathbf{m}_d)} - C_{112}^{(\mathbf{m}_d)} C_{122}^{(\mathbf{m}_d)} \end{aligned} \qquad (13)$$

(as was mentioned in Introduction, the components of tensor $C_{ikm}^{(\mathbf{m})}$ in piezoelectric crystals should be complemented with the additional terms [2] corresponding to the contribution of electromechanical coupling). Thus, $p^{(2\omega)}$ can take the values 0 or ± 2, i. e., the rotation of vector $\mathbf{A}^{(d)}$ through an angle of π makes the polarization vector $\mathbf{a}^{(2\omega)}$ of the second harmonic return to its initial position either without the complete revolution or by the revolution through an angle of 2π or -2π (i.e., either to the same or to the opposite direction with respect to $\mathbf{A}^{(d)}$). Criterion (12) shows which of these scenarios would take place for the given acoustic axis (the additional variants of the behavior of $\mathbf{a}^{(2\omega)}$ arise under the conditions $4B_1B_2 = B_3^2$ and $B_i = 0$, $i = 1, 2, 3$, which, in fact, can be fulfilled only in theory).

It is important that the reversal of the unit polarization vector of the reference wave $\mathbf{A}^{(d)}$ affects not only the orientation of the vector $\mathbf{a}^{(2\omega)}$ but also its magnitude, i.e., the second-harmonics amplitude (a similar dependence of the orientation and the amplitude on the polarization of the degenerate elastic wave is also characteristic of the electromechanical interaction in piezoelectrics [4]). It should also be indicated that if $4B_1B_2 \neq B_3^2$, the magnitude of vector $\mathbf{a}^{(2\omega)}$ does not tend to zero. It can be shown that the extremum (maximum and minimum) values of $|\mathbf{a}^{(2\omega)}| = \sqrt{\mathbf{a}^{(2\omega)} \cdot \mathbf{a}^{(2\omega)}}$ and the corresponding orientations $\mathbf{A}^{(d)}$ in the plane $\mathbf{P}$ are the eigenvalues and the eigenvectors, respectively, of the 2×2 matrix $C_{ijk}^{(\mathbf{m}_d)} A_k^{(d)}$ (the convolution of the sought vector $\mathbf{A}^{(d)}$ in the $\mathbf{P}$ plane), i.e.,

$$[C_{ijk}^{(\mathbf{m}_d)} A_k^{(d)}] A_j^{(d)} = |\mathbf{a}^{(2\omega)}| A_i^{(d)}, \quad i, j, k = 1, 2. \qquad (14)$$

In the particular case of an acoustic axis parallel to the 3-fold symmetry axis of the trigonal crystal, a degenerate wave with polarization given by Eq. (9) generates the second transverse harmonic with the polarization $\mathbf{a}^{(2\omega)}$ given by Eq. (11), with the following components in the X_1X_2 plane:

$$\mathbf{a}^{(2\omega)} = \begin{pmatrix} c_{555}\cos 2\Omega - c_{444}\sin 2\Omega \\ -c_{444}\cos 2\Omega - c_{555}\sin 2\Omega \end{pmatrix}. \qquad (15)$$

Equation (15) clearly demonstrates that $p^{(2\omega)} = -2$. Moreover, in the given symmetrical case, the number of rotations $p^{(2\omega)}$ relates not only to the complete revolutions (multiple to π), but also local rotations. An arbitrary rotation $\Delta\Omega$ of the reference-wave polarization gives rise to the rotation of the second-harmonic polarization by $-2\Delta\Omega$. In addition, the magnitude of the vector $\mathbf{a}^{(2\omega)}$ turns out to be independent of the reference-wave polarization. If the crystal is described by any of the symmetry groups 32, $3m$, or $\bar{3}m$, then $c_{555} = 0$ and Equation (15) takes the form derived in [14].

Of course, the above formulation of the problem, where any given rotation of the polarization vector of the reference wave $\mathbf{A}^{(1)}$ is always the same at each point of the wave path (e.g., it can simply be the source rota-

[1] According to the definition, the Poincaré index for a singular point for the planar vector field (not necessarily even) indicates the number of rotations through an angle of 2π corresponding to the rotation of the radius vector by the angle 2π about the singular point.

tion), differs from the situation characteristic of the propagation of the reference wave with the circular polarization along the acoustic axis $\mathbf{m}_d$. In this case, the second harmonic described by Eq. (10) has, should be circularly polarized. Its polarization vector (in the complex representation), $\mathbf{a}^{(2\omega)} = \mathbf{a}' + i\mathbf{a}''$ lies in the **P** plane and has the following components in this plane

$$a_i' = C_{i11}^{(\mathbf{m}_d)} - C_{i22}^{(\mathbf{m}_d)}, \quad a_i'' = 2C_{i12}^{(\mathbf{m}_d)}, \quad i = 1, 2. \quad (16)$$

Note that if the polarization vector of the reference wave in the **P** plane runs around the circumference with the angular velocity ω, then the second-harmonic polarization vector runs around the ellipse with the angular velocity $2\omega|\mathbf{a}' \times \mathbf{a}''|/(\mathbf{a}'^2 + \mathbf{a}''^2)$. In the particular case of the circularly polarized reference wave propagating along the threefold symmetry axis, we have $\mathbf{a}' = 2(c_{555}, -c_{444})^T$ and $\mathbf{a}'' = 2(c_{444}, c_{555})^T$, i.e., the second harmonic is also circularly polarized, but its polarization vector runs with angular velocity 2ω around the circumference in the opposite direction.

Consider the distribution of polarization vectors of the second harmonics excited by the reference wave for one of the branches $\alpha = 1, 2$ (say, $\alpha = 1$) as function of the propagation direction ***m*** in the close vicinity of the conical axis $\mathbf{m}_d$. If ***m*** deviates from $\mathbf{m}_d$ by a small angle $\theta \ll 1$, the second harmonic continues growing linearly until the wave path x is much less than the coherence length $l = \frac{\lambda}{4}(v_d/\Delta v)$, where $\Delta v \equiv |v_1(\mathbf{m}) - v_2(\mathbf{m})| \sim \theta$. The rotation of the vector $\delta\mathbf{m}$ about $\mathbf{m}_d$ through an angle of 2π is accompanied by the rotation of the polarization vector of the reference wave $\mathbf{A}^{(1)}(\mathbf{m})$, (which, in the leading approximation, lies in the **P** plane) by the angle of $2\pi n_d^{(\omega)} = \pm\pi$ in the local polarization field $\mathbf{A}^{(1)}(\mathbf{m})$ ($n_d^{(\omega)} = \pm 1/2$ is the Poincaré index for the point of conic degeneracy $\mathbf{m}_d$). Correspondingly, the vector $\mathbf{A}^{(2\omega)}(\mathbf{m})$ rotates through an angle of $2\pi p^{(2\omega)} n_d^{(\omega)}$ in the p plane, i.e., the Poincaré index of the point $\mathbf{m}_d$ in field $\mathbf{A}^{(2\omega)}(\mathbf{m})$ equals $p^{(2\omega)} n_d^{(\omega)}$.

COLLINEAR INTERACTION OF DEGENERATE WAVES ALONG AN ACOUSTIC AXIS

Consider the propagation of two degenerate wave with different frequencies ω_1 and ω_2 and polarizations $\mathbf{A}^{(1)}, \mathbf{A}^{(2)} \in \mathbf{P}$ along the acoustic axis $\mathbf{m}_d$ set by Eq. (8),

$$\mathbf{u}^{(l)} = U_1\mathbf{A}^{(d1)}\cos\left[\omega_1\left(\frac{x}{v_d} - t\right)\right] + U_2\mathbf{A}^{(d2)}\cos\left[\omega_2\left(\frac{x}{v_d} - t\right)\right]. \quad (17)$$

According to Eq. (7), the nonlinear wave with the sum and the difference frequencies includes the beating mode polarized along $\mathbf{A}^{(3)}$ and the combination harmonic $\mathbf{u}^{(\omega_1 \pm \omega_2)}$ with a linearly increasing amplitude,

$$\mathbf{u}^{(\omega_1 \pm \omega_2)} = \frac{1}{8}U_1U_2\frac{\omega_1\omega_2 x}{\rho v_d^4}\mathbf{a}^{(\omega_1 \pm \omega_2)}\cos\left[(\omega_1 \pm \omega_2)\left(\frac{x}{v_d} - t\right)\right], \quad (18)$$

where $\mathbf{a}^{(\omega_1 \pm \omega_2)}$ is the non-normalized polarization vector lying in the plane **P** and having the following in-plane components

$$a^{(\omega_1 \pm \omega_2)} = C_{ikm}^{(\mathbf{m}_d)} A_k^{(d1)} A_m^{(d2)}, \quad i, k, m = 1, 2. \quad (19)$$

The combination harmonics cannot arise during propagation of degenerate waves along the four- and sixfold symmetry axes. In these cases, $\mathbf{a}^{(\omega_1 \pm \omega_2)} = 0$ at any $\mathbf{A}^{(1)}$, $\mathbf{A}^{(2)} \in \mathbf{P}$. Similar to the previous section, we consider here the conic-type degeneracy (acoustic axes with non-symmetric orientations or those parallel to the threefold axis).

Above, we considered the case of one degenerate wave. The use of two independent degenerate reference modes provides additional opportunities to control the amplitude and polarization properties of the nonlinear harmonic. First, assume that the polarization of one of the reference waves (e.g., $\mathbf{A}^{(d1)}$) remains unchanged, whereas the polarization of the other wave ($\mathbf{A}^{(d2)}$) is rotated through an angle of π in **P**. Following [13], we can see that the vector $\mathbf{a}^{(\omega_1 \pm \omega_2)}$ given by Eq. (19) is rotated through an angle of $\pi p^{(\omega_1 \pm \omega_2)} = \pm\pi$, whose sign is determined by the following criterion

$$p^{(\omega_1 + \omega_2)} = \mathrm{sgn}\det(C_{ikm}^{(\mathbf{m}_d)} A_k^{(d1)}), \quad i, k, m = 1, 2. \quad (20)$$

In the general case of a non-symmetric acoustic axis, there exists a pair of preferential orientations $\mathbf{A}^{(d1)}$ for which $\det(C_{ikm}^{(\mathbf{m}_d)} A_k^{(d1)}) = 0$. Choosing any of them as the fixed polarization of one of the reference waves in Eq. (18), we see that the polarization direction of the combined harmonic $\mathbf{a}^{(\omega_1 \pm \omega_2)}$ remains unchanged during the rotation of the polarization $\mathbf{A}^{(d2)}$ of another reference wave. At the same time, the value of $\left|\mathbf{a}^{(\omega_1 \pm \omega_2)}\right|^2$ depends, in general, on the variations in the orientation of the vector $\mathbf{A}^{(d1)}$ irrespectively of the chosen fixed vector $\mathbf{A}^{(d2)}$. The extremum values of $\left|\mathbf{a}^{(\omega_1 \pm \omega_2)}\right|^2$, equal to the eigenvalues of the squared $C_{ikm}^{(\mathbf{m}_d)} A_k^{(d1)}$ of the 2×2 matrix, correspond to the situation where the vector $\mathbf{A}^{(d2)}$ turns out to be the eigenvector of the given matrix.

Now, assume that the polarization vectors of both reference waves are rotated through an angle of π in the

P plane in a correlated way, so that the angle $\Omega_{12} = \Omega_1 - \Omega_2$ between these rectors remains constant, i.e.,

$$\mathbf{A}^{(d2)} = \mathbf{T}\mathbf{A}^{(d1)}, \quad (21)$$

where **T** is the rotation matrix (through an angle of Ω_{12} in the **P** plane),

$$T_{ij} = \begin{pmatrix} \cos\Omega_{12} & \sin\Omega_{12} \\ -\sin\Omega_{12} & \cos\Omega_{12} \end{pmatrix}. \quad (22)$$

Substituting the result into Eq. (19), we find that the polarization vector of combined harmonic,

$$a_i^{(\omega_1 \pm \omega_2)} = C_{ikn}^{(\mathbf{m}_d)} T_{nm} A_k^{(1)} A_m^{(1)}, \quad i, k, m, n = 1, 2, \quad (23)$$

which differs from the second-harmonic polarization described by Eq. (11), only by the following change

$$C_{ikm}^{(\mathbf{m}_d)} \longrightarrow C_{ikn}^{(\mathbf{m}_d)} T_{nm} \quad (24)$$

(it should be noted that the right-hand side loses its full symmetry with respect to all the subscripts). Using this formal analogy, we find that the correlated rotation of the polarization vectors for both reference waves through the angle π results in the rotation of the vector $\mathbf{a}^{(\omega_1 \pm \omega_2)}$ in the same plane, **P**, through an angle of $2\pi p^{(\omega_1 \pm \omega_2)} = 0, \pm 2\pi$ in full accordance with the criterion

$$p^{(\omega_1 \pm \omega_2)} = [1 + \mathrm{sgn}(4\tilde{B}_1 B_2 - \tilde{B}_3^2)]\,\mathrm{sgn}\,\tilde{B}_1. \quad (25)$$

Criterion (25) differs from Eq. (12) by the use of, instead of B_1 and B_3, the following quantities in Eq. (13):

$$\tilde{B}_1 = B_1\cos^2\Omega_{12} + B_2\sin^2\Omega_{12} - \frac{1}{2}B_3\sin\Omega_{12},$$
$$\tilde{B}_3 = \frac{1}{2}(B_1 - B_2)\sin 2\Omega_{12} + B_3\cos^2\Omega_{12}. \quad (26)$$

The principal difference between this case and the case of the second harmonic generated by a single reference wave is the fact that the characteristic behavior of the combined harmonic can be controlled by the choice of the misorientation angle Ω_{12} between them, depending on the correlated rotation of the polarization of reference waves $\mathbf{A}^{(d1)}$ and $\mathbf{A}^{(d2)}$. According to Eqs. (25) and (26), if, e.g., $\Omega_{12} = \pi/2$, then $p^{(\omega_1 \pm \omega_2)}$ cannot go to zero. If $B_1 \geq 0$ and the angle Ω_{12} can be chosen in such a way that $4\tilde{B}_1 B_2 = \tilde{B}_3^2$, then there should exist such an orientation of the vectors $\mathbf{A}^{(d1)}$ and $\mathbf{A}^{(d2)}$, that $\mathbf{a}^{(\omega_1 \pm \omega_2)} = 0$.

At the same time, the polarization characteristics of the combined harmonic arising from two degenerate waves propagating along the threefold axis, are simplified, as in the case of the second harmonic. The magnitude of the polarization vector $\mathbf{a}^{(\omega_1 \pm \omega_2)}$ in the X_1X_2 plane of the trigonal crystal,

$$\mathbf{a}^{(\omega_1 \pm \omega_2)} = \begin{pmatrix} c_{555}\cos(\Omega_1 + \Omega_2) - c_{444}\sin(\Omega_1 + \Omega_2) \\ -c_{444}\cos(\Omega_1 + \Omega_2) - c_{555}\sin 2(\Omega_1 + \Omega_2) \end{pmatrix} \quad (27)$$

is independent of the rotation of the polarization of the reference waves and is rotated through an angle of $-\Delta\Omega$ or $-2\Delta\Omega$ at the local rotation of the polarization in one or both reference waves by $\Delta\Omega$. In the case of the space groups 32, $3m$, $\bar{3}m$ when $c_{555} = 0$, Equation (27) takes the form reported in [11].

NONLINEAR QUASI-LONGITUDINAL WAVE PROPAGATING ALONG THE ACOUSTIC AXIS

Consider the possibility of controlling the amplitude of a nonlinear wave with the polarization parallel to the polarization $\mathbf{A}^{(3)}$ of the nondegenerate (usually quasi-longitudinal) linear wave. As an example, consider the beating mode excited by the degenerate reference wave. According to Eq. (6), the amplitude of these beatings is proportional to

$$\mathbf{F}^{(11)} \cdot \mathbf{A}^{(3)} = C_{ikm}^{(\mathbf{m}_d)} A_i^{(3)} A_k^{(d1)} A_m^{(d1)}. \quad (28)$$

For degeneracy along the symmetry axes higher than twofold ones we have $\mathbf{F}^{(11)} \cdot \mathbf{A}^{(3)} = c_{33} + c_{344} = \mathrm{const}$. However, for nonsymmetric acoustic axes, the beating amplitude turns out to be additionally modulated with the orientation of the reference-wave polarization $\mathbf{A}^{(d1)}$. There are two such orientations, for which $\mathbf{F}^{(11)} \cdot \mathbf{A}^{(3)} = 0$, and, hence, the beating mode completely disappears.

The nonlinear wave polarized along $\mathbf{A}^{(3)}$ and having the linearly increasing amplitude arises at the sum frequency $\omega_1 + \omega_2$ because of the interaction of two counterpropagating degenerate waves with frequencies meeting the lock-in condition $\omega_1/\omega_2 = (v_3 - v_d)/(v_3 + v_d)$ [2]. The amplitude of this combined harmonic is proportional to the parameter

$$\mathbf{F}^{(12)} \cdot \mathbf{A}^{(3)} = C_{ikm}^{(\mathbf{m}_d)} A_i^{(3)} A_k^{(d1)} A_m^{(d2)}, \quad (29)$$

dependent on the misorientation angle $\Omega_{12} = \Omega_1 - \Omega_2$ between the $\mathbf{A}^{(d1)}$ and $\mathbf{A}^{(d2)}$ polarizations of the reference waves. For example, at the interaction of the waves counterpropagating along the axes with the symmetry higher than twofold, we obtain

$$\mathbf{F}^{(12)} \cdot \mathbf{A}^{(3)} = (c_{33} + c_{344})\cos\Omega_{12}. \quad (30)$$

Therefore, if $\mathbf{A}^{(d1)}$ and $\mathbf{A}^{(d2)}$ are orthogonal, then the harmonic is excited, whereas if $\mathbf{A}^{(d1)}$ and $\mathbf{A}^{(d2)}$ are parallel, the generation is the most efficient.

Finally, the combined harmonic with the linearly increasing amplitude polarized along $\mathbf{A}^{(3)}$ arises at the sum frequency $\omega_1 + \omega_2$ because of the interaction of degenerate and nondegenerate waves copropagating along the nonsymmetric acoustic axis and meeting the lock-in condition $\omega_1/\omega_2 = (v_3 - v_d)/2v_d$ [2]. The amplitude of this harmonic is proportional to

$$\mathbf{F}^{(13)} \cdot \mathbf{A}^{(3)} = C_{ikm}^{(\mathbf{m}_d)} A_i^{(d1)} A_k^{(3)} A_m^{(3)}, \qquad (31)$$

and, thus, linearly depends on controlled polarization given by Eq. (9) for a degenerate reference wave.

POLARIZATION-CONTROLLED EFFECTS IN ACOUSTOOPTICS AND NONLINEAR OPTICS

The rotation of the degenerate-wave polarization can be used to control the acousto-optic interactions. Consider, e.g., the diffraction of electromagnetic waves from one of symmetry planes m in the uniaxial crystal, which pass through the direction X_3 of the principal symmetry axis. Let the mode $\mathbf{E}^{(1)}$ of the electromagnetic field be diffracted into the mode $\mathbf{E}^{(2)}$ because of the non-collinear interaction with the degenerate acoustic wave propagating along X_3. The acousto-optic coupling constant is equal to $\mathbf{E}^{(1)}\Delta\boldsymbol{\eta}\mathbf{E}^{(2)}$, where $\Delta\eta_{ij}$ is the variation in the dielectric impermeability tensor related to the photoelastic effect [15] and dependent on the acoustic-wave polarization. One can readily see that the coupling constant in our case is proportional to the component of polarization vector $\mathbf{A}^{(d)}$ of the degenerate acoustic wave, which is orthogonal to m. Rotating the vector $\mathbf{A}^{(d)}$ in the $\mathbf{P}$ plane orthogonal to m, one can control the diffracted-wave amplitude varying it from a certain maximum value at $\mathbf{A}^{(d)}$ oriented normally to the m plane down to zero at $\mathbf{A}^{(d)} \in m$. A similar effect in the m plane also arises in the case of the collinear acousto-optic interaction along the acoustic axis with a nonsymmetric orientation.

The idea to control the polarization properties of nonlinear harmonics is also applicable to electromagnetic waves propagating along the direction X_3 of the optical axis in some uniaxial crystals (in biaxial crystals, the direction of degeneracy with due regard for the frequency dispersion is frequency-dependent. Let $\mathbf{E}^{(d)}$ be an arbitrary unit vector in the plane $\mathbf{P}$ orthogonal to X_3, which indicates the field direction for the degenerate wave. As is well known [16], the optical nonlinearity results in the generation of the second harmonic with the linearly increasing amplitude and the field direction in the $\mathbf{P}$ plane parallel to the vector with components

$$e_i^{(2\omega)} = \chi_{ijk} E_j^{(d)} E_k^{(d)}, \quad i, j, k = 1, 2, \qquad (32)$$

where χ_{ijk} are the coefficients characterizing the nonlinear permittivity. (Under the condition $\chi_{3jk} \neq 0$, the double-frequency mode with constant amplitude and the polarization along X_3 is excited.) The vector described by Eq. (32) has the form the most general for the crystals of groups 3 and $\bar{6}$,

$$\mathbf{e}^{(2\omega)} = \begin{pmatrix} \chi_{111}\cos 2\Omega + -\chi_{222}\sin 2\Omega \\ -\chi_{222}\cos 2\Omega - \chi_{111}\sin 2\Omega \end{pmatrix}, \qquad (33)$$

where the angle Ω determines the orientation of the reference wave polarization $\mathbf{E}^{(d)}$. It is seen that its local rotation in the plane $\mathbf{P}$ through an angle of $\Delta\Omega$ causes the rotation of the second-harmonic field by the angle $-2\Delta\Omega$, whereas the second-harmonic amplitude is independent of Ω. For the groups 32, $3m$, $\bar{6}m2$, one of components (χ_{111} or χ_{222}), goes to zero, whereas for all the other symmetry groups of uniaxial crystals, $\mathbf{e}^{(2\omega)} = 0$ is an identical, zero, in other words, no second harmonic is generated.

ACKNOWLEDGMENTS

The study was supported by the Russian Foundation for Basic Research, project no. 97-02-16338.

REFERENCES

1. V. I. Alshits and J. Lothe, Kristallografiya **24** (4), 672 (1979) [Sov. Phys. Crystallogr. **24**, 387 (1979)]; Kristallografiya **24** (4), 683 (1979) [Sov. Phys. Crystallogr. **24**, 393 (1979)]; Kristallografiya **24** (6), 1122 (1979) [Sov. Phys. Crystallogr. **24**, 644 (1979)].
2. V. E. Lyamov, *Polarization Effects and Anisotropy in the Interaction of Acoustic Waves in Crystals* (Mosk. Gos. Univ., Moscow, 1983).
3. V. I. Alshits, A. V. Sarychev, and A. L. Shuvalov, Zh. Éksp. Teor. Fiz. **89**, 922 (1985) [Sov. Phys. JETP **62**, 531 (1985)].
4. V. I. Alshits, V. N. Lyubimov, A. V. Sarychev, and A. L. Shuvalov, Zh. Éksp. Teor. Fiz. **93**, 723 (1987) [Sov. Phys. JETP **66**, 408 (1987)].
5. V. I. Alshits, A. N. Darinskiĭ, and A. L. Shuvalov, Zh. Éksp. Teor. Fiz. **96**, 1958 (1989) [Sov. Phys. JETP **69**, 1105 (1989)].
6. A. L. Shuvalov and A. G. Every, Phys. Rev. B **53**, 14906 (1996).

7. A. L. Shuvalov and A. G. Every, J. Acoust. Soc. Am. **101**, 2381 (1997).
8. A. L. Shuvalov, Proc. R. Soc. London, Ser. A **454**, 2911 (1998).
9. A. L. Shuvalov, J. Acoust. Soc. Am. **104**, 2008 (1998).
10. A. L. Shuvalov and N. H. Scott, Acta Mech. **140**, 1 (1999).
11. K. K. Ermilin, V. A. Krasil'nikov, V. E. Lyamov, and V. M. Prokhorov, Fiz. Tverd. Tela (Leningrad) **18**, 3133 (1976) [Sov. Phys. Solid State **18**, 1828 (1976)].
12. M. A. Krasnosel'skiĭ, A. I. Perov, A. I. Povolotskiĭ, and P. P. Zabreĭko, *Vector Fields in a Plane* (Fizmatgiz, Moscow, 1963).
13. A. L. Shuvalov, Math. Mech. Solids **5**, 499 (1999).
14. K. K. Ermilin, V. A. Krasil'nikov, V. E. Lyamov, and V. M. Prokhorov, Fiz. Tverd. Tela (Leningrad) **15**, 2251 (1973).
15. E. Dieulesaint and D. Royer, *Elastic Waves in Solids* (Wiley, New York, 1981; Nauka, Moscow, 1982).
16. A. Yariv and P. Yeh, *Optical Waves in Crystals: Propagation and Control of Laser Radiation* (Wiley, New York, 1984; Mir, Moscow, 1987).

Translated by K. Kugel

Crystallography Reports, Vol. 46, No. 5, 2001, pp. 820–825. Translated from Kristallografiya, Vol. 46, No. 5, 2001, pp. 894–899.

PHYSICAL PROPERTIES OF CRYSTALS

Dedicated to the memory of B.K. Vainshtein

Mechanical Properties of Organic Alkali Metal and Ammonium Hydrophthalate Single Crystals

V. R. Regel, N. L. Sizova, G. S. Belikova, and T. N. Turskaya

Shubnikov Institute of Crystallography, Russian Academy of Sciences, Leninskiĭ pr. 59, Moscow, 117333 Russia

e-mail: aopt@ns.crys.ras.ru

Received April 10, 2001

Abstract—The mechanical parameters characterizing the deformation and fracture of acid salts of orthophtalic acid (alkali metals and ammonium hydrophthalates) have been determined. It is shown that the mechanical properties of these crystals are considerably anisotropic and can be either deformed plastically, form kink bands, or undergo brittle fracture depending on the direction of the compression axis with respect to the cleavage plane. © *2001 MAIK "Nauka/Interperiodica".*

INTRODUCTION

Single crystals of acid salts of orthophtalic acid, $C_8H_5O_4X$ hydrophthalates (X = K, Rb, Cs, NH_4), belong to the orthorhombic system, the point symmetry group *mm*2 for potassium and rubidium hydrophthalates and *mmm* for cesium and ammonium hydrophthalates. Potassium and rubidium hydrophthalate single crystals are piezoelectrics with high coefficients of acoustooptical interaction [1, 2]. This feature allows one to use them for data processing and intralaser modulation in various acoustooptical devices. The temperature stability of potassium and ammonium hydrophthalate crystals has been studied by the mass-spectrometric method [3, 4]. According to these data, during cleavage in vacuum at 400 K, potassium hydrophthalate decomposes with separation of water, whereas ammonium hydrophthalate evolves ammonium at 370 K. The hydrophthalate $C_8H_5O_4X$ crystals possess a low surface energy of the cleavage plane (perfect cleavage) and have a large value of the maximum interplanar spacing (e.g., ~26 Å for a potassium hydrophthalate). Therefore, hydrophthalates are widely used as X-ray analyzers in the spectral range from 8 to 26 Å and as monochromators for the preliminary formation of the parallel monochromatic radiation in high-resolution X-ray apparatus such as double-crystal vacuum spectrometers [5].

The $C_8H_5O_4X$ hydrophthalates crystals are characterized by various bonding types in different crystallographic planes—ionic, molecular, and hydrogen. The specific character of their structure and chemical bonding, as well as the insufficient information on the mechanical properties of the orthorhombic crystals, motivates the interest in their studies. A high anisotropy of mechanical properties of $C_8H_5O_4X$ hydrophthalates depending on the direction of the compression axis with respect to the cleavage plane was observed in [6–11], where the basic plastic and strength parameters were also measured.

Because of a great interest in this class of crystals in recent years, it seems expedient to review the results on the mechanical properties of hydrophthalates obtained for about the last 10 years. The knowledge of the mechanical properties of $C_8H_5O_4X$ hydrophthalates would help to solve an important technical problem, of bending of plates along a cylindrical surface of the Rowland circle in the preparation of elements for focusing spectrographs.

EXPERIMENTAL

The $C_8H_5O_4X$ hydrophthalate single crystals were grown from aqueous solutions on seeds oriented along the (010) face (the cleavage plane) by the method of temperature decrease. The crystals were grown within 2.5–4 months at the temperature decrease from 40 to 25°C and the supersaturation of 2.5–3%. The $14 \times 5 \times 4$ to $8 \times 3 \times 3$-mm-long specimens of different cleavage-plane orientations with respect to the compression axis were cut out from the crystals grown. The orientation of ground and polished specimens varied within 2°, which was checked by the conoscopic figures with an accuracy of 0.1°. The compression tests of the specimens were made on an Instron test machine and a special device for compression and stress relaxation for small specimens [12] at a deformation rates ranging within 1×10^{-6}–1×10^{-5} m/s and the temperatures ranging within 300–473 K. The microstructure of the

1063-7745/01/4605-0820$21.00 © 2001 MAIK "Nauka/Interperiodica"

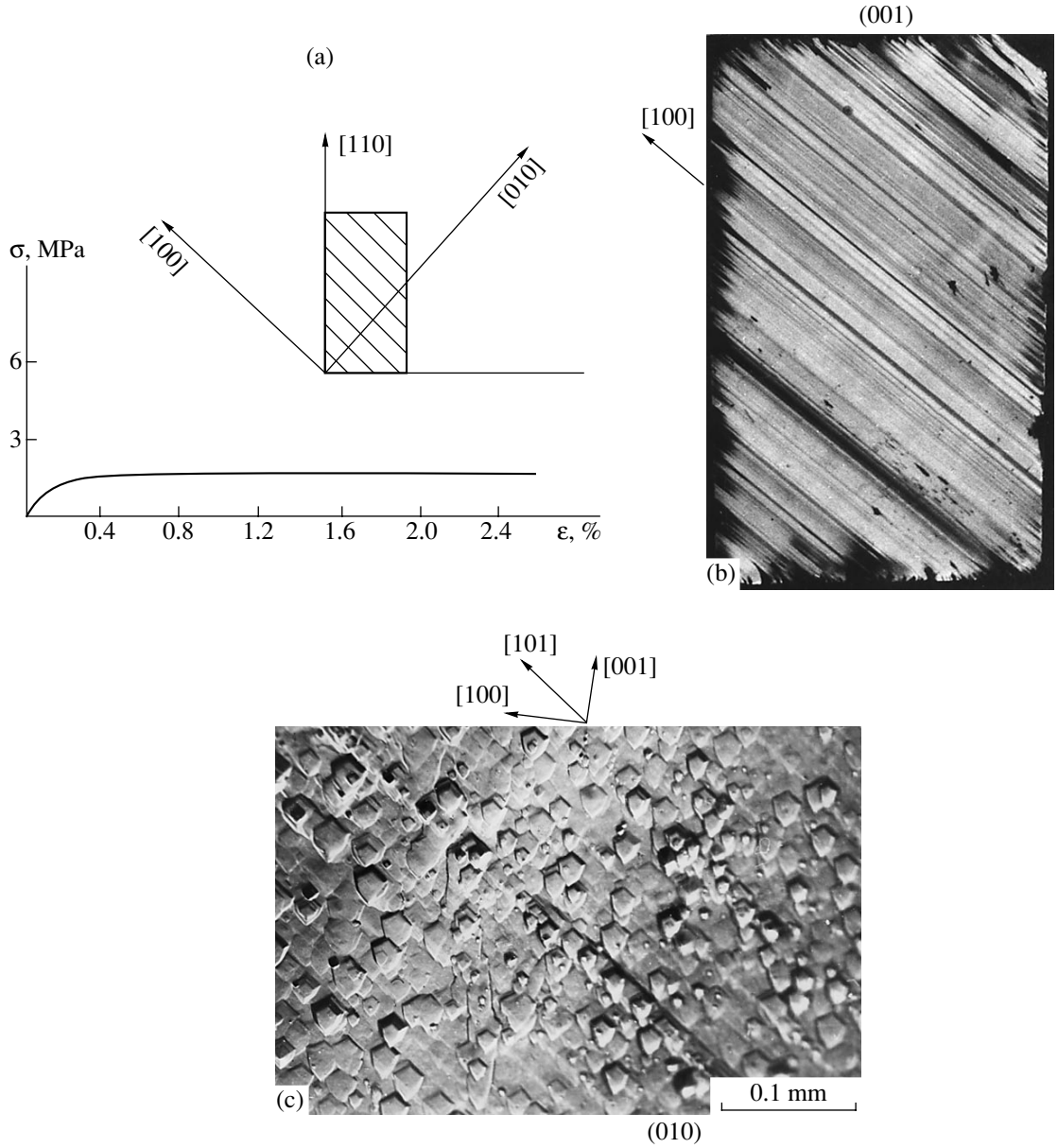

Fig. 1. (a) Compression curve for potassium hydrophthalate specimen taken along the [011] direction and the orientation of the crystallographic axes in the specimen; (b) the (001) surface of the specimen after deformation; (c) selective etching pattern of the (010) plane.

deformed specimens was revealed by chemical etching in dehydrated alcohol.

EXPERIMENTAL RESULTS

Plastic Deformation of $C_8H_5O_4X$ Hydrophthalate Crystals and Study of Stress Relaxation [6, 8]

For potassium hydrophthalate specimens oriented so that the compression axis forms an angle of 45° to the (010) cleavage, the maximum tangential stresses arise in this plane, and the crystal turns out to be highly plastic (Fig. 1a). The specimen is elastically deformed at stresses lower than ~1.5 MPa; then the moderate plastic deformation is observed almost without hardening up to high strains (50% and higher). The specimen starts "flowing" similar to a metal. The study of the shear in strained potassium hydrophthalate specimens showed that the slip plane coincides with the (010) cleavage (Fig. 1b). The crystal relief and the surface microstructure shows the [001] slip direction under the compression along the [011] and [100] slip direction under the compression along the [110] direction. The third slip direction, [101], is determined from the selective etching pattern of the cleavage plane of the strained specimens (the slip bands in the [101] direction) (Fig. 1c). The compression test of other $C_8H_5O_4X$

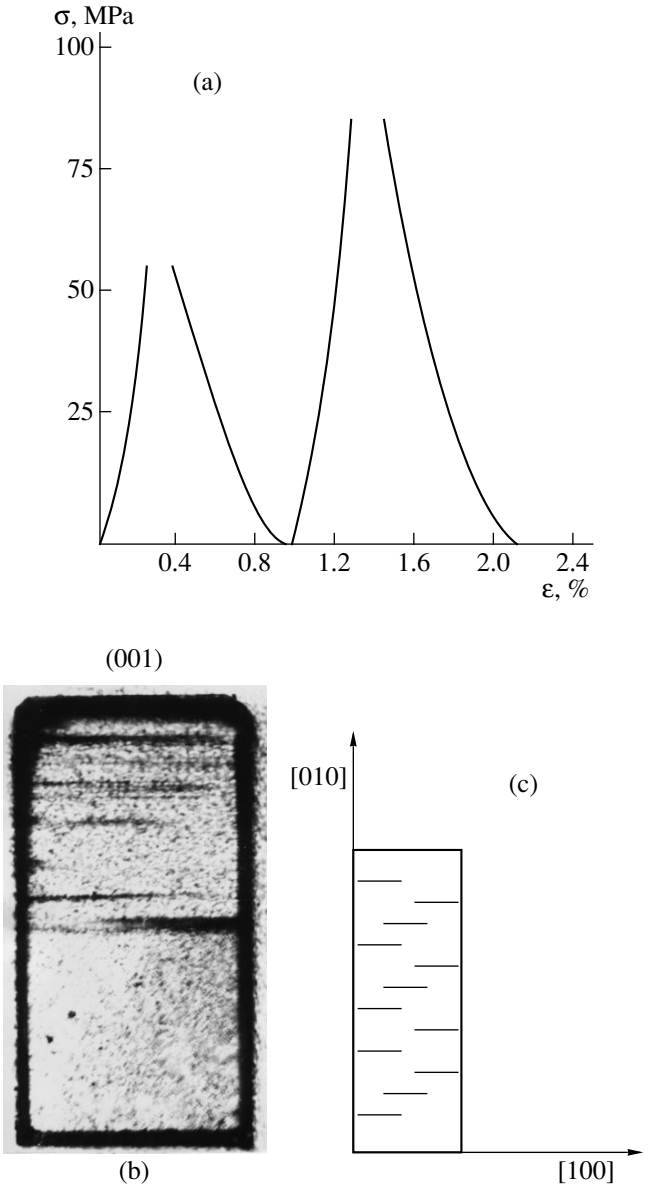

Fig. 2. (a) Compression and unloading curves for potassium hydrophthalate along the [010] direction; (b) the (001) surface of the specimen after deformation; (c) orientation of the crystallographic axes.

hydrophthalates showed that plastic deformation in rubidium and cesium hydrophthalates is also observed along the [011] and [110] directions. Plastic deformation of ammonium hydrophthalate is observed only under compression in the [110] direction, whereas compression in the [011] direction leads to brittle fracture of the crystal.

To obtain information on the kinetic parameters of such deformation—the activation energy and the activation volume—we studied the stress relaxation in potassium hydrophthalates in more detail [8]. Using a set of the stress-relaxation curves taken at different initial stresses σ with due regard for internal stresses σ_{int} determined from asymptotic values of σ at $t \longrightarrow \infty$, we constructed the $\log(d\sigma/dt)$ versus $(\sigma-\sigma_{int})$ curves. The activation volume q was determined as the slope of these curves. The distance L between the points of dislocation pinning was determined from the activation volume $q = L\mathbf{b}^2$, where $\mathbf{b}$ is the Burgers vector. The activation energy U_0 of the dislocation motion was estimated from the measured rates of stress decrease $d\sigma/dt$ on the stress-relaxation curves taken at two temperatures, $T_1 = 291$ and $T_2 = 400$ K. This estimation yields an activation energy of $U_0 \approx 100$ kcal/mol (4 eV) and $q \approx 16 \times 10^{-18}$ cm^3. The q/b^3 value is about 3.7×10^3 and allows one to understand the character of obstacles met by dislocations in their motion in potassium hydrophthalate crystals. This value is consistent in the opinion that forest dislocations intersecting the (010) slip plane in potassium hydrophthalates are the obstacle in the dislocation motion in this plane [8].

Brittle Fracture of $C_8H_5O_4X$ Hydrophthalate Crystals [6, 11]

The study of the specimens with the compression axis normal to the (010) cleavage and coinciding with the [010] direction (Fig. 2) shows that in this case there is no microscopic plastic deformation. The behavior of the crystal under loading and unloading is unusual. Under the first loading cycle, the crystal is elastically strained with an increase of a load up to $\sigma = 100$ MPa; then, being unloaded, it underwent brittle fracture. If the specimen was loaded to less than 100 MPa, the subsequent unloading proceeds nonlinearly, whereas the specimen size in the compression direction after unloading increases (Fig. 2a). Microscopic observations showed that such specimen behavior is associated with formation of microcracks along the cleavages (Figs. 2b, 2c). During unloading, the cracks open, and during loading, they "collapse."

Study of Kink Formation Processes in $C_8H_5O_4X$ Hydrophthalates [6, 7, 9]

The compression axis of the specimen lies in the (010) cleavage plane and coincides with the [100] and [001] crystallographic directions. The stress-strain curves for the specimens of both orientations show that, first, the specimen is elastically strained and then, at a load of ~25 MPa, one observes an abrupt stress drop to a value of ~4–5 MPa accompanied by a bound sound. For the specimen oriented along the [100] axis, upon the first kink, oscillating kinks are developed in the stress range 5–6 MPa with further specimen deformation (Fig. 3a). The specimen oriented along the [001] axis usually undergoes fracture in the kink range immediately after the first main decrease in stress. To study kink formation, two types of the boundary condition were created; namely, we used "hard" dies excluding any lateral displacements, and "soft" dies, which

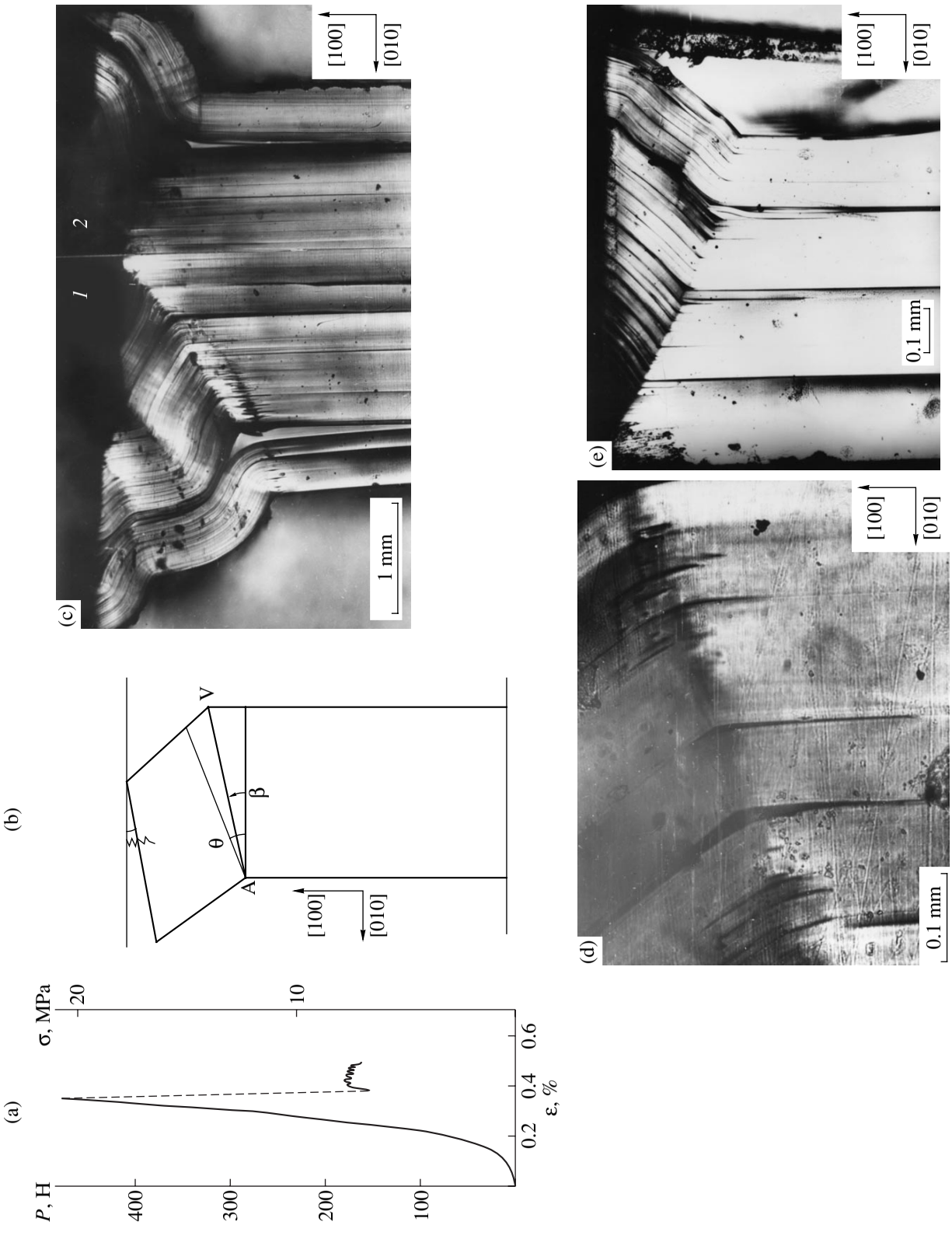

Fig. 3. (a) Compression curve for a potassium hydrophthalate specimen along the [100] direction (*P* is the load 8H); (b) the position of the specimen under compression by the "soft" dies; (c)–(e) reorientation of a potassium hydrophthalate specimen under compression along the [100] direction by (c) "hard" dies; (d) "soft" dies; (e) "hard" dies with the use of a lubricant.

allowed lateral displacements during rotation (Fig. 3b). In the first case, a relaxometer-type machine [12] was used; in the second case, an Instron machine. Under compression of $C_8H_5O_4X$ hydrophthalate crystals by both "hard" and "soft" dies along both directions, we observed the formation of reorientation kink-type regions near the specimen ends in the temperature range 300–473 K. In both cases, this process is caused by the fact that the nonuniform stress state and macrobending moments providing kink nucleation and development appear mainly at the specimen ends [13]. It is also known that if a crystal is deformed by "hard" dies with considerable friction coefficients between the dies and the specimen ends, a formation of the reoriented regions occurs only in the ways that do not allow any displacement of the specimen ends with respect to one another [13, 14]. A characteristic view of the regions formed under a crystal deformation by "hard" dies is shown in Fig. 3c. A complex kink consists of two bands (*1* and *2*) having equal widths, but different crystallographic directions. A specific feature of "soft" dies used in our study is that one die is rigidly fixed, whereas another is hinged with a lever of ≅600 mm. Such dies allow one to change the crystal shape by rotating its ends to a small angle of order of 1°: $\xi = \arctan d/D \approx 1°$, where d is the value of lateral displacement, D is the lever length in a hinge die. This angle is sufficient for the formation of a kink band with one misorientation direction (Fig. 3d). A similarly fixed elastic rod acquires the same shape upon the external field attains the critical value and also loses its elastic stability [15]. In the case of deformation by the "hard" dies, the analogous kinks can be obtained if one specimen end is lubricated with molybdenum bisulfate (Fig. 3e).

We studied the angular characteristics of the kink bands, where θ is the misorientation angle between the planes of a crystal lattice of the kink and a lattice of the matrix; β is the angle between a kink boundary and the normal to acting slip planes (Fig. 3b). It is known that the non-symmetrical slope boundary is a source of long-range stresses $\delta = E\rho b \sin(\theta/2 - \beta)$, where ρ is the linear density of dislocations in the boundary. At $\theta > 2\beta$, the kink band is extended, and at $\theta < 2\beta$ the matrix is also extended. The tensile stresses along the kink boundaries relax by the forming of a hierarchic system of microcracks with lengths $\langle C_1\rangle$, $\langle C_2\rangle$ … $\langle C_n\rangle$ and the spaces in between $\langle d_1\rangle$, $\langle d_2\rangle$ … $\langle d_n\rangle$. We managed to measure $\langle C_i\rangle$ and $\langle d_i\rangle$ on four scale levels for the case $\theta < 2\beta$ when the cracks are developed mainly in the matrix. It turned out that the system of microcracks is of a fractal character [16]. Indeed, $\langle C_{i+1}\rangle/\langle C_i\rangle \approx 4 \approx \langle d_{i+1}\rangle/\langle d_i\rangle$ and, therefore, the dependence $\log C_i$ versus $\log d_i$ is a straight line. We believe that the fractal character of microcracks is caused by the corresponding decrease of the volume "supplying" the crack with elastic energy necessary for the transition to a lower scale level. The action of the (010) slip plane in this crystal promotes kink formation due to dislocation motion at an angle to the direction of kink propagation and generation of microcracks by the mechanism similar to that suggested by Rozhanskii [17].

Specific Features of Ammonium Hydrophthalate Single Crystals

All the above results on plastic deformation, brittle fracture, and kink formation are valid for the whole series of $C_8H_5O_4X$ hydrophthalate single crystals except for ammonium hydrophthalate whose deformation behavior has a number of specific features. Thus, plasticity in ammonium hydrophthalate is only observed along [110], whereas under compression along [011], the crystal undergoes brittle fracture [6]. The formation of kink bands in ammonium hydrophthalate also differs from kink formation in other $C_8H_5O_4X$ hydrophthalates. Indeed, a kink band in ammonium hydrophthalate is not formed under compression along [001] direction and the crystal undergoes brittle fracture [6]. The maximum anisotropy in microdensity of the ammonium hydrophthalate was observed in the experiments on a Knoop microindentation [11].

Along with the maximum anisotropy in the mechanical properties of the ammonium hydrophthalate in the $C_8H_5O_4X$ hydrophthalate series, it also shows anomalous anisotropy in thermal expansion [10]. The thermal expansion coefficient α was measured on a quartz dilatometer along the [100], [010], and [001] directions. It is shown that specimen heating decreases its length along the [100] axis, i.e., $\alpha_{[100]} < 0$ along [010] and [001] axes. The $\alpha_{[010]}$ and $\alpha_{[001]}$ are positive, but have different values and temperature dependences. The maximum anisotropy characteristic of an ammonium hydrophthalate was also confirmed in studies of the X-ray spectral properties [18]. The strong forbidden (001) reflection was found for ammonium hydrophthalate single crystal in the range of ultra-soft X-rays near the absorption edge with the wavelength of 44 Å. This reflection may be used to record the emission spectrum of carbon. A study with the copper-anode X-ray tube showed that the high reflection "efficiency" at the absorption edge is observed if the optical axis of the spectrometer coincides with the [100]-axis of a single crystal. If it coincides with the [001] axis of the crystal, the forbidden first-order reflection is not observed.

The maximum anisotropy in the mechanical properties, the thermal expansion coefficient, and the X-ray sensitivity in the $C_8H_5O_4X$ hydrophthalate series is observed for ammonium hydrophthalate because of anisotropy of chemical bonding in the crystal, i.e., because of the structure and location of benzene rings.

CONCLUSIONS

The compression test of organic single crystals of potassium, rubidium, cesium, and ammonium hydrophthalates provided the determination of their mechanical parameters characterizing the deformation and fracture processes. It is shown that depending on orientation, crystals can undergo either plastic deformation or brittle fracture and can form kink bands.

The analysis of the relaxation curves for potassium hydrophthalate single crystals allowed us to determine the kinetic parameters of deformation such as the activation energy (100 kcal/mol) and the activation volume (16×10^{-18} cm^3). The data obtained are consistent with the idea that the main obstacle to the dislocation motion in the slip plane (010) are forest dislocations intersecting this plane.

Ammonium hydrophthalate crystals show the maximum anisotropy in mechanical properties, the thermal expansion coefficient, and the X-ray sensitivity in the $C_8H_5O_4X$ hydrophthalate series.

REFERENCES

1. L. M. Belyaev, G. S. Belikova, A. B. Gil'varg, *et al.*, Kristallografiya **14** (4), 645 (1969) [Sov. Phys. Crystallogr. **14**, 544 (1969)].
2. G. S. Belikova, L. M. Belyaev, M. P. Goloveĭ, *et al.*, Kristallografiya **19** (3), 566 (1974) [Sov. Phys. Crystallogr. **19**, 351 (1974)].
3. O. F. Pozdnyakov, B. P. Redkov, A. S. Smirnov, *et al.*, Kristallografiya **33** (4), 994 (1988) [Sov. Phys. Crystallogr. **33**, 588 (1988)].
4. V. R. Regel, L. A. Lutfullaeva, T. M. Muinov, *et al.*, Izv. Akad. Nauk Tadzh. SSR **111** (1), 26 (1989).
5. G. S. Belikova, Yu. I. Grineva, V. V. Korneev, *et al.*, in *Apparatus and Methods of X-ray Analysis* (Nauka, Leningrad, 1983), Vol. 31, p. 171.
6. V. R. Regel, V. I. Vladimirov, N. L. Sizova, *et al.*, Kristallografiya **34** (6), 1490 (1989) [Sov. Phys. Crystallogr. **34**, 892 (1989)].
7. V. I. Vladimirov, A. A. Birkovskiĭ, V. R. Regel, *et al.*, Fiz. Tverd. Tela (Leningrad) **31** (10), 125 (1989) [Sov. Phys. Solid State **31**, 1722 (1989)].
8. V. R. Regel, N. L. Sizova, and T. N. Turskaya, Kristallografiya **41** (5), 918 (1996) [Crystallogr. Rep. **41**, 875 (1996)].
9. V. R. Regel, N. L. Sizova, G. S. Belikova, *et al.*, Fiz. Tverd. Tela (St. Petersburg) **41** (2), 265 (1999) [Phys. Solid State **41**, 236 (1999)].
10. V. R. Regel, N. L. Sizova, V. V. Zhdanova, *et al.*, Kristallografiya **39** (6), 1097 (1994) [Crystallogr. Rep. **39**, 1008 (1994)].
11. N. L. Sizova, L. A. Lutfullaeva, V. R. Regel, *et al.*, Kristallografiya **37** (4), 1047 (1992) [Sov. Phys. Crystallogr. **37**, 558 (1992)].
12. V. R. Regel, G. A. Dubov, and V. N. Glazunov, in *Crystals: Growth, Structure, and Properties* (Nauka, Moscow, 1993), p. 263.
13. A. A. Birkovskiĭ, V. I. Vladimirov, and A. E. Romanov, in *Disclinations and Rotary Deformation of Solids* (Fiziko-tekhn. Inst., Leningrad, 1988), p. 5.
14. V. I. Vladimirov and A. E. Romanov, in *Disclinations in Crystals* (Nauka, Leningrad, 1986), p. 818.
15. S. P. Timoshenko, *Stability of Bars, Plates and Shells* (Nauka, Moscow, 1971), p. 818.
16. B. M. Smirnov, Usp. Fiz. Nauk **149** (2), 177 (1986) [Sov. Phys. Usp. **29**, 481 (1986)].
17. V. N. Rozhanskiĭ, Fiz. Tverd. Tela (Leningrad) **2** (6), 1082 (1960) [Sov. Phys. Solid State **2**, 978 (1960)].
18. A. V. Okotrub, L. G. Bulusheva, L. N. Mazalov, *et al.*, Mol. Mater. **10**, 213 (1998).

Translated by T. Dmitrieva

Crystallography Reports, Vol. 46, No. 5, 2001, pp. 826–829. Translated from Kristallografiya, Vol. 46, No. 5, 2001, pp. 900–903.

PHYSICAL PROPERTIES OF CRYSTALS

Dedicated to the memory of B.K. Vainshtein

Absorption Spectra and Circular Dichroism of $Sr_3Ga_2Ge_2O_{14}$: Cr and $Ca_3Ga_2Ge_2O_{14}$: Cr Crystals

Z. B. Perekalina[1], V. P. Orekhova[1], K. A. Kaldybaev[2], B. V. Mill[3], and D. V. Isakov[1]

[1] *Shubnikov Institute of Crystallography, Russian Academy of Sciences, Leninskiĭ pr. 59, Moscow, 117333 Russia*

[2] *Issyk-Kul State University, Karakol, Kyrgizstan*

[3] *Moscow State University, Vorob'evy gory, Moscow, 119899 Russia*

Received December 27, 2000

Abstract—Absorption spectra and circular dichroism spectra of chromium-doped Sr-gallogermanate crystals of different colors and doped and pure Ca-gallogermanate crystals have been studied. It is shown that chromium ions enter the Sr-gallogermanate crystals in two valence states—Cr^{3+} and Cr^{4+}. It is assumed that Cr^{4+} ions replace Ge^{4+} in the tetrahedra. © *2001 MAIK "Nauka/Interperiodica".*

INTRODUCTION

Below we describe the study of the optical properties of trigonal gallogermanate $A_3Ga_2Ge_2O_{14}$ crystals (A = Ca, Sr) of different compositions and colors. These crystals have a set of important optical (including non-linear), spectroscopic, lasing, piezoelectric, etc., properties [1].

Gallogermanate $Ca_3Ga_2Ge_2O_{14}$ (CGGO) and $Sr_3Ga_2Ge_2O_{14}$ (SGGO) crystals belong to the class symmetry 32 of the trigonal system, sp. gr. $D_3^2 - P321$, $Z = 1$ [2]. The unit-cell parameters are a = 8.076, c = 4.974 Å for CGGO and a = 8.270, c = 5.040 Å for SGGO. The ionic radii are equal to 1.12 for Ca^{2+}, and 1.26 Å for Sr^{2+} in the eightfold coordination and 0.62 for Ga^{3+}, 0.53 for Ge^{4+}, 0.615 for Cr^{3+}, and 0.55 Å for Cr^{4+} in the sixfold coordination [3].

The structures of CGGO and SGGO crystals consist of layers normal to the c-axis and oxygen octahedra and two types of oxygen tetrahedra. Between the layers Thompson cubes occupied by large Ca^{2+} or Sr^{2+} ions are located [the 3(*e*) position with the local symmetry 2]. Some tetrahedra lie on the threefold axes (the central 2(*d*) position with the local symmetry 3); and some other tetrahedra are grouped around the octahedra by the symmetry of the threefold axis [the 3(*f*) position with the local symmetry 2]. The 2(*d*) tetrahedra are occupied by the Ge^{4+} ions and the 3(*f*) tetrahedra, by Ga^{3+} and Ge^{4+} ions in the ratios 3 : 2 and 7 : 8 for Ca- and Sr-gallogermahate, respectively. The 1(*a*) octahedra (the symmetry 32) are statisfically occupied by Ge^{4+} and Ga^{3+} ions in the ratios 4 : 1 and 3 : 2 for Ca- and Sr-gallogermanate, respectively. In chromium-doped crystals, the Cr^{3+} ions enter the octahedra and replace Ga^{3+} ions there; the Cr^{4+} ions enter the 2(*d*) and 3(*f*) tetrahedra and replace the Ge^{4+} ions. The statistical filling of the 1(*a*) and 3(*f*) positions by Ga^{3+} and Ge^{4+} ions results in a partial disorder of the crystal structure and the fluctuation of the crystal field in the positions of chromium ions, thus, changing the spectral and generation characteristics of the crystal [1, 2, 4, 5].

We studied the physical properties on chromium-doped strontium gallogermanate crystals $Sr_3Ga_2Ge_2O_{14}$: Cr (SGGO : Cr) of different colors and a $Ca_3Ga_2Ge_2O_{14}$: Cr (CGGO : Cr) crystal.

EXPERIMENTAL

A transparent $Sr_3Ga_2Ge_4O_{14}$: Cr single crystal of the mass 210 g, 100 mm in length and 25 mm in cross section was grown from the platinum crucible 45 mm in length containing 240 g of the melt by the Czochzalski method (0.1 at. % of Cr_2O_3 in the charge with respect to Ga_2O_3) on an automated Malvern MSR-2 setup. Crystals were grown on a ⟨0001⟩-oriented seed in the O_2 atmosphere (P = 2 atm) at the pulling velocity 2.5 mm/h and the rotation velocity 40 rpm. In the cross-section with a constant diameter, the crystal habit was close to that of the (1010) hexagonal prism with the rounded edges and the flat crystallization front. The crystal grown has an unusual color. The neck and the initial part of the cone are reddish, then the crystal grew green up to the end of the widened part, which coincided with inversion of the crystallization front. Upon the crystallization-front inversion, the crystal acquired the structure consisting of alternating 1–5-mm-thick reddish and green layers. However, the central part (6–7 mm in

1063-7745/01/4605-0826$21.00 © 2001 MAIK "Nauka/Interperiodica"

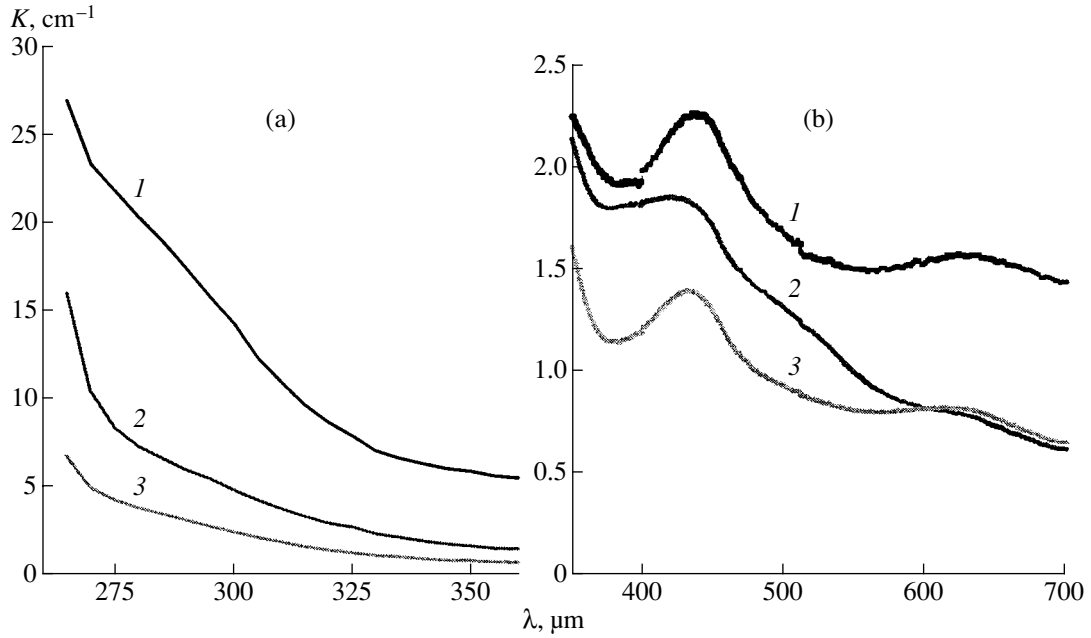

Fig. 1. Absorption spectra of (*1*) $Ca_3Ga_2Ge_2O_{14}$: Cr, (*2*) $Sr_3Ga_2Ge_2O_{14}$: Cr (reddish), and (*3*) $Sr_3Ga_2Ge_2O_{14}$: Cr (green) crystals in the (a) ultraviolet and (b) visible spectrum ranges.

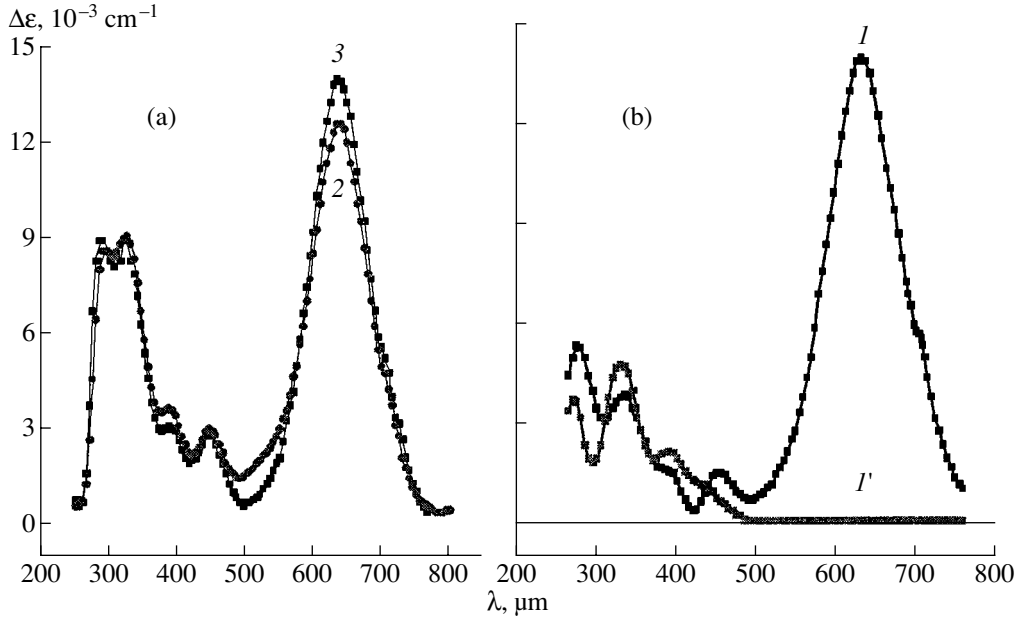

Fig. 2. Circular-dichroism spectra for (a) $Sr_3Ga_2Ge_2O_{14}$:Cr ((*2*) reddish, (*3*) green); (b) (*1*) $Ca_3Ga_2Ge_2O_{14}$: Cr crystals, and (*1'*) undoped $Ca_3Ga_2Ge_2O_{14}$ crystal.

diameter) of the green layers also has a reddish color. The reddish layers thin toward the lower part of the crystal, and the lowest part is green.

A transparent green CGGO : Cr single crystal of the mass 244 g was grown from melt (268 g) under similar conditions. In contrast to the SGGO : Cr crystal, the CGGO : Cr crystal has a homogeneous color without shades.

The specimens were prepared from green chromium-doped CGGO crystals and green and reddish chromium-doped SGGO crystals. The specimens were 0.5–1.5-mm-thick plates oriented normally to the optical axis. The absorption spectra were measured on Hitachi and Specord-40 spectrophotometers in the range of 250–700 nm. The circular-dichroism spectra were studied on a dichrograph designed and manufac-

Basic spectroscopic parameters of $Sr_3Ga_2Ge_4O_{14}$: Cr^{3+} (SGGO : Cr) and $Ca_3Ga_2Ge_4O_{14}$ (CGGO) crystals

Crystals	Optical transitions from $^4A_2$ to the next levels				Color centers
	b^4T_1	a^4T_1	$^4T_2$	^2E	
SGGO : Cr (reddish)	290*	430*	640*		
	295**	445**	635**	700**	320.385
		2.8***	12.4***		
		0.69****	4****		
SGGO : Cr (green)	295*	435*	630*		
	290**	445**	635**	700**	320.385
		2.9***	14***		
		0.64***	5.6****		
CGGO : Cr (green)	285*	440*	635*		
	275**	450**	630**	700**	335.390
		1.5***	14***		
		1.2****	6.3****		
CGGO (undoped)					275.330.390.440

Note: The crystal-field parameters are: Dq = 1560 cm^{-1}; B = 690 cm^{-1}; Dq/B =2.26 for SGGO : Cr (reddish) Dq = 1590 cm^{-1}; B = 690 cm^{-1}; Dq/B =2.3 for SGGO : Cr (green) Dq = 1570 cm^{-1}; B = 660 cm^{-1}; Dq/B =2.0 for CGGO : Cr (green).

* Positions of the absorption-band peaks, nm.

** Positions of the peaks of the circular-dichroism bands, nm.

*** Intensity of the peaks of the circular-dichroism bands, $\Delta\varepsilon$, 10^{-2} cm^{-1}.

**** Rotational forces of the circular dichroism bands, R, 10^{-40} CGS units.

tured at the Institute of Crystallography in the range of 250–800 nm [6].

RESULTS AND DISCUSSION

The absorption spectra of the green and reddish SGGO : Cr crystals (curves *3* and *2*, respectively) and a green CGGO : Cr crystal (curve *1*) are shown in Figs. 1a and 1b, where K is the absorption factor. All the spectra have broad electronic-vibrational absorption bands typical for Cr^{3+} ions—one in the ultraviolet (Fig. 1a) and two in the visible (Fig. 1b) ranges of spectra. The positions of the band maxima for all the specimens are indicated in table. The crystal-field parameters Dq and B (see the table) were evaluated from the experimental data and agreement with the data in [4, 5].

The absorption spectra of green CGGO : Cr and SGGO : Cr specimens (Fig. 1b, curves *1* and *3*) are similar, which indicates that the replacement of Ca by Sr in gallogermanates almost did not affect the intensity and the symmetry of the crystal field in the center of the octahedron in the position 1(*a*) occupied by Cr^{3+} ions. As is seen from Fig. 1b, the intensity of the broad absorption band in the red spectrum range of SGGO : Cr is lower for a reddish specimen (curve *2*) than the intensity of that of the green specimen (curve *3*). This indicates a lower Cr^{3+} concentration in the reddish specimen. It should be noted that, apart from the bands due to Cr^{3+} ions, an additional broad band is observed in the green range (470–580 nm) of the absorption spectra of the reddish specimen. This absorption can be attributed to broad absorption bands of Cr^{3+} ions with the peaks at 500 and about ~550 nm [4]. Since the intensities of the broad absorption bands in the red range of the spectrum (at 625 and 630 nm) are low for both reddish and green specimens, the contribution of these bands to the crystal color is insignificant. The largest contribution to the crystal color comes from the Cr^{3+} and Cr^{4+} absorption in the green spectrum range.

Figure 2a shows the circular-dichroism spectra of reddish (curve *2*) and green (curve *3*) SGGO : Cr specimens. It is established that circular dichroism is present in all the three broad bands of the absorption spectra and also in the R-line (about 700 nm) of the Cr^{3+} ion (Fig. 2a, curves *1* and *2*). Moreover, the circular-dichroism (Fig. 2a, curve *2*) and the absorption (Fig. 1b, curve *2*) spectra of the reddish SGGO : Cr specimen has a broad low-intensity absorption band in the green range (470–580 nm). This band may be attributed to the circular dichroism of Cr^{4+} ions. As is seen from Fig. 2a, the circular-dichroism spectra for the reddish and the green SGGO : Cr specimens slightly differ—the positions of all the bands almost coincide and their intensities differ only slightly. The peaks of the absorption bands and circular dichroism are listed in table.

Comparing the circular-dichroism spectra of green SGGO : Cr and CGGO : Cr specimens (Fig. 2b, curve *1* [5] and Fig. 2a, curve *3*) one can see that the intensity ratios of the bands (at the maxima) for the same electron transitions of Cr^{3+} ions are different and are equal

to ~1 at λ about 630 nm, ~0.5 at λ about 440 nm and ~0.6 in the ultraviolet range. Since the selection rules for the transitions in the absorption and circular dichroism spectra are different, the intensity ratios for these spectra are different.

The circular-dichroism spectra of SGGO : Cr crystals are show some additional broad bands that cannot be attributed to chromium ions. Earlier, such bands were observed in the circular-dichroism spectra of undoped CGGO crystals (Fig. 2b, curve *1'*) [5]. These bands with the maxima in the range 330–390 nm can be attributed to color centers (see table) related to structural defects formed during crystal growth.

The rotational forces of the electron $^4A_2 \longrightarrow a^4T_1$ and $^4A_2 \longrightarrow {}^4T_2$ transitions were calculated by the formula $R = 0.407 \times 10^{-38}\Delta\varepsilon_{0i}\Delta_i/\nu_{0i}$, where $\Delta\varepsilon_0$, Δ_i and ν_{0i} were determined from the absorption bands corresponding to these transitions in the circular-dichroism spectra ($\Delta\varepsilon_{0i}$ is the band intensity at the maximum, Δ_i is the band halfwidth, and ν_{0i} is the transition frequency). The optical parameters of the specimens studied are indicated in table.

CONCLUSIONS

The study of the absorption and circular-dichroism spectra of undoped and chromium-doped CGGO and SGGO crystals provided the separation of the absorption and circular-dichroism bands caused not only by octahedrally coordinated Cr^{3+} ions, but with Cr^{4+} ions in the tetrahedral coordination, as well as the bands caused by defect centers.

The presence of Cr^{4+} ions in the CGGO and SGGO crystals can be explained by the conditions of their growth under the pressure of the oxidizing atmosphere. These conditions can provide the transition of some Cr^{3+} ions to the tetravalent state. A presence in the structure of tetrahedra 2(*d*)- and 3(*f*)-positions with the symmetry 3 and 2, respectively, occupied by Ge^{4+} ions (whose radius is close to that of the Cr^{4+} ion) allows the incorporation of Cr^{4+} ions into the crystal structure. The symmetry of these tetrahedra opens the way for the appearance of circular dichroism in the electron transitions of the Cr^{4+} ions.

The observation of the additional circular-dichroism bands not caused by chromium ions in undoped and chromium-doped CGGO and SGGO crystals was assumed to be associated with defects formed during crystal growth.

ACKNOWLEDGMENTS

This study was supported by the Russian Foundation for Basic Research, project no. 99-02-17242.

REFERENCES

1. *Physics and Spectroscopy of Lasing Crystals*, Ed. by A. A. Kaminskii (Nauka, Moscow, 1986).
2. E. L. Belokoneva and B. V. Mill', in *Crystallochemical Systematics of Minerals*, Ed. by V. S. Urusov (Mosk. Gos. Univ., Moscow, 1985), p. 140.
3. R. D. Shanon, Acta Crystallogr., Sect. A: Cryst. Phys., Diffr., Theor. Gen. Crystallogr. **A32**, 751 (1976).
4. P. I. Macfarlane, T. P. J. Han, B. Henderson, and A. A. Kaminskii, Opt. Mater., No. 3, 15 (1994).
5. Z. B. Perekalina, T. F. Veremeĭchik, K. A. Kaldybaev, and A. D. Tynaev, Kristallografiya **45** (2), 337 (2000) [Crystallogr. Rep. **45**, 304 (2000)].
6. Z. B. Perekalina, V. I. Vologin, I. A. Kudryashov, and K. A. Kaldybaev, Zh. Prikl. Spektrosk. **43**, 328 (1985).

Translated by T. Dmitrieva

Crystallography Reports, Vol. 46, No. 5, 2001, pp. 830–834. Translated from Kristallografiya, Vol. 46, No. 5, 2001, pp. 904–908.

PHYSICAL PROPERTIES OF CRYSTALS

Dedicated to the memory of B.K. Vainshtein

Growth Conditions and Electric Properties of KDP Crystals. I. Conductivity Measurements

E. D. Yakushkin, E. P. Efremova, and A. I. Baranov

Shubnikov Institute of Crystallography, Russian Academy of Sciences, Leninskiĭ pr. 59, Moscow, 117333 Russia

e-mail: yakushkin@ns.crys.ras.ru

Received December 20, 2000

Abstract—Conductivity of potassium dihydrophosphate (KDP) crystals grown from solutions with different pH has been studied with due regard for the sectorial structure and the impurity composition of the crystals grown. The dependence of the conductivity parameters on these two factors is established. The data obtained lead to a conclusion on the formation of the real structure important for various electro-optical applications of KDP crystals and provide the optimization of growth conditions. *© 2001 MAIK "Nauka/Interperiodica".*

INTRODUCTION

Physical properties of ferroelectric potassium dihydrophosphate (KDP) crystals of the composition KH_2PO_4 have been studied for more than 60 years. Despite the great importance of these crystals for the theory of phase transitions and various electrooptical applications, no systematic studies of physical properties of KDP crystals depending on growth conditions have been performed as yet. The present article partly closes this gap. We studied for the first time the high-temperature dielectric properties such as conductivity and dielectric permittivity of KDP crystals synthesized from solutions with different pH with due regard for their sectorial structure and the impurity composition.

Below, we present the results of the conductivity measurements of KDP crystals.

As is well known, ionic conductivity is essentially dependent on the structural defects. Conductivity of KDP single crystals was repeatedly studied on preliminarily doped crystals [1, 2], crystals characterized by the high-temperature reconstructive phase transition [3], and the crystals with the complex impedance analyzed in the high-temperature range [4]. Nevertheless, the role played by the real structure of a nominally pure single crystal in the formation of its electric properties is still unclear. In particular, we have established that the conductivity of specimens prepared from one growth sector of a KDP crystal can differ by three to four orders of magnitude, which indicates the complexity of the process of formation of real structure in KDP single crystals during their growth.

EXPERIMENTAL

Potassium dihydrophosphate crystals were grown onto a point seed fixed in the center of a reversibly rotating platform by the method of continuous temperature decrease (from 50°C). The solution supersaturation was about 3% during the whole growth process. The growth rates of the prism and pyramid faces were up to 3 mm/day (24 h), i.e., were sufficient for the formation of the well-developed {100} and {101} growth sectors and comparison of their defect structures. The starting KDP salt was synthesized from the extra-pure grade H_3PO_4 and KOH reagents (Russia). The acidity (pH) of the solutions obtained was purposefully varied within (2.35–4.82) ± 0.04 by adding either H_3PO_4 acid or KOH alkali to the solution. At the stoichiometric component ratio, the pH value of the solution was 4.0 ± 0.2.

The specimens were $5 \times 5 \times 0.5$-mm^3-large *z*-cut plates of KDP single crystals prepared from the prism and the pyramid growth sectors located at different distances from the seed (Fig. 1).

Conductivity and complex impedance were measured by the bridge method at the frequencies ranging from 100 Hz to 1 MHz. The corresponding temperature curves were measured in the mode of stabilized specimen temperature with the use of thermally deposited silver electrodes. Prior to measurements, the specimens were annealed for ten hours in air at the temperature 150°C.

The composition, concentration, and the spatial distribution of impurities were controlled by the method of emission spectral analysis, which allowed us to study the chosen specimens with both considerably different and close impurity concentrations.

1063-7745/01/4605-0830$21.00

RESULTS AND DISCUSSION

It is well known that conductivity in KDP crystals is provided by the motion of proton defects. It was reasonable to assume that the stoichiometry variation with respect to hydrogen during KDP growth from solutions with different pH values is the most important factor affecting the conductivity parameters. We could expect that a crystal grown from the solution of the highest acidity would contain an excessive number of protons, whereas an increase of the solution alkalinity would increase the number of proton vacancies and that with the deviation of the solution composition from stoichiometric, the crystal conductivity would increase. However, the real situation is much more complicated, which is well seen from the table. Thus, the "alkali crystal" really possesses high conductivity, but the conductivity of the specimens prepared even from the same single crystal can differ by several orders of magnitude (from 3.8×10^{-11} to 3.5×10^{-7} Ω^{-1} cm^{-1}). The activation enthalpy of single-crystal conductivity also varies over a wide range (from 0.9 to 0.3 eV).

The table lists the data obtained for 14 specimens prepared from three single crystals. The ordinal numbers of the specimens correspond to three pH values of the solutions used for crystallization and the location of a future specimen in the single crystal bulk (Fig. 1). Of all the impurities present in KDP crystals, we studied Fe^{3+} and Al^{3+} whose concentrations are usually higher than the concentrations of all the other cationic impurities, and because it is just these impurities that determine the formation of the "defect structure" of KDP crystals during growth [5, 6]. Thus, it is well known that the incorporation of iron into the KDP lattice should give rise to the formation of two potassium and one hydrogen vacancies.

The activation enthalpies H listed in the table were obtained by approximating the measured conductivity by the following "thermoactivation" relationship:

$$\sigma = \frac{A}{T}\exp\left[-\frac{H}{KT}\right], \quad (1)$$

where A is the so-called pre-exponential factor dependent on the concentrations of mobile defects—protons or proton vacancies. Moreover, both A and H parameters depend on the crystal structure and the conductivity mechanism. Obviously, the parameter H has different physical meanings in different cases: if the impurity conductivity prevails, it has the meaning of the enthalpy of migration of a given ion or proton defect; if the intrinsic conductivity prevails (i.e., conductivity provided by thermally activated defects), it has the meaning of the enthalpy of their formation and migration. Figure 2 shows the characteristic temperature dependence of conductivity for four specimens cut out from KDP single crystals (the measuring-field frequency was 1 kHz). We obtained the curves similar to those shown in Fig. 2, which were described quite well by the exponential relationship (1) with different parameters

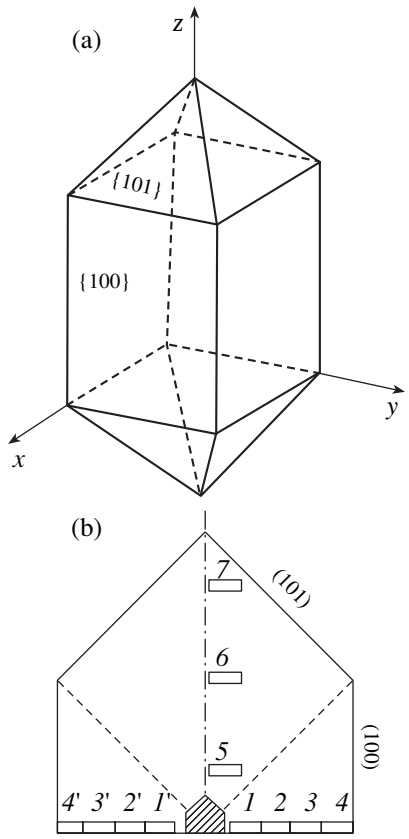

Fig. 1. (a) KDP crystal and (b) scheme illustrating specimen preparation.

in the whole temperature range of all the 14 specimens. The H values given in the table were averaged by the least-squares procedure. For specimens II(2) and II(5) prepared from the KDP single crystal with the "normal" pH value, one can establish two modes of the change in conductivity depending on the temperature. At the first mode at about 375 K, the temperature dependence of conductivity has a kink [Figure 2 shows the conductivity only for specimen II(5)]. The activation enthalpy in this case is determined from the high-temperature parts of the curves, i.e., from the range of the intrinsic conductivity of the crystal, with the conductivities at all the frequencies being almost the same. The activation enthalpies for the second mode [low-temperature (impurity) branches] are indicated in parentheses.

In correspondence with Eq. (1), the analysis of the temperature dependences of conductivity provides the classification of the specimens over three groups with considerably different values of the parameters (the groups *A*, *B*, and *C*), although in the region $H \approx 0.7$ eV, the boundary between the groups A and B is only conditional because of the close enthalpy values. The error in the H value indicated in table (±20%) is purposefully overestimated because, generally speaking, conductivity depends on the frequency of measurements. Never-

Conductivity parameters of the specimens cut out from different growth sectors of KDP crystals grown from solutions with different pH values and characterized by different impurity concentrations

Crystal	pH of the solution	Specimen	Growth sector	Total concentration of Fe and Al impurities, 10^{-3} mol %	H, eV ±20%	σ, Ω^{-1} cm^{-1} (at room temperature)	Group of conductivity mechanism
I	2.35	I(2)	100	8.2	1.0	2.82×10^{-11}	A
		I(4)	100	8.4	0.9	3.80×10^{-11}	A
		I(5)	101	6.8	0.7	1.20×10^{-10}	B
		I(6)	101	6.2	0.6	1.64×10^{-10}	B
II	3.84	II(1)	100	9.9	0.6	1.06×10^{-10}	B
		II(2)	100	2.8	0.8(0.5)	2.60×10^{-11}	A(B)
		II(5)	101	6.9	0.8(0.5)	6.85×10^{-11}	A(B)
		II(6)	101	1.6	0.8	2.61×10^{-10}	A
III	4.82	III(2)	100	4.5	0.5	2.55×10^{-10}	B
		III(3)	100	5.9	0.6	1.28×10^{-10}	B
		III(4')	100	13.9	0.3	2.15×10^{-7}	C
		III(4)	100	14.4	0.3	3.55×10^{-7}	C
		III(6)	101	5.9	0.8	5.6×10^{-11}	A
		III(7)	101	12.3	0.3	7.03×10^{-8}	C

theless, even the measurements made at the same frequency show that the conductivity mechanisms in these three groups of specimens are different.

Different conductivity mechanisms can be illustrated proceeding from the known models of crystal disorder [7]. The pre-exponential factor is determined in such a way that higher values of the factor A correspond to higher values of the activation enthalpy, whereas the low values of A correspond to the low values of H. In other words, within the chosen model, $\ln A$ should be proportional to H, $\ln A \sim H$. Since $A = A'\exp[\Delta S'k]$ (where ΔS is the change in entropy), this signifies that the more pronounced the disorder caused by the formation of defects, the higher the values of the angular coefficient in the proportion $\ln A \sim H$. Figure 3 shows the dependence of the logarithm of the pre-exponential factor on the activation enthalpy for all the specimens studied. Unlike H-values given in the table, we used here the exact H values measured at a frequency of 1 kHz. Different angular coefficients of the dashed lines in Fig. 3 indicate different conductivity mechanisms in the above groups of specimens (in correspondence with the slightly different models). In the range of the H values $H \approx 0.5$–0.7 eV, a crossover can be formed, i.e., the change in the conductivity mechanism—from the impurity mechanism to the intrinsic-conductivity one. It is clear that for KDP crystals, the term "impurity" can indicate an increase both in the concentration of proton vacancies and in the number of excessive protons at low pH values caused by the presence of a cationic impurity.

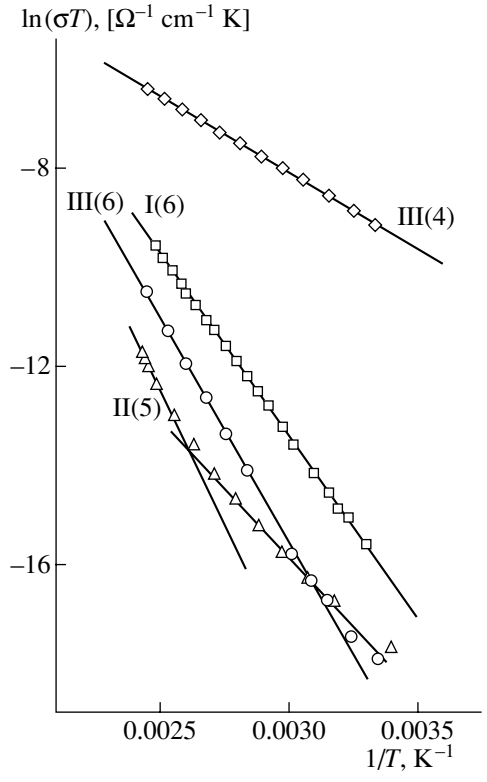

Fig. 2. Temperature dependence of conductivity of KDP crystals in the Arrhenius coordinates.

Thus, it can be concluded that crystals of the group A are the most ordered and their conductivity is determined mainly by intrinsic thermally activated proton defects with rather high enthalpies of formation and migration. It is clear that these crystals have the highest degree of perfection. The conductivity parameters of the crystals of the group B correspond to the impurity mode of conductivity. The line coefficient for the group

B, which is higher than for the group *A* in Fig. 3, also indicates the higher defect concentration in the proton sublattice of these crystals. Two specimens of the group A show the transition from the mode of low-temperature impurity conductivity with $H \approx 0.5$ eV to the high-temperature intrinsic conductivity with $H \approx 0.8$ eV. Figure 3 shows both *H*-values. It is seen from the table and Figs. 2 and 3 that the group C combines the crystals whose conductivity parameters and, therefore, also their defect structures, considerably differ from those of all the other crystals. This group is formed by three specimens of "alkali" crystal.

Different conductivities of the specimens can be understood if one takes into account the distribution of the cationic impurities in the crystals and the sectorial structure of the latter. The most specific situation is observed in an "alkali" crystal (pH 4.82). The change in the impurity concentration by a factor of 2.5 in the specimens prepared from one growth sector of the crystal is accompanied by the change in conductivity by three orders of magnitude. The absolute value of the impurity concentration and, thus, also the concentration of proton vacancies thus formed are not high enough to give rise to the change in the conductivity mechanism. Earlier, the topographs of this crystal showed the existence of growth macroinhomogeneities—the layers parallel to the {100} and {101} faces, characterized by elevated defect concentrations [5]. It seems that this results in an increase of the effective mobility of proton defects and the reduction of the enthalpy of conductivity activation.

The defect structure of "acid" crystals (pH 2.35) is formed in different way. These single crystals are characterized by homogeneous distribution of the cationic impurities and close conductivity parameters inside each growth sector. Thus, the temperature dependences of conductivity for specimens I(2) and I(4) are almost equivalent. On the other hand, the differences between the {100} and {101} growth sectors in these crystals are more pronounced than for other sectors: the conductivity of the specimens cut out from the {101} sector is three to four times higher than the conductivity of the specimens cut out from the {100} sector even at a somewhat lower impurity concentration. The same specimens are also characterized by lower activation energies, which seems to be associated with a more pronounced defect structure of the {101} growth sectors characteristic of the growth technology used and especially well seen on crystals grown from nonstoichiometric solutions. We mean here the symmetric rotation of the crystal in a crystallizer with the rotation axis coinciding with the *z*-axis of the crystal. In this case, the solution oversaturation decreases more pronouncedly at the (101) face, and, in growth from an acid solution, it should be accompanied by a more pronounced decrease of pH at the surfaces of growing faces of the pyramid. The latter fact can give rise to certain changes in the hydrogen stoichiometry in the {101} sector, e.g., to a higher proton concentration in interstitials in this sector than in the {100} sector or the replacement of some potassium ions by hydroxonium (H_3O^+). Proton migration over interstitials requires lower energy than the formation and migration of intrinsic thermally activated defects, which may result in a reduction of the energy of conductivity activation from a value of 0.9 eV in the {100} sector to 0.7 eV in the {101} one.

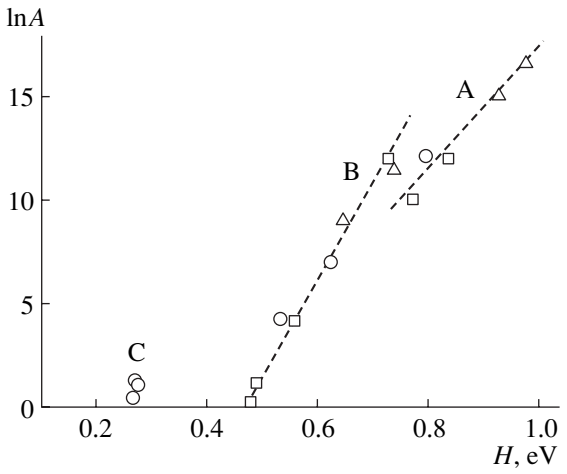

Fig. 3. Dependence of the logarithm of the coefficient *A* from Eq. (1) on the enthalpy of conductivity activation for three single crystals: (△) I, (□) II, and (○) III.

The defect structure of the hydrogen sublattice of the crystal grown under the normal conditions (pH 3.84) is formed mainly because of the appearance of proton vacancies during incorporation of natural cationic impurities. The concentration of such defects in a "normal" crystal is approximately equal to the total concentration of the cationic impurities (in molar fractions). In this crystal, the variations in the impurity concentration do not considerably change conductivity. Thus, a decrease of the impurity concentration in the {100} sector by a factor of about 3.5 is accompanied by a similar decrease of the specimen conductivity. An increase of conductivity of the specimen cut out from the {101} sector with a decrease of the impurity concentration is somewhat surprising and can be associated, e.g., with the effect of the intersectorial pyramid–pyramid boundary, in the direct vicinity of which the specimen II(6) was cut out. Thus, the conductivity parameters of the "normal" crystal are not worse than those of the "acid" one, moreover, the impurity concentration in the normal crystal decreases in the process of its growth.

CONCLUSION

It has been shown that conductivity can be strongly influenced by both hydrogen nonstoichiometry of the crystal during its growth from solutions of various acidities and the presence of impurities in the crystal, which give rise to the formation of defects in the proton sublattice. The results obtained show that the influence of

hydrogen nonstoichiometry on conductivity of KDP crystals is comparable with the effect of uncontrolled cationic impurities. Indeed, in the transitions from an acid to a normal and to an alkali crystal, the conductivity value changes but not more pronouncedly than it changes with the distance from the seed within one growth sector of an alkali crystal. The conductivity parameters of crystals grown from solutions with different pH values but the same variation in the impurity concentration change in different ways. Thus, if at the normal pH value, an increase of the impurity (Fe^{3+} and Al^{3+}) concentration by a factor from three to four in the {100} sector results in an increase of conductivity also by a factor from three to four at pH 4.82, an increase in the impurity concentration by a factor of 2.5 results in an increase of conductivity by more than three orders of magnitude. In this case, the specimens are characterized by the maximum impurity concentration ($>10^{-2}$ mol %) and the presence of macroinhomogeneities. The following conclusions seem to be important for practice.

Conductivity and dielectric properties of KDP crystals are essentially dependent on all the three factors studied—the sectorial structure, the pH value of the crystallization solution, and the related distribution of cationic impurities, mainly, Fe^{3+} and Al^{3+}.

The parameters characterizing conductivity of KDP crystals can pronouncedly differ even within one growth sector. This is most clearly seen on crystals with pH 4.82, where specimen conductivities differ by three orders of magnitudes.

The energy of conductivity activation tends to decrease, whereas the conductivity itself tends to increase with an increase of the pH value of the crystallization solution and the impurity concentration, which depends on an increase in the proton-vacancy concentration responsible for conductivity. Thus, the KDP crystals optimal for electrooptical applications should be grown at pH 2.3–4.0 with due regard for the characteristic features of the defect-structure formation considered above.

ACKNOWLEDGMENTS

This study was supported by the Russian Foundation for Basic Research, project no. 99-02-17443 and the Shuvalov Leading Scientific School, project no. 96-15-504.

REFERENCES

1. M. O'Keefe and C. T. Perrino, J. Phys. Chem. Solids **28**, 211 (1967).
2. L. B. Harris and G. J. Vella, J. Chem. Phys. **58**, 4550 (1973).
3. A. I. Baranov, V. P. Khiznichenko, and L. A. Shuvalov, Ferroelectrics **100**, 135 (1989).
4. O. O. Damasceno, J. Oliveira, and A. L. Oliveira, Solid State Ionics **31**, 49 (1988).
5. E. P. Efremova, V. A. Kuznetsov, A. Yu. Klimova, *et al.*, Kristallografiya **38** (5), 171 (1993) [Crystallogr. Rep. **38**, 674 (1993)].
6. T. A. Eremina, V. A. Kuznetsov, T. M. Okhrimenko, and N. G. Furmanova, Kristallografiya **41** (4), 717 (1996) [Crystallogr. Rep. **41**, 680 (1996)].
7. N. F. Mott and R. W. Gurney, *Electronic Processes in Ionic Crystals* (Clarendon, Oxford, 1948; Inostrannaya Literatura, Moscow, 1950).

Translated by L. Man

Crystallography Reports, Vol. 46, No. 5, 2001, pp. 835–841. Translated from Kristallografiya, Vol. 46, No. 5, 2001, pp. 909–915.

PHYSICAL PROPERTIES OF CRYSTALS

Dedicated to the memory of B.K. Vainshtein

Analytical Description of the Yield Drop in the Alexander–Haasen Model

B. V. Petukhov

Shubnikov Institute of Crystallography, Russian Academy of Sciences, Leninskiĭ pr. 59, Moscow, 117333 Russia

e-mail: petukhov@ns.crys.ras.ru

Received May 15, 2000

Abstract—The analytical solution of the equations of the Alexander–Haasen model, which describes the shape of the deformation-curve peak (the so-called yield drop), has been obtained for the case of a low initial dislocation density. It is shown that the self-development of the dislocation structure results in the specific kinetic transition with a dramatic decrease of the elastic-deformation rate and an increase of the plastic-flow rate. It is natural to interpret this phenomenon as an elastoplastic transition, and to consider the corresponding stress as the yield stress despite the fact that, being considered in the traditional way, its value does not coincide with either the upper or lower yield stress. The conditions of the existence of the yield drop are studied, and the quantitative criterion of the corresponding change in the deformation-curve shape is proposed. © *2001 MAIK "Nauka/Interperiodica".*

INTRODUCTION

As is well known, deformation of materials with an increasing stress results in the transition from the elastic deformation to the plastic flow of the material. The initial section of the stress-strain or stress-time curve, hereafter called the deformation curve, is characterized by a pronounced slope determined by the elastic moduli of the material. In the vicinity of a certain stress τ_0 (the so-called yield stress), it is changed into the section with a relatively small slope, which describes the so-called easy-slide stage of deformation. In some cases, the more complicated behavior of the deformation curve is observed, with the formation of an additional peak of the deforming stress in the transition region. In this case, one considers the upper τ_u and the lower τ_l yield stresses.

The yield stresses are the most important characteristics of the mechanical properties of materials; they were considered in a large number of publications [1–4]. The behavior of the yield stresses depending on the temperature and deformation-rate variations allows one to determine the mechanisms controlling the plastic flow of materials—kinetics of dislocation multiplication and mobility, the spectrum of dislocation sources, etc. To establish the quantitative relationships, various theoretical models were proposed to describe the behavior of loaded materials. Depending on the aim with which these models were developed, they are divided into the dynamic models (in which the transition to easy gliding is associated with the laws of the temporal evolution of the processes) and the static models (in which the yield stress is determined by the characteristic stress providing the operation of the dislocation sources) [5]. Various dislocation mechanisms associated with the yield stress are considered in [6]. The interpretation of the yield stress in the static models is relatively simple, and the sharp transition from the elastic to plastic deformation is predetermined by the steep change in the stress spectrum of the source. The situation with the dynamic models is less obvious [7–10], and the transition to the yield stage is associated with the self-organization of the kinetic process. One of the most successful and popular dynamic models was developed by Alexander and Haasen [10]. The dependences of the upper and the lower yield stress on various parameters calculated within this model provided the explanation of numerous characteristic features of the behavior of silicon. This model satisfactorily agrees with the experimental data, and does not become less attractive despite the appearance of promising new alternative approaches based on the mesoscopic models of the dislocation dynamics [11].

The present study is aimed at the further development of the Alexander–Haasen model, which seems to be important because of a number of serious problems encountered in the interpretation of the experimental data on the yield point of materials. The formulation of these problems reflects the ambiguous interpretation of the transition from the elastic to the plastic behavior even within the framework of well-known models, because there is no sufficiently complete analytical solution for these models and explicit description of the

1063-7745/01/4605-0835$21.00

deformation curves in the vicinity of this transition. We attempt to close this gap for the generalized Alexander–Haasen model. Not going into all the details of the determination of the yield point, we should like to remind here the simplest method of its determination (with due regard for its shortcoming) in order to provide better understanding of the problem formulation. The conventional definition of the yield stress as a stress above which the irreversible plastic deformation is observed [12] is quite sufficient in many occasions, but, at the same time, it is also only approximate, because some plastic deformation arises due to dislocation motion irrespectively of the load applied. Therefore, in many instances, the yield point is defined rather formally as a stress corresponding to a certain fixed deformation, e.g., 0.2%. This definition has nothing to do with the physics of yield appearance if does not even foresee the possibility of the occurrence of a specific phenomenon that can manifest itself in the formation of some specific features of the deformation curve in mechanical tests. Below, considering a simple example of the kinetic Alexander–Haasen model, we shall show that this specific phenomenon, which attributes the qualitative aspect to the yield stress, is really possible and study the conditions of its manifestation.

ALEXANDER–HAASEN MODEL

Within the Alexander–Haasen model, the transition to the plastic flow of a material is associated with the avalanche-like multiplication of dislocations. The corresponding experimental data are generalized by the following phenomenological equation [10]

$$d\rho/dt = w\tau_e\rho v, \tag{1}$$

where ρ is the density of mobile dislocations, v is the velocity of their motion, w is the multiplication constant, τ_e is the effective stress equal to the difference of the external, τ, and the internal $\tau_i = \alpha\rho^{1/2}$, stresses

$$\tau_e = \tau - \tau_i = \tau - \alpha\rho^{1/2}. \tag{2}$$

Here α is the coefficient of the so-called Taylor hardening, which determines the contribution of random elastic fields of dislocations to the large-scale potential relief hindering the dislocation motion. It was shown that equation (1) also describes the dislocation multiplication in quasicrystals [13].

In accordance with the dislocation-mobility measurements [14–16], the dependence of the dislocation velocity on stress and temperature is given by the expression

$$v = \tau_e^m B(T), \tag{3}$$

where $B(T)$ is the temperature-dependent part, e.g., the Arrhenius factor

$$B(T) = v_0\exp(-G/kT). \tag{4}$$

Here G is the activation energy, k is the Boltzmann constant, T is the temperature, and v_0 is the constant preexponential factor. The original Alexander–Haasen model was used for silicon (the case $m = 1$). We shall consider here the generalized model at arbitrary m values. The method of the solution used here also allows the generalization of the equation, which describes the kinetics of dislocation multiplication (1), but below we limit ourselves to a simpler case.

The deformation kinetics is described by the expression

$$(1/S)d\tau/dt = \dot\varepsilon - \rho b v, \tag{5}$$

where S is the combined elastic modulus, $\dot\varepsilon$ is the deformation rate, and b is the magnitude of the Burgers vector.

Alexander and Haasen solved Eqs. (1)–(5) separately in the vicinity of the upper and the lower yield stresses and used different approximations. The upper stress τ_u was determined without the allowance for hardening by the method of iterations of kinetic equations (1)–(5). The lower yield stress τ_l was determined under the assumption that the elastic component of the deformation rate can be ignored, i.e., by replacing Eq. (5) by the Orowan equation $\dot\varepsilon = \rho b v$. These approximations are efficient at comparatively low values of the hardening coefficient α. At the same time, it is obvious that this description is far from being exhaustive. The transitions from the dramatic behavior of deformation in the vicinity of the yield drop to the smooth behavior in the vicinity of τ_l have not been studied as yet. Moreover, since the approximations made in the calculation of τ_u and τ_l are inconsistent, the deformation behavior at a high hardening coefficient α, when τ_u and τ_l merge together, the yield drop disappears, and the deformation curves become monotonic, has not been studied.

Now consider the solution within the Alexander–Haasen model in more detail. To simplify the formulas to be derived, we write the model equations in the dimensionless form by measuring the dislocation density ρ in the units

$$\rho_1 = (\dot\varepsilon/B(T))^{2/(m+2)}(w/S)^{m/(m+2)}, \tag{6}$$

the stresses, in the units

$$\tau_1 = (S\dot\varepsilon/(wB(T)))^{1/(m+2)}, \tag{7}$$

and time, in the units

$$t_1 = (wB(T))^{-1/(m+2)}(S\dot\varepsilon)^{-(m+1)/(m+2)}. \tag{8}$$

To avoid the cumbersome formulas, we retain the notation used earlier for the dimensionless variables τ, ρ, and t. Then the equations take the form

$$d\rho/dt = \rho\tau_e^{m+1}, \tag{9}$$

$$d\tau_e/dt = 1 - \rho\tau_e^m - 0.5a\rho^{1/2}\tau_e^{m+1}. \tag{10}$$

Here $a = \alpha(w/(bS))^{1/2}$ is the dimensionless hardening parameter. Now, reduce the system (9) and (10) to one

equation. With this aim, integrate Eq. (9) with respect to time

$$\rho = \rho_0 \exp(\varphi), \tag{11}$$

where

$$\varphi = \int_0^t \tau_e^{m+1}(t')dt', \tag{12}$$

so that $\dot{\varphi} = \tau_e^{m+1}$. Here ρ_0 is the initial value of the dislocation density (measured in the ρ_1 units) assumed to have small but finite value.

Now change from the variable t to the variable φ in Eq. (10) using the equations $d\tau_e/dt = (d\tau_e/d\varphi)\dot{\varphi} = \tau_e^{m+1} d\tau_e/d\varphi$. We arrive at the closed equation

$$\tau_e^{m+1} d\tau_e/d\varphi = 1 - \rho_0 e^{\varphi}\tau_e^m - 0.5a\rho_0^{1/2} e^{\varphi/2}\tau_e^{m+1}. \tag{13}$$

Knowing the solution of Eq. (13), $\tau_e(\varphi)$, we can readily obtain the complete kinetics of the deformation process from the equation

$$t = \int_0^{\varphi} \frac{d\varphi'}{\tau_e^{m+1}(\varphi')}, \tag{14}$$

relating the variables φ and t.

The transformation of the above equations allowed us to single out the dependence of various quantities on most of the problem parameters in the form of the explicit scale factors (6)–(8) and to determine those parameters which are essential for characterization of the solution types. There are only two such parameters in (13)—ρ_0 and a. Consider first the important particular case of negligible hardening, $a \longrightarrow 0$.

THE YIELD STRESS AS A POINT WHERE THE KINETIC DEPENDENCES CHANGE THEIR CHARACTER

At $a = 0$, equation (13) takes the form

$$\tau^{m+1} d\tau/d\varphi = 1 - \rho_0 e^{\varphi}\tau^m. \tag{15}$$

The low initial dislocation density ($\rho_0 \ll 1$) allows one to solve Eq. (15) by the method of successive approximations. In the zero approximation, we begin the consideration with the equation $\tau^{m+1} d\tau/d\varphi = 1$ having the solution $\tau = \tau_0(\varphi) = [(m+2)\varphi]^{1/(m+2)}$. Substituting this equation into the right-hand side of Eq. (15) and performing integration, we arrive at the next approximation. Because of smallness of ρ_0, we can expect noticeable deviations from the zero approximation only at high φ values, $\varphi \gg 1$. Then, the first iteration in this region yields

$$\tau_1(\varphi) \approx \tau_0(\varphi) - \rho_0 e^{\varphi}/\tau_0(\varphi). \tag{16}$$

Although the correction to $\tau_0(\varphi)$ in the applicability range of perturbation theory, $\delta\tau = -\rho_0 e^{\varphi}/\tau_0(\varphi)$, is relatively small, its pronounced exponential dependence on φ can make the derivative of $\delta\tau$ with respect to φ equal to the derivative of $\tau_0(\varphi)$. Having the opposite sign, the change in $\delta\tau$ can compensate an increase in $\tau_0(\varphi)$, which would result in the nonmonotonic behavior of $\tau_1(\varphi)$ and the formation of the maximum corresponding to the upper yield stress.

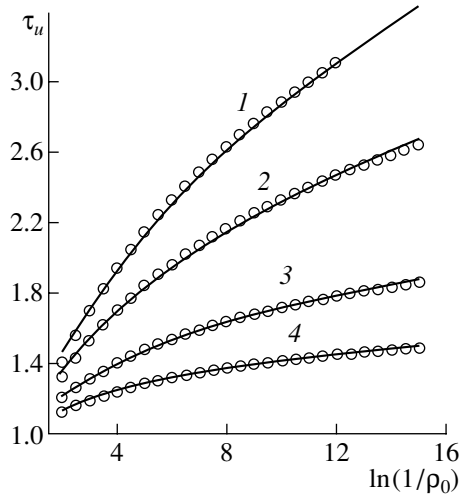

Fig. 1. Upper yield stress as a function of the initial dislocation density at different values of m estimated by Eq. (17): m is equal to (*1*) 1, (*2*) 2, (*3*) 5, and (*4*) 10. Circles indicate the results of the numerical solution of Eqs. (9) and (10) at $a = 0$.

Figure 1 illustrates the dependence of the upper yield stress on the initial dislocation density ρ_0 for m values obtained in the numerical calculation with the use of Eq. (16). For a more convenient use of the model during processing of the experimental data, it is useful to obtain the explicit analytical approximation of τ_u. Here is one of the possible approximations

$$\tau_u = \ln^n(1.44/\rho_0), \tag{17}$$

where

$$n = 1.188/(m + 2.226)^{0.83}. \tag{18}$$

The correspondence of this approximation (circles) to the numerical solution of Eq. (15) is illustrated by Fig. 1.

Because of the exponential increase of the contribution containing ρ_0 to Eq. (15) with an increase of φ, this iteration procedure has a very limited applicability range. One can readily see that $\tau_0(\varphi)$ corresponds to the stress variation along the elastic part of the deformation curve. In terms of physics, the applicability of the iteration procedure signifies that the stress change is the key factor at the first stage of this process, whereas the dislocation-density change is rather small and, therefore, cannot seriously affect the deformation process. An increasing contribution of the plastic component to the material deformation results in an unloading stress $\delta\tau$. At the beginning, the unloading stress is relatively low, but upon some time, the rate of its variation

becomes not only comparable with the rate of the elastic-stress change, but even much higher than it. As a result, the deformation stress first stops increasing at the point corresponding to the upper yield stress and then starts decreasing, which, finally, provides the yield drop. This stage of the process cannot be described by the solution corresponding to the iteration procedure.

Thus, a more detailed solution requires another approach. Now, we have to describe the deformation curve in a wider interval outside the immediate vicinity of the maximum. This description would allow revealing the specific role of the yield stress and the corresponding appearance of a certain qualitative new phenomenon.

Now, represent Eq. (15) in a more convenient form with the aid of a new unknown function $w = \tau^{m+2}/(m+2)$,

$$dw/d\varphi = 1 - \rho_{01}\exp(\varphi)w^{m/(m+2)}. \quad (19)$$

Here $\rho_{01} = \rho_0(m+2)^{m/(m+2)}$. The zero iteration yields $w \approx \varphi$. For the deviation of the function w_1 from φ at the initial interval of φ variation, φ $w_1 = w - \varphi$, we obtain $w_1 \ll \varphi$. Then the next iteration of Eq. (19) yields

$$w_1 \approx -\rho_{01}\int_0^\varphi \varphi'^{\frac{m}{m+2}} e^{\varphi'} d\varphi', \quad (20)$$

At $\varphi \gg 1$, the approximate calculation of the integral in Eq. (20) gives

$$w_1 \approx -\rho_{01} e^{\varphi}\varphi^{m/(m+2)}. \quad (21)$$

Approximation (21) is valid in the range of moderately large φ unless $|w_1| \ll \varphi$. The derivative of w_1 with respect to φ has the exponential term e^{φ} and, therefore, has a high value to the right of the point of the maximum in the applicability range of Eq. (21) and is approximately equal to $dw_1/d\varphi \approx w_1$ [which is obvious from the comparison of Eqs. (20) and (21)]. In the wider range we are interested in, this relationship is valid only within the order of magnitude. Thus, it can be used for determining w in a wider range of φ values. Let us assume that $w_1 = \varphi u$ and write the equation for u with due regard for the fact that $dw_1/d\varphi = \varphi du/d\varphi - u \approx \varphi du/d\varphi$. The approximate equality is based on the fact that, similar to w_1, the analogous relationship should also take place for u, i.e., $du/d\varphi \sim u$, and, therefore, the first term predominates at $\varphi \gg 1$. As a result, we arrive at the equation for u with the separable variables

$$du/d\varphi \approx -\rho_{01} e^{\varphi}\varphi^{-2/(m+2)}(1+u)^{m/(m+2)}, \quad (22)$$

which can readily be integrated to yield

$$((m+2)/2)(1+u)^{2/(m+2)} = -\rho_{01}\int_0^\varphi \varphi'^{-\frac{2}{m+2}} e^{\varphi'} d\varphi' + C \approx -\rho_{01} e^{\varphi}\varphi^{-2/(m+2)} + C. \quad (23)$$

Here C is the integration constant, which can be determined from the comparison of Eq. (23) with Eq. (21) which is valid at moderately high φ values. One can readily see that good correspondence is attained at $C = (m+2)/2$.

Thus, coming back from the function u to stresses, we obtain

$$\tau(\varphi) = \tau_0(\varphi) \times \left[1 - \frac{2\rho_0}{(m+2)^{2/(m+2)}}\int_0^\varphi \varphi'^{-\frac{2}{m+2}} e^{\varphi'} d\varphi'\right]^{1/2}. \quad (24)$$

At high φ values, the integral in Eq. (24) can easily be evaluated and the formula is simplified,

$$\tau(\varphi) = \tau_0(\varphi)[1 - 2\rho_0 e^{\varphi}/\tau_0^2(\varphi)]^{1/2}. \quad (25)$$

One can also see that at relatively low dislocation density, expansion (25) in ρ agrees quite well with Eq. (16). Therefore, Eq. (25) smoothly matches the solution in the vicinity of the maximum and extends the solution of Eq. (15) to a larger range.

As is seen from Fig. 2, at small ρ_0 values, this equation describes quite well the stress in the large region around the maximum (curve *1*). Equation (25) shows that the $\tau(\varphi)$ value drastically decreases with an increase of φ to the right of the point of the maximum. As will be shown somewhat later, a decrease in $\tau(\varphi)$ down to the zero value "dictated" by Eq. (25) does not really happen, but this requirement indicates the drastic change in the solution nature. Equation (25) is valid if $\varphi du/d\varphi \gg u$ and can become invalid if $u \longrightarrow -1$ [when φ approaches the point φ_0, i.e., the zero value of the square bracket in (25)]. Using Eq. (25) and the conditions $\varphi du/d\varphi \sim u$, we arrive at the range where the solution becomes invalid:

$$\delta\varphi = \varphi - \varphi_0 \sim \varphi_0^{-2/m}. \quad (26)$$

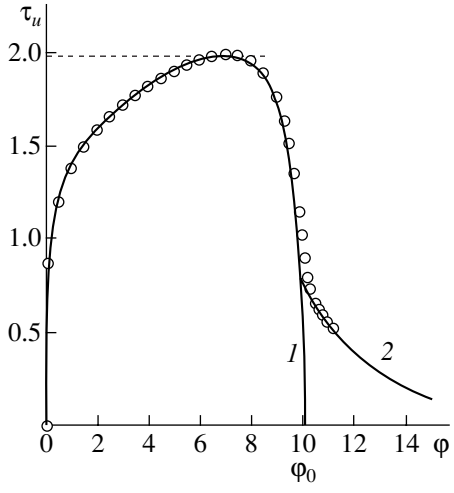

Fig. 2. Illustrating the change of the type of the solution of Eq. (15) ($m = 3$, $\rho_0 = 10^{-4}$). Curve *1* represents Eq. (24) and curve (*2*), Eq. (27). Circles are the results of the numerical solution of the differential equation (15).

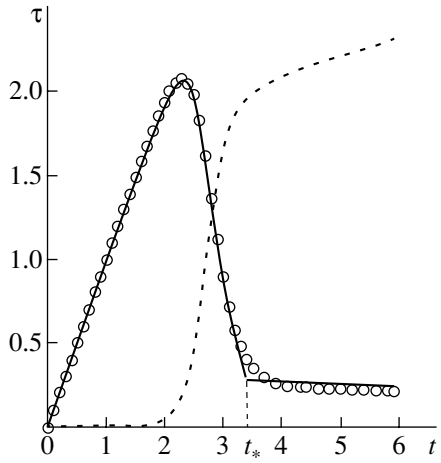

Fig. 3. Deformation curve at $m = 1$ and $\rho_0 = 10^{-2}$. Circles are the results of the numerical solution of differential Eqs. (9) and (10) at $a = 0$ and t_* is the point, where the solution changes its nature. Dashed line describes the function $0.5\rho(t)$.

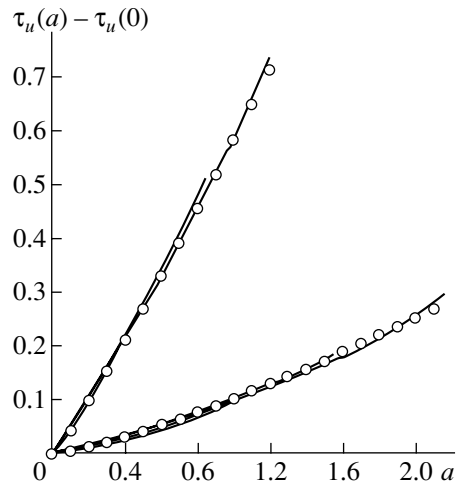

Fig. 4. Upper yield stress as a function of the hardening coefficient a. The upper family of curves corresponds to $\ln(1/\rho_0) = 10$ and $m = 1, 2, 5, 10$ and the lower family of curves, to $\ln(1/\rho_0) = 2$ at $m = 1, 2, 5, 10$ (the shorter lines correspond to higher m values).

Since $\varphi_0 \gg 1$ at small ρ_0, the solution becomes invalid only in a comparatively narrow neighborhood of the point φ_0.

At $\varphi > \varphi_0$, the solution is obtained from the condition $d\tau/d\varphi \longrightarrow 0$ in the "quasistationary approximation" and has qualitatively different form:

$$\tau(\varphi) \approx (\rho_0 e^{\varphi})^{-1/m}. \quad (27)$$

To be sure of the validity of the above solution, estimate the value of $d\tau/dt = \tau^{m+1} d\tau/d\varphi$. Differentiating Eq. (27), we obtain $d\tau/d\varphi \approx -\tau/m$. As follows from Eq. (25), in the vicinity of φ_0, we have $\rho(\varphi) \approx \tau_0^2(\varphi)/2$ (in virtue of the continuity of $\rho(\varphi$ and $\tau(\varphi)$, the latter relationship can also be used at $\varphi > \varphi_0$). Thus, $\tau \approx (2/\tau_0^2(\varphi))^{1/m}$ and $d\tau/dt \approx -\{[2/\tau_0^2(\varphi)]^{(m+2)/m)}\}/m \ll 1$, because $\tau_0(\varphi)$ at large φ is also large. Therefore, the neglect of the left-hand side of Eq. (15) at $\tau(\varphi)$ values determined by Eq. (27) is quite admissible.

In principle, one can smoothly change from solution (25) to solution (27) in the vicinity of the point φ_0. However, because of the narrow interval of transition indicated above, this refinement is not especially important, and, in the first approximation, one can limit the consideration to a simple intersection of the dependences described by Eqs. (25) and (27) at a certain "transition point" $\varphi = \varphi_*$.

The dramatic change in the behavior of the deformation curve indicates that, ignoring the width of the transient region, we can state that, at a certain moment, the kinetics of deformation undergoes the qualitative change. In this case, the elastic-deformation rate $d\tau/dt$ changes from the value of the order of unity (in $\sim[2/\tau_0^2(\varphi)]^{(m+2)/m}/m$ dimensionless units) to a low value $d\tau/dt$, so that the plastic deformation of the material becomes the prevalent process. This change in the character of the deformation curve can be interpreted as an elastoplastic transition. The solution obtained gives the complete quantitative description the appearance of yield and allows the expression of the width of the transition region via the system parameters such as the initial dislocation density ρ_0, the exponent of the stress sensitivity m, etc.

As has already been indicated, the transition from the curve $\tau(\varphi)$ to the true deformation curve is made with the use of Eq. (14) and the equation relating the dimensionless time and deformation $\varepsilon = \dot{\varepsilon}\, t/t_1$. The equation

$$t = \int_0^{\varphi} \frac{d\varphi'}{[\tau_0^2(\varphi') - 2\rho_0 \exp(\varphi')]^{(m+1)/2}} \quad (28)$$

and Eq. (25) provide the parametric representation (with the parameter φ) of the dependence $\tau(t)$ in the region preceding the transition $t < t_*$. The transition moment t_* is determined by Eq. (28) with $\varphi = \varphi_*$. Applying Eq. (27) to the region on the right from the transition point, we obtain the smooth monotonic dependence

$$\tau(t) = [((m+1)/m)(t - t_*) + 1/\tau_*^{m+1}]^{-1/(m+1)}. \quad (29)$$

Figure 3 compares the curves obtained analytically from Eqs. (25) and (27) with the numerical solution of

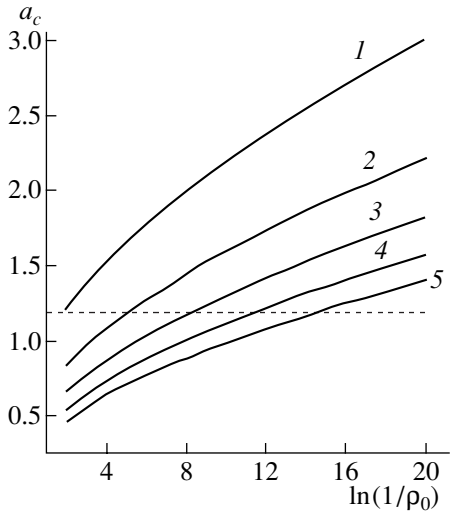

Fig. 5. The dependence of a_c on ρ_0 at various m (*1*, *2*, *3*, *4*, and *5*). The dashed line separates the regions of the parameters which satisfy (above the line) and do not satisfy (below the line) criterion (33) of existence of the yield drop at a certain fixed hardening level.

Eq. (10). It is seen that these curves agree quite satisfactorily everywhere except for a narrow transition region.

CRITERION OF YIELD-DROP EXISTENCE

The method used for solving Eq. (15) can also be used to solve the general equation (13) with an arbitrary hardening value. However, the formulas obtained are too cumbersome, and, therefore, the general analytical solution in the explicit form is omitted here. We limit ourselves to some qualitative results and analytical approximations.

Unlike the upper yield stress τ_u weakly dependent on the hardening coefficient a, the lower yield stress τ_l noticeably increases with an increase of a. As a result, at high $a = a_c$ value, the maximum of the curve $\tau(\varphi)$ or $\tau(t)$ coincides with the minimum corresponding to the lower yield stress, whereas at higher a values, the deformation curve becomes monotonic.

Following Alexander and Haasen, we can determine the lower yield stress in the quasistationary approximation ignoring the contribution of the elastic deformation on the right of the transition point. To do so, we assume that $d\tau/dt = 1 - \rho\tau_e^m \approx 0$, and obtain $\tau_e \approx \rho^{-1/m}$. Therefore, the total stress is

$$\tau \approx \rho^{-1/m} + a\rho^{1/2}. \tag{30}$$

Determining the minimum of the τ_l curve with respect to ρ, we obtain the lower yield stress

$$\tau_l = ((m+2)/m)(ma/2)^{2/(m+2)}. \tag{31}$$

It should be indicated that the value of τ_l is independent of both initial dislocation density and the characteristics of the kinetics of dislocation multiplication w (the latter takes place for the dimensional quantity). This independence is, of course, only approximate, because it takes place within the quasistationary approximation.

As the numerical solution of Eq. (13) shows, the contribution of hardening to the upper yield stress only weakly depends on m. This is illustrated by Fig. 4 for two considerably different ρ_0 values—$\ln(1/\rho_0) = 2$ and $\ln(1/\rho_0) = 10$. Therefore, in this case, a simplified analytical formula approximately valid for all the m values should be more useful than the exact solution. As such an approximation of the hardening-dependent addition to the upper yield stress, $\Delta\tau_u(a) = \tau_u(a) - \tau_u(0)$, one can use the following expression

$$\Delta\tau_u(a) \approx \frac{103.5}{[\ln(380/\rho_0)]^{2.5}} a^p, \tag{32}$$

where

$$p = 0.8041 - 0.231[\ln(1.44/\rho_0)]^{1/3}.$$

The correspondence of this approximation to the numerical solution of Eq. (13) is illustrated by Fig. 4.

In the publications on yield stress, one often raises the question on the conditions for the yield-drop formation and formulates the approximate qualitative criteria of its formation such as the existence of the low initial dislocation density and low sensitivity of the dislocation velocity to stresses [10, 11]. The calculation made in our study provides the quantitative formulation of such a criterion.

The yield drop can exist if the hardening coefficient a is less than the value of $a_c(\rho_0, m)$ at which the upper and lower yield stresses coincide $\tau_u(a_c) = \tau_l(a_c)$:

$$a < a_c(\rho_0, m). \tag{33}$$

The function $a_c(\rho_0, m)$ calculated with the use of the above expressions for $\tau_u(a)$ and $\tau_l(a)$ is illustrated by Fig. 5. One can see that the above qualitative conditions of the yield-drop appearance on the deformation curves are satisfied. The lower the initial dislocation density and the exponent of the stress sensitivity m, the wider the region of the yield-drop manifestation. Moreover, criterion (33) clarifies the role of the remaining parameters of the problem such as T, $\dot{\varepsilon}$, and w that influence the scale factors in ρ_0 and a.

Although at $a > a_c$, no yield drop is formed and the deformation curve is monotonic, the above phenomenon of the dramatic change in the character of the kinetic curves in the vicinity of a certain stress is preserved and attributes the "qualitative sense" to the notion of the yield stress concept.

CONCLUSION

Numerous experiments on semiconductor materials showed that both upper and lower yield stresses show the same dependence on the deformation rate and the temperature

$$\tau_{u,l} \sim \dot{\varepsilon}^{1/n} \exp(U/kT) \quad (34)$$

with approximately equal n and U values [10]. In the formulation of the model suggested here, this fact obviously follows from the possible scale transformation, which singles out the main dependences of various quantities on the parameters in the form of dimensional factors still prior to the solution of the equations. For stresses, this factor is given by Eq. (7) which, at the thermally activated dislocation motion, acquires the form of Eq. (34). For silicon, the experimental data correspond to $n \approx 3$, which determines the choice of the exponent $m = 1$ in the dislocation mobility (3). To interpret most of the experimental data, e.g., a decrease of the yield stress with an increase of the temperature, it is sufficient to know only the scale factors. The solution of the equations allows the study of finer effects associated with the changes in the deformation-curve shape. It is shown that the transition of the elastic deformation of the material to predominantly plastic deformation occurs in a relatively narrow interval. Denoting the deformation value prior to the attainment of the yield stress by ε_p, the prevailing contribution to the deformation rate changes from elastic to plastic in the range $\delta\varepsilon \ll \varepsilon_p$. This interval is the narrower, the lower the initial dislocation density or, in terms of the dimensional quantities, the lower the value of the parameter ρ_0/ρ_1, where ρ_1 is given by Eq. (6).

Ignoring the width of the transition region, one can consider "the point" of elastoplastic transition. This point does not coincide either with the upper or the lower yield stresses and, we believe, is an important characteristic of the kinetics of the deformation process in materials. The existence of sharp elastoplastic transition is a specific feature of the self-development of the kinetic process inherent in the model considered.

REFERENCES

1. R. Berner and H. Kronmuller, *Plastische Verformung von Einkristallen*, in *Moderne Probleme der Metallphysik*, Ed. by A. Seeger (Springer-Verlag, Berlin, 1965; Mir, Moscow, 1969).
2. B. I. Smirnov, *Dislocation Structure and Crystal Hardening* (Nauka, Leningrad, 1981).
3. A. A. Urusovskaya, in *Modern Crystallography*, Vol. 4: *Physical Properties of Crystals*, Ed. by B. K. Vainshtein, A. A. Chernov, and L. A. Shuvalov (Nauka, Moscow, 1981; Springer-Verlag, Berlin, 1988), Chap. 2.
4. T. Suzuki, H. Yosinaga, and S. Takeuti, *Dislocation Dynamics and Plasticity* (Syokabo, Tokyo, 1986; Mir, Moscow, 1989).
5. A. N. Orlov, Fiz. Tverd. Tela (Leningrad) **8**, 832 (1966) [Sov. Phys. Solid State **8**, 666 (1966)].
6. V. Z. Bengus, T. P. Kovalenko, and E. D. Tabachnikova, Izv. Vyssh. Uchebn. Zaved., Fiz. **27** (6), 56 (1984).
7. W. G. Johnston, J. Appl. Phys. **33**, 2716 (1962).
8. V. G. Govorkov, V. L. Indenbom, V. S. Papkov, and V. R. Regel, Fiz. Tverd. Tela (Leningrad) **6** (4), 1039 (1964) [Sov. Phys. Solid State **6**, 802 (1964)].
9. B. Sestak and A. Seeger, Z. Metallkd. **69**, 195 (1978).
10. H. Alexander and P. Haasen, Solid State Phys. **22**, 27 (1968).
11. A. Moulin, M. Condat, and L. P. Kubin, Acta Mater. **47** (10), 2879 (1999).
12. J. Friedel, *Dislocations* (Pergamon, Oxford, 1964; Mir, Moscow, 1967).
13. U. Messerschmidt, M. Bartsch, M. Feuerbacher, *et al.*, Philos. Mag. A **80** (5), 1165 (2000).
14. B. Ya. Farber, Yu. L. Iunun, V. I. Nikitenko, *et al.*, Phys. Status Solidi A **138**, 557 (1993).
15. M. Imai and K. Sumino, Philos. Mag. A **47**, 599 (1983).
16. A. George and J. Rabier, Rev. Phys. Appl. **22**, 941 (1987); **22**, 1327 (1987).

Translated by L. Man

Crystallography Reports, Vol. 46, No. 5, 2001, pp. 842–844. Translated from Kristallografiya, Vol. 46, No. 5, 2001, pp. 916–918.

PHYSICAL PROPERTIES OF CRYSTALS

Dedicated to the memory of B.K. Vainshtein

Dispersionless Polaritons on a Twist Boundary in Optically Uniaxial Crystals

A. N. Darinskiĭ

Shubnikov Institute of Crystallography, Russian Academy of Sciences, Leninskiĭ pr. 59, Moscow, 117333 Russia
e-mail: ADar@ns.crys.ras.ru

Received February 2, 2001

Abstract—It has been shown that the so-called dispersionless localized waves (polaritons) can exist in a bicrystal formed by two identical crystals. The optical axes of these crystals lie at the interface at a certain angle to one another. The exact analytic expression is derived for the velocity of the wave propagating along the bisector of the angle between the optical axes in the upper and the lower parts of the bicrystal. The wave structure is analyzed for several limiting cases. *© 2001 MAIK "Nauka/Interperiodica".*

Let a bulk electromagnetic wave propagate in an optically anisotropic medium with the group velocity parallel to a plane. Now, cut the medium along this plane and rotate both parts so that they would form an angle φ with respect to one another. Then a natural question arises: what would happen with the bulk wave? We shall show that under certain conditions, the bulk wave would be "localized" and give rise to polaritons on the surface at $\varphi \neq 0$. These polaritons have no frequency dependence of the dielectric permittivity and, thus, they can be referred to as dispersionless.

The existence of dispersionless polaritons was considered in [1], where the localized waves were considered at the isotropic medium—uniaxial crystal interface. These polaritons appear within a certain range of propagation directions. Also, the permittivity of the isotropic medium must exceed unity. It is worth noting that the condition for polariton existence at the interface of semiinfinite media is a certain dependence of the dielectric permittivity on frequency [2, 3]. In particular, if there are two isotropic media, the dielectric permittivity of one of these media should be negative.

Consider an optically uniaxial crystal with the dielectric permittivity $\hat{\varepsilon} = \varepsilon_0 + (\varepsilon_e - \varepsilon_o)\mathbf{c} \otimes \mathbf{c}$, where c ($|\mathbf{c}| = 1$) is the direction of the optical axis and the symbol $\otimes$ denotes the dyadic multiplication. The vector $\mathbf{n}$ ($|\mathbf{n}| = 1$) is the normal to the crystal boundary and the vector $\mathbf{m}$ ($|\mathbf{m} = 1$) lies in the boundary plane and specifies the direction of the wave propagation (Fig. 1). We assume that $\mathbf{c}$ also lies in the boundary plane and forms an angle $(\pi/2 - \varphi)$ with $\mathbf{m}$.

Using the well-known expressions for $\mathbf{E}_{o\,e}$ and $\mathbf{H}_{o\,e}$ ([4], p. 317), we find the tangential components of these vectors:

$$E_{o\,m} = -p_o\cos\varphi, \quad E_{o\,t} = -p_o\sin\varphi,$$
$$H_{o\,m} = -\frac{p_o^2}{v}\sin\varphi, \quad H_{o\,t} = v\varepsilon_o\cos\varphi, \tag{1}$$

$$E_{e\,m} = \frac{p_o^2}{v}\sin\varphi, \quad E_{e\,t} = -\varepsilon_o\cos\varphi,$$
$$H_{e\,m} = -\frac{\varepsilon_o p_e}{v}\cos\varphi, \quad H_{e\,t} = -\frac{\varepsilon_o p_e}{v}\sin\varphi, \tag{2}$$

where the subscripts m and t indicate the projections onto $\mathbf{m}$ and $\mathbf{t} = [\mathbf{n} \times \mathbf{m}]$, respectively, $v = \omega/ck$ is the wave velocity along the boundary measured in the units of the light speed c in vacuum (k is the tangential projection of the wavevector);

$$p_o = i\sqrt{1 - v^2/v_o^2}, \quad p_e = i\sqrt{\varepsilon_e(v_e^2 - v^2)} \tag{3}$$

are the decay factors of the ordinary and extraordinary waves (it is assumed that the medium occupies the half-space $(\mathbf{nr}) > 0$ and $\mathbf{E}, \mathbf{H} \propto \exp ik[(\mathbf{m} + p\mathbf{n})\mathbf{r} - vt]$), and v_e and v_0 are the velocities of the ordinary and the extraordinary waves along $\mathbf{m}$ in the c units, respectively.

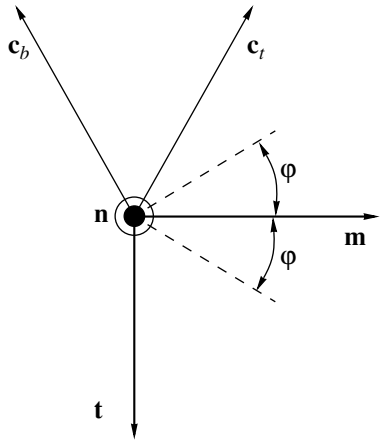

Fig. 1. Geometry of the problem, $\mathbf{c}_t$ and $\mathbf{c}_b$ are the optical axes in the upper and lower parts of the bicrystal.

1063-7745/01/4605-0842$21.00 © 2001 MAIK "Nauka/Interperiodica"

Let the bicrystal be composed of two identical uniaxial media. Their optical axes lie in the interface plane (Fig. 1). We are interested in the localized waves propagating along **m**.

The change $p_{oe} \longrightarrow -p_{oe}$, $\varphi \longrightarrow -\varphi$ in (1) and (2) yields the tangential components of the electric and the magnetic fields of the inhomogeneous waves in the lower medium. The determinant of boundary conditions is represented as the product of two functions:

$$\begin{aligned} f_1(v, \varphi) &= E_{ot}H_{et} - E_{et}H_{ot}, \\ f_2(v, \varphi) &= E_{om}H_{em} - E_{em}H_{om}, \end{aligned} \tag{4}$$

whence it follows that the polariton velocity should satisfy one of the following conditions:

$$f_1(v, \varphi)\frac{v}{\varepsilon_o} \equiv p_o p_e \sin^2\varphi + \varepsilon_0 v^2 \cos^2\varphi = 0, \tag{5}$$

$$f_2(v, \varphi)\frac{v^3}{p_o} \equiv v^2 \varepsilon_o p_e \cos^2\varphi + p_o^3 \sin^2\varphi = 0. \tag{6}$$

Consider the first equation. Substituting p_o and p_e from Eq. (3) into Eq. (5), we arrive at the quadratic equation with respect to v^2. One of its roots is known *a priori*—$v^2 = v_d^2 = \sin^2\varphi/\varepsilon_o$. This root corresponds to the degeneracy $p_o = p_e = i\cos\varphi$ (a reader is referred to [5] for more detail). The second root,

$$v^2 = \frac{\bar{\varepsilon} v_e^2 \sin^2\varphi}{\bar{\varepsilon}\sin^4\varphi - \cos^4\varphi}, \tag{7}$$

where $\bar{\varepsilon} = \varepsilon_e/\varepsilon_o$, does not meet the physical requirement $v < v_o$, v_e either in the optically positive or optically negative media (the polariton velocity must be lower than the velocity of bulk waves). Thus, equation (5) does not describe localized waves.

Now, consider Eq. (6). In optically positive crystals ($\bar{\varepsilon} > 1$), the "polariton" solution of this equation at small φ has the form

$$\begin{aligned} v &\approx v_e\{1 - 0.5\bar{\varepsilon}^2(1 - 1/\bar{\varepsilon})^3 \sin^4\varphi\}, \\ &\varphi \ll 1. \end{aligned} \tag{8}$$

In this case, the polariton is a weakly localized extraordinary wave with the imaginary p_e:

$$|p_e| \approx \bar{\varepsilon}(1 - 1/\bar{\varepsilon})^{3/2} \sin^2\varphi. \tag{9}$$

This quantity should be complemented with the inhomogeneous ordinary wave with $|p_o| \approx (1 - 1/\bar{\varepsilon})^{1/2}$ is each part of the bicrystal.

The localized solution cannot "disappear" unless it goes through $v = v_e$. In other words it, first, must be transformed into the extraordinary bulk wave. However, v_e satisfies Eq. (6) at $\varphi = 0$ and $\pi/2$. Therefore, the solution exists within the whole interval of $[0, \pi/2]$ and is transformed into the bulk wave at its boundaries.

The polariton velocity can exactly be found for arbitrary φ. Upon the substitution of Eq. (3) into Eq. (6), we arrive at a cubic equation with respect to v^2. Again, one of its roots is $v^2 = v_d^2$. One of the two remaining roots obeying the conditions $v < v_o$, v_e and $v^2 > 0$ is

$$\begin{aligned} \frac{v^2}{v_e^2} &= \frac{\bar{\varepsilon}[1 - 3\sin^2\varphi + \cos^2\varphi[1 + 4\sin^2\varphi(\bar{\varepsilon} - 1)]^{1/2}]}{2[1 + (\bar{\varepsilon} - 1)\sin\varphi][\bar{\varepsilon}\cos^4\varphi - \sin^4\varphi]}. \end{aligned} \tag{10}$$

In optically negative crystals, both roots do not obey the above requirements. Note that at $\bar{\varepsilon} = \tan^4\varphi$, both denominator and numerator in Eq. (10) vanish so that at this point no divergence is observed.

The amplitude ratio for the ordinary and the extraordinary waves in the polariton equals $\Delta = p_o \tan\varphi/v$. At low φ values, $\Delta \approx i\sqrt{\varepsilon_e - \varepsilon_o}\sin\varphi$, i.e., is small in the measure of smallness of φ. At the same time, if φ is close to $\pi/2$ (**m** is the bisector of the small angle $2\psi = \pi - 2\varphi$ formed by the optical axes), $\Delta \approx i\sqrt{\varepsilon_0(\sqrt{4\bar{\varepsilon} - 3} - 1)/2}$, and, in this limiting case, the amplitudes of the ordinary and the extraordinary waves are of the same order of magnitude. Note that in the vicinity of $\varphi \approx \pi/2$, the decay factors of both components depend linearly on the small parameter ψ,

$$\begin{aligned} p_o &\approx i|\sin\psi|\sqrt{(\sqrt{4\bar{\varepsilon} - 3} - 1)/2}, \\ p_e &\approx i|\sin\psi|\sqrt{\bar{\varepsilon}(2/\bar{\varepsilon} + \sqrt{4\bar{\varepsilon} - 3} - 3)/2}, \end{aligned} \tag{11}$$

and not quadratically like p_e at $\varphi \approx 0$ (see Eq. (9)). Moreover, unlike the situation at $\varphi \approx 0$, the difference between v_e and the polariton velocity at $\varphi \approx \pi/2$,

$$v \approx v_e[1 - 0.25(2/\bar{\varepsilon} + \sqrt{4\bar{\varepsilon} - 3} - 3)\sin^2\psi] \tag{12}$$

varies proportionally to the squared small parameter and not as this parameter in degree four.

Thus, in the bicrystal under consideration, a localized electromagnetic wave is generated only if the bicrystal is formed by optically positive crystals. The wave exists at arbitrary $\varepsilon_e/\varepsilon_o > 1$ and arbitrary angles between the optical axes of the parts of the bicrystal. At $\varphi = 0$ and $\varphi = \pi/2$, a localized wave is transformed into a bulk wave. However, the structure of the wave localized in the vicinity of $\varphi = 0$ and the structure of the wave localized in the vicinity of $\varphi = \pi/2$ are different.

Figure 2 shows v/v_e as a function of φ at various $\bar{\varepsilon}$. It is seen that the polariton velocity is almost equal to v_e even at pronounced optical anisotropy.

It is apparent that polaritons can exist not only along the bisector of the angle formed by the optical axes, but

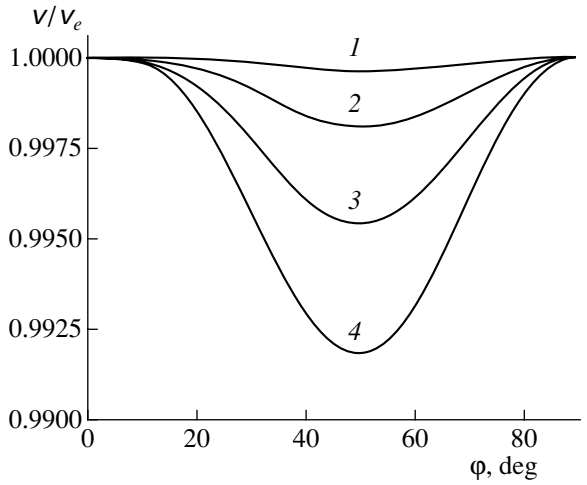

Fig. 2. Polariton velocity as a function of the angle between the optical axes: (*1*) $\bar{\varepsilon}$ = 1.2; (*2*) $\bar{\varepsilon}$ = 1.4; (*3*) $\bar{\varepsilon}$ = 1.6; (*4*) $\bar{\varepsilon}$ = 1.8.

also close to the bisector. However, in the latter case, the problem does not have any simple analytic solution.

ACKNOWLEDGMENTS

The authors is grateful to V.I. Alshits and V.N. Lyubimov for useful discussions. The study was supported by the Russian Foundation for Basic Research, project no. 98-02-16069.

REFERENCES

1. M. I. D'yakonov, Zh. Éksp. Teor. Fiz. **94** (4), 119 (1988) [Sov. Phys. JETP **67**, 714 (1988)].
2. V. N. Lyubimov and D. G. Sannikov, Fiz. Tverd. Tela (Leningrad) **14**, 675 (1972) [Sov. Phys. Solid State **14**, 575 (1972)].
3. V. M. Agranovich and V. L. Ginzburg, *Crystal Optics with Spatial Dispersion and Excitons* (Nauka, Moscow, 1979; Springer-Verlag, New York, 1984).
4. F. I. Fedorov, *Optics of Anisotropic Media* (Akad. Nauk BSSR, Minsk, 1958).
5. F. I. Fedorov, *Theory of Gyrotropy* (Nauka i Tekhnika, Minsk, 1976).

Translated by A. Darinskiĭ

Crystallography Reports, Vol. 46, No. 5, 2001, pp. 845–847. Translated from Kristallografiya, Vol. 46, No. 5, 2001, pp. 919–921.

PHYSICAL PROPERTIES OF CRYSTALS

Low-Frequency Dielectric Properties of DMAAS Crystals in the Vicinity of 110 K

A. M. Lotonov*, L. F. Kirpichnikova, and N. D. Gavrilova***

** Moscow State University, Moscow, 119899 Russia*

*** Shubnikov Institute of Crystallography, Russian Academy of Sciences, Leninskiĭ pr. 59, Moscow, 117333 Russia*

e-mail: luba@ns.crys.ras.ru

Received December 29, 2000

Abstract—Dielectric properties in "pure" and partly deuterated DMAAS crystals have been studied within the frequency range 40^{-2}–10^{7} Hz in the vicinity of 110 K. It is established that the crystals possess relatively high conductivity, 10^{-4}–10^{-7} Ω^{-1} m^{-1}, which is explained by their crystal structure. The frequency dependence of the complex dielectric constant has two linear segments, which indicate the change in the charge-carriers motion in the vicinity of 110 K. It is revealed that at low temperatures, conductivity increases at higher frequencies. © *2001 MAIK "Nauka/Interperiodica".*

The ferroelectric–ferroelastic $(CH_3)_2NH_2Al(SO_4)_2 \cdot 6H_2O$ (DMAAS) crystals have a complex system of hydrogen bonds between three main structural complexes of the three-dimensional framework [1]: $[Al(H_2O)]^{3+}$ hexaaluminium cations, sulfate anions $[SO_4]^{2-}$, and the molecular $[(CH_3)_2NH_2]^+$ (DMA) cations, the O–H···O bonds being shorter and stronger than the N–H···O ones. A second-order ferroelectric phase transition of the order-disorder type with symmetry change $2/m \longrightarrow m$ in the vicinity of the tricritical point occurs at T_C = 152 K [2]. The partial replacement of hydrogen by deuterium does not change the phase-transition temperature. The dielectric relaxation in DMAAS crystals was measured mainly in the range of the ferroelectric phase transition [3–6]. The measurements of the complex dielectric constant at the frequencies 120 Hz–56 GHz revealed the fundamental dielectric dispersion described by the Debye formula in the vicinity of T_C [3], with the activation energy of dipole groups and the relaxation time of dipoles being equal to E_a = 0.112 eV and $\tau = 1.6 \times 10^{-7}$ s, respectively. Two types of low-frequency dielectric relaxation mechanisms with the activation energies E_1 = 0.16 and E_2 = 0.49 eV are established [4]. The second mechanism is associated with domain motion. The X-ray studies showed that above T_C, the DMA ions perform hoppings and rotations around the axis connecting two carbon atoms, and are located pairwise in four positions with the probabilities 0.4 and 0.1 [7]. Neutron inelastic-scattering experiments showed that below T_C, the rotational motion of DMA ions is transformed into librational oscillations [8, 9]. The EPR studies showed that the ferroelectric phase transition is associated with the cooperative ordering of DMA cations and aluminum and sulfate complexes [10, 11], with hydrogen bonds playing the part of the trigger mechanism in the ordering of all the structural elements. The EPR measurements also showed that DMA ions decelerate their motion in the vicinity of 110 K, and are frozen in one of the structurally nonequivalent positions. The NMR measurements revealed a small anomaly at 110 K [12]. The optical studies of DMAAS crystals led to the assumption about a possible phase transition at 110 ± 5 K [13, 14]. The dielectric measurements and the mechanical tests [15, 16] revealed the anomalies in the respective properties in the vicinity of 110 K not necessarily indicating a phase transition. Within the phenomenological theory [17], these anomalies were considered as the consequences of isostructural ordering in one of the sublattices. At present, there is no proof of the occurrence of a phase transition in this temperature range. Thus, further studies of these crystals in the vicinity of 110 K are of particular interest.

We had the aim to study the dielectric constant and conductivity in pure and partly deuterated (30% of deuterium) DMAAS crystal in the frequency range $(40–2) \times 10^5$ Hz in the vicinity of 110 K.

Dielectric constant and dielectric-loss tangent used in the calculation of conductivity were measured with the aid of an R 551 bridge (Russia) in the mode of stabilized temperature. The specimens were $5 \times 5 \times 0.5$-mm^3-large single-crystal plates with applied silver electrodes. The *X*-axis coincided with the spontaneous-polarization axis (at 130 K), the *Y*-axis coincided with the twofold axis of the crystal.

The frequency dependences of the real and the imaginary parts of dielectric constant, $\varepsilon = \varepsilon' + i\varepsilon''$, at various temperatures close to 110 K are shown in Fig. 1. The characteristic feature is the existence of two

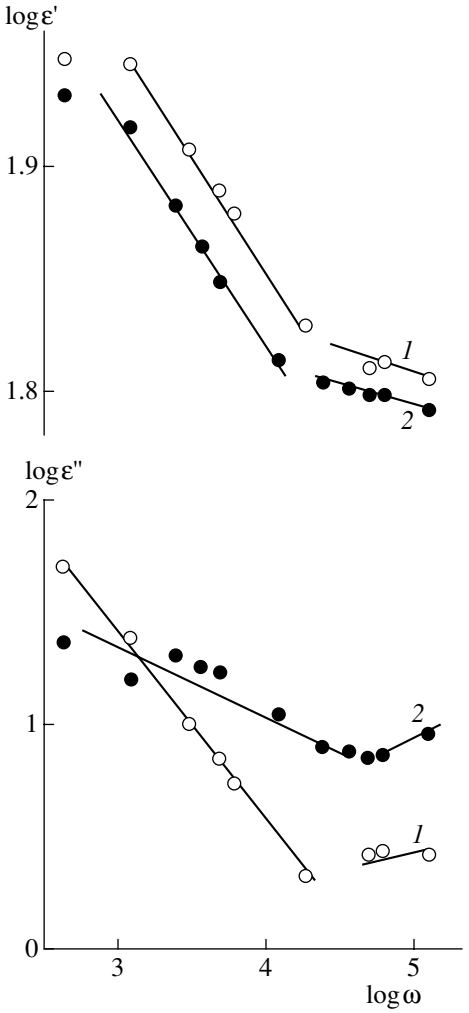

Fig. 1. Frequency dependences of the real and the imaginary parts of the dielectric constant of DMAAS crystals in the log–log coordinates at two temperatures (*1*) 112.4 and (*2*) 107.6 K.

linear segments, ε' and ε", in log–log plot. The slopes of the dependences logε' versus logω are almost the same for the left-side portions of the curves (–0.142 at 107.6 K and –0.147 at 112.4 K), but are slightly different for their right-side portions (–0.027 at 107.6 K and –0.044 at 112.4 K). It is clearly seen that the slopes of the frequency dependences of ε" are essentially different above and below 110 K. The slopes of the linear segments of the left branches (–0.409 at 107.6 K and –0.898 at 112.4 K) and right branches (0.186 at 107.6 K and 0.123 at 112.4 K) of the logε" (logω) curves also differ considerably. The linear segments prove the validity of the universal fractal–power law [18] which states that for a broad class of materials, the power dependence of the dielectric properties on frequency is fulfilled ($\varepsilon' \approx \omega^{-n}$; $\varepsilon'' \approx \omega^{k}$). The values of the *n* and *k* constants allow one to estimate the transport mechanism in the system. In accordance with the model of universal dielectric response, the *n* and *k* val-

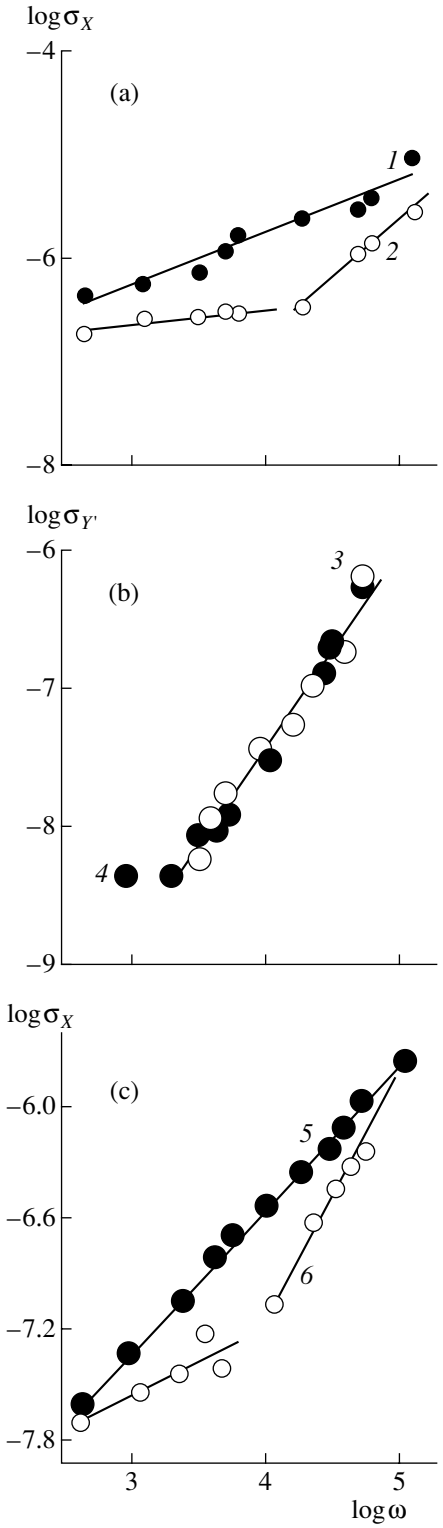

Fig. 2. Frequency dependences of conductivity of (a, b) pure and (c) partly deuterated DMAAS crystals in the log–log coordinates at various temperatures in the vicinity of 110 K: (*1*) 107.8, (*2*) 112.4, (*3*) 106.5, (*4*) 112.9, (*5*) 89.5, and (*6*) 113.4 K.

ues can change from zero to unity. The changes in the slopes indicate different mechanisms of charge transfer above and below 110 K.

Figure 2 shows the dependence of conductivity σ on cyclic frequency ω on the log–log scale for pure (Figs. 2a, 2b) and partly deuterated ferroelectric phase of the DMAAS crystals near 110 K (several tens of degrees below T_C). The conductivity and its frequency dependence are the most important here: the conductivity values ranging within 10^{-4}–10^{-7} Ω^{-1} m^{-1} are typical of ferroelectrics with hydrogen bonding above 0°C. It is well known that conductivity of this type is caused by the motion of protonic structural defects. In DMAAS crystals, along with the defects inherent in a real crystal, there are also protonic defects caused by motion of DMA ions. The hopping-rotational motion of DMA ions above T_C between different orientational states is accompanied by the break of N–H···O bonds and appearance of new ones [1, 8]. Below T_C, the rotation of DMA ions with partly broken bonds is transformed into the librational motion with thermal oscillations with large amplitudes. It seems that the observed high conductivity is determined by the structural characteristics of DMA ions in DMAAS crystals.

An increase of conductivity with frequency can indicate the hopping mechanism of proton conductivity. The typical feature of the polar cuts of DMAAS crystals is the existence of two linear segments on the "σ versus ω" curves above 110 K; below this temperature, conductivity is described by a straight line. In this temperature range, the coefficient of pyroelectric effect has a low peak, which results in an increase in spontaneous polarization, a pronounced increase of the coercive field, EPR and NMR anomalies in the respective spectra and change in the optical and mechanical characteristics. The nature of these anomalies is still unclear; however, it should be indicated that similar behavior in the vicinity of 110 K was also observed in other ferroelectrics with hydrogen bonds (KDP, MASD), which may be associated with certain ordering (change in occupancies of the energy levels) in the system of hydrogen bonds and its effect on the structure and properties of DMAAS crystals.

REFERENCES

1. G. A. Kiosse, I. M. Razdobreev, L. F. Kirpichnikova, *et al.*, Kristallografiya **39** (1), 34 (1994) [Crystallogr. Rep. **39**, 27 (1994)].
2. L. F. Kirpichnikova, L. A. Shuvalov, N. R. Ivanov, *et al.*, Ferroelectrics **96**, 313 (1989).
3. Z. Sobiestianskas, J. Grigas, and E. F. Andreev, Izv. Akad. Nauk SSSR, Ser. Fiz. **55** (3), 548 (1991).
4. J. Wolak, B. Hilczer, L. F. Kirpichnikova, *et al.*, Kristallografiya **40** (6), 1069 (1995) [Crystallogr. Rep. **40**, 994 (1995)].
5. V. Kapustianik, M. Fally, H. Kabelka, *et al.*, J. Phys.: Condens. Matter **9**, 723 (1997).
6. N. Yasuda and H. Tajima, J. Korean Phys. Soc. **32**, S283 (1998).
7. A. Pietraszko, K. Lukaszewicz, and L. F. Kirpichnikova, Pol. J. Chem. **68**, 1877 (1994).
8. V. Yu. Kazimirov, A. V. Belushkin, and L. A. Shuvalov, Kristallografiya **42** (3), 471 (1997) [Crystallogr. Rep. **42**, 425 (1997)].
9. V. Yu. Kazimirov, E. É. Rider, V. A. Sarin, *et al.*, Kristallografiya **43** (2), 228 (1998) [Crystallogr. Rep. **43**, 193 (1998)].
10. W. Bednarski, S. Waplak, and L. F. Kirpichnikova, J. Phys.: Condens. Matter **11**, 1567 (1999).
11. W. Bednarski, S. Waplak, and L. F. Kirpichnikova, J. Phys. Chem. Solids **60**, 1669 (1999).
12. J. Dolinsek, D. Klanjek, D. Arkon, *et al.*, Phys. Rev. B **59** (5), 3460 (1999).
13. O. G. Vlokh, B. B. Kapustianik, I. I. Polovinko, *et al.*, Ferroelectrics **111**, 333 (1990).
14. O. G. Vlokh, V. B. Kapustyanyk, I. I. Polovinko, *et al.*, Kristallografiya **36** (4), 919 (1991) [Sov. Phys. Crystallogr. **36**, 516 (1991)].
15. L. F. Kirpichnikova, N. R. Ivanov, N. D. Gavrilova, *et al.*, Kristallografiya **36** (5), 1246 (1991) [Sov. Phys. Crystallogr. **36**, 702 (1991)].
16. L. F. Kirpichnikova, A. A. Urusovskaya, V. I. Mozgovoĭ, *et al.*, Kristallografiya **36** (6), 1516 (1991) [Sov. Phys. Crystallogr. **36**, 859 (1991)].
17. S. V. Pavlov and L. F. Kirpichnikova, Ferroelectrics **144**, 185 (1993).
18. A. K. Jonscher, *Universal Relaxation Law* (Chelsea Dielectric Press, London, 1996).

Translated by A. Zalesskiĭ

Crystallography Reports, Vol. 46, No. 5, 2001, pp. 848–849. Translated from Kristallografiya, Vol. 46, No. 5, 2001, pp. 922–923.

THIN FILMS

Epitaxial (001) Fe Films with Unidirectional Anisotropy

A. A. Potseluĭko* and V. G. Pyn'ko**

** Krasnoyarsk State Institute of Trade and Economy, Krasnoyarsk, 660049 Russia*
e-mail: apotz@www.kgtei.kts.ru
*** Kirenskiĭ Institute of Physics, Siberian Division, Russian Academy of Sciences, Krasnoyarsk, 660036 Russia*
Received February 9, 2000; in final form, August 31, 2000

Abstract—It has been shown that single-crystal (001) Fe films grown on the cleaved LiF substrates in the presence of NaCl vapor are characterized by an asymmetric and displaced hysteresis loop of a transitional antiferromagnetic layer of a metamagnetic nature in a certain range of remagnetizing fields. Such shape of the hysteresis loop is explained by possible existence between the film and the substrate. *© 2001 MAIK "Nauka/Interperiodica".*

The orientational growth of a material film on a substrate of another single crystal (epitaxy) is often considered as the formation of an interlayer with a certain crystal structure and corresponding to a equilibrium phase diagram between the crystal-substrate and a film have been considered in a number of papers (see, e.g., [1]). We believe that this approach adequately describes the process in many instances. However, one should take into consideration that the intermediate layer between the substrate and a growing film (interlayer) may contain in addition to the elements contained in the film and substrate, also the atoms from the residual gases in the evacuated chamber. In some cases, this can promote better epitaxy [2].

As is shown below, the introduction into a transitional layer of certain atoms can considerably influence the magnetic properties of an epitaxial ferromagnetic film, in particular, of an iron film.

The films were deposited onto the substrates in a vacuum chamber of a commercial UVR-2 (apparatus

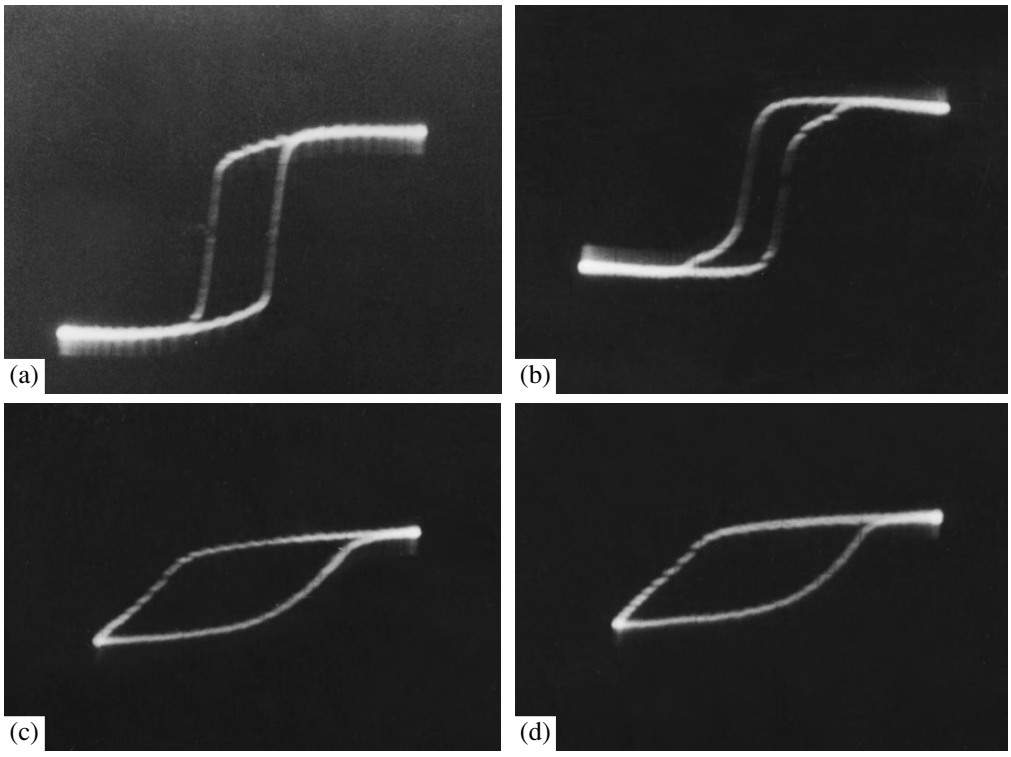

Fig. 1. Hysteresis loops of the (001) Fe film obtained in NaCl vapor: (a) H = 270 Oe, $H \parallel$ [110]; (b) H = 270 Oe, H forms an angle of 25° with [110]; (c) H = 50 Oe, $H \parallel$ [110]; (d) H = 50 Oe, H forms an angle of 25° with [110].

1063-7745/01/4605-0848$21.00

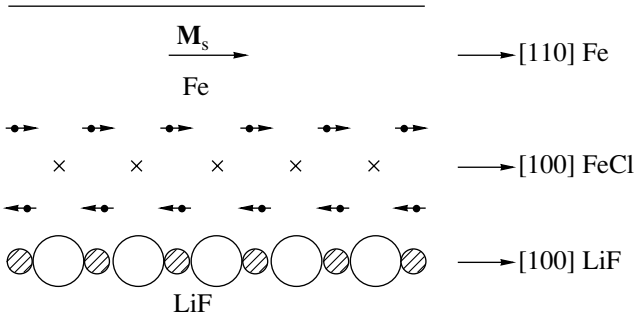

Fig. 2. Possible arrangement of the Fe–LiF interface and the orientations of magnetic moments of Fe atoms in the absence of an external magnetic field; $\mathbf{M}_s$ is a component of the spontaneous magnetization in the Fe film; Fe atoms are shown by small filled circles; Cl atoms in a transitional layer are indicated by crosses; F atoms, by large open circles; Li atoms, by hatched circles.

Russia) under the residual pressure of about 10^{-4} torr. The sputtering was performed on conical tungsten spirals at a deposition rate of about 100 Å s^{-1}. The hysteresis loop was measured by the conventional method with the use of an inductive pickup.

Figure 1 shows the hysteresis loops from Fe films grown on a cleaved LiF substrate in the presence of NaCl vapors. Upon substrate annealing at 250°C and their subsequent cooling down to 170–180°C in the evacuated chamber, a certain amount of NaCl was sputtered without the deposition of sodium and chloride onto the LiF substrate. Immediately after NaCl sputtering, the iron films were deposited onto the substrates. The electron-diffraction patterns showed that the films thus obtained were single crystalline and were oriented with respect to the LiF substrate as follows: (001) $[100]_{Fe} \parallel (001)\ [110]_{LiF}$. The hysteresis loops were measured in the 270-Oe- (Figs. 1a, 1b) and 50-Oe-fields (Figs. 1c, 1d). The remagnetizing field was applied either along the [110] direction in the film or at an angle of 25° to this direction. The loop shape measured along the [110] direction in a 270-Oe-field was the same as for the films obtained by the standard technology (without preliminary sputtering of sodium chloride) for remagnetization along the [110] direction. The loop recorded in a 50-Oe-field was shifted along the abscissa, which is characteristic of the films with the unidirectional magnetic anisotropy. The loop recorded in a 270-Oe-field applied at the 25° to the [110] direction had the same shape as in Fe films prepared by the standard technology and remagnetized along the same field direction. A decrease of the amplitude of the remagnetizing 50-Oe-field changed the loop shape; in addition to the loop shift, the loop also became asymmetrical.

The above characteristics of the loop shape for Fe film observed in different fields lead to the assumption about the existence of a certain antiferromagnetic layer between the LiF substrate and the Fe film, which possesses metamagnetic properties (the metamagnetic state is formed if the energy of anisotropy within ferromagnetic layers is higher than the negative exchange energy between ferromagnetic layers). The metamagnetic properties are inherent in $FeCl_2$ with the trigonal lattice and the Néel temperature 24 K [3].

We assume that the transitional antiferromagnetic layer between the LiF substrate and the Fe film consists of a metastable compound formed by Fe and Cl atoms. Sodium atoms resulting from decomposition of NaCl molecules are deposited onto the LiF substrate can contaminate the Fe film, however, this contamination is inessential for the magnetic properties of this film. The structure of the film formed on the metamagnetic layer and the film orientation relative to the LiF substrate are the same as those for the films grown by a conventional technology.

The film–substrate interface is schematically shown in Fig. 2. This scheme is favored by the fact that the hysteresis loop in Fe film measured in the field applied along the [100] direction preserves its shape and shows no shift irrespective of the field intensity.

The interface retains its antiferromagnetic properties when heated to at least 200°C.

REFERENCES

1. Yu. D. Chistyakov and Yu. P. Raĭnova, *Physicochemical Principles of Microelectronic Technology: Textbook for Institutes of Higher Education* (Metallurgiya, Moscow, 1979).
2. B. V. Vasil'ev, A. A. Potseluĭko, and V. G. Pyn'ko, in *Proceedings of the School-Workshop "Physics and Chemistry of Solid State" Blagoveshchensk, 1985*, p. 154.
3. S. V. Vonsovskiĭ, *Magnetism* (Nauka, Moscow, 1971; Wiley, New York, 1974).

Translated by A. Zalesskiĭ

Crystallography Reports, Vol. 46, No. 5, 2001, pp. 850–855. Translated from Kristallografiya, Vol. 46, No. 5, 2001, pp. 924–929.

SURFACE

Dedicated to the memory of B.K. Vainshtein

Structure of the Polar (010) Cleavage of a Ferroelectric TGS Crystal from the Atomic–Force Microscopy Data

N. V. Belugina and A. L. Tolstikhina

Shubnikov Institute of Crystallography, Russian Academy of Sciences,
Leninskiĭ pr. 59, Moscow, 117333 Russia
e-mail: alla@ns.crys.ras.ru

Received October 24, 2000

Abstract—The atomically smooth polar (010) cleavage of a ferroelectric triglycine sulfate (TGS) crystal has been studied by the method of atomic-force microscopy. It is shown that the rounded 0.6-nm-high (deep) protrusions and pits with nanometer lateral dimensions revealed on the surfaces of TGS crystals are characteristic of their microrelief. These microrelief details can be formed either as a result of crystal cleavage in the ferroelectric phase or the mechanical action of a cantilever onto the crystal surface. These two-dimensional formations are relatively stable and genetically related to the layer structure of the ferroelectric phase of TGS crystals.

INTRODUCTION

An important role of crystal surfaces in various phenomena of the ferroelectric nature is well known. Along with the defects in the crystal bulk, the surface layers seriously (and in very thin layers, even decisively) influence the dielectric parameters of ferroelectric crystals. The advent of atomic-force microscopy (AFM) based on measuring very weak (~10^{-6}–10^{-13} N) forces acting between the surface atoms and the atoms of the cantilever tip opened new possibilities for studying ferroelectric crystals or simply ferroelectrics. Today, AFM is an efficient method for direct observation of the statics and dynamics of the domain structure and the surface morphology of ferroelectrics at a high spatial resolution [1–3]. The practical use of AFM for designing various ferroelectric-based devices for recording and reading information [4–7] is also of great importance.

One of the most popular objects for microscopy studies is triglycine sulfate crystal (TGS), a typical ferroelectric at room temperature, showing perfect cleavage along the (010) plane. However, the images obtained from the surface of TGS crystals in different AFM modes are differently, and often even inconsistently, interpreted. Thus, the rounded formations observed on the polar surface of TGS crystals are often explained by the processes of surface etching by water from the atmosphere [8–14]. The same formations are often interpreted as subsurface domains [3]. Such inconsistent interpretation is explained by the insufficiently studied mechanism of contrast formation in AFM and the difficulties encountered in the attempts to distinguish numerous configurations of the irregular domain structure from the topographic relief of the surface. The present study was undertaken with the aim to establish the nature of these two-dimensional formations first observed by the AFM method on the polar surfaces of TGS crystals. To solve this problem, we investigated the crystals whose morphology and domain structure had been studied in detail by the methods of optical and electron microscopies.

EXPERIMENTAL

Triglycine sulfate crystals $(NH_3^+CH_2COOH)_2 \cdot (NH_3^+CH_2COO^-)SO_4^{2-}$ for our study were grown by the method of isothermal evaporation at $T > T_C = 49.5$°C at the Institute of Crystallography of the Russian Academy of Sciences. The unit-cell parameters of a TGS crystal in the crystallographic setting described in [15] are $a = 0.915$, $b = 1.269$, $c = 0.573$ nm, $\beta = 105°40'$. The unit cell contains two formula units. The bars with the major axis parallel to the ferroelectric *b*-axis were cut out from the growth pyramid of the face *m* and then were cut into 1.5 to 2.0-mm-thick specimens along the (010) cleavage normal to the *b*-axis.

The images of the TGS surface were obtained in several modes on Solver P4 and P47 and NT-MDT scanning probe microscopes. As is well known, the diagnostics of the surface properties of specimens in AFM is based on the consideration of various force interactions between the cantilever and the surface. The contributions made by different acting forces to the total force interaction depend on various parameters, and, first and foremost, on the distance between the

cantilever tip and the specimen surface. An atomic-force microscope and, in particular, its cantilever are designed to provide its operation in different modes of imaging (based on different interactions between various forces).

We studied TGS crystals in the contact and the resonance (interruptive contact) operating modes of an atomic-force microscope. In the contact mode, the major contribution to the total interaction is made by short-range repulsive forces acting between the atoms of the cantilever tip and the atoms of the crystal surface. The force acting onto the surface is usually of the order of $F \sim 10^{-6}$–10^{-7} N. In the contact mode, the cantilever tip is in a "soft" physical contact with the specimen surface. Mutual repulsion of the tip and the surface atoms results in overlap of their electron shells and the Coulomb repulsion of their nuclei, which causes the cantilever deviation. The surface topographs can be obtained under the condition of conservation of the force acting between the tip and the surface. In the side-force mode, one records the lateral deviations of the cantilever tip, e.g., the deviation caused by different friction coefficients in different chemically nonequivalent surface regions. This mode is often used in the studies of the surfaces of inhomogeneous crystals and of specimens with comparatively smooth surfaces. The side deviations of the cantilever from the well-developed microrelief hinder the interpretation of the image.

In the resonance mode, the surface is scanned by a cantilever tip vibrating with the frequency either of the resonance or forced vibrations with the amplitudes amounting up to tens of nanometers. The cantilever tip gently touches the specimen surface. The forces acting between the tip and the surface atoms are of the mixed nature. The effect of capillary forces is weakened. In our experiments, the force acting onto the specimen in the resonance mode was $F \sim 10^{-8}$ N. The backfeed provided the constant variation of the vibration amplitude. Thus, we recorded only the vibration phases.

If not specified otherwise, we studied as-cleaved (in air) surfaces. In the contact mode, we used 85-μm-long Si_3N_4 cantilevers at the resonance frequencies of 120 kHz with the tip curvature radius of 50 nm; in the resonance mode, we used 110-μm-long Si (NT-MDT) conductive (titanium-oxide coated) cantilevers with the curvature radius of the tip $R \leq 20$ nm and the resonance frequency f = 210 kHz, an uncoated 200-μm-long cantilever at the resonance frequency f = 40 kHz, and 90 μm-long cantilever at the resonance frequency f = 360 kHz.

RESULTS AND DISCUSSION

Figures 1.1 and 1.2 show the images of the surface region of a weakly unipolar aged crystal obtained by scanning along the direction $+X$ in the contact side-force and the topograph modes, respectively. In the side-force mode (Fig. 1.1), a lenslike formation with the dimensions 1800 nm along the "short" axis and about 4000 nm along the "long" axis is seen. As a rule, the domains in TGS crystals are of the lenslike shape and arranged in the growth pyramid of the *m* face in such a way that the long axis of the lens is parallel to the [102] direction. The "walls" of this formation (which, we believe, is a domain) are filled with rounded islands from 100 to 150 nm in diameter. On the images obtained in the topography mode at opposite scanning directions ($+X$ in Fig. 1.2 and $-X$ in Fig. 1.2), large lenslike domain can hardly be seen, whereas in the side-force mode (Fig. 1.1); scanning along $+X$ in Fig. 1.1, along $-X$ in Fig. 1.3, and along $+Y$ in Fig. 1.5) this domain is seen quite clearly. It is well known that domains with opposite polarizations (+ and –domains) in TGS crystals have different chemical compositions. The positive domains are formed by the glycinium cation G1 ($NH_3^+CH_2COOH$) emerging on the surface and two sulfate SO_4 groups, whereas the negative ones, by the glycinium cation G_2 ($NH_3^+CH_2COOH$) and a zwitter-ion G_3 ($NH_3^+CH_2COO^-$) [16]. Therefore, the mode sensitive to the chemistry of the surface allows one to reveal the domains of opposite polarities with a rather high contrast. However, the contrast of the lenslike domain obtained in the contrast mode is unstable and is considerably deteriorated during the repeated scanning of the surface (Figs. 1.1–1.5).

Scanning of the images obtained in the topography and side-force modes along different directions reveals rounded islands along the domain boundaries (Fig. 1). Their contrast differs from the contrast of domains and can be attributed either to the regions with opposite polarities (subsurface ferroelectric domains [3]) or simply to protrusions and hollows of the surface microrelief of the crystal. The first assumption seems to be more natural, because the islands are located along the domain boundaries similar to the nuclei of the opposite polarities at the impurity centers decorating the domain boundary. Figure 1.6 shows the image of the same surface region on a larger scale obtained by multiple scanning in the side-force mode. It is seen that the contact of the cantilever with the surface causes relative displacement of the lenslike domain and rounded islands. Moreover, some additional islands appear in the vicinity of the domain boundary. Similar formation of islands in the vicinity of the lenslike domain was also observed in the side-force mode in [3], where it was explained by branching of the domain structure.

In our experiments, we also often observed the formation of rounded islands and pits during multiple scanning by a cantilever of the polar TGS crystals in the contact mode [17, 18]. The height (depth) of these islands and pits was about 0.6 nm. As a rule, upon a certain time after scanning cessation, the "induced" islands and pits disappeared [18]. It seems that formations observed along the boundaries or in the vicinity of the lenslike domains on as-cleaved surfaces and those

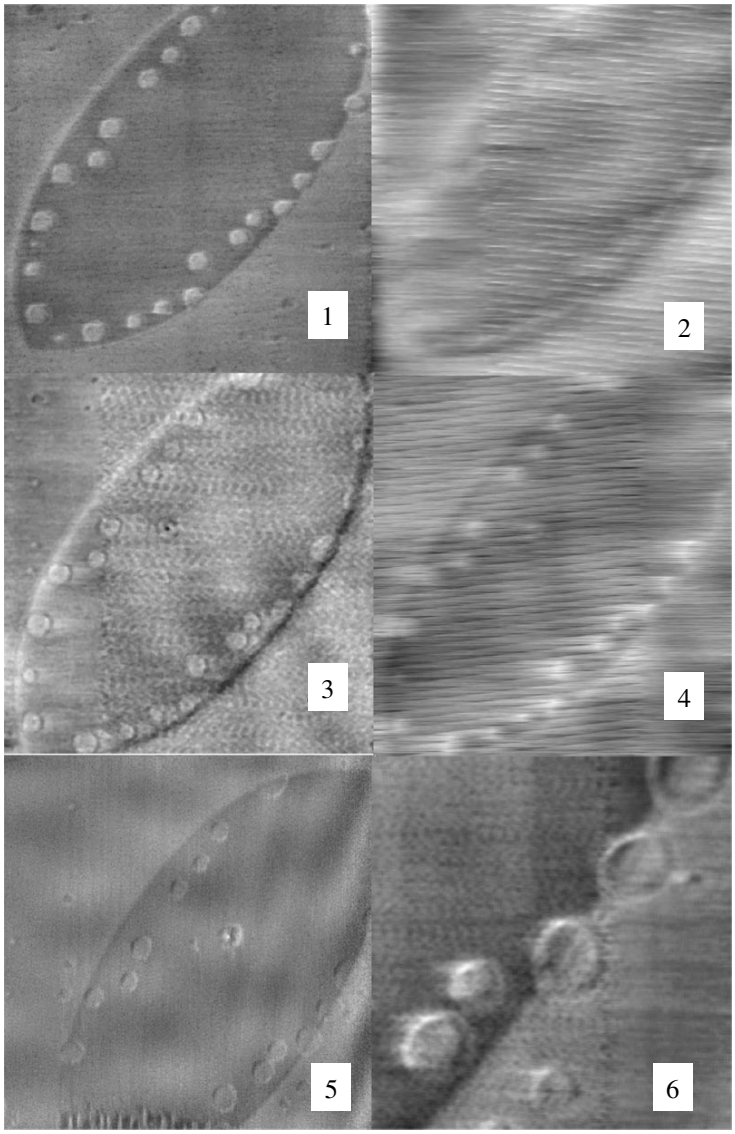

Fig. 1. Image of a lenslike domain in a unipolar TGS crystal obtained by scanning along the $+X$ direction in the (1) side-force and (2) the topography modes; scanning in the $-X$ direction in the (3) side-force and (4) the topography modes; (5) scanning in the $+Y$ direction in the side-force mode; and (6) scanning along the $+Y$ direction in the side-force mode on a larger scale.

observed upon their multiple scanning are of the same nature.

There are several contradictory and, sometimes, even mutually excluding standpoints on the nature of the island (protrusions) and pit formation. In most cases, they are attributed to partial dissolution of the surface by the adsorbed water molecules always present on the surface of a crystal cleaved in air. These islands are either two-dimensional nuclei formed due to recrystallization in the presence of adsorbed water [10, 19] or the remaining fragments of the etched-off monolayer [11]. However, the appearance and disappearance of islands and pits can hardly be explained by conventional surface etching by atmospheric water, because similar islands and pits are also observed on the vacuum-cleaved TGS surfaces [20], which also makes the decisive role of water molecules in the formation of such a relief somewhat dubious. At the same time, the cleavages obtained and studied at temperatures considerably exceeding the Curie point showed no such formations, which led to the assumption that, in actual fact, these formations are the "nuclei" of the domains of opposite polarities inside the rounded domains. However, unlike the contrast from the lenslike domain, the stable high-quality contrast from two-dimensional formations observed in the contact mode, the mutual displacement of the domain boundary and islands, and the appearance of new islands during multiple scanning makes the conclusion about the ferroelectric nature of these surface formations somewhat dubious.

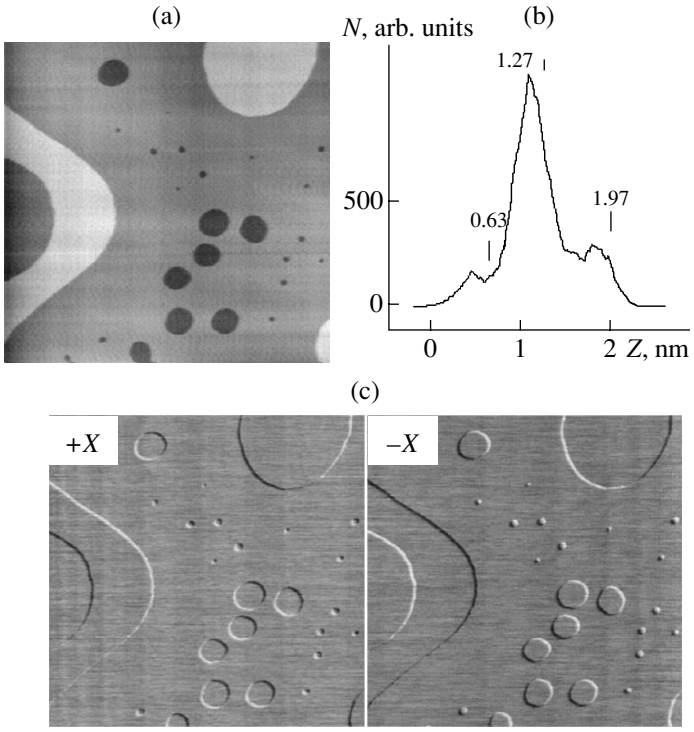

Fig. 2. (a) Topographs of the atomically smooth region of the (010) polar surface of a TGS crystal obtained in the resonance mode and (b) the corresponding histogram of heights. The abscissa shows the height Z and the ordinate, the number N of points lying at such heights. In fact, the histogram reflects the ratio of the areas occupied by pits (the darkest region) and islands (the lightest region) to the area of the main cleavage surface (the grey region). (c) The image of the same region obtained by scanning along different directions in the phase-contrast mode. The dimensions of the scanned surface region are 6500×6900 nm^2.

The rounded islands and the pits of various dimensions characteristic of the polar cleavage surface were observed in our and other experiments in an atomic-force microscope operating in the contact and in the resonance modes [3, 8–14, 19, 21]. These experiments also showed that the lateral dimensions of the islands and the pits vary over a wide range, but their heights (depths) are constant and are about $1/2b \sim 0.6$ nm. Figure 2a shows the topograph from a polar surface of an aged TGS crystal obtained in the resonance mode. The atomically smooth 6500×6900-nm^2 region shows islands (protrusions) of different shapes and rounded pits. The diameter of the rounded islands range from 1300 to 2600 nm, and those of the pits, from 50 to 600 nm. The difference in the roughness heights S_Y of such a surface is 2.59 nm, whereas the root-mean square roughness S_Q equals 0.41 nm. The protrusion heights and the pit depths are usually constant $1/2b = 0.6$ nm with respect to the surface plane. This also follows from the histogram of the heights (Fig. 2b) characterized by three maxima corresponding to the heights 0.63, 1.27, and 1.97 nm, which are practically the multiples of $1/2b$. The study of the images obtained in recording the phase shift (cantilever vibrations with respect to the excitation signal) showed that this surface region is a single domain (because of the change of the contrast with the change of scanning direction from $+X$ to $-X$ only at the protrusion and pit boundaries) (Fig. 2c). This also indicates the topographic nature of the contrast from the islands and the pits with the same polarities coinciding with the polarity of the matrix.

To clarify the nature of the islands and pits and the contradictory conclusions following from our and other experiments, we have analyzed the problem in terms of crystal cleavage. As is well known, cleavage is the consequence of the specific features of the ideal crystal lattice, i.e., the geometry of the spatial lattice and the nature of the binding forces. In practice, this phenomenon is provided not only by the specific features of the ideal lattice but also by the characteristics of the real structure. N.V. Belov and M.V. Klassen-Neklyudova [22] considered the conditions for cleavage in crystals with different chemical bonding and formulated the so-called "cleavage rules." One of these rules states that the crystallographic plane along which the crystal can be cleaved should not pass through a molecule. The unit cell of a TGS crystal contains two formula units (two molecules) "threaded" onto the b-axis which, thus, double the lattice parameter along this axis. Therefore, theoretically, two variants of TGS cleavage normal to the [010] direction are possible—cleavage multiple of b and cleavage multiple of $(1/2)b$. We believe that the formation of islands and pits in some surface regions

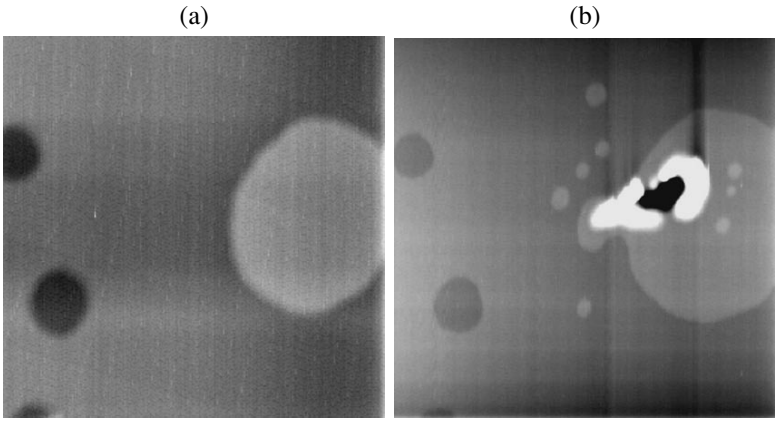

Fig. 3. Image of a 3000×3000-nm^2 surface region with a large rounded protrusion (1300 nm in diameter) and pits (a) prior to and (b) upon the short mechanical contact of the cantilever tip with the crystal surface.

during cleavage corresponds to the second variant and is a multiple of (1/2)*b*.

To confirm this hypothesis, we used the approach based on simulation of island and pit formation under the action of the mechanical factors onto the surface of a ferroelectric crystal. We studied the impact of the cantilever tip on the surface in the resonance mode. Figure 3 shows the image of the 3000×3000-nm^2-large rounded protrusion (about 1300 nm in diameter) and small pits existing prior to (Fig. 3a) and upon (Fig. 3b) the disrupted mechanical contact of the cantilever tip with the surface. The probe impact resulted in local damage of the protrusion surface (Fig. 3b) and the formation of a 23-nm-deep crater. Moreover, the cantilever impact also initiated the formation of small rounded islands on the protrusion and around it, with some of them having the same diameter of about 112 nm. These islands also play the role of ~0.6-nm-high surface protrusions. Ten minutes upon the cantilever impact, these small islands disappeared. In the first approximation, one can assume that the mechanical impact of the probe on the specimen surface is similar to cleavage of a ferroelectric crystal. Therefore, the formation of rounded protrusions on the polar surface of a TGS crystal (genetically related to energy-inhomogeneous layer structure of the crystal) can also occur irrespectively of the adsorbed water. The islands thus formed are similar to the formations observed upon multiple scanning of the surface by a cantilever in the contact mode (under the conditions that the tip exerts a pressure of F in the contact mode $F \sim 10^{-6}$ N) in our earlier studies [17, 18]. The energetic stability of the monolayer corresponding to the level (1/2)*b* in the unit cell manifests itself in the constancy of the surface response to the mechanical action—the formation of ~0.6-nm-high (deep) protrusions (pits).

We believe that rounded protrusions and submicron pits formed during crystal cleavage multiple of (1/2)*b* should not be considered as ferroelectric domains or the traces of etching by adsorbed water. Rather, they demonstrate the property of surface self-ordering under the action of decompensating fields and surface tension during cleavage. Upon cleavage, these pits and protrusions become the details of a stable specific surface microrelief. The rounded shape of two-dimensional formations is explained by the effect of surface-tension forces. According to our observations, these formations are stable against heating and preserve their dimensions in the reversible ferroelectric–paraelectric phase transitions. Crystal cleavage in the paraelectric phase proceeds without the formations observed in the ferroelectric phase [20]. At the moment of appearance of these formations, they can be associated with point defects and their accumulations, which is seen from the characteristic arrangement of islands (pits) along the domain boundaries (Fig. 1), i.e., in the traditional sites of point-defect accumulations in TGS crystals. Moreover, the density of rounded protrusions at the sites of their accumulations coincides with the density of decorating particles at point defects (10^{17}–10^{18} m^{-2}) observed in electron microscopy studies of TGS crystals.

The results obtained show that islands and pits induced either by multiple scanning or the cantilever impact on the surface have the same nature as the islands and pits formed during cleavage of a ferroelectric crystal. The only difference between the two reduces to the protrusion and pit stabilities, which can be explained as follows. As is well known, cleavage is closely related to the surface energy (minimal at the cleavage planes). In the cleavage of a TGS crystal, some energy is consumed for the formation of a microrelief on the cleavage plane, but then the crystal remains in the equilibrium state. During surface scanning by a cantilever, the microrelief is changed because of newly formed islands and pits, which requires the additional work of the friction forces. In turn, this increases the specific surface of the newly formed microrelief and, thus, also the surface energy. Therefore, the microrelief formed under the action of the cantilever tip can be less stable than the microrelief formed

due to cleavage. Upon the cessation of the action of the external factor, the scanning-induced islands (pits) disappear, because the system always tends to the state with a lower surface energy, whereas the microrelief tends to return to the initial state.

The rounded ~0.6-nm-high two-dimensional formations on the atomically smooth polar surface of a TGS crystal observed by the method of atomic-force microscopy are, in fact, the stable details of the surface microrelief. They are formed in cleavage of a TGS crystal in the ferroelectric phase and also upon scanning with a cantilever and reflect the real layer structure of a ferroelectric TGS crystal.

ACKNOWLEDGMENTS

We are grateful to Professor L.A. Shuvalov for his interest in our investigation. The study was supported by the Russian Foundation for Basic Research, project no. 99-02-17303.

REFERENCES

1. F. Saurenbach and B. D. Terris, Appl. Phys. Lett. **56** (17), 1703 (1990).
2. O. Kolosov, A. Gruverman, J. Hatano, *et al.*, Phys. Rev. Lett. **74** (21), 4309 (1995).
3. A. Correia, J. Massanell, N. Garcia, *et al.*, Appl. Phys. Lett. **68** (20), 2796 (1996).
4. T. Hidaka, T. Maruyama, M. Saitoh, *et al.*, Appl. Phys. Lett. **68** (17), 2358 (1996).
5. C. H. Ahn, T. Tybell, L. Antognazza, *et al.*, Science **276**, 1100 (1997).
6. L. M. Eng, Nanotechnology **10**, 405 (1999).
7. L. M. Eng, M. Bammerlin, Ch. Loppacher, *et al.*, Ferroelectrics **222**, 153 (1999).
8. H. Haefke, R. Luthi, K.-P. Meyer, and H.-J. Güntherodt, Ferroelectrics **151**, 143 (1994).
9. K. Hara, M.-K. Bae, H. Okabe, *et al.*, Ferroelectrics **170**, 101 (1995).
10. J. Ohgami, Y. Sugawara, S. Morita, *et al.*, Jpn. J. Appl. Phys., Part 1 **35** (5A), 2734 (1996).
11. H. Bluhm, R. Wiesendanger, and K.-P. Meyer, J. Vac. Sci. Technol. B **14** (2), 1180 (1996).
12. H. Bluhm, K.-P. Meyer, and R. Wiesendanger, Ferroelectrics **200**, 327 (1997).
13. H. Bluhm, U. D. Schwarz, and R. Wiesendanger, Phys. Rev. B **57** (1), 161 (1998).
14. L. M. Eng, M. Friedrich, J. Fousek, and P. Gunter, J. Vac. Sci. Technol. B **14** (2), 1191 (1996).
15. E. A. Wood and A. N. Holden, Acta Crystallogr. **10**, 145 (1957).
16. F. Jona and G. Shirane, *Ferroelectric Crystals* (Pergamon, Oxford, 1962; Mir, Moscow, 1965).
17. N. V. Belugina, A. L. Tolstikhina, and S. A. Shikin, Poverkhnost, No. 2, 22 (2000).
18. A. L. Tolstikhina, N. V. Belugina, and S. A. Shikin, Ultramicroscopy **82**, 149 (2000).
19. J. Ohgami, Y. Sugawara, S. Morita, *et al.*, J. Phys. Soc. Jpn. **66** (9), 2747 (1997).
20. L. M. Eng, M. Bammerlin, Ch. Loppacher, *et al.*, Appl. Surf. Sci. **140**, 253 (1999).
21. L. M. Eng, H.-J. Guntherodt, G. Rosemann, *et al.*, J. Appl. Phys. **83** (11), 5973 (1998).
22. N. V. Belov and M. V. Klassen-Neklyudova, Zh. Tekh. Fiz. **18**, 265 (1943).

Translated by L. Man

Crystallography Reports, Vol. 46, No. 5, 2001, pp. 856–859. Translated from Kristallografiya, Vol. 46, No. 5, 2001, pp. 930–933.

Dedicated to the memory of B.K. Vainshtein

Compaction of Adsorbed Alkali Metal Submonolayers on the {111} and {0001} Surfaces of Metal Crystals

V. F. Dvoryankin and G. G. Dvoryankina

Institute of Radio Engineering and Electronics, Russian Academy of Sciences, Fryazino, Moscow oblast, 141120 Russia

Received December 13, 2000

Abstract—The structural mechanism has been suggested of formation of the ordered surface hexagonal structures with an increase of the coverage during adsorption of alkali metal atoms on the {111} surfaces of face-centered cubic and {0001} surfaces of a hexagonal metal crystal. The coverage θ_s providing the formation of close-packed hexagonal adsorbed layers in adsorption systems is determined for alkali metals. The theoretically calculated and the experimentally obtained θ_s values are in good agreement. *© 2001 MAIK "Nauka/Interperiodica".*

INTRODUCTION

At present, considerable experimental material has been accumulated on the surface structures formed by alkali metal atoms adsorbed on the {111} and {0001} faces of metal crystals [1–4]. Since the lateral interactions between the adsorbed alkali metal atoms are of the isotropic nature, then, in accordance with the symmetry of the {111} and {0001} faces, the two-dimensional surface structures are formed. These structures have rhomblike primitive unit cells consisting of two regular triangles and are formed within the large range of coverages θ until the complete filling of the first adsorbed layer.

We had the aim to establish the structural mechanism providing the change of the primitive unit cells of the surface structure with an increase of coating θ. The knowledge of such mechanism would allow one to predict which atomic structures would be observed by the electron diffraction method in a certain range of coverages and identify the corresponding diffraction patterns.

With an increase of the coverage θ, the adsorbed alkali metal atoms tend to form the hexagonal close-packed structures, whose formation indicates the completion of growth of the first adsorbed layer. It is very important to determine the coverage θ_s value at which the saturated hexagonal close-packed layers are formed, because the formation of the second adsorbed layer can occur at coverages θ lower than θ_s. This would break the growth of adsorbed layers and results in the erroneous interpretation of the experimental data. The problem of θ_s determination for various adsorption systems is reduced to the determination of the atomic radii of alkali metal atoms which then can be used for determination of interatomic distances in hexagonal close-packed layers. The atomic radii in adsorptive metal systems were discussed earlier [5]. However, the atomic radii appropriate for the determination of interatomic distances in adsorbed close-packed layers have not been considered.

Below, we suggest the structural mechanism of the changes in the surface structures during compaction of adsorbed layers of alkali metals and calculate the θ_s values for various adsorptive systems with the participation of Cs, Rb, K, and Na adsorbates.

STRUCTURAL MECHANISM OF COMPACTION OF ADSORBED ALKALI METAL LAYERS

The figure shows the scheme of compaction of the alkali metal layers on the {111} planes of cubic face centered and {0001} hexagonal metal crystals. It is seen that compaction of the layers occurs via successive rotations of the primitive unit cell by 30° with the simultaneous reduction of its dimensions by a factor of $\sqrt{3}/2$. In the analytical form, this mechanism can be represented as

$$\ldots(2\times 2)[0.25] \longrightarrow (\sqrt{3}\times\sqrt{3})R30^\circ[0.33] \longrightarrow 3/2\times 3/2[0.44] \longrightarrow (3\sqrt{3}/4\times 3\sqrt{3}/4)R30^\circ[0.59]. \quad (1)$$

The figures in square brackets indicate the corresponding coverages θ. At the coverages $\theta < 0.25$, the compac-

1063-7745/01/4605-0856$21.00

tion mechanism can be written as

$$\begin{aligned}&\ldots(16/9\sqrt{3}\times 16/9\sqrt{3})R30°[0.11]\\&\longrightarrow (8/3\times 8/3)[0.14]\\&\longrightarrow (4/3\sqrt{3}\times 4/3\sqrt{3})R30°[0.18]\ldots\end{aligned}\qquad(2)$$

These surface structures can be transformed in the following way:

$$\begin{aligned}&\ldots(3.08\times 3.08)R30°[0.11]\\&\longrightarrow (2.67\times 2.67)[0.14]\\&\longrightarrow (2.31\times 2.31)R30°[0.19]\ldots\end{aligned}\qquad(3)$$

These are only hypothetical structures, which cannot be obtained in practice. Therefore, series (3) are written in another form

$$\begin{aligned}&\ldots(3\times 3)[0.11]\ (\sqrt{7}\times\sqrt{7})R19.1°[0.14]\\&\longrightarrow 1/2\sqrt{21}\times 1/2\sqrt{21}R10.9°[0.19]\ldots\end{aligned}\qquad(4)$$

The unit-cell dimensions and the coverages θ in series (3) and (4) of atomic surface structures practically coincide. The total rotation of the unit-cells, $(\sqrt{7}\times\sqrt{7})R19.1°$ and $(1/2\sqrt{21}\times 1/2\sqrt{21})R10.9°$, equals 30°.

The study of the adsorption system Cs/Ag {111} by the low-energy electron diffraction method at low temperatures (40–50 K) [6] revealed the following series of atomic surface structures with an increase of the coverage θ:

$$\begin{aligned}&\ldots(2\sqrt{3}\times 2\sqrt{3})R30°[0.08]\\&\longrightarrow (3\times 3)[0.11]\\&\longrightarrow (\sqrt{7}\times\sqrt{7})R19.1°[0.14]\\&\longrightarrow (A\times B)[0.18]\longrightarrow (2\times 2)[0.25]\longrightarrow [\theta_s = 0.32].\end{aligned}\qquad(5)$$

Comparison of (1) with (4) and (5) shows that the experimental data are consistent with the mechanism of compaction of the alkali metal adsorbed layer suggested in this study. To confirm this conclusion, consider one more example. In the adsorption system K/Pt{111} [7], the following series of atomic surface structures are formed with an increase of the coverage θ

$$\begin{aligned}&\ldots(3\times 3)[0.11]\longrightarrow (\sqrt{7}\times\sqrt{7})R19.1°[0.14]\\&\longrightarrow (2\times 2)[0.25]\longrightarrow (\sqrt{3}\times\sqrt{3})R30°[0.33]\\&\longrightarrow 3/2\times 3/2[0.44].\end{aligned}\qquad(6)$$

It is seen that the structure $(1/2\sqrt{21}\times 1/2\sqrt{21})R10.9°[0.19]$ is omitted in (6), and in (5), it is not identified.

The suggested structural mechanism allows the determination of all the atomic surface structures depending on the coverage θ. Only some fragments of this mechanism are considered in numerous publications which can be explained either by the difficulties encountered in the formation of ordered structures in concrete adsorption systems or by non-optimum experimental conditions.

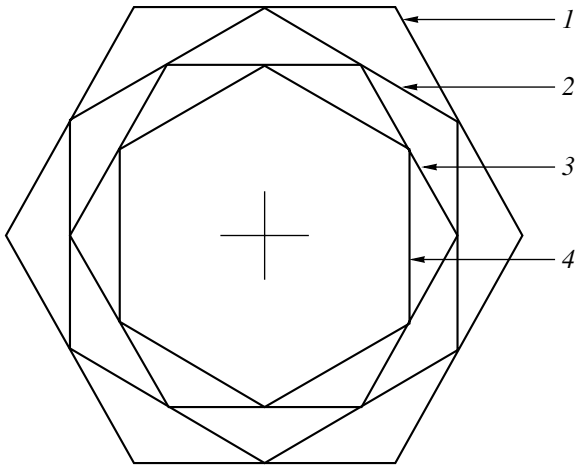

Schematic changes in the surface structures occurring with an increase of θ: (*1*) (2 × 2), (*2*) ($\sqrt{3}\times\sqrt{3}$)*R*30°, (*3*) (3/2 × 3/2), and (*4*) ($3\sqrt{3}/4\times 2\sqrt{3}/4$)*R*30°.

CALCULATION OF COVERAGE θ_s FOR HEXAGONAL CLOSE-PACKED ALKALI METAL LAYERS

The coverage θ_s corresponding to the formation of hexagonal close-packed layers on metal substrates can be calculated if the area occupied by the primitive unit cells on the surface of the metal crystal, S_s, and the hexagonal close packed layer, S_A are known. In this case, the value of θ_s equals S_s/S_A. The value of S_s for the surface with a certain orientation can be determined from the unit-cell dimensions of metal crystals [8]. To determine S_A, one has to know the atomic radii of Cs, Rb, K, and Na characterizing the interatomic distances in close-packed adsorbed layers. The atomic radii used for calculating interatomic distances in bulk metal crystals cannot be used in this case because the coefficient of close packing of spheres in two-dimensional space ($\pi/2\sqrt{3}$ = 0.9069) exceeds the corresponding coefficient for the three-dimensional space ($\pi/3\sqrt{2}$ = 0.7404). In Cs, Rb, K, and Na crystals, each atom has

Table 1. Atomic radii (Å) of alkali metals used for calculating θ_s

Na	K	Rb	Cs	Reference
1.80	2.20	2.35	2.60	[9, 10]
–	2.162	2.287	2.518	[11]
1.79	2.21	2.33	2.51	[12]

Table 2. Coverage θ_s of the alkali metal-saturated {111} and {0001} surfaces of metal crystals

Surface	S_p, Å	θ_s			
		Cs	Rb	K	Na
Ni{111}	5.377	0.23–0.25	0.28–0.30	0.32–0.33 (0.31 [13])	0.48 (0.49 [14])
Co{0001}	5.451	0.23–0.25	0.28–0.30	0.33–0.34 (0.31 [15])	0.49
Fe{111}	5.584	0.24–0.26	0.29–0.31	0.33–0.35	0.50
Cu{111}	5.658	0.24–0.26 (0.25 [16])	0.30–0.31 (0.31 [17])	0.34–0.35 (0.33 [18])	0.50 (0.54 [19])
Zn{0001}	6.150	0.26–0.28	0.32–0.34	0.37–0.38	0.55
Rh{111}	6.263	0.27–0.29	0.33–0.34	0.37–0.39 (0.36 [20])	0.56
Ru{0001}	6.331	0.27–0.29 (0.29 [21])	0.33–0.35 (0.33 [22])	0.38–0.39 (0.37 [23])	0.56 (0.58 [24])
Ir{111}	6.383	0.27–0.29	0.33–0.35	0.38–0.39	0.57
Cr{0001}	6.416	0.27–0.29	0.34–0.35	0.38–0.40	0.57
Os{0001}	6.479	0.28–0.30	0.34–0.36	0.39–0.40	0.58
Pd{111}	6.552	0.28–0.30	0.34–0.36	0.39–0.41	0.58
Re{0001}	6.601	0.28–0.30	0.34–0.36	0.39–0.41	0.59
Pt{111}	6.664	0.28–0.30 (0.30 [25])	0.35–0.37	0.40–0.41 (0.40 [26])	0.59 (0.59 [25])
Al{111}	7.101	0.30–0.32 (0.33 [27])	0.37–0.39	0.42–0.44 (0.45 [28])	0.63
Au{111}	7.203	0.31–0.33	0.37–0.40	0.43–0.45	0.64
Ag{111}	7.230	0.31–0.33 (0.33 [6])	0.38–0.40 (0.37 [6])	0.43–0.45 (0.40[6])	0.64
Ti{0001}	7.536	0.32–0.34	0.39–0.41	0.45–0.47	0.67
Cd{0001}	7.685	0.33–0.35	0.40–0.42	0.46–0.47	0.68

eight nearest neighbors located at distances $a_0\sqrt{3}/2$, where a_0 is the parameter of the body-centered cubic unit cell. The packing coefficient for such crystals equals 0.681. Thus, the interatomic distances in adsorbed hexagonal close-packed layers should be shorter than the corresponding distances in bulk alkali metal crystals.

In this study, the interatomic distances in hexagonal close-packed layers of alkali metals were characterized with the use of the following radii (Table 1): ionic–atomic radii [9, 10], orbital radii for Cs, Rb, and K [11], and octahedral covalent radii [12]. It is seen that covalent radii are close to ionic–atomic ones. We used the following values: for Cs 2.51 and 2.60 Å, for Rb 2.29 and 2.35 Å, for K 2.16 and 2.21 Å, for Na 1.80 Å, and calculated the areas of the primitive unit cells S_A and determined the values θ_s (Table 2). The experimental values of θ_s are indicated in brackets together with the corresponding references. It is seen that the calculated θ_s values agree quite well with the experimental data.

It should also be indicated that the atomic radii of alkali metals chosen for characterization of interatomic distances in adsorbed close-packed layers on the {111} surface of face-centered cubic and {0001} hexagonal metal crystals can also be used for the determination of interatomic distances in adsorbed close-packed layers of alkali metals on other surfaces of metal crystals.

The θ_s values characterize the termination of series (1) of the ordered surface structures. Since the alkali metal atoms are rather large, series (1) are terminated at low θ_s values (Table 2).

CONCLUSION

The structural mechanism of compaction of adsorbed layers of alkali metals on the surfaces of metal crystals suggested in the present study is consistent with the modern concepts on the changes in chemical bonding between the adsorbed atoms of alkali metals with an increase in coverage. Thus, it was shown [29] that the transition from the ionic to metallic bonding takes place in the process of filling the first adsorbed layer of the alkali metal. Ionic bonding at low coverage is provided by the transition of electrons from adsorbed atoms to the substrate, which results in the partial ionization of these adsorbed atoms. With an increase of the coverage, the adsorbed atoms got back their valence electrons and can be considered as metal atoms, which can approach one another to distances comparable with the dimensions of the nS^1-orbital and, thus, can form either metal or covalent bonds. Finally, this results in the formation of hexagonal close-packed layers with the coverage θ_s.

It is expedient to study the structural mechanisms of compaction of adsorbed layers formed by metal ions with the electronic structure different from the electronic structure of alkali metal atoms. Such studies would make an essential contribution to understanding

and interpretation of the processes of adsorbed submonolayer formation on the metal surface with an increase of coverage.

REFERENCES

1. *Physics and Chemistry of Alkali Metal Adsorption*, Ed. by H. P. Bonzel *et al.* (Elsevier, Amsterdam, 1989).
2. R. D. Diehl and R. McGrath, Surf. Rev. Lett. **2**, 387 (1995).
3. R. D. Diehl and R. McGrath, Surf. Sci. Rep. **23**, 43 (1996).
4. R. D. Diehl and R. McGrath, J. Phys.: Condens. Matter **9**, 951 (1997).
5. C. T. Cambell, Surf. Sci. **167**, L181 (1986).
6. G. S. Leetherman and R. D. Diehl, Phys. Rev. B **53**, 4939 (1996).
7. S. Moré, W. Berndt, A. M. Bradshaw, and R. Stumpt, Phys. Rev. B **57**, 9246 (1998).
8. *Crystallographic Data on Metal and Alloy Structures*, Ed. by A. Taylor and J. Kogle Brenda (Dover, New York, 1963).
9. J. C. Slater, J. Chem. Phys. **41**, 3199 (1964).
10. V. I. Lebedev, *Ionic Atomic Radii and Their Role in Geochemistry and Chemistry* (Leningr. Gos. Univ., Leningrad, 1969).
11. J. T. Waber and D. T. Cromer, J. Chem. Phys. **42**, 4116 (1965).
12. S. S. Batsanov, Zh. Strukt. Khim. **3**, 616 (1962).
13. D. Fisher, Z.-Y. Li, and R. D. Diehl, Surf. Sci. **259**, 85 (1991).
14. R. L. Gerlach and T. N. Rhodin, Surf. Sci. **17**, 32 (1969).
15. T. Vaara, J. Vaari, and J. Lahtinen, Surf. Sci. **395**, 28 (1998).
16. S. A. Lindgren, L. Walldén, J. Rundgren, *et al.*, Phys. Rev. B **28**, 6707 (1983).
17. X. Shi, C. Su, D. Heskett, *et al.*, Phys. Rev. B **49**, 14638 (1994).
18. R. L. Adler, I. R. Collins, S. J. Murray, *et al.*, Phys. Rev. B **48**, 17445 (1993).
19. D. Tang, D. McIlroy, X. Shi, *et al.*, Surf. Sci. **255**, 497 (1991).
20. J. E. Crowell and G. A. Somorjai, J. Vac. Sci. Technol. A **2**, 881 (1984).
21. M. Kiskinova, G. Rangelov, and L. Surnev, Surf. Sci. **147**, 57 (1986).
22. T. Hertel, H. Over, H. Bludau, *et al.*, Phys. Rev. B **50**, 8126 (1994).
23. R. Duszak and R. H. Prince, Surf. Sci. **216**, 14 (1989).
24. T. Hertel, H. Over, H. Bludau, *et al.*, Surf. Sci. **301**, 1 (1994).
25. J. Cousty and R. Riwan, Surf. Sci. **204**, 45 (1988).
26. K. G. Pirug and H. P. Bonzel, Surf. Sci. **194**, 159 (1988).
27. D. L. Adams, Appl. Phys. A: Mater. Sci. Process. **A62**, 123 (1996).
28. S. V. Christensen, K. T. Neilsen, J. Nerlov, *et al.*, Surf. Sci. **339**, 919 (1995).
29. K. Horn, J. Somers, Th. Linder, and A. M. Bradshaw, in *Physics and Chemistry of Alkali Metal Adsorption* (Elsevier, Amsterdam, 1989), p. 55.

Translated by L. Man

Crystallography Reports, Vol. 46, No. 5, 2001, pp. 860–863. Translated from Kristallografiya, Vol. 46, No. 5, 2001, pp. 934–937.

Dedicated to the memory of B.K. Vainshtein

Dependence of the Step Velocity on Its Length on the (010) Face of the Orthorhombic Lysozyme Crystal

L. N. Rashkovich[1], N. V. Gvozdev[1], M. I. Sil'nikova[1], I. V. Yaminskiĭ[1], and A. A. Chernov[2]

[1] *Physics Faculty, Moscow State University, Vorob'evy gory, Moscow, 119899 Russia*

e-mail: rashk@polc49.phys.msu.su

[2] *NASA Marshall Space Flight Center, Huntsville, AL 35812, USA*

e-mail: alex.chernov@msfc.nasa.gov

Received December 6, 2000

Abstract—The length of a two-dimensional critical nucleus has been measured, and the Gibbs–Thomson formula has been experimentally verified on orthorhombic lysozyme crystals. The step velocity was found to be independent of its length. The critical length initiating the step motion can be determined by a low density of kinks on a step, and not the critical-nucleus size. The invalidity of the Gibbs–Thomson formula in this case is discussed. © *2001 MAIK "Nauka/Interperiodica".*

The steps on the growing (010) face of an orthorhombic lysozyme crystals (grown at pH 4.6 from the reactive agents supplied to us by Seikagaku Co., Japan) were observed in an atomic force microscope. The mass concentration of the salting-out agent (NaCl) was equal to 5 mass %, the equilibrium and actual concentrations of lysozyme were $C_0 = 0.35$ mass % [1] and $C = 0.95$ mass %, respectively. Thus, the relative supersaturation was $\sigma = (C - C_0)/C_0 = 1.7$ (i.e., $C/C_0 = 2.7$).

Studying the faces of the lysozyme crystal, we revealed a stacking fault in the form of an 8-μm-long step parallel to [100] which was not overgrown during growth. The step height ranged within (0.5–1.5)b (b = 7.37 nm) of the lysozyme crystal (Fig. 1). The rectilinear steps generated by a dislocation source along the c-axis propagate normally and along the stacking fault (above and below it).

The motion below the defect was begun upon the attainment by the step of the critical length l_c (Fig. 2). A part of a step indicated by the letter A had advanced for a considerable distance above the defect (right-hand part in Fig. 2), while the other part of this step indicated by the letter B did not start moving because the length of this part was still less than l_c. Taking successive frames of the process and measuring the time dependences of the following distances from the clearly seen point of the stacking fault emergence (shown by the arrow in Fig. 1): (i) to the step edge along the c-axis (curve *1*, Fig. 3), (ii) normally to the part of the step moving above the defect (curve *2*, Fig. 3), (iii) normally to the part of a step moving below the defect (at the left-hand side of Fig. 2, curve *3* in Fig. 3). All these dependences turned out to be linear. These straight lines are described by the following equations: (*1*) $x = 680 \pm 24 + (17.3 \pm 0.3)t \pm 31$; (*2*) $x = 745 \pm 27 + (2.4 \pm 0.2)t \pm 41$; (*3*) $x = -(58 \pm 9) + (2.2 \pm 0.1)t \pm 7$ nm.

Thus, the step velocity along the c-axis was $V_{001} \equiv V_{\parallel} = 17.3 \pm 0.3$ nm/s; along the a-axis above the defect, $V_{100} \equiv V_{\perp} = 2.4 \pm 0.2$ nm/s; and below the defect, $V = 2.2 \pm 0.$ nm/s. It is seen that the two latter velocities are indistinguishable within the experimental accuracy. The step below the defect started moving only after the step length along the c-axis attained the value $l_c = 1140 \pm 150$ nm. Consider Fig. 3. The time was measured from the moment when the length of an immobile step segment was 680 nm, although the segment started increasing at the moment when the straight line *1* intersected the time axis, i.e., at the moment earlier by 680 nm : 17.3 nm/s ≅ 40 s.

The constancy of velocity V indicates that it does not depend on varying of the step length as is shown by the curve *3* in Fig. 3. This is inconsistent with the Gibbs–Thomson formula

$$V = V_{\infty}(1 - l_c/l), \qquad (1)$$

where V_{∞} is the velocity of an infinitely long step, l is

its length, and

$$l_c = 8.2\Omega\alpha/kT\ln C/C_0. \quad (2)$$

Here $\Omega = 3.16 \times 10^{-20}$ cm^3 is the volume of a molecule in the lysozyme unit cell, α is the free surface energy of a step rise, k is the Boltzmann constant, and T is the temperature. The numerical coefficient is obtained under the assumption that the two-dimensional critical nucleus has a rectangular shape with the ratio of the sides equal to $V_{001}/V_{100} = 7.2$ (l_c is the longer side of a rectangle).

Taking the measured value of l_c and the step length $l \approx 2700$ nm (for the second experimental point on the lowest curve in Fig. 3), we obtain $l_c/l = 0.42$. It follows from Eq. (1) that the V/V_∞ ratio should be equal to 0.58. In other words, the second point should be located lower by a factor of almost two, which considerably exceeds the experimental error.

The value $\alpha = 20 \pm 2$ erg/cm^2 ($kT = 4.25 \times 10^{-14}$ erg) calculated by Eq. (2) is higher by an order of magnitude than the values typical of protein crystals. However, assuming that the volume of a building unit is equal to the unit-cell volume ($\Omega' = 4\Omega$), we obtain $\alpha = 5 \pm 0.5$ erg/cm^2, which is closer to typical values (1 erg/cm^2) [2]. Unfortunately, the number of molecules the building unit consists of is still unclear.

The velocity V is independent of l, which can be explained considering the motion of steps with the length comparable with l_c [3, 4]. According to [3, 4], the step edge should have the equilibrium shape, and the step velocity is limited to a straight portion of the length $l - l_c/2$. The resulting expression relating a step length and the step velocity has the form

$$l/l_c - 1 = A(V/V_0) \times (1 - V/V_0)^{-1/2}\left(1 + \frac{2}{\pi}\arcsin V/V_0\right), \quad (3)$$

where the constant A for a critical nucleus having the assumed shape is $A = 0.38kT/\alpha ab \approx 0.008$ (the lattice parameter $a = 5.65$ nm and α is taken to be equal to the lowest of the values indicated above, ~5 erg/cm^2).

It follows from Eq. (3) that if $A \ll 1$, then even a small excess of a step length l over l_c makes the step velocity equal to the velocity of an infinite step, in other words, V is independent of l. According to [4], the surface energy is related to the kink density as $\alpha \approx kT/ca^2\rho_\infty$. Using the parameters of the building unit equal to the unit cell, we have $\alpha \approx 7$ erg /cm^2, which is close to the value calculated by Eq. (2).

Another approach to the interpretation of the data obtained is as follows. A rectilinear step parallel to the c-axis starts moving parallel to itself only with the formation of the nuclei of new molecular rows and motion of kinks limiting these nuclei.

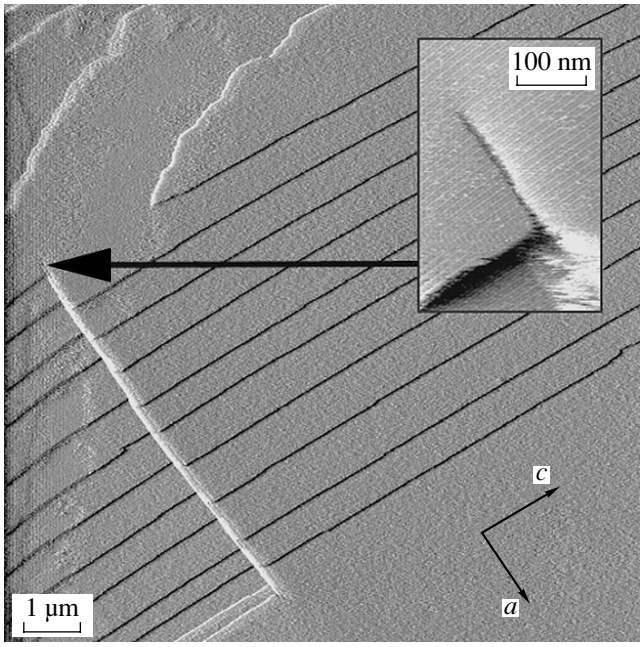

Fig. 1. Stacking fault on a crystal face. Contact mode, scanning frequency 15 Hz. A dislocation source of steps is not seen because it is located on the upper right-hand side.

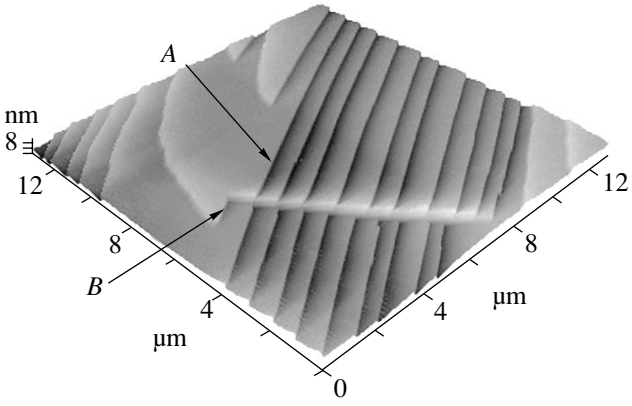

Fig. 2. Three-dimensional image of steps passing by a stacking fault. The experimental conditions are the same as in Fig. 1. For notation see the text.

A step segment having the finite length $l - V_\parallel t$ limited from one side by the stacking fault (right-hand side in Fig. 2) cannot acquire any kinks from the outside. Therefore, it can move in the direction normal to itself only due to the formation of nuclei of new rows, i.e., pairs of kinks having the opposite signs on this segment. At small segment length l, the segment has no kinks (they had no time to appear). During this period, the segment is static, $V = 0$. As soon as the first nucleus is generated, a new row is formed along the segment

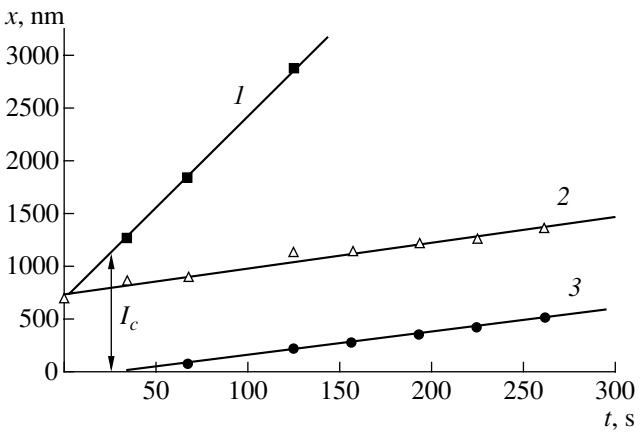

Fig. 3. To the determination of the step velocity. The temporal dependence of distances from the point of emergence of a stacking fault: (*1*) to the step edge along the *c*-axis; (*2*) along the normal to the segment of the same step moving above the defect; (*3*) the same for the segment moving below the defect.

and the segment is displayed by a distance equal to the kink depth, i.e., a single lattice parameter $a = 5.65$ nm. Then, the second nucleus appears, etc. With an increase of the segment length l, the nuclei of new rows can appear on the segment even prior to the complete formation of the preceding rows. When the segment length l considerably exceeds the mean interkink distance on an infinite step, $1/\rho_\infty = (v_k/2J)^{1/2}$ [5], the velocity of the segment reaches a steady-state value $V = a(2v_kJ)^{1/2}$, where v_k is the kink velocity along the step, J is the rate of nucleation of one-dimensional nucleus. Curve *3* in Fig. 3 shows that the initial nonstationary period of nucleation corresponds to the absence of any growth; then the growth at the constant rate corresponds to the linear increase of length with time.

The expectation time t_1 for the appearance of the first nucleus can be determined from the condition that the number of nuclei formed on the measuring (growing) segment is equal to unity:

$$\int_0^{t_1} d\tau \int_0^{v_\parallel \tau} J\, d\xi = 1. \qquad (4)$$

Here ξ is the coordinate along the segment from the immovable contact point at the stacking fault and the time τ, similar to the time t, is measured from the moment when the segment starts increasing. Assuming that J is independent of the coordinate and time, we obtained from Eq. (4)

$$t_1 = (2/JV_\parallel)^{1/2}. \qquad (5)$$

Now evaluate t_1. The velocity of one-dimensional nucleation $J_0 = 2.7 \times 10^{-5}$ nm^{-1} s^{-1} was determined earlier with the use of atomic force microscopy [6]. We measured the kink density $\rho_{\infty 0} = 1.74 \times 10^{-3}$ nm^{-1}, the velocity of step motion $V_{\perp 0} = a(2v_kJ)^{1/2} = a\rho_\infty v_k = 0.19$ nm/s, and the velocity of kink motion $v_{k0} = V_{\perp 0}/a\rho_{\infty 0} = 19.3$ nm/s. However, we failed to measure supersaturation σ with satisfactory precision [6].

Within the only existing classical Kossel model, $J \approx \sigma(1 + \sigma)$ [5], $v_k \sim \sigma$, and, thus, $V_\perp \sim \sigma(1 + \sigma)^{1/2}$. Now apply this model to our experiments and assume that the kinetic coefficients in our experiments and in [6] are the same. Then, using the ratio of step velocities $V_\perp = 2.4$ nm/s in our earlier [6] and the present experiments, one can yield the value of the supersaturation unknown in the present experiment, σ_0, via the $\sigma = 1.7$ in the form

$$\sigma_0(1 + \sigma_0)^{1/2} = (V_{\perp 0}/V_\perp)\sigma(1 + \sigma)^{1/2}. \qquad (6)$$

Then we find $\sigma_0 = 0.21$. Similarly, $v_k = v_{k0}(1.7/0.21) = 156$ nm/s, and

$$J = [\sigma(1 + \sigma)/\sigma_0(1 + \sigma_0)]J_0 = 4.9 \times 10^{-4} \text{ nm}^{-1} \text{ s}^{-1}. \qquad (7)$$

Then the kink density is $\rho_\infty = 2.6 \times 10^{-3}$ nm^{-1}. Substituting J from Eq. (7) and $V_\parallel = 17.33$ nm/s into Eq. (5), we obtain $t_1 = 15$ s.

The time experimentally obtainable from Fig. 3, $t_c = l_c/V_\parallel = 66$ s (at the moment when the velocity of a step segment reaches a steady-state value) corresponds to the condition at which the ratio of the step length to the interkink distance ($1/\rho_\infty = l/(v_{k/2}J)^{1/2}$) equals several units. In our case, $1/\rho_\infty = 385$ nm and $l_c = 1140$ nm $\cong 3/\rho_\infty$. In actual fact, this ratio is much less, because for short steps $\rho < \rho_\infty$ [7, 8]. By the moment t_c, the number of nuclei formed on the growing segment would have been less than $JV_\parallel t_c^2 = Jl_ct_c/2 = 18$, i.e., the segment should be displaced to a distance much shorter than $18 \times 5.65 \cong 100$ nm and which is close to the measurement accuracy. At $l > l_c$, the velocity $V_\perp$ becomes constant, and the nonstationary approach described by Eq. (4) becomes inapplicable.

Thus, the study of a step on the (010) face of an orthorhombic lysozyme crystal shows that the critical length of a step segment at the beginning of its displacement and the dependence of its velocity on the segment length seem to be of purely kinetic origin. The large value of l_c (>1 μm) seems to be determined by a small kink density on the step rather than high surface energy. The same cause also explains the independence of the step velocity of its length. Of course, the thermodynamic Gibbs–Thomson relation remains valid, but only

at lower ($\ll 1$) supersaturations at the steps with low kink density where the kinetic effects become unimportant.

ACKNOWLEDGMENTS

This study was supported by the Russian Foundation for Basic Research, projects nos. 00-02-16701 and 00-04-55020, the NATO grant PST.CLG 975240, and the NASA grants NCC8-66-50 and NAG-1454.

REFERENCES

1. M. Ataka and M. Asai, J. Cryst. Growth **90**, 86 (1988).
2. A. A. Chernov, Phys. Rep. **288**, 61 (1997).
3. V. V. Voronkov, Kristallografiya **18**, 32 (1973) [Sov. Phys. Crystallogr. **18**, 19 (1973)].
4. V. V. Voronkov, in *Crystals: Growth, Properties and Applications*, Ed. by A. A. Chernov and H. Muller-Krumbhaar (Springer-Verlag, Berlin, 1983), Vol. 9, p. 74.
5. V. V. Voronkov, Kristallografiya **15** (1), 135 (1970) [Sov. Phys. Crystallogr. **15**, 108 (1970)].
6. A. A. Chernov, L. N. Rashkovich, I. V. Yaminski, and N. V. Gvozdev, J. Phys.: Condens. Matter **11**, 9969 (1999).
7. F. C. Frank, J. Cryst. Growth **22**, 233 (1974).
8. T. A. Onishchenko, G. T. Moldazhanova, O. V. Monovskiĭ, and L. N. Rashkovich, Kristallografiya **41** (3), 413 (1996) [Crystallogr. Rep. **41**, 389 (1996)].

Translated by A. Zalesskiĭ

Crystallography Reports, Vol. 46, No. 5, 2001, pp. 864–867. Translated from Kristallografiya, Vol. 46, No. 5, 2001, pp. 938–941.

CRYSTAL GROWTH

Growth and Ionic Conductivity of γ-Li_3PO_4

A. K. Ivanov-Shitz, V. V. Kireev, O. K. Mel'nikov, and L. N. Demianets

Shubnikov Institute of Crystallography, Russian Academy of Sciences, Leninskiĭ pr. 59, Moscow, 117333 Russia

e-mail: ivanov@ns.crys.ras.ru

Received December 18, 2000

Abstract—Single crystals of γ-Li_3PO_4 have been grown from flux. The $4 \times 8 \times 9$-mm crystals have the cleavage along the [010] and [120] directions. The anisotropy in ionic conductivity in the grown crystals, $((\sigma \parallel a)/(\sigma \parallel b) = 2.5$ and $(\sigma \parallel a)/(\sigma \parallel c) = 1.3)$, is explained by specific features of the γ-Li_3PO_4 structure. © *2001 MAIK "Nauka/Interperiodica".*

INTRODUCTION

One of the best studied and most interesting families of solid electrolytes consists of materials with the γ-Li_3PO_4-type structure such as Li_4GeO_4- and Li_4SiO_4-based solid solutions [1–3]. The nonstoichiometric phases in the Li_4GeO_4–Li_3VO_4, and Li_4GeO_4–Li_3PO_4 systems have high values of ionic conductivity (up to 10^{-4}–10^{-5} Ω/cm) even at room temperature [1–3], which makes these materials very promising for practical application in lithium-based current sources. Solid electrolytes with the γ-Li_3PO_4-type structures can also be model objects for studying the effect of various factors on ionic conductivity. However, up to now, no detailed study of ionic conductivity in lithium orthophosphate has been made, which is explained, first of all, by the absence of bulk single crystals necessary for such study. Therefore, the present study was aimed at growth of γ-Li_3PO_4 single crystals, the study of anisotropy in ionic conductivity, and the determination of the mechanism of ion transport in these crystals.

EXPERIMENTAL

The initial material used for growing γ-Li_3PO_4 crystals was polycrystalline lithium orthophosphate synthesized from LiH_2PO_4 and Li_2CO_3 by the standard solid-phase technology with the annealing temperature being 800°C. The γ-Li_3PO_4 single crystals were grown by crystallization from flux with the Li_2MoO_4–LiF mixture as a solvent. The initial components in the mass ratio $Li_3PO_4 : Li_2MoO_4 : LiF = 50 : 34 : 16$ were placed into a 60-ml platinum vessel. The platinum rod served as a seed. Upon the complete dissolution of lithium orthophosphate in the melt at 1030°C, the system was rapidly cooled down to 990°C, and then the crystallization was performed by cooling the melt at a rate of 0.15°C to the temperature 950°C. The crystals grown were taken from the melt and cooled to room temperature at a rate of 30°C/h.

The crystals grown were identified by the X-ray phase analysis on a Rigaku D maxIIIc diffractometer (CuK_α radiation).

Since the γ-Li_3PO_4 crystals are orthorhombic, the ionic conductivity (σ) was measured along the three directions (crystallographic *a*-, *b*-, and *c*-axes). To measure the ionic conductivity, silver electrodes were applied to the ends of the oriented γ-Li_3PO_4 crystals (the silver paste was applied onto the preliminary polished surfaces of the crystals then annealed at 500–550°C). The ionic conductivity was measured by the method of impedance spectroscopy in the frequency range 50 Hz–500 kHz. The impedance spectra were processed using the EQUIVCRT complex of programs written by Boucamp [4].

RESULTS AND DISCUSSION

The crystallization experiments yielded colorless intergrowths of lithium orthophosphate crystals about 25 mm in diameter. Single crystal domains had the maximum dimensions $4 \times 8 \times 9$ mm and were studied in a polarization microscope. The crystals had the cleavages normal to the [010] and [120] directions. The angle formed by the cleavage planes was 40.2°. According to the X-ray phase analysis data, the crystals were identified with γ-lithium orthophosphate.

Figure 1 shows the hodographs of the total resistance of γ-Li_3PO_4 crystals (σ measured along the *b*-axis) and the equivalent electric circuit for determining the hodograph parameters. The resistance *R* of the equivalent electric circuit corresponds to the bulk resistance of the crystal. The form of the impedance hodograph was the same for the conductivity measured

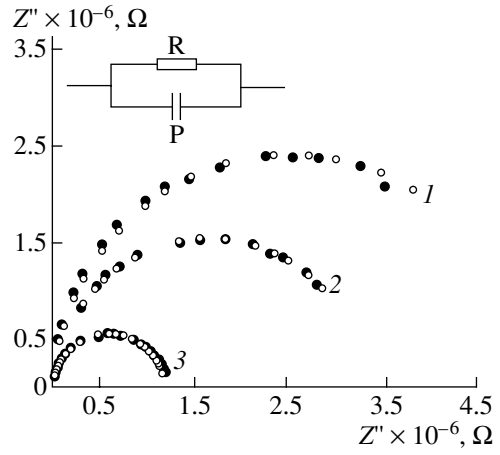

Fig. 1. Frequency dependence of total complex resistance in γ-Li_3PO_4 crystals measured along the *b*-axis at the temperatures (*1*) 330, (*2*) 345, (*3*) 374°C. Filled circles correspond to the experimental data; light circles, to the calculated data.

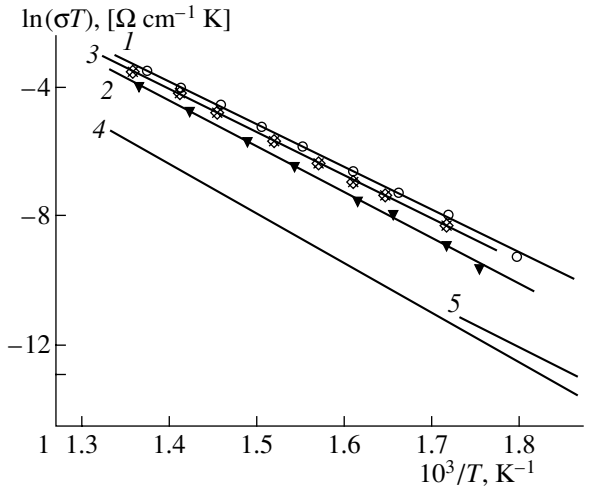

Fig. 2. Temperature dependences of conductivity in γ-Li_3PO_4: (*1–3*) for single crystals measured along the (*1*) *a*-axis, (*2*) *b*-axis, (*3*) *c*-axis and (*4*, *5*) for a polycrystal (*4*) according to [4, 5] and (*5*) according to [7].

along all the three crystallographic axes. As is seen from Fig. 1, the impedance hodograph has the shape of a distorted semicircumference. At temperatures lower than 350°C, the high resistance of γ-Li_3PO_4 crystals allowed the observation of only a part of the semicircumference.

The temperature dependence of ionic conductivity in γ-Li_3PO_4 single crystals obeys the Arrhenius law,

$$\sigma T = \sigma_0 \exp(-E_{\sigma T}/kT), \quad (1)$$

in the whole temperature range (Fig. 2), which is quite consistent with the well-known data [5–7]. For comparison, Figure 2 also shows the results obtained on polycrystalline specimens [5–7]. Table lists the data obtained in the present study and on other studies of ionic conductivity in γ-Li_3PO_4.

As is seen from Fig. 2 and the table, the γ-Li_3PO_4 single crystals are characterized by low anisotropy in ionic conductivity ($\sigma_{300} \parallel a$)/($\sigma_{300} \parallel b$) = 2.5 and ($\sigma_{300} \parallel a$)/($\sigma_{300} \parallel c$) = 1.3. It is well known that the anisotropy in σ in layer and tunneling conductors attains the values up to several orders of magnitude, and, therefore, the anisotropy in γ-Li_3PO_4 conductivity indicates that the material is a three-dimensional conductor.

The σ values determined in the present study considerably exceed the values indicated in [5–7], which is explained by different properties of single crystals and ceramic specimens (conductivity of a ceramic is usually lower than conductivity of single crystals of the same composition).

Lithium orthophosphate is a typical representative of the compounds with framework structures [3, 7] (Fig. 3). Lithium cations fully occupy two types of positions, Li1 and Li2. The γ-Li_3PO_4 structure is rather loose, i.e., the framework voids comprise a considerable part of the total volume and penetrate the structure in all directions, thus creating favorable conditions for ionic conductivity. Nevertheless, one can expect a low value of ionic conductivity in γ-Li_3PO_4 (Fig. 2 and table), since in an ideal crystal, all the lithium cations fully occupy their positions and are rigidly bonded to the framework, which creates no prerequisites for ion transport. However, in real crystals, ionic conductivity can be associated with the formation of temperature-induced defects such as Frenkel defects. The interstitial-ion concentration in this case is rather low, which results in low conductivity in pure γ-Li_3PO_4. A considerable increase of σ with the preservation of the structure is possible if the matrix material is doped with heterovalent impurities. This was actually observed in solid solutions with the γ-Li_3PO_4 structure [1–3]. It should be indicated that the high conductivity of lithium orthophosphate reported in [8] seems to be

The experimental data on ionic conductivity and the energy of conductivity activation in γ-Li_3PO_4 at 300 and 450°C and the similar data obtained in other studies

Type of material	$E_{\sigma T}$, eV	σ, S/cm at 300°C	σ, S/cm at 450°C
Single crystal, σ∥*a*-axis	1.14	4.1×10^{-7}	4.1×10^{-5}
Single crystal, σ∥*b*-axis	1.23	1.6×10^{-7}	2.2×10^{-5}
Single crystal, σ∥*c*-axis	1.14	3.1×10^{-7}	3.1×10^{-5}
Polycrystal [5, 6]	1.31	1.5×10^{-8}	2.9×10^{-5}
Polycrystal [7]	1.24	2.2×10^{-8}	

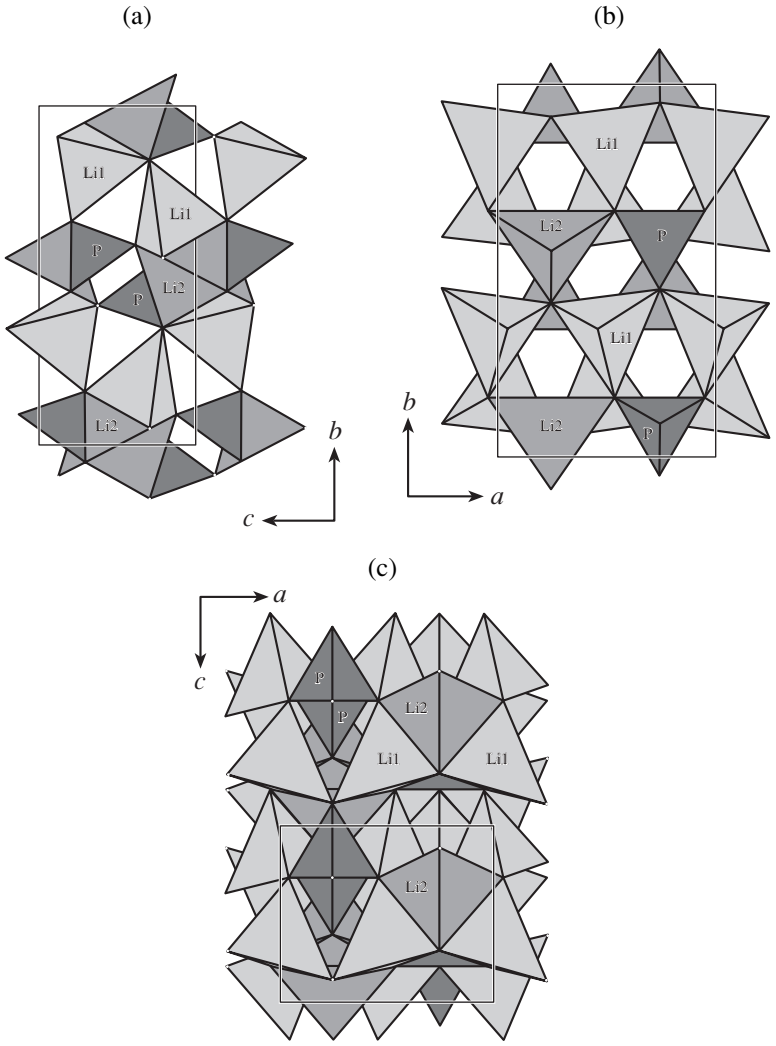

Fig. 3. Model of the γ-Li_3PO_4 structure projected onto the (a) *bc*, (b) *ac*, and (c) *ab* planes (the LiO_4 and PO_4 tetrahedra are indicated as Li1. Li2, and P).

explained by the presence of noncontrolled impurities in the specimen.

Unlike the layer and tunneling structures, the framework structures usually show low anisotropy in conductivity. As is seen from Fig. 2 and the table, ionic conductivity of γ-Li_3PO_4 (a typical representative of the framework materials) is close to isotropic. The deviation from isotropy is seen from the lower value of ionic conductivity and higher values of the energy of conductivity activation along the *b*-axis in comparison with the corresponding values measured along the *a*- and *c*-axes. This fact can be explained by the specific features of the γ-Li_3PO_4 structure [7] (Fig. 3): the voids in the crystal framework penetrate this structure in all directions, so that the channels formed along the *a*- and *c*-axes are rectilinear, whereas the channels along the *b*-axis have the zig-zag shape, which is seen from the comparison of the projections of the γ-Li_3PO_4 structure onto the *bc* and *ab* planes, on the one hand, and the projection onto the *ac* plane, on the other hand (Fig. 3). The through channels are formed along the *a*- and *c*-axes, whereas along the *b*-axis, the structure is "closed," which hinders migration of Li^+ ions along the *b* axis.

The data on anisotropy in the γ-Li_3PO_4 phase can be used to interpret the data for high-conducting solid solutions with the γ-Li_3PO_4 structure. The anisotropy in conductivity in the latter compounds should be slightly higher than in pure (undoped) γ-Li_3PO_4, because conductivity in lithium phosphate is reduced by the insufficient number of mobile ions, whereas the structural factors play only the role of secondary effects. In the solid solutions with the framework voids filled with a large number of Li^+ ions, the structural factors play the key part in ion transport.

ACKNOWLEDGMENTS

This study was supported by the Russian Foundation for Basic Research, project no. 99-03-32726.

REFERENCES

1. A. K. Ivanov-Shits and I. V. Murin, *Ionic Conductivity in Solids* (S.-Peterb. Gos. Univ., St. Petersburg, 2000).
2. J. T. S. Irvine and A. R. West, in *High Conductivity Solid Ionic Conductors*, Ed. by T. Takahashi (World Scientific, Singapore, 1989), p. 201.
3. E. I. Burmakin, in *Solid Electrolytes with Alkali Metal Cation Conductivity* (Nauka, Moscow, 1992), p. 215.
4. B. A. Boukamp, Solid State Ionics **18**/**19**, 136 (1986).
5. Y.-W. Hu, I. D. Raistrick, and R. A. Huggins, J. Electrochem. Soc. **124** (8), 1240 (1977).
6. R. A. Huggins, Electrochim. Acta **22**, 773 (1977).
7. B. Wang, B. C. Chakoumakos, B. C. Sales, *et al.*, J. Solid State Chem. **115**, 313 (1995).
8. E. I. Burmakin, G. K. Stepanov, and S. V. Zhidovinova, Élektrokhimiya **18** (5), 649 (1982).

Translated by L. Man

Crystallography Reports, Vol. 46, No. 5, 2001, pp. 868–875. Translated from Kristallografiya, Vol. 46, No. 5, 2001, pp. 942–949.

CRYSTAL GROWTH

Electron Microscopy of Epitaxial Structures of Pseudobinary $A^{III}B^{V}$ Solid Solutions and the Model of Nonequilibrium Ordering in Epitaxial Growth

S. K. Maksimov and K. S. Maksimov

Moscow Institute of Electronic Technology, Moscow, 103498 Russia

e-mail: lemi@mx.iki.rssi.ru

Received November 1, 1999; in final form, November 10, 2000

Abstract—The results of the electron microscopy studies of self-modulated GaAlAs, GaAsP, and InGaP layers have been generalized, and the laws governing the self-oscillatory growth of these materials have been formulated. The growth characteristics under the autocatalysis conditions were established from a computer simulation of the epitaxial process. It is demonstrated that the autocatalytic model of crystallization corresponds to the experimental characteristics of self-modulation. The anomalies in electron microscopy images of the boundaries were revealed, which can be interpreted only with the invocation of the autocatalytic model. The reliabilities of various theoretical self-modulation models are also discussed. © *2001 MAIK "Nauka/Interperiodica".*

INTRODUCTION

As is well known, epitaxial crystallization occurs at the deviations from the equilibrium growth process under the conditions of particle and energy flows providing the occurrence of self-organization processes [1]. The pseudobinary $A^{III}B^{V}$ (GaAlAs, GaAsP, etc.) solid solutions are characterized by positive mixing energies Ω [2] and the propensity to stratification at temperatures lower than the epitaxial-growth temperature. Therefore, epitaxial growth should result in the formation of homogeneous structures with a short-range order of the stratification type [2]. However, the process can also be accompanied by the formation of a long-range atomic order and composition self-modulation [3–10]. The mechanism of nonequilibrium order is also very important in the light of the general problems of self-organization and the practical formation of epitaxial $A^{III}B^{V}$ structures. At present, atomic ordering and self-modulation in epitaxially grown semiconductor heterostructures are usually associated with the manifestation of the self-organization processes [11–17], but the suggested interpretation of the phenomenon and its possible mechanisms are still inconsistent.

At present, there are no models explaining the self-organization from the unified standpoint. Most scientists explain atomic ordering by the changes in the nature of atomic interactions at the surfaces of semiconductor crystals caused by the surface reconstruction [5, 6], whereas the self-modulation is interpreted based on several different hypotheses, which can be divided into three major groups. The hypotheses of the first group are based on the consideration of misfit elastic stresses [14, 16]. Those of the second group are based on the consideration of the growth-surface relief [15, 17], and finally, the hypotheses of the third group are associated with the autocatalysis provided by the positive mixing energy Ω [11, 12, 13].

CHARACTERISTICS OF SELF-ORGANIZATION IN HETEROEPITAXIAL CRYSTALLIZATION AND THEORETICAL MODELS OF THE PHENOMENON

In the present study, self-modulation is interpreted with the invocation of the generalized data of the experimental investigations of $Ga_{1-x}Al_xAs$/(001)GaAs heterostructures [10, 13] grown by the MOCVD method from arsine and alkyl compounds of Ga and Al [18] in an open-type reactor, $GaAs_{1-y}P_y$/(001)GaAs [3, 8, 19] formed by gas-phase epitaxy by the chloride–hydride technology [3], and $In_{1-x}Ga_xP$/(111)GaAs [4] grown by the liquid-phase method [20]. Analyzing the results of these experiments, we established the following characteristic features:

(1) Self-modulation and atomic order can coexist within a structure formed under constant growth conditions [9].

(2) Modulation amplitude attains several tens of mole percent [7, 13, 19].

(3) Modulation direction does not necessarily coincide with the maximum elastic-compliance direction [001] [4, 10, 19] and, as a rule, coincides with the growth direction [4, 8, 10, 19].

(4) As a result of self-modulation, the regions of almost pure AlAs [13] arise in $Ga_{0.7}Al_{0.3}As$ and of $GaAs_{0.95}P_{0.05}$ in $GaAs_{0.95}P_{0.05}$ layers [3], with the modulation amplitude attaining tens of mole percent (the process of fitting to the average composition is provided by varying the layer thickness of the strata

1063-7745/01/4605-0868$21.00 © 2001 MAIK "Nauka/Interperiodica"

Typical parameters used in the simulation of epitaxial-layer growth under the autocatalytic conditions

Parameter	Parameter value	Dimension
Initial dimensionless parent-phase composition η_m	0.0357	
	0.0363	
Initial composition of the crystal η_c	1	
Total concentration of the components in the parent phase	(1.5×10^{22})	cm^{-3}
Efficient diffusion coefficient	(4×10^{-5})	cm^2/s
Total concentration of the components in the crystal	(2.2×10^{22})	cm^{-3}
$q_1 = 2.7(1 + 1.0006\eta_c^+ + 0.0011\eta_c^{+2})$		nm/s
$q_2 = 2.9(1 - 1.0005\eta_c^+ + 0.001\eta_c^{+2})$		nm/s
Remote boundary (infinitely remote source)		cm
Depth of the parent-phase layer	0.5	cm
	1	cm
Number of points	500	
Duration of the process	16	min
Temporal integration step	0.015625	s
Thickness of the crystal grown	1.95	μm

enriched with As and P) [3].[1] Under the equilibrium conditions, neither AlAs formation nor $GaAs_{0.95}P_{0.05}$ decomposition can occur even at the liquid nitrogen temperature.

(5) The fixed modulation amplitude Δx attains 60 mol % AlAs [13] for GaAlAs, 30 mol % GaP [19] for GaAsP, and 20 mol % GaSb for GaAsSb [7], in other words, the modulation amplitude decreases with an increase of the mismatch in the lattice parameters of the components.

(6) The transition to the oscillatory growth mode giving rise to the formation of a modulated structure is provided by a higher growth rate [10]. This is also indicative of the kinetic nature of the phenomenon.

(7) The modulation amplitude does not depend on the composition either of the parent phase or the growth surface and is constant over the whole range of thicknesses of the epitaxial layer [3], whereas the modulation period does depend on these parameters and decreases with the distance from the heterojunction.

(8) The transition to the oscillatory growth mode is preceded by the steady-state mode and the formation of unmodulated layer even in those cases where the crystallization conditions for the formation of the unmodulated layer are closer to the conditions for formation of a two-phase structure than to those necessary for the formation of a modulated volume [4].

Some experimental characteristics of self-modulation are inconsistent with the predictions based on some of the theoretical models. The self-modulation whose direction coincides with the growth direction and the constancy of the self-modulation amplitude over the epitaxial-layer thickness contradict the predictions based on the model explaining the phenomenon by misfit stresses [14, 16]. The modulation periods and amplitudes observed can hardly be interpreted within the model explaining the phenomenon by the surface relief, which is recognized even by the authors of this model themselves [15, 17]. The autocatalytic model [13] is more consistent with the experimental characteristics, despite the fact that the assumption underlying this model (the statement that the sign of the mixing energy on the surface coincides with the sign of the mixing energy in the crystal bulk) is inconsistent with the main statement providing the interpretation of the atomic order by the sign reversal of the mixing energy on the reconstructed surfaces [5, 6]. This inconsistency is essential if the self-modulation and the atomic order are observed in the same epitaxial-layer volumes, as is the case, e.g., in [9].

All the facts considered above dictated the further study of the phenomenon in the framework of the self-catalytic model.

CHARACTERISTICS OF MODULATION IN THE SELF-CATALYTIC MODEL

It was shown [13] that crystallization of a binary crystal under the condition of autocatalysis results in an *S*-like dependence of the crystal composition on the parent-phase composition (resulting, in turn, in a self-modulation) if the adsorption coefficients, which describe the appearance of the parent-phase components on the growth surface, have the form

$$q_i = \alpha_i \pm \beta_i\eta_c^+ + \gamma_i\eta_c^{+2}, \quad (1)$$

[1] The term "stratum" corresponds to a concentration domain with the dimensions in the foil plane multiply exceeding its dimension along the growth direction.

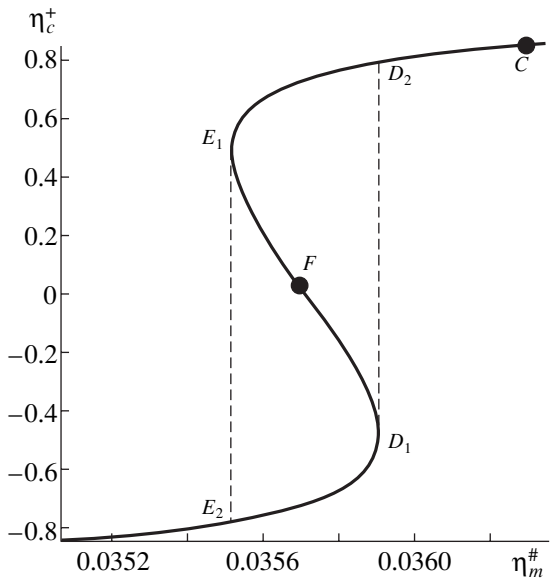

Fig. 1. Composition of a growing crystal as a function of the parent-phase composition under the same adsorption coefficients and at the computational parameters as in Figs. 1–4: η_c^+ is the crystal composition, η_m^+ is the parent-phase composition, $E_1E_2D_1D_2$ is the region of the nonunique dependence of η_c^+ on η_m^+.

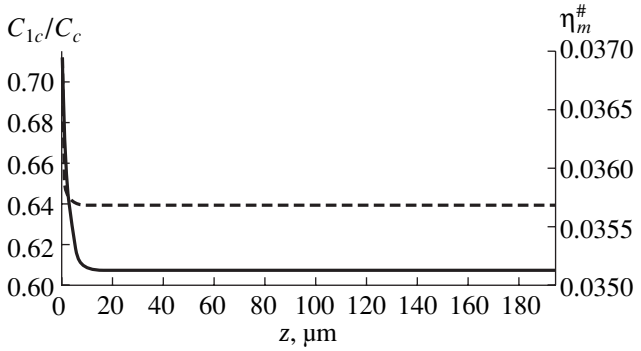

Fig. 2. Calculated variations in the compositions of the crystal and the subsurface layers of the parent phase as functions of the epitaxial-payer thickness at $\eta_m = 0.0363$ nm/s and the parent-phase thickness $\tau = 5$ mm. Solid line indicates the variations in η_c, the dashed line, the variations in $\eta_m^\#$; z is the distance from the initial crystal surface.

where η is the composition parameter, $\eta = (C_1 - C_2)/(C_1 + C_2)$, C_i are the component concentrations, the superscript "plus" indicates that the coefficient is considered at the crystal–parent phase interface, and the subscript "minus" indicates that the parameter η belongs to the crystal.

A modulation arises if $|\beta_i| > |\alpha_i|$, which corresponds to the probability of autocatalytic adsorption exceeding the probability of random adsorption. To verify the hypothesis of the autocatalytic self-modulation mechanism, we numerically simulated epitaxial growth under the autocatalytic conditions.

A autocatalytic growth was described by the system of the following equations:

the continuity equation

$$\partial C_i/\partial t = -\partial J_i/\partial z, \quad (2)$$

the flow (Fick) equation

$$J_i = -D_i\partial C_i/\partial z + \nu C_i, \quad (3)$$

the equation of the interface motion

$$u = dZ/dt, \quad (4)$$

the adsorption equation

$$I_i = C_i^\# q_i, \quad (5)$$

and the continuity equation at the interface

$$uC_i^+ = I_i, \quad (6)$$

$$uC_i^\# = I_i + J_i^\#. \quad (7)$$

Here u is the velocity of the interface motion, t is the time, and z is the spatial coordinate along the surface normal measured from the initial surface of the crystal, Z is the current position of the crystal–parent phase interface, J_i is the flux of the ith component, D_i is the diffusion coefficient of this component, ν is the component of the drift velocity, I_i is the flow of the ith component through the interface, $q_i = q_i(C_1^+/C_2^+)$ is the adsorption rate of the ith component dependent on the composition of the crystal surface, and the superscript "#" indicates that the quantity is considered in the vicinity of the interface in the parent phase.

The numerical simulation was based on Eq. (2); the boundary conditions at the parent phase–crystal interface were Eqs. (3)–(6). At the second (remote) interface, we used the conditions of the composition constancy (for an infinitely remote source) and the zero redistribution flow (i.e., the condition of an impenetrable interface). Because of the function discontinuity at the parent-phase–growing crystal interface, we had to use the explicit difference scheme. In accordance with (1), the basic parameters determining the possible formation of an S-like dependence are the adsorption coefficients. In the model under consideration, the component flows are taken into account by the computational procedure, so that the adsorption coefficients also determine the growth rate of the crystal. Therefore, these coefficients were chosen (by the order of magnitude) in such a way that the growth rate of the crystal corresponded to the growth rates observed in real technological processes. Our computations showed that the modulation period depends on the difference between the probabilities of random and autocatalytic adsorption. Therefore, the value of $|\beta_i| - |\alpha_i|$ was selected in such a way that the modulation periods corresponded to the experimentally observed modulated periods. The remaining parameters in our computations corresponded to the parameters of the simulated epitaxial

processes. Their typical values are listed in table. The results of these computations are shown in Figs. 1–5.

The analysis of the calculated data showed the following:

Autocatalysis can also be accompanied by the steady-state growth of a crystal having a constant composition (Fig. 2) and the formation of the oscillatory crystallization mode providing growth of a modulated crystal (Fig. 3). The steady-state growth is preceded by either a transient mode or monotonic variations of the composition (Fig. 2).

In oscillatory growth, composition oscillations in the subsurface layers of the parent phase and a growing crystal occur synchronously (the curves corresponding to the composition variations in the subsurface layer of the parent phase and the growing crystal are shown in Figs. 3 and 4). The modulation is observed along the growth direction. Preferential adsorption of one of the components results in the second-component accumulation in the subsurface layer of the parent phase. The motion of the crystallization front provides the generation of a concentration wave of this component and, as a result, the concentration of this component in the subsurface layer of the parent phase continuously increases.

The rate of the latter process is limited by diffusion. As a consequence, the component flow to the growing crystal increases because of random adsorption. In turn, an increase of the second-component concentration at the growth surface stimulates an increase of the autocatalytic component of the second-component flow. This stage continues until the moment when the second-component concentration in the parent phase at the growth surface attains the critical value providing a jumpwise change of the resulting flow of this component to the crystal surface.

The self-oscillatory growth mechanism is observed at certain ratios of the quantities characterizing the diffusion coefficients and the thickness of the parent phase, on the one hand, and the growth rate, on the other hand (Figs. 3 and 4). An increase of the growth rate of the crystal and the hindered mass transfer in the parent phase (a decrease of the diffusion coefficients and an increase of the parental-phase thickness) provide the transition to the oscillatory crystallization mechanism. An increase of the growth rate with the change of the layer growth mechanism to the multicenter mechanism explains the transition from the steady-state to the oscillatory mechanism in GaAlAs epitaxial growth.

For the initial parent phase, the compositions outside the $E_1E_2D_1D_2$ region (Fig. 1), i.e., the region of nonunique dependence of the crystal composition on the parent-phase composition or the region of the optimum composition for the modulation formation, the initial epitaxy stages result in the formation of an unmodulated layer (Fig. 4). The region of the nonunique dependence is shifted toward the component with

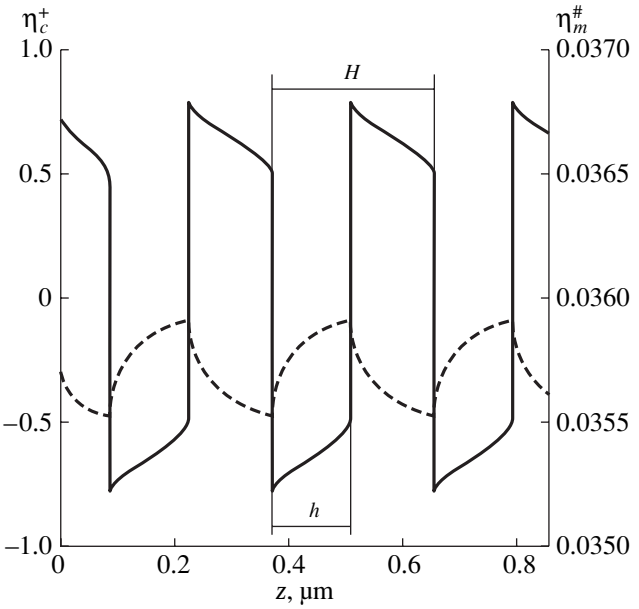

Fig. 3. Calculated variations in η_c (solid line) and $\eta_m^\#$ (dashed line) at τ = 10 mm and η_m corresponding to the point *F* in Fig. 1, with all the remaining parameters being the same as in Fig. 2.

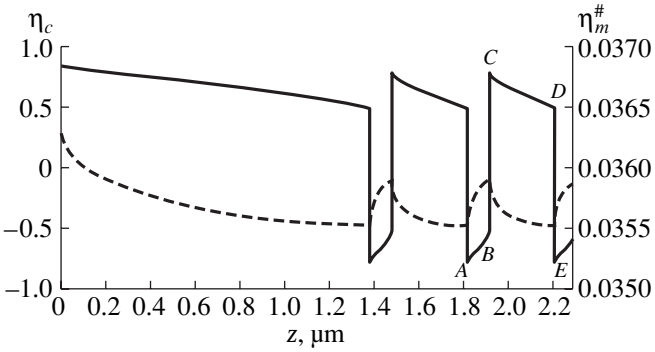

Fig. 4. Calculated variations in η_c (solid line) and $\eta_m^\#$ (dashed line) at τ = 10 mm and η_m = 0.0363, with all the remaining parameters being the same as in Fig. 2. The thicknesses *h* of the strata are *AB* = 0.279 μm, *h CD* = 0.625 μm; *H* is the modulation period.

a lower adsorption coefficient. The formation of transitional unmodulated layers explains the fact that we observe the $In_{0.65}Ga_{0.35}P$ and not the $In_{0.52}Ga_{0.48}P$ modulation in InGaP [4].

Even a slight increase of the autocatalytic adsorption coefficients $|\beta_i|$ above the coefficients of random adsorption $|\alpha_i|$ (of the order of 10^{-4} of the absolute value of the adsorption coefficients) results in the self-oscillatory growth mode. In this case, the composition variations in the boundary layers of the parent phase do not exceed (of about 10^{-4} of the absolute value of the adsorption coefficients), whereas the variation in the crystal composition can attain tens of mole percent

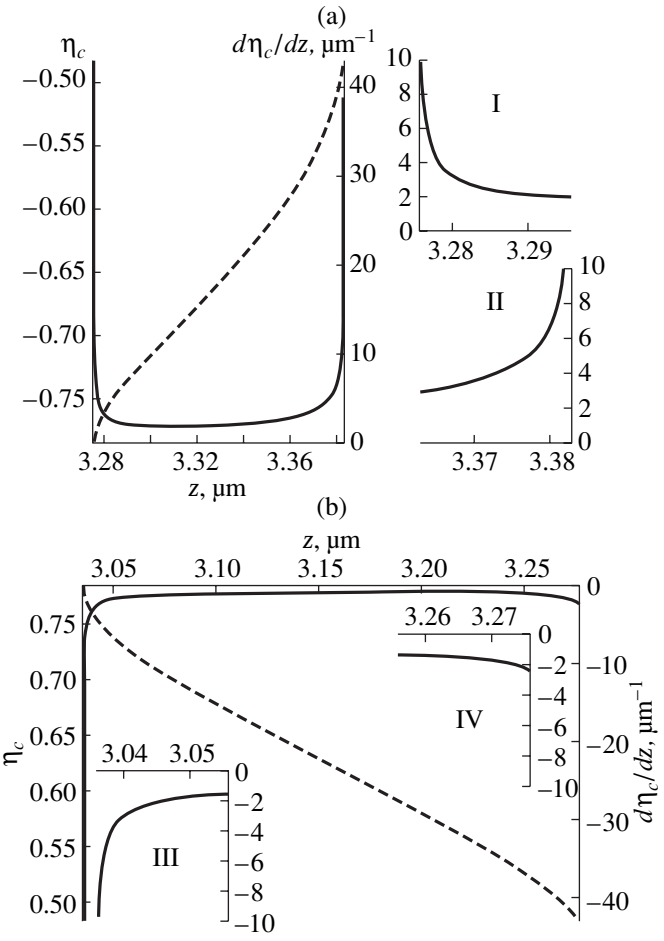

Fig. 5. (a) Detailed composition variations and the composition gradient for the stratum *AB* in Fig. 4.; (b) the same for the stratum *CD* in Fig. 4. Solid lines indicate the variations in the composition gradients, the dashed lines indicate the composition variations. In the insets, the variations in the composition gradients in the vicinity of the boundaries: I and II, at the stratum *AB*; I, in the vicinity of the point *A*; II, in the vicinity of the point *B*; III, IV, at the stratum *CD*; III, in the vicinity of the point *C*; IV, in the vicinity of the point *D*.

(Figs. 3 and 4). This fact is consistent with the experimental data [3, 4, 7, 8, 10, 13].

The modulation period decreases with a reduction of the difference between $|\beta_i|$ and $|\alpha_i|$. The modulation periods observed range within 5–15 nm in GaAlAs and 40–200 nm in GaAsP. The modulation period in InGaP exceeds 500 nm, which allows one to estimate the excess in the coefficients of the autocatalytic adsorption over the coefficients of random adsorption for these structures. The estimates based on fitting of the calculated and the observed modulation periods yield $(|\beta_i| - |\alpha_i|) > 2 \times 10^{-4}\ q_i$ for InGaP, $(|\beta_i| - |\alpha_i|) \approx (5 \times 10^{-5}$–$10^{-4})q_i$ for GaAsP, and $(|\beta_i| - |\alpha_i|) \approx 10^{-5} q_i$ for GaAlAs. The mixing energies Ω for InGaP, GaAsP, and GaAlAs structures are $\Omega_{InGaP} > 3.5$, 1.8 and 1.2 kcal/mol, respectively. Thus, the difference $(|\beta_i| - |\alpha_i|)$ is minimal in GaAlAs and, therefore, the phenomenon in this compound is observed very rarely, whereas the difference $(|\beta_i| - |\alpha_i|)$ in InGaP is maximal, and the phenomenon is quite characteristic of this compound [21].

The modulation period depends on the parent phase composition and decreases with an approach of the composition to the region of its nonunique dependence (the differences in the periodicities are illustrated by Figs. 3 and 4) and with the duration of self-oscillatory growth (the first and the second composition oscillations in Fig. 4). The amplitude modulation is almost independent of the parent-phase and growth-surface compositions, in full accordance with the variations of the modulation parameters observed in the formation of GaAsP layers [3, 8, 19].

In autocatalysis, the composition varies in a complicated manner (Figs. 3–5). The neighboring concentration strata show mirror-symmetric changes only at the optimum compositions of the parent phase and close values and structures of the adsorption coefficients (Fig. 3). Inside a stratum, an increase of the distance from the entrance interstratum boundary results in the formation of the minimum of the composition curve, whereas with an approach to the second interstratum boundary, the gradient of the composition variation tends to infinity (Fig. 5). At this boundary, the composition varies in the jumpwise manner.

If the initial composition of the parent phase differs from the optimum composition, the symmetry is broken and the strata of different compositions are characterized by different dimensions (Figs. 4 and 5). The composition of a growing crystal is determined by the composition of the boundary layer of the parent phase, which, in turn, varies because of the preferential adsorption of one of the components at the surface of the growing crystal, the accumulation of the second component in the boundary layers caused by the concentration wave and the diffusion exchange between the components of the subsurface layers of the parent phase and its bulk. At the preferential adsorption of the component prevalent in the parent phase, the diffusion flows decelerate the composition variations in the subsurface layers. However, at the preferential adsorption of the second component, these flows accelerate the composition variations in the subsurface layers. As a result, the strata formed have different dimensions: the broad stratum enriched with the prevalent component and a narrow stratum enriched with the second component.

Two boundaries should be distinguished for each stratum—the entrance one, which is closest the substrate, and the exit one, which is most remote from this substrate. At the moment of the change of the adsorption mode, the flows incident onto the crystal surface and the flows propagating inside the parent phase are drastically changed, but upon the passage of the points where the mode changes the component distributions in the boundary layer become similar to the distributions

observed at the previous stages. As a result, in the vicinity of the entrance boundaries, the regions of nonsteady-state growth with the monotonic variation of the composition gradient arise (Fig. 5). The characteristics of nonsteady-state growth for the strata of various types have close absolute values of the gradients and similar shapes of the curves which reflect their variations. However, the strata of various types are characterized by different types of the composition variations in the vicinity of the exit boundaries. The slower the composition variations inside the strata, the closer the composition variations to the stepwise ones at the exit boundaries.

In the vicinity of the entrance boundary of a broad stratum, there exists a region where the composition gradient tends to infinity from the side of the narrow stratum. This region penetrates the narrow stratum for several tens of nanometers; from the side of a broad stratum, there is a 10-nm-long region of moderate gradients. In the vicinity of the exit boundary of the broad stratum, the composition variations are close to stepwise ones; from the side of the narrow stratum, there is an approximately 10-nm-long region of moderate gradients.

The characteristic features of the composition variations following from the autocatalytic model considerably differ from the composition variations following from the models considered in [14–17], for which the composition is constant within the strata and varies in the jumpwise manner at the interstratum boundaries.

DETECTION OF COMPOSITION VARIATIONS IN THE VICINITY OF BOUNDARIES

To verify the self-modulation mechanism, one has to carefully study the interstratum boundaries. The difficulties encountered here are associated with the fact that the images with the lattice resolution [22] are insensitive to slight near-boundary variations of the composition following from the model considered in [13], whereas the unambiguous interpretation of the corresponding conversion-beam electron diffraction patterns is rather difficult because the electron beam is scattered from an object whose lattice constant varies in two different ways—(1) in a jumpwise manner (at a certain point) and (2) monotonically by an unknown law (in the neighborhood of this point). Moreover, the spatial resolution attained by the convergent-beam method does not exceed 15–20 nm [23], which is insufficient for our purpose. Therefore, the composition variations in the vicinity of the boundaries were studied by the method of inclined stratum boundaries [24] in its quantitative variant [25].

Neglecting the differences in the structure factors in various parts of a bicrystal (which are unimportant in practice), we analyzed the intensity distribution (contrast) on the images of inclined stratum boundaries having different values of the lattice constants within the

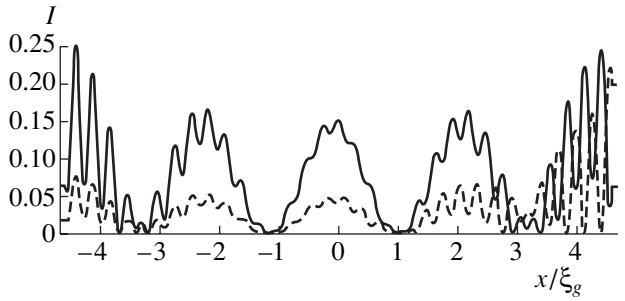

Fig. 6. Theoretical bright-field intensity profiles for the simple stepped boundary and the GaAsP structure with the modulation amplitude equal to 20 mol % GaP. Solid line corresponds to the layer characterized by a smaller lattice constant located above the boundary, the dashed line, for the layer located below the boundary; ξ_g is the extinction length.

theoretical model, which takes into account the following phenomena: (a) scattering of electron waves in the first volume characterized by the diffraction vector $\mathbf{g}_1$ and the excitation error s_1, (b) scattering in the second volume characterized by the diffraction vector $\mathbf{g}_2$ and the excitation error s_2, (c) the jumpwise variation in the phases of scattered electrons at the interstratum boundaries, and (d) interference of the waves scattered by various parts of a bicrystal on the exit surface [26]. The resulting contrast is of the interference nature and is essentially dependent on the structure of the interstratum boundary. The theoretical analysis showed [24, 25] that the specific features of this contrast can be characterized, in the first approximation, by the following three simple rules:

If the composition within the strata is approximately constant and changes at the interstratum boundary in a jumpwise manner (a simple stepped boundary), then the images of inclined boundaries are characterized by intensity oscillations of two types—those of the moiré fringes and those of the displacement bands [24, 25].

If the strata are separated not by simple stepped boundaries but by certain regions with the composition gradient, the intensity oscillations are suppressed already at gradient-region thicknesses as low as ~2 nm [24].

If the interstratum boundary is stepped, but there are regions of the composition gradient close to it, then, at slight variations in the dimensions and composition of the near-boundary regions, two systems of intensity oscillations are substituted by only one system, and, with an increase of the oscillations and dimensions of this region, the interference intensity oscillations are completely suppressed [25].

The periodicity of moiré fringes and oscillations in case (c) are uniquely related to the difference in the lattice constants of the neighboring layers; the constancy of this periodicity indicates the constancy of the modulation amplitude [24, 25].

In passing through an interface, the entrance and exit boundaries of each stratum are characterized by

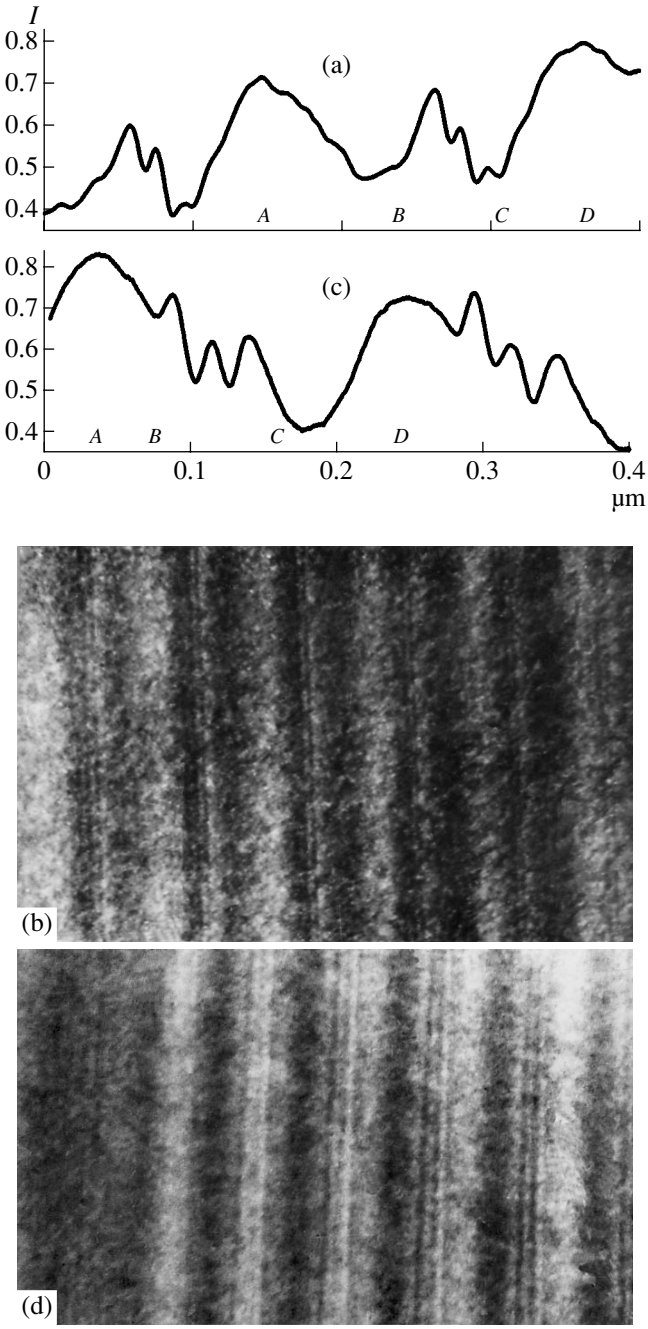

Fig. 7. Dark-field electron micrographs and the corresponding intensity profiles of the self-modulated GaAsP/GaAs structure; $[\bar{1}\bar{2}5]$ direction is the projection of the modulation direction [001]: (a, b) $\mathbf{g} = [20\bar{2}]$, $(\mathbf{g} \cdot \mathbf{R})s < 0$ and $s > 0$; (c, d) $\mathbf{g} = [1\bar{1}1]$, $(\mathbf{g} \cdot \mathbf{R})s > 0$, and $s < 0$. The intensity profiles are averaged over 500 scans; the relative intensity is plotted along the *y*-axis.

different signs of the changes in the lattice constants. In electron imaging, different signs of the changes in the lattice constants correspond to different signs of the variations of the excitation error *s*, i.e., the electron microscopy images of the boundaries with different signs of the lattice-constant changes are formed under different diffraction conditions. Therefore, the intensity distribution on the images of the entrance and exit boundaries of a stratum cannot be identical. However, the micrographs of the stepped boundaries should show both these boundaries. At the same time, the different character of oscillations on the images of different boundaries provides the unambiguous interpretation of the boundaries of each type.

In order to obtain the images of the inclined boundaries of the GaAsP layers with the self-modulation along the [001] direction, we used projections along the [121] direction, in which these boundaries are inclined by an angle of about 30° to the electron beam. Figure 7 shows such a projection and the structure region in the vicinity of the line of transition from the unmodulated epitaxial-layer volume to the modulated one, i.e., to the epitaxial-layer region where the mole fraction of GaP does not exceed 10–15%. Figure 7 shows the periodic intensity oscillations provided by the lattice-constant variation of the dilatation nature superimposed onto the interference oscillations. The comparison of the interference oscillations for the epitaxial-layer volumes with different GaP concentrations shows that their periodicity is constant over the whole modulated volume. Thus, at the characteristic modulation amplitude of about 10–30 mol % GaP in GaAsP, the changes in the growth conditions in the transition from the region close to the heterojunction to the region with the "constant composition" do not exceed 1–2 mol %. The interference intensity oscillations on the images of the boundary uniquely indicate that the visible boundaries are of the jumpwise and not of the gradient character.

The character of the interference intensity oscillations varies with the change of the sign of the excitation error *s*. However, the boundary images in Fig. 7 have only one subsystem of intensity oscillations on micrographs corresponding to the same excitation errors *s*, and the intensity distributions on the images of different boundaries are identical. Thus, first, the micrographs show the boundaries of only one type; second, the boundary structures correspond to the case (c), in other words, close to the boundaries, one observes the composition variations, and, third, the boundaries of different types differ by both the values of composition variations close to these boundaries and the dimensions of the regions where these composition variations are localized.

If crystal is set in such a way that the diffraction vector $\mathbf{g}_{av}$ and the composition intermediate between the concentration-domain compositions is in the reflection position, then the domain images corresponding to $|\mathbf{g}_1| > |\mathbf{g}_{av}|$are bright, whereas the images of the domains with $|\mathbf{g}_2| < |\mathbf{g}_{av}|$ are dark [27]. This rule allows one to establish the component prevalent in a stratum.

At an excess of AsH_3, the parent phase forms broad strata enriched with GaAs and narrow strata enriched with GaP. In this case, one can see only the boundaries

corresponding to the transitions from the broad to the narrow strata; the images of these boundaries show interference intensity oscillations. The fact that only the boundaries corresponding to the transitions from the GaAs-enriched strata to GaP-enriched strata along the growth direction are observed is confirmed by the contrast analysis of micrographs in Fig. 7c, where $s \approx 0$, and the micrographs corresponding to the projection along the [010] direction at $s \equiv 0$, i.e., on micrographs obtained under the conditions of pure dilatation contrast [27]. If the AsH_3 and PH_3 concentrations in the parent phase become comparable, the micrographs show the boundaries between the strata enriched with GaP and the strata enriched with GaAs, but no interference oscillations. At the same time, the intensities of these oscillations on the images of the first-type boundaries are also reduced.

CONCLUSION

The results of the electron microscopy study performed can be interpreted only in terms of the autocatalytic model, which predicts the composition variations close to the boundaries and different character of these variations in the vicinity of the entrance and the exit boundaries. These results and the correlations between the predictions of the autocatalytic model and the experimental features of self-modulation considered above indicate the adequacy of the autocatalytic mechanism of the phenomenon. The validity of the autocatalytic model is indirectly confirmed by the fact that the morphology of spontaneously modulated GaAsSb layers [7] grown in the two-phase region (where the role of the Gibbs potential is analogous to the role of a positive mixing energy in the model suggested in [13]) is consistent with the morphology of the nonequilibrium self-modulation in GaAsP [3, 8, 19].

The data obtained in the present study together with the experimental results in which the self-modulation and the atomic order were observed in the same epitaxial volumes (see, e.g., [9]) make the reconstruction model of atomic ordering somewhat doubtful. As far as we know, experimentally, this model was confirmed only indirectly, because of the correlation between the order types at the crystalline-substrate surface and in the epitaxial-layer bulk [6].

ACKNOWLEDGMENTS

This study was supported by the Russian Foundation for Basic Research, project no. 97-02-17990 and the Project on the Studies in the Field of Fundamental Natural Sciences, project no. 97-0-7.2-200.

REFERENCES

1. G. Nicolis and I. Prigogine, *Self-Organization in Non-Equilibrium Systems* (Wiley, New York, 1977; Mir, Moscow, 1979).
2. V. T. Bublik and B. N. Leikin, Phys. Status Solidi A **46**, 365 (1978).
3. S. K. Maksimov and E. N. Nagdaev, Dokl. Akad. Nauk SSSR **245**, 1369 (1979) [Sov. Phys. Dokl. **24**, 297 (1979)].
4. S. K. Maksimov, L. A. Bondarenko, A. S. Petrov, and V. V. Kuznetsov, Fiz. Tverd. Tela (Leningrad) **24**, 628 (1982) [Sov. Phys. Solid State **24**, 355 (1982)].
5. J.-P. Chevalier and R. Portier, Inst. Phys. Conf. Ser. **117**, 453 (1991).
6. A. Zunger, MRS Bull. **22** (7), 20 (1997).
7. T.-Y. Seong, A. G. Norman, J. L. Hutchison, *et al.*, Inst. Phys. Conf. Ser. **117**, 485 (1991).
8. S. K. Maksimov, Kristallografiya **39** (2), 315 (1994) [Crystallogr. Rep. **39**, 269 (1994)].
9. P. Bellon, G.-P. Chevalier, G. P. Martin, *et al.*, Appl. Phys. Lett. **52**, 567 (1988).
10. S. K. Maksimov, Kristallografiya **42** (1), 157 (1997) [Crystallogr. Rep. **42**, 145 (1997)].
11. L. A. Bondarenko, S. K. Maksimov, and E. N. Nagdaev, in *Proceedings of the 4th All-Union Conference on Physicochemical Foundations of Doping of Semiconductor Material* (Baĭkov Inst. of Metallurgy, Akad. Nauk SSSR, Moscow, 1979), p. 138.
12. O. D. Chernavskaya, D. S. Chernavskiĭ, and R. A. Suris, *Structural Defects, Methods of Their Study and Their Effect on the Properties of Crystals* (Inst. Élektronnoĭ Tekhniki, Moscow, 1982), p. 3.
13. S. K. Maksimov, K. S. Maksimov, and É. A. Il'ichev, Pis'ma Zh. Éksp. Teor. Fiz. **63**, 412 (1996) [JETP Lett. **63**, 433 (1996)].
14. J. E. Guyer and P. W. Voorhees, Phys. Rev. B **54**, 11710 (1996).
15. J. Tersoff, Phys. Rev. B **56**, R4394 (1997).
16. I. P. Ipatova, V. G. Malyshkin, A. A. Maradudin, *et al.*, Phys. Rev. B **57**, 12968 (1998).
17. P. Venezuela, J. Tersoff, and M. G. Legally, Nature **397** (6721), 678 (1999).
18. É. A. Il'ichev, V. M. Maslovskiĭ, and É. A. Poltoratskiĭ, Fiz. Tekh. Poluprovodn. (Leningrad) **20**, 594 (1986) [Sov. Phys. Semicond. **20**, 378 (1986)].
19. S. K. Maksimov, Inst. Phys. Conf. Ser. **117**, 491 (1991).
20. I. N. Batov, Yu. D. Il'in, and A. S. Petrov, Izv. Leningr. Élektrotekh. Inst. im. V. I. Ul'yanova **220**, 71 (1978).
21. J. E. Bernard, S. Froyen, and A. Zunger, Phys. Rev. B **44**, 11178 (1991).
22. M. J. Hytch, E. Snoeck, and R. Kilaas, Ultramicroscopy **74**, 131 (1998).
23. N. I. Borgardt, Kristallografiya **40** (2), 228 (1995) [Crystallogr. Rep. **40**, 206 (1995)].
24. S. K. Maksimov and E. N. Nagdaev, Phys. Status Solidi A **72**, 135 (1982).
25. K. S. Maksimov and S. K. Maksimov, Pis'ma Zh. Tekh. Fiz. **24** (12), 76 (1998) [Tech. Phys. Lett. **24**, 489 (1998)].
26. R. Gevers, Philos. Mag. **7** (83), 1720 (1962).
27. S. K. Maksimov and E. N. Nagdaev, Phys. Status Solidi A **69**, 505 (1982).

Translated by L. Man

Crystallography Reports, Vol. 46, No. 5, 2001, pp. 876–879. Translated from Kristallografiya, Vol. 46, No. 5, 2001, pp. 950–954.

CRYSTALLOGRAPHIC SOFTWARE

MINCRYST: a Crystallographic Database for Minerals, Local and Network (WWW) Versions

A. V. Chichagov, D. A. Varlamov, R. A. Dilanyan, T. N. Dokina, N. A. Drozhzhina, O. L. Samokhvalova, and T. V. Ushakovskaya

Institute of Experimental Mineralogy, Russian Academy of Sciences, Chernogolovka, Moscow oblast, 142432 Russia

e-mail: avchicha@issp.ac.ru

Received November 3, 1999; in final form, October 10, 2000

Abstract—MINCRYST is an original interrelated combination of the Crystal Structure Database for Minerals, Subbase of Calculated Polycrystal Standards (Calculated Powder X-ray Diffraction Standard Subbase, CPDS Subbase), and the Applied Program Package. The Information fund of the Crystal Structure Database comprises about 4800 files. Two MINCRYST versions are developed—the local (L) version with the original Database Management System designed for use on a personal computer and the WWW version with an original interface integrated into the WWW server of the Institute of Experimental Mineralogy of the Russian Academy of Sciences (Chernogolovka) accessible to all the Internet users.[1] © *2001 MAIK "Nauka/Interperiodica"*.

The MINCRYST Database has already been described in a number of publications [1–6]. Since the time of these publications, this database has been considerably developed. Below, we describe the refined version.

MINCRYST is the crystallographic database of minerals, which is an original system involving as interrelated components the Database of Crystal Structures, the automatically formed Database of Calculated Polycrystal Standards (Calculated Powder X-ray Diffraction Standards, CPDS), and the interactive Program Package.

MINCRYST is a unique system having neither Russian nor foreign analogues. It is characterized by the following three principal features:

(1) MINCRYST is a universal system containing information on the chemical compositions, crystal structures, and X-ray diffraction properties of minerals and their structural analogues, which characterize each mineral, on the one hand, as a "single crystal" (whose fundamental characteristic is its atomic coordinates) and, on the other hand, as a "polycrystal" (whose fundamental characteristic is interplanar distances).

(2) MINCRYST is a complex system because it operates with the newly created information resources (Crystal Structure Database), increases the body of the information resources by including calculated data (the automatically formed Database of calculated polycrystal standards), and also incorporates the program package utilizing the created resources for the appropriate analysis (crystallochemical and X-ray diffraction analyses, qualitative and quantitative X-ray phase analyses).

(3) MINCRYST solves the very important problem of polycrystal standards for minerals which uses the automatically formed database of calculated polycrystal standards instead of the database of experimental standards [3] in the qualitative X-ray phase analysis.

Databases of various crystallostructural characteristics of various substances (including minerals) are continuously being developed abroad. First, these are the widely known Database of Polycrystal Standards (Powder Diffraction Files, PDF) with the respective data being accumulated, edited, published, and distributed by the International Center of Diffraction Data (ICDD) and the Inorganic Crystal Structure Database (ICSD), FIZ-Karlsruhe (Germany), and NIST (USA). The cooperation of the above institutions and organizations resulted in the accumulation of about 40 000 calculated polycrystal standards in PDF (1998) supplied with the corresponding cross references. There is an obvious tendency to integrate the data on crystal structures and the data on polycrystal standards, first considered in 1990 [1]. Also the Internet versions of crystallographic databases of inorganic substances are being actively developed, such as the WWW version of the Database of Zeolite Structures (Structure Commission of the International Zeolite Association; http://www.iza-structure.org/databases/).

The WWW version of FIZ-Karlsruhe ICSD is developed by the ILL-Grenoble (France). However, only the demonstrational version (http://193.49.43.4/dif/icsd/) is presently accessible to the external users.

The Mineral Structure Data (J. Smith, University of Colorado, http://ruby.colorado.edu/~smyth/min/miner-

[1] http://database.iem.ac.ru/mincryst/.

als.html) and the Database of Crystal Structures published in *American Mineralogist* (B. Downs and P. Heese, University of Arizona and Mineralogical Society of America, http://www.geo.arizona.edu/xtal-cgi/test) are being developed.

MINCRYST also continues to be developed. By April 1, 2001, the MINCRYST Information fund of the Crystal Structure Database includes about 4800 files about 2700 unique minerals, 2100 different compositional varieties, the structure, the pressure–temperature conditions of their synthesis, etc.

The main MINCRYST component—the Crystal Structure Database—includes the data published in various scientific journals and also some special files (Crystallographic Information Files) from the Internet. The crystallostructural information in the original format is introduced from the keyboard into the ASCII files (then into BDM files). After special examination, these data are transferred to MINCRYST along with the additionally calculated BDP, BDI, and INF files with the aid of the original programs for single and batch import.

Presently, there exist two MINCRYST versions—the L version with the original Database Management System and the WWW version with the original WWW interface. Prior to 1996, the MINCRYST Database involved the ASCII files in alphabetical order and was designed for use only on a PC. At present, the MINCRYST information fund is incorporated into two databases with the corresponding management systems [7, 9–11].

The L version of MINCRYST can be used either on an individual PC or in the Organization network [PC 486 and more modern generations (RAM 16 Mb) up to HDD (30 Mb)]. The L version includes the database in the Paradox-5.0 format and is supplied with the Database Management System based on Borland Delphi 2.0 system operating within Microsoft Windows 3.x/9.x.

In the L version, the Main Database (MAIN_DB) and the User Database (USER_DB) are organized with the equitable service. The files in MAIN_DB are formed and edited by the programmer and the files in USER_DB are formed and introduced by the user.

The WWW version containing the database in the SQL format is integrated into the WWW Database Server of the Institute of Experimental Mineralogy of the Russian Academy of Sciences (http://database.iem.ac.ru/mincryst/) and provides global access to MINCRYST for any Internet user working on any-type computers supplied with any graphical WWW browser supporting the JavaScript and Java languages. The server part of MINCRYST was created within the Digital Unix operation system on a DEC Alpha workstation with the use of the DB server mySQL, the HTTP server Apache, the Script Languages PHP and JavaScript, and Java applets (all server programs are distributed freely among Russian users [8]).

Presently, the database cards in MINCRYST are formed as follows. The BDM files containing the initial primary "single-crystal" information are used by the Applied Program Package for calculating the additional BDP, BDI, and INF files [1, 4–6]. The BDF file comprises the calculated polycrystal standard. The BDI file contains the calculated data necessary for plotting the crystal structure on a monitor screen. The INF file involves the complete calculated X-ray diffraction characteristics of the crystal phase. The BDM and BDP files are imported to the L version, and the BDM, BDP, BDI, and INF files are imported to the WWW version of MINCRYST using the original programs for the batch and single import.

The contents of the database cards in both versions are virtually identical with one difference—the BDI and the INF files in the L version are calculated with the use of the incorporated part of the program package and are used as such in the Applied Program Package, whereas in the WWW version, these files are calculated preliminarily and then are incorporated into the database card. Hence, we describe here only the content of the database card in the WWW version accessible to the user. It is structurized as follows.

MAIN DATA:

—mineral name;

—composition, structure, and pressure–temperature parameters of the synthesis;

—crystallochemical formula;

—space group;

—number of formula units;

—unit-cell volume (calculated);

—molar volume (calculated);

—density (calculated);

—linear and mass absorption coefficients (calculated);

—R factor and the number of reflections used in the solution of the structure;

—linear and angular unit-cell parameters;

—number of atomic positions per unit cell;

—X-ray wavelength to be used in the calculation of X-ray powder characteristics of the mineral;

—the angular range of the calculated X-ray powder pattern of the mineral;

—the date of the last editing of the file.

ATOMIC POSITIONS (parameters of the basis atomic positions):

—serial numbers;

—coordinates;

—isotropic thermal parameters;

—occupancies.

CPDS CARD (parameters of the reflections of the calculated polycrystal standard):

—*hkl* indices;

—interplanar spacings $d(hkl)$;

relative integrated intensities $I(i)/I(m) \times 100$.[2]

INFO CARD:

—information card containing the crystallostructural characteristics of the mineral, including the calculated complete and reduced forms of its X-ray powder pattern.

CRYSTAL STRUCTURE:

—the model of the crystal structure, whose graphic image is constructed with the aid of the Java applet.

X-RAY LINE DIAGRAM:

—the model of the X-ray powder pattern of the mineral (the line diagram, whose graphic image is constructed with aid of the Java applet).

REFERENCES:

—references to the publications on the refinement or solution of the crystal structure and the additional reference containing a brief comment and the name of the operator who input and examined the file.

The original interface to the WWW variant of MINCRYST provides the user not only with the complete crystallostructural information on the mineral in the text–tabular form but also with the graphical depiction of the crystal structure and the calculated X-ray diffraction pattern. The graphical image is obtained with the aid of the Java applet containing the corresponding initial data for displaying the image on a PC. This procedure increases the rate of graphical-information processing controlled only by the speed of the PC and provides the animation and examination of the graphic image in the interactive mode. In particular, the current MINCRYST version already involves the procedures for the interactive continuous rotation about the arbitrary direction and discrete rotation of the crystal-structure model about three coordinate axes along with the fragmentation of the structure over the atomic sorts. For the model of the X-ray powder pattern, one can change the vertical scale, scan the horizontal scale and change it (d, θ, 2θ), determine the indices, angles, and the intensities of the *hkl* reflections.

The user queries can be prepared either through the dynamically formed HTML pages with the standard HTML and JavaScript languages or through Java applets (graphics). The query preparation involves the translation of rather simple user's queries to the complex structured SQL queries for the database and provides screening, search for, and retrieval of information based on the complex of parameters and allows the user to export the chosen information.

[2] The polycrystal–standard has only 20 strongest reflections from the total number of reflections on the X-ray powder pattern of the mineral.

The special form of the search based on the CPDS part of the database card enables the user to perform the qualitative X-ray phase analysis based on the given experimental interplanar spacings with due regard for possible composition of atoms in the crystallochemical formula of the mineral.

The answers to the queries in the text–tabular form are presented in the form of dynamically formed HTML pages. The objects containing any graphical information are displayed with the aid of automatically loaded Java applets. The cards are edited and imported through the WWW interface.

In the L version of MINCRYST, the following operation modes are maintained by the Database Management System:

—screening of the database content (MAIN_DB and USER_DB) according to the characteristic list containing the name of the mineral, the number of the Information card, the specification, and the crystallochemical formula;

—simultaneous screening of the characteristic list and the related information cards;

—display of the chosen information cards (up to ten cards simultaneously) on a monitor screen;

—the search for a card in accordance by the specially selected signs—mineral name, specification, crystallochemical formula, space group, crystal system, references (authors, journal, year of publication), and the serial number of the information card;

—the calculation of the file containing the crystallostructural characteristics of the mineral and the input files for the Applied Program Package, which are automatically exported to the corresponding subdirectories on a hard disc;

—the calculation of the RENTPOL file, which includes all the basic BDP records in the ASCII form and is automatically exported for its subsequent use by the Applied Program Package for the automated qualitative X-ray phase analysis [2, 3];

—import of the records to MAIN_DB and USER_DB;

—export of the information card on the mineral as the BDM and BDP files (ASCII format) to the corresponding subdirectories on a hard disc;

—editing MIAN_DB by the programmer.

All the computations are performed by the Program Package incorporated into the Database Management System of the L version.

Using the program package incorporated into the L version and employing the calculated and exported input files, the user can:

—calculate and display the crystal-structure model of the mineral, manipulate the image in the interactive mode, select *hkl*-oriented fragments, and calculate interpositional (interatomic) distances, bond lengths, and bond angles;

—calculate and display the complete profile of the X-ray diffraction pattern of an individual polycrystal phase of the mineral or a mixture of polycrystal phases at the given concentrations.

Other possibilities provided by the program package incorporated into the L version have been considered earlier [5, 6].

CONCLUSIONS

The Russian Crystallographic Database for Minerals, which represents a universal and complex system including the Crystal Structure Database, the Polycrystal Standard Database of Minerals, and the Program Package, was developed and is available both in the WWW and the local versions (the latter can be installed on a PC).

The use of modern network technologies in the development of the WWW version of MINCRYST allowed the design of the versatile and fast WWW interface and provided the interactive mode of manipulating the graphical images.

Recently, the WWW MINCRYST has been cross-linked with the International Network of Mineralogical Databases (e.g., with the Mineralogy Database, USA, http://web.wt.net/~daba/Mineral/) and supplements the latter with a new crystallographic information.

As a result, WWW MINCRYST, which has accumulated the information on the composition, structure, and X-ray diffraction characteristic of various minerals, can use this information for analytical purposes with the aid of the available on-line program package, and is cross-linked with the international network of mineralogical WWW databases, is the unique crystallographic database which provides the most complete information of the fundamental mineralogical triad—composition–structure–property.

MINCRYST has been registered in the Russian State Database Register (the Scientific Technical Center *Informregister*) (WWW version, no. 0229805169, Registration Certificate no. 4873, February 11, 1999; L version, no. 0229805170, Registration Certificate no. 4874, February 11, 1999).

All the questions about the further information on MINCRYST and the purchase of the L-version should be addressed to the author to the Institute of Experimental Mineralogy, Russian Academy of Sciences, Chernogolovka, Moscow oblast, 142432 Russia; e-mail: avch@iem.ac.ru A.V. Chichagov.[3]

ACKNOWLEDGMENTS

From 1996 to 1998, this study was supported by the Russian Foundation for Basic Research, project nos. 96-07-89162 and 96-07-89323.

REFERENCES

1. A. V. Chichagov, A. B. Belonozhko, A. L. Lopatin, *et al.*, Kristallografiya **35**, 610 (1990) [Sov. Phys. Crystallogr. **35**, 356 (1990)].
2. A. V. Chichagov, Mater. Sci. Forum **79–82**, 257 (1991).
3. A. V. Chichagov, Z. V. Shilova, and A. L. Lopatin, Kristallografiya **37**, 942 (1992) [Sov. Phys. Crystallogr. **37**, 500 (1992)].
4. A. V. Chichagov, A. L. Lopatin, Ju. I. Molchanov, *et al.*, Exp. Geosci. **2**, 9 (1993).
5. A. V. Chichagov, Mater. Sci. Forum **166–169**, 193 (1994).
6. A. V. Chichagov, in *Proceedings of the Second International Workshop on Advances in Databases and Information System, ADBIS'95, Moscow, 1995*, Vol. 2, p. 6.
7. A. V. Chichagov, D. A. Varlamov, R. A. Dilanyan, *et al.*, Exp. Geosci. **7**, 61 (1998).
8. D. A. Varlamov, in *Scientific Service in Internet* (Mosk. Gos. Univ., Moscow, 1999), p. 311.
9. A. V. Chichagov and D. A. Varlamov, in *Proceedings of the 2nd Ural Crystallographic Conference "Theoretical, Mineralogical and Technical Crystallography, Crystallography-98, Syktyvkar, 1998*, p. 36.
10. A. V. Chichagov, D. A. Varlamov, and R. A. Dilanyan, in *Proceedings of the XIV International Conference on X-ray Radiography of Minerals, St. Petersburg, 1999*, p. 301.
11. A. V. Chichagov, D. A. Varlamov, and R. A. Dilanyan, in *Proceedings of the 2nd National Conference on Application of X-ray, Synchrotron Radiation, Neutrons, and Electrons, RSNÉ-99, Moscow, 1999*, p. 439.

Translated by T. Safonova

[3] All the programs used for designing MINCRYST are unlicensed and can be freely distributed.

Crystallography Reports, Vol. 46, No. 5, 2001, pp. 880–882. Translated from Kristallografiya, Vol. 46, No. 5, 2001, pp. 955–957.

CRYSTALLOGRAPHIC SOFTWARE

Dedicated to the memory of B. K. Vainshtein

Data Collection in Single-Crystal Diffractometry Equipped with a Zero-Dimensional Detector: Planning and Optimization

Yu. V. Nekrasov

Shubnikov Institute of Crystallography, Russian Academy of Sciences,
Leninskiĭ pr. 59, Moscow, 117333 Russia
e-mail: nekrasov@ns.crys.ras.ru

Received April 16, 2001

Abstract—The algorithm of statistical optimization providing the best quality of the measurements within the planned time of data collection has been improved. The algorithm is characterized by high efficiency, simplicity, and flexible distribution of the time necessary for estimating and main measurements of the reflections.

INTRODUCTION

Generally, single-crystal diffractometry uses the standard optimization procedure of data collection [1]. In this procedure, the time necessary for the second (main) measurement of reflections is determined from the result of the first (estimating) measurement. This provides approximately equal accuracy in measuring the intensities of strong and moderate reflections. However, the constant time of the estimating measurements not correlated with the average diffraction intensity necessarily leads to losses in the diffractometer efficiency or the measurement quality. Moreover, the unpredictable number of repeated measurements hinders planning of the experiment.

The procedure of statistical optimization [2] is free from the above drawbacks. In 1978, we used this procedure in the control program for a Syntex $P2_1$ diffractometer. A large number of various protein and mineral crystals and organic molecules, have been studied with the use of this program. The procedure provided the best statistical accuracy during the collection of the X-ray data at the given survey rate. However, it was not possible to distribute the time among the estimating and main measurements; the number of parameters used was too large.

Now, we improved the algorithm of the statistical optimization and freed it from the above drawbacks. We developed a reliable procedure for averaging the intensities of multiply measured reflections.

OPTIMIZATION OF DATA COLLECTION

Collection of the X-ray data was controlled by the special optimization program. The program operates with two types of parameters—control and variable ones.

The control parameters include the survey rate R_0 (reflections/h) and the relative number of reflections measured with a higher accuracy (HAM reflections) q_0. The variable parameters include the time t_1 or the scan rate V_1 of the first measurement, the time t_2 or the scan rate V_2 of the second measurement, and the threshold accuracy of the first measurement $(I/\sigma)_1$ providing the second measurement.

The values of the control parameters are specified by a user.

The variable parameters are regularly corrected upon each measurement of the group of n_0 reflections with due regard for the measurement of the previous m groups (the typical values are $n_0 = 5$ and $m = 5$). The correction is based on the comparison of the current and set values of the control parameters (the reference reflections are excluded from the calculations).

The time of the first measurement is calculated from the survey rate and the number of HAM reflections (the latter implicitly enter the $\bar{R}$ value):

$$t_1 = (\bar{R}/R_0)\bar{t}_1. \quad (1)$$

Here, $\bar{t}_1 = \sum wt_1 / \sum w$ is the average time of the first measurement, $\bar{R} = \sum wR / \sum w$ is the average survey rate, $R = n_0/\Delta t$ is the survey rate for the mth group, Δt is the measurement time for the mth group, and w is the individual weight of the mth group.

The time of the second measurement is equal to the time of the first measurement multiplied by the coefficient γ. The maximum γ value is specified by the

user and is varied depending on the actual number of HAM reflections:

$$t_2 = \gamma t_1, \quad (2)$$

the empirical formula is

$$\gamma = (\bar{q}/q_0)^{1/2}\gamma_{\max}. \quad (3)$$

Here, $\bar{q} = \sum wn/n_0\sum w$ is the average number of HAM reflections, and n is the real number of HAM reflections in the mth group,

$$\gamma_{\min} \le \gamma \le \gamma_{\max}.$$

The number of HAM reflections is maintained at the set level by varying the threshold accuracy of the estimating measurement:

$$(I/\sigma)_1 = (\bar{q}/q_0)(\overline{I/\sigma})_1, \quad (I/\sigma)_{\min} \le (I/\sigma)_1. \quad (4)$$

Here, $(\overline{I/\sigma})_1 = \sum w(I/\sigma)_1/\sum w$ is the average threshold accuracy of the first measurement. The summation is performed over m groups.

If instead of the measurement time one corrects the scan rate, the following formulas are used:

$$V_1 = (R_0/\bar{R})\bar{V}_1, \quad (1')$$

$$V_2 = V_1/\gamma. \quad (2')$$

In the latter case, the minimum scanning rate provided by the apparatus $V_{\min}$ is taken into account. The number of scans in the main measurement is

$$Z = V_{\min}/V_2 + 0.5,$$

$$Z_{\min} \le Z \le Z_{\max}.$$

The mutual dependence of the basic parameters of data collection leads automatically to the optimum time distribution between the first and second measurements over a wide range of the average intensity variation. When the intensity is high and the number of HAM reflections corresponds to the set number, the main measurement is performed slowly, while the estimating measurement is made fast. If the average intensity is less high, the number of HAM reflections is reduced, and the time of the first measurement is increased. The time of the second measurement is also increased, but to a somewhat lesser degree (because both parameters determining its value "act" in opposite ways).

Unlike the standard optimization procedure, the time of the main measurement is always maximal (except for reference reflections). Thus, strong reflections are measured with high accuracy in accordance with their contribution to the structural information [3].

The overall operating efficiency of the diffractometer is tested simultaneously with the correction of the parameters of the data collection. If the groups of reflections measured contain no HAM reflections, one has to check the peak intensity of the first matrix reflection. If this intensity is lower than one-half of the initial value, one has to refine the orientation matrix. If the attempt to refine the orientation matrix fails, the data collection is stopped. (The control can be disabled.)

Scan rates V_1 and V_2 for the first and the second measurements of a reflection and the coefficient γ as functions of the set number of HAM reflections, q_0, and its actual number, $\bar{q}$. The survey rate R_0 equals 20 reflections per hour

q_0		0.95		0.20	
$\bar{q}/q_0$	V_2	V_1	V_2	V_1	γ
1.00	8	2.15	0.27	0.65	0.081
0.25	4	0.49	0.12	0.30	0.075

Knowing the total number of reflections (determined by the unit-cell parameters of the crystal and the set minimum spacing), the survey rate (rigidly controlled by the program), one can plan the time and, to some extent, the quality of data collection at the set values of the control parameters.

Now illustrate the optimization of X-ray data collection by the model computation performed by the following formulas:

$$t_0 = 60/R_0; \quad t_1 = t_0/(q\gamma + 1);$$

$$t_2 = \gamma t_1; \quad V_1 = \Delta\omega/t_1; \quad V_2 = V_1/t,$$

which are the equivalents to Eqs. (1) and (2). (The scan range $\Delta\omega = 0.5°$; the ratio of the time of background measurement to the time of scan is $t_B/t_P = 0.5$. This is equivalent to the scan time at $\Delta\omega = 0.75°$ without measuring the background.)

The results are listed in the table.

CALCULATION OF THE AVERAGE INTENSITY OF HAM REFLECTIONS

Generally, the multiply measured intensities of the same reflection are averaged with the corresponding weights inversely proportional to the dispersion of the intensity calculated from each individual measurement, $w = \sigma^{-2}$.

It was demonstrated [4] that in the case of scatter in the results, this procedure leads to a small systematic shift of the average.

For correct averaging, one has to use the following quantities as the weights: $w_P = t_P/t_0 = V_0/V$ and $w_B = t_B/t_0 = V_0/(t_P/t_B)V$, where t_P and t_B are the times of measuring the peak and the background, respectively; t_0 is the standard measurement time determining the intensity scale; and V and V_0 are the individual and the stan-

dard scan rates, respectively. Then, the average intensity is

$$\bar{I} = \bar{P} - \bar{B}, \quad (5)$$

where

$$\bar{P} = t_0 \sum P / \sum t_p = V_0^{-1} \sum P / \sum V^{-1}, \quad (6)$$

$$\bar{B} = t_0 \sum B / \sum t_B = V_0^{-1} \sum B / \sum (t_B/t_P) V^{-1}, \quad (7)$$

where $\bar{P}$ and $\bar{B}$ are the average numbers of quanta recorded in the peak and background measurements, respectively; V_0 is the standard scan rate (deg/min); and *P*, *B*, and *V* refer to the individual measurements.

The dispersion in the average intensity is

$$\sigma_I^2 = \sigma_P^2 + \sigma_B^2, \quad (8)$$

$$\sigma_P^2 = t_0^2 / \sum (t_p^2/P) = V_0^{-2} / \sum P^{-1} V^{-2}, \quad (9)$$

$$\sigma_B^2 = t_0^2 / \sum (t_B^2/B) = V_0^{-2} / \sum (t_B/t_P)^2 B^{-1} V^{-2}. \quad (10)$$

Summation is performed over all the multiple measurements of the reflection.

CONCLUSIONS

The proposed algorithm ensures data collection with optimal quality at the set rate and allows one to plan the experiment with respect to its duration and the number of reflections measured with higher accuracy.

If the instrument works normally, no operator intervention in the course of the experiment is necessary.

Statistical optimization based on the prediction of the nearest future from the results of the recent past will be the more effective the higher the homogeneity of the intensity. Therefore, it is advisable to make the measurements in spherical layers in reciprocal space by inverted passage of the rows and with allowance for absences.

ACKNOWLEDGMENTS

The study was supported by the Russian Foundation for Basic Research, project no. 99-04-48570.

REFERENCES

1. D. F. Grant, Acta Crystallogr., Sect. A: Cryst. Phys., Diffr., Theor. Gen. Crystallogr. **A29**, 217 (1973).
2. Yu. V. Nekrasov, Kristallografiya **32** (5), 1261 (1987) [Sov. Phys. Crystallogr. **32**, 744 (1987)].
3. B. K. Vainshtein and R. L. Kayushina, Kristallografiya **11** (4), 468 (1967) [Sov. Phys. Crystallogr. **11**, 417 (1967)].
4. Yu. K. Nekrasov, Kristallografiya **32** (3), 779 (1987) [Sov. Phys. Crystallogr. **32**, 459 (1987)].

Translated by T. Safonova

Crystallography Reports, Vol. 46, No. 5, 2001, pp. 883–884. Translated from Kristallografiya, Vol. 46, No. 5, 2001, pp. 958–959.

JUBILEES

Boris Borisovich Zvyagin (on the Occasion of His 80th Birthday)

On April 14, 2001, an outstanding scientist and a well-known expert in electron diffraction analysis and structural crystallography of minerals celebrated his 80th birthday. Professor Zvyagin is a principal scientist of the Institute of Geology of Ore Deposits, Petrography, Mineralogy and Geochemisty (IGEM) of the Russian Academy of Sciences, doctor in physics and mathematics. Zvyagin graduated with distinction from the Physics Faculty of the Moscow State University in 1944 (the Chair of Theoretical Physics) and became a post-graduate student under the supervision of the late Professor Z.G. Pinsker at the Institute of Soils of the USSR Academy of Sciences where he was engaged in electron diffraction studies of clay minerals. Zvyagin proved the importance and efficiency of electron diffraction as an independent method of the structural analysis providing original structural information not on about the clay minerals, but also on a large number of mineral substances; first, in his Candidate dissertation (the electron diffraction study of the crystal structure of montmorillonite, 1949) and then in his research at the All-Union Institute of Geology (VSEGEI) in Leningrad, where he worked in 1949–1963, beginning as a senior scientist and, later, as head of the laboratory. At that time, Zvyagin also performed the first studies on a unique electron diffraction camera–microscope at the accelerating voltage up to 400 kV designed and constructed by N.M. Popov. The results obtained in that period were summarized in his Doctoral dissertation on electron diffraction and structural crystallography of clay minerals defended at the Institute of Crystallography of the USSR Academy of Sciences in 1963.

By the initiative of F.V. Chukhrov, Zvyagin entered the IGEM and created there the electron diffraction laboratory on the basis of the high-voltage electron diffraction camera. For more than half a century, Zvyagin has been faithful to his scientific vocation—electron diffraction structure analysis and structural crystallography. Zvyagin was the first to apply oblique-texture electron diffraction patterns to the structural study of layer minerals and proved its efficiency. Using electron diffraction, Zvyagin managed to solve numerous complicated problems of structural and genetic mineralogy, polytipism, and systematics of such complicated objects as halloysites, copper- and zinc-containing clay minerals, molybdenites, graphites, oxides and iron hydroxides, micas with noncentrosymmetric layers, and inhomogeneous mica polytypes. A number of new minerals were discovered among which the surprising structures of ferripyrophillite and hydroferripyrophillite are of special crystallochemical interest.

In 1957, Zvyagin was the first to use oblique-texture electron diffraction patterns for refinement of crystal structures of finely dispersed layer silicates—kaolinite and celadonite. Later, using high-voltage electron diffraction, he studied the crystal structures of a number of minerals—muscovites 1*M* and $2M_2$; paragonites 1*M*, $2M_1$, and 3*T*; nacrite; chapmanite; and bismutoferrite. Zvyagin took an active part in the development of electron diffractometry at the IGEM. The method provided the high-precision determination of the positions and the state of hydrogen atoms in the brucite and lizardite 1*T* structures.

His lengthy experience promoted the development of a new scientific discipline—modular crystallography—which included the most important concepts of such fields of crystal chemistry as polymophism, polytypism, and the theory of the OD structures. He made

1063-7745/01/4605-0883$21.00

the fundamental generalizations of the modular systems including biopyriboles, sapphirines, ferrites, spinelloids, and also the systems of complex reyerite–gyrolite–fedorite-type silicates. Zvyagin considered in terms of modular crystallography the problems of the nomenclature for micas. Zvyagin is the author and coauthor of more than 370 scientific publications mainly on the structure and crystal chemistry of layer and clay minerals, structural electron diffraction, polytypism, and modular crystallography.

Under Zvyagin supervision, ten Candidate dissertations were successfully made and defended. Later, three of these Candidates defended Doctoral dissertations. In 1986, Zvyagin became a Professor. His fruitful activity as a researcher has not passed unnoticed, and in 1986 he was awarded the Fedorov Prize of the USSR Academy of Sciences. He also received international recognition and was given the highest award of the Clay Mineral Society of the USA in 2000.

Zvyagin is an active member of the National Committee of Russian Crystallographers, the Scientific Council on Electron Microscopy of the Presidium of the Russian Academy of Sciences, Scientific Councils of the IGEM and the Institute of Crystallography, the Commissions on Electron Diffraction and International Tables on Crystallography of the International Union of Crystallography, and the Nomenclature Commission of the International Clay Association. He was often invited as a lecturer to numerous National and International conferences and schools on electron diffractions, crystallography, and electron microscopy and was an active organizer of these meetings.

The Editorial Board of *Kristallografiya*, numerous collegues, and friends congratulate Professor Zvyagin with his 80th birthday and wish him good health and new scientific achievements.

Translated by L. Man

Crystallography Reports, Vol. 46, No. 5, 2001, p. 885. Translated from Kristallografiya, Vol. 46, No. 5, 2001, p. 960.

REVIEWS

Review of *Physics of Condensed Media*, volume 5 of the Encyclopedia of *Modern Natural Sciences*

in 10 volumes. Moscow, MAGISTR PRESS, 2000 (288 pp.)

As is well known for all those working in the fields of physics, biology, chemistry, and other closely related fields the last few decades have shown the development of natural sciences at an ever-increasing rate. It became very important that an ever-increasing audience, including students, postgraduates, and teachers of secondary and higher schools, coincide with all the new achievements of these sciences. Undoubtedly, the publication of the multivolume encyclopedia of *Modern Natural Sciences* would promote more solutions to this problem.

Volume 5 is devoted to the physics of the condensed state of matter and includes sections that consider the most urgent problems of this field. The results of modern studies to the effect, which have not yet received adequate reflection in a form accessible to the common reader, are presented in this volume in a lively and intelligible form, which is especially important today, when even conventional textbooks are lacking.

Almost all the most interesting results obtained in solid state physics within the last two–three decades are reflected in this volume. Articles written by well-known experts allow the reader to get acquainted with the modern concepts of physics of strengths and plasticity of crystals, phase transitions, the effect of shape memory, high-temperature superconductivity, quantum dimensional effects in semiconductors, magnetism of properties of nanostructures, new effects in magnetics and ferroelectrics and many other fields of physics of condensed media, and ferroelectricity, etc. The high qualifications and talents of the authors (the Soros professors) provided the optimum level of the material statement for all those who are interested in physics and who possess a secondary-school knowledge of the subject, as well as for teachers, students, post-graduates, and lecturers of physics who wish to improve their knowledge in the respective fields.

The book would no doubt be useful and interesting for a large circle of readers. This encyclopedia will soon appear on the shelves of libraries in schools, universities, and research institutes, as well as bookstores. Unfortunately, the edition of 5500 copies is too small and should be increased considerably.

Professor L.A. Shuvalov,
Chief Scientist of the Shubnikov Institute
of Crystallography
of the Russian Academy of Sciences

Translated by L. Man

1063-7745/01/4605-0885$21.00